Faculty of Mathematics and Natural Sciences | RWTH AACHEN UNIVERSITY

1,4-Aminoarylation of 1,3-Dienes via Photoexcited Palladium Catalysis and Phenol Synthesis from Fluorinated Drug Scaffolds as a Precursor Strategy for ^{18}F-Radiodeoxyfluorination

Von der Fakultät für Mathematik und Naturwissenschaften der RWTH Aachen University zur Erlangung des akademischen Grades eines Doktors der Naturwissenschaften genehmigte Dissertation

vorgelegt von

Gaurav Gaurav (Master of Science)

aus

Delhi, India

Berichter: *Prof. Dr. Tobias Ritter*

Prof. Dr. Daniele Leonori

Tag der mündlichen Prüfung: *03.08.2026*

Diese Dissertation ist auf den Internetseiten der Universitätsbibliothek online verfügbar.

Dissertation advisor: Prof. Dr. Tobias Ritter Gaurav Gaurav

SUMMARY

This thesis addresses two challenges at the interface of synthetic methodology and radiopharmaceutical chemistry: the selective multicomponent functionalization of 1,3-dienes under mild conditions, and the preparation of phenol precursors for ^{18}F-radiodeoxyfluorination from commercially available fluorinated drug scaffolds.

Chapter I describes the development of a visible-light-induced three-component 1,4-aminoarylation of 1,3-butadiene using photoexcited palladium catalysis. Classical palladium-catalysed aminoarylation requires elevated temperatures, suffers from competing β-hydride elimination, and affords mixtures of regio- and stereoisomers within the thermal Pd(0)/Pd(II) manifold. Visible-light irradiation of a Pd(0)–phosphine complex generates an excited state capable of single-electron activation of aryl bromides, producing a hybrid aryl-Pd(I) radical that adds regioselectively across the diene to afford a homoallylic radical, which undergoes oxidative ligation to a π-allylpalladium(II) intermediate subsequently intercepted by the amine. The transformation proceeds at room temperature with $Pd(PPh_3)_4$, rac-BINAP, and K_2CO_3 in acetonitrile under 450 nm irradiation, affording aryl-substituted allylic amines in up to 82% yield with excellent E-selectivity (>20:1 E/Z) across a broad range of aryl bromides, secondary amines, and substituted 1,3-dienes. Synthetic utility was demonstrated through late-stage functionalization of 11 bioactive molecules and the three-step synthesis of clofilium in 50% overall yield. Mechanistic investigations, including TEMPO radical trapping, ESI-MS detection of the π-allylpalladium(II) intermediate, and Hammett analysis, are consistent with the proposed radical Pd(0)/Pd(I)/Pd(II)/Pd(0) catalytic cycle.

Chapter II addresses the preparation of phenol precursors for ^{18}F-radiodeoxyfluorination from fluorinated pharmaceutical scaffolds. The development of ^{18}F-labeled isotopologues of fluorine-containing drugs is of high translational value for pharmacokinetic PET studies, as ^{19}F to ^{18}F substitution preserves the carbon framework and pharmacological identity of the parent compound. Classical hydroxylation methods fail on the moderately activated aryl fluorides characteristic of fluorinated pharmaceuticals, motivating a radical $S_{RN}1$ approach using benzaldoxime as a metal-free hydroxide surrogate. Application to a panel of eleven fluorinated CNS drugs and PET imaging ligands afforded the corresponding phenols in isolated yields of 29–88%, with yields correlating with the degree of electronic activation at the aryl C–F bond. For [^{18}F]FPEB, the required phenol precursor is directly accessible from the commercial drug in one step, completing a three-molecule sequence to the ^{18}F-labeled PET tracer without bespoke precursor synthesis. The method provides a direct and operationally simple route to ^{18}F-labelled isotopologues of fluorinated pharmaceutical scaffolds from commercially available starting materials, bypassing the need for bespoke precursor synthesis.

This thesis contributes photocatalytic and radical methods to the modular synthesis of allylic amines and to a general precursor strategy for ^{18}F-labeling of fluorinated pharmaceuticals by PET.

Dissertation advisor: Prof. Dr. Tobias Ritter Gaurav Gaurav

ZUSAMMENFASSUNG

Diese Dissertation befasst sich mit zwei Herausforderungen an der Schnittstelle zwischen synthetischer Methodenentwicklung und radiopharmazeutischer Chemie: der selektiven Mehrkomponentenfunktionalisierung von 1,3-Dienen unter milden Bedingungen sowie der Herstellung von Phenolvorstufen für die ^{18}F-Radiodeoxyfluorierung aus kommerziell erhältlichen fluorierten Wirkstoffgerüsten.

Kapitel I beschreibt die Entwicklung einer lichtinduzierten Dreikomponenten-1,4-Aminoarylierung von 1,3-Butadien mittels fotoinduzierter Palladiumkatalyse. Die klassische palladiumkatalysierte Aminoarylierung erfordert erhöhte Temperaturen, leidet unter konkurrierender β-Hydrid-Eliminierung und liefert Gemische von Regio- und Stereoisomeren innerhalb des thermischen Pd(0)/Pd(II)-Manifolds. Die Bestrahlung eines Pd(0)–Phosphin-Komplexes mit sichtbarem Licht erzeugt einen angeregten Zustand, der zur Einelektronen-Aktivierung von Arylbromiden befähigt ist und ein hybrides Aryl-Pd(I)-Radikal erzeugt, das regioselektiv an das Dien addiert und ein homoallylisches Radikal liefert, welches eine oxidative Ligation zu einem π-Allylpalladium(II)-Intermediat eingeht, das anschließend durch das Amin abgefangen wird. Die Reaktion verläuft bei Raumtemperatur mit $Pd(PPh_3)_4$, rac-BINAP und K_2CO_3 in Acetonitril unter 450 nm Bestrahlung und liefert arylsubstituierte Allylamine in bis zu 82% Ausbeute mit ausgezeichneter E-Selektivität (>20:1 E/Z) über eine breite Palette von Arylbromiden, sekundären Aminen und substituierten 1,3-Dienen. Der synthetische Nutzen wurde durch die Spätphasenfunktionalisierung von elf bioaktiven Molekülen und die dreistufige Synthese von Clofilium in 50% Gesamtausbeute demonstriert. Mechanistische Untersuchungen, einschließlich TEMPO-Radikalabfang, ESI-MS-Nachweis des π-Allylpalladium(II)-Intermediats und Hammett-Analyse, sind konsistent mit dem vorgeschlagenen radikalischen Pd(0)/Pd(I)/Pd(II)/Pd(0)-Katalysezyklus.

Kapitel II befasst sich mit der Herstellung von Phenolvorstufen für die ^{18}F-Radiodeoxyfluorierung aus fluorierten Wirkstoffgerüsten. Die Entwicklung ^{18}F-markierter Isotopologe fluorhaltiger Arzneistoffe ist von hohem translationalem Wert für pharmakokinetische PET-Studien, da der ^{19}F zu ^{18}F-Austausch das Kohlenstoffgerüst und die pharmakologische Identität der Ausgangsverbindung bewahrt. Klassische Hydroxylierungsmethoden versagen bei den moderat aktivierten Arylfluoriden fluorierter Pharmazeutika, was einen radikalischen $S_{RN}1$-Ansatz mit Benzaldoxim als metallfreiem Hydroxid-Surrogat motiviert. Die Anwendung auf ein Panel aus elf fluorierten ZNS-Wirkstoffen und PET-Bildgebungsliganden lieferte die entsprechenden Phenole in isolierten Ausbeuten von 29–88%, wobei die Ausbeuten mit dem Grad der elektronischen Aktivierung an der Aryl-C–F-Bindung korrelieren. Für [^{18}F]FPEB ist die benötigte Phenolvorstufe in einem einzigen Schritt aus dem kommerziellen Wirkstoff zugänglich, womit eine Drei-Molekül-

Sequenz zum ^{18}F-markierten PET-Tracer ohne maßgeschneiderte Vorstufen-Synthese realisiert wird. Die Methode bietet einen direkten und praktisch einfach umzusetzenden Zugang zu ^{18}F-markierten Isotopologen fluorierter Wirkstoffgerüste aus kommerziell erhältlichen Ausgangsmaterialien und umgeht dabei die Notwendigkeit einer zielspezifischen Vorläufersynthese.

Diese Dissertation leistet einen Beitrag durch photokatalytische und radikalische Methoden zur modularen Synthese von Allylaminen sowie zu einer allgemeinen Vorläuferstrategie für die ^{18}F-Markierung fluorierter Pharmazeutika mittels PET.

ACKNOWLEDGMENTS

First and foremost, I would like to express my deepest and most sincere gratitude to Professor Dr. Tobias Ritter, whose mentorship has been one of the most formative and cherished experiences of my scientific life. His unwavering guidance, profound expertise, and remarkable patience have been instrumental in shaping not only this research, but the way I think about and approach science as a whole. His genuine belief in my potential, his encouragement to always pursue excellence, and his ability to inspire curiosity and rigor in equal measure have left an indelible mark on me as a researcher and as a person. I feel deeply privileged and grateful to have had the opportunity to pursue my doctoral studies within the Ritter Group at the Max-Planck-Institut für Kohlenforschung, and I will carry the lessons learned under his supervision with me throughout my career. I would also like to extend my heartfelt gratitude to Professor Dr. Daniele Leonori for so generously agreeing to be part of this journey as an examiner. His invaluable contributions have meant a great deal to me, and I am truly thankful for his time and thoughtfulness in supporting the completion of this dissertation.

I wish to extend my most heartfelt gratitude to Dr. Yuan Cai, whose kindness, patience, and generosity have left a lasting impression on me both as a scientist and as a person. His thorough instruction on a wide range of laboratory instruments, his readiness to offer guidance at every turn, and his genuine care for those around him made the laboratory a truly wonderful place to grow and learn. I am deeply fortunate to have had the privilege of working alongside him.

I am also deeply thankful to my colleagues and friends at the Max-Planck-Institut für Kohlenforschung, namely Neha, Dilgam, Tim, Yuanhao, Felix, Roland, Pia, and Luca, for their stimulating scientific discussions and collegial camaraderie. I would additionally like to acknowledge Sylwia for her kind and efficient assistance with various administrative matters. My sincere gratitude extends to the entire Ritter Group for fostering such a professional, collaborative, and intellectually enriching environment during my tenure in Mülheim an der Ruhr.

On a personal note, I owe an immeasurable debt of gratitude to my family, including my parents, sister, and extended family, for their unconditional love, enduring encouragement, and unwavering emotional support throughout every stage of this doctoral journey. Their belief in me has been a constant source of strength during the most demanding periods of this endeavor. I also wish to express my deepest gratitude to Anushka Dayal, whose love, patience, and unwavering support, especially through my most difficult periods of health, have meant more to me than words can adequately express. There are no words sufficient to capture how much your presence means to me.

I also wish to sincerely thank Vivek, a cherished friend since my time at Hansraj College, for his enduring friendship and for always being a dependable source of help and support whenever it was needed most. I would further like to extend my warm gratitude to my dear friends from RPVV,

whose friendship, forged during my formative school years, has remained a steadfast and joyful presence throughout my life. Their camaraderie and encouragement have continued to mean a great deal to me, even across the distances that time and circumstance have brought.

Finally, I would like to express my appreciation to the Max-Planck-Institut für Kohlenforschung for providing an exceptional research environment and world-class resources. I am grateful to all those who have contributed, directly or indirectly, to this remarkable and transformative chapter of my life.

"To my family and Anushka Dayal, whose unwavering support and boundless love have been the foundation of everything.

TABLE OF CONTENTS

SUMMARY II
ZUSAMMENFASSUNG IV
ACKNOWLEDGMENTS VI
TABLE OF CONTENTS IX
NOTE XI
LIST OF ABBREVIATIONS XII
CHAPTER I — 1,4-AMINOARYLATION OF BUTADIENES VIA PHOTOINDUCED PALLADIUM CATALYSIS 1
I.1 Introduction 1
I.1.1 Historical Foundations and Conceptual Development of Photochemistry 1
I.1.2 Constraints of High-Energy UV Excitation in Organic Synthesis 4
I.1.3 Classical Molecular Photochemistry and Excited-State Reactivity in Transition-Metal Complexes 5
I.1.4. Activation Manifolds in Visible-Light-Induced Catalysis 9
I.1.4.1 Single Electron Transfer (SET) 11
I.1.4.2 Energy Transfer (EnT) mediated Process 14
I.1.4.3 Proton–Coupled Electron Transfer (PCET) and Atom-Transfer Pathways 17
I.1.5. Dual Photocatalysis and Metallaphotoredox Catalysis 20
I.1.6 Visible-Light-Induced Transition-Metal Catalysis 24
I.1.7 Microsecond Triplets to Visible-Light-Induced Palladium Catalysis 30
I.1.8 Photoexcited Palladium as a Single-Electron Platform 33
I.1.9 Expansion and Mechanistic Diversification of Visible-Light-Induced Palladium Catalysis 35
I.2 RESULTS AND DISCUSSION 38
I.2.1 Research Summary 38
I.2.2 Reaction Background 38
I.2.3 Reaction Development and Optimization 43
I.2.4 Substrate Scope 49
I.2.4.1 Scope of Aryl Halides 50
I.2.4.2 Scope of Amines and Late-Stage Functionalization 51
I.2.4.3 Scope of 1,3-Dienes 51
I.2.4.4 Synthetic Application: Synthesis of Clofilium 52
I.2.4.5 Limitations of the Substrate Scope 53
I.2.5 Mechanistic Investigations 54
I.2.5.1 Control Experiments 54
I.2.5.2 UV–Vis Absorption Study 55
I.2.5.3 Radical Trapping Experiments with TEMPO 55
I.2.5.4 Detection of the π-Allylpalladium(II) Intermediate 56
I.2.5.5 Correlation of Reactivity with Reduction Potential and Mesolytic Cleavage Rate 57
I.2.5.6 Hammett Analysis 60
I.2.5.7 Aryl Iodide Reactivity and Mechanistic Implications 61
I.2.5.8 Amine Nucleophilicity and the π-Allylpalladium Interception Step 62
I.2.5.9 Proposed Catalytic Cycle 63
I.2.6 Conclusion 64
CHAPTER II — PHENOL SYNTHESIS FROM FLUORINATED DRUG SCAFFOLDS AS A PRECURSOR STRATEGY FOR ^{18}F-RADIODEOXYFLUORINATION 65
II.1 Introduction 65
II.1.1 Positron Emission Tomography: Physical Basis, Historical Development, and Clinical Significance 65
II.1.2 Radionuclides and FDA-Approved ^{18}F Tracers 66

II.1.3 Fundamental Constraints of ^{18}F Labeling....68
II.1.4 Nucleophilic Aromatic Substitution for ^{18}F-Labeling....69
II.1.5 Advanced Radiofluorination Strategies....71
II.1.5.1 Transition-Metal-Mediated Radiofluorination....71
II.1.5.2 Diaryliodonium Salts and Hypervalent Iodine Precursors....74
II.1.5.3 Radiofluorination of Aryl Sulfonium Salts....76
II.1.6 The Persistent Precursor Problem: A Critical Evaluation....78
II.1.7 Deoxyfluorination of Phenols: PhenoFluor and the Concerted S_NAr Mechanism....79
II.1.8 Ruthenium-Mediated Radiodeoxyfluorination of Electron-Rich Phenols....81
II.1.9 Phenol-to-Fluoride Disconnection as a Strategic Principle....83
II.1.10 Phenol Synthesis as the Bottleneck: Classical Methods and Radical Hydroxylation Strategy....84

II.2 RESULTS AND DISCUSSION....87

II.2.1 Reaction Design and Mechanistic Rationale....87
II.2.2 Substrate Scope and Translational Rationale....88
II.2.3 Limitations, Outlook, and Downstream Radiofluorination Potential....92
II.2.4 Conclusion....93

CHAPTER III — EXPERIMENTAL DATA....95

III.1 Materials and Methods....95
III.2 *1,4-Aminoarylation of Butadienes*....96
III.2.1 General Procedure for 1,4-aminoarylation of butadienes....96
III.2.2 Detection of allyl Pd(II) species by ESI-MS....109
III.2.3 Radical trapping experiment with TEMPO....110
III.3 Synthesis of Fluorinated Substrates....110
III.3.1 Synthesis of 4-(4-fluorophenyl)-3-nitropyridine S55....110
III.3.2 Synthesis of 3-Fluoro-5-[(pyridin-3-yl)ethynyl]benzonitrile (FPEB) S58....111
III.3.3 Synthesis of Iloperidone S59....112
III.3.4 Synthesis of Blonanserin S60....112
III.3.5 Synthesis of Melperone, S61....115
III.3.6 Synthesis of p-MPPF, S64....115
III.4 General Procedure for Radical Hydroxylation....118

IV. SPECTROSCOPIC DATA....126

V. REFERENCES....220

VI. APPENDIX....228

VII. LIST OF PUBLICATIONS....228

VIII. CURRICULUM VITAE....230

NOTE

Portions of this thesis have been taken, with permission, from the following publication:

- Cai, Y.; Gaurav, G.; Ritter, T. 1,4-Aminoarylation of Butadienes via Photoinduced Palladium Catalysis, *Angew. Chem. Int. Ed.* **2024**, *63*, e202311250.
- *Chapter II results have not been published anywhere yet (Manuscript in Preparation)*

Additional work performed during my doctoral study that does not appear in this thesis has been published in:

- Cai, Y.; Dawor, M.; Gaurav, G.; Ritter, T. Kharasch-Type Haloalkylation of Alkenes by Photoinduced Copper Catalysis. *J. Am. Chem. Soc.* **2025**, *147*, 18438–18444

LIST OF ABBREVIATIONS

The following abbreviations were used in the writing of the thesis.

[^{18}F]FDG	2-[^{18}F]fluoro-2-deoxy-D-glucose
[^{18}F]FPEB	[^{18}F]3-fluoro-5-[(pyridin-3-yl)ethynyl]benzonitrile
[^{18}F]p-MPPF	[^{18}F]N-{2-[4-(2-methoxyphenyl)piperazin-1-yl]ethyl}-N-(pyridin-2-yl)-4-fluorobenzamide
^{18}F	fluorine-18
^{1}H NMR	proton nuclear magnetic resonance spectroscopy
^{13}C NMR	carbon-13 nuclear magnetic resonance spectroscopy
^{19}F NMR	fluorine-19 nuclear magnetic resonance spectroscopy
^{3}MLCT	triplet metal-to-ligand charge transfer
Ar	aryl
ArBr	aryl bromide
ArX	aryl halide
BDFE	bond dissociation free energy
BET	back electron transfer
BINAP	2,2′-bis(diphenylphosphino)-1,1′-binaphthyl
calc'd	calculated
cb-DBT	4-(2-cyanobenzyl)dibenzothiophene
cGMP	current good manufacturing practice
CNS	central nervous system
COD	1,5-cyclooctadiene
Cp	cyclopentadienyl
CS_NAr	concerted nucleophilic aromatic substitution
CT	computed tomography
D_2	dopamine D_2 receptor
D_3	dopamine D_3 receptor
dba	dibenzylideneacetone
DBTO	dibenzothiophene sulfoxide
DFT	density functional theory
DPEphos	bis[2-(diphenylphosphino)phenyl]ether
dppf	1,1′-bis(diphenylphosphino)ferrocene
d.r.	diastereomeric ratio
E/Z	geometric isomer descriptor (entgegen/zusammen)
E_{00}	zero-zero excitation energy
ee	enantiomeric excess
EI	electron ionisation
EnT	energy transfer
equiv.	equivalents
ESI	electrospray ionisation
FDA	Food and Drug Administration
FDG	fluorodeoxyglucose
FPEB	3-fluoro-5-[(pyridin-3-yl)ethynyl]benzonitrile
GMP	good manufacturing practice

HAT	hydrogen atom transfer
HOMO	highest occupied molecular orbital
HPLC	high-performance liquid chromatography
HRMS	high-resolution mass spectrometry
5-HT_{1A}	serotonin 5-HT_{1A} receptor
5-HT_{2A}	serotonin 5-HT_{2A} receptor
^{ipr}ImCl	2-chloro-1,3-bis(2,6-diisopropylphenyl)imidazolium chloride
ISC	intersystem crossing
LC	ligand-centered
LED	light-emitting diode
LMCT	ligand-to-metal charge transfer
LUMO	lowest unoccupied molecular orbital
MC	metal-centered
$mGluR_5$	metabotropic glutamate receptor subtype 5
MLCT	metal-to-ligand charge transfer
mol%	mole percent
MRI	magnetic resonance imaging
m/z	mass-to-charge ratio
NHC	N-heterocyclic carbene
NHPI	N-hydroxyphthalimide
NMR	nuclear magnetic resonance
OAc	acetate
OTf	triflate (trifluoromethanesulfonate)
PC	photoredox catalyst
PCET	proton-coupled electron transfer
PET	positron emission tomography
Ph	phenyl
PhenoFluor	N,N′-1,3-bis(2,6-diisopropylphenyl)-2,2-difluoroimidazolidene
p-MPPF	N-{2-[4-(2-methoxyphenyl)piperazin-1-yl]ethyl}-N-(pyridin-2-yl)-4-fluorobenzamide
ppm	parts per million
PPh_3	triphenylphosphine
rac	racemic
R_f	retention factor
rt	room temperature
S_0	ground singlet state
S_1	first excited singlet state
SCE	saturated calomel electrode
SCIDY	spirocyclic iodonium ylide
SEAr	electrophilic aromatic substitution
SET	Single electron transfer
S_NAr	Nucleophilic aromatic substitution
$S_{RN}1$	Radical nucleophilic substitution
T_1	lowest excited triplet state
TEMPO	2,2,6,6-tetramethylpiperidin-1-yl)oxidanyl

TM	Transition metal
TLC	thin-layer chromatography
TMEDA	N,N,N′,N′-tetramethylethylenediamine
UV	ultraviolet
vis	visible (light)
XAT	halogen atom transfer

CHAPTER I — 1,4-AMINOARYLATION OF BUTADIENES VIA PHOTOINDUCED PALLADIUM CATALYSIS

I.1 Introduction

I.1.1 Historical Foundations and Conceptual Development of Photochemistry

The history of photochemistry spans over two centuries, reflecting the gradual realization that light can initiate and direct chemical reactions.[1] The foremost example of photochemistry is photosynthesis (Greek: photo: light; synthesis: putting together). Photosynthesis is the fundamental bioenergetic process carried out by photoautotrophs (plants, algae, and cyanobacteria) that converts solar electromagnetic radiation into stable chemical potential energy.[2] The earliest documented photochemical reaction was reported in 1777 by Carl Wilhelm Scheele, who observed that silver chloride (AgCl) darkens upon exposure to sunlight due to its photodecomposition into metallic silver and chlorine gas.[3]

Grotthuss (1817) showed that only absorbed light can cause a photochemical transformation, an insight drawn from the photo-bleaching of colored thiocyanate and cyanide complexes of iron(III) and cobalt(II).[4] After 24 years, unaware of Grotthuss's work, the American chemist John William Draper demonstrated that the rate of the photoreaction between moist hydrogen and chlorine gases is directly proportional to the intensity of the absorbed light, providing the first explicit quantitative confirmation of Grotthuss's earlier insight.[5] These findings led to the formulation of the first law of photochemistry, the Grotthuss–Draper law, which states that only light that is absorbed by a system can induce a photochemical change.

Over the course of the nineteenth century, such principles were extended from inorganic salts to organic substrates.[1] Irradiation was found to promote bond cleavage[6], rearrangement[7], and radical formation in a range of molecules, establishing photochemistry as a distinct mode of activation. Characteristic reaction types gradually emerged: photoreduction of carbonyl compounds,[8,9] halogenation of hydrocarbons,[10] isomerization of alkenes,[11] the reactivity of diazo and diazonium compounds[1], and cycloaddition processes such as the dimerization of anthracene[12,13] (Figure 1). These reactions demonstrated that exposure to light could induce transformations not readily accessible under thermal conditions and that light-driven chemistry followed its own kinetic and mechanistic patterns.

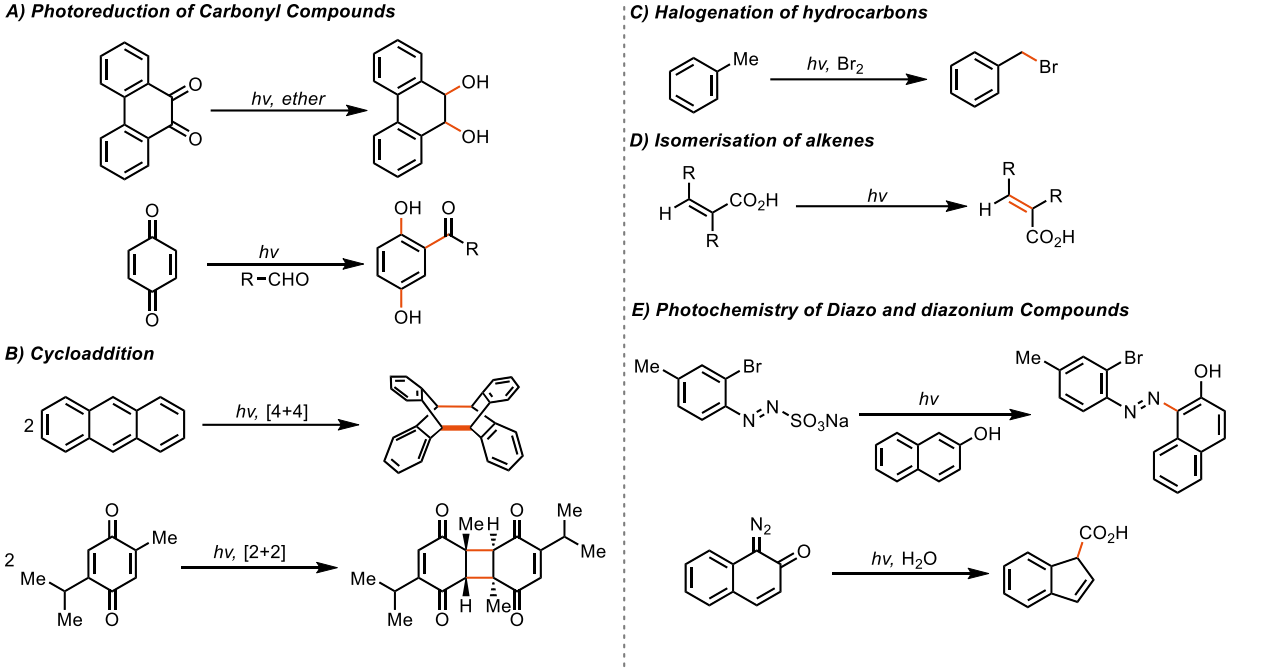


Figure 1. Representative early photochemical transformations of classical organic photochemistry

At this stage, interpretation remained largely phenomenological. Reactions were described as “light-induced decompositions” and the role of radiation was understood in terms of activation rather than electronic structure. Only toward the end of the nineteenth and beginning of the twentieth century did the picture become more precise. Quantitative studies and the development of spectroscopic methods clarified that photon absorption generates a discrete activated species and that each absorbed photon can initiate a single primary event.[4,14] With the emergence of early quantum theory, this activated species came to be understood as an electronically excited state.[15,16]

At the beginning of the twentieth century, photochemistry began to be examined with greater experimental control and conceptual clarity. The work of Giacomo Ciamician and Paul Silber signifies a crucial advancement in this development. Through systematic solar irradiation of diverse organic compounds, they demonstrated that light could induce oxidation, reduction, rearrangement, and C–C bond formation under relatively mild conditions.[1,17] Aromatic ketones underwent bimolecular photoreduction to afford phenols; alcohols and alkenes were oxidized under atmospheric oxygen;[18,19] ketones and aldehyde displayed α-fragmentation reactivity later known as Norrish type reactions;[20,21] and unsaturated systems engaged in dimerization and addition processes.[8,22] Notably, these transformations were carried out under prolonged solar irradiation, featuring the deliberate use of sunlight as the driving energy source. Collectively, these studies demonstrated that light-driven reactions could proceed along pathways distinct from those observed under thermal conditions and that irradiation could generate reactive intermediates not readily accessible by conventional means.

Ciamician, in his 1912 visionary lecture, reflected on the progress of organic photochemistry and proposed that solar radiation could, in principle, serve as a practical driving force for chemical synthesis.[23] Drawing inspiration from natural photosynthesis, he suggested that systematic use of sunlight might enable chemical transformations under comparatively mild conditions, potentially reducing reliance on high temperatures and harsh reagents.[23] Photochemistry had thus evolved from descriptive observation to deliberate experimental exploitation, creating the need for a theoretical framework capable of rationalizing how light interacts with molecules at the electronic level.[24,25]

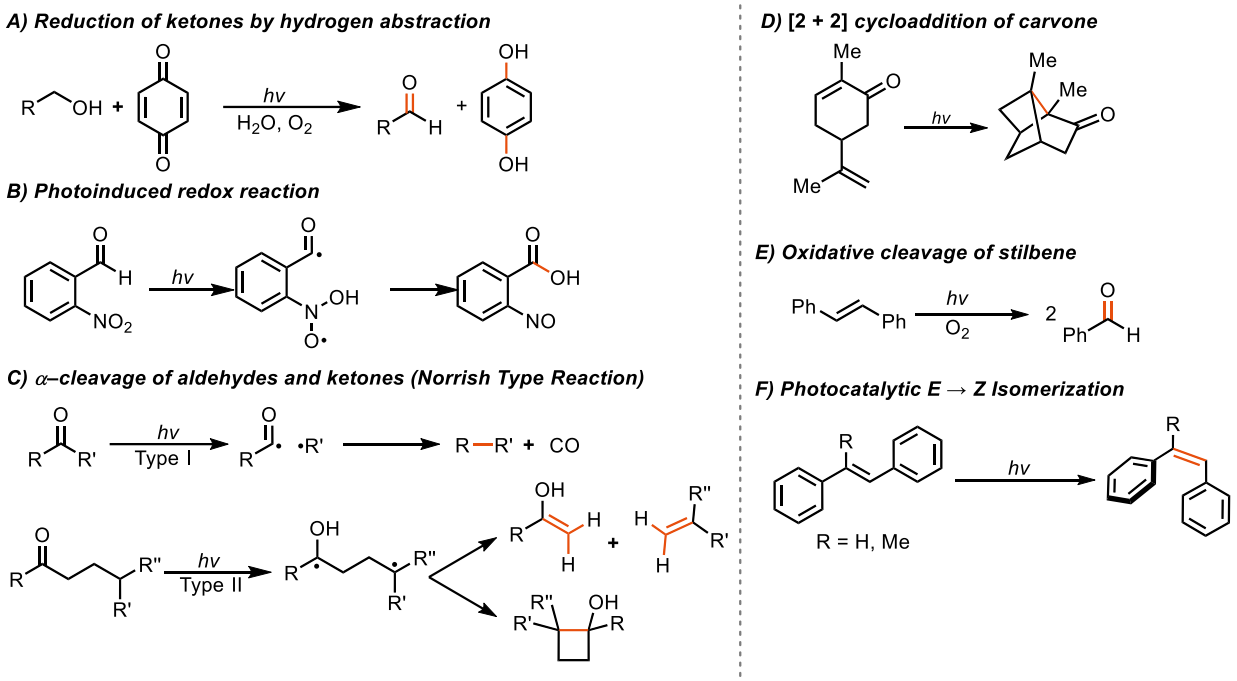


Figure 2. Representative classes of photochemical transformations from 1900s. (A) Hydrogen abstraction–initiated ketone reduction. (B) Photoinduced redox reaction of nitroarenes. (C) Norrish type I and type II α-cleavage processes of carbonyl compounds. (D) Intramolecular [2+2] cycloaddition of carvone. (E) Oxidative cleavage of stilbene under irradiation. (F) Photochemical E→Z isomerisation of alkenes.

Over time, photochemistry has developed from empirical observations into a mechanistically understood approach for controlling chemical reactivity. Electronic excitation induced by light opens reaction pathways that are inaccessible in the ground state under thermal conditions.[26] This transformation is based on the recognition that photon absorption alters the electronic structure, generating transient species with distinct geometries, spin states, and redox properties.[25,26] Advances in photophysical understanding, catalyst design, and light sources have expanded the practical scope of photochemistry. In particular, selective excitation under visible irradiation reduces the unselective decomposition commonly associated with high-energy UV light, thereby broadening the applicability of light-driven methods in synthesis.[27,28] The progression from early solar experiments to modern photocatalytic systems highlights the need for a thorough mechanistic understanding of excited-state structures and reactivity.

I.1.2 Constraints of High-Energy UV Excitation in Organic Synthesis

Classical organic photochemistry has traditionally relied on ultraviolet (UV) irradiation to excite substrates to reactive electronically excited states directly.[29] This dependence reflects the intrinsic photophysical characteristics of most small organic molecules, which absorb only weakly in the visible region and therefore require higher-energy, short-wavelength light to reach productive excited-state manifolds (Figure 3).[29] Consequently, UV-driven activation enabled many foundational photochemical transformations and shaped the development of synthetic photochemistry for more than a century.[30]

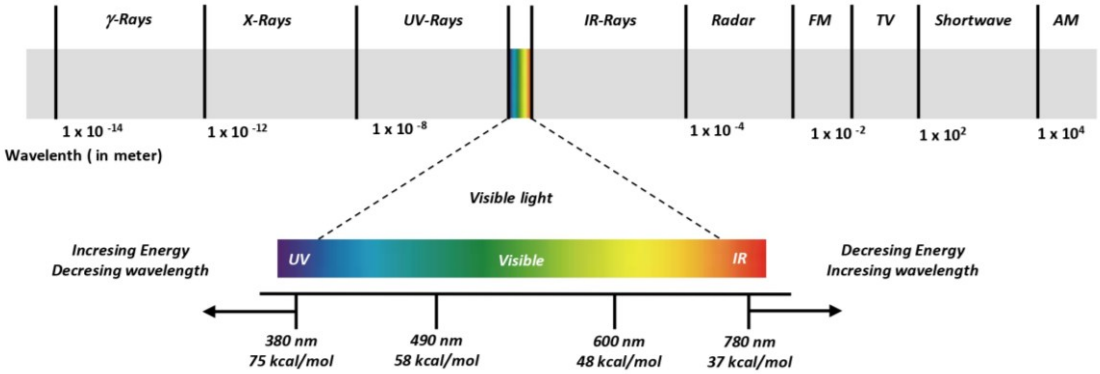


Figure 3. Electromagnetic spectrum and corresponding photon energies

The repertoire of directly excited substrates in UV-driven photochemistry was primarily dictated by the presence of suitable chromophores, with carbonyl compounds, conjugated alkenes, and arenes constituting the principal substrate classes.[31] Halogenated substrates and unsaturated nitrogen-containing molecules have also been found to be photochemically active, and irradiation of molecular oxygen can generate reactive excited states that enable synthetically useful oxidative transformations.[32] Nonetheless, the practical application of UV photochemistry remained constrained, particularly in the synthesis of complex molecules and late-stage functionalization.[31] Direct excitation of ketones requires irradiation in the range of 260–300 nm, corresponding to photon energies of 95–110 kcal·mol^{-1}, while conjugated alkenes require excitation in the range of 270–340 nm.[33,34] Such short-wavelength excitation frequently populates highly reactive excited states that undergo unproductive relaxation or unselective reactivity, manifesting as competing side reactions and photodecomposition of substrate or product.[27] UV-driven photochemistry has therefore historically been associated with limited generality and reduced predictability relative to thermal catalysis, constraints that motivated the development of visible-light activation strategies capable of operating under milder and more selective conditions.[30]

Beyond these intrinsic selectivity constraints, UV photochemistry has faced substantial operational barriers. Conventional irradiation sources such as mercury or xenon lamps produce broad emission profiles, increasing the likelihood of non-selective excitation of substrates, intermediates, or products.[27,30] Effective implementation further requires UV-transparent reaction

vessels, appropriate shielding, and careful temperature control, factors that have collectively restricted broad adoption and contributed to reproducibility challenges.[30]

The emergence of visible-light photocatalysis addressed many of these limitations and has since become a central platform in modern organic synthesis.[35] Visible light (ca. 380–750 nm, corresponding to ca. 38–75 kcal·mol^{-1}) provides sufficient energy to access reactive intermediates while avoiding the excessive energy input associated with UV irradiation.[28] Critically, visible-light photocatalysis proceeds via catalyst-controlled activation rather than direct substrate excitation, in which selective excitation of a photoactive species triggers regulated electron- and energy-transfer processes, suppressing background reactivity and improving chemoselectivity and functional-group tolerance.[29,35,36] This mechanistic shift from substrate-centered to catalyst-centered excitation represents a conceptual turning point in the development of synthetic photochemistry.

I.1.3 Classical Molecular Photochemistry and Excited-State Reactivity in Transition-Metal Complexes

Photon absorption promotes a molecule vertically from its ground state (S_0) to an electronically excited state without significant nuclear rearrangement, as described by the Franck-Condon principle, producing a species with distinct electronic structure, geometry, and reactivity relative to the ground-state species.[25] As illustrated in the Jablonski diagram (Figure 4), this vertical excitation generates an excited singlet state (S_1), which rapidly undergoes vibrational relaxation prior to further evolution through competing pathways including fluorescence, non-radiative internal conversion, and intersystem crossing to the triplet manifold.[37] Although singlet–triplet transitions are formally spin-forbidden ($\Delta S \neq 0$), strong spin–orbit coupling in heavy transition-metal complexes enables efficient intersystem crossing, populating triplet states that exhibit lifetimes in the nanosecond to microsecond range sufficient to enable bimolecular electron or energy transfer with substrates at synthetically relevant concentrations.[25] The lifetime of the resulting excited state governs whether productive chemistry can occur, as it determines the probability of encountering a substrate molecule before non-radiative decay.[26]

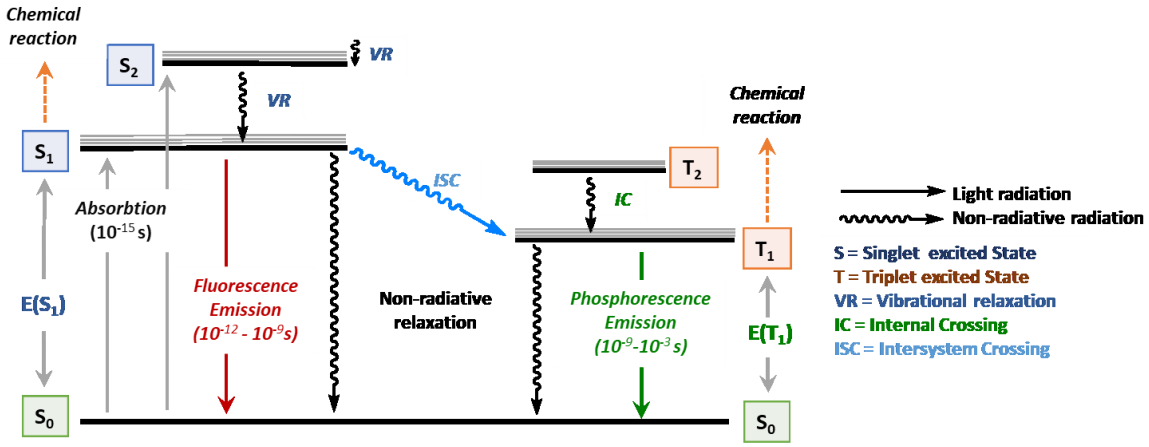


Figure 4. Simplified Jablonski diagram illustrating the principal photophysical pathways following photon absorption. S_0, ground singlet state; S_1, lowest excited singlet state; T_1, lowest triplet state.

In transition-metal complexes, electronic excitation encompasses multiple classes of transitions beyond localised π→π* processes, including metal-centered (MC or d–d), ligand-centered (LC), metal-to-ligand charge-transfer (MLCT), and ligand-to-metal charge-transfer (LMCT) transitions (Figure 5).[38] Their relative energies are governed by ligand-field splitting (Δ_0), metal oxidation state, and d-electron configuration. In octahedral transition-metal complexes, ligand coordination splits the metal d orbitals into lower-energy t_{2g} and higher-energy e_g sets. For many first-row transition metals, relatively small Δ_0 values result in low-lying MC excited states that provide efficient non-radiative relaxation pathways via metal–ligand bond distortion, leading to rapid deactivation on picosecond timescales.[38] By contrast, second- and third-row d^6-complexes such as Ru(II) and Ir(III) exhibit larger Δ_0 values, which destabilize MC states relative to MLCT states. The resulting ^{3}MLCT states are energetically isolated from upper-lying MC states and comparatively long-lived, properties that underlie their widespread application in visible-light photocatalysis.[39] Beyond these canonical systems, the same principles extend to first-row and late transition-metal complexes, where the interplay between metal oxidation state, ligand-field strength, and d-electron configuration determines the accessibility and lifetime of photoactive excited states, thereby defining the scope of metals amenable to visible-light activation.[38] Whilst MLCT excited states are characteristic of low-valent metal centers bearing π-acceptor ligands, LMCT excited states arise in complexes with high-valent metal centers and strongly donating σ or σ+π ligands, representing a photophysically distinct activation mode with markedly different reactivity profiles (Figure 6).

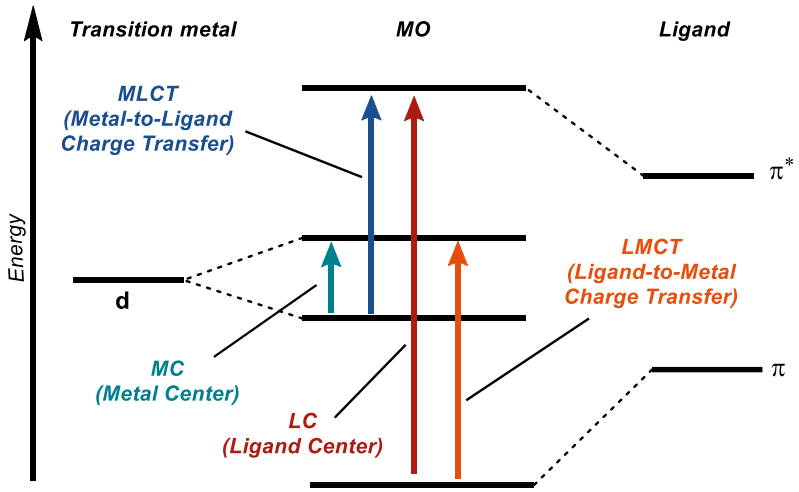


Figure 5. Simplified molecular orbital diagram illustrating the four principal classes of electronic transition in TM complexes. MC, metal-centered (d–d) transition; LC, ligand-centered transition; MLCT, metal-to-ligand charge transfer; LMCT, ligand-to-metal charge transfer. M, metal; L, ligand.

The probability of a given electronic transition is governed by selection rules that determine absorption intensity. In centrosymmetric complexes, d–d transitions are Laporte-forbidden (g→g or u→u) and therefore exhibit low molar extinction coefficients ($\varepsilon \lesssim 10^1$–$10^2$ M^{-1} cm^{-1}). Spin selection rules further restrict transitions with $\Delta S \neq 0$, although spin–orbit coupling in heavy metals can partially relax this prohibition. Vibronic coupling and geometric distortion can also partially relax the Laporte constraint, though metal-centered transitions generally remain weak.[40] In

contrast, MLCT transitions involve a change in orbital symmetry (g→u) and are therefore Laporte-allowed, leading to substantially higher extinction coefficients (ε ≈ 10^3–10^5 M^{-1} cm^{-1}). The strong absorption associated with MLCT bands enables efficient light harvesting under visible irradiation and facilitates formation of reactive excited states under synthetically relevant conditions.[40]

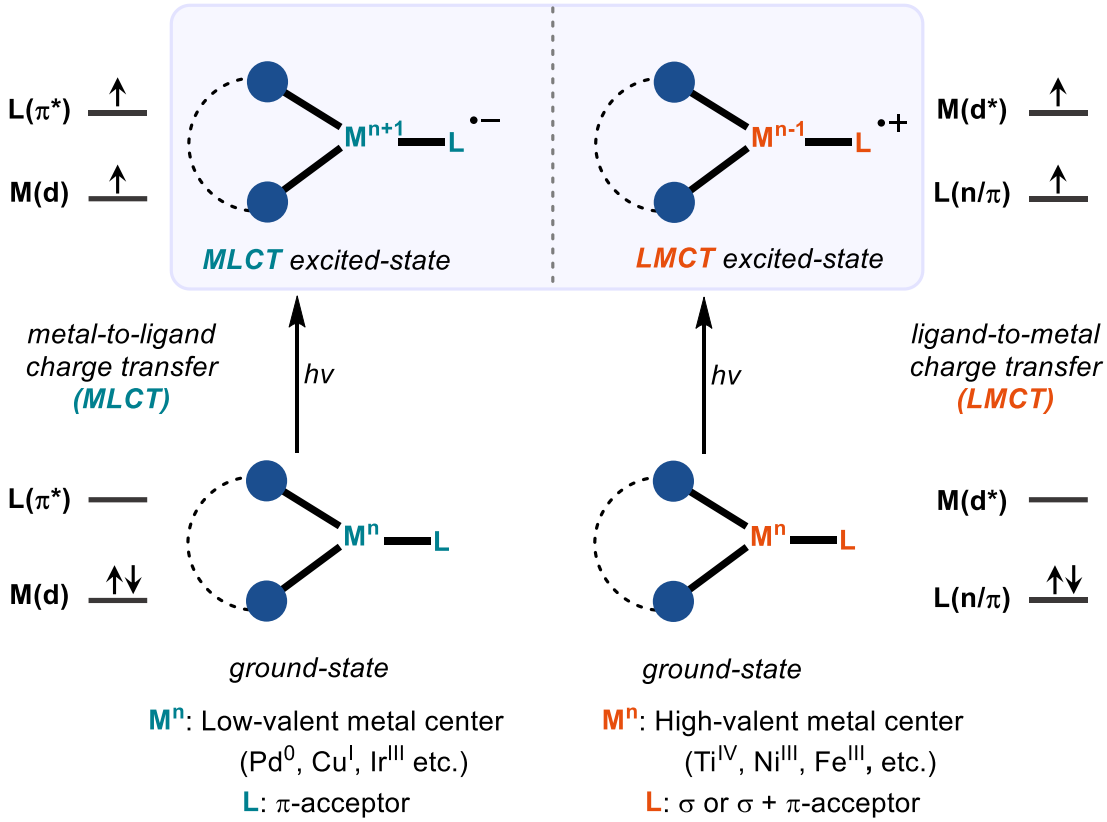


Figure 6. Comparison of metal-to-ligand charge-transfer (MLCT) and ligand-to-metal charge-transfer (LMCT) excited states in TM complexes.

Upon irradiation at 375 nm, fac-Ir(ppy)$_3$ undergoes MLCT excitation followed by rapid intersystem crossing to a long-lived ^{3}MLCT state (Figure 7). In this excited configuration, electron density is transferred from the metal-centered t_{2g} manifold to a ligand-centered π* orbital, resulting in transient oxidation at the iridium center and reduction at the ligand framework.[40] Photoexcitation does not alter the ground-state redox potentials themselves; instead, it generates an electronically excited species (PC*) whose free energy exceeds that of the ground state by E_{00}, corresponding to the vertical displacement between ground- and excited-state potential energy surfaces. As illustrated in Figure 7B (eqs. 1–2), this energy term modifies the thermodynamic potentials for electron transfer such that oxidation of PC* becomes more favourable (shifted by $-E_{00}$) and reduction of PC* becomes more favourable (shifted by $+E_{00}$) relative to the ground state. The excited-state complex therefore exhibits distinct oxidation and reduction potentials, enabling both oxidative and reductive quenching pathways. This photoinduced enhancement of redox driving force provides the thermodynamic basis for SET processes central to visible-light photocatalysis.[41]

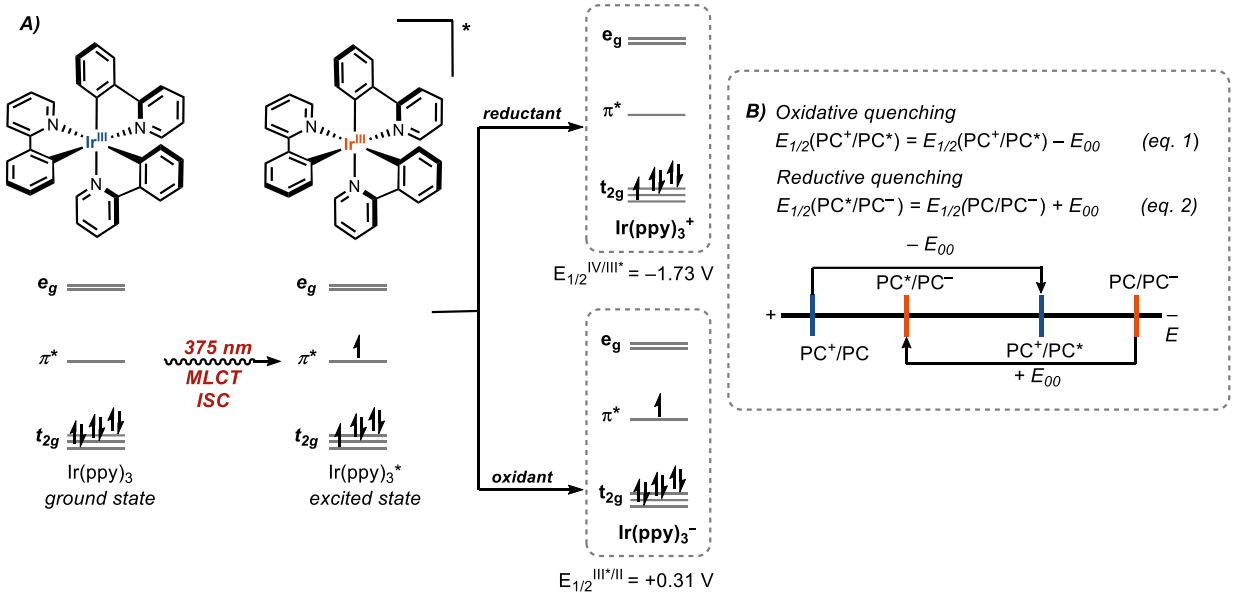


Figure 7. (A) Schematic representation of MLCT excitation and excited-state redox properties of fac-Ir(ppy)$_3$. (B) Relationship between the ground-states and excited-states redox potentials and its connection with E_{00}.

The thermodynamic driving force alone does not guarantee productive catalysis. For efficient intermolecular electron or energy transfer in solution, the excited-state lifetime (τ) must be sufficient to allow diffusion-controlled encounter between reactants, with a characteristic diffusion timescale of approximately 10^{-8} s. An excited state with τ below approximately 1 ns is generally unable to participate in efficient bimolecular quenching, while τ above approximately 10 ns is typically required for effective quenching at synthetically relevant concentrations.[36,40] Short-lived excited states are more likely to undergo non-radiative decay prior to productive interception. Consequently, the interplay between ligand-field effects, absorption intensity, excited-state redox potential, and lifetime defines the operational window for photocatalytic performance, while competing deactivation pathways, including fluorescence, phosphorescence, internal conversion, and metal-centered relaxation, continually compete with productive chemical engagement.[42] These photophysical principles collectively define the design criteria for transition-metal complexes capable of harnessing visible light to drive productive chemical transformations under mild and selective conditions.

I.1.4. Activation Manifolds in Visible-Light-Induced Catalysis

The development of visible-light photocatalysis over the past two decades has established a mechanistically diverse set of strategies for activating organic substrates under mild conditions.[29,43] These strategies share a common feature: the absorption of visible-light photons generates electronically excited states whose chemical potential drives productive bond-forming and bond-breaking events that are inaccessible on the ground-state potential energy surface.[29] Within this broad framework, three mechanistically distinct activation manifolds can be identified, distinguished by the relationship between the light-absorbing species, the substrate, and the bond-forming catalytic cycle.[43]

The essential mechanistic distinction between thermal and photochemical activation lies in how the reaction coordinate is accessed. Thermal catalysis lowers the activation barrier while remaining confined to the ground-state potential energy surface (Figure 8A).[26] Direct photoexcitation of a substrate promotes the system onto an excited-state surface, generating a new electronic configuration with reactivity distinct from the ground state (Figure 8B).[26] When an exogenous photocatalyst or sensitizer mediates excitation rather than the substrate absorbing directly, the system accesses the excited-state surface through an intermediate excited species, enabling selective activation under conditions where direct substrate excitation would be inefficient or unselective (Figure 8C, 8D).[29,40,42]

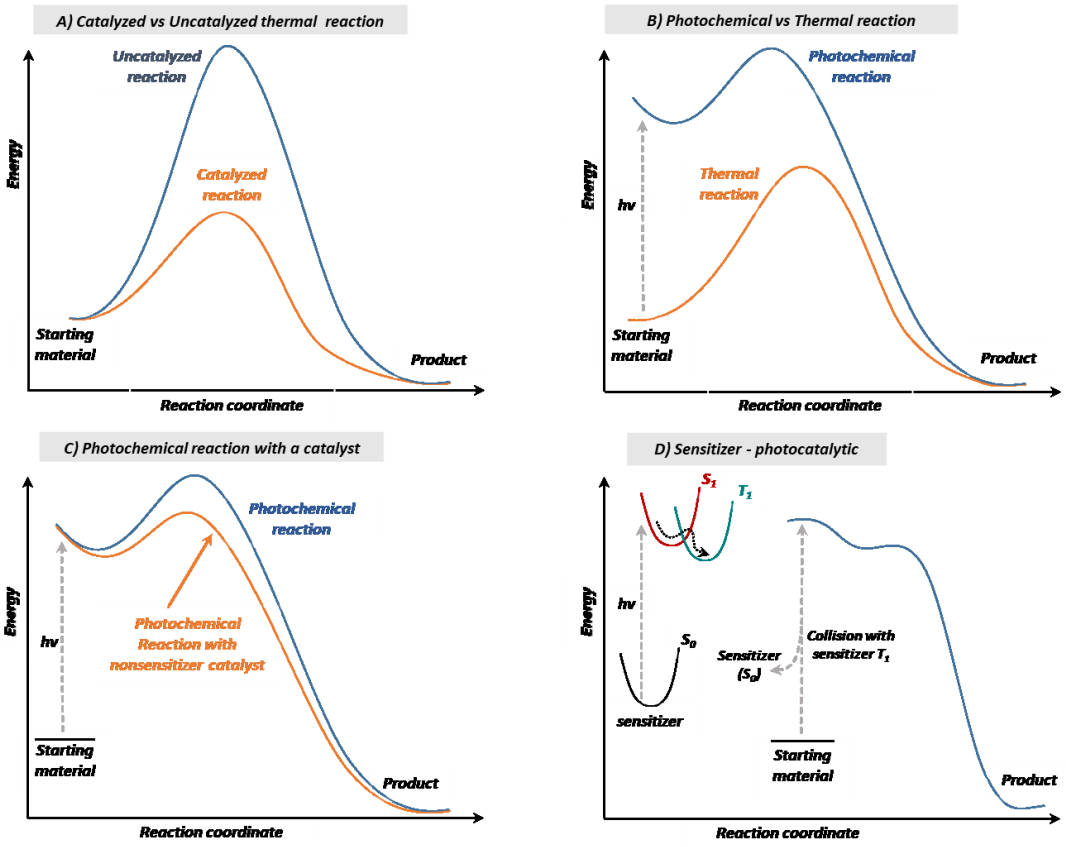


Figure 8. Reaction coordinate diagrams; A) Ground-state thermal reaction (uncatalyzed and catalyzed); B) Direct photochemical excitation to an excited-state surface; C) Photochemical reaction with a catalyst; D) Sensitizer- or photocatalyst-mediated pathway

Photoredox catalysis relies on an exogenous photocatalyst that absorbs visible light and accesses a long-lived excited state (Figure 9A).[29] This excited state engages with substrates through outer-sphere processes including single electron transfer (SET), energy transfer (EnT), hydrogen-atom transfer (HAT), or proton-coupled electron transfer (PCET) (Figure 10).[29,42] SET generates radical ion intermediates through oxidative or reductive quenching of the excited photocatalyst; EnT populates an electronically excited substrate directly; HAT produces substrate-centered radicals through hydrogen abstraction; and PCET enables bond activation through the concerted movement of a proton and an electron.[29,42,44–46] The photocatalyst is not involved in the subsequent bond-forming or bond-breaking step; its role is confined to substrate activation, after which it is returned to its ground state upon completion of the catalytic cycle.[29] The broad tunability of excited-state redox potentials through systematic ligand modification has rendered this manifold widely applicable across synthetic methodology.

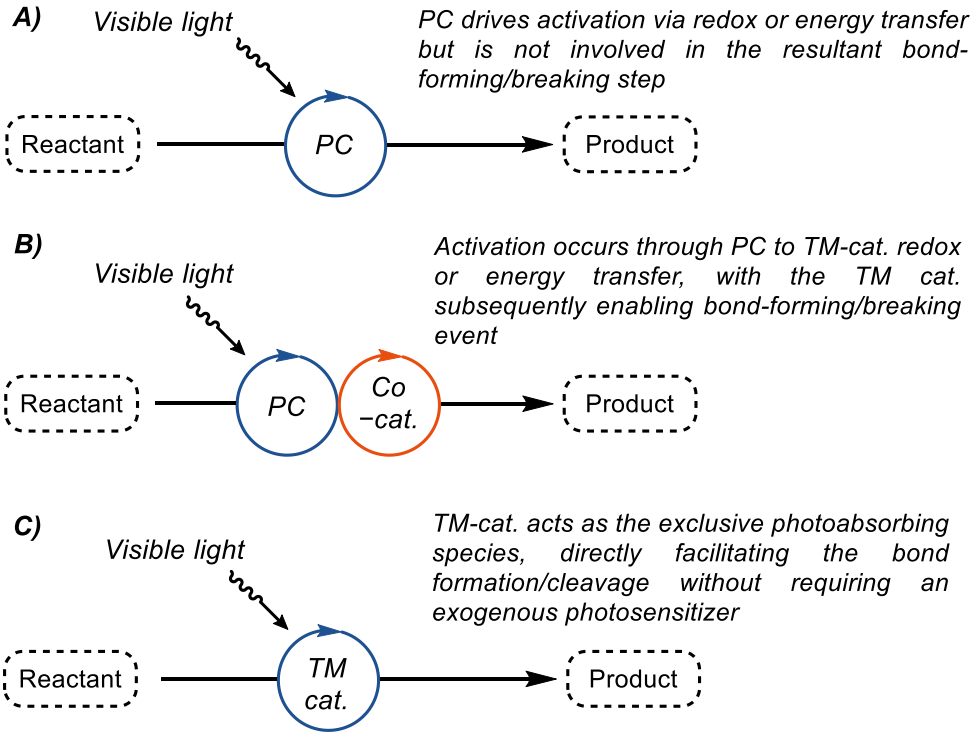


Figure 9. Visible light-induced transformations via (A) photoredox catalysis, (B) dual photocatalysis and co-catalysis, and (C) visible-light-induced transition-metal catalysis.

Metallaphotoredox catalysis integrates visible-light activation with a separate transition-metal catalytic cycle operating in parallel (Figure 9B).[41,47] Activation occurs through the photocatalyst via redox or energy transfer to the transition-metal co-catalyst, which subsequently governs substrate coordination and the elementary steps of bond formation, including oxidative addition, transmetalation, and reductive elimination.[47] Product formation depends on the coordinated operation of these two mechanistically distinct cycles, with SET events connecting them at defined points in the catalytic sequence.[47] This cooperative architecture has been demonstrated with nickel, palladium, copper, gold, and cobalt co-catalysts, and has substantially expanded the scope of cross-coupling chemistry by enabling the use of radical precursors incompatible with two-electron organometallic pathways.[47]

Visible-light-induced transition-metal catalysis is defined by the transition-metal complex acting as the exclusive photoabsorbing species, directly facilitating bond formation or cleavage without requiring an exogenous photosensitizer (Figure 9C).[43] Excitation and organometallic reactivity are integrated within a single catalytic entity, and bond formation proceeds through metal-bound intermediates generated upon photoexcitation.[43] This places specific demands on the electronic structure of the metal complex: it must absorb in the visible region, access an excited state of sufficient energy and appropriate geometry to undergo productive organometallic reactivity, and do so without rapid non-radiative deactivation to the ground state.[43,48] This manifold is mechanistically distinct from both photoredox catalysis and metallaphotoredox catalysis, and its realization in palladium complexes bearing suitable ligand environments forms the conceptual basis for the photocatalytic strategy described in this thesis.[48,49] The mechanistic diversity of these three manifolds reflects the broad range of strategies by which visible-light energy can be converted into chemical reactivity, and provides the conceptual context within which visible-light-induced palladium catalysis operates.

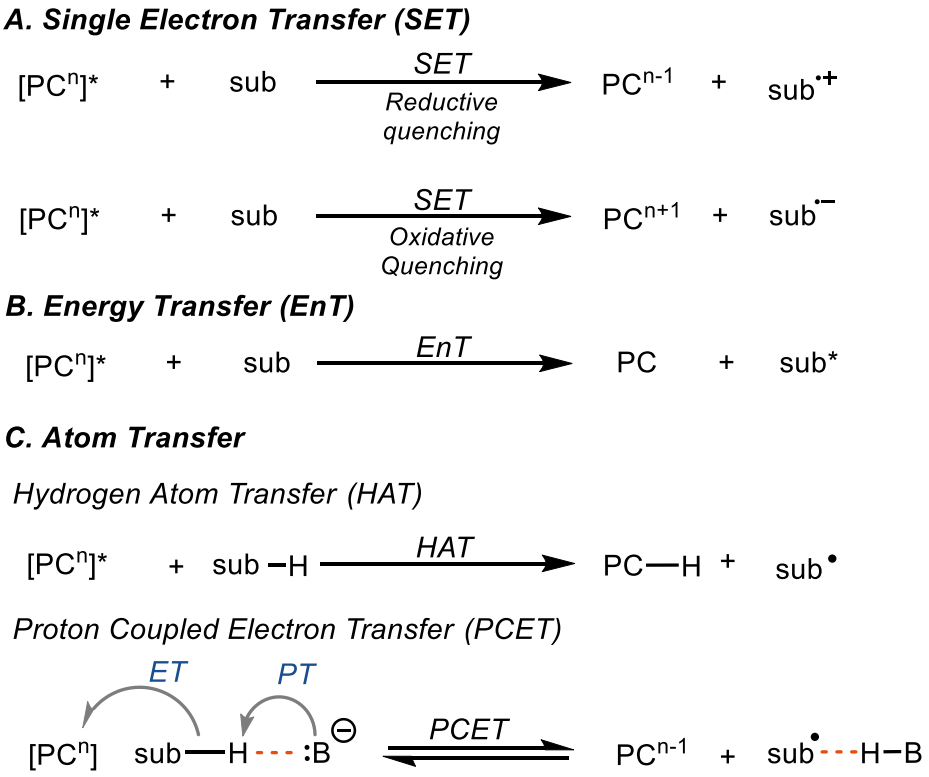


Figure 10. Principal activation modes available to photoexcited catalysts in visible-light photocatalysis. (A) Single electron transfer (SET) through reductive and oxidative quenching pathways, (B) Energy transfer (EnT) from the excited catalyst to the substrate, (C) Hydrogen atom transfer (HAT) and proton-coupled electron transfer (PCET) processes.

I.1.4.1 Single Electron Transfer (SET)

Single-electron transfer (SET) photocatalysis involves outer-sphere electron exchange between a photoexcited catalyst and an organic substrate, generating radical cationic or radical anionic intermediates.[29] Upon visible-light absorption, the photocatalyst is promoted to a long-lived excited state with substantially higher redox potentials than in its ground state, thereby enabling

single-electron oxidation or reduction under mild conditions (Figure 11).[40]

In the reductive quenching pathway, the excited photocatalyst accepts an electron from an electron donor to form the reduced photocatalyst, which subsequently transfers an electron to an electron acceptor to regenerate the ground-state catalyst. In the oxidative quenching pathway, the excited photocatalyst donates an electron to an electron acceptor, generating the oxidised photocatalyst, which is then reduced by an electron donor to close the catalytic cycle (Figure 11).[29] Depending on the reaction partners, SET pathways may therefore operate under net-oxidative, net-reductive, or redox-neutral conditions. The defining mechanistic feature of SET photocatalysis is that electron transfer constitutes the primary activation event, with subsequent reactivity controlled by the chemistry of the resulting radical species.[29]

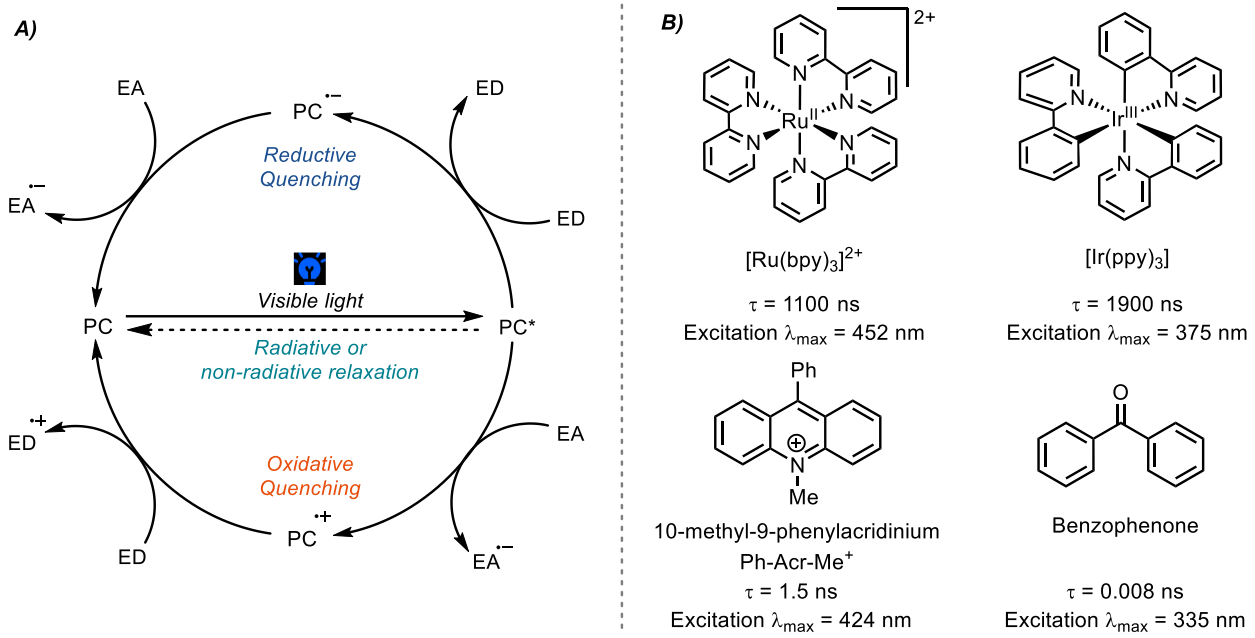


Figure 11. Photoredox catalysis under visible-light irradiation: (A) reductive and oxidative quenching cycles showing single-electron transfer pathways involving an electron donor and acceptor, and (B) structures and photophysical properties of common photoredox catalysts. PC, photoredox catalyst; ED, electron donor; EA, electron acceptor; τ, excited-state lifetime; λ_{max}, excitation wavelength maximum.

The earliest demonstrations of visible-light SET photocatalysis employed photoexcited ruthenium polypyridyl complexes. Kellogg demonstrated in 1978 that $Ru(bpy)_3^{2+}$ under visible-light irradiation can promote reductive activation of sulfonium salts in the presence of a stoichiometric dihydropyridine electron donor, providing one of the first clear illustrations that excited-state electron transfer could be harnessed catalytically under mild conditions.[50] Deronzier showed in 1984 that SET-initiated Pschorr-type cyclizations of stilbenediazonium salts catalyzed by $Ru(bpy)_3^{2+}$ could operate under overall redox-neutral conditions within a closed catalytic cycle.[51] Fukuzumi demonstrated in 1990 that reductive cleavage of phenacyl halides using $Ru(bpy)_3^{2+}$ and an acridine-based reductant could be controlled between competing reductive and oxidative quenching pathways through acid catalysis.[52] Okada showed in 1991 that single-electron reduction of N-(acyloxy)phthalimides induces mesolytic bond cleavage, generating alkyl radicals,

thereby establishing decarboxylative fragmentation as a general radical-generation strategy under mild photocatalytic conditions.[53] Collectively, these early studies defined the fundamental SET manifolds, reductive, redox-neutral, and fragmentation-driven, that underpin later developments in visible-light photoredox catalysis.[54]

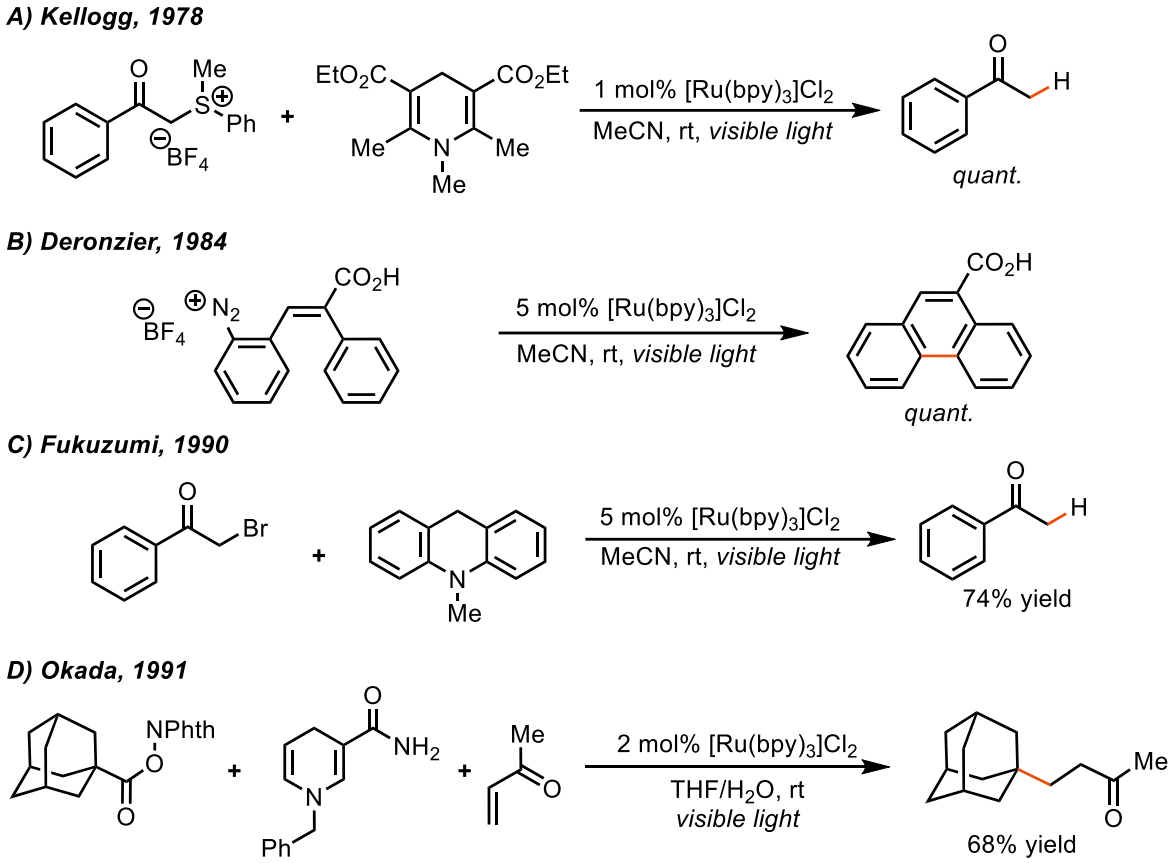


Figure 12. Selected early examples of visible-light photoredox catalysis using $[Ru(bpy)_3]Cl_2$, reported by (A) Kellogg (1978), (B) Deronzier (1984), (C) Fukuzumi (1990), (D) Okada (1991).

Despite these early demonstrations, the synthetic application of photoinduced electron-transfer processes remained limited for several decades. MacMillan and co-workers reported in 2008 that the merger of photoredox catalysis with organocatalysis could achieve asymmetric α-alkylation of aldehydes, enabling stereocontrolled C–C bond formation through the combination of $Ru(bpy)_3^{2+}$ generated radicals and organocatalytically generated enamines.[55] Yoon and co-workers demonstrated in the same year that enone [2+2] cycloadditions could proceed via SET to form enone radical anions, opening cycloaddition pathways inaccessible under thermal conditions.[56] Stephenson and co-workers established visible-light-mediated reductive dehalogenation as a general SET-based approach for generating carbon-centered radicals from alkyl and benzylic halides without use of stoichiometric tin-based reductants.[57] These reports collectively demonstrated that SET photocatalysis had matured into a practically applicable activation mode for radical-mediated bond construction in organic synthesis.[29]

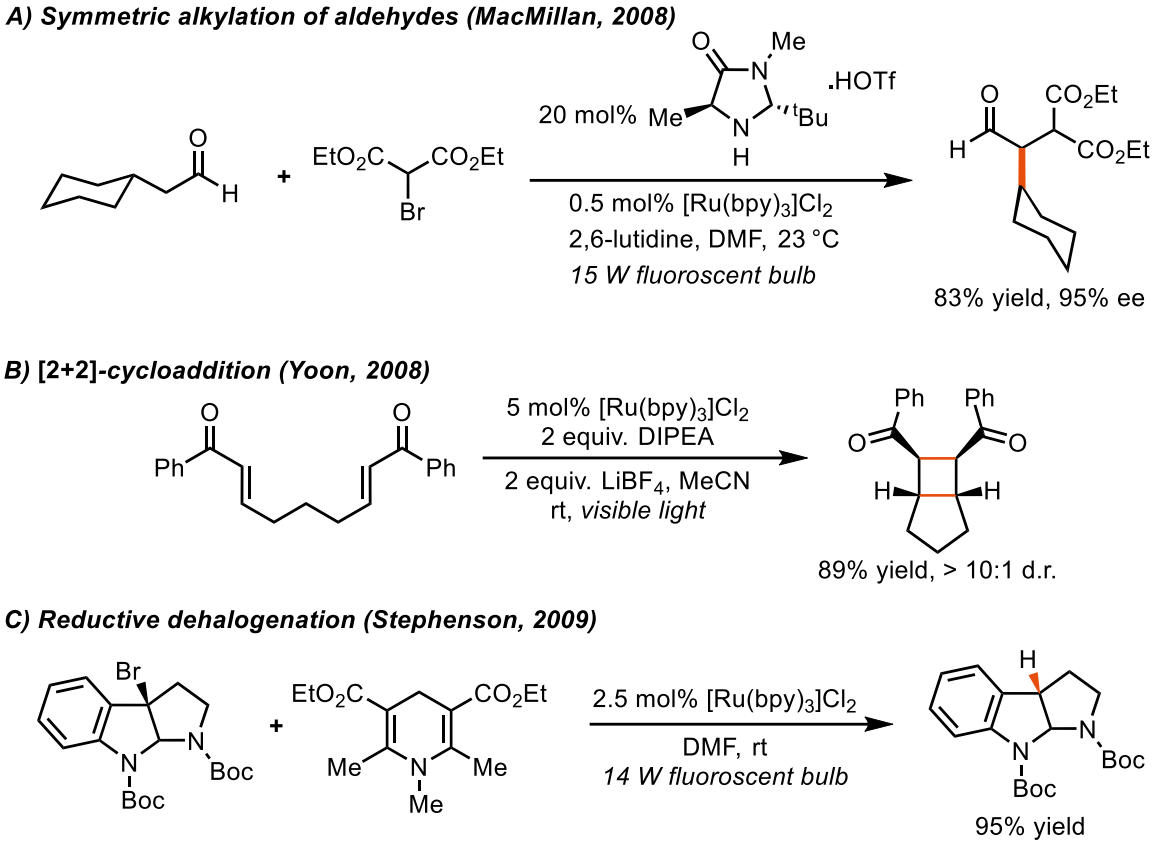


Figure 13. Early visible-light photoredox transformations. (A) Enamine-mediated α-alkylation of aldehydes (MacMillan, 2008). (B) [2+2] cycloaddition via SET (Yoon, 2008). (C) Reductive dehalogenation via a radical pathway (Stephenson, 2009).

Following these pioneering contributions, visible-light photoredox catalysis underwent rapid expansion, evolving from isolated transformations into a broadly applicable synthetic strategy.[29] This growth was driven not only by the versatility of SET-based radical generation but also by the integration of photoredox activation with complementary catalytic manifolds, including organocatalysis, Lewis acid catalysis, and transition-metal catalysis.[41] Within these cooperative frameworks, the photoredox catalyst functions as a controlled source of redox activity, while a co-catalyst governs substrate coordination and bond-forming elementary steps. The development of such dual catalytic systems provided the conceptual foundation for visible-light-induced transition-metal catalysis, a distinct activation manifold in which photoexcitation is directly coupled to metal-centered organometallic reactivity.[41,47]

I.1.4.2 Energy Transfer (EnT) mediated Process

Energy transfer (EnT) photocatalysis represents a mechanistically distinct activation mode in which the photocatalyst operates as a sensitiser rather than as a redox-active species.[42,44] Upon irradiation with visible light, the photocatalyst absorbs a photon and is promoted to an electronically excited singlet state, which rapidly undergoes intersystem crossing to generate a relatively long-lived triplet excited state (Figure 14).[25] This triplet state subsequently transfers its excitation energy to a ground-state substrate via triplet–triplet energy transfer, populating the substrate triplet excited state whilst regenerating the photocatalyst in its ground state.[44] In contrast to SET pathways, EnT photocatalysis proceeds without net electron transfer or changes in

oxidation state, and the observed reactivity arises from the biradical character and altered spin multiplicity of triplet-state substrates rather than from radical ion intermediates.[42,44]

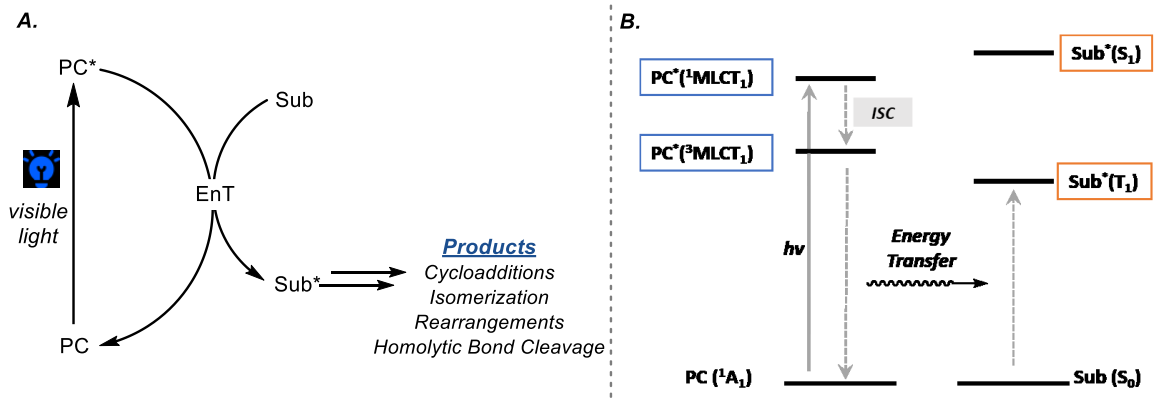


Figure 14. (A) General scheme for Energy-transfer photocatalysis; (B) Jablonski diagram with singlet and triplet states and triplet energy transfer

EnT photocatalysis is governed predominantly by a Dexter-type exchange mechanism involving short-range, orbital-overlap-dependent electron exchange between donor and acceptor, which is intrinsically spin-allowed for triplet–triplet transfer.[44,58] In contrast, Förster energy transfer operates through long-range dipole–dipole coupling and is restricted to singlet–singlet processes, rendering it mechanistically irrelevant for productive triplet sensitisation in homogeneous solution-phase catalysis (Figure 15).[44] The requirement for orbital overlap explains the distance dependence, diffusion sensitivity, and steric constraints characteristic of EnT processes.[58]

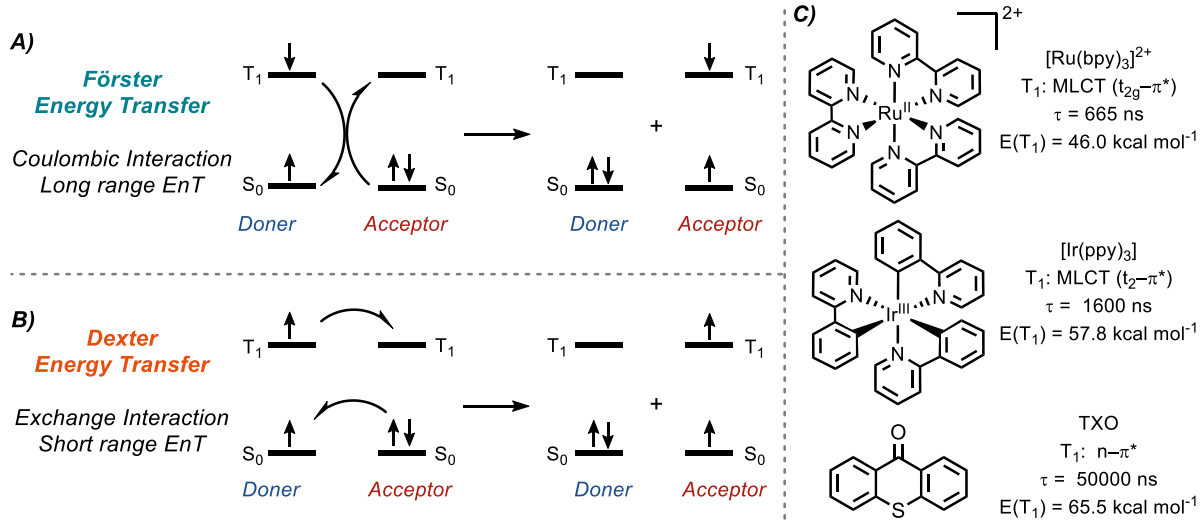


Figure 15. Mechanistic pathways for energy transfer, (A) Förster energy transfer via long-range Coulombic interactions, (B) Dexter energy transfer via short-range exchange interactions, (C) representative photocatalysts with triplet energies and excited-state lifetimes.

The efficiency of EnT reactions is governed primarily by three factors: the triplet energy of the photocatalyst must exceed that of the substrate (E_T(PC) > E_T(substrate)), the triplet-state lifetime must be sufficient for productive bimolecular encounter, and the probability of productive donor–acceptor contact must be adequate under the reaction conditions.[44,58] $Ru(bpy)_3^{2+}$ exhibits a ^{3}MLCT triplet state with $E(T_1)$ = 46.0 kcal mol^{-1} and τ = 665 ns, whereas $Ir(ppy)_3$ displays a higher triplet energy of $E(T_1)$ = 57.8 kcal mol^{-1} and a longer triplet lifetime of $\tau \approx 1.6$ μs, enabling

sensitisation of more energetically demanding substrates.[44] Organic sensitisers such as thioxanthone possess even higher triplet energies of $E(T_1)$ = 65.5 kcal mol^{-1} and extended triplet lifetimes of approximately 50 μs, substantially expanding the accessible energetic window for substrate activation.[44]

The experimental basis for visible-light EnT photocatalysis was established by Kutal and co-workers, who demonstrated that $Ru(bpy)_3^{2+}$ could sensitise the norbornadiene–quadricyclene valence isomerisation under visible-light irradiation, with the incompatibility of the substrate's redox potentials with SET processes providing compelling mechanistic evidence that the transformation proceeded through triplet energy transfer (Figure 16A).[59] Yoon and co-workers subsequently demonstrated that visible-light-mediated intramolecular [2+2] cycloadditions of styrenes proceed efficiently via triplet sensitisation using fac-$Ir(ppy)_3$ complex, a transformation inaccessible through electron-transfer photoredox chemistry owing to the high oxidation potential of the styrene substrates (Figure 16B).[60]

Weaver and co-workers showed that E/Z isomerisation of styrenyl alkenes can be achieved through selective triplet sensitisation, demonstrating contra-thermodynamic geometric control through excited-state energy transfer (Figure 16C).[61] Gilmour and co-workers introduced bio-inspired E/Z isomerisation of activated olefins using riboflavin as an inexpensive organic sensitiser, demonstrating that EnT strategies can be implemented with metal-free photocatalysts while retaining high stereochemical control (Figure 16D).[62]

The synthetic scope of EnT photocatalysis has been substantially advanced by Glorius and co-workers, whose contributions have defined the conceptual and practical boundaries of the field.[58,63] A significant development was the demonstration that triplet energy transfer can enable intermolecular [2π+2σ]-photocycloadditions of bicyclo[1.1.0]butanes with heterocyclic alkenes, a reaction class inaccessible under thermal conditions or conventional photoredox chemistry, unlocking strain-release reactivity as a new dimension of EnT synthesis.[64] More recently, the scope of EnT catalysis has been extended to include triplet-sensitised sigma-bond fragmentation. Ritter and co-workers demonstrated that arylthianthrenium salts undergo Dexter-type triplet energy transfer-induced homolytic $C(sp^2)$–S bond cleavage upon sensitisation with thioxanthone under visible-light irradiation, generating aryl radicals and the persistent thianthrenium radical cation under redox-neutral conditions (Figure 16E).[65] The low triplet energy of arylthianthrenium salts, attributed to the electronic interplay of the sulfur atoms within the tricyclic thianthrene scaffold, enables this transformation with high energy efficiency compared to aryl pseudohalides, substantially expanding the synthetic utility of EnT catalysis in arylation chemistry.[65]

These developments establish EnT photocatalysis as a general and mild strategy for accessing excited-state reactivity under visible-light irradiation, with reactivity orthogonal to SET photoredox pathways and governed by triplet energy alignment rather than by substrate redox potential.[42,44,58,63]

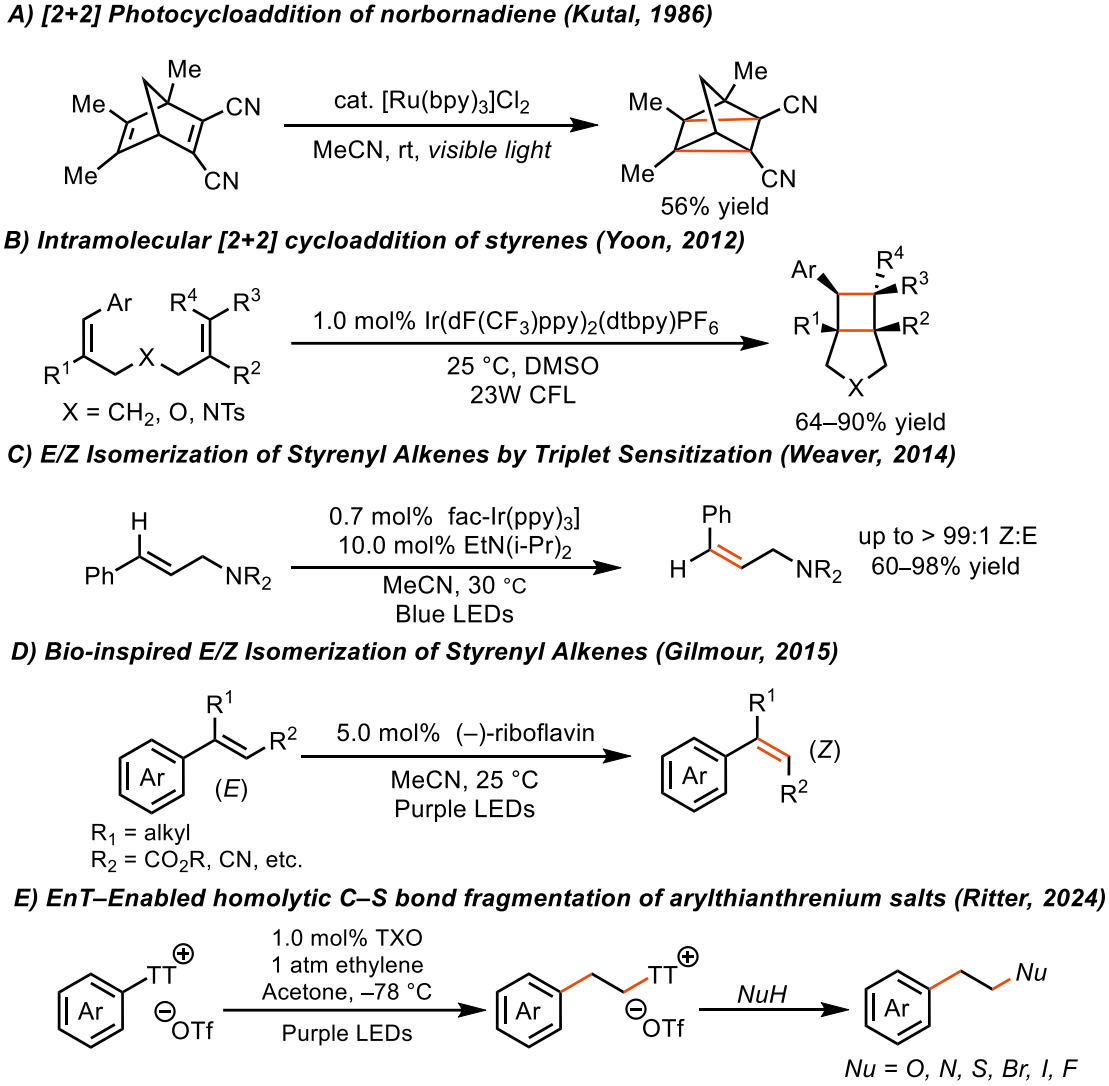


Figure 16. Representative transformations enabled by energy transfer photocatalysis: (A) [2+2] photocycloaddition of norbornadiene, (B) intramolecular [2+2] cycloaddition of styrenes (C) E/Z isomerisation of styrenyl alkenes by triplet sensitisation (D) bio-inspired E/Z isomerisation of activated olefins using riboflavin (E) EnT-enabled homolytic C–S bond fragmentation of arylthianthrenium salts.

I.1.4.3 Proton–Coupled Electron Transfer (PCET) and Atom-Transfer Pathways

Proton-coupled electron transfer (PCET) describes redox processes in which proton and electron transfer are thermodynamically and kinetically linked, enabling bond activation through coupled rather than isolated charge-transfer events.[46] Distinct from SET and EnT pathways, PCET proceeds through linked redox and acid–base processes and frequently culminates in homolytic X–H bond cleavage. In this way, the reactivity of PCET is governed by the interplay of redox potential, proton-transfer free energy, and bond dissociation free energy (BDFE) rather than by any single thermodynamic parameter.[46,66]

Hydrogen atom transfer (HAT) may be viewed as a limiting case of concerted PCET in which a proton and an electron originate from the same σ(X–H) bond and are delivered to the same acceptor in a single elementary step.[45,67] Reactivity in this regime is primarily determined by BDFE, radical stabilization, steric accessibility, and polarity matching between the abstractor and the substrate.[67,68] Under visible-light irradiation, HAT proceeds through two general pathways. In direct HAT, the photoexcited catalyst itself serves as the hydrogen abstractor, enabling homolytic X–H cleavage through excited-state reactivity.[67] In indirect HAT, photocatalytically generated radical intermediates, such as aminium, thiyl, or nitrogen-centered radicals, function as transient hydrogen abstractors following initial activation via SET or EnT pathways, allowing independent modulation of site selectivity and reactivity (Figure 17).[69,70]

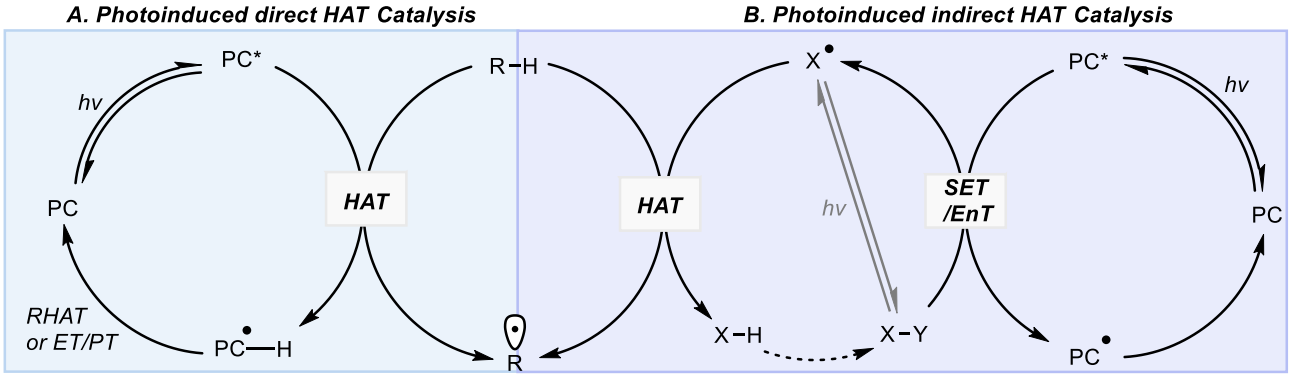


Figure 17. Photochemical hydrogen atom transfer catalysis: (A) direct hydrogen atom transfer from a substrate to an excited photocatalyst, and (B) indirect hydrogen atom transfer mediated by a radical intermediate generated through single-electron or energy transfer processes.

Concerted PCET (cPCET) represents a mechanistically distinct mode in which proton and electron transfer occur in a single kinetic event but proceed through separate donor–acceptor channels rather than from a common σ-bond, with reactivity governed by thermodynamic coupling between redox potential and proton-transfer energetics rather than by BDFE alone (Figure 18).[46]

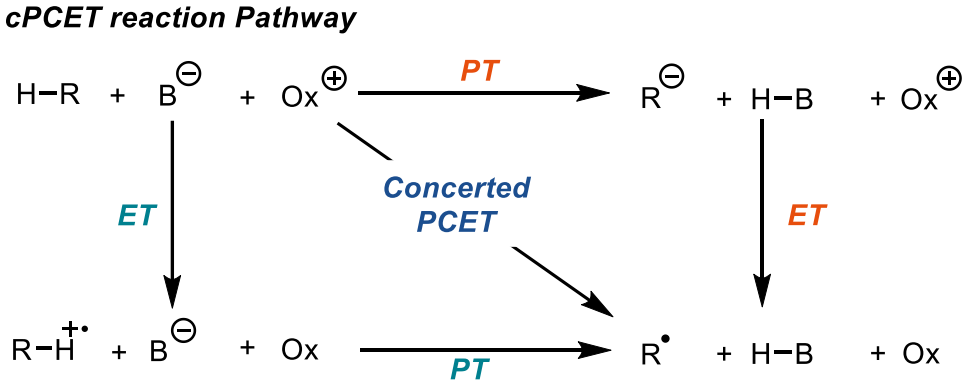


Figure 18. Reaction pathways for proton-coupled electron transfer, showing concerted transfer proceeding through simultaneous movement of an electron and a proton alongside stepwise pathways involving sequential electron and proton transfer with discrete intermediates.

Stepwise pathways, wherein electron and proton transfer occur sequentially through discrete charged intermediates and multisite PCET, in which a proton and an electron are transferred to

spatially distinct acceptors through hydrogen-bond preorganisation, occupy further regions of this mechanistic landscape.[66] Knowles and co-workers provided the first visible-light implementation of concerted PCET in organic synthesis through catalytic ketyl–olefin cyclization, employing a photoredox catalyst and Brønsted acid cooperatively to generate ketyl radicals under mild conditions (Figure 19A).[71] This was extended to an asymmetric aza-pinacol cyclization in which a chiral phosphoric acid provided both the proton-transfer partner and stereochemical control, establishing PCET as a viable platform for enantioselective radical generation.[72]

Within visible-light catalysis, HAT further extends to photoexcited transition-metal systems in which metal-centered excited states directly mediate inner-sphere HAT processes.[48,67] Gevorgyan and co-workers demonstrated that visible-light excitation of a Pd(0) complex generates a hybrid aryl Pd-radical species capable of an intramolecular 1,5-HAT event, enabling selective desaturation of silyl ethers into silyl enol ethers at room temperature without an exogenous photosensitizer or oxidant (Figure 19B).[73] This reactivity mode, in which single-electron Pd(I)/aryl radical intermediates combine both radical character and organometallic reactivity, established photoinduced transition-metal-mediated HAT as a mechanistically distinct and synthetically powerful activation pathway.[48,49]

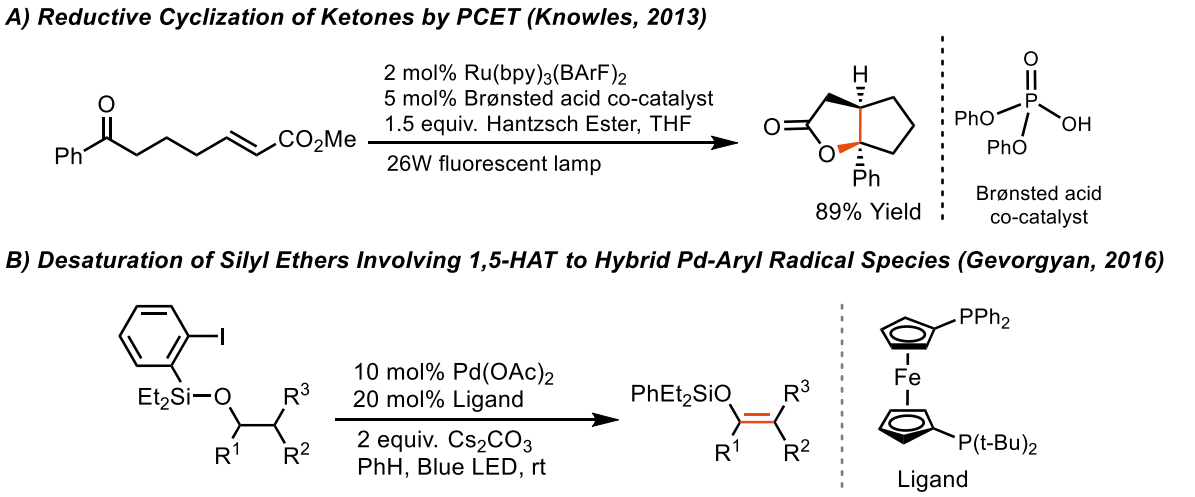


Figure 19. Representative transformations involving proton-coupled electron transfer and hydrogen atom transfer: (A) reductive ketyl–olefin cyclization enabled by proton-coupled electron transfer, and (B) desaturation of silyl ethers via intramolecular 1,5-hydrogen atom transfer to a hybrid palladium aryl radical intermediate.

I.1.5. Dual Photocatalysis and Metallaphotoredox Catalysis

Over the past decade, visible-light photoredox catalysis has developed into a general and reliable platform for controlled radical generation, establishing light as a practical source of redox activation for complex synthetic systems.[29,54] Building on this foundation, methodological development shifted beyond single-catalyst photoredox systems toward cooperative dual catalytic cycles, in which photoredox activation is integrated with a second catalytic manifold.[27] Within this framework, the photocatalyst provides controlled excited-state redox or energy-transfer events, while a separate co-catalyst directs substrate activation and bond formation, enabling reactivity that cannot be achieved under single-photocatalyst conditions (Figure 20).[27,47]

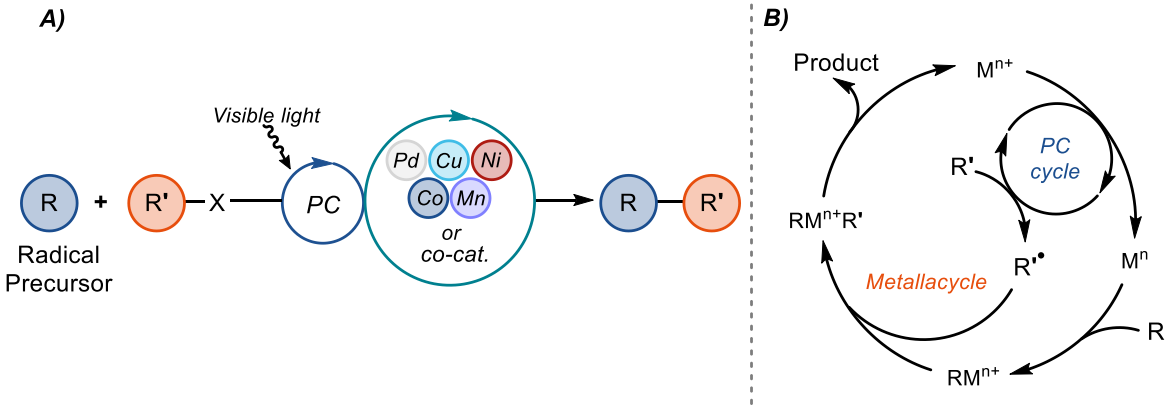


Figure 20. General schemes for dual photocatalysis: (A) coupling of a photoredox cycle with a transition-metal catalytic cycle leading to product formation, and (B) dual photocatalysis cycle

A defining feature of dual photocatalytic systems is the ability of photocatalysts to generate reactive intermediates without requiring strong substrate coordination, thereby enabling broad compatibility with diverse co-catalysts. Photoredox catalysis can therefore be merged with Brønsted and Lewis acids, organocatalysts, and transition-metal complexes without fundamentally perturbing their intrinsic activation modes. Rather than constituting a single mechanistic system, dual photocatalysis functions as a modular design framework in which photonic energy is converted into open-shell intermediates that are subsequently directed into selective bond-forming pathways by complementary co-catalysts.[27]

The integration of photoredox catalysis with Brønsted and Lewis acid activation demonstrated that PCET pathways can facilitate activation of otherwise inert X–H bonds under mild conditions.[46,71] Merger with organocatalytic manifolds showed that radicals generated by photoinduced SET can be intercepted within independent catalytic cycles. Rovis and co-workers developed a photoredox/NHC dual catalytic system in which a $Ru(bpy)_3^{2+}$ photocatalyst and a chiral N-heterocyclic carbene organocatalyst operate cooperatively, generating a radical intermediate from an aldehyde-derived Breslow intermediate under visible-light excitation to enable enantioselective C–C bond formation with high yield and enantioselectivity (Figure 21A).[74] Knowles and co-workers reported a catalytic asymmetric aza-pinacol cyclization in which an Ir-based photocatalyst promotes single-electron reduction of an imine to generate a nitrogen-centered radical that undergoes intramolecular cyclization, with a chiral Brønsted acid controlling

enantioselectivity to afford cyclic amines in high yield and ee (Figure 21B).[72]

MacMillan and co-workers introduced aldehyde β-arylation via tandem photoredox/organocatalysis, wherein the Ir photocatalyst generates aryl radicals from cyanoarenes while an enamine formed from the aldehyde engages in radical coupling at the β-position, enabling direct C–H functionalization of aldehydes under mild conditions (Figure 21C).[75] Yoon and co-workers developed an enantioselective [2+2] cycloaddition using visible-light photocatalysis in combination with a chiral Lewis acid, wherein the Ru photocatalyst mediates SET to generate an enone radical anion while the Lewis acid organises the substrate environment to suppress racemic background reactivity and induce high enantioselectivity (Figure 21D).[76] The scope of dual photocatalysis was further extended to radical thiol–ene reactions, wherein a Ru-based photocatalyst generates thiyl radicals under visible-light irradiation and aniline derivatives function as redox mediators to facilitate efficient radical generation and propagation across alkenes to form C–S bonds (Figure 21E).[77] These studies collectively established that open-shell intermediates generated by photoredox activation can be incorporated into distinct catalytic manifolds while maintaining catalyst turnover and reaction control.[27]

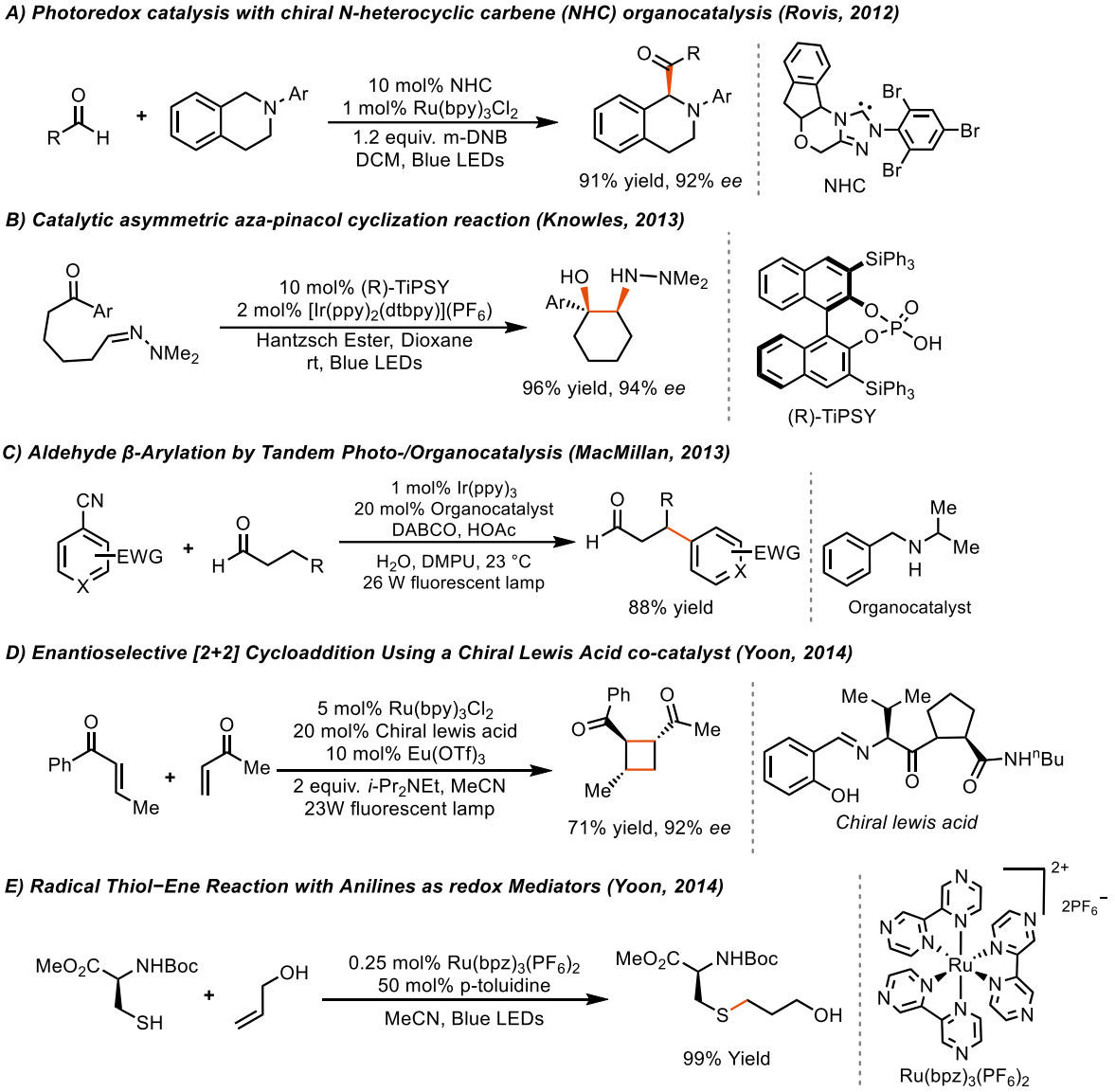


Figure 21. Representative dual photoredox catalytic reactions: (A) NHC/photoredox dual catalysis; (B) Brønsted acid-enabled photoredox PCET for asymmetric aza-pinacol cyclization; (C) enamine-mediated aldehyde β-arylation under photoredox conditions; (D) dual photoredox/chiral Lewis acid [2+2] cycloaddition; (E) photoredox-mediated radical thiol–ene reaction employing aniline redox mediators.

A defining advance in dual photocatalysis was the integration of photoredox activation with transition-metal catalysis in metallaphotoredox systems. MacMillan and co-workers reported that nickel/photoredox dual catalysis enables decarboxylative C(sp^3)–C(sp^2) cross-coupling of α-amino acids with aryl halides under mild visible-light conditions, demonstrating that radicals generated by single-electron oxidation can be incorporated directly into a nickel catalytic cycle (Figure 22).[78] In this system, an Ir-based photocatalyst mediates radical generation from the carboxylate precursor, while the nickel catalyst undergoes oxidative addition to an aryl halide, intercepts the resulting α-amino radical to form a Ni(III) intermediate, and furnishes the product through reductive elimination.[47,78]

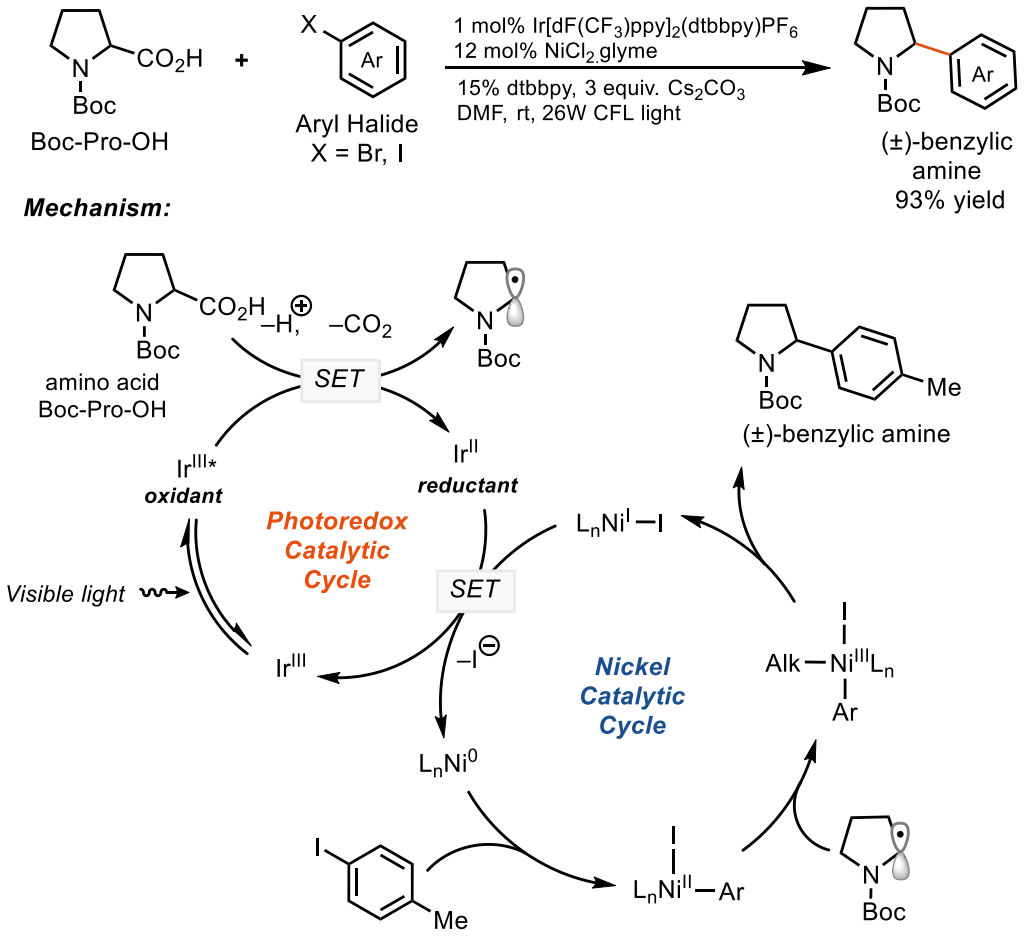


Figure 22. General mechanism of nickel/photoredox metallaphotocatalysis showing intersecting photoredox and nickel catalytic cycles connected through SET.

Related dual photoredox–palladium systems reported by Sanford and co-workers demonstrated that aryl radicals generated under visible-light conditions can engage Pd(II)/Pd(III)/Pd(IV) manifolds to enable directed C–H arylation at room temperature in the absence of stoichiometric oxidants (Figure 23).[79] In these reactions, photoredox activation generates the aryl radical partner from an aryldiazonium salt, whilst the palladium catalyst mediates organometallic bond formation within a thermally driven catalytic cycle. These studies established radical–metal cross-coupling as a general mechanistic platform and demonstrated that photoredox and palladium catalysis can operate synergistically within a single reaction manifold.[41,79]

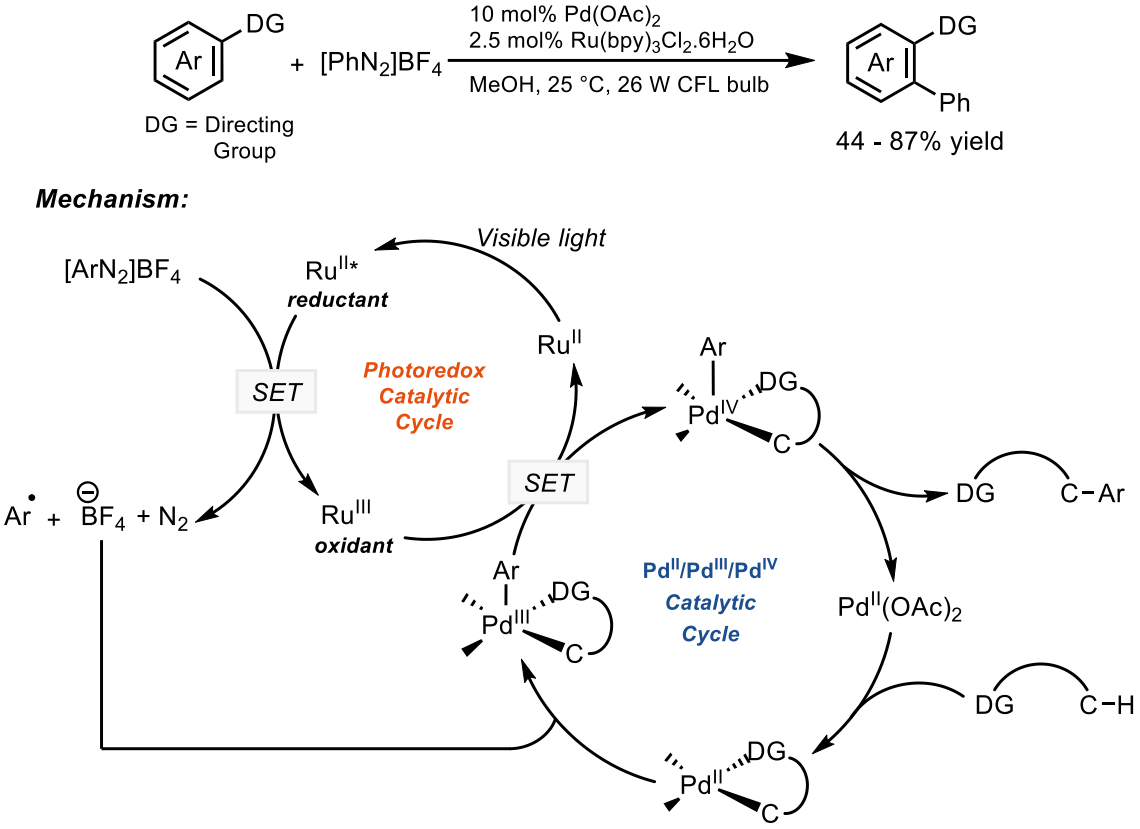


Figure 23. General mechanistic framework for dual photoredox–palladium catalysis involving directed C–H arylation, showing aryl radical generation by single-electron reduction of an aryldiazonium salt and interception by a Pd(II) palladacycle intermediate.

In dual photoredox–palladium catalysis, light serves primarily to generate radical intermediates that are subsequently captured by a thermally operating palladium cycle. In contrast, visible-light-induced palladium catalysis involves direct excitation of the palladium complex itself, altering its electronic structure and the elementary steps available to it. The evolution from dual photoredox–Pd systems to photoexcited Pd catalysis therefore represents not merely an extension of dual catalysis but a fundamental shift in activation mode, from photoredox-initiated radical generation to metal-centered photoactivation, in which the distinction between the photoabsorbing species and the bond-forming catalyst collapses into a single entity.[43,48]

I.1.6 Visible-Light-Induced Transition-Metal Catalysis

Transition-metal catalysis has transformed modern organic synthesis through well-defined two-electron redox manifolds in which oxidative addition, migratory insertion, transmetalation, and reductive elimination proceed along thermally accessible potential energy surfaces.[80] The efficacy of palladium and nickel catalysis within these ground-state cycles arises from closed-shell metal–substrate coordination, yet this same framework inherently disfavors homolytic bond cleavage and open-shell intermediates.[81] Consequently, oxidative addition of unactivated alkyl electrophiles is kinetically disfavoured, competitive β-hydride elimination limits the utility of alkyl coupling partners, and transformations that depend on discrete radical intermediates remain largely outside the intrinsic scope of thermal two-electron cycles.[47,82]

The conceptual framework for addressing these limitations dates back nearly four decades. Scheffold and co-workers reported in 1983 that vitamin B_{12a} catalyzes the reductive acylation of Michael acceptors under photoelectrochemical conditions via photoinduced homolysis of an acyl Co(III) intermediate (Figure 24).[83] Electrochemical reduction of vitamin B_{12a} generates nucleophilic Co(I), which reacts with acid anhydrides to form an acyl Co(III) species; subsequent visible-light irradiation induces homolytic cleavage of the Co–C bond, releasing an acyl radical that adds to the electron-deficient alkene. Although catalyst turnover in this system required electrochemical regeneration of the reduced cobalt species, the critical mechanistic insight was that excitation of a discrete organometallic intermediate provides access to a radical manifold unavailable under thermal conditions. This limitation was later resolved by Carreira and co-workers, who demonstrated that base-mediated deprotonation of a Co(III)H intermediate by diisopropylethylamine regenerates the active Co(I) species without recourse to electrochemistry, establishing a synthetically practical cobalt photocatalytic system.[84]

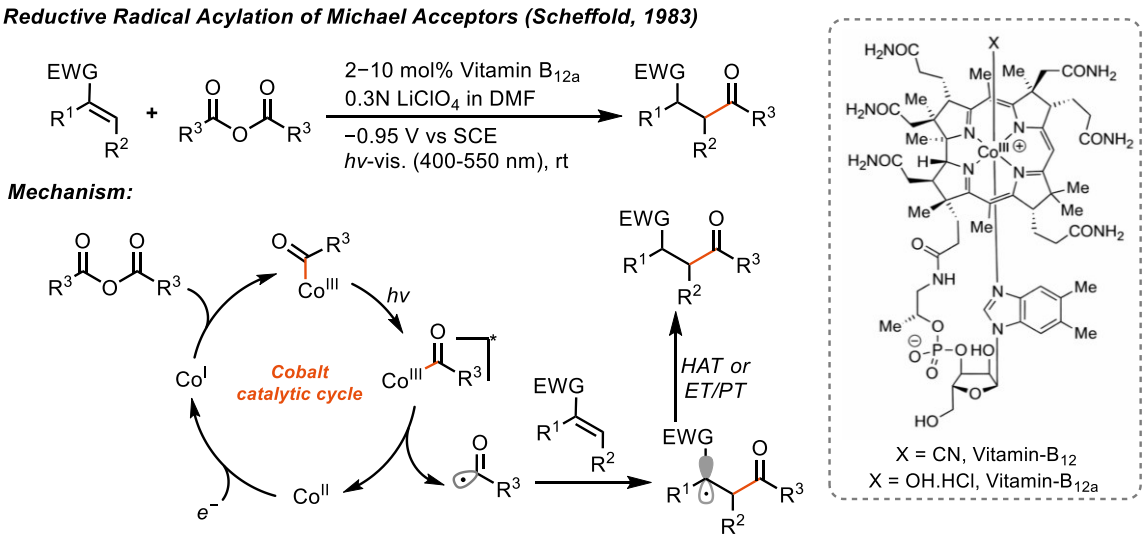


Figure 24. Vitamin B_{12a}-catalyzed reductive acylation of Michael acceptors under photoelectrochemical conditions.

Building on this foundation, Carreira and co-workers employed cobaloxime complexes for the intramolecular Heck-type cyclization of alkyl iodides and the intermolecular trifluoroethylation of styrene derivatives under visible light and continuous-flow conditions (Figure 25A and 25B).[84,85] Rovis and co-workers subsequently disclosed a mechanistically distinct excited-state manifold, demonstrating that LMCT activation of Co(II) acetylide complexes enables [2+2+2] cycloaddition of diynes with terminal alkynes (Figure 25C).[86] Coordination of the diyne substrate induces a bathochromic shift of approximately 100 nm, rendering the complex photoactive in the visible region. Photoexcitation generates an LMCT state in which electron density transfers from the acetylide ligand to the cobalt center, transiently generating an electron-enriched cobalt species that undergoes oxidative cyclization with the ligated diyne; subsequent alkyne insertion and reductive elimination furnish substituted arenes. Fluorimetric analysis confirmed the LMCT assignment through an inverse correlation between emission energy and alkyne electron density.[86] This LMCT pathway is mechanistically distinct from the Co–C bond homolysis central

to the earlier cobalt systems, underscoring the multiple excited-state activation modes accessible to first-row transition-metal complexes.

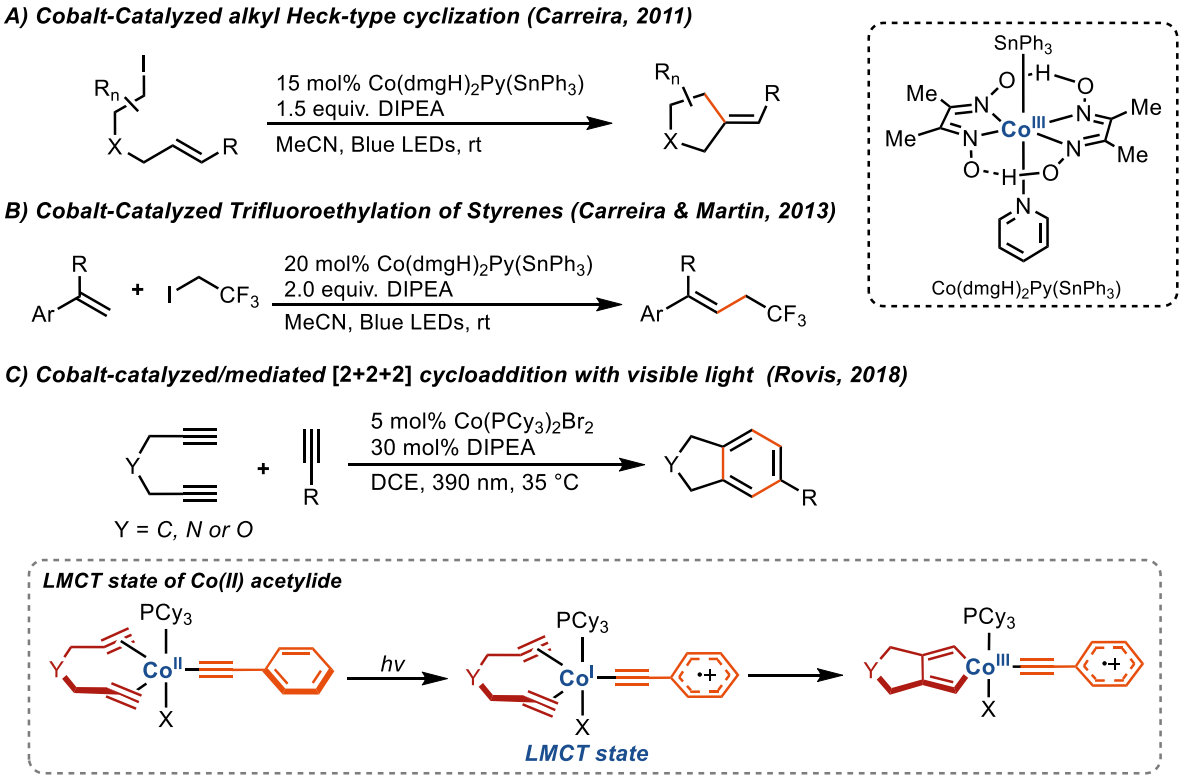


Figure 25. Cobalt-catalyzed visible-light-induced transformations: (A) intramolecular alkyl Heck-type cyclization of alkyl iodides enabled by cobaloxime photocatalysis, (B) intermolecular trifluoroethylation of styrene derivatives under continuous-flow conditions, and (C) diyne–alkyne [2+2+2] cycloaddition proceeding via photoinduced LMCT activation of a Co(II) acetylide complex.

Many transition-metal complexes absorb visible light through MLCT or LMCT transitions, whose molar absorptivities are several orders of magnitude greater than those of Laporte-forbidden d–d transitions in centrosymmetric complexes.[40,43] Upon photon absorption, vertical Franck-Condon excitation redistributes electron density across the metal-ligand framework.[25] Rapid intersystem crossing, driven by spin-orbit coupling that scales with atomic number, converts the initially formed singlet state into a longer-lived triplet configuration that constitutes the reactive manifold in most catalytic systems.[25,39] The excitation energy E_{00} places the complex on an excited-state surface with shifted redox potentials and modified bond dissociation energies relative to the ground state (Figure 26), permitting bonds that are robust thermally to become susceptible to homolytic cleavage and enabling redox events that are thermodynamically inaccessible under thermal conditions.[41,43] Although spin–orbit coupling and the resulting excited-state lifetimes are longest for second- and third-row metals, productive photocatalytic reactivity has been demonstrated for first-row transition metals including cobalt, nickel, copper, and iron.[43]

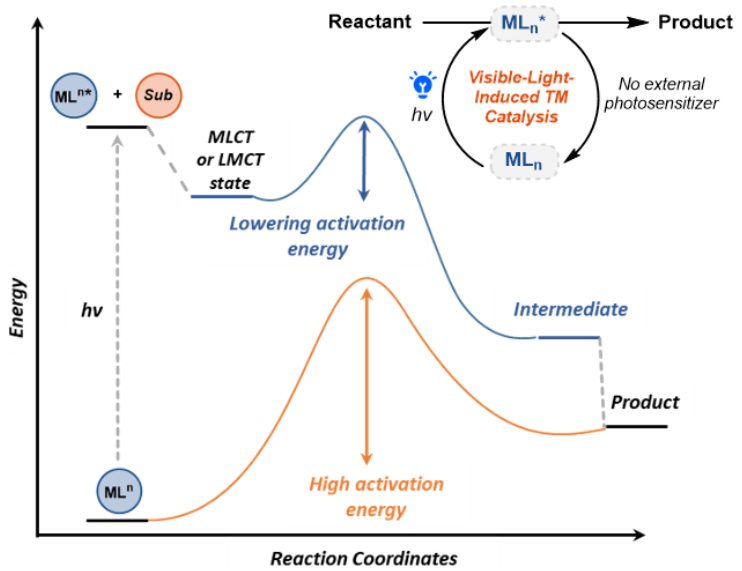


Figure 26. Reaction coordinate diagram comparing ground-state transition-metal catalysis (orange) and visible-light-induced transition-metal catalysis (blue), showing photoexcitation to an excited-state surface with a reduced activation barrier for bond activation.

The scope of first-row metal photocatalysis extends well beyond cobalt. Iron catalysis has been demonstrated by Jin and co-workers, who reported that Fe(III) carboxylate complexes undergo photoinduced LMCT upon blue-light irradiation, generating a carboxyl radical and a Fe(II) intermediate; decarboxylation of the carboxyl radical produces a nucleophilic alkyl radical that undergoes Minisci-type addition to protonated heteroarenes, enabling decarboxylative C–H alkylation under mild conditions (Figure 30A).[87] Visible-light-induced catalysis has also been demonstrated for late transition metals traditionally associated with two-electron reactivity. Hashmi and co-workers reported that Au(I) complexes catalyse the intermolecular 1,2-difunctionalization of alkynes with aryl diazonium salts under visible-light irradiation, proceeding through a Au(I)/Au(III) redox cycle without an external photosensitizer or stoichiometric oxidant (Figure 30B).[88] In this system, visible-light irradiation enables direct oxidative addition of the diazonium salt to the Au(I) complex, generating an arylgold(III) intermediate that undergoes subsequent alkyne activation and reductive elimination to afford the difunctionalized products. In a distinct copper manifold, Liu and co-workers demonstrated that a copper photocatalyst generated in situ from $Cu(OAc)_2$ and ammonium thiocyanate promotes the cyclization of vinyl azides to afford 4-alkyl/aryl-2-aminothiazoles under visible-light irradiation without an exogenous photoredox catalyst (Figure 30C).[89] The copper LMCT manifold was further extended by Ritter and co-workers to decarboxylative functionalization of benzoic acids: photoinduced LMCT within a copper carboxylate complex generates an aryl radical via low-barrier radical decarboxylation, which is captured by the copper center to form a high-valent arylcopper(III) intermediate; reductive elimination then affords aryl fluorides and phenols from abundant benzoic acid precursors under mild conditions (Figure 30D).[90,91] These iron, copper, and gold examples share a common mechanistic feature with the cobalt systems: direct excitation of the metal complex enables inner-sphere SET that bypasses the requirement for an exogenous photoredox sensitiser.[43]

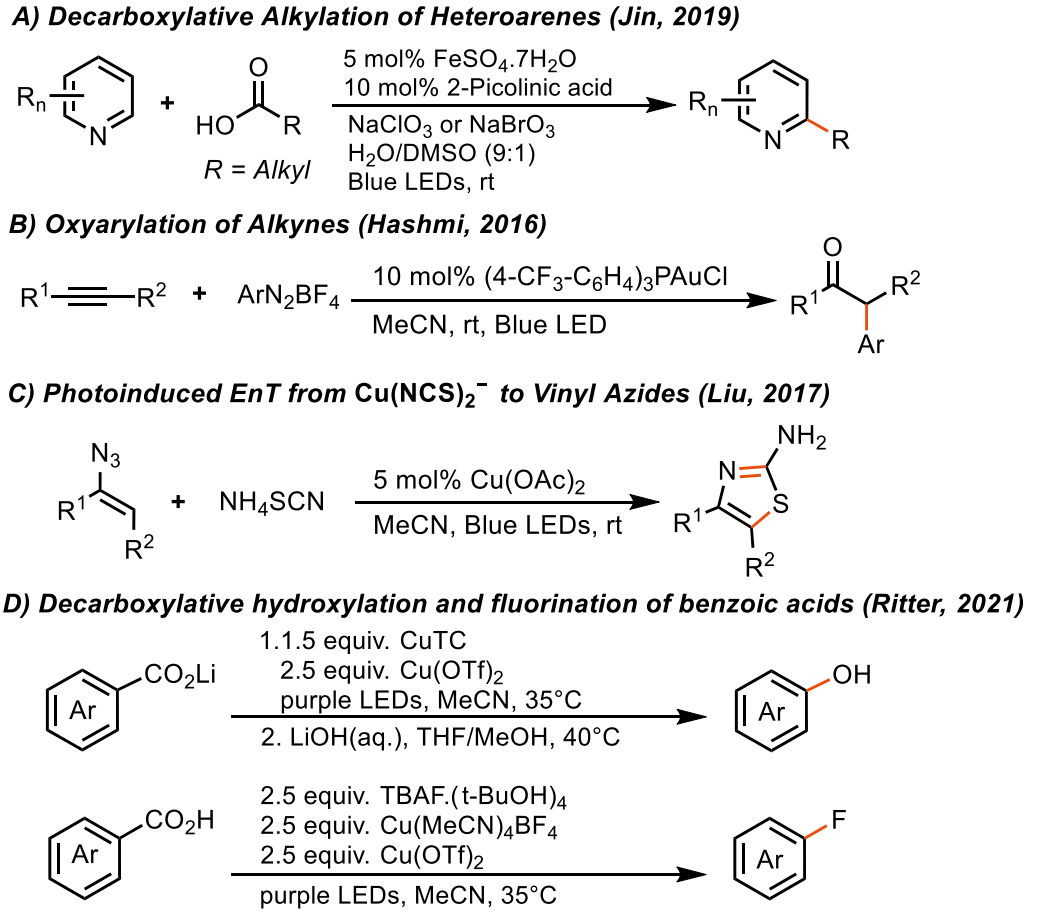


Figure 27. Representative visible-light-induced TM transformations: (A) Fe(III)-catalyzed decarboxylative C–H alkylation of heteroarenes via LMCT-generated carboxyl radicals (B) photosensitizer-free Au(I)-catalyzed 1,2-difunctionalization of alkynes with aryl diazonium salts, (C) visible-light-driven synthesis of 2-aminothiazoles from vinyl azides via an in situ generated copper photocatalyst (D) Cu-LMCT-enabled decarboxylative fluorination and hydroxylation of benzoic acids

Systematic photophysical and computational studies by Doyle and co-workers delineated the excited-state pathway responsible for Ni–aryl bond weakening in nickel aryl halide complexes (Figure 28).[92,93] Initial ultrafast transient absorption spectroscopy revealed that photoexcitation generates a singlet excited state that undergoes intersystem crossing with τ_{ISC} = 1.1 ps, initially forming a state computationally assigned as ^{3}MLCT with a decay lifetime of τ = 4.1 ns.[92] Subsequent experimental reinvestigation revised this assignment, demonstrating that this long-lived state is a tetrahedral ^{3}d–d excited state rather than ^{3}MLCT in character, lying approximately 0.5 eV above the ground state.[93] Structural reorganization accompanying population of this ^{3}d–d state elongates the Ni–aryl bond and predisposes it toward homolytic cleavage, yielding a Ni(I) complex and a discrete aryl radical; spin-trapping experiments confirmed aryl radical formation and excluded alternative cleavage pathways.[93] Because the transition state for bond homolysis lies substantially lower in energy on the excited-state surface than on the ground-state surface, irradiation grants access to an alternative reaction coordinate rather than simply accelerating a pre-existing thermal process. The synthetic relevance of this manifold was demonstrated in C–O cross-coupling between 4-bromoacetophenone and n-butanol, where visible-light irradiation substantially increased product formation relative to thermal conditions.[92]

Photoinduced Homolysis of Ni–Ar Bond, ^{3}d–d Excited State of Aryl Ni(II) Complexes (Doyle, 2018)

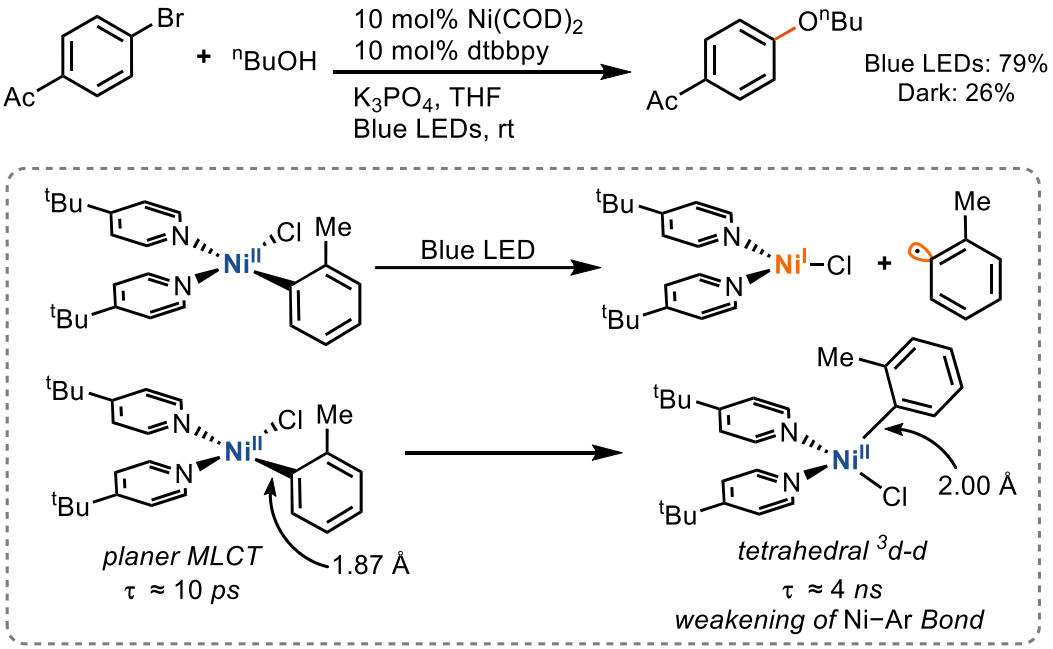


Figure 28. Photoinduced homolysis of Ni–Ar bonds in aryl Ni(II) complexes, showing excitation to a short-lived ^{3}MLCT state followed by population of a longer-lived ^{3}d–d metal-centered excited state associated with Ni–aryl bond elongation, together with the C–O bond-forming cross-coupling enabled by irradiation.

Gevorgyan and co-workers demonstrated that photoexcitation of $Pd(PPh_3)_4$ redirects the two-electron oxidative addition of aryl iodides toward a single-electron pathway, generating hybrid aryl-Pd(I) species capable of 1,5-hydrogen atom transfer.[73] The annual number of publications in this field expanded substantially following these foundational examples, with particularly rapid growth observed after the introduction of photoexcited palladium catalysis in 2016 (Figure 29).[43] Subsequent work showed that this excited-state manifold extends to unactivated alkyl and aryl electrophiles that resist thermal two-electron activation, enabling C–C and C–heteroatom bond formation under mild conditions.[48] Critically, the photoexcited palladium complex serves simultaneously as the light-absorbing species and the organometallic catalyst within a single catalytic cycle, without recourse to an exogenous photosensitizer.[43] This integration of photon absorption and organometallic bond-forming reactivity within a single metal center defines the mechanistic boundary between dual photoredox–metal catalysis and visible-light-induced transition-metal catalysis.

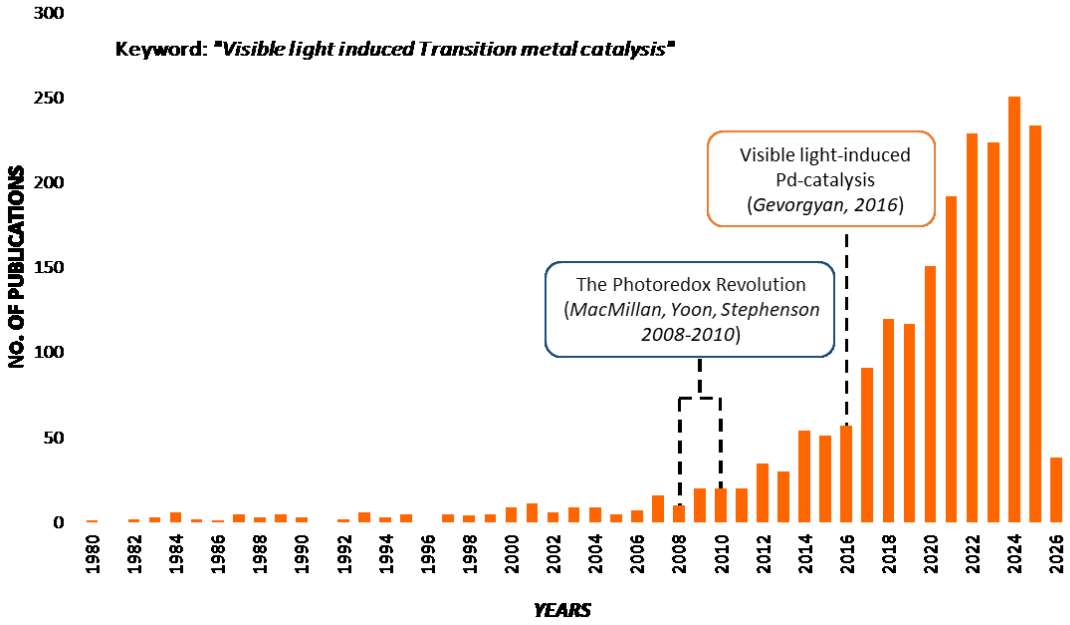


Figure 29. Annual publication count for visible-light-induced transition-metal catalysis showing growth in research activity, with highlighted periods corresponding to the expansion of photoredox catalysis (2008–2010), the introduction of visible-light-induced palladium catalysis (2016), and the subsequent rapid increase in publications. Data retrieved from SciFinder on 23 February 2026 using the search term “visible-light induced-transition metal catalysis”.

I.1.7 Microsecond Triplets to Visible-Light-Induced Palladium Catalysis

Classical palladium catalysis operates predominantly within a closed-shell Pd(0)/Pd(II) redox manifold defined by two-electron elementary steps: oxidative addition, transmetalation, migratory insertion, and reductive elimination.[47] These processes proceed on a single ground-state potential energy surface and are rationalized as concerted two-electron bond reorganization at the metal center.[47] Open-shell intermediates are not considered productive elements of the catalytic cycle; when radical species arise under thermal conditions, they are typically interpreted as off-cycle phenomena. Within this framework, electronically excited palladium complexes were not regarded as catalytically relevant for nearly three decades following Caspar and co-workers foundational 1985 report demonstrating that Pd(0) phosphine complexes possess microsecond-lived triplet excited states.[94]

Early photophysical investigations of closed-shell d^{10} phosphine complexes established that palladium chemistry is not intrinsically confined to the ground-state surface. Homoleptic and chelating phosphine complexes of Pd(0) exhibit phosphorescence from low-lying triplet states of predominantly metal-centered d→p character with varying degrees of MLCT admixture.[94–96] Excitation promotes electron density from filled metal d orbitals into orbitals of mixed metal p and ligand π^* character, generating triplet configurations populated efficiently via intersystem crossing. These studies demonstrated that electronically excited states of Pd(0) complexes are accessible under near-UV irradiation and possess microsecond lifetimes at ambient temperature.[94]

Within this class, $Pd(PPh_3)_4$ exhibits measurable emission in deoxygenated solution with a lifetime

of 3.61 μs.[94] In solution, $Pd(PPh_3)_4$ exists in equilibrium with the three-coordinate species $Pd(PPh_3)_3$, and the emissive state has been attributed primarily to this coordinatively unsaturated complex.[94,97] Since homogeneous catalysis is conducted in solution, the three-coordinate species should be regarded as the photochemically relevant state under catalytic conditions. Quenching experiments with organic triplet acceptors confirmed the triplet nature of the excited state and placed the Pd(0)* state approximately 46–50 kcal mol^{-1} above the ground state, defining the energetic regime accessible to photoexcited palladium.[94]

The photophysical data for representative Pd(0) complexes are compiled in Table 1. In the solid state at 298 K, $Pd(PPh_3)_4$ exhibits biexponential decay with lifetime components of 3.1 and 10 μs and a triplet energy of 53.6 kcal mol^{-1}, whereas $Pd(PPh_3)_3$ displays components of 3.7 and 78 μs with a triplet energy of 47.7 kcal mol^{-1}.[97] In degassed toluene solution, $Pd(PPh_3)_3$ exhibits single-exponential decay with τ = 6.0 μs and E_T = 43.8 kcal mol^{-1}.[97] Related chelating diphosphine complexes display comparable microsecond lifetimes and triplet energies spanning approximately 38–54 kcal mol^{-1} (Table 1).[95,96] These triplet energies place photoexcited Pd(0) within the energetic regime required for activation of carbon–iodine bonds via SET or excited-state bond homolysis.[94,97]

Complex	Absorption, λ_{max} (nm)	Emission, λ_{max} (nm)	Lifetime, t (μs)	Triplet Energy (kcal/mol)	Quantum Yield, Φ	Excited State Character	Conditions (T = 298 K)
$[Pd(PPh_3)_4]$	322	533	3.1, 10	53.6	0.33	MLCT (Pd→π*Ph)	Solid state
$[Pd(PPh_3)_3]$	322	600	3.7, 78	47.7	0.46	Mixed MLCT/MC (d→p)	Solid state
$[Pd(PPh_3)_3]$	322	653	6.0	43.8	0.13	Mixed MLCT/MC (d→p)	Toluene solution
$[Pd(P(m\text{-}tol)_3)_3]$	320	635	3.9	45.0	0.29	Mixed MLCT/MC	Toluene solution
$[Pd(binap)_2]$	420	746	2.6	38.3	0.32	MLCT	Toluene solution
$[Pd(biphep)_2]$	400	667	3.2	42.9	0.38	MLCT	Toluene solution
$[Pd(dppp)_2]$	380	580	4.5	49.3	0.25	MLCT	Toluene solution

Table 1. Photophysical properties of representative palladium(0) complexes, including absorption and emission maxima, excited-state lifetimes, triplet energies, quantum yields, and excited-state character.[95–97]

The electronic structure of these excited states refines the mechanistic picture. Extended Hückel calculations indicated that the lowest-energy transition in three-coordinate Pd(0) complexes involves promotion of an electron from a metal d orbital to the vacant $(n+1)p_z$ orbital, confirming that the excited state is anchored at the metal center.[94] Time-dependent DFT studies validated this assignment quantitatively, with natural transition orbital analysis of $Pd(PPh_3)_3$ revealing excitation from a HOMO of approximately 55% Pd-4d character to a LUMO dominated by Pd-$5p_z$

contribution.[97] In contrast, $Pd(PPh_3)_4$ exhibits predominantly MLCT character with a largely ligand-based LUMO, and the calculated energy separation of approximately 6400 cm^{-1} between the tetra- and tricoordinate species accounts for their distinct emission energies.[97] These data establish that low-coordinate Pd(0) complexes possess long-lived, energetically accessible, and partially metal-centered excited states under synthetically relevant conditions.

Despite this photophysical foundation, the implications of photoexcited palladium for catalytic design remained largely unexplored for nearly three decades, as the Pd(0)/Pd(II) two-electron manifold dominated cross-coupling chemistry and radical pathways were considered mechanistically peripheral.[47,48]

The first indications that light could influence palladium-catalyzed cross-couplings emerged as kinetic acceleration rather than mechanistic redefinition. Köhler and co-workers reported in 2009–2010 that UV and visible irradiation enhanced the rate of the Heck reaction by accelerating the reduction of Pd(II) precatalysts to Pd(0), thereby shortening induction periods (Figure 30A).[98] When a pre-formed Pd(0) catalyst was employed, irradiated and non-irradiated reactions proceeded identically, demonstrating that light facilitated entry into the established two-electron cycle without altering the catalytic manifold itself.[98] A more mechanistically developed example was reported by Abdiaj and co-workers in 2018, who demonstrated that visible-light irradiation enables Negishi cross-couplings of challenging aryl halides via excitation of a Pd–Zn complex absorbing at 430 nm (Figure 30B).[99] ^{31}P NMR monitoring showed that this intermediate was consumed more rapidly under irradiation, correlating with accelerated product formation, though the transformation remained interpretable within a closed-shell two-electron manifold.[99]

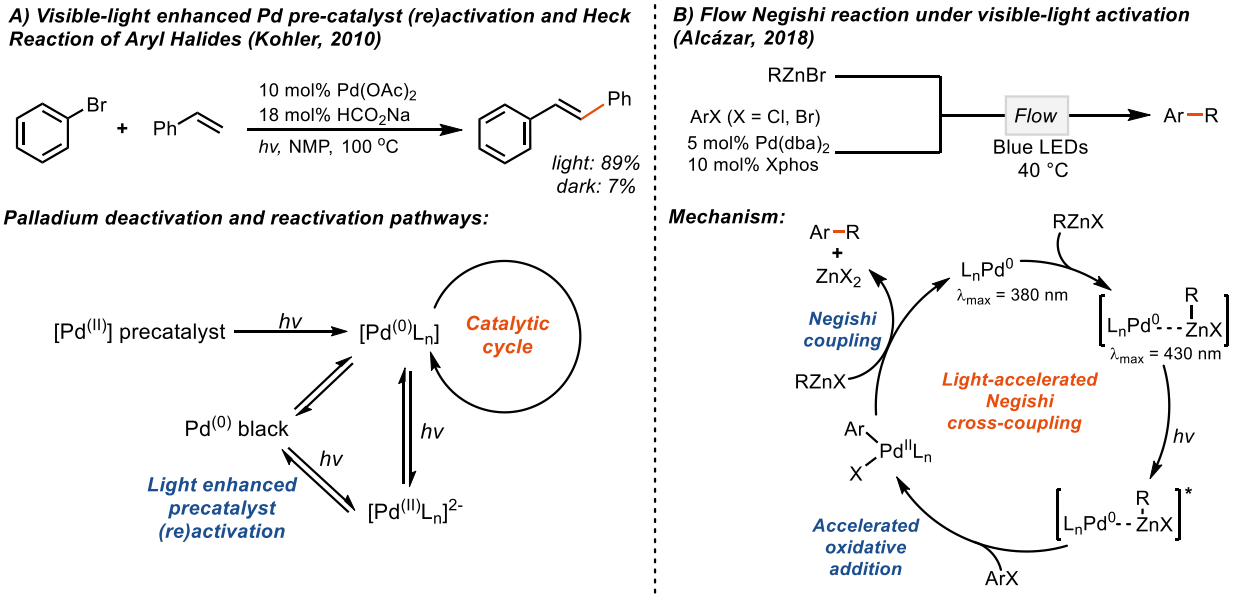


Figure 30. Early visible-light-accelerated palladium catalysis: (A) light-enhanced reduction of Pd(II) precatalysts in the Heck reaction shortening induction periods without altering the Pd(0)/Pd(II) catalytic manifold, and (B) visible-light-enabled Negishi cross-coupling via excitation of a Pd–Zn intermediate accelerating oxidative addition while preserving the closed-shell two-electron cycle.

The mechanistic boundary between light-accelerated and light-redirected palladium catalysis was established by Gevorgyan and co-workers, who demonstrated that photoexcitation of $Pd(PPh_3)_4$ redirects the two-electron oxidative addition of aryl iodides toward a discrete single-electron pathway, generating hybrid aryl-Pd(I) radical species as key intermediates.[73] These hybrid Pd(I)/aryl radical intermediates combine organometallic and radical reactivity within a single species, merging the substrate control of classical palladium cross-coupling with the bond-activation versatility of open-shell chemistry.[48,49] The photoexcited palladium complex serves simultaneously as the light-absorbing species and the organometallic catalyst within a single catalytic cycle, without recourse to an exogenous photosensitizer, distinguishing this manifold from the dual photoredox–palladium systems.[42]

I.1.8 Photoexcited Palladium as a Single-Electron Platform

The light-accelerated Heck and Negishi reactions discussed above demonstrated that visible irradiation can shorten induction periods or facilitate oxidative addition without fundamentally altering the underlying Pd(0)/Pd(II) catalytic manifold.[98,99] In each case, light functioned as a kinetic tool, accelerating entry into a pre-existing two-electron cycle. A mechanistically distinct advance emerged when visible-light irradiation was shown to redirect aryl iodide activation into a single-electron pathway, generating hybrid Pd–radical intermediates under mild conditions (Figure 31A).[73]

Desaturation of silyl ethers bearing pendant aryl iodides proceeds under blue LED irradiation at room temperature, in the absence of exogenous photosensitizers or stoichiometric oxidants, to furnish silyl enol ethers via an intramolecular 1,5-hydrogen atom transfer sequence (Figure 31A).[73] The occurrence of remote C–H functionalization through 1,5-HAT is incompatible with a closed-shell aryl–Pd(II)–iodide intermediate generated via concerted oxidative addition, since classical Pd(II) species do not participate in radical HAT processes. The reaction outcome, therefore, implies the involvement of open-shell intermediates.

Mechanistic validation experiments support this interpretation (Figure 31B).[73] Radical clock substrates undergo selective cyclopropyl ring opening, consistent with discrete aryl radical formation prior to hydrogen abstraction. Radical scavengers suppress product formation, and deuterium-labeling studies exclude concerted metalation–deprotonation and direct Pd(II)-mediated β-hydride elimination pathways.[73] These observations cannot be reconciled with a purely two-electron catalytic cycle.

Single-electron activation of the aryl iodide under photoexcitation provides a coherent explanation for the observed reactivity (Figure 31C).[73] Photoexcited Pd(0)* engages the C–I bond through SET to generate an aryl radical and a Pd(I) species. The aryl radical undergoes intramolecular 1,5-HAT to produce a secondary alkyl radical, which recombines with palladium prior to β-hydride elimination, restoring Pd(0) and delivering the desaturated product. Radical relay chemistry and organometallic β-hydride elimination therefore operate within a unified catalytic manifold.

The feasibility of this pathway is fully consistent with the photophysical properties of phosphine-ligated Pd(0) complexes established in section I.1.7. Microsecond-lived triplet excited states of three-coordinate Pd(0) species possess excitation energies of approximately 46–50 kcal mol^{-1}, sufficient to enable homolytic activation of aryl iodides under ambient conditions.[94,97] The lowest-energy transitions exhibit significant metal-centered d→p character, indicating direct perturbation of the palladium valence manifold upon excitation.[97] These excited-state properties provide the energetic basis for single-electron bond activation at palladium.

The Gevorgyan desaturation occupies a foundational position in the evolution of photoinduced palladium catalysis.[73] The microsecond-lived excited states of phosphine-ligated Pd(0) complexes, long characterised as photophysical properties of academic interest, were shown to be synthetically accessible and mechanistically consequential under visible light.[73] The single-electron manifold established by this transformation provided the mechanistic foundation upon which subsequent advances in visible-light-induced palladium catalysis were built.[49]

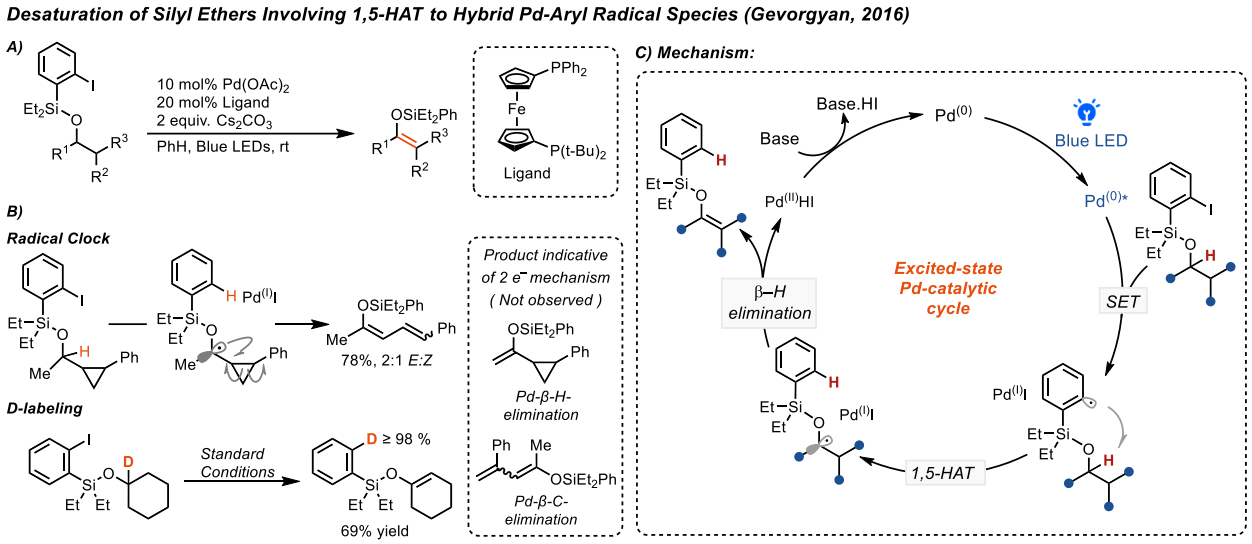


Figure 31. Visible-light-induced palladium-catalyzed desaturation of silyl ethers via 1,5-hydrogen atom transfer: (A) reaction of aryl iodide-tethered silyl ethers under blue LED irradiation to afford silyl enol ethers, (B) radical clock and deuterium-labeling experiments supporting a single-electron pathway, and (C) proposed mechanism featuring Pd(0)*-mediated SET, hybrid Pd(I)–radical intermediates, 1,5-HAT, and β-hydride elimination.

I.1.9 Expansion and Mechanistic Diversification of Visible-Light-Induced Palladium Catalysis

The discovery that photoexcited palladium activates aryl iodides through SET rapidly transformed an initial mechanistic observation into a broadly applicable catalytic platform.[73] Subsequent investigations revealed that visible-light excitation can perturb multiple elementary steps of palladium catalysis beyond oxidative addition, opening mechanistic pathways inaccessible under thermal conditions (Figure 32).[48,49] In addition to enabling single-electron activation of electrophiles through SET from the photoexcited Pd(0) center (Figure 32A), photoexcitation has been shown to facilitate homolysis of Pd–C bonds, modulating reductive elimination processes and enabling C–C and C–heteroatom bond formation under mild conditions (Figure 32B).[48,49] A central mechanistic feature emerging from these studies is the concept of radical–polar crossover, in which radicals generated under photoexcited palladium catalysis recombine with palladium intermediates to form classical Pd(II) species that undergo conventional organometallic steps such as β-hydride elimination, nucleophilic substitution, or reductive elimination. This convergence of radical and two-electron palladium chemistry provides a general framework for understanding the diverse reactivity patterns observed across the field.[48]

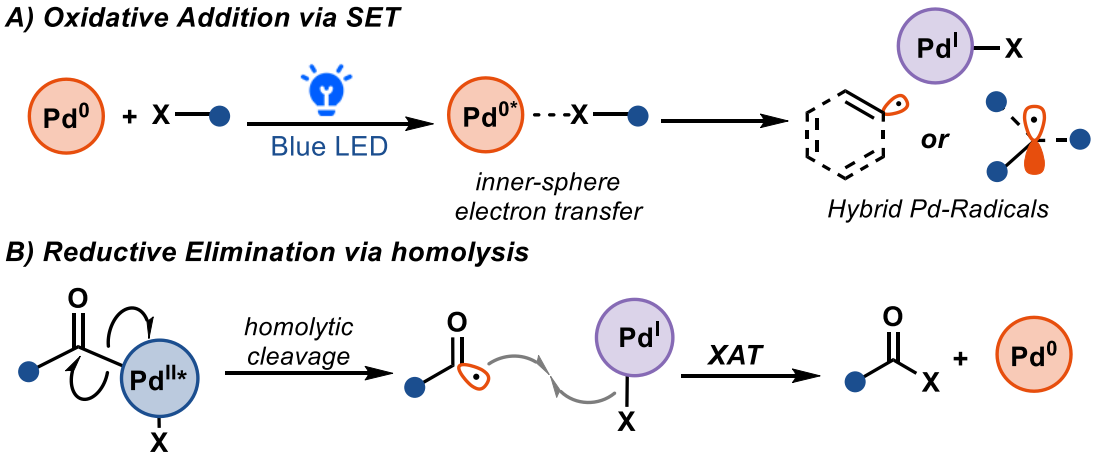


Figure 32. Mechanistic diversification of visible-light-induced palladium catalysis: (A) inner-sphere SET from photoexcited Pd(0) to electrophiles generating hybrid Pd(I)–radical intermediates; (B) photoinduced homolysis of Pd–C bonds facilitating reductive elimination processes inaccessible under thermal conditions.

One of the earliest intermolecular extensions of the hybrid Pd–radical manifold was the alkyl–Heck coupling of α-heteroatom-substituted primary and secondary alkyl halides with vinyl arenes and heteroarenes reported by Gevorgyan and co-workers (Figure 33A).[100] Under blue LED irradiation at room temperature and without an exogenous photosensitizer, photoexcited Pd(0) promotes single-electron activation of the alkyl halide to generate an alkyl radical, which undergoes addition to the vinyl arene; subsequent recombination with palladium and β-hydride elimination furnishes synthetically valuable allylic silanes, boronates, phosphonates, and phthalimide derivatives with high stereoselectivity. This reactivity was subsequently extended to unactivated tertiary alkyl halides, which are entirely resistant to classical two-electron oxidative addition, further underscoring the unique capacity of photoexcited palladium to engage

electrophiles beyond the reach of ground-state catalysis.[101] Parallel developments revealed that radical precursors other than alkyl halides can be incorporated into this manifold (Figure 33B). Glorius and co-workers reported a decarboxylative Heck reaction of N-hydroxyphthalimide esters with vinyl arenes under visible-light irradiation, in which mechanistic studies implicated single-electron reduction of the NHPI ester by photoexcited $Pd(PPh_3)_4$, generating an alkyl radical through decarboxylation; subsequent alkene addition and palladium-mediated β-hydride elimination afforded exclusively (E)-configured olefins without an exogenous photosensitizer or base.[102]

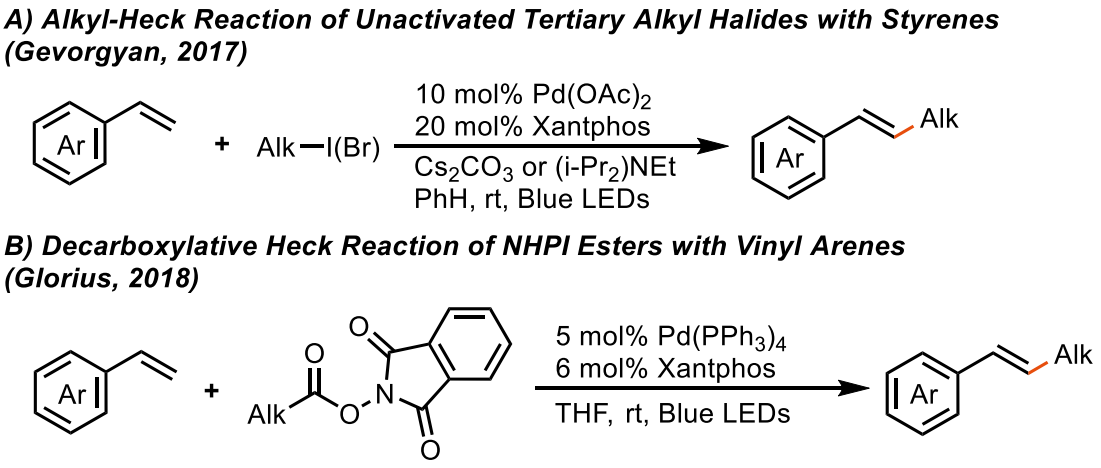
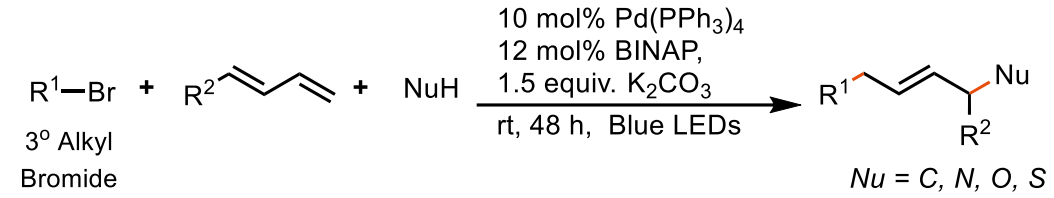


Figure 33. Extension of visible-light-induced palladium catalysis through radical coupling reactions: (A) alkyl–Heck coupling of unactivated tertiary alkyl halides with styrenes; (B) decarboxylative Heck reaction of N-hydroxyphthalimide esters with vinyl arenes.

The radical–polar crossover concept reached its most synthetically significant expression through the 1,4-difunctionalization of 1,3-dienes. Glorius and co-workers demonstrated that a three-component palladium-catalyzed cascade involving an interrupted radical Heck/allylic substitution sequence enables selective 1,4-difunctionalization of unactivated 1,3-dienes, including butadiene, with unactivated alkyl bromides and a broad range of nitrogen-, oxygen-, sulfur-, and carbon-based nucleophiles (Figure 34A).[103] Radical addition of the alkyl radical to the diene generates an allylic radical that is intercepted by palladium to form a π-allylpalladium intermediate; nucleophilic attack then delivers the 1,4-difunctionalized product with high regio- and stereoselectivity. In a complementary approach, Gevorgyan and co-workers reported the photoinduced palladium-catalyzed 1,2-carbofunctionalization of conjugated dienes, enabling three-component synthesis of allylic amines from 1,3-dienes, alkyl iodides, and amines via a radical–polar crossover pathway (Figure 34B).[104] These transformations established 1,3-dienes as uniquely versatile substrates for photoexcited palladium catalysis, capable of intercepting radical intermediates at the allylic position and channeling them through classical π-allylpalladium chemistry.

A) Photoinduced palladium-catalysed 1,4-aminoalkylation of 1,3-dienes (Glorius, 2020)



B) Photoinduced Palladium catalysed 1,2-aminoalkylation of 1,3-dienes (Gevorgyan, 2020)

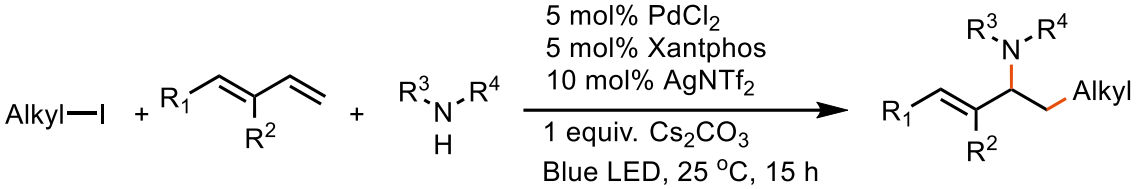


Figure 34. Visible-light-induced palladium-catalyzed difunctionalization of 1,3-dienes via radical–polar crossover: (A) three-component interrupted radical Heck/allylic substitution enabling 1,4-difunctionalization of dienes (B) photoinduced 1,2-carbofunctionalization of conjugated dienes for three-component synthesis of allylic amines from 1,3-dienes

Whilst the Glorius and Gevorgyan diene functionalization reactions demonstrate the power of the radical–polar crossover manifold in constructing allylic C–N and C–heteroatom bonds via alkylation,[104,105] the installation of an aryl group at the remote position of the diene, affording a 1,4-aminoarylation motif, remained unaddressed. The 1,4-aminoarylation of butadiene developed in the present work addresses this challenge directly, employing the same photoexcited palladium manifold to achieve conjunctive arylation rather than alkylation at the terminal position of the diene.

I.2 RESULTS AND DISCUSSION

Note: This chapter includes work that has been published in *Angew. Chem.*[106] and is presented here with permission. The 1,4-aminoarylation reaction was designed and developed entirely by Dr. Yuan Cai. The substrate scope with respect to aryl bromides, aryl halides, amines, and dienes was explored jointly by Dr. Yuan Cai and the author. Mechanistic investigations, including HRMS analysis, TEMPO radical trapping experiments, and identification of the telomerization by-product, were conducted by the author. The manuscript was prepared collaboratively by Prof. Dr. Tobias Ritter, Dr. Yuan Cai, and the author of the thesis. Within the substrate scope, compounds 1, 5, 6, 7, 8, 12, 15–26, 34, and 48 were synthesized by the author.

I.2.1 Research Summary

The three-component coupling of aryl halides, 1,3-dienes, and amines to afford aryl-substituted allylic amines represents a long-standing challenge in synthesis. Classical palladium catalysis requires elevated temperatures, suffers from competing β-hydride elimination, and delivers mixtures of regio- and stereoisomers, limiting both the efficiency and scope of diene aminoarylation.[107,108] This chapter describes the development of a 1,4-aminoarylation of butadienes using aryl bromides and aliphatic amines under photoexcited palladium catalysis. The transformation proceeds at room temperature under blue LED irradiation with $Pd(PPh_3)_4$, rac-BINAP, and K_2CO_3 in acetonitrile, affording aryl-substituted allylic amines in up to 82% yield with excellent E-selectivity (>20:1 E/Z) and high chemo-, regio-, and stereoselectivity across a broad range of aryl bromides, secondary amines, and conjugated dienes, including direct use of 1,3-butadiene. Mechanistic investigations are consistent with a photoinduced radical Pd(0)/Pd(I)/Pd(II)/Pd(0) Heck–Tsuji–Trost allylation cascade, in which single-electron activation of the aryl bromide by photoexcited Pd(0) generates a hybrid aryl-Pd(I) radical species that adds to the diene, producing a π-allylpalladium intermediate subsequently intercepted by the amine nucleophile.[48,94,103] The synthetic utility of this approach is demonstrated through late-stage functionalization of bioactive molecules, establishing photoexcited palladium catalysis as a practical platform for the modular assembly of complex allylic amine scaffolds from abundant feedstock starting materials.

I.2.2 Reaction Background

Multicomponent reactions enable the efficient construction of complex molecules by forming multiple bonds in a single catalytic operation.[109] Three-component coupling reactions that simultaneously establish C–C and C–N bonds across unsaturated systems provide an efficient route to nitrogen-containing compounds from simple building blocks, and the selective coupling of aryl halides, dienes, and amines provides a direct and modular approach to allylic amine synthesis.[104]

Allylic amines are common structural motifs in pharmaceuticals, natural products, and biologically

active molecules.[110] Their synthetic utility arises from the characteristic reactivity of the allylic position, which permits a range of downstream transformations including oxidation, reduction, and cyclization, making allylic amines valuable building blocks in complex molecule synthesis.[111]

Among conjugated dienes, 1,3-butadiene is one of the most industrially abundant feedstock chemicals, produced primarily as a by-product of steam cracking during ethylene manufacture, with global output exceeding 14 million metric tons annually.[112] The ready availability of this substrate has made butadiene a widely used C_4-synthon in catalytic transformations.[112] In addition to its industrial relevance, the electronically coupled π-system of 1,3-butadiene permits bond formation at multiple positions along the diene framework, making regioselective control of 1,2- versus 1,4-functionalization a central challenge. Other conjugated dienes are likewise industrially significant: isoprene is produced on approximately 800,000 metric tons per year for synthetic rubber manufacture, whilst naturally occurring terpenoid dienes such as myrcene can be accessed from renewable biomass at approximately 2,000 metric tons per year (Figure 35A).[112]

The earliest examples of palladium-catalyzed three-component coupling between aryl halides, conjugated dienes, and amines were reported by Heck and co-workers in 1978 and subsequently expanded by Dieck and co-workers in 1983, demonstrating that allylic amines could be accessed through palladium-mediated diene aminoarylation.[107,108] In these transformations, oxidative addition of the aryl halide to Pd(0) generates an aryl–palladium intermediate that subsequently reacts with the diene to form a π-allylpalladium intermediate, which an amine nucleophile can intercept to afford the corresponding allylic amine (Figure 35B).

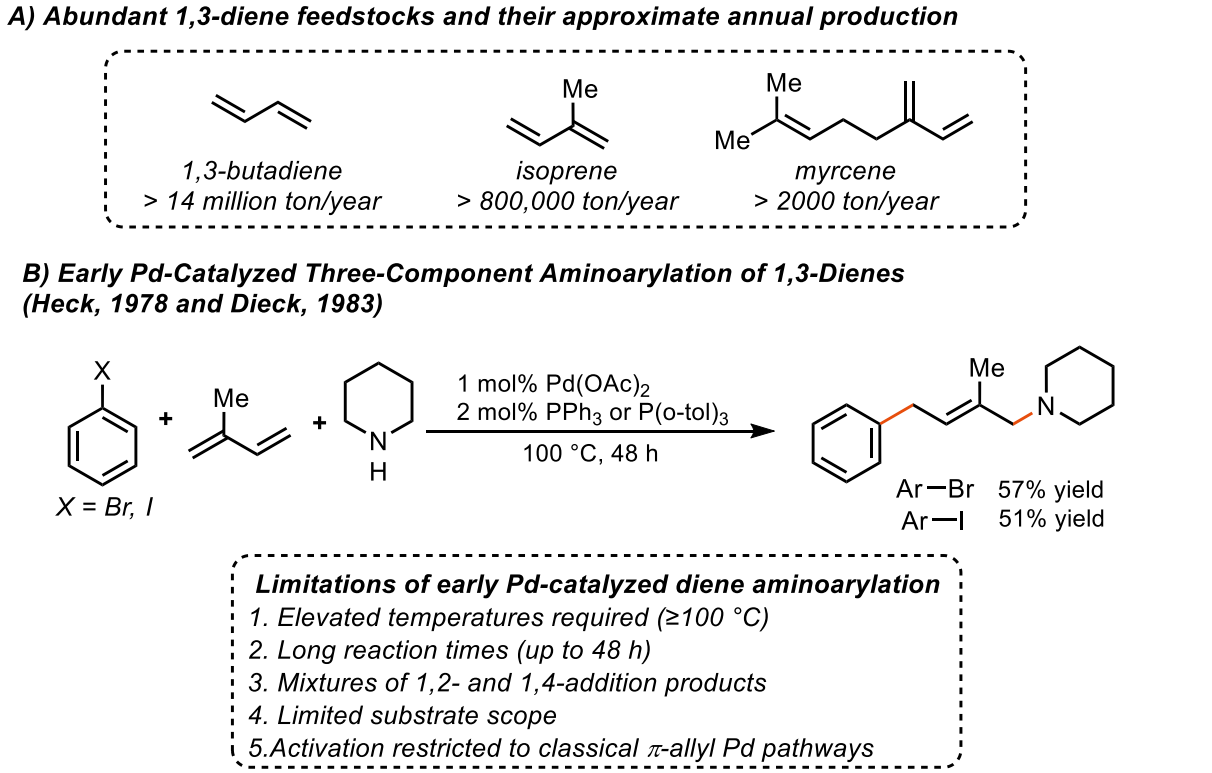


Figure 35. Conjugated diene feedstocks and early palladium-catalyzed three-component aminoarylation of 1,3-dienes: (A) representative 1,3-diene feedstocks and approximate annual production volumes, and (B) early palladium-catalyzed three-component aminoarylation of 1,3-dienes with aryl bromides and aryl iodides.[107,108]

Although these pioneering reactions established the feasibility of diene aminoarylation, they suffered from fundamental limitations inherent to the Pd(0)/Pd(II) two-electron manifold. In representative examples with piperidine as the nucleophile, bromobenzene afforded the allylic amine in 57% yield, whilst iodobenzene gave 51% yield, both requiring temperatures of 115–120 °C and reaction times of up to 48 hours.[107] Competing β-hydride elimination pathways frequently generated Heck-type by-products, eroding yield and complicating purification, whilst poor functional-group tolerance restricted applicability to simple substrates.

These limitations originate from fundamental mechanistic features of the classical π-allyl palladium manifold (Figure 36). Following oxidative addition of the aryl halide to Pd(0), migratory insertion into the conjugated diene generates a σ-alkyl Pd(II) intermediate that undergoes rapid equilibration to the corresponding η³-allyl palladium complex. Product formation can proceed via two mechanistically distinct pathways: outer-sphere nucleophilic attack on the π-allyl complex leading predominantly to 1,4-functionalized products, or direct trapping of the σ-alkyl intermediate favouring 1,2-functionalization.[111] The relative contribution of these pathways is governed by ligand environment, nucleophile identity, and the dynamics of π–σ–π interconversion within the allyl palladium manifold. The fluxional nature of η³-allyl complexes, together with low barriers for syn–anti interconversion of the allyl fragment, further generates mixtures of E and Z-olefin isomers as well as regioisomeric products, whilst β-hydride elimination competes with nucleophilic substitution to afford Heck-type by-products. Regioselective and stereoselective control over diene aminoarylation, therefore, remained an unresolved problem within the classical two-electron Pd manifold.

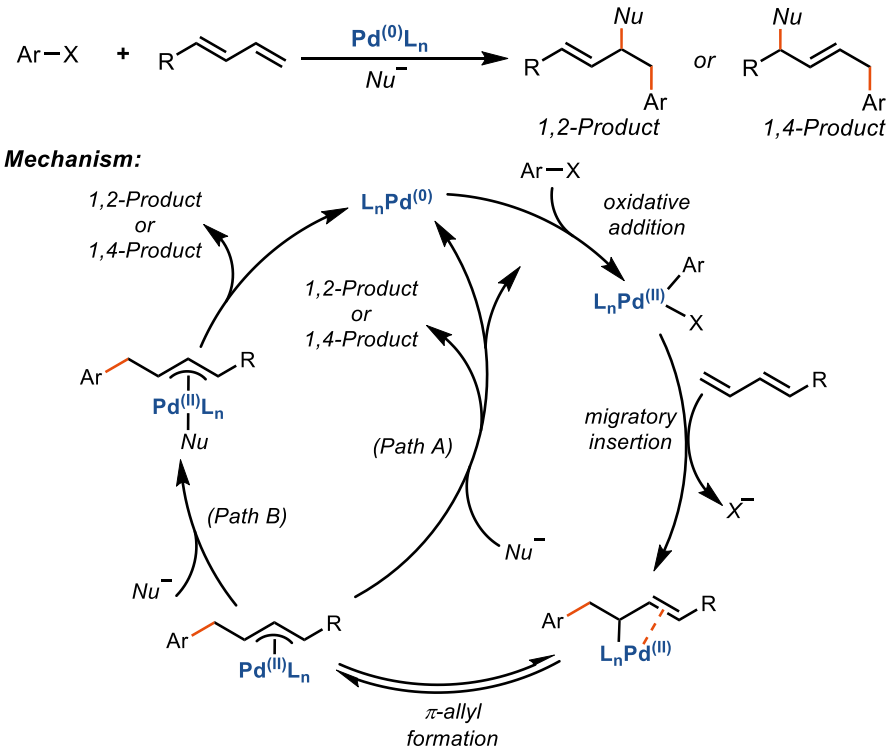


Figure 36. Classical Pd(0)/Pd(II) catalytic cycle for the difunctionalization of 1,3-dienes via π-allyl palladium intermediates.

A further challenge inherent to palladium-catalyzed diene functionalization is the competing telomerization pathway. In the presence of a palladium catalyst, two equivalents of 1,3-butadiene undergo oxidative coupling to generate a bis-π-allyl palladium intermediate, which can react with the amine nucleophile to furnish a C_8 telomer rather than the desired three-component coupling product.[113] telomerization is thermodynamically favourable and proceeds efficiently under mild conditions, making it a persistent competing pathway that is difficult to suppress without precise control of catalyst and ligand environment. In three-component aminoarylation reactions, telomerization consumes both the diene and the amine whilst incorporating no aryl fragment, directly competing with the desired manifold.[112,113]

Asymmetric variants of diene aminoarylation present additional challenges that have prevented their development within classical palladium manifolds. The allylic amine products bear a stereogenic center at the allylic position, yet control over the prochirality of π-allyl intermediates generated directly from unactivated dienes through radical-mediated sequences remains unsolved: the radical addition step is not stereocontrolled, and the resulting allyl radical can recombine with palladium from either face. Existing diene aminoarylation reactions therefore afford racemic products, and enantioselective variants of this three-component coupling remain undeveloped.

The choice of electrophilic coupling partner further constrains the scope of diene aminoarylation. Aryl halides represent the most attractive class of aryl radical precursors owing to their broad commercial availability, structural diversity, and the range of electronic and steric properties accessible through synthetic modification. Aryl bromides alone represent over 1.1 million registered compounds (Reaxys structure search, accessed 8 March 2026), and are available from commercial suppliers in diverse structural configurations spanning electron-rich, electron-deficient, sterically hindered, and heteroaromatic variants. However, the direct activation of aryl bromides by single-electron reduction is thermodynamically demanding, typically requiring potentials of approximately −2.4 V vs SCE,[29] substantially more negative than the reducing capacity of most photoredox catalysts in their excited states.[29] This barrier arises from the strong C(sp^2)–Br bond and the aromatic stabilization of the radical anion intermediate, which raises the energetic cost of SET relative to aliphatic counterparts.[29] Thermal two-electron oxidative addition of aryl bromides to Pd(0) requires elevated temperatures incompatible with selective diene functionalization.[107] These combined barriers explain why selective three-component aminoarylation of unactivated 1,3-dienes with aryl bromides had not been achieved prior to the present work.

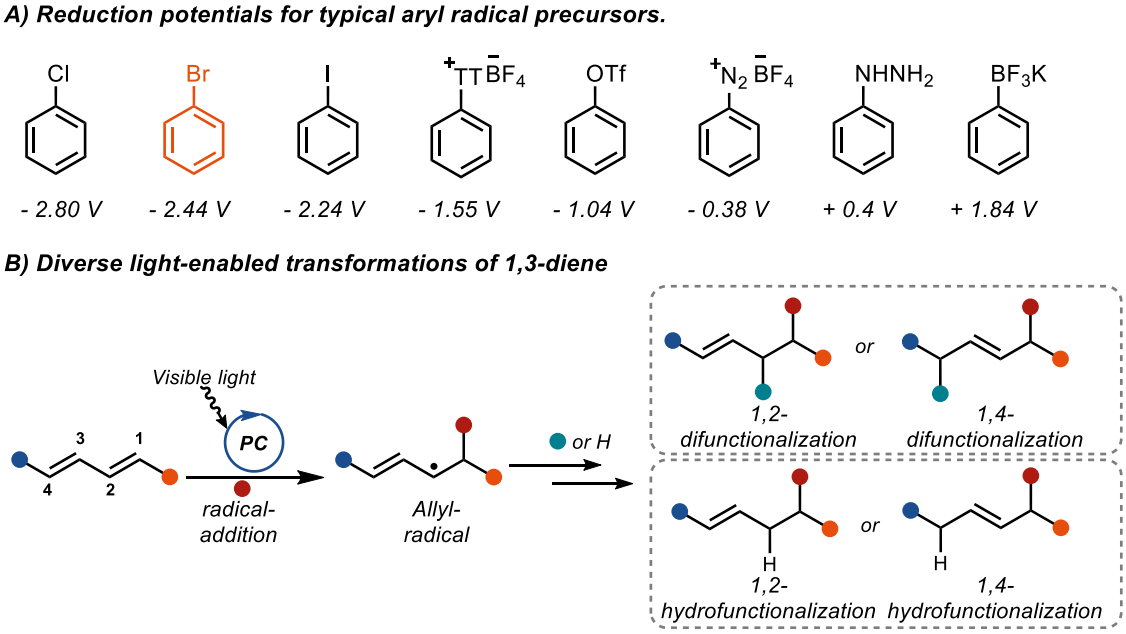


Figure 37. Aryl radical generation and addition to conjugated dienes: (A) representative aryl radical precursors and their reduction potentials, and (B) visible-light-induced radical addition to conjugated dienes generating allylic radical intermediates that can evolve through competing 1,2- and 1,4-difunctionalization or hydrofunctionalization pathways.

The conceptual foundation for overcoming these barriers was established by Gevorgyan and co-workers in 2016, who demonstrated for the first time that photoexcitation of a Pd(0)–phosphine complex generates a hybrid aryl-Pd(I) radical species capable of effecting transformations inaccessible to ground-state palladium, as discussed in the introduction.[48,73] The application of this platform to diene functionalization was subsequently realized by Glorius and co-workers, who demonstrated 1,4-difunctionalization of unactivated dienes with alkyl bromides via an interrupted radical Heck/allylic substitution cascade,[103,114] and by Gevorgyan and co-workers, who reported 1,2-carbofunctionalization of conjugated dienes through a radical–polar crossover pathway.[104] Both approaches, however, employed alkyl radical precursors. The generation of aryl radicals from aryl bromides presents a mechanistically distinct challenge: aryl bromides require substantially more negative reduction potentials for single-electron activation, and the resulting ambiphilic aryl radicals are more reactive towards undesired hydrogen atom abstraction from allylic C–H bonds and α-C–H positions of amines than nucleophilic alkyl radicals.[29,48] Photoexcited palladium catalysis, therefore, provides the conceptual basis for a selective three-component 1,4-aminoarylation of butadiene, provided that the competing pathways of hydrodehalogenation, Heck coupling, Buchwald-Hartwig amination, and telomerization can be suppressed within a single catalytic manifold.[48,103,104]

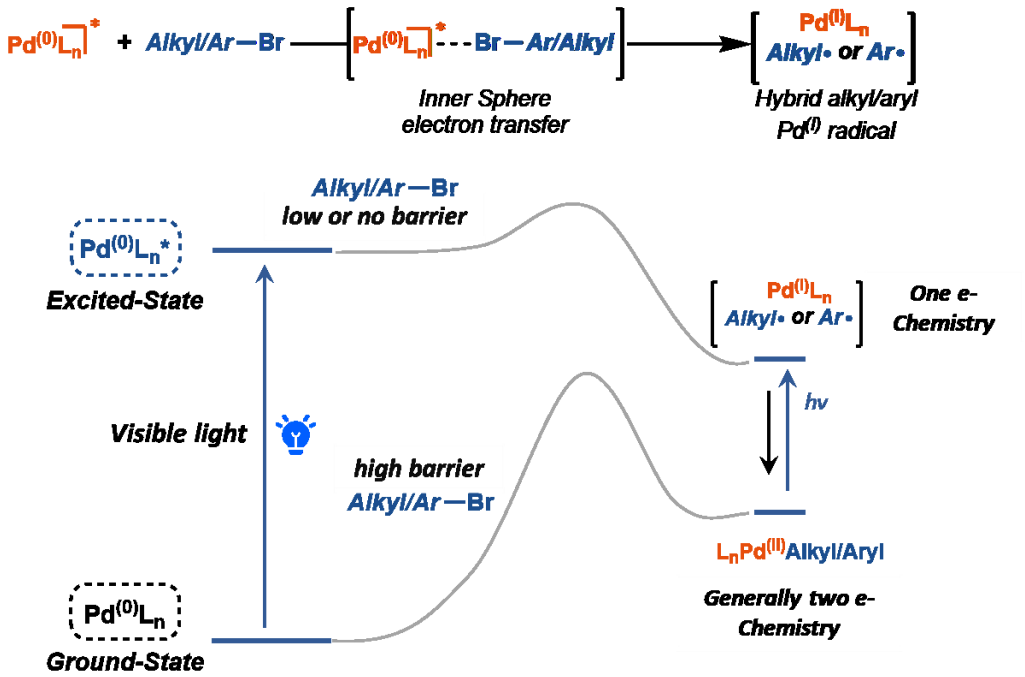


Figure 38. Reaction coordinate diagram illustrating photoexcitation of a palladium(0) complex and subsequent activation of aryl or alkyl bromides. Visible-light excitation generates an excited-state Pd(0) species that undergoes inner-sphere electron transfer with the substrate, enabling formation of hybrid Pd(I)–radical intermediates through a low-barrier pathway, in contrast to the higher-barrier ground-state pathway associated with two-electron reactivity.

I.2.3 Reaction Development and Optimization

Photoexcited palladium catalysis provides a mechanistically distinct entry into hybrid radical–organometallic pathways, enabling aryl radical generation via excited-state SET and subsequent interception through π-allylpalladium intermediates.[106] Translating this reactivity into a selective three-component 1,4-aminoarylation of 1,3-butadiene requires simultaneous control over three interdependent steps: activation of the aryl bromide via SET from the photoexcited Pd(0)* complex, regioselective radical addition across the diene to generate an allylic radical intermediate, and efficient nucleophilic trapping of the resulting π-allylpalladium complex by the amine. Four competing pathways must be suppressed within the same catalytic manifold: Heck coupling, which arises from β-hydride elimination from an allylpalladium intermediate before amine trapping to afford a styrene-derived arylbutadiene byproduct; telomerization, which results from Pd(0)-catalyzed oxidative coupling of two equivalents of 1,3-butadiene with the amine to furnish a C_8 octa-2,7-dien-1-yl amine product lacking any aryl fragment; Buchwald–Hartwig amination, which affords an N-aryl amine through direct coupling of the aryl bromide with the amine in the absence of diene insertion; and hydrodehalogenation, which converts the aryl bromide to the corresponding arene through reductive cleavage of the C–Br bond without formation of any new C–C or C–N bond (Figure 39).

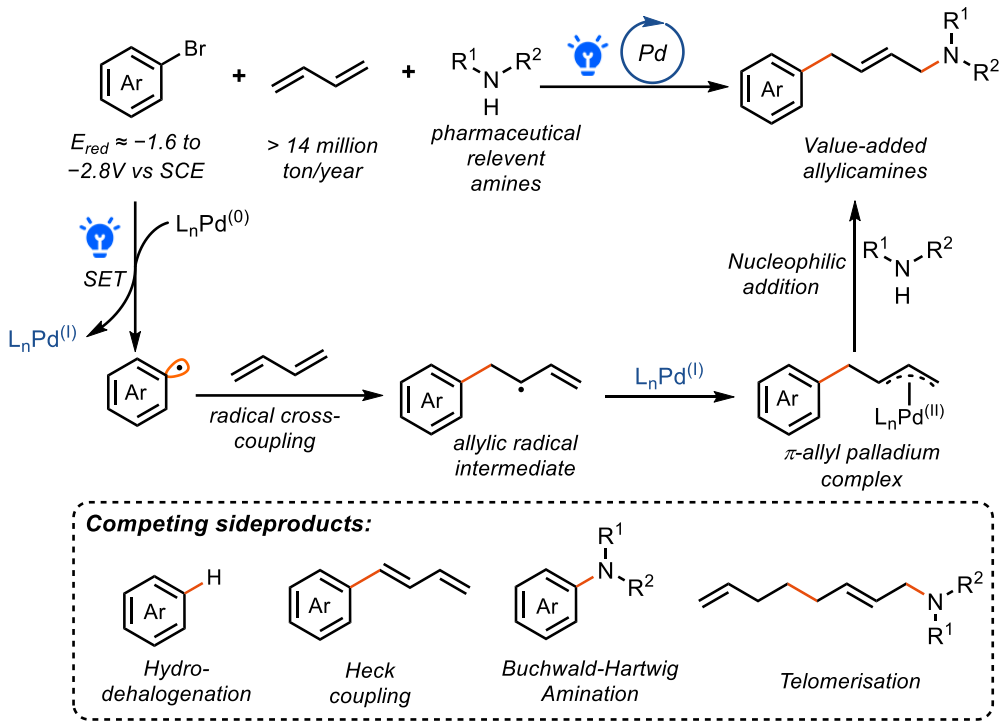


Figure 39. Proposed catalytic manifold for the visible-light-induced three-component 1,4-aminoarylation of 1,3-butadiene via photoexcited palladium catalysis, and principal competing pathways requiring suppression: hydrodehalogenation, Heck coupling, Buchwald–Hartwig amination, and telomerization.

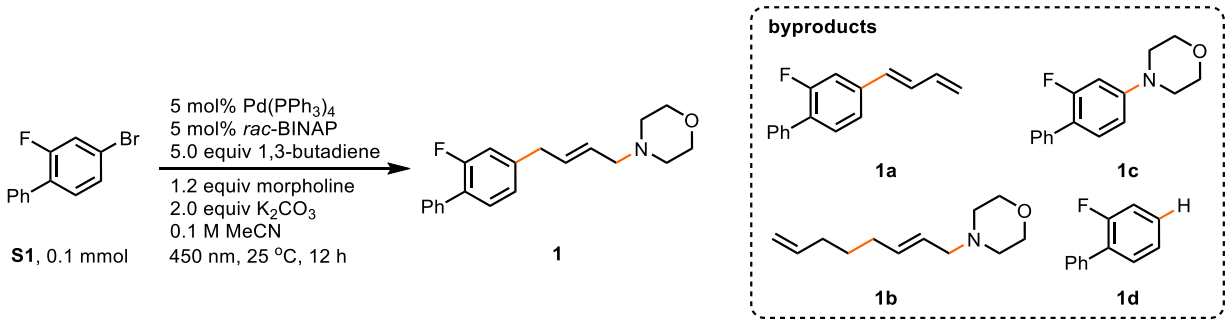
Aryl bromides were selected as the aryl radical precursors owing to their broad commercial availability and their capacity for single-electron activation under photoexcited palladium conditions, whilst avoiding the competing two-electron oxidative addition associated with aryl iodides. Although aryl iodides possess weaker C–X bonds and generally faster mesolytic cleavage rates, they undergo rapid oxidative addition to Pd(0) before photoexcitation can occur, diverting the catalyst into a conventional two-electron manifold and suppressing productive radical formation (Figure 39). 1,3-Butadiene was chosen as the diene coupling partner on account of its industrial abundance and its capacity to act both as a radical acceptor and as a precursor to π-allylpalladium intermediates, enabling direct access to allylic amine products.[112] Butadiene was employed in excess (5.0 equivalents) to suppress hydrodehalogenation byproduct 1d to below 5%, ensuring that productive radical addition across the diene outcompetes reductive protonation of the aryl radical. Morpholine was employed as the nucleophilic amine partner owing to its strong nucleophilicity towards π-allylpalladium intermediates and its low propensity to coordinate irreversibly to palladium or to undergo competing oxidation under photochemical conditions.

Within this framework, the palladium source, ancillary ligand, base, and solvent were each varied in turn, with 1-bromo-3-fluoro-4-phenylbenzene (S1), 1,3-butadiene, and morpholine as the model substrates. Yields of desired product 1 and byproducts 1a–1d were monitored by ^{1}H and ^{19}F NMR spectroscopy using an internal standard, and the results are summarised in Table 2.

The three-component coupling of S1, 1,3-butadiene, and morpholine using $Pd(PPh_3)_4$ (5 mol%), rac-BINAP (5 mol%), and K_2CO_3 (2.0 equiv.) in acetonitrile under 450 nm irradiation at 25 °C

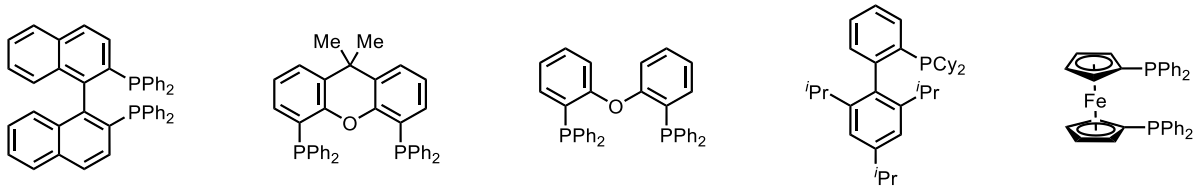
afforded the desired allylic amine product 1 in 82% yield with excellent E-selectivity (>50:1 E/Z), with full conversion of S1 and none of byproducts 1a–1d detected above 2% (entry 1, Table 2).

The influence of the palladium source was examined first. Substitution of $Pd(PPh_3)_4$ with $Pd(OAc)_2$ led to a marked decrease in both conversion (35%) and yield (28%), consistent with the requirement for a pre-formed Pd(0) complex capable of direct photoexcitation under visible light (entry 2, Table 2). $Pd_2(dba)_3$ was essentially ineffective, affording less than 2% yield from less than 5% conversion (entry 3, Table 2), indicating that the dba ligand suppresses productive photochemical activation, most likely by competing for coordination and attenuating the excited-state reducing power of the Pd(0) center. $(PhCN)_2PdCl_2$ afforded 32% yield from 41% conversion, with hydrodehalogenation byproduct 1d present at 3% as the principal side product, confirming that reduction to Pd(0) under these conditions is partial and inconsistent (entry 4, Table 2). Among all palladium sources examined, $Pd(PPh_3)_4$ was uniquely effective and was retained as the precatalyst of choice.



entry	changes from reaction conditions	conv. of **S1**/%	yield of **1**/%	E/Z of **1**	**1a:1b:1c:1d**
1	no change	>99	82	>50:1	<2:<2:<2:4
2	10 mol% *rac*-BINAP, 5 mol% $Pd(OAc)_2$	35	28	>50:1	<2:<2:<2:2
3	2.5 mol% $Pd_2(dba)_3$ instead of $Pd(PPh_3)_4$	<5	<2	ND	ND
4	5 mol% $(PhCN)_2PdCl_2$ instead of $Pd(PPh_3)_4$	41	32	>50:1	<2:<2:<2:3
5	Xantphos instead of *rac*-BINAP	>99	59	>50:1	<2:<2:<2:6
6	X-phos instead of *rac*-BINAP	>99	73	32:1	<2:<2:<2:7
7	DPEphos instead of *rac*-BINAP	>99	77	24:1	<2:<2:<2:3
8	dppf instead of *rac*-BINAP	37	13	>50:1	<2:<2:<2:2
9	KOAc instead of K_2CO_3	55	34	>50:1	<2:<2:<2:4
10	Cs_2CO_3 instead of K_2CO_3	>99	61	>50:1	6:<2:<2:5
11	K_3PO_4 instead of K_2CO_3	>99	71	>50:1	<2:<2:<2:5
12	$PhCF_3$ instead of MeCN	>99	72	>50:1	<2:<2:<2:12
13	w/o light	<5	<2	ND	ND
14	w/o *rac*-BINAP	>99	66	34:1	<2:<2:<2:12
15	w/o light, 100 °C, 48 h	29	4	>50:1	<2:<2:<2:5
16	w/o light, w/o *rac*-BINAP, 100 °C, 48 h	66	16	>50:1	<2:4:<2:9

ND = not detected



rac-BINAP Xantphos DPEphos X-phos dppf

Table 2. Optimisation of reaction conditions for the visible-light-induced three-component 1,4-aminoarylation of 1,3-butadiene with 1-bromo-3-fluoro-4-phenylbenzene (S1) and morpholine; byproducts arising from competing pathways are shown: 1a (Heck coupling), 1b (telomerization), 1c (Buchwald–Hartwig amination), and 1d (hydrodehalogenation).[106]

The effect of the ancillary ligand was then investigated with $Pd(PPh_3)_4$ held constant. Xantphos gave 59% yield with maintained E-selectivity (>50:1 E/Z) but an increase in hydrodehalogenation byproduct 1d to 6%, suggesting that this wide bite-angle geometry supports productive π-allyl substitution but at a cost to chemoselectivity (entry 5, Table 2). X-Phos and DPEphos each

afforded higher yields of 73% and 77% respectively, but with substantially reduced E/Z ratios of 32:1 and 24:1 (entries 6 and 7, Table 2), indicating that these ligand geometries permit productive reactivity yet compromise the stereochemical outcome of the π-allyl substitution step. In contrast, dppf afforded only 13% yield despite 37% conversion, with a byproduct distribution consistent with unproductive off-cycle pathways dominating (entry 8, Table 2), suggesting that the ferrocene-based bidentate framework is poorly suited to sustaining the photochemical manifold. These results demonstrate that bidentate phosphine ligands with appropriate geometry are required for both reactivity and E-selectivity, with rac-BINAP providing the optimal balance.

The base was varied next. KOAc gave reduced conversion (55%) and yield (34%), consistent with insufficient deprotonation of the morpholinium salt under the reaction conditions and a consequently slower rate of π-allyl substitution (entry 9, Table 2). Cs_2CO_3 maintained full conversion but afforded only 61% yield, with telomerization byproduct 1b detected at 6%, suggesting that the stronger basicity of cesium carbonate promotes off-cycle diene oligomerization (entry 10, Table 2). K_3PO_4 gave 71% yield with full conversion (entry 11, Table 2), indicating broad compatibility of inorganic phosphate bases, with K_2CO_3 remaining optimal overall.

The effect of the solvent was examined by replacing acetonitrile with $PhCF_3$. Full conversion was maintained and yield of product 1 reached 72%, but the hydrodehalogenation byproduct 1d increased substantially to 12% (entry 12, Table 2). This increase in 1d under $PhCF_3$ conditions indicates that acetonitrile provides superior chemoselectivity, consistent with its capacity to stabilise cationic palladium intermediates involved in the π-allyl substitution step and to moderate the reactivity of aryl radical intermediates in solution.

The photochemical requirement was confirmed by a series of control experiments. In the absence of light, conversion dropped to less than 5% and product yield to less than 2% (entry 13, Table 2), demonstrating that the transformation does not proceed via thermal activation under the standard conditions and is strictly dependent on visible-light excitation. Removal of rac-BINAP under otherwise standard conditions gave 66% yield but with reduced E-selectivity (34:1 E/Z) and a substantial increase in hydrodehalogenation byproduct 1d to 12% (entry 14, Table 2), highlighting the dual role of rac-BINAP in enforcing stereoselectivity at the π-allyl substitution step and in suppressing unproductive reductive dehalogenation within the catalytic cycle. Thermal activation at 100 °C in the absence of light afforded only 4% yield after 48 hours from 29% conversion (entry 15, Table 2), and conducting the same thermal reaction without rac-BINAP gave 16% yield from 66% conversion with 4% telomerization byproduct 1b and 9% hydrodehalogenation byproduct 1d (entry 16, Table 2), consistent with the low efficiency and poor selectivity reported under classical thermal aminoarylation conditions and confirming that the photochemical pathway is essential for productive and selective reactivity.[107,108]

A competing pathway that requires particular attention at the level of catalyst design is telomerization, which proceeds through a mechanistically distinct Pd(0)-catalyzed oxidative coupling pathway entirely independent of the radical manifold. In this process, Pd(0) promotes the oxidative coupling of two equivalents of 1,3-butadiene to generate a bis-π-allylpalladium intermediate, upon which nucleophilic attack by morpholine affords the C_8 telomer product 1b, a linear octa-2,7-dien-1-yl morpholine, without incorporation of any aryl fragment (Figure 40). The suppression of this pathway under the optimised conditions is attributable primarily to the role of rac-BINAP, as evidenced by the increase in 1d and the emergence of 1b observed upon its removal (entry 14, Table 2), and to the use of the aryl bromide as a radical trap that captures photoexcited Pd(0) before it can enter the thermal telomerization manifold.

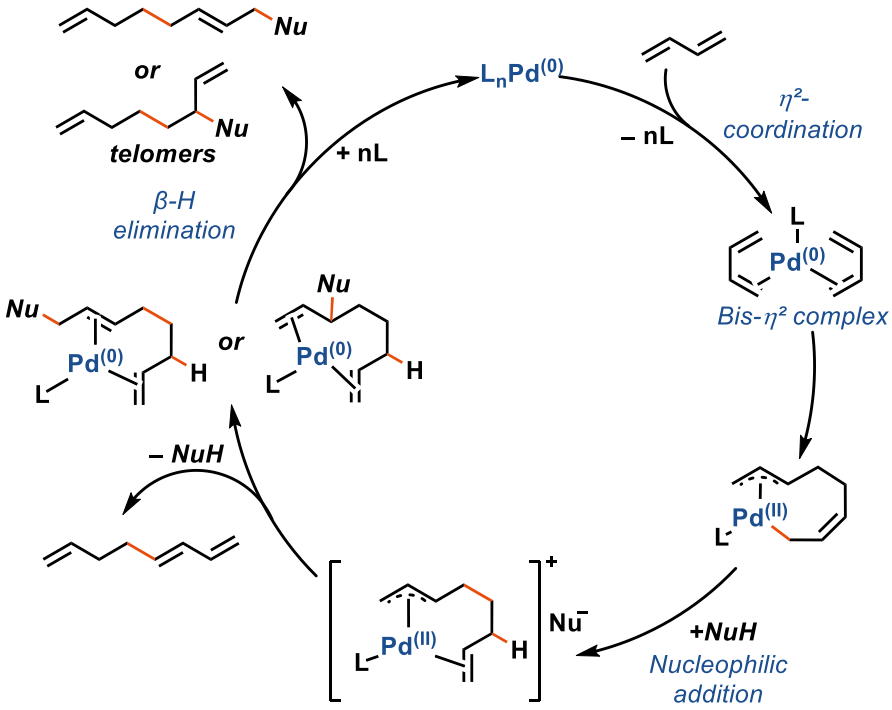


Figure 40. Telomerization mechanism showing the competing Pd(0)-catalyzed oxidative coupling of two equivalents of 1,3-butadiene to generate a bis-π-allylpalladium intermediate, followed by nucleophilic attack by nucleophile to afford the telomer products.[113]

Based on these results, $Pd(PPh_3)_4$, rac-BINAP, and K_2CO_3 in acetonitrile under 450 nm irradiation at 25 °C were identified as the optimal conditions and were carried forward for subsequent substrate scope investigations.

I.2.4 Substrate Scope

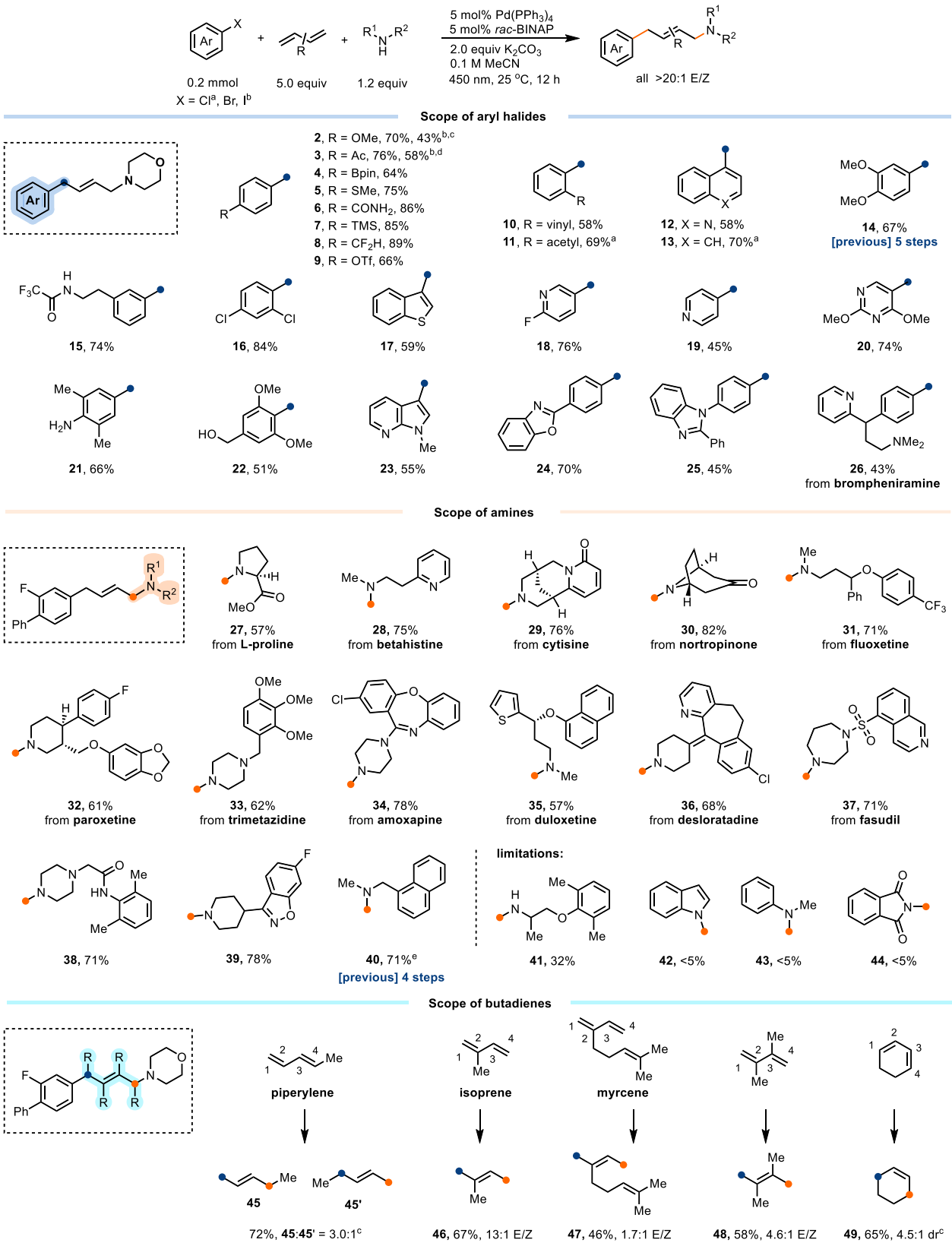


Figure 41. Substrate scope of the 1,4-aminoarylation of 1,3-butadiene via Photoinduced palladium catalysis. [a] aryl chloride used; [b] aryl iodide used; [c] 24 h; [d] 48 h; [e] bromobenzene used. Yields are isolated yields.

I.2.4.1 Scope of Aryl Halides

A broad range of aryl bromides was first examined. Electron-rich, neutral, and poor substrates all participated efficiently, affording allylamines in 43–89% yield with uniformly high *E*-selectivity. The absence of a clear electronic trend is consistent with a radical mechanism in which reactivity is governed primarily by C–X bond fragmentation kinetics rather than by the electronic demands of oxidative addition.

Electron-neutral and electron-poor aryl bromides gave consistently high yields. 4-Acetylbromobenzene afforded **3** in 76% yield, and electron-withdrawing groups were broadly tolerated, including carbonyl-containing substituents such as amide (**6**, 86%) and trifluoroacetamide (**15**, 74%), as well as difluoromethyl (**8**, 89%) and vinyl (**10**, 58%). These electrophilic functionalities, which are typically incompatible with classical palladium catalysis, remained intact under the present photochemical conditions.

Electron-donating groups were equally compatible. Aryl bromides bearing boronic acid pinacol ester (**4**, 64%), thioether (**5**, 75%), trimethylsilyl (**7**, 85%), and methoxy (**2**, 70%) substituents were all accommodated. 4-Bromodimethoxybenzyl alcohol (**22**, 51%), bearing a free primary alcohol, also reacted without protection, with the boronate and alcohol products providing useful handles for further derivatisation. Protic groups, which would require protection under classical Buchwald-Hartwig conditions, were tolerated without modification.

Substrates bearing potentially catalyst-inhibiting functionalities were also well tolerated, including free thioethers (**5**, 75%) and Lewis-basic pyridyl nitrogen atoms (**19**, 45%; **20**, 74%). Sterically demanding 2,6-disubstituted aryl bromides, which are typically sluggish in classical cross-coupling due to steric shielding during oxidative addition, reacted in moderate yield (**22**, 51%), consistent with the radical mechanism bypassing the steric demands of the two-electron pathway.

Heteroaryl bromides were also well tolerated. Benzothiophene (**17**, 59%), fluorobenzene (**18**, 76%), N-methylindole (**23**, 55%), benzofuran (**24**, 70%), benzimidazole (**25**, 45%), and pyrimidine (**20**, 74%) derivatives all afforded the desired allylamines. The compatibility of nitrogen-containing heterocycles is noteworthy, given their propensity to coordinate to palladium and inhibit catalysis under thermal conditions.

Aryl chlorides are inherently less reactive than aryl bromides, consistent with their more negative reduction potentials and slower mesolytic cleavage rates of the corresponding radical anions.[115,116] Nevertheless, 1-naphthyl chloride and 2-acetylphenyl chloride (**11**, **13**) afforded products in 69–70% yield under standard conditions, demonstrating that aryl chlorides, the most abundant and cost-effective class of aryl halides, are viable substrates. Importantly, the chemoselectivity of the transformation allows selective conversion of aryl bromides in the presence of aryl chlorides and aryl triflates (**9**, **16**), as triflates are not competent substrates under these conditions, providing a useful handle for selective functionalization in polyhalogenated molecules.

Aryl iodides, which are preferred aryl radical precursors over aryl bromides in many photoredox reactions owing to their less negative reduction potentials, afforded lower yields in this transformation.[116,117] This counterintuitive result is attributed to the rapid two-electron oxidative addition of aryl iodides to Pd(0) prior to photoexcitation, diverting the catalyst into the two-electron manifold before radical generation can occur. Consistent with this interpretation, electron-rich aryl iodides, which are less susceptible to thermal oxidative addition, provided higher conversions than electron-deficient aryl iodides. With extended reaction times (48 h), aryl iodides were converted to the corresponding allylamines in 43–58% yields (**2**, **3**).

I.2.4.2 Scope of Amines and Late-Stage Functionalization

The amine scope was next evaluated using 1-bromo-3-fluoro-4-phenylbenzene as the aryl partner. Secondary aliphatic amines proved optimal, affording allylamines in 57–82% yield. Cyclic amines, including morpholine, piperidine, and pyrrolidine, as well as bicyclic and acyclic dialkyl amines spanning five-, six-, and seven-membered ring systems, were all effective nucleophiles. The efficiency of these substrates reflects the rapid interception of the π-allylpalladium(II) intermediate by a strong nucleophile.

The utility of the method for late-stage functionalization of medicinally relevant compounds was demonstrated through the direct incorporation of complex amine fragments derived from bioactive molecules (compounds **27**–**37**). Allylamines were obtained in good yields from amines derived from L-proline (**27**, 57%), betahistine (**28**, 75%), cytisine (**29**, 76%), nortropinone (**30**, 82%), fluoxetine (**31**, 71%), paroxetine (**32**, 61%), trimetazidine (**33**, 62%), amoxapine (**34**, 78%), duloxetine (**35**, 57%), desloratadine (**36**, 68%), and fasudil (**37**, 71%). The successful functionalization of these structurally complex, polyfunctional amines without the need for protective group manipulation demonstrates the direct compatibility of the method with pharmaceutical synthesis.

Primary aliphatic amines (**41**, 32%) displayed significantly lower reactivity owing to their reduced nucleophilicity toward the π-allylpalladium(II) intermediate, leading to competitive Heck coupling as the dominant side pathway. Amines with poor nucleophilicity, including N-heteroaromatics, anilines, sulfonamides, imides, and carbamates (**42**–**44**), did not furnish the desired products (<5% yield), even in the presence of a strong base for deprotonation, reflecting the fundamental kinetic requirement for rapid nucleophilic attack on the allylpalladium(II) complex to compete with β-hydride elimination. Importantly, the selectivity differential between secondary aliphatic amines and the weaker nucleophiles allows for chemoselective allylation in the presence of amide and aniline functionalities (**15**, **21**, **38**), which is of synthetic value for the functionalization of polyfunctional molecules bearing multiple nitrogen-containing groups.

I.2.4.3 Scope of 1,3-Dienes

Substituted 1,3-dienes were examined to probe the influence of diene structure on reactivity and selectivity. Terminal substitution, as in piperylene (**45**), reduced conversion (~60% after 12 h) and

gave two regioisomeric products in a 3.0:1 ratio (72% combined yield), reflecting competing radical-addition orientations across the unsymmetrical diene and slower nucleophilic attack on the hindered π-allylpalladium intermediate.

Substituents at the internal 2-position of the diene, as in isoprene (**46**) and myrcene (**47**), did not significantly attenuate reactivity but resulted in mixtures of Z/E isomers (13:1 and 1.7:1, respectively), owing to 1,3-allylic strain in the substituted π-allylpalladium(II) intermediate that erodes the facial selectivity observed with unsubstituted butadiene. A 2,3-disubstituted butadiene afforded the tetrasubstituted allylamine **48** in 58% yield with 4.6:1 E/Z selectivity, demonstrating that even highly substituted diene systems are accessible substrates. 1,3-Cyclohexadiene afforded cyclic allylamine **49** in 65% yield with 4.5:1 dr, consistent with diastereoselective trapping of the π-allylpalladium complex from the less hindered face. Across all diene substrates, 1,2-addition products were not detected, confirming the complete regioselectivity of the radical addition step.

I.2.4.4 Synthetic Application: Synthesis of Clofilium

To further illustrate the synthetic utility of the method, the 1,4-aminoarylation was applied as the key step in the synthesis of clofilium (**51**), a quaternary ammonium antiarrhythmic agent.[118] The three-component coupling of 4-chlorobromobenzene, 1,3-butadiene, and triethylamine under the standard photochemical conditions afforded allylamine **50** in 81% yield with >20:1 E-selectivity. Subsequent hydrogenation and N-alkylation with ethyl iodide in acetone delivered clofilium (**51**) in 50% overall yield over three steps. This compares favorably with the previously reported four-step synthetic route, which afforded clofilium in only 24% overall yield.[119] The convergent single-step construction of the allylamine core from three commercially available components highlights the step-economy of the photocatalytic approach.

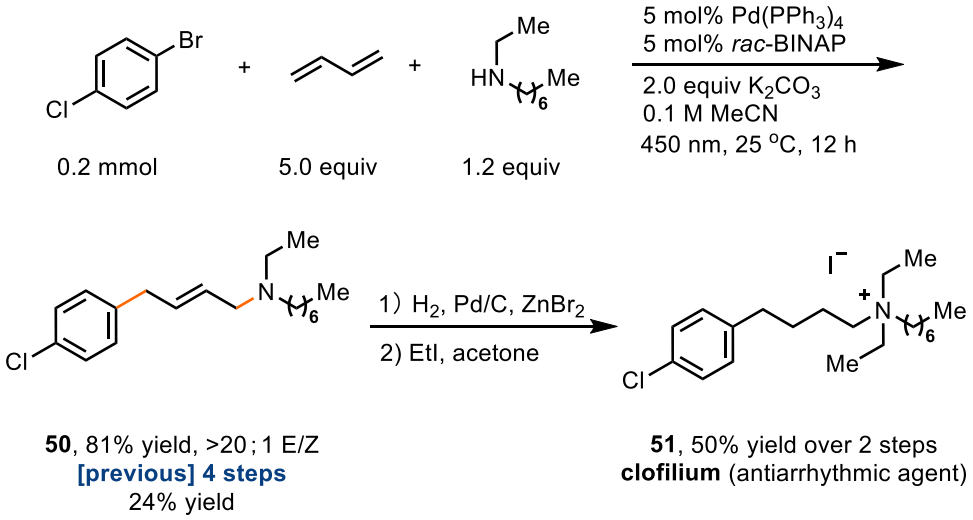


Figure 42. Synthesis of clofilium (**51**) using the visible-light-induced 1,4-aminoarylation of 1,3-butadiene as the key step, compared with the previously reported four-step route affording 24% overall yield.[119]

I.2.4.5 Limitations of the Substrate Scope

Despite the broad substrate scope and demonstrated utility in the synthesis of pharmaceutically relevant molecules, several limitations were identified across each component class (Figure 43).[106] Within the aryl halide series, substrates bearing sensitive functional groups such as epoxides gave only moderate yields (48%), reflecting competing ring-opening under the reaction conditions. Electron-deficient heterocyclic bromides, including imidazole and pyrimidine derivatives, gave diminished yields of 40% and 31%, respectively. Substrates with mesolytic cleavage rate constants k_c below 10^5 s^{-1}, such as thiazole- and thiophene-based aryl bromides, afforded less than 5% yield, consistent with slow radical anion fragmentation allowing back electron transfer to outcompete productive C–X bond cleavage. Aryl chlorides gave only trace to moderate yields of 6–23%, consistent with less favorable activation under the reaction conditions, whilst aryl triflates were not compatible, affording less than 5% yield. 4-Fluoroiodobenzene gave 43% yield despite its weaker C(sp^2)–I bond, suggesting that competing ground-state oxidative addition reduces access to the photoexcited pathway.

Within the amine series, secondary aliphatic amines were required for productive reactivity. Primary aliphatic amines (**41**) gave low yields of 28–29% with significant Heck coupling byproduct formation, consistent with reduced nucleophilicity toward the π-allylpalladium(II) intermediate compared with secondary amines. Weakly nucleophilic amines, including anilines, N-heteroaromatics, sulfonamides, imides, and carbamates (**42**–**44**), gave less than 5% yield under the standard conditions and did not furnish the desired product even in the presence of a strong base, establishing a minimum nucleophilicity requirement for productive π-allyl substitution. The relationship between amine nucleophilicity and reaction outcome is examined quantitatively in the mechanistic investigations.

Within the diene series, reactivity and selectivity were sensitive to substitution pattern. 1-Substituted dienes such as piperylene gave approximately 60% conversion after 12 hours with reduced yield, attributed to slower nucleophilic attack at the more sterically hindered π-allylpalladium intermediate. 2-Substituted dienes, including isoprene and myrcene, maintained conversion but resulted in mixtures of E/Z isomers, consistent with reduced geometric control in the substituted π-allylpalladium intermediate. Cyclooctadiene gave less than 5% yield, indicating that conformationally restricted cyclic dienes are poorly compatible, likely owing to steric constraints affecting both radical addition and subsequent nucleophilic trapping.

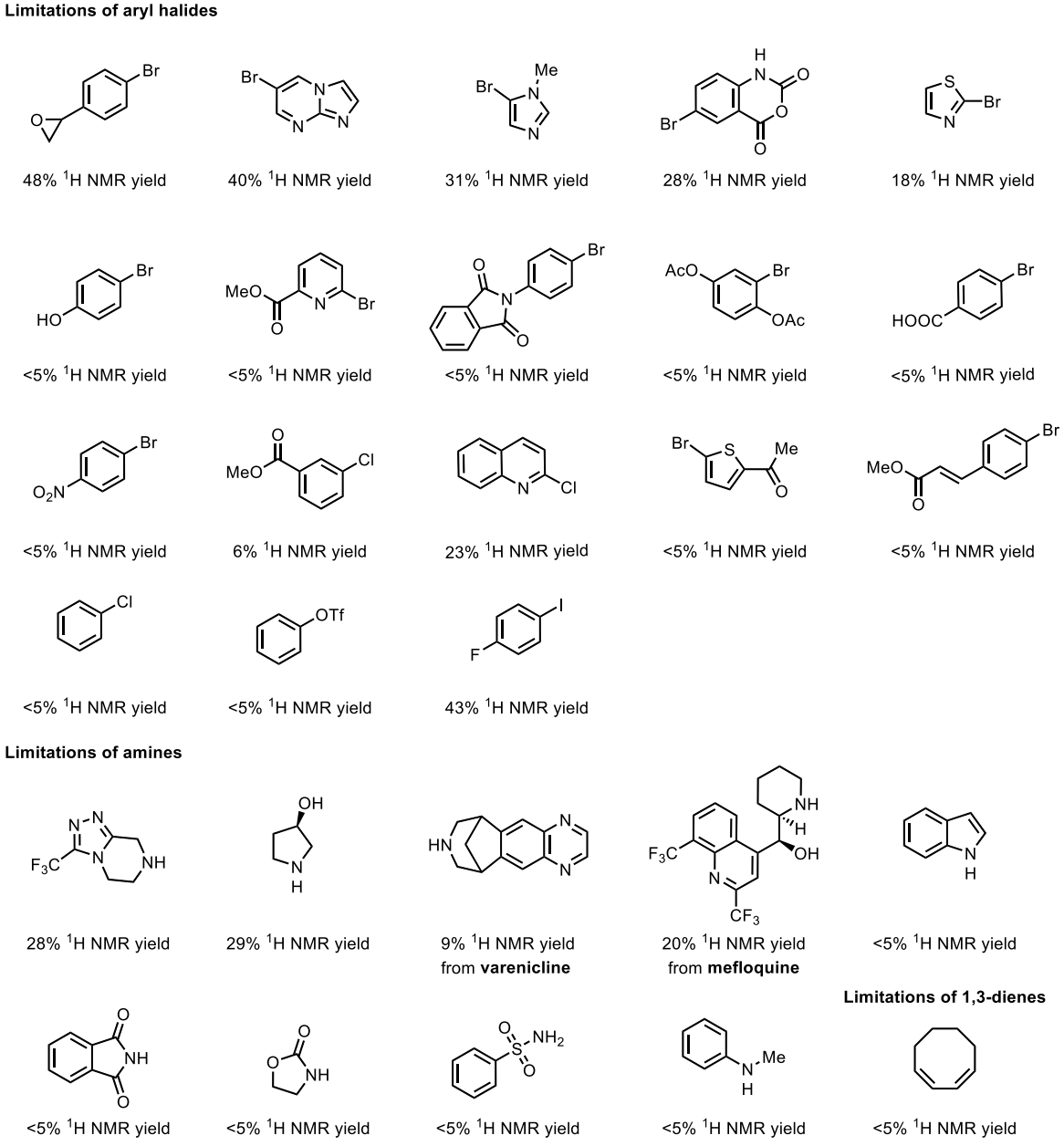


Figure 43. Unsuccessful substrates for the 1,4-aminoarylation of 1,3-butadiene via Photoinduced palladium catalysis, showing limitations across aryl halide (A), amine (B), and diene (C) component classes.

I.2.5 Mechanistic Investigations

I.2.5.1 Control Experiments

The photochemical requirement for the 1,4-aminoarylation was established through a series of control experiments, the results of which are summarised in Table 2. In the absence of light, conversion dropped to less than 5% and the yield of product 1 to less than 2% (entry 13, Table 2), demonstrating that the transformation does not proceed via thermal activation under the standard conditions and is strictly dependent on visible-light excitation. Heating to 100 °C without irradiation for 48 hours afforded only 4% yield from 29% conversion (entry 15, Table 2), and conducting the same thermal reaction without rac-BINAP gave 16% yield from 66% conversion (entry 16, Table 2), consistent with the low efficiency and poor chemoselectivity reported under

classical thermal aminoarylation conditions.[107,108]

Removal of rac-BINAP under otherwise standard photochemical conditions maintained full conversion and afforded 66% yield of product 1. However, the E/Z ratio decreased from greater than 50:1 to 34:1, and hydrodehalogenation byproduct 1d increased substantially to 12% (entry 14, Table 2), demonstrating two distinct roles for rac-BINAP within the catalytic cycle. First, rac-BINAP governs the stereochemical outcome of the Tsuji–Trost allylation step, as evidenced by the erosion of E-selectivity upon its removal. Second, rac-BINAP suppresses unproductive reductive dehalogenation, as evidenced by the increase in byproduct 1d, most likely by stabilising the Pd(I) intermediate and preventing premature reduction within the catalytic cycle.

I.2.5.2 UV–Vis Absorption Study

To identify the operative chromophore under the reaction conditions, UV–Vis absorption spectra of the individual reaction components and their combinations were recorded in acetonitrile (Figure 44).[106] $Pd(PPh_3)_4$ alone absorbs to approximately 400 nm. Addition of rac-BINAP produces a broad absorption extending to 500 nm, consistent with formation of a Pd–BINAP complex in solution. The complete reaction mixture closely resembles this Pd–BINAP profile, identifying the palladium–BINAP complex as the operative chromophore and confirming its competence to absorb 450 nm irradiation under the standard conditions. Addition of 1,3-butadiene, aryl bromide S1, or morpholine did not alter the absorption profile, ruling out these components as light-absorbing species and establishing that excitation occurs exclusively at the palladium–BINAP complex.

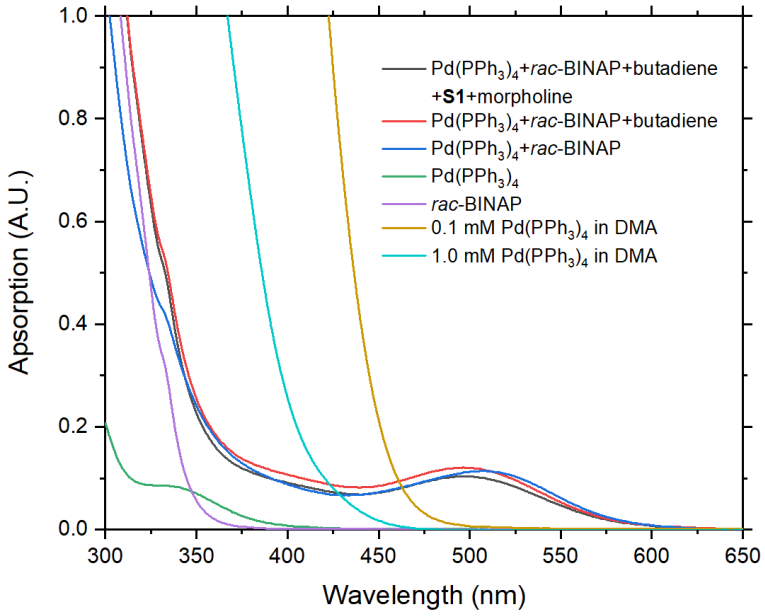


Figure 44. UV–Vis absorption spectra of $Pd(PPh_3)_4$, rac-BINAP, and their combinations with reaction components in acetonitrile, identifying the palladium–BINAP complex as the operative chromophore under 450 nm irradiation.[106]

I.2.5.3 Radical Trapping Experiments with TEMPO

The intermediacy of free radical species within the catalytic cycle was established by conducting the reaction in the presence of 2,2,6,6-tetramethylpiperidine-1-oxyl (TEMPO, 2.0 equiv.) as a

radical scavenger.[106] Formation of product 1 was fully suppressed, and overall conversion was reduced to approximately 5%, consistent with the interception of radical intermediates prior to productive catalytic turnover. High-resolution mass spectrometry identified two TEMPO adducts in the reaction mixture (Figure 45). Adduct 52 (calcd for $C_{21}H_{27}FNO$ $[M+H]^+$, 328.2071; found, 328.2071; deviation +0.2 ppm) corresponds to the aryl radical adduct, confirming generation of Ar• from S1 under the photocatalytic conditions. Adduct 53 (calcd for $C_{25}H_{33}FNO$ $[M+H]^+$, 382.2541; found, 382.2541; deviation −0.1 ppm) corresponds to the homoallylic radical adduct formed after addition of Ar• to 1,3-butadiene, providing direct evidence for the allylic radical intermediate proposed in the catalytic cycle. The detection of both 52 and 53 establishes that aryl radical generation and subsequent radical addition to butadiene are both kinetically accessible steps under the reaction conditions.

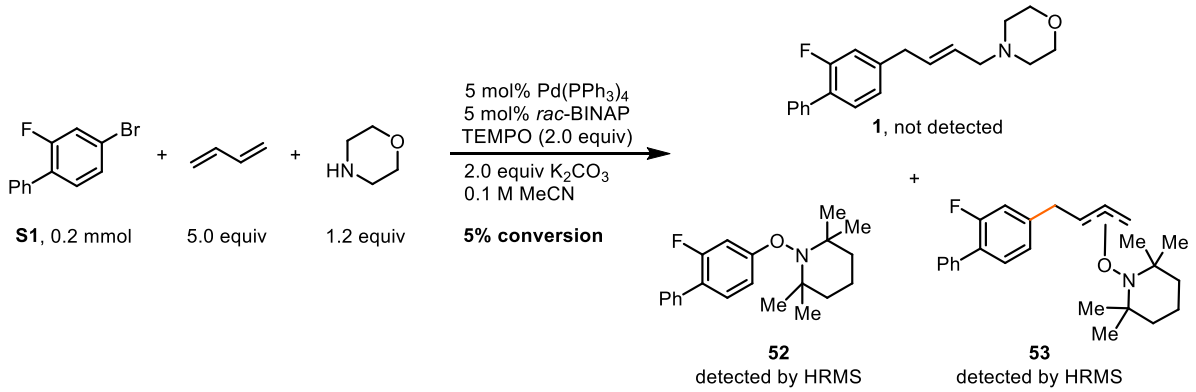


Figure 45. Radical trapping experiment with TEMPO (2.0 equiv.) showing suppression of product 1 and detection of aryl radical adduct 52 and homoallylic radical adduct 53 by HRMS.

I.2.5.4 Detection of the π-Allylpalladium(II) Intermediate

Direct evidence for the π-allylpalladium(II) intermediate was obtained by quenching the reaction at −78 °C after one hour of irradiation and analysing the mixture immediately by electrospray ionisation mass spectrometry.[106] Allyl–Pd(II)–Br complex Pd-1, incorporating the rac-BINAP ligand, bromide, and the aryl-functionalized allyl fragment derived from S1 and 1,3-butadiene, was detected by ESI-MS and confirmed by exact mass measurement (calcd for $C_{60}H_{46}FP_2Pd$ $[M-Br]^+$, 953.2088; found, 953.2090; deviation −0.2 ppm) (Figure 46). The detection of Pd-1 under catalytic conditions is consistent with its role as the electrophilic π-allylpalladium(II) species intercepted by the amine nucleophile in the Tsuji–Trost allylation step, and supports the proposed Pd(0)/Pd(I)/Pd(II)/Pd(0) oxidation state sequence.

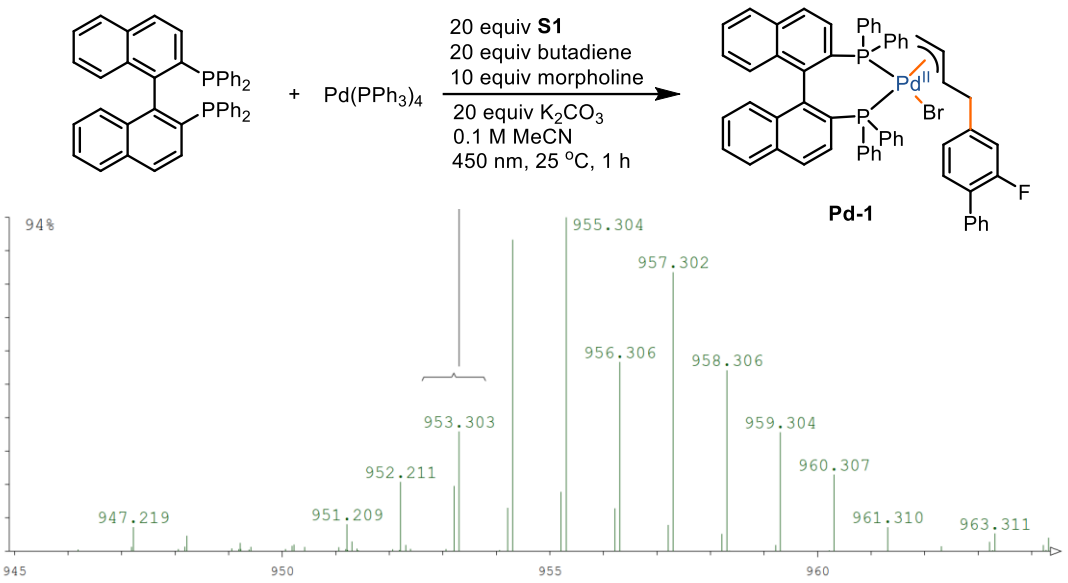


Figure 46. High-resolution mass spectrum of π-allylpalladium(II) complex Pd-1, detected by ESI-MS after quenching the reaction at −78 °C following 1 hour of irradiation.[106]

I.2.5.5 Correlation of Reactivity with Reduction Potential and Mesolytic Cleavage Rate

To probe the mechanism of aryl radical generation from aryl bromides, the reaction was evaluated with a series of aryl halides of systematically varied reduction potential (E°) and mesolytic cleavage rate constant kc of the corresponding radical anion (Table 3, Figure 47).[106] Aryl halides with k_c above 10^5 s^{-1} afforded yields above 74% within 12 hours irrespective of halide type, whilst substrates with lower kc values gave reduced yields that improved with extended reaction times of 48 hours. This behavior is consistent with slow mesolytic cleavage of the $ArX^{\bullet -}$ radical anion competing with unproductive back electron transfer (BET) from $ArX^{\bullet -}$ to L–Pd(I), which regenerates ground-state Pd(0) and ArX without productive radical formation. A positive correlation between yield and reduction potential E° further supports an SET/mesolytic cleavage component, in which more easily reduced aryl halides generate $ArX^{\bullet -}$ more efficiently and thereby increase the probability of productive C–X bond fragmentation before BET can occur (Figure 48).

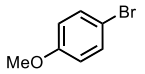
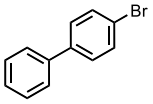
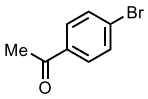
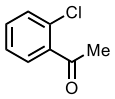
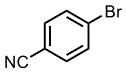
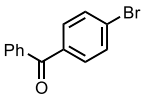
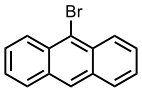
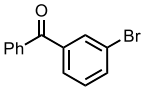
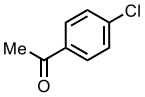
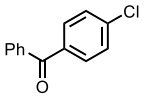
aryl halides	reduction potentials/E°	log k_c	time	conv.	yield	yield of Heck byproduct
	-2.72	–	12 h	>99%	74%	<2%
	-2.43	10.5	12 h	>99%	88%	<2%
	-1.84	7.5	12 h	>99%	81%	9%
	-2.21	7.4	12 h	87%	76%	<2%
	-1.90	5.5	12 h	>99%	75%	3%
	-1.94	8.7	12 h	>99%	74%	10%
	-1.63	4.95	12 h 48 h	25% 71%	28% 53%	<2% 3%
	-1.70	5.9	12 h	>99%	26%	<2%
	-1.53	2.9	12 h 48 h	16% 87%	12% 72%	<2% 3%
	-1.90	3.5	12 h 48 h	24% 55%	10% 22%	<2% 3%
	-1.64	1.7	12 h 48 h	<5% 15%	<1% <1%	<2% <2%

Table 3. Reaction yields as a function of reduction potential (E°) and mesolytic cleavage rate constant (k_c) of aryl halides.[106]

Notably, 4-bromoanisole (E° = −2.72 V vs SCE) participated with greater than 99% conversion and 74% yield despite possessing one of the most negative reduction potentials in the series and a kc value that could not be reliably determined (Figure 47). This reactivity is exceptional for reactions employing aryl halides as aryl radical precursors via SET, and is attributed either to a direct halogen atom transfer (XAT) pathway, which is not subject to the same thermodynamic constraints as SET, or to the strong reducing power of photoexcited $Pd(PPh_3)_4$, reported at E°red = −2.51 V vs Fc^+/Fc.[120]

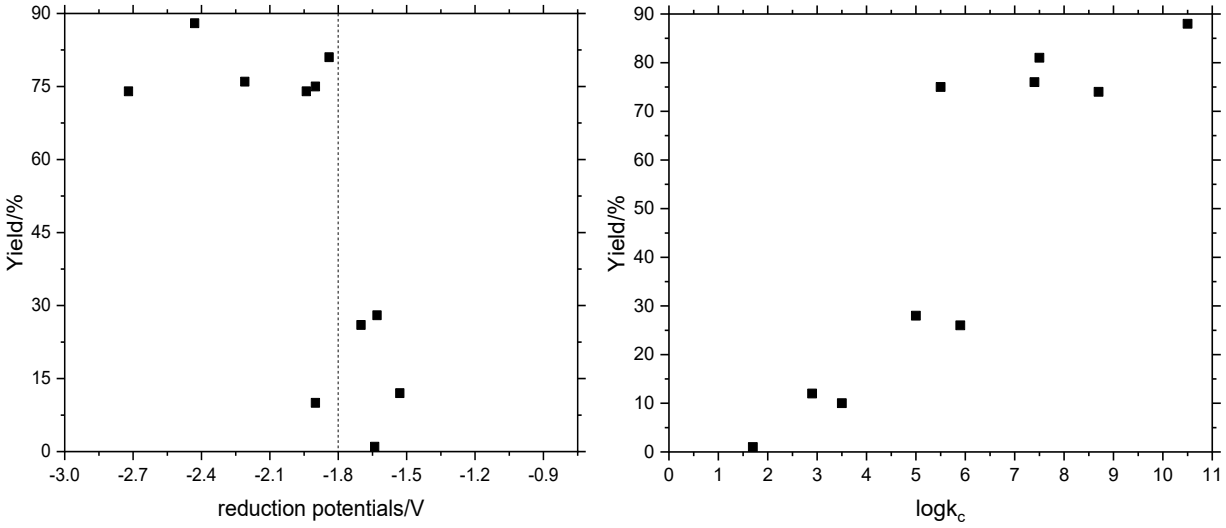


Figure 47. Correlation of isolated yield with reduction potential E° (left) and log k_n (right), and three-dimensional representation showing the combined dependence.

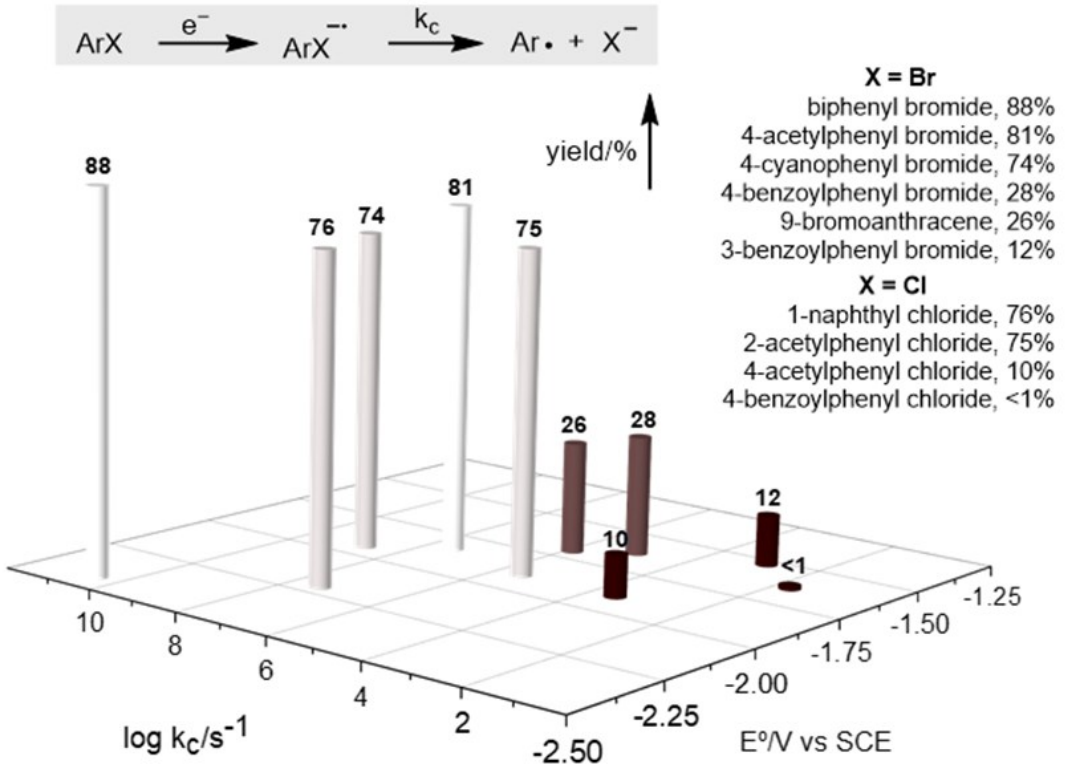


Figure 48. Relationship between the yields achieved in the reactions and the reduction potential (E°) of aryl halides and dissociation rate constant of the corresponding radical anion (k_c).

I.2.5.6 Hammett Analysis

A Hammett competition experiment was conducted by reacting phenyl bromide and a series of para-substituted aryl bromides (0.5 equiv. each) under standard conditions with a limiting quantity of morpholine (0.2 equiv.), such that relative rates could be determined from product ratios at low conversion. A linear free energy relationship was obtained (R^2 = 0.84) with a reaction constant ρ = +0.5 (Figure 49). The small positive value of ρ indicates modest accumulation of negative charge at the reaction center in the transition state for C–X bond fragmentation, consistent with partial electron transfer from palladium to the aryl halide at the transition state. The limited magnitude of ρ reflects the restricted delocalisation of negative charge into the aromatic π-system at the transition state, which rationalises the broad electronic tolerance observed across the aryl halide substrate scope and is consistent with both XAT and SET/mesolytic cleavage pathways contributing to aryl radical generation.

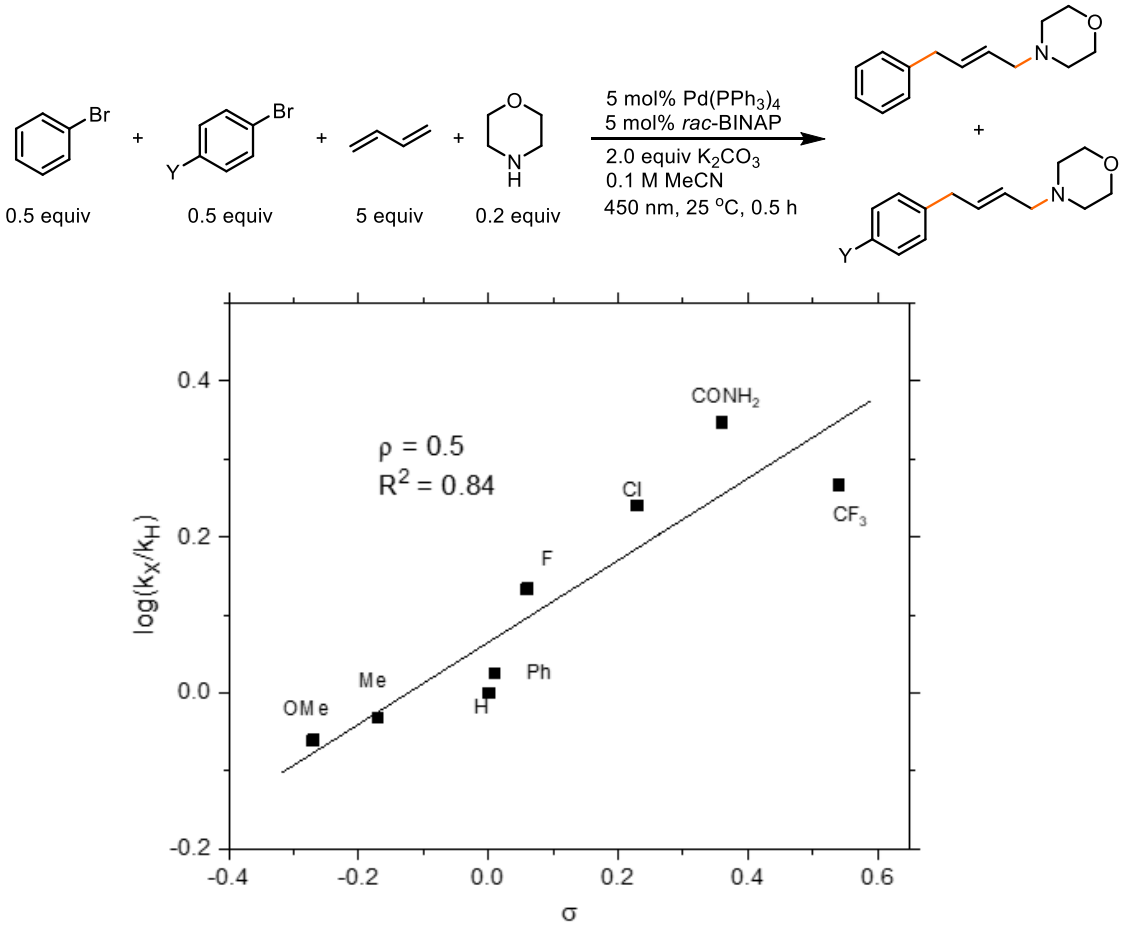


Figure 49. Hammett correlation for the visible-light-induced 1,4-aminoarylation of 1,3-butadiene using para-substituted aryl bromides in competition with phenyl bromide.[106]

I.2.5.7 Aryl Iodide Reactivity and Mechanistic Implications

The behavior of aryl iodides under the standard reaction conditions provided additional mechanistic insight into the mode of palladium activation (Table 4).[106] Despite possessing weaker C–X bonds and less negative reduction potentials than the corresponding aryl bromides, aryl iodides afforded markedly lower yields of 15–55% and required extended reaction times. More significantly, reactivity within the aryl iodide series was inversely correlated with electron-withdrawing character: 4-iodoanisole gave 42% yield at 12 hours, whilst 4-iodotrifluoromethylbenzene gave only 5% yield. This trend is opposite to what would be expected from SET or XAT kinetics alone, where electron-deficient aryl halides with less negative reduction potentials and faster mesolytic cleavage rates would be predicted to give higher yields.

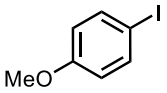
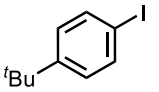
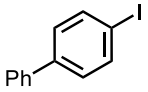
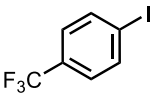
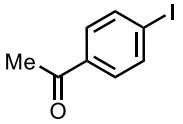
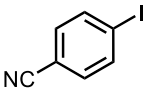
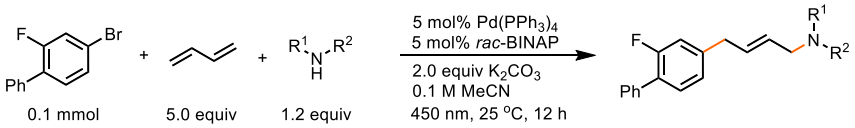
aryl halides	time	conv.	yield
	12 h	85%	42%
	24 h	>99%	55%
	12 h	42%	21%
	12 h	45%	15%
	12 h	34%	5%
	12 h	49%	22%
	48 h	>99%	62%
	12 h	40%	12%
	48 h	83%	43%

Table 4. Reaction yields for aryl iodides of varied electronic character in the visible-light-induced 1,4-aminoarylation of 1,3-butadiene.[106]

This counterintuitive electronic trend is attributed to competitive two-electron oxidative addition of aryl iodides to ground-state Pd(0) prior to photoexcitation, which diverts the catalyst into the classical two-electron Pd(0)/Pd(II) manifold before radical generation can occur. Electron-rich aryl iodides, being inherently less reactive toward oxidative addition, remain more available for activation via the photoexcited Pd(0) pathway, which accounts for their superior performance relative to electron-deficient aryl iodides within this series. This interpretation is fully consistent with the observation that extended reaction times improve yields for aryl iodides, since slower oxidative addition at room temperature under continuous irradiation allows a greater fraction of the catalyst to be intercepted in the excited state.

I.2.5.8 Amine Nucleophilicity and the π-Allylpalladium Interception Step

The Tsuji–Trost allylation step was probed systematically using a series of amines of varying nucleophilicity, as quantified by Mayr and co-workers' nucleophilicity parameter N.[121] The results are summarised in Table 5.[106] Pyrrolidine (N = 18.64) afforded 79% yield of the desired allylamine with only 8% Heck coupling byproduct 1a. Trimethylamine (N = 15.10) gave 62% yield, benzylamine (N = 14.29) gave 42% yield with 13% Heck byproduct, and tert-butylamine (N = 12.35) gave only 22% yield, accompanied by 40% Heck coupling byproduct (Table 5).



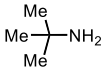
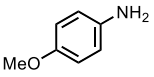
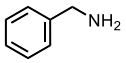
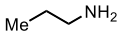
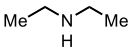
amines	*N* Parameter	conv.	yield	yield of Heck byproduct	yield of hydrodefunctionalization byproduct
	12.35	>99%	22%	40%	3%
	13.42	94%	34%	18%	2%
	13.77	>99%	27%	15%	6%
	14.29	>99%	42%	13%	5%
	15.11	>99%	48%	10%	5%
	15.10	>99%	62%	24%	5%
	18.64	>99%	79%	8%	8%

Table 5. Correlation of amine nucleophilicity (Mayr N parameter)[121] with isolated yield of allylamine product 1 and Heck coupling byproduct 1a formation in the visible-light-induced 1,4-aminoarylation of 1,3-butadiene.[106]

The progressive increase in Heck coupling byproduct 1a with decreasing N value confirms that β-hydride elimination from the π-allylpalladium(II) intermediate competes directly with nucleophilic substitution by the amine. At sufficiently low N values, β-hydride elimination becomes the dominant pathway, and Heck coupling product 1a is the major product. These data establish that the Tsuji–Trost allylation step is selectivity-determining with respect to the amine component, and define a minimum nucleophilicity threshold below which productive π–allyl substitution cannot compete with β-hydride elimination under the standard conditions. This quantitative nucleophilicity dependence also accounts for the practical limitations of the amine substrate scope described in

section I.2.4.5, where primary amines, anilines, sulfonamides, and carbamates all fall below this threshold.

I.2.5.9 Proposed Catalytic Cycle

The mechanistic data presented in sections I.2.5.1–I.2.5.8 are collectively consistent with the Pd(0)–Pd(I)–Pd(II)–Pd(0) catalytic cycle shown in Figure 50.[106] Photoexcitation of the L–Pd(0) complex (L = PPh_3 or rac-BINAP) under 450 nm irradiation generates the excited-state species L–Pd(0)*, identified as the operative chromophore by UV–Vis absorption spectroscopy (section I.2.5.2). This excited species activates aryl bromides via SET, XAT, or a combination of both pathways, generating the aryl radical Ar• and L–Pd(I)–Br. The Hammett analysis (ρ = +0.5) and the k_c/E° correlations are consistent with both pathways contributing without permitting a definitive mechanistic assignment. For substrates with slow mesolytic cleavage, unproductive BET from $ArX^{\bullet -}$ to L–Pd(I) competes with productive C–X bond fragmentation, accounting for the reduced yields observed at low kc values.

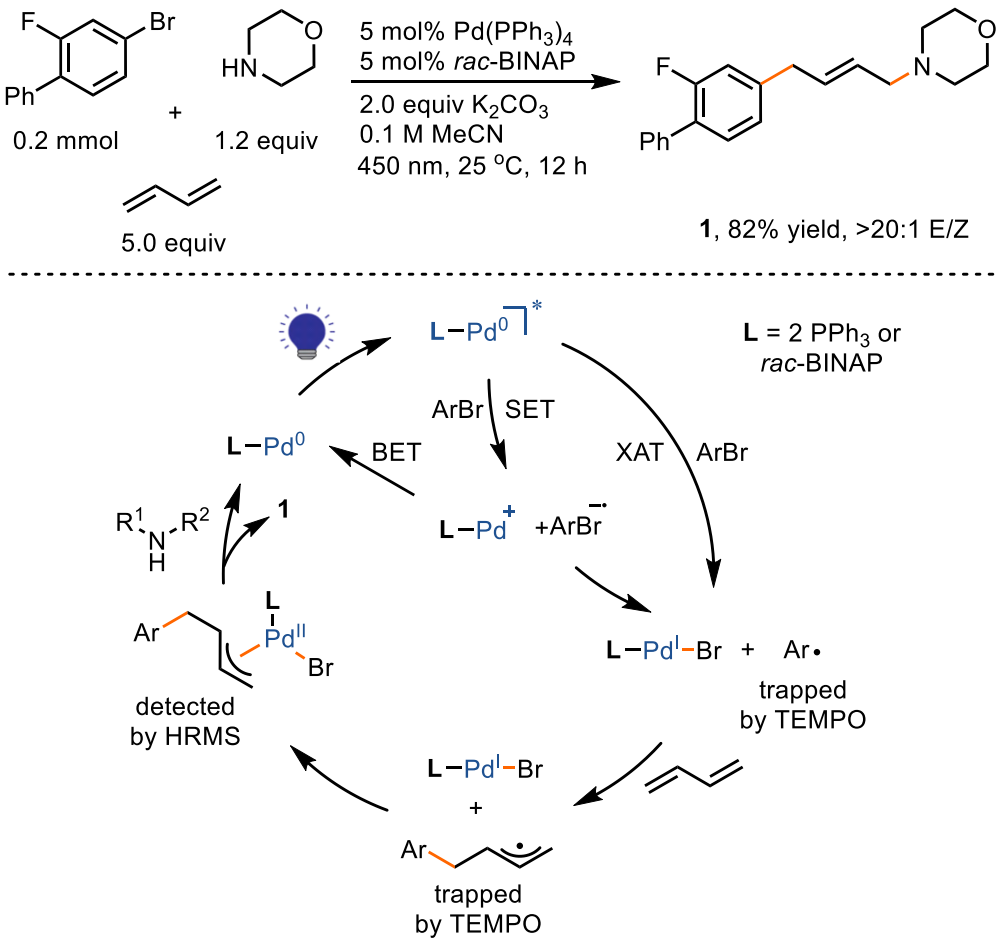


Figure 50. Proposed catalytic cycle for 1,4-aminoarylation of 1,3-butadiene via photoinduced palladium catalysis, showing aryl radical generation via SET or XAT from photoexcited L–Pd(0)*, radical addition to butadiene, oxidative ligation to afford the π-allylpalladium(II) intermediate, and Tsuji–Trost allylation to deliver the allylamine product.

The aryl radical Ar• adds regioselectively to the terminal carbon of 1,3-butadiene, generating a homoallylic radical intermediate, the formation of which was confirmed by TEMPO trapping and HRMS detection of adduct S52 (section I.2.5.3). The homoallylic radical undergoes oxidative

ligation to L–Pd(I)–Br to afford the π-allylpalladium(II) complex, confirmed by direct ESI-MS detection of Pd-1 (section I.2.5.4). Nucleophilic attack by the secondary aliphatic amine on the π-allylpalladium(II) complex via Tsuji–Trost allylation delivers the allylamine product with greater than 20:1 E-selectivity, controlled by the rac-BINAP ligand (section I.2.5.1), and regenerates L–Pd(0) to close the catalytic cycle.

The mechanistic data do not permit a definitive distinction between SET and XAT pathways for aryl radical generation, and both are likely operative depending on substrate electronics. The exceptional reactivity of 4-bromoanisole despite its highly negative reduction potential suggests a direct XAT contribution for electron-rich substrates, whilst the positive k_c/E° correlations support SET involvement for more easily reduced aryl halides. This mechanistic duality is consistent with the broad electronic tolerance observed across the aryl halide substrate scope and represents a distinctive feature of photoexcited palladium catalysis relative to conventional photoredox systems.

I.2.6 Conclusion

A visible-light-induced three-component 1,4-aminoarylation of 1,3-butadiene has been developed using photoexcited palladium catalysis, providing direct access to aryl-substituted allylamines from commercially available aryl halides and aliphatic amines in a single synthetic step with excellent E-selectivity.[106] The transformation proceeds via a radical Pd(0)/Pd(I)/Pd(II)/Pd(0) manifold, bypassing the limitations of classical thermal aminoarylation and enabling mild reaction conditions at room temperature that are broadly compatible with sensitive functional groups. A wide range of aryl bromides, secondary aliphatic amines, and substituted 1,3-dienes were accommodated, including complex pharmaceutical fragments demonstrated through the late-stage functionalization of eleven bioactive molecules and the concise three-step synthesis of the antiarrhythmic agent clofilium in 50% overall yield, compared with 24% over four steps by the previously reported route.[119,122] The method is limited to secondary aliphatic amines, as weakly nucleophilic amines fail to intercept the π-allylpalladium(II) intermediate competitively, and aryl triflates and strongly electron-deficient heterocyclic bromides are not compatible under the standard conditions.

CHAPTER II — PHENOL SYNTHESIS FROM FLUORINATED DRUG SCAFFOLDS AS A PRECURSOR STRATEGY FOR ^{18}F-RADIODEOXYFLUORINATION

II.1 Introduction

II.1.1 Positron Emission Tomography: Physical Basis, Historical Development, and Clinical Significance

Positron emission tomography (PET) is a non-invasive nuclear imaging modality that enables quantitative three-dimensional mapping of radiolabeled compounds within living organisms. The physical basis of the technique rests on positron–electron annihilation: a positron emitted from a decaying radionuclide travels a short distance in tissue before annihilating with an electron, producing two coincident 511 keV gamma photons emitted at approximately 180° to one another (Figure 51).[123] Detection of these collinear photon pairs by a circumferential scintillation detector array enables tomographic reconstruction of the tracer's spatial concentration profile, with sensitivity extending to the picomolar regime and thereby exceeding the detection limits of conventional anatomical imaging by several orders of magnitude.[123]

The conceptual foundations of PET were established by Wrenn, Good, and Handler in 1951 through the proposal of positron-emitting radioisotopes for tumor localization.[124] The technique was subsequently realized instrumentally with the construction of the first dedicated PET scanner by Ter-Pogossian and co-workers in 1975.[125] Over subsequent decades, PET evolved from a specialized research tool into a clinically established modality with applications across oncology, neurology, and cardiology. A defining distinction between PET and anatomical imaging modalities such as computed tomography (CT) or magnetic resonance imaging (MRI) lies in the nature of the detected signal: whereas CT and MRI report structural variation, PET directly measures biochemical and molecular processes in vivo.[123] These processes frequently precede macroscopic pathology and are therefore inaccessible to structural imaging. This capacity to quantify early-stage biological function underpins PET's central role in drug development, enabling non-invasive measurement of target engagement, biodistribution, and pharmacokinetic–pharmacodynamic relationships in living systems.[123]

The information content of a PET experiment is defined entirely by the chemical structure of the administered tracer. Two broad classes of tracers can be distinguished. Radiolabeled drug analogs provide direct information on the pharmacokinetics and target engagement of the labeled compound, whilst receptor-targeted radiotracers report on the abundance and accessibility of a specific molecular target. In both cases, the imaging output is inseparable from molecular structure, and tracer synthesis therefore defines the accessible chemical space of PET imaging rather than serving solely as an enabling step.[123] This dependence places synthetic methodology at the center of PET tracer development and establishes arene fluorination as a central transformation for accessing structurally diverse radiotracers.

The dominance of fluorine-18 across approved radiopharmaceuticals is reflected in the breadth of clinically deployed tracers spanning diverse structural classes. Clinically approved tracers spanning oncology, neurology, and metabolic imaging, including glucose metabolism agents, amino acid analogs, and tau protein imaging agents, demonstrate that a single radiochemical strategy based on arene fluorination provides access to mechanistically and structurally distinct biological targets.[123,126] Despite substantial variation in molecular architecture and function, these tracers share a requirement for late-stage fluorine-18 incorporation into structurally complex frameworks, underscoring the central role of synthetic methodology in tracer design. Small molecules constitute the dominant targeting vector class across approved diagnostic radiopharmaceuticals, substantially exceeding peptide- and antibody-based constructs in number, and fluorine-18 is used predominantly in oncological and neurodegenerative disease imaging.[126] This distribution establishes that PET imaging is predominantly enabled by fluorine-18-labeled small molecules, and it is this class of tracer that defines the synthetic challenge addressed in the present work.

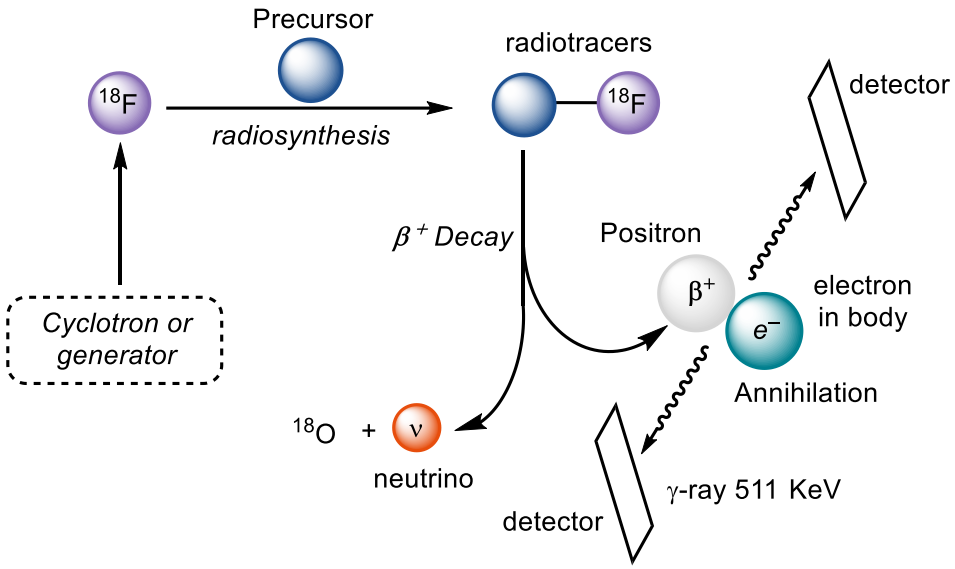


Figure 51. Principle of positron emission tomography (PET).[125]

II.1.2 Radionuclides and FDA-Approved ^{18}F Tracers

Several positron-emitting radionuclides have been employed in clinical and research PET; however, their utility is governed by nuclear decay characteristics, production accessibility, and compatibility with synthetic chemistry (Table 6).[123,127] Carbon-11 (t½ = 20.4 min) is isotopically well-suited for incorporation into organic molecules and is widely used in neuroimaging, but its short half-life confines radiosynthesis, purification, and quality control to facilities equipped with an on-site cyclotron, thereby precluding distribution beyond the site of production.[127] Nitrogen-13 (t½ = 9.97 min) and oxygen-15 (t½ = 2.04 min) impose even stricter constraints, limiting their application to rapid, single-step radiosyntheses performed in immediate proximity to the imaging facility.[127] Gallium-68 (t½ = 67.7 min), in contrast, is generator-produced and well-suited to peptide-based imaging, particularly in neuroendocrine tumor and prostate-specific membrane

antigen applications; however, its coordination-driven chemistry restricts its use primarily to biomolecular constructs and limits its applicability to small-molecule, multi-step organic radiosynthesis.[126]

Isotope	Half-life	Production	Max β^+ Energy (keV)	Decay Mode	Typical Application
^{11}C	20.4 min	$^{14}N(p,\alpha)^{11}C$	960	β^+ (99.8%)	Neuroimaging, receptor studies
^{13}N	9.97 min	$^{16}O(p,\alpha)^{13}N$	1190	β^+ (99.8%)	Cardiac perfusion
^{15}O	2.04 min	$^{14}N(d,n)^{15}O$	1720	β^+ (99.9%)	Blood flow, oxygen metabolism
^{18}F	109.7 min	$^{18}O(p,n)^{18}F$	635	β^+ (97%), EC (3%)	Oncology, neurology, drug development
^{68}Ga	67.7 min	$^{68}Ge/^{68}Ga$ generator	836	β^+ (89%)	Neuroendocrine tumours, PSMA imaging

Table 6. Comparison of common PET radionuclides and their key properties.[128]

Fluorine-18 (t½ = 109.7 min) occupies a distinct position within this landscape. Its half-life permits multi-step radiosynthesis, analytical quality control, and distribution of the finished tracer from a centralised radiopharmacy to distant imaging centers, whilst remaining sufficiently short to maintain acceptable radiation exposure to the patient.[123] Its low positron emission energy (E_{max} = 635 keV) results in a short positron range in tissue of approximately 0.6 mm, which directly translates into high spatial resolution.[123,127] Fluorine-18 is produced via proton bombardment of ^{18}O-enriched water through the $^{18}O(p,n)^{18}F$ nuclear reaction, affording no-carrier-added aqueous [^{18}F]fluoride as a chemically versatile synthon for nucleophilic radiofluorination.[123] These combined nuclear and chemical features have established fluorine-18 as the dominant radionuclide for the development of small-molecule PET tracers.[123,126]

This dominance is reflected in clinically deployed tracers spanning diverse structural classes (Figure 52A), where representative fluorine-18-labeled radiopharmaceuticals such as [^{18}F]FDG, [^{18}F]fluorodopa, Amyvid™, Vizamyl™, and Tauvid™ illustrate the breadth of biological targets accessible through a common labeling strategy.[126,127] Despite substantial variation in molecular architecture and function, these tracers share a requirement for late-stage fluorine-18 incorporation into structurally complex frameworks, underscoring the central role of synthetic methodology in tracer design. A quantitative representation of radionuclide usage across approved PET radiopharmaceuticals further reinforces this trend (Figure 52B), with fluorine-18 constituting the largest fraction by absolute count, whilst isotopes such as ^{11}C, ^{13}N, and ^{82}Rb appear only in proportions consistent with their operational constraints.[126] A complementary perspective is provided by the distribution of targeting modalities (Figure 52C), where small molecules constitute the dominant vector class across approved diagnostic radiopharmaceuticals, substantially exceeding peptide- and antibody-based constructs.[126]

The same half-life that enables multi-step synthesis, however, imposes a strict temporal constraint. The interval from radionuclide production to patient administration must not exceed

approximately three half-lives, placing the labeling step under a practical completion window of approximately 30 minutes.[123] This requirement restricts viable transformations to those that are rapid, high-yielding, and operationally robust under highly dilute conditions. The clinical impact of fluorine-18 is therefore inseparable from the development of general, reliable arene fluorination strategies capable of accommodating electronically and sterically diverse substrates, establishing arene radiofluorination as the central synthetic transformation in PET tracer development.

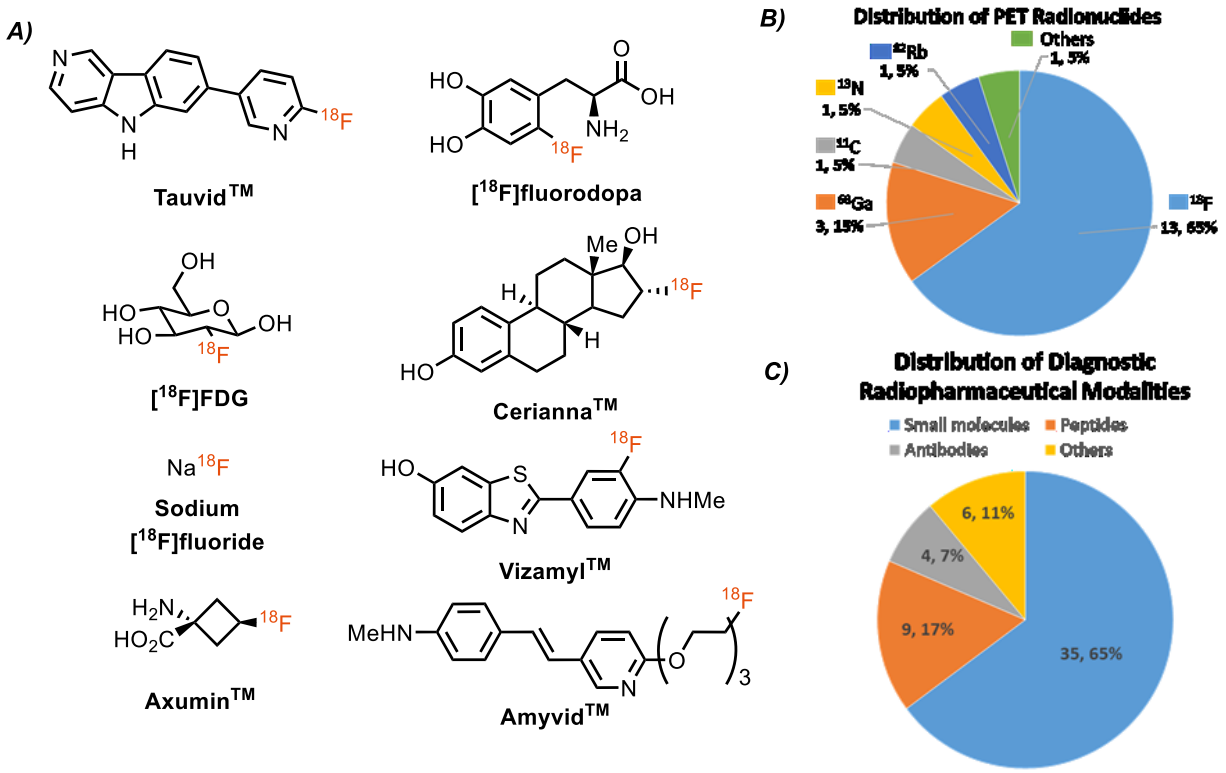


Figure 52. Overview of PET radiopharmaceuticals illustrating the dominance of fluorine-18-labeled small molecules across approved clinical tracers, shown as (A) representative ^{18}F-labeled compounds, (B) distribution of radionuclides across approved PET radiopharmaceuticals by reported tracer count, and (C) distribution of targeting modalities across approved diagnostic radiopharmaceuticals, highlighting the predominance of small-molecule tracers.[123,126]

II.1.3 Fundamental Constraints of ^{18}F Labeling

The properties that make fluorine-18 attractive for PET also impose constraints that collectively define the design space for viable radiofluorination chemistry. These are not incidental limitations to be minimised but hard boundary conditions that any practical labeling method must satisfy, and understanding them precisely is essential for evaluating the chemical strategies described in the remainder of this chapter.[123,129]

The kinetic constraint is the most immediately apparent. With a half-life of 109.7 min, the labeling reaction itself must be complete within approximately 30 minutes to leave adequate time for downstream purification by semi-preparative HPLC, formulation, sterility and quality control testing, and transport before patient injection.[123,130] This requirement disfavours any chemistry that demands extended reaction times, iterative condition adjustment, or complex multi-step sequences under radioactive conditions. Equally important, reliability and reproducibility are

paramount: a reaction that achieves acceptable radiochemical yield in the majority of attempts but fails intermittently is clinically unacceptable in a regulated radiopharmacy environment where batch failure carries both patient and financial consequences.[129]

The stoichiometric constraint is equally important but more frequently underappreciated in discussions of radiochemical method development. Cyclotron-produced [^{18}F]fluoride is invariably the limiting reagent, present at nanomolar to picomolar concentrations and reacting with a labeling precursor present in large molar excess, typically at millimolar concentrations.[123] This asymmetry differs from conventional fluorine-19 organic chemistry by many orders of magnitude, and its consequences for reaction kinetics, competing side pathways, and solvation behavior are profound.[131] Many fluorine-19 reactions optimised under comparable concentrations of both reactants do not translate to the radiochemical regime, where even minor side reactions involving the precursor in excess can compete productively with the desired fluorination pathway.[130]

The strategic constraint of late-stage radiolabel incorporation is the most consequential for synthetic planning. Because the half-life does not permit early installation of fluorine-18 followed by further chemical transformations, the C–^{18}F bond must be formed at or near the very end of the synthetic sequence, with all other functional groups present in their final form.[123,129] This requirement inverts conventional synthetic logic: rather than planning a synthesis around a pre-installed fluorine atom, the radiochemist must append the radiolabel to a fully assembled, functionally complex molecule in a single late-stage step.[123] The demand for simultaneous functional group tolerance, speed, reliability, and operational simplicity, all compressed into one transformation, represents the central unsolved challenge that motivates the development of precursor-based radiofluorination strategies described in this chapter.[129]

A fourth constraint, often overlooked in academic method development, is regulatory compliance. The production of ^{18}F-labeled radiopharmaceuticals for clinical use must comply with current good manufacturing practice (cGMP) regulations to meet quality and safety criteria specified by pharmacopoeia standards.[123] This imposes requirements on reaction design well beyond chemical yield alone: reagents must be commercially available, traceable, and of documented purity; the synthesis must be automated on validated modules; residual solvents, metals, and unreacted precursor must be removed to specified limits; and the entire process must be documented and reproducible across operators and sites.[123] These requirements exclude many otherwise promising laboratory-scale radiofluorination methods from clinical translation and represent a genuine and frequently underappreciated filter on the practical utility of new radiochemistry.[132]

II.1.4 Nucleophilic Aromatic Substitution for ^{18}F-Labeling

Nucleophilic aromatic substitution (S_NAr) has been the dominant method for ^{18}F incorporation into arenes since the earliest clinical applications of fluorine-18 and remains the workhorse for routine radiopharmaceutical synthesis of electron-deficient aryl fluorides.[123] Its adoption in clinical

radiopharmacy reflects operational practicality rather than chemical generality: [^{18}F]fluoride reacts directly with a suitably activated precursor in a single transition-metal-free step, the reaction is readily automated, and it tolerates the aqueous conditions inherent to cyclotron-produced [^{18}F]fluoride.[123] These features enabled the implementation of S_NAr in the synthesis of [^{18}F]FDG, which remains the most widely used clinical PET radiotracer and whose landmark radiosynthesis was established by Hamacher and co-workers in 1986, and they continue to underpin routine radiopharmaceutical production worldwide.[133]

The mechanism proceeds through a stepwise addition–elimination sequence. Fluoride attacks the arene ipso to the leaving group in the rate-determining step, generating an anionic Meisenheimer σ-complex stabilized by electron-withdrawing substituents positioned ortho or para to the leaving group.[134] Elimination of the leaving group restores aromaticity and furnishes the aryl fluoride product.[123] The requirement for stabilization of this high-energy intermediate defines the electronic scope of the reaction.[123] A mechanistically important consequence of this pathway is the leaving group reactivity order ArF >> ArCl > ArBr > ArI, which reflects the ability of the fluorine substituent to stabilize negative charge in the Meisenheimer complex through the polarity of the C–F bond rather than through simple bond dissociation energy considerations (Figure 53).[123,134]

Activating groups are necessary rather than merely beneficial in classical S_NAr radiofluorination. In the absence of ortho- or para-electron-withdrawing substituents, the addition step is prohibitively endergonic and cannot be rendered productive by adjusting temperature, solvent, or base. This limitation is intrinsic to the reaction coordinate rather than kinetic in origin. Electron-neutral and electron-rich arenes, which constitute the majority of drug-like aromatic scaffolds, are therefore inaccessible under classical S_NAr conditions.[123,135] In practical ^{18}F chemistry, substrates bearing nitro or trialkylammonium leaving groups typically exhibit higher reactivity than aryl halides, whilst halogen exchange on aryl fluorides is disfavoured due to a reduction in molar activity from isotopic dilution with the carrier fluorine-19.[123]

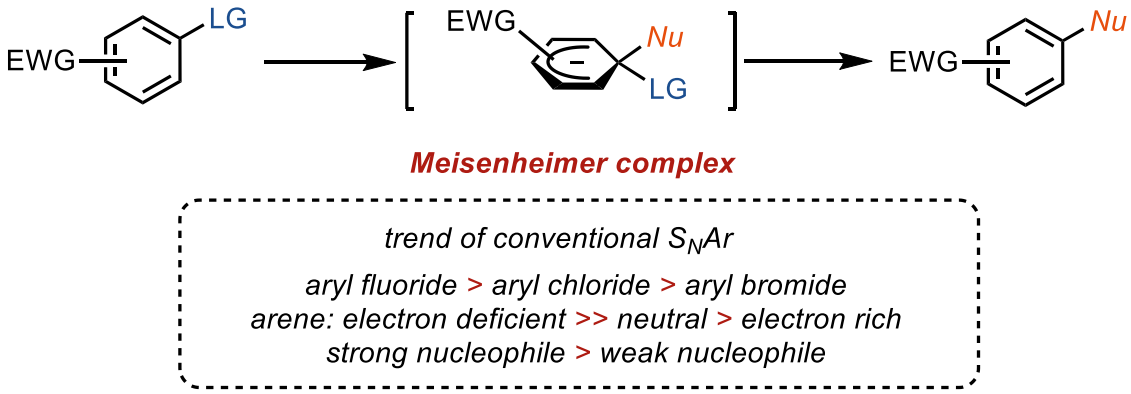


Figure 53. Classical S_NAr reaction of electron-deficient arenes showing the stepwise addition–elimination mechanism, the anionic Meisenheimer σ-complex intermediate stabilised by ortho- or para-electron-withdrawing groups, and the leaving group reactivity order ArF >> ArCl > ArBr > ArI.[123]

Classical S_NAr provides reliable access to electron-deficient aryl fluorides and remains the operational backbone of clinical radiopharmacy. However, it does not provide a general solution for the radiofluorination of electronically diverse arenes encountered in modern pharmaceutical targets.[123,135] This mechanistic limitation defines the boundary of classical nucleophilic substitution in ^{18}F chemistry and directly motivates the development of alternative strategies that operate beyond electronically activated substrates, as described in the sections that follow.

II.1.5 Advanced Radiofluorination Strategies

The limitations of classical S_NAr have prompted the development of a range of alternative ^{18}F-radiofluorination strategies over the past two decades. The practical value of these methods is ultimately constrained by the 109.7 min half-life of ^{18}F, which imposes strict limits on reaction time, purification, and formulation within the radiopharmacy workflow. Rather than providing an exhaustive catalog, this section evaluates the most practically significant approaches with explicit attention to three criteria that determine whether a radiofluorination method has genuine translational impact: (i) the substrate space it enables, (ii) the limitations it leaves unresolved, and (iii) the operational burden it introduces under time-constrained conditions. These criteria structure the discussion of each approach in the sections that follow, from transition-metal-mediated platforms to hypervalent iodine and sulfonium strategies, culminating in a critical assessment of the limitations that persist across current methodologies.[123,129]

II.1.5.1 Transition-Metal-Mediated Radiofluorination

The emergence of transition-metal-mediated radiofluorination marked a decisive conceptual shift away from the electronic constraints of classical S_NAr. In these approaches, reactivity is no longer governed primarily by the intrinsic electrophilicity of the substrate arene, but by the ability of an organometallic intermediate to engage fluoride at a high-valent metal center and undergo C–F reductive elimination. This transition effectively replaces substrate-controlled reactivity with catalyst-controlled bond formation, enabling access to aryl fluorides beyond the electronic limits of classical nucleophilic substitution.[123]

The conceptual foundation of this strategy was established by Buchwald and co-workers in 2009 through the Pd(0)-catalyzed fluorination of aryl triflates.[136] Electron-rich biaryl monophosphine ligands were shown to facilitate reductive elimination from ArPd(II)F intermediates, demonstrating for the first time that palladium could be used for catalytic C–F bond formation from a nucleophilic fluoride source. The requirement for carrier-added CsF in this pioneering work precluded direct translation to no-carrier-added ^{18}F labeling, but the mechanistic precedent it established directly informed subsequent radiochemical developments.[123,136]

The palladium-mediated radiofluorination platform was subsequently realised in fully ^{18}F-compatible form by the Ritter group, as shown in Figure 54.[137] Oxidative fluorination of arylpalladium(II) precursors with [^{18}F]fluoride generates high-valent Pd(IV)–fluoride intermediates that undergo C–F reductive elimination, enabling ^{18}F incorporation without dependence on substrate electron density. The procedure employs a Pd(II) complex bearing a tridentate pyrazolylborate ligand framework; fluoride capture occurs under mild conditions at 23 °C, followed by reductive elimination at 85 °C in the presence of a sulfonamide-ligated aryl–Pd(II) transmetalating partner. Representative radiochemical yields of 10–33% reflect the inherent complexity of the precursor-to-product sequence, but the method demonstrated that high-valent Pd intermediates can be exploited for ^{18}F incorporation into structurally demanding substrates, including steroid frameworks and cyclopropane-containing architectures.[137]

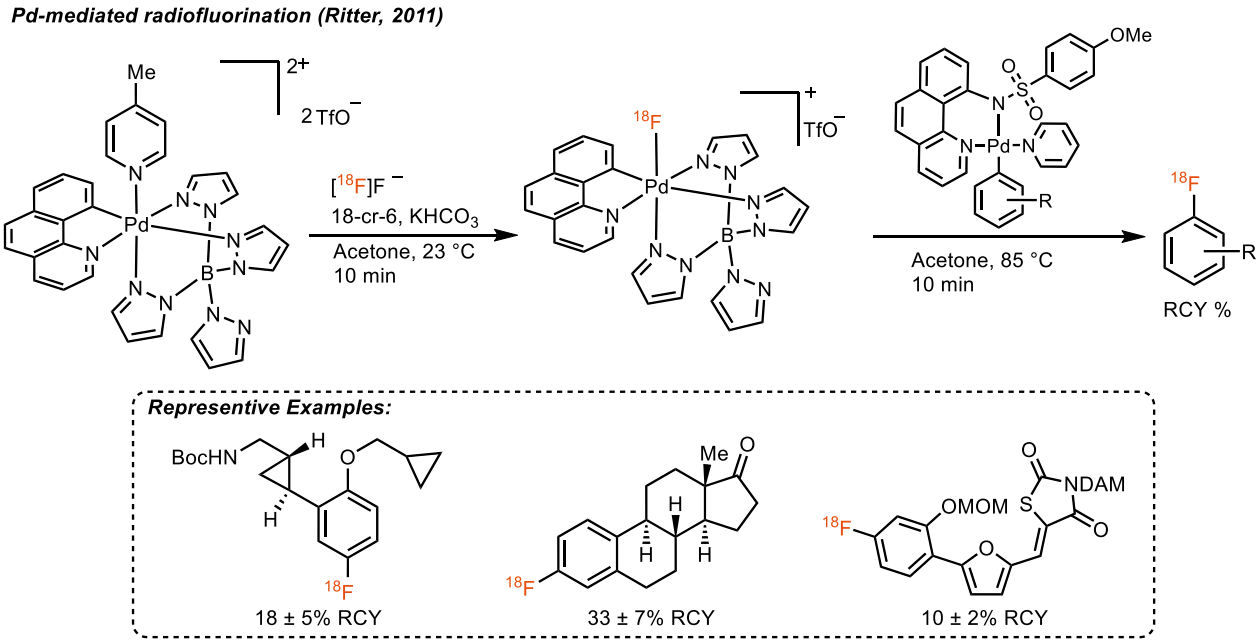


Figure 54. Palladium-mediated ^{18}F-radiofluorination of arylpalladium(II) precursors via oxidative fluorination and C-F reductive elimination from a high-valent Pd(IV)-fluoride intermediate.[137]

A nickel-mediated variant, introduced by the Ritter group in 2012, reduced the operational complexity inherent to the palladium platform by enabling oxidative radiofluorination of pre-formed aryl–Ni(II) complexes under comparatively accessible conditions (Figure 55).[138] Aryl bromides are treated with $Ni(COD)_2$ and TMEDA to furnish the aryl–Ni(II)–Br intermediate, which undergoes ligand exchange to install a sulfonamide-based ancillary ligand. Subsequent exposure to aqueous [^{18}F]fluoride in the presence of an oxidant at ambient temperature achieves fluorination in a single radiochemical step. The method provides access to a range of electron-neutral and electron-rich substrates with radiochemical yields of 13–58%, and the use of aryl bromide starting materials reduces the burden of precursor synthesis relative to the palladium manifold.[138]

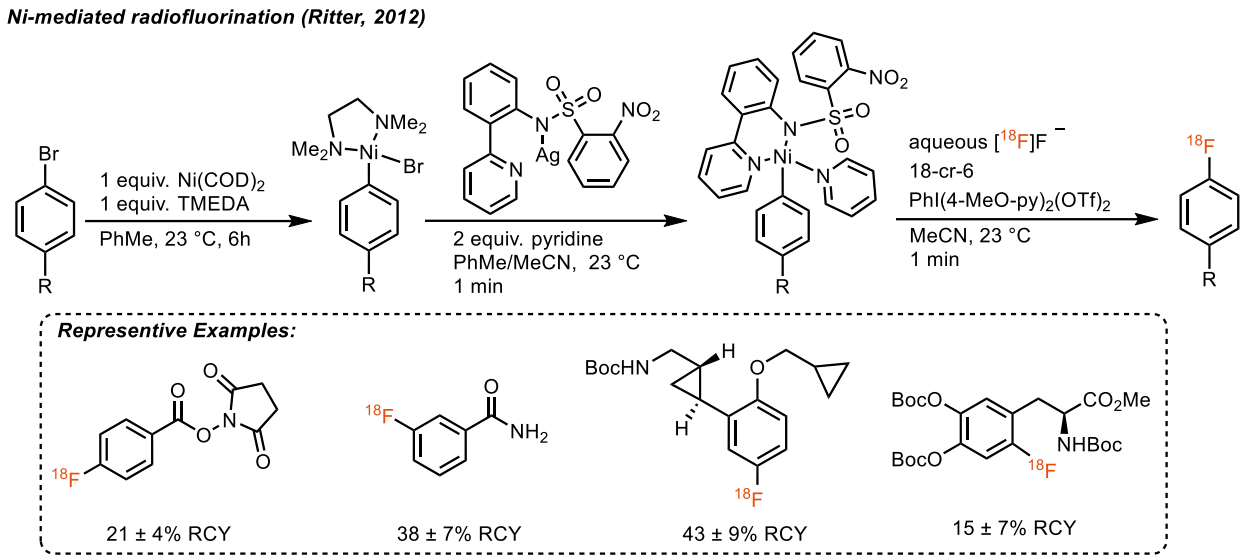


Figure 55. Nickel-mediated radiofluorination through sequential oxidative addition, ligand exchange, and oxidative fluorination of aryl–Ni(II) complexes.

Copper-mediated radiofluorination of aryl boronic esters, developed by Gouverneur and co-workers and illustrated in Figure 56, further broadened the scope of transition-metal-mediated ^{18}F chemistry by providing access to electron-rich, electron-neutral, and electron-poor arenes from stable and synthetically accessible boronate precursors.[139] The use of $[Cu(OTf)_2(py)_4]$ with $[^{18}F]KF/K_{222}$ in DMF at 110 °C allows efficient labeling of substrates inaccessible by S_NAr, including electron-rich methoxy arenes, whilst retaining chemoselectivity for the boronate in the presence of aryl halides. Radiochemical conversions ranging from 26–59% demonstrate the breadth of the method, and clinically relevant tracers including [^{18}F]DAA1106 and 6-[^{18}F]fluoro-L-DOPA have been prepared under these conditions, demonstrating applicability to complex, drug-like molecules.[139]

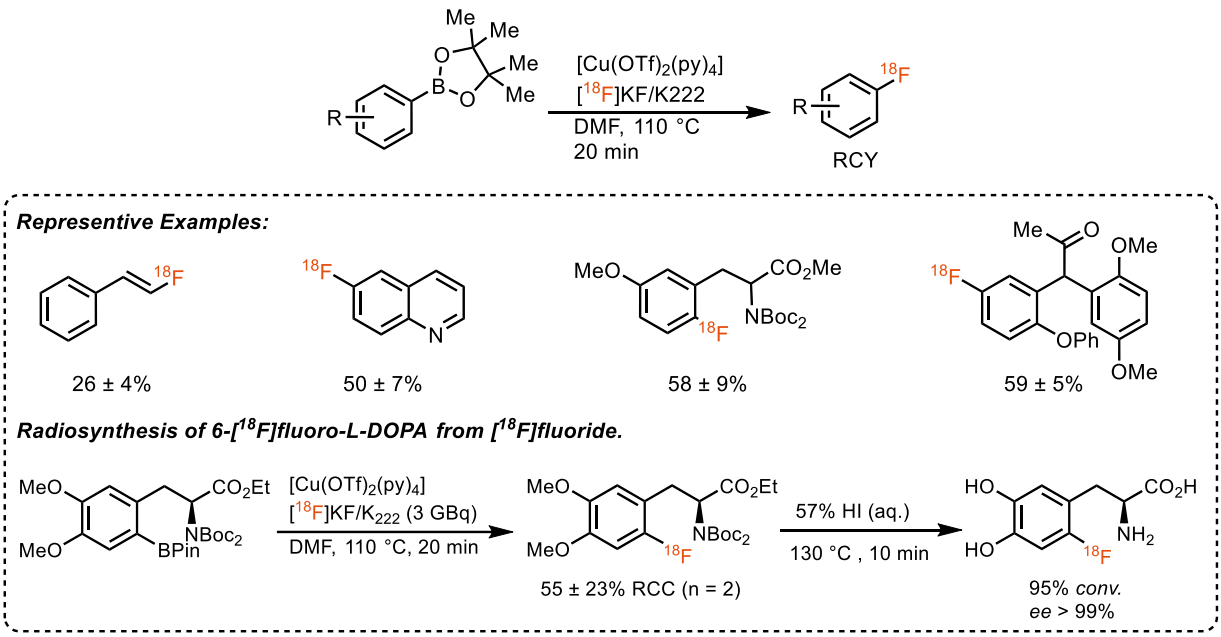


Figure 56. Copper-mediated nucleophilic ^{18}F-fluorination of aryl boronic pinacol esters using $[Cu(OTf)_2(py)_4]$ and $[^{18}F]KF/K_{222}$ in DMF.

These three platforms represent complementary solutions to the electronic limitations of S_NAr: palladium provides high-valent fluorination reactivity, nickel simplifies the precursor-to-product sequence, and copper provides the broadest practical substrate scope from the most accessible precursor class.[123,129] However, none eliminates the precursor requirement. Each demands a pre-formed organometallic or organoboron intermediate that must be synthesized, characterized, and quality-controlled prior to the radioactive step. The requirement for substrate prefunctionalization introduces an additional synthetic sequence independent of the radiochemical transformation, and residual metal removal must meet cGMP limits for clinical batches, thereby imposing a purification burden that reduces radiochemical yield and extends total processing time.[123]

II.1.5.2 Diaryliodonium Salts and Hypervalent Iodine Precursors

Diaryliodonium salts occupy a distinctive position in the landscape of ^{18}F-radiofluorination precursors because they provide a metal-free alternative to transition-metal platforms whilst extending the accessible substrate space beyond the electronic constraints of classical S_NAr. The approach was introduced by Pike and co-workers in 1995, who demonstrated that treatment of diaryliodonium salts with cyclotron-produced no-carrier-added [^{18}F]fluoride in the presence of K_2CO_3/K_{222} provides [^{18}F]fluoroarenes in a single radiochemical step.[140] The reaction tolerates electron-rich arenes and proceeds without pre-formed organometallic complexes, representing an important conceptual departure from both S_NAr and transition-metal approaches.

The mechanism of fluorination in diaryliodonium salts proceeds through a ligand coupling pathway on the hypervalent iodine center. In an unsymmetrical salt, regioselectivity is governed primarily by the electronic disparity between the two aryl ligands, with [^{18}F]fluoride being preferentially delivered to the more electron-deficient ring. A well-established empirical refinement

of this selectivity is the ortho-effect: the introduction of ortho-substituents on the spectator arene diverts fluoride transfer to the target ring with high selectivity regardless of its electronic character, thereby enabling ^{18}F incorporation into arenes that would otherwise be inaccessible by electronic discrimination alone. The electron-rich 2-thienyl and mesityl groups are the most widely used spectator arenes for this purpose, and their use in unsymmetrical iodonium precursors allows predictable, regioselective labeling across a broad substrate range.[123,139–141]

The principal limitation of diaryliodonium salts is precursor synthesis. The preparation of unsymmetrical salts requires electrophilic iodination conditions, typically using strong Lewis or Brønsted acids and oxidants such as *m*-CPBA or Oxane, which are incompatible with a wide range of pharmacophoric functional groups. The two-arene constitution of the precursor also introduces an atom-economy penalty, as only one of the two aryl groups is transferred to the product, and careful selection of the spectator group is required to ensure selectivity. Late-stage installation of the iodonium motif onto complex drug-like scaffolds, therefore, remains synthetically demanding.[123]

Spirocyclic iodonium ylides (SCIDY precursors), introduced by Vasdev, Liang, and co-workers in 2014, address several of these limitations through a modified hypervalent iodine architecture (Figure 57).[142] In place of a second arene, the iodine center bears a β-dicarbonyl auxiliary in a spirocyclic arrangement, which eliminates the counterion and the spectator aryl group. The spirocyclopentane-derived iodonium ylide provides superior regiospecificity, bench stability, and flash-chromatographic purifiability compared with conventional diaryliodonium salts, and the absence of a competing arene removes the regioselectivity ambiguity inherent to asymmetric salts. Radiofluorination of diverse non-activated and sterically hindered arenes, including electron-rich anisoles, pyridines, and indoles, was demonstrated with radiochemical conversions of up to 85% and sufficient specific activity for human PET imaging.[142] The SCIDY approach has been translated to the preparation of [^{18}F]FPEB and validated for clinical use, representing one of the very few iodonium-based methods to have progressed to GMP-compliant radiopharmaceutical production.[123,142]

Despite these advances, precursor accessibility remains a practical constraint for both diaryliodonium and SCIDY strategies. The multi-step synthesis of the iodine(III) precursor constitutes a significant workload upstream of the radiochemical step, and precursor stability under radiolabeling conditions requires careful optimisation for each new substrate. No-carrier-added iodonium radiofluorination thus offers broad substrate scope but at the cost of a synthetic overhead that limits its utility for rapid tracer discovery.[123]

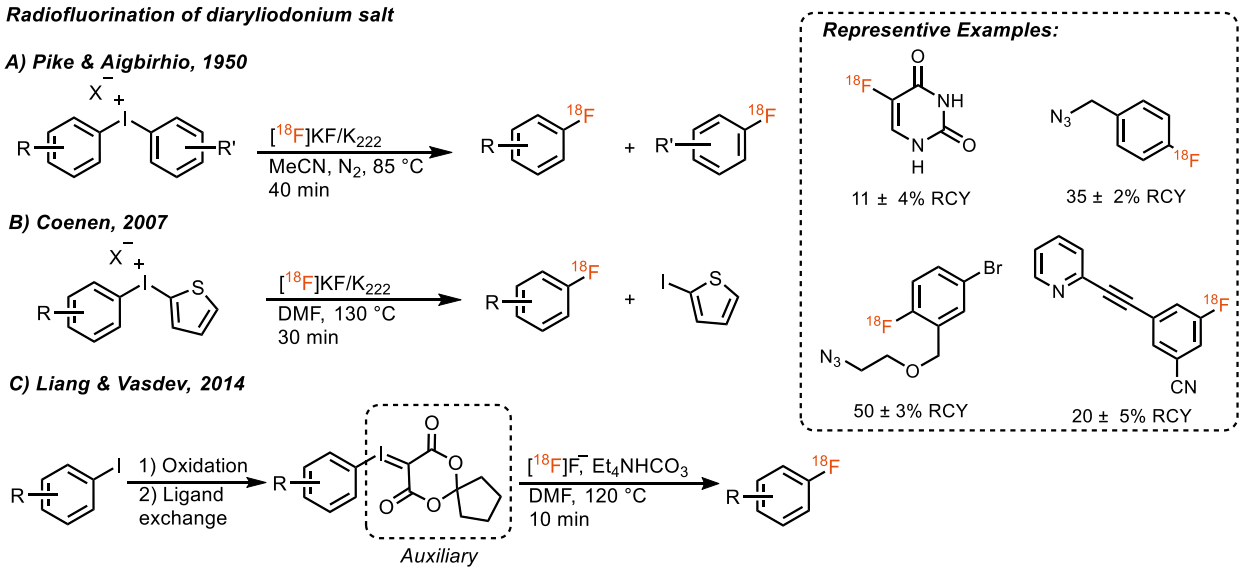


Figure 57. Diaryliodonium salt and spirocyclic iodonium ylide precursors for ^{18}F-radiofluorination showing (A) the original diaryliodonium salt approach providing access to electron-neutral and electron-rich aryl ^{18}F products, (B) the 2-thienyl auxiliary strategy for improved regioselectivity, and (C) the spirocyclic iodonium ylide platform offering enhanced precursor stability and simplified purification.[123,141,142]

II.1.5.3 Radiofluorination of Aryl Sulfonium Salts

Aryl sulfonium salts represent a structurally distinct class of ^{18}F-radiofluorination precursor that operates through S_NAr mechanism but circumvents the electronic limitations of classical S_NAr by employing the sulfonium group as the activating leaving group rather than a conventional electron-withdrawing substituent. Two complementary strategies for the synthesis of dibenzothiophene sulfonium precursors and their application to ^{18}F-radiofluorination have been developed by the Årstad and Ritter groups, respectively, each addressing the challenge of precursor accessibility from a distinct retrosynthetic direction (Figure 58).[143,144]

Årstad and co-workers reported in 2018 that dibenzothiophene sulfonium salts are accessible through a mild intramolecular ring-closing reaction of biaryl thioethers under N-chlorosuccinimide-mediated conditions, providing bench-stable, column-chromatographically purifiable precursors for ^{18}F-radiofluorination.[143] The ring-closing strategy circumvents the principal synthetic limitation of triarylsulfonium salts, which require harsh, selective S-arylation conditions incompatible with many pharmacophoric functional groups, by generating the dibenzothiophene sulfonium motif through cyclization of a biaryl thioether intermediate that is itself readily assembled from aryl halide starting materials by palladium-catalyzed C–S coupling. The mechanism of

radiofluorination proceeds by ipso-attack of [^{18}F]fluoride at the carbon bearing the sulfonium leaving group, with regioselectivity confirmed through DFT calculations showing a linear correlation between radiochemical yields and the Hammett substituent constant σ (R^2 = 0.97), providing a predictive tool for reaction outcome without the need for full radiochemical optimisation of each new substrate.[143] Radiochemical yields across the substrate scope ranged from 27 ± 5% for an electron-rich methoxyphenyl substrate to 65 ± 5% for 3-[^{18}F]fluoropyridine at 110 °C in dimethylsulfoxide over 15 minutes, with the unsubstituted analog affording 45 ± 3%, and electron-deficient aryls and pyridines consistently labeled in the highest yields, consistent with the S_NAr mechanism.[143]

Ritter and co-workers in 2020 addressed the remaining limitation of precursor-dependent synthesis, specifically the requirement for pre-functionalized aryl halide starting materials, through direct aromatic C–H dibenzothiophenylation.[144] In this approach, bench-stable dibenzothiophene sulfoxide (DBTO) reacts with the arene substrate in the presence of an acid anhydride activator to deliver the sulfonium salt with high site-selectivity directly from the carbon–hydrogen bond, bypassing the need for any prior arene functionalization. Positional selectivity for the para carbon–hydrogen bond was demonstrated with ratios of up to 50:1 (para/ortho) and 100:1 (para/meta), and a set of three /electronically differentiated dibenzothiophenes was introduced to enable matched reactivity across a wide range of substrates.[144] The two-step sequence of carbon–hydrogen dibenzothiophenylation followed by ^{18}F-radiofluorination was applied to a series of marketed small-molecule drugs, with radiochemical yields of 55–94% for the fluorination step depending on the choice of dibenzothiophene reagent and substrate electronics, demonstrating that site-selective late-stage ^{18}F-labeling of complex molecules is achievable from C–H functionalization without upstream precursor synthesis specific to the fluorination step.[144]

Both approaches are metal-free in the radiofluorination step and do not require azeotropic drying of [^{18}F]fluoride, conferring a practical advantage over transition-metal platforms with respect to GMP compliance and residual metal analysis. Årstad and co-workers approach is most suitable for substrates assembled convergently from aryl halide building blocks, where the biaryl thioether can be introduced at a defined synthetic stage, whilst the Ritter and co-workers approach extends the accessible substrate space to finished molecules bearing no prior activating group, representing a conceptual step towards truly late-stage ^{18}F-radiofluorination.[123,143,144]

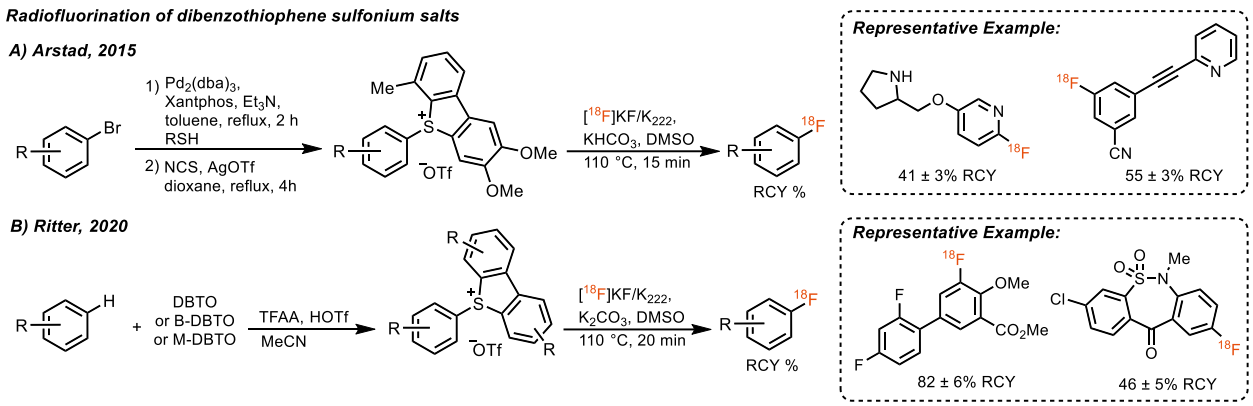


Figure 58. Dibenzothiophene sulfonium salt-mediated ^{18}F radiofluorination. Arstad approach (2015): Pd-catalyzed C–S coupling from aryl bromides. Ritter approach (2020): direct C–H dibenzothiophenylation.

II.1.6 The Persistent Precursor Problem: A Critical Evaluation

The advanced ^{18}F-radiofluorination strategies presented in Sections II.1.5.1–II.1.5.3 reveal a structural pattern that cuts across all platform types: every method described, whether palladium-, nickel-, or copper-mediated, or based on hypervalent iodine or sulfonium precursors, requires the synthesis of a dedicated organometallic or organoheteroatom intermediate before the radioactive step can be initiated. This precursor requirement is not merely a synthetic inconvenience; it imposes a fundamental kinetic and logistical constraint on the translational utility of each method.[123,129]

The synthesis of a ^{18}F-radiofluorination precursor constitutes an entirely independent synthetic campaign. For transition-metal platforms, this means the iterative preparation and characterization of arylpalladium, arylnickel, or arylboron derivatives, each of which must meet purity and stability standards suitable for GMP use. For iodonium and sulfonium approaches, multi-step synthesis of the hypervalent heteroatom precursor is required, and the atom economy is inherently poor: in diaryliodonium chemistry, only one aryl group is converted to the labeled product, whilst the spectator group, synthesized at equivalent cost, is discarded. In each case, the precursor synthesis introduces a lead time of days to weeks that is incompatible with the exploratory pace of drug development and tracer screening programs.[123]

A further concern is precursor availability and regulatory status. For a ^{18}F-labeled radiopharmaceutical to enter clinical use, the radiolabeling precursor must be produced at a sufficient scale, with appropriate quality control, and available commercially or from a validated in-house source. This manufacturing requirement has been met for a small number of precursors, most notably aryl boronic esters for the Gouverneur copper-mediated method and spirocyclic iodonium ylide precursors for a handful of validated tracers, but it represents a genuine barrier to the translation of newly developed ^{18}F-radiofluorination methods, as precursor supply chains require substantial investment to establish and maintain.[139,142]

This limitation can be reframed as a strategic question: if the ideal late-stage ^{18}F-radiofluorination

strategy converts a commercially available, multistep-free precursor to a ^{18}F-labeled product within the radioactive half-life constraint and without transition metal residues, then the question becomes whether any such precursor can serve as a ^{18}F-radiofluorination handle with broad generality. The phenol presents itself as a compelling answer, given its ubiquity in natural products and pharmaceutical frameworks, its ready availability through biosynthetic and synthetic routes, and its inherent reactivity towards deoxyfluorination. This strategic logic, namely the phenol-to-fluoride disconnection as an enabling transform, motivates the deoxyfluorination strategies discussed in the sections that follow.[123,129]

II.1.7 Deoxyfluorination of Phenols: PhenoFluor and the Concerted S_NAr Mechanism

The potential of phenols as ^{18}F-radiofluorination precursors was first realised in preparative fluorine chemistry through the development of PhenoFluor (N,N′-1,3-bis(2,6-diisopropylphenyl)-2,2-difluoroimidazolidene) by Ritter and co-workers in 2011.[145] PhenoFluor enables a one-step ipso fluorination of phenols to aryl fluorides under mild conditions, with yields of 74–95% across a structurally diverse substrate range including electron-rich arenes, heteroaromatics, and complex natural products. The transformation is operationally simple, proceeds without transition metals, and tolerates moisture in a manner atypical of conventional nucleophilic fluorination chemistry, which ordinarily requires rigorously anhydrous conditions owing to the diminished nucleophilicity of hydrated fluoride.[145] The chemoselectivity profile of PhenoFluor is particularly notable: selective deoxyfluorination occurs at the least electron-rich phenol in polyhydroxylated systems, providing a predictable and programmable selectivity of direct relevance to the labeling of complex substrates.[123,146]

The mechanistic basis of PhenoFluor reactivity, elucidated by Ritter and co-workers in 2016, proved to be fundamentally distinct from classical S_NAr and was the key insight that enabled translation of the deoxyfluorination to ^{18}F-radiochemistry (Figure 59).[147] Mechanistic investigation revealed that the PhenoFluor-mediated transformation proceeds via a concerted nucleophilic aromatic substitution (CS_NAr) pathway, in which C–F bond formation and C–O bond cleavage occur simultaneously through a single neutral four-membered transition state without the intermediacy of a discrete Meisenheimer complex. The computed activation barrier of $\Delta G^{\ddagger}$ = 21.8 kcal·mol^{-1} reflects the synchronous nature of this process, and stands in contrast to the two-barrier energy profile of classical stepwise S_NAr in which the Meisenheimer intermediate constitutes a local minimum on the reaction coordinate.[146,147] The mechanistic distinction has direct practical consequences: because CS_NAr does not require charge build-up on the intermediate ring, the reaction is not restricted to electron-poor arenes. The substrate scope extends to electron-rich phenols, including methoxy- and amino-substituted substrates, that are completely inert under conventional S_NAr conditions.[147]

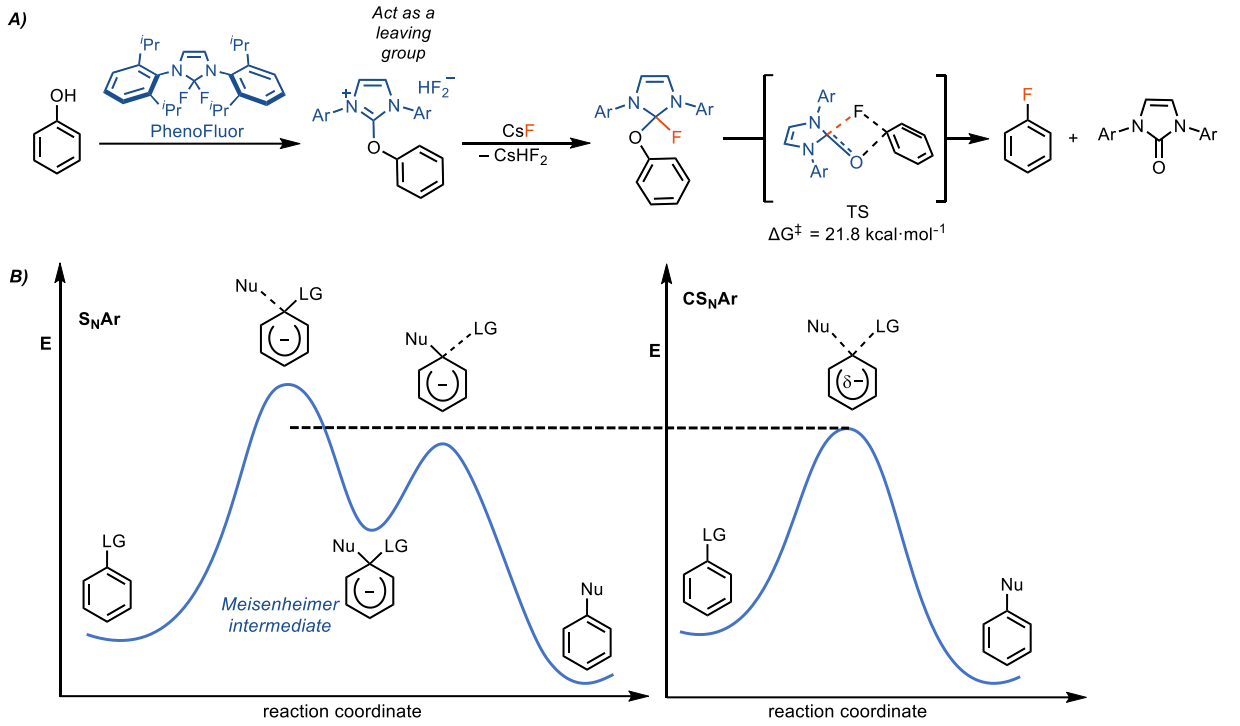


Figure 59. PhenoFluor-mediated deoxyfluorination of phenols via the concerted nucleophilic aromatic substitution mechanism showing (A) in situ activation of the hydroxyl group to a cationic uronium leaving group followed by fluoride substitution through a concerted transition state (B) comparative reaction coordinate diagrams for classical stepwise nucleophilic aromatic substitution proceeding via a Meisenheimer intermediate with two activation barriers and the concerted pathway proceeding through a single transition state.[145–147]

This mechanistic insight directly enabled ^{18}F-radiofluorination. The CS_NAr pathway is operative at the nanomolar fluoride concentrations characteristic of no-carrier-added ^{18}F-chemistry, and the absence of a Meisenheimer intermediate means that the reaction does not require the electronic activation of the arene that renders classical S_NAr inapplicable to electron-rich substrates.[146,147] The ^{18}F-deoxyfluorination protocol employs the operationally stable ^{ipr}ImCl reagent with Ag_2CO_3 as base to form the uronium intermediate in situ, followed by [^{18}F]fluoride incorporation via an exchange cartridge and thermal CS_NAr at 130 °C over 20 minutes in butanone/ethanol (Figure 60).[147] The method proceeds without azeotropic drying of [^{18}F]fluoride and tolerates a broad range of functional groups, including amines, thioethers, sulfonamides, amides, and basic heterocycles, with decay-corrected radiochemical conversions of 76–98% across representative arene and heteroarene substrates.[147] The method provides ^{18}F-labeled aryl fluorides directly from commercially available phenols without any upstream precursor synthesis specific to the fluorination step, representing a qualitative departure from the precursor-dependent paradigm of all previously discussed ^{18}F-radiofluorination strategies.[123,145,147]

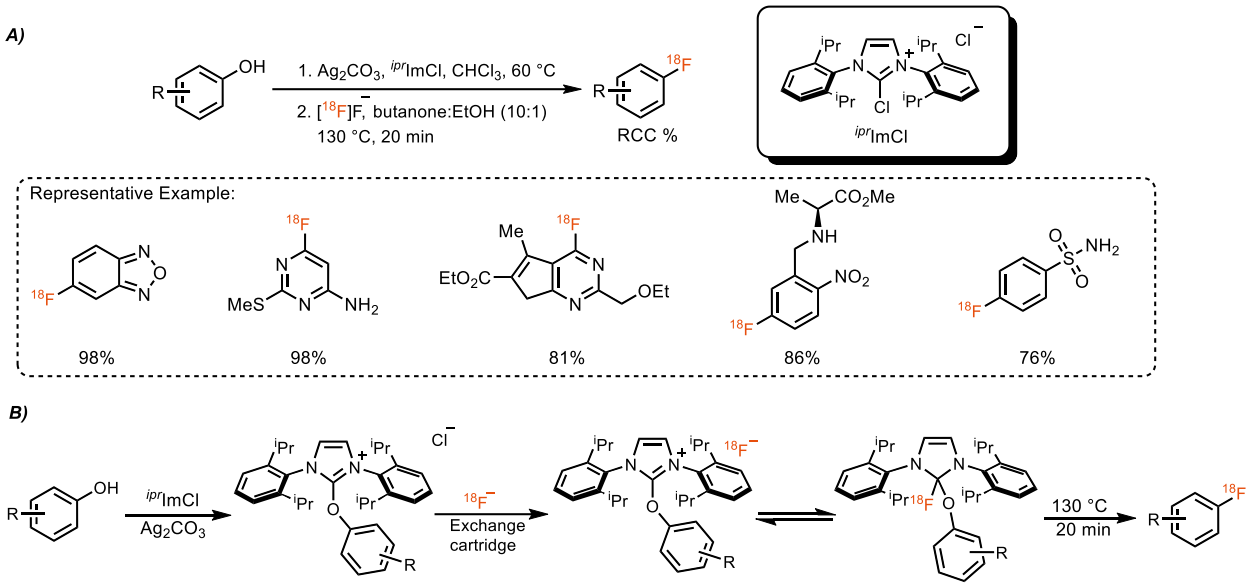


Figure 60. ^{18}F-Deoxyfluorination of phenols using the ^{ipr}ImCl reagent: (A) representative arene and heteroarene substrates affording 76–98% radiochemical conversion, and (B) proposed mechanistic sequence from uronium formation to concerted C-F bond formation.[147]

II.1.8 Ruthenium-Mediated Radiodeoxyfluorination of Electron-Rich Phenols

The electron-rich phenol limitation of PhenoFluor under no-carrier-added ^{18}F conditions was addressed by Ritter and co-workers in 2017 through a strategy that exploits ruthenium η⁶-coordination to simultaneously increase the population of the reactive tetrahedral adduct and lower the activation barrier for C–F bond formation on electron-rich substrates.[148] The phenol substrate is first treated with CpRu(COD)Cl in ethanol at 80 °C for 30 minutes to give the η⁶-coordinated arene–ruthenium complex (Figure 61). This complexation withdraws electron density from the arene ring, converting the electron-rich phenol into an electronically activated substrate competent for deoxyfluorination. The positively charged RuCp fragment also increases the Coulombic attraction between fluoride and the phenol–reagent complex, shifting the equilibrium towards the reactive tetrahedral adduct and directly addressing the concentration problem that prevents electron-rich phenol labeling under standard no-carrier-added conditions.[148]

The mechanistic sequence proceeds by treating the η⁶-coordinated complex with ^{ipr}ImCl and [^{18}F]fluoride in acetonitrile/DMSO (1:1) at 125 °C for 30 minutes to generate the uronium intermediate, which equilibrates with the tetrahedral adduct, which serves as the reactive species for fluorination.[148] The RuCp fragment stabilizes the Meisenheimer complex sufficiently that a classical stepwise S_NAr mechanism is favored over the CS_NAr pathway even for electron-rich substrates, with demetallation as the rate-determining step. UV irradiation of the Ru-complexed aryl fluoride intermediate liberates the free ^{18}F-labeled aryl fluoride and the urea byproduct. The method demonstrates broad applicability to structurally complex electron-rich targets, with representative radiochemical conversions of 85–99% across substrates including an NHBoc-protected amino acid derivative, an indole ester, a quinoline-containing substrate, a morpholine-containing biaryl, and a benzamide.[148]

The ruthenium complexation strategy has also been extended beyond simple arene substrates. Ritter and co-workers demonstrated in 2018 that site-specific ^{18}F-radiofluorination of phenol-containing peptides is achievable by incorporating tyrosine(CpRu) building blocks into solid-phase peptide synthesis protocols, demonstrating compatibility with late-stage functionalization of structurally complex, biologically relevant targets and enabling access to ^{18}F-labeled peptide tracers that are inaccessible by conventional ^{18}F-radiofluorination methods.[149]

The PhenoFluor CS_NAr and Ru-mediated strategies are therefore precisely complementary: the former operates most efficiently on electron-neutral to moderately electron-poor phenols via a metal-free concerted pathway, whilst the latter extends radiodeoxyfluorination to electron-rich substrates and peptide frameworks through transient organometallic activation. Their combined substrate coverage spans the full electronic range of phenols encountered in pharmaceutical and biological contexts. The radiodeoxyfluorination step is now well-defined across this entire range, and the primary synthetic challenge in the tracer development pipeline has consequently shifted upstream to the preparation of the phenol precursor itself, which becomes the rate-limiting creative problem in any new ^{18}F-radiofluorination campaign based on the deoxyfluorination strategy.[145,147–149]

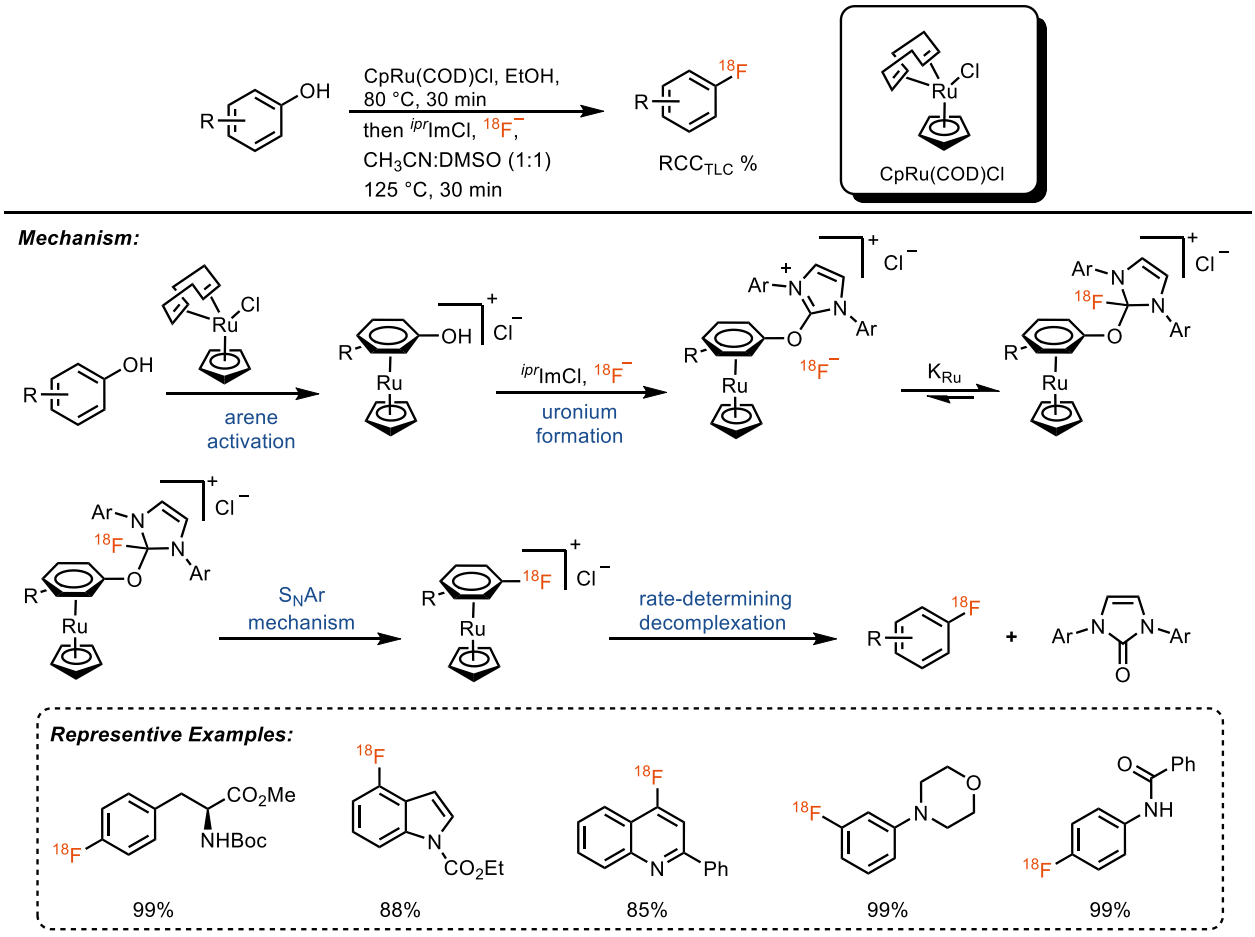


Figure 61. Ruthenium-mediated ^{18}F-radiodeoxyfluorination of electron-rich phenols via Ru π-complex activation, extending the substrate scope of PhenoFluor-based deoxyfluorination to electronically demanding substrates.[148]

II.1.9 Phenol-to-Fluoride Disconnection as a Strategic Principle

The developments described in Sections II.1.4 through II.1.8 collectively validate a general retrosynthetic principle for ^{18}F PET tracer development. Any ^{18}F-labeled aryl fluoride target can be conceptually disconnected into two sequential operations: preparation of the corresponding aryl phenol precursor by conventional synthetic chemistry, and subsequent conversion of that phenol to the aryl fluoride by ^{18}F-radiodeoxyfluorination with [^{18}F]fluoride.[145,147,148] This phenol-to-fluoride disconnection is strategically powerful because the phenol intermediate is a stable and fully characterisable non-radioactive compound that can be prepared, purified, and quality-controlled independently of radioactive decay constraints. It can be synthesized in bulk, stored at the radiopharmacy site, and used as the substrate for a single well-defined ^{18}F-radiodeoxyfluorination step when required.[123] The rate-determining factor in the tracer development pipeline, therefore, becomes phenol synthesis rather than the radiochemical transformation.[123,129]

A particularly important application of this disconnection is in the development of ^{18}F-labeled isotopologues of fluorine-containing drugs for pharmacokinetic PET studies. Such molecules are of high translational value because structural identity is preserved during isotopic substitution. The ^{19}F to ^{18}F substitution does not alter the carbon framework, substitution pattern, or pharmacological identity of the molecule, enabling non-invasive imaging of true drug disposition rather than a structurally modified surrogate.[123,126,127] The disconnection maps directly onto a retrosynthetic aryl fluoride-to-phenol transform, and the central synthetic question becomes whether phenol precursors can be prepared from commercially available fluorinated drug scaffolds using methods compatible with their structural and functional group complexity (Figure 62).[145,147]

The strategic advantage of this approach relative to existing ^{18}F-radiofluorination practice is the decoupling of precursor synthesis from the radiopharmacy workflow. Classical ^{18}F-radiofluorination strategies require preparation of a bespoke, target-specific precursor for each tracer, a process that must be completed prior to the radioactive step and that constitutes the principal bottleneck in tracer development.[123,129,130] By contrast, the phenol-to-fluoride disconnection places the synthetic burden entirely on conventional chemistry applied to commercially available starting materials, leaving the radiopharmacy step as a single, well-defined transformation applied to a pre-characterised substrate. The breadth of the radiodeoxyfluorination substrate scope, spanning electron-neutral through electron-rich phenols via the complementary PhenoFluor CS_NAr and Ru-mediated platforms, ensures that the disconnection is applicable across the electronic diversity of aryl fluoride targets encountered in drug development and molecular imaging.[145–148]

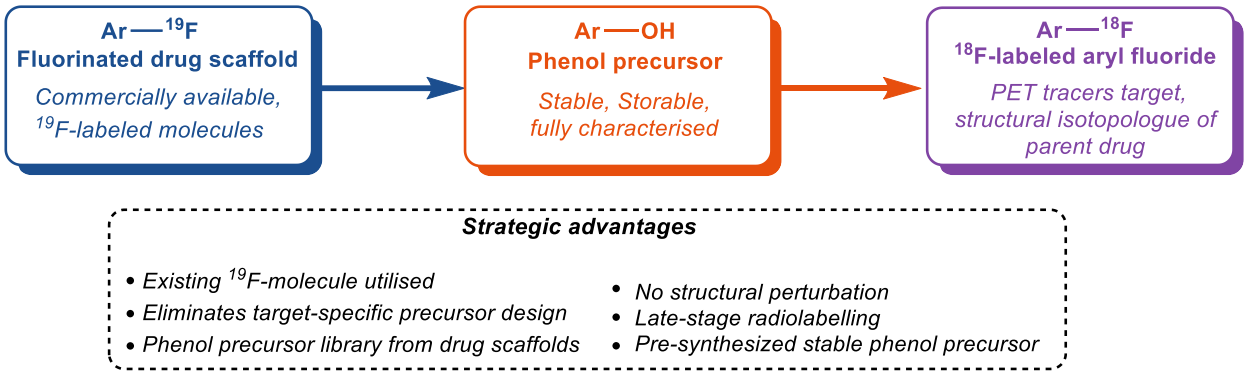


Figure 62. Phenol-to-fluoride disconnection for PET tracer development. Fluorinated scaffolds are converted to stable phenol precursors, enabling subsequent radiodeoxyfluorination to ^{18}F-labeled aryl fluorides.[145,147,148]

II.1.10 Phenol Synthesis as the Bottleneck: Classical Methods and Radical Hydroxylation Strategy

The preparation of phenol precursors for ^{18}F-radiodeoxyfluorination is inseparable from the broader precursor problem that limits all existing radiofluorination strategies. Every transition-metal-mediated and hypervalent heteroatom-based ^{18}F-radiofluorination method requires the synthesis of a bespoke, target-specific precursor before the radioactive step can be initiated, and phenol synthesis for radiodeoxyfluorination is no exception. Classical nucleophilic aromatic substitution with hydroxide requires strongly electron-withdrawing substituents to stabilise the Meisenheimer intermediate and fails entirely for the moderately activated aryl fluorides characteristic of fluorinated pharmaceuticals, as illustrated by the hydroxylation of 4-fluorotoluene with NaOH giving only 2% yield at 309 °C.[150,151] Transition-metal-catalyzed approaches extend the substrate scope to aryl bromides, chlorides, and iodides, but copper-catalyzed methods require strongly basic conditions incompatible with sensitive pharmacophoric groups, whilst palladium-catalyzed methods suffer from competing N-arylation and O-arylation at Ar–Pd–OH intermediates.[152,153] The use of benzaldehyde oxime as a hydroxide surrogate in palladium and copper catalysis improved functional group tolerance considerably, with Fier and Maloney and co-workers demonstrating late-stage hydroxylation of functionally dense drug-like aryl halides under mildly basic conditions using both palladium and copper catalysis.[152,153] Shi and co-workers subsequently extended the scope further to electron-rich and neutral aryl fluorides through rhodium-catalyzed η^6-coordination-mediated activation of the C–F bond, isolating a rhodium η^5-cyclohexadienyl Meisenheimer-type intermediate as direct mechanistic evidence for the stepwise S_NAr pathway.[151] Both approaches nonetheless require a transition-metal catalyst, reintroducing the metal contamination, cost, and ligand optimisation concerns that restrict utility in pharmaceutical and radiopharmaceutical contexts.

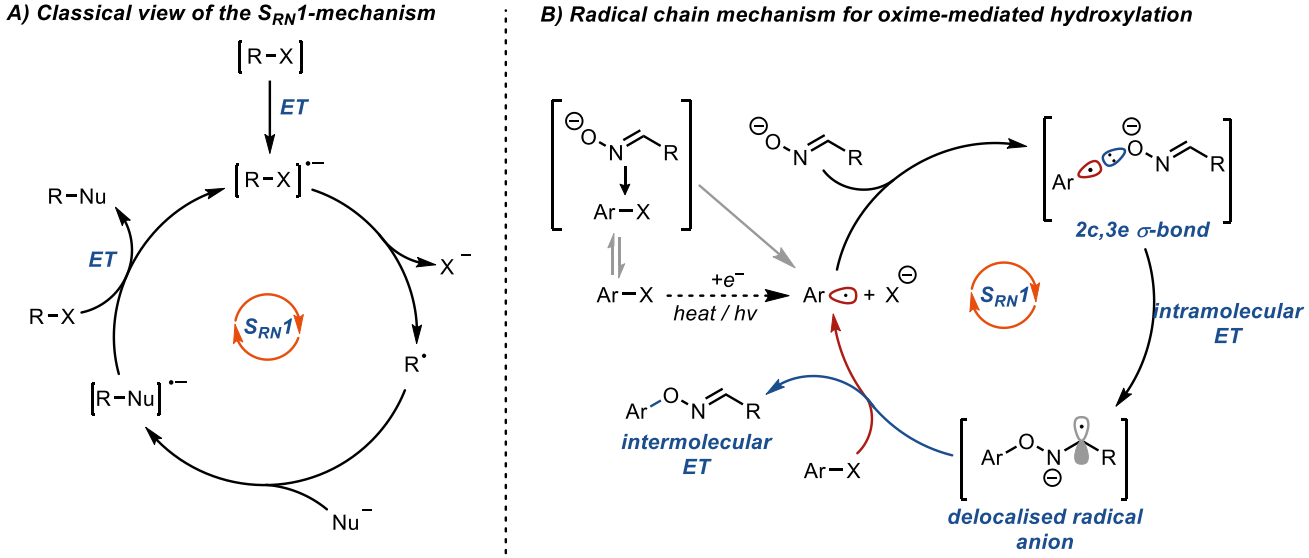


Figure 63. A) General $S_{RN}1$ cycle. B) Radical chain mechanism for oxime-mediated hydroxylation of aryl fluorides.

A transition-metal-free solution was reported by James and co-workers in 2021, involving the radical hydroxylation of aryl halides using a rationally designed oxime as a hydroxide surrogate via a radical-nucleophilic substitution chain mechanism.[154] Conventional hydroxide anions cannot participate in such radical chain processes because they are poor single-electron donors, and no oxygen-based anion had previously been shown capable of intermolecular coupling with aryl radicals to form C–O bonds. The oxime reagent overcomes this limitation by functioning simultaneously as a single-electron donor for radical chain initiation and as a hydroxyl-delivery agent, releasing the free phenol in situ via N–O bond fragmentation, with benzonitrile as the only byproduct, without requiring a separate deprotection step.[154] The method converts aryl fluorides, chlorides, bromides, and iodides to phenols under operationally simple, metal-free conditions with broad functional group compatibility encompassing amines, amides, nitriles, ethers, and basic heterocycles.[154]

The combination of this radical hydroxylation with the ^{18}F-radiodeoxyfluorination platforms described in Sections II.1.7 and II.1.8 dissolves the precursor problem entirely for the substrate class of fluorinated pharmaceuticals and PET imaging ligands. Rather than requiring a bespoke precursor synthesized specifically for the radiofluorination step, the fluorinated drug itself serves as the commercially available starting material. Radical hydroxylation converts it directly to the phenol precursor in a single late-stage step, and ^{18}F-radiodeoxyfluorination of that phenol installs [^{18}F]fluoride at the same position previously occupied by ^{19}F, delivering the ^{18}F-labeled isotopologue with full preservation of the carbon framework, substitution pattern, and pharmacological identity of the parent drug. The three-molecule sequence; fluorinated drug, phenol, and ^{18}F-labeled drug proceeds entirely from commercially available starting materials without any target-specific precursor synthesis. The electronic requirements of the radical hydroxylation, which operates most efficiently on aryl fluorides bearing electron-withdrawing substituents, converge precisely with the structural features of fluorinated central nervous system

drugs and PET imaging ligands, which characteristically incorporate electron-withdrawing heterocyclic cores, carbonyl groups, and cyano substituents as integral pharmacophoric elements. The systematic application of this two-step sequence to this pharmaceutically important substrate class constitutes the focus of the present work.[123,145,147,154]

II.2 RESULTS AND DISCUSSION

Note: The radical aromatic hydroxylation strategy described in this chapter applies the $S_{RN}1$ methodology reported by James and co-workers[154] as the synthetic platform for the preparation of phenol precursors from fluorinated pharmaceutical scaffolds. The synthesis of the fluorinated substrate library, the assembly of the hydroxylation substrate panel, and all experimental work described in this chapter were designed and performed entirely by the author. This work is unpublished.

II.2.1 Reaction Design and Mechanistic Rationale

Commercially available fluorinated pharmaceuticals and PET imaging ligands represent an underexploited starting point for the preparation of ^{18}F-labeled isotopologues: if the aryl C–F bond present in the drug scaffold can be selectively converted to a phenol, the resulting precursor becomes directly amenable to ^{18}F-radiodeoxyfluorination, establishing a two-step route from commercial fluorinated drug to ^{18}F-labeled tracer that bypasses the need for bespoke precursor synthesis entirely. Realizing this concept required a hydroxylation strategy capable of operating on aryl fluorides specifically, under conditions compatible with the functional group complexity characteristic of pharmaceutical targets, and without reliance on transition metal catalysis that could be compromised by the basic nitrogen heterocycles, free hydroxyl groups, and metal-coordinating functionality present in many drug scaffolds. Radical $S_{RN}1$ hydroxylation, as developed by James and co-workers, satisfies each of these requirements: it proceeds via single-electron reduction of the arene to generate a radical anion that fragments selectively at the C–F bond with release of fluoride, it is inherently suited to electron-poor aryl fluorides of the type found in CNS drugs and PET imaging ligands, and it operates without any metal catalyst under mildly basic conditions.[154]

The selection of benzaldoxime as the hydroxide surrogate was informed by two complementary bodies of precedent. Fier and Maloney demonstrated that benzaldoxime functions as an effective and practical hydroxide surrogate for the late-stage synthesis of phenols from functionally dense drug-like aryl halides under both Pd-catalyzed and Cu-catalyzed cross-coupling conditions, establishing that this reagent is compatible with the structural complexity of pharmaceutical substrates and operates under mildly basic conditions without degradation of base-sensitive functional groups.[152,153] James and co-workers subsequently demonstrated that benzaldoxime functions equivalently as the oxygen-atom source in the metal-free radical $S_{RN}1$ manifold.[154] Whilst Fier and Maloney and co-workers established the utility of benzaldoxime for phenol synthesis from aryl chlorides, bromides, and iodides under transition metal catalysis, the palladium and copper-catalyzed manifolds are inherently less suited to aryl fluorides owing to the kinetic barrier associated with oxidative addition into the strong aryl C–F bond.[152,153] The radical $S_{RN}1$ pathway proceeds instead via thermodynamically favorable radical anion fragmentation at the C–F bond, making it the strategically correct choice for the aryl fluoride substrate class

investigated here.[154] This mechanistic alignment, in which both the hydroxylation and the subsequent radiodeoxyfluorination operate at the same aryl C–F bond, is a defining strategic feature of the two-step route developed in this chapter.

Cesium carbonate (Cs_2CO_3) was selected as base on the basis of its compatibility with the basic nitrogen heterocycles present across the substrate panel, including piperazine, piperidine, and pyridine rings, which may be sensitive to the strongly basic conditions employed in alternative protocols. Benzaldoxime was employed as the hydroxide surrogate on the basis of its commercial availability, low cost, and established compatibility with the structural complexity of drug-like molecules under mildly basic conditions, without the need to prepare a specialised surrogate reagent. The reaction temperature of 100 °C was employed throughout to ensure productive reactivity across substrates of varying electronic character.[152–154]

II.2.2 Substrate Scope and Translational Rationale

A structurally diverse panel of fluorinated pharmaceuticals and PET imaging ligands was subjected to radical $S_{RN}1$ hydroxylation using benzaldoxime as the hydroxide surrogate and Cs_2CO_3 as base in DMSO at 100 °C, affording the corresponding phenol products in isolated yields ranging from 29% to 88% (Figure 64). Substrate selection was guided by two complementary criteria operating in parallel. The first was structural: each substrate bears an aryl C–F bond in an electronic environment expected to sustain productive radical anion formation and chain propagation under the $S_{RN}1$ conditions. The second was pharmacological and translational: each substrate is either a clinically validated ^{18}F-labeled PET imaging agent for which the phenol product would enable a more accessible radiosynthetic route, or a fluorinated CNS drug whose ^{18}F-labeled isotopologue would be of direct value for pharmacokinetic and receptor occupancy studies by PET, but for which no suitable radiolabeling precursor currently exists. Six substrates required synthesis prior to the hydroxylation study; the remainder were obtained from commercial sources.

Fluorinated quinoline and pyridine heterocycles constitute the pharmacophoric cores of a large number of CNS-active drugs and PET imaging ligands, and four commercially available substrates bearing these motifs were included in the panel on the basis of their direct structural relevance to this drug class. The fluoroquinaldine S54, the difluorophenylpyridine S56, the fluorophenyl nitropyridine S55, and the fluoromethylquinolinyl methyl ketone S57 afforded phenols 54, 56, 55, and 57 in 58%, 48%, 43%, and 29% isolated yield respectively. The yield trend across this series is broadly consistent with the degree of electronic activation available at the C–F bond in each substrate, with S57 giving the lowest yield in the panel at 29%.

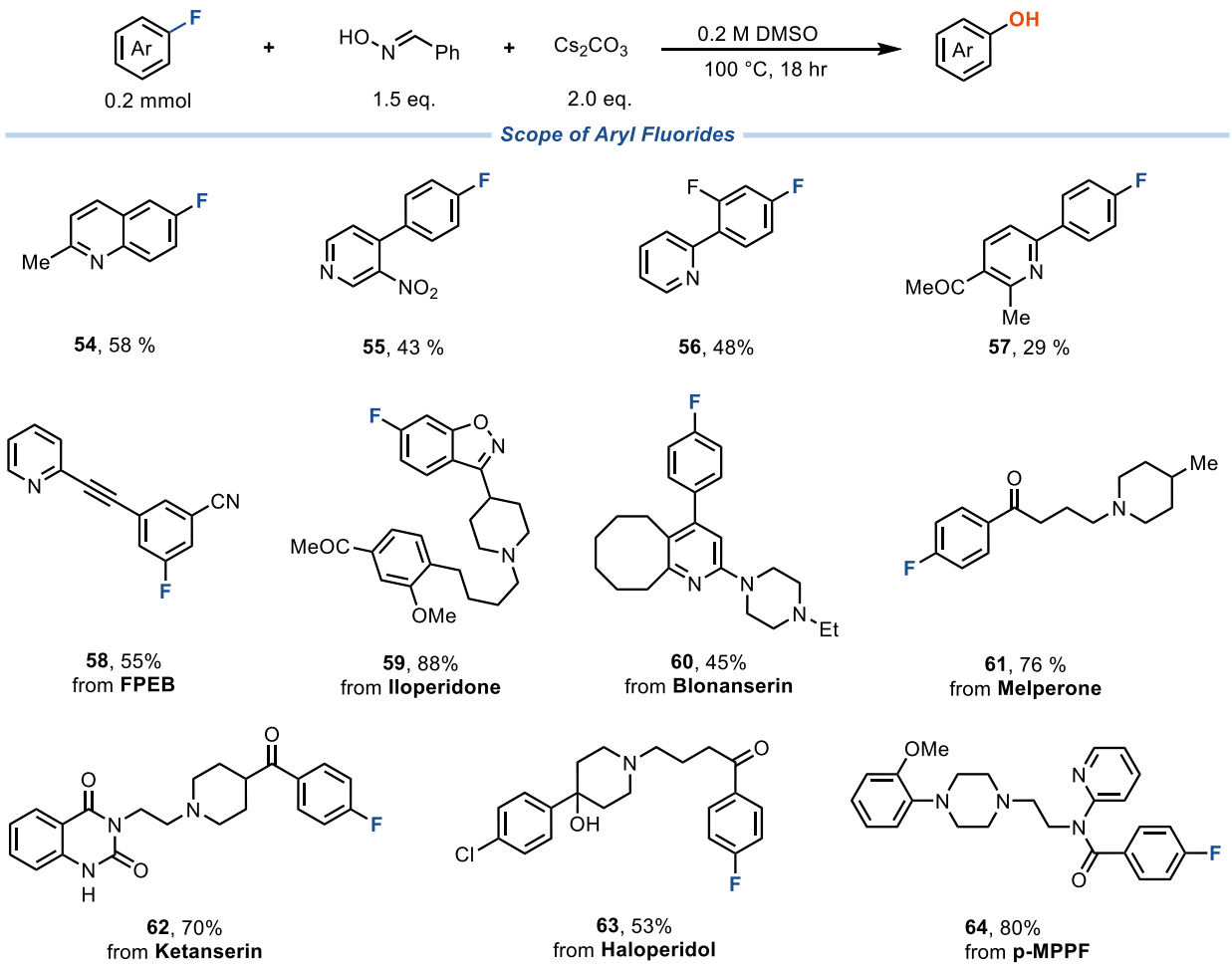


Figure 64. Radical $S_{RN}1$ hydroxylation of fluorinated pharmaceuticals and positron emission tomography (PET) imaging ligands using benzaldoxime.

[^{18}F]FPEB is a potent and selective antagonist of the metabotropic glutamate receptor subtype 5 validated in first-in-human studies as a quantitative PET radioligand for mapping mGluR5 distribution in the living human brain, with demonstrated clinical utility in neuropsychiatric research and drug occupancy measurement.[155] The radiosynthesis of [^{18}F]FPEB has historically posed a significant challenge. Conventional nucleophilic ^{18}F-for-nitro substitution on a nitrobenzonitrile precursor affords [^{18}F]FPEB in poor radiochemical yields of 1–5% under standard heating conditions, a consequence of the competing side reactions and precursor decomposition that accompany the harsh basic conditions required for this transformation.[156] Copper-mediated ^{18}F-radiofluorination of aryl boronic ester precursors, pioneered by Gouverneur and co-workers and subsequently applied to [^{18}F]FPEB by Gouverneur and Sanford group, broadened the accessible precursor space but requires the synthesis of a dedicated arylboronic ester or arylboronic acid that is structurally distinct from the parent drug.[139,157,158] The use of arylstannane precursors, also demonstrated by Sanford and co-workers, raises significant concerns about the inherent toxicity of organotin compounds and their suitability for clinical radiopharmaceutical production.[159] Ritter and co-workers subsequently demonstrated that a phenol precursor of FPEB could be converted directly to [^{18}F]FPEB via PhenoFluor-mediated concerted nucleophilic aromatic substitution, establishing the phenol as the ideal radiofluorination precursor for this tracer but leaving the

preparation of that phenol as an unresolved synthetic challenge.[147] Radical hydroxylation of commercially available FPEB (S58) under the conditions described in Section II.1.2 afforded phenol 58 in 55% isolated yield, providing direct access to the established PhenoFluor radiofluorination precursor from the commercial drug in a single synthetic step and completing the three-molecule sequence from commercially available fluorinated drug to ^{18}F-labeled PET tracer without requiring any bespoke precursor synthesis.

[^{18}F]p-MPPF is the most widely used ^{18}F-labeled antagonist radiotracer for the serotonin 5-HT$_{1A}$ receptor, validated for quantitative imaging of 5-HT$_{1A}$ receptor distribution in the human brain across a broad range of clinical applications, including studies of depression, anxiety, and epilepsy.[160,161] Existing radiosynthetic routes to [^{18}F]p-MPPF rely on nucleophilic ^{18}F-for-nitro substitution on a bespoke fluorobenzamide nitro-precursor that must be prepared by multi-step synthesis independently of the parent drug.[142] Radical hydroxylation of commercially available p-MPPF (S64) afforded phenol 64 in 80% isolated yield. The para-fluorobenzamide unit in p-MPPF carries a carbonyl group in direct conjugation with the aryl fluoride, providing strong electronic activation of the C–F bond, consistent with the S$_{RN}$1 mechanism, as reflected in the high yield obtained.[154] Phenol 64 is directly suitable as a radiodeoxyfluorination precursor for [^{18}F]p-MPPF, providing a single-step route to this precursor from the commercial drug that replaces the existing multi-step bespoke precursor synthesis.

Iloperidone (S59) is an atypical antipsychotic with high affinity for dopamine D$_2$, D$_3$, and serotonin 5-HT$_{1A}$ receptors.[162] No radiolabeled isotopologue of iloperidone has been reported, and its receptor occupancy in vivo has been characterised exclusively through indirect PET displacement approaches using established radioligands. The fluorobenzisoxazole unit in iloperidone places the aryl C–F bond in direct conjugation with both the isoxazole nitrogen creating one of the most electronically activated C–F environments in the substrate panel. Radical hydroxylation of S59 afforded phenol 59 in 88% isolated yield, the highest yield in the series, consistent with this high degree of electronic activation. Phenol 59 is a precursor suitable for ^{18}F-labeling of iloperidone by radiodeoxyfluorination, enabling the prospect of direct pharmacokinetic characterisation of this drug's CNS distribution by PET.

Melperone (S61) is a butyrophenone antipsychotic bearing a para-fluorophenyl ketone motif in which the carbonyl group is in direct conjugation with the fluorinated ring.[162] No radiolabeled isotopologue of melperone has been reported. The para-carbonyl activation pattern represents one of the most favorable electronic environments for S$_{RN}$1 reactivity and radical hydroxylation of S61, affording phenol 61 in 76% isolated yield, reflecting this favorable electronic activation. Phenol 61 is a precursor suitable for ^{18}F-labeling of melperone by radiodeoxyfluorination.

Ketanserin (S62) is a serotonin 5-HT$_{2A}$ receptor antagonist whose radiolabeled history illustrates the limitations of existing ^{18}F-labeling strategies for this drug class. [^{11}C]Ketanserin was the first 5-HT$_{2A}$ receptor PET tracer studied in humans, but was discontinued owing to low target-to-nontarget ratios and rapid metabolism in vivo.[163] The discontinuation of [^{11}C]ketanserin reflected

unfavorable tracer kinetics and the inherent practical constraints of the short ^{11}C half-life rather than any deficiency in the 5-HT_{2A} receptor affinity or selectivity of ketanserin itself. A subsequent ^{18}F-labeled fluoroethyl analog, [^{18}F]FEK, was developed to address the isotope limitation and demonstrated improved in vivo characteristics in baboon brain, but no human PET studies have been published.[164] The fluoroethyl modification in [^{18}F]FEK introduces a structural change relative to the parent drug that alters its pharmacological and metabolic profile, precluding its use as a structurally faithful pharmacokinetic isotopologue of ketanserin. A direct ^{18}F-labeled isotopologue of ketanserin, preserving the native drug structure whilst benefiting from the practical advantages of the longer ^{18}F half-life for quantitative PET receptor imaging, has never been prepared. Radical hydroxylation of S62 afforded phenol 62 in 70% isolated yield. The para-fluorophenyl ring in ketanserin carries an electron-withdrawing carbonyl substituent in direct conjugation with the C–F bond, and the 70% yield is consistent with this degree of electronic activation. Phenol 62 is a precursor suitable for the preparation of such a structurally faithful ^{18}F-isotopologue of ketanserin by radiodeoxyfluorination, addressing the structural limitation of [^{18}F]FEK and reopening the prospect of direct quantitative PET imaging of 5-HT_{2A} receptors with a ketanserin-based radioligand.

Haloperidol (S63) is a classical D_2 receptor antipsychotic for which ^{18}F-labeling has been attempted but with limited success. [^{18}F]Haloperidol was first prepared via nucleophilic ^{18}F-for-nitro substitution on a nitrobenzonitrile precursor, followed by multi-step elaboration, and applied in preclinical PET studies in baboons, where it produced widespread non-selective brain binding that precluded its use as a selective dopamine receptor imaging agent.[165] Receptor occupancy studies of haloperidol in humans have consequently relied on indirect displacement of established radioligands rather than direct ^{18}F-labeling of the drug itself.[166] Radical hydroxylation of S63 afforded phenol 63 in 53% isolated yield. Phenol 63 is a precursor suitable for the preparation of the ^{18}F-isotopologue of haloperidol by radiodeoxyfluorination.

Blonanserin (S60) is an atypical antipsychotic with high affinity for dopamine D_2, D_3, and serotonin 5-HT_{2A} receptors that has been characterized in PET studies using [^{11}C]raclopride for striatal D_2 receptor occupancy and [^{11}C]FLB for extrastriatal occupancy in schizophrenic patients, but no radiolabeled isotopologue of blonanserin has been reported.[167] The fluorophenyl group in the blonanserin scaffold is located within a fused polycyclic framework that reduces the electronic activation at the C–F bond. Radical hydroxylation of S60 afforded phenol 60 in 45% isolated yield, providing a precursor suitable for ^{18}F-labeling of blonanserin by radiodeoxyfluorination.

Across the full substrate panel, yields correlate with the electronic character of the aryl C–F bond, consistent with the $S_{RN}1$ mechanism established by James and co-workers.[154] Substrates bearing electron-withdrawing substituents in direct conjugation with the C–F bond gave the highest yields, whilst substrates in which electronic activation at the C–F bond is reduced gave lower yields. All substrates in the panel were tolerated under the radical chain conditions, and the phenol products were isolated in good purity, as confirmed by NMR spectroscopy and HRMS. The combined

substrate panel demonstrates that radical $S_{RN}1$ hydroxylation is a broadly applicable and functionally tolerant strategy for converting fluorinated pharmaceutical scaffolds to phenol precursors suitable for downstream ^{18}F-radiodeoxyfluorination, with a practical yield range of 29–88% across structurally and electronically diverse drug molecules.

II.2.3 Limitations, Outlook, and Downstream Radiofluorination Potential

Productive radical $S_{RN}1$ hydroxylation requires sufficient electronic activation of the aryl C–F bond to sustain radical anion formation and chain propagation under the thermal conditions employed, and this electronic requirement defines the practical boundary of the method. Attempted hydroxylation of flurbiprofen methyl ester, rucaparib, and olaparib, each bearing a fluorine atom on an aryl ring without strong electron-withdrawing substituents in direct conjugation with the C–F bond, afforded no productive conversion under the standard conditions (Figure 65). Apalutamide, which bears a fluorobenzamide unit in which the amide carbonyl is positioned meta rather than para to the C–F bond, also failed to undergo productive hydroxylation, consistent with the weaker through-ring activation available at the meta position relative to the para-substituted fluorobenzamide units present in the successful substrates ketanserin, melperone, and p-MPPF. These results are fully consistent with the yield trend observed across the successful panel and confirm that substrates bearing insufficiently activated aryl C–F bonds fall outside the practical scope of the present conditions.

Ester-containing substrates represent a further limitation of the method. Attempted hydroxylation of flumequine methyl ester and flurbiprofen methyl ester resulted in ester hydrolysis rather than productive C–F hydroxylation, reflecting the incompatibility of ester functionality with the reaction conditions.

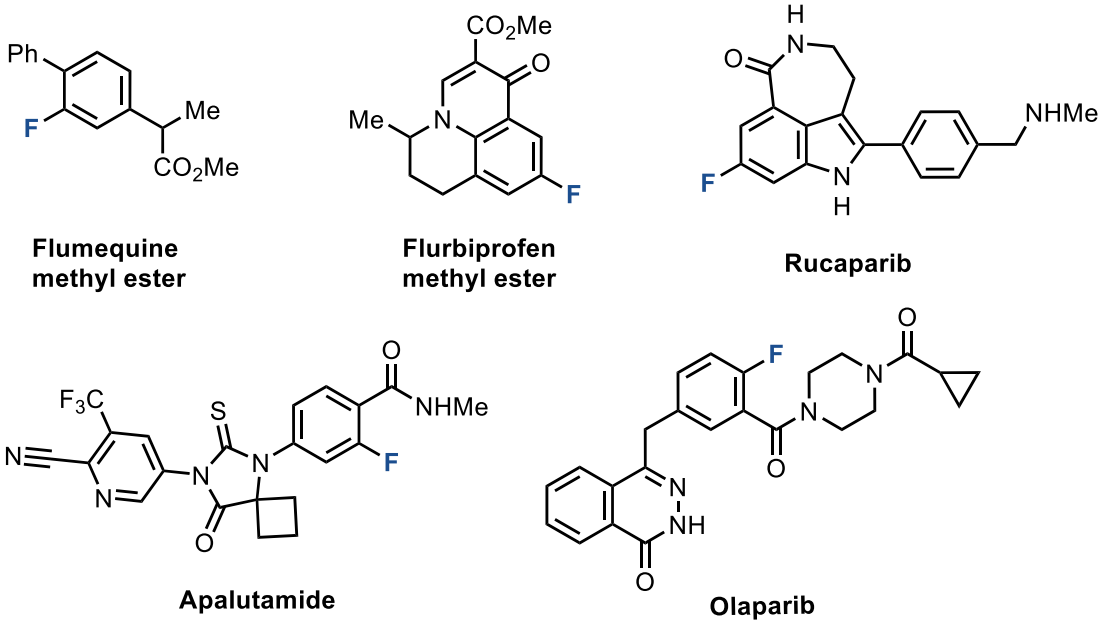


Figure 65. Failed fluorinated pharmaceuticals substrate under the standard conditions of radical hydroxylation.

Fluorine is routinely incorporated into CNS drug scaffolds and PET imaging ligands in electron-withdrawing contexts, on heterocyclic rings, adjacent to carbonyl groups, and in positions that enhance metabolic stability and CNS penetration,[168,169] and the structural features that confer pharmacological utility to these compounds are therefore broadly convergent with the electronic requirements of the $S_{RN}1$ mechanism. The same electron-withdrawing heterocyclic cores, carbonyl groups, and cyano substituents that are incorporated into CNS drugs to achieve target binding affinity, metabolic stability, and CNS penetration also provide the electronic activation required for productive radical chain hydroxylation, and this convergence underpins the broad practical utility of the present approach for this drug class despite the electronic and functional group limitations.

The phenol products prepared in Section II.2.2 are direct precursors for downstream ^{18}F-radiodeoxyfluorination via PhenoFluor-mediated concerted nucleophilic aromatic substitution.[147] The complete three-molecule sequence from commercially available fluorinated drug to ^{18}F-labeled PET tracer has been established for [^{18}F]FPEB by the Ritter group, and phenol 58 prepared in the substrate scope provides the required precursor for this sequence from commercially available FPEB in a single synthetic step. For the remaining phenols in the panel, the downstream radiofluorination step remains to be demonstrated, and the phenol precursors prepared here provide the essential intermediates for this work.

II.2.4 Conclusion

Radical $S_{RN}1$ hydroxylation of fluorinated pharmaceuticals and PET imaging ligands using benzaldoxime as a metal-free hydroxide surrogate provides direct synthetic access to phenol precursors suitable for downstream ^{18}F-radiodeoxyfluorination from commercially available fluorinated starting materials in a single late-stage step, without requiring any target-specific precursor design or multi-step bespoke synthesis. Application of the method to a panel of eleven fluorinated CNS drugs and PET imaging ligands afforded the corresponding phenols in isolated yields of 29–88%, demonstrating broad applicability across structurally and electronically diverse pharmaceutical scaffolds. For [^{18}F]FPEB, the phenol precursor required for PhenoFluor-mediated radiofluorination is directly accessible from the commercial drug in one step, completing a three-molecule sequence from fluorinated drug to ^{18}F-labeled PET tracer that requires no bespoke chemistry at any stage. The method offers a direct and scalable entry to ^{18}F-labelled isotopologues of fluorinated pharmaceutical scaffolds from commercially available starting materials, enabling practical pharmacokinetic and receptor occupancy characterisation by PET without requiring target-specific precursor design. The electronic boundary of the method, defined by the requirement for sufficient activation of the aryl C–F bond to sustain radical chain turnover, and the incompatibility of ester functionality with the basic conditions, were identified through investigation of substrates outside the successful substrate. The convergence between the electronic requirements of the $S_{RN}1$ mechanism and the pharmacophoric features characteristic of CNS-active fluorinated drugs suggests that the present approach is broadly applicable to this

therapeutically important compound class.[168,170] The downstream radiofluorination of the phenol precursors prepared here remains the subject of ongoing investigation.

CHAPTER III — EXPERIMENTAL DATA

III.1 Materials and Methods

All air- and moisture-insensitive reactions were carried out under ambient atmosphere and monitored by thin-layer chromatography (TLC). Concentration under reduced pressure was performed by rotary evaporation at 25–40 °C at an appropriate pressure. Purified compounds were further dried under high vacuum (0.010–0.005 mbar). Yields refer to purified and spectroscopically pure compounds. All air- and moisture-sensitive manipulations were performed using oven-dried glassware (120 °C for a minimum of 12 hours) and standard Schlenk techniques under an atmosphere of argon.

Solvents

Anhydrous MeCN, THF was obtained from *Phoenix Solvent Drying Systems*. Anhydrous acetone, DMF, DMSO, and AcOMe were dried by storage over 4Å molecular sieves. All deuterated solvents were purchased from *Euriso-Top*.

Chromatography

Thin-layer chromatography (TLC) was performed using EMD TLC plates pre-coated with 250 µm thickness silica gel 60 F254 plates and visualized by fluorescence quenching under 254 nm UV light, permanganate stain, cerium ammonium molybdate stain, or phosphomolybdic acid stain. Flash chromatography was performed using silica gel (40–63 µm particle size) purchased from Geduran®

Spectroscopy and Instruments

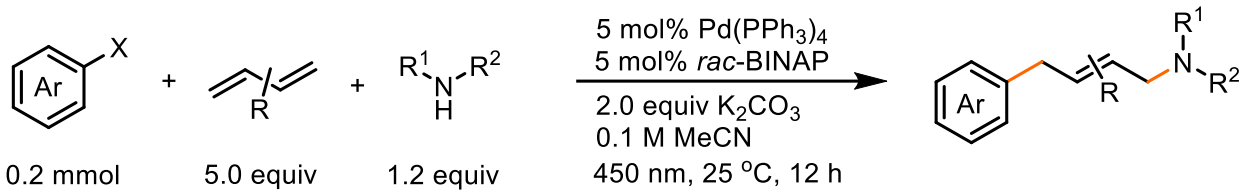
NMR spectra were recorded on a *Bruker Ascend*™ 500 spectrometer operating at 500 MHz, 471 MHz, and 126 MHz, for ^{1}H, ^{19}F, and ^{13}C acquisitions, respectively. Chemical shifts are reported in ppm with the solvent residual peak as the internal standard. For ^{1}H NMR: $CDCl_3$, 7.26; DMSO-d_6, 2.50; CD_3CN, 1.96; CD_2Cl_2, 5.32; For ^{13}C NMR: $CDCl_3$, 77.16; DMSO-d_6, 39.52; CD_3CN, 1.32; CD_2Cl_2, 53.84. ^{19}F NMR spectra were referenced using a unified chemical shift scale based on the ^{1}H resonance of tetramethylsilane (1% v/v solution in the respective solvent). Data is reported as follows: s = singlet, d = doublet, t = triplet, q = quartet, quin = quintet, sext = sextet, sept = septet, m = multiplet, bs = broad singlet; coupling constants in Hz; integration

Starting materials

All substrates were used as received from commercial suppliers or prepared according to published procedures unless otherwise stated. Chemicals were purchased from *Sigma-Aldrich*, *TCI*, *Alfa Aesar, Activate Scientific*, and *BLD Pharma*.

III.2 *1,4-Aminoarylation of Butadienes*

III.2.1 General Procedure for 1,4-aminoarylation of butadienes



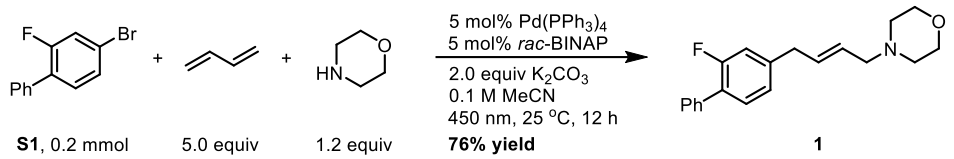
0.2 mmol 5.0 equiv 1.2 equiv

General procedure using Schlenk line: To a 4-mL borosilicate vial containing a Teflon-coated magnetic stirring bar were added aryl bromide (if solid) (0.200 mmol, 1.00 equiv), *rac*-BINAP (6.2 mg, 10 μmol, 5.0 mol%), amine (if solid) (0.240 mmol, 1.20 equiv), K_2CO_3 (56 mg, 0.40 mmol, 2.0 equiv), and $Pd(PPh_3)_4$ (12 mg, 10 μmol, 5.0 mol%). The vial was sealed with a Teflon-lined screw cap, and evacuated and backfilled with argon three times using a Schlenk line. Dry MeCN (2 mL, c = 0.1 M), butadiene (1.0 mmol, 5.0 equiv), aryl bromide (if liquid) (0.200 mmol, 1.00 equiv), and amine (if liquid) (0.240 mmol, 1.20 equiv) were added via syringe. The vial was sealed with parafilm, stirred for 5 min without irradiation, and then irradiated with 450 nm LEDs for 12 h at 25 °C. Subsequently, silica gel (5-10 mL) was added, and the reaction mixture was concentrated to dryness under reduced pressure. The resulting residue was purified by chromatography on silica gel to afford the desired product.

General procedure using glovebox: To a 4-mL borosilicate vial containing a Teflon-coated magnetic stirring bar were added aryl bromide (if solid) (0.200 mmol, 1.00 equiv), *rac*-BINAP (6.2 mg, 10 μmol, 5.0 mol%), amine (if solid) (0.240 mmol, 1.20 equiv), and K_2CO_3 (56 mg, 0.40 mmol, 2.0 equiv). The vial was transferred into a nitrogen-filled glovebox. $Pd(PPh_3)_4$ (12 mg, 10 μmol, 5.0 mol%), dry MeCN (2 mL, c = 0.1 M), butadiene (1.0 mmol, 5.0 equiv), aryl bromide (if liquid) (0.200 mmol, 1.00 equiv), and amine (if liquid) (0.240 mmol, 1.20 equiv) were added. The vial was sealed with a Teflon-lined screw cap, stirred for 5 min without irradiation, and then irradiated with 450 nm LEDs for 12 h at 25 °C. Subsequently, silica gel (5–10 mL) was added, and the reaction mixture was concentrated to dryness under reduced pressure. The resulting residue was purified by chromatography on silica gel to afford the desired product.

For simplicity, in our research, we have opted to execute the transformation for most compounds by using a glovebox. Control experiments showed that yields were within error of measurement.

Allylamine 1



S1, 0.2 mmol | 5.0 equiv | 1.2 equiv | **76% yield** | **1**

To a 4-mL borosilicate vial containing a Teflon-coated magnetic stirring bar were added aryl bromide **S1** (50.0 mg, 0.200 mmol, 1.00 equiv), *rac*-BINAP (6.2 mg, 10 μmol, 5.0 mol%), and K_2CO_3 (56 mg, 0.40 mmol, 2.0 equiv). The vial was transferred into a nitrogen-filled glovebox. $Pd(PPh_3)_4$ (12 mg, 10 μmol, 5.0 mol%), dry MeCN (1 mL, c = 0.1 M), butadiene (1.0 mL, 1.0 M in MeCN, 1.0 mmol, 5.0 equiv), and morpholine (20.9 mg, 20.8 μL, 0.240 mmol, 1.20 equiv) were added. The vial was sealed with a Teflon-lined screw cap, stirred for 5 min without irradiation, and then irradiated with 450 nm LEDs for 12 h at 25 °C. Subsequently, silica gel (5–10 mL) was added, and the reaction mixture was concentrated to dryness under reduced pressure. The resulting residue was purified by chromatography on silica gel (hexanes/EtOAc/Et_3N = 20:10:1) to afford **1** as a light yellow solid in 76% yield (47.3 mg).

$\mathbf{R_f}$ = 0.20 (hexanes/EtOAc/Et_3N = 20:10:1).

NMR Spectroscopy:

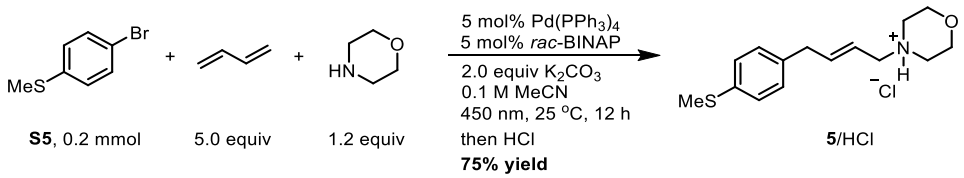
^{1}H NMR (500 MHz, $CDCl_3$, 23 ºC, δ): 7.57 – 7.55 (m, 2H), 7.46 (t, *J* = 7.7 Hz, 2H), 7.41 – 7.36 (m, 2H), 7.05 (dd, *J* = 7.8, 1.7 Hz, 1H), 7.00 (dd, *J* = 11.6, 1.6 Hz, 1H), 5.86 – 5.77 (m, 1H), 5.69 – 5.55 (m, 1H), 3.77 (t, *J* = 4.6 Hz, 4H), 3.44 (d, *J* = 6.7 Hz, 2H), 3.04 (d, *J* = 6.7 Hz, 2H), 2.50 (t, *J* = 4.7 Hz, 4H).

^{13}C NMR (125 MHz, $CDCl_3$, 23 ºC, δ): 159.7 (d, *J* = 248.2 Hz), 141.8 (d, *J* = 7.3 Hz), 135.7, 132.4, 130.6 (d, *J* = 4.1 Hz), 128.9 (d, *J* = 2.9 Hz), 128.4, 128.2, 127.5, 126.8 (d, *J* = 13.5 Hz), 124.5 (d, *J* = 3.1 Hz), 116.1 (d, *J* = 23.1 Hz), 67.0, 61.1, 53.6, 38.3.

^{19}F NMR (471 MHz, $CDCl_3$, 23 ºC, δ): –118.4 (dd, *J* = 11.4, 8.3 Hz).

HRMS-ESIpos (m/z) calc'd for $C_{20}H_{23}FNO$ $[M+H]^+$, 312.1758; found, 312.1755; deviation: +1.1 ppm.

Allylamine hydrochloride 5/HCl



S5, 0.2 mmol | 5.0 equiv | 1.2 equiv | then HCl | **75% yield** | **5**/HCl

To a 4-mL borosilicate vial containing a Teflon-coated magnetic stirring bar were added aryl bromide **S5** (40.6 mg, 0.200 mmol, 1.00 equiv), *rac*-BINAP (6.2 mg, 10 μmol, 5.0 mol%), and K_2CO_3 (56 mg, 0.40 mmol, 2.0 equiv). The vial was transferred into a nitrogen-filled glovebox. $Pd(PPh_3)_4$ (12 mg, 10 μmol, 5.0 mol%), dry MeCN (1 mL, c = 0.1 M), butadiene (1.0 mL, 1.0 M in MeCN, 1.0 mmol, 5.0 equiv), and morpholine (20.9 mg, 20.8 μL, 0.240 mmol, 1.20 equiv) were added. The vial was sealed with a Teflon-lined screw cap, stirred for 5 min without irradiation, and then irradiated with 450 nm LEDs for 12 h at 25 °C. Subsequently, silica gel (5–10 mL) was added, and the reaction mixture was concentrated to dryness under reduced pressure. The resulting residue was purified by chromatography on silica gel (EtOAc/Et_3N = 100:1). To remove $OPPh_3$ in the product, ether (5 mL) was added, followed by the addition of HCl (0.10 mL, 0.40 mmol,

4.0 M in dioxane, 2.0 equiv), and subsequent washing of the precipitate with ether (2 × 2 mL) to afford **5**/HCl as a colorless solid in 75% yield (44.7 mg).

R*f* = 0.23 (EtOAc/Et_3N = 100:1).

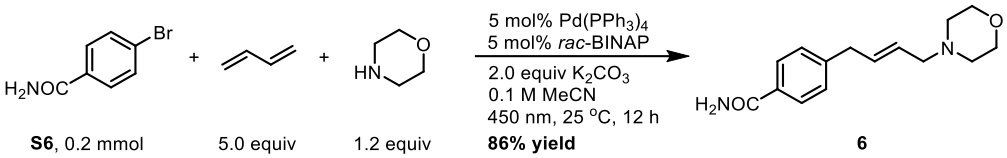
NMR Spectroscopy:

^{1}H NMR (500 MHz, $CDCl_3$, 23 ºC, δ): 13.04 (s, 1H), 7.19 (d, *J* = 8.2 Hz, 2H), 7.07 (d, *J* = 8.2 Hz, 2H), 6.16 – 5.98 (m, 1H), 5.88 (dt, *J* = 15.0, 7.3 Hz, 1H), 4.24 (td, *J* = 12.4, 12.0, 2.1 Hz, 2H), 3.95 (dd, *J* = 13.0, 3.5 Hz, 2H), 3.59 (dd, *J* = 7.5, 3.7 Hz, 2H), 3.43 – 3.31 (m, 4H), 2.88 – 2.74 (m, 2H), 2.46 (s, 3H).

^{13}C NMR (125 MHz, $CDCl_3$, 23 ºC, δ): 142.0, 136.6, 135.3, 129.0, 127.1, 118.3, 63.6, 59.3, 51.1, 38.3, 16.0.

HRMS-ESIpos (m/z) calc'd for $C_{15}H_{22}NOS$ $[M–Cl]^+$, 264.1417; found, 264.1416; deviation: +0.2 ppm.

Allylamine 6



S6, 0.2 mmol | 5.0 equiv | 1.2 equiv | **86% yield** | **6**

To a 4-mL borosilicate vial containing a Teflon-coated magnetic stirring bar were added aryl bromide **S6** (40.0 mg, 0.200 mmol, 1.00 equiv), *rac*-BINAP (6.2 mg, 10 μmol, 5.0 mol%), and K_2CO_3 (56 mg, 0.40 mmol, 2.0 equiv). The vial was transferred into a nitrogen-filled glovebox. $Pd(PPh_3)_4$ (12 mg, 10 μmol, 5.0 mol%), dry MeCN (1 mL, c = 0.1 M), butadiene (1.0 mL, 1.0 M in MeCN, 1.0 mmol, 5.0 equiv), and morpholine (20.9 mg, 20.8 μL, 0.240 mmol, 1.20 equiv) were added. The vial was sealed with a Teflon-lined screw cap, stirred for 5 min without irradiation, and then irradiated with 450 nm LEDs for 12 h at 25 °C. Subsequently, silica gel (5–10 mL) was added, and the reaction mixture was concentrated to dryness under reduced pressure. The resulting residue was purified by chromatography on silica gel (EtOAc/Et_3N = 20:1) to afford **4** as a light yellow solid in 86% yield (44.8 mg).

R*f* = 0.15 (EtOAc/Et_3N = 20:1).

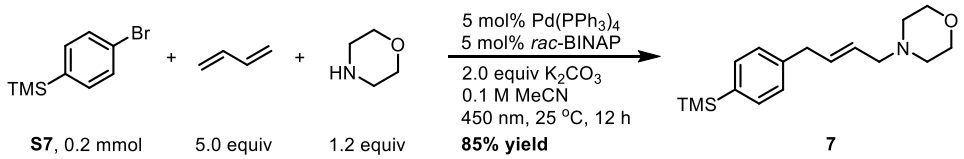
NMR Spectroscopy:

^{1}H NMR (500 MHz, $CDCl_3$, 23 ºC, δ): 7.78 (d, *J* = 8.1 Hz, 2H), 7.27 (d, *J* = 7.9 Hz, 2H), 6.09 (br, 2H), 5.87 – 5.72 (m, 1H), 5.64 – 5.56 (m, 1H), 3.75 (t, *J* = 4.7 Hz, 4H), 3.45 (d, *J* = 6.7 Hz, 2H), 3.01 (d, *J* = 6.8 Hz, 2H), 2.47 (br, 4H).

^{13}C NMR (125 MHz, $CDCl_3$, 23 ºC, δ): 169.2, 144.7, 132.4, 131.2, 128.8, 128.2, 127.6, 66.9, 61.0, 53.6, 38.7.

HRMS-ESIpos (m/z) calc'd for $C_{15}H_{21}N_2O_2$ $[M+H]^+$, 261.1598; found, 261.1598; deviation: –0.1 ppm.

Allylamine 7



S7, 0.2 mmol | 5.0 equiv | 1.2 equiv | **85% yield** | **7**

To a 4-mL borosilicate vial containing a Teflon-coated magnetic stirring bar were added aryl bromide **S3** (45.8 mg, 0.200 mmol, 1.00 equiv), *rac*-BINAP (6.2 mg, 10 μmol, 5.0 mol%), and K_2CO_3 (56 mg, 0.40 mmol, 2.0 equiv). The vial was transferred into a nitrogen-filled glovebox. $Pd(PPh_3)_4$ (12 mg, 10 μmol, 5.0 mol%), dry MeCN (1 mL, c = 0.1 M), butadiene (1.0 mL, 1.0 M in MeCN, 1.0 mmol, 5.0 equiv), and morpholine (20.9 mg, 20.8 μL, 0.240 mmol, 1.20 equiv) were added. The vial was sealed with a Teflon-lined screw cap, stirred for 5 min without irradiation, and then irradiated with 450 nm LEDs for 12 h at 25 °C. Subsequently, silica gel (5–10 mL) was added, and the reaction mixture was concentrated to dryness under reduced pressure. The resulting residue was purified by chromatography on silica gel (hexanes/EtOAc/Et_3N = 20:10:1) to afford **3** as a light yellow oil in 85% yield (49.2 mg).

R_f = 0.21 (hexanes/EtOAc/Et_3N = 20:10:1).

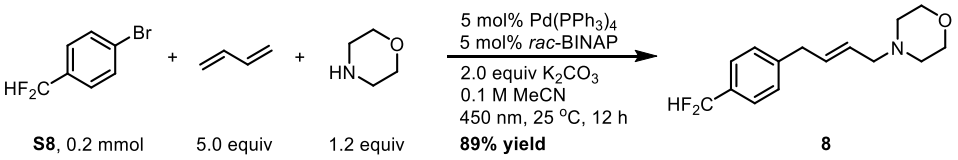
NMR Spectroscopy:

^{1}H NMR (500 MHz, $CDCl_3$, 23 ºC, δ): 7.49 (d, *J* = 7.9 Hz, 2H), 7.20 (d, *J* = 7.6 Hz, 2H), 5.81 (dt, *J* = 15.1, 6.8 Hz, 1H), 5.60 (dt, *J* = 15.2, 6.7 Hz, 1H), 3.76 (t, *J* = 4.7 Hz, 4H), 3.41 (d, *J* = 6.7 Hz, 2H), 3.01 (d, *J* = 6.4 Hz, 2H), 2.48 (t, *J* = 4.7 Hz, 4H), 0.29 (s, 9H).

^{13}C NMR (125 MHz, $CDCl_3$, 23 ºC, δ): 140.8, 137.8, 133.6, 133.4, 128.0, 127.3, 66.9, 61.1, 53.6, 38.9, -1.0.

HRMS-ESIpos (m/z) calc'd for $C_{17}H_{28}NOSi$ $[M+H]^+$, 290.1935; found, 290.1932; deviation: +0.9 ppm.

Allylamine 8



S8, 0.2 mmol | 5.0 equiv | 1.2 equiv | **89% yield** | **8**

To a 4-mL borosilicate vial containing a Teflon-coated magnetic stirring bar were added aryl bromide **S8** (41.4 mg, 0.200 mmol, 1.00 equiv), *rac*-BINAP (6.2 mg, 10 μmol, 5.0 mol%), and K_2CO_3 (56 mg, 0.40 mmol, 2.0 equiv). The vial was transferred into a nitrogen-filled glovebox. $Pd(PPh_3)_4$ (12 mg, 10 μmol, 5.0 mol%), dry MeCN (1 mL, c = 0.1 M), butadiene (1.0 mL, 1.0 M in MeCN, 1.0 mmol, 5.0 equiv), and morpholine (20.9 mg, 20.8 μL, 0.240 mmol, 1.20 equiv) were added. The vial was sealed with a Teflon-lined screw cap, stirred for 5 min without irradiation, and then irradiated with 450 nm LEDs for 12 h at 25 °C. Subsequently, silica gel (5–10 mL) was added, and the reaction mixture was concentrated to dryness under reduced pressure. The resulting residue was purified by chromatography on silica gel (hexanes/EtOAc/Et_3N = 10:15:1) to afford **8** as a light yellow solid in 89% yield (59.5 mg).

R_f = 0.27 (hexanes/EtOAc/Et_3N = 10:15:1).

NMR Spectroscopy:

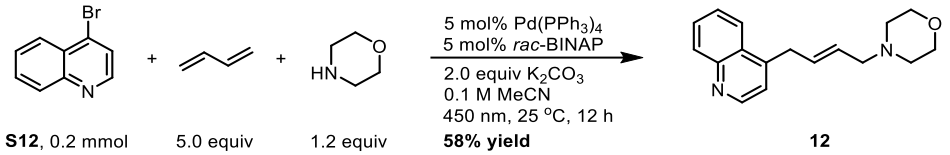
^{1}H NMR (500 MHz, $CDCl_3$, 23 ºC, δ): 7.43 (d, *J* = 7.7 Hz, 2H), 7.25 (d, *J* = 7.7 Hz, 2H), 6.61 (t, *J* = 56.6 Hz, 1H), 5.81 – 5.71 (m, 1H), 5.61 – 5.52 (m, 1H), 3.71 (t, *J* = 4.7 Hz, 4H), 3.41 (d, *J* = 6.7 Hz, 2H), 2.97 (d, *J* = 6.7 Hz, 2H), 2.43 (br, 4H).

^{13}C NMR (125 MHz, $CDCl_3$, 23 ºC, δ): 143.2, 132.7, 132.4 (t, *J* = 22.3 Hz), 128.9, 128.1, 125.8 (t, *J* = 6.0 Hz), 114.9 (t, *J* = 238.2 Hz), 67.1, 61.2, 53.7, 38.8.

^{19}F NMR (471 MHz, $CDCl_3$, 23 ºC, δ): −109.95 (d, *J* = 56.5 Hz).

HRMS-EI (m/z) calc'd for $C_{15}H_{19}NOF_2$ $[M]^+$, 267.1429; found, 267.1432; deviation: –1.1 ppm.

Allylamine 12



To a 4-mL borosilicate vial containing a Teflon-coated magnetic stirring bar were added aryl bromide **S12** (41.6 mg, 0.200 mmol, 1.00 equiv), *rac*-BINAP (6.2 mg, 10 μmol, 5.0 mol%), and K_2CO_3 (56 mg, 0.40 mmol, 2.0 equiv). The vial was transferred into a nitrogen-filled glovebox. $Pd(PPh_3)_4$ (12 mg, 10 μmol, 5.0 mol%), dry MeCN (1 mL, c = 0.1 M), butadiene (1.0 mL, 1.0 M in MeCN, 1.0 mmol, 5.0 equiv), and morpholine (20.9 mg, 20.8 μL, 0.240 mmol, 1.20 equiv) were added. The vial was sealed with a Teflon-lined screw cap, stirred for 5 min without irradiation, and then irradiated with 450 nm LEDs for 12 h at 25 °C. Subsequently, silica gel (5–10 mL) was added, and the reaction mixture was concentrated to dryness under reduced pressure. The resulting residue was purified by chromatography on silica gel (EtOAc/Et_3N = 5:1) to afford **12** as a brownish oil in 58% yield (31.1 mg).

R_f = 0.37 (EtOAc/Et_3N = 5:1).

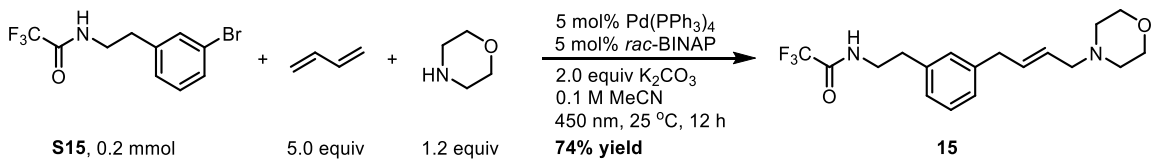
NMR Spectroscopy:

^{1}H NMR (500 MHz, $CDCl_3$, 23 ºC, δ): 8.85 (d, *J* = 4.4 Hz, 1H), 8.14 (d, *J* = 8.9 Hz, 1H), 8.03 (d, *J* = 8.4 Hz, 1H), 7.72 (ddd, *J* = 8.3, 6.8, 1.4 Hz, 1H), 7.57 (ddd, *J* = 8.2, 6.7, 1.3 Hz, 1H), 7.25 (d, *J* = 4.3 Hz, 1H), 5.95 – 5.85 (m, 1H), 5.69 – 5.57 (m, 1H), 3.85 (d, *J* = 6.4 Hz, 2H), 3.71 (t, *J* = 4.7 Hz, 4H), 3.00 (d, *J* = 7.8 Hz, 2H), 2.43 (t, *J* = 4.6 Hz, 4H).

^{13}C NMR (125 MHz, $CDCl_3$, 23 ºC, δ): 150.3, 148.4, 146.0, 130.9, 130.3, 129.3, 129.1, 127.4, 126.4, 123.7, 121.1, 66.9, 61.0, 53.5, 35.1.

HRMS-EI (m/z) calc'd for $C_{17}H_{20}N_2O$ $[M]^+$, 268.1570; found, 268.1572; deviation: –0.7 ppm.

Allylamine 15



To a 4-mL borosilicate vial containing a Teflon-coated magnetic stirring bar were added aryl bromide **S15** (59.2 mg, 0.200 mmol, 1.00 equiv), *rac*-BINAP (6.2 mg, 10 μmol, 5.0 mol%), and K_2CO_3 (56 mg, 0.40 mmol, 2.0 equiv). The vial was transferred into a nitrogen-filled glovebox. $Pd(PPh_3)_4$ (12 mg, 10 μmol, 5.0 mol%), dry MeCN (1 mL, c = 0.1 M), butadiene (1.0 mL, 1.0 M in MeCN, 1.0 mmol, 5.0 equiv), and morpholine (20.9 mg, 20.8 μL, 0.240 mmol, 1.20 equiv) were added. The vial was sealed with a Teflon-lined screw cap, stirred for 5 min without irradiation, and then irradiated with 450 nm LEDs for 12 h at 25 °C. Subsequently, silica gel (5–10 mL) was added, and the reaction mixture was concentrated to dryness under reduced

pressure. The resulting residue was purified by chromatography on silica gel (EtOAc/Et_3N = 100:1) to afford **15** as a light yellow oil in 74% yield (52.9 mg).

R_f = 0.18 (EtOAc/Et_3N = 100:1).

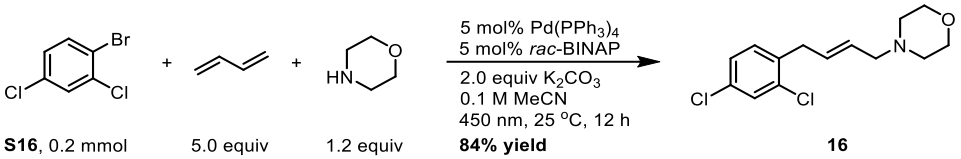
NMR Spectroscopy:

^{1}H NMR (500 MHz, $CDCl_3$, 23 ºC, δ): 7.26 (t, *J* = 7.6 Hz, 1H), 7.08 (d, *J* = 8.0 Hz, 1H), 7.03 (d, *J* = 7.6 Hz, 1H), 7.00 (s, 1H), 6.66 (s, 1H), 5.77 (dt, *J* = 15.3, 6.7 Hz, 1H), 5.56 (dt, *J* = 15.2, 6.8 Hz, 1H), 3.71 (t, *J* = 4.7 Hz, 4H), 3.59 (q, *J* = 6.8 Hz, 2H), 3.37 (d, *J* = 6.8 Hz, 2H), 2.98 (d, *J* = 7.0 Hz, 2H), 2.86 (t, *J* = 7.1 Hz, 2H), 2.44 (t, *J* = 4.7 Hz, 4H).

^{13}C NMR (125 MHz, $CDCl_3$, 23 ºC, δ): 157.2 (q, *J* = 36.9 Hz), 140.9, 137.8, 133.1, 129.0, 129.0, 127.6, 127.2, 126.4, 115.8 (q, *J* = 287.8 Hz), 66.9, 61.1, 53.5, 41.1, 38.7, 34.9.

HRMS-ESIpos (m/z) calc'd for $C_{18}H_{23}N_2O_2NaF_3$ $[M+Na]^+$, 379.1604; found, 379.1605; deviation: –0.2 ppm.

Allylamine 16



To a 4-mL borosilicate vial containing a Teflon-coated magnetic stirring bar were added aryl bromide **S16** (45.2 mg, 0.200 mmol, 1.00 equiv), *rac*-BINAP (6.2 mg, 10 μmol, 5.0 mol%), and K_2CO_3 (56 mg, 0.40 mmol, 2.0 equiv). The vial was transferred into a nitrogen-filled glovebox. $Pd(PPh_3)_4$ (12 mg, 10 μmol, 5.0 mol%), dry MeCN (1 mL, c = 0.1 M), butadiene (1.0 mL, 1.0 M in MeCN, 1.0 mmol, 5.0 equiv), and morpholine (20.9 mg, 20.8 μL, 0.240 mmol, 1.20 equiv) were added. The vial was sealed with a Teflon-lined screw cap, stirred for 5 min without irradiation, and then irradiated with 450 nm LEDs for 12 h at 25 °C. Subsequently, silica gel (5–10 mL) was added, and the reaction mixture was concentrated to dryness under reduced pressure. The resulting residue was purified by chromatography on silica gel (hexanes/EtOAc/Et_3N = 10:5:1) to afford **16** as a light yellow oil in 84% yield (47.9 mg).

R_f = 0.29 (hexanes/EtOAc/Et_3N = 10:5:1).

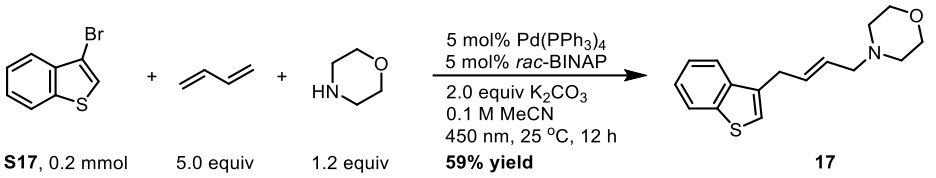
NMR Spectroscopy:

^{1}H NMR (500 MHz, $CDCl_3$, 23 ºC, δ): 7.35 (d, *J* = 2.1 Hz, 1H), 7.16 (dd, *J* = 8.2, 2.1 Hz, 1H), 7.11 (d, *J* = 8.2 Hz, 1H), 5.71 (dt, *J* = 15.2, 6.4 Hz, 1H), 5.50 (dt, *J* = 15.2, 6.8 Hz, 1H), 3.70 (t, *J* = 4.7 Hz, 4H), 3.43 (d, *J* = 6.4 Hz, 2H), 2.96 (d, *J* = 6.8 Hz, 2H), 2.42 (t, *J* = 4.8 Hz, 4H).

^{13}C NMR (125 MHz, $CDCl_3$, 23 ºC, δ): 136.5, 134.7, 132.7, 131.3, 131.0, 129.4, 128.5, 127.2, 67.0, 61.1, 53.6, 35.9.

HRMS-ESIpos (m/z) calc'd for $C_{14}H_{18}NOCl_2$ $[M+H]^+$, 286.0760; found, 286.0758; deviation: +0.6 ppm.

Allylamine 17



S17, 0.2 mmol | 5.0 equiv | 1.2 equiv | **59% yield** | **17**

To a 4-mL borosilicate vial containing a Teflon-coated magnetic stirring bar were added aryl bromide **S17** (42.6 mg, 0.200 mmol, 1.00 equiv), *rac*-BINAP (6.2 mg, 10 μmol, 5.0 mol%), and K_2CO_3 (56 mg, 0.40 mmol, 2.0 equiv). The vial was transferred into a nitrogen-filled glovebox. $Pd(PPh_3)_4$ (12 mg, 10 μmol, 5.0 mol%), dry MeCN (1 mL, c = 0.1 M), butadiene (1.0 mL, 1.0 M in MeCN, 1.0 mmol, 5.0 equiv), and morpholine (20.9 mg, 20.8 μL, 0.240 mmol, 1.20 equiv) were added. The vial was sealed with a Teflon-lined screw cap, stirred for 5 min without irradiation, and then irradiated with 450 nm LEDs for 12 h at 25 °C. Subsequently, silica gel (5–10 mL) was added, and the reaction mixture was concentrated to dryness under reduced pressure. The resulting residue was purified by chromatography on silica gel (hexanes/EtOAc/Et_3N = 10:5:1) to afford **17** as a light yellow oil in 59% yield (32.3 mg).

R_f = 0.35 (hexanes/EtOAc/Et_3N = 10:5:1).

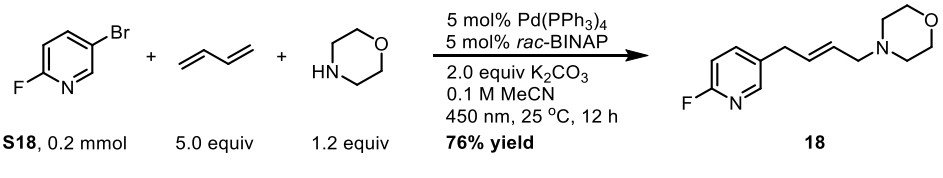
NMR Spectroscopy:

^{1}H NMR (500 MHz, $CDCl_3$, 23 ºC, δ): 7.88 (dd, *J* = 7.8, 1.2 Hz, 1H), 7.76 (dd, *J* = 6.9, 2.0 Hz, 1H), 7.42 – 7.33 (m, 2H), 7.12 (s, 1H), 5.94 – 5.84 (m, 1H), 5.72 – 5.62 (m, 1H), 3.73 (t, *J* = 4.7 Hz, 4H), 3.62 (d, *J* = 6.5 Hz, 2H), 3.02 (d, *J* = 6.1 Hz, 2H), 2.46 (t, *J* = 4.6 Hz, 4H).

^{13}C NMR (125 MHz, $CDCl_3$, 23 ºC, δ): 140.6, 138.7, 134.7, 131.5, 128.3, 124.2, 123.8, 122.9, 122.1, 121.8, 67.0, 61.1, 53.6, 31.8.

HRMS-EI (m/z) calc'd for $C_{16}H_{19}NOS$ $[M]^+$, 273.1182; found, 273.1184; deviation: –0.6 ppm.

Allylamine 18



S18, 0.2 mmol | 5.0 equiv | 1.2 equiv | **76% yield** | **18**

To a 4-mL borosilicate vial containing a Teflon-coated magnetic stirring bar were added aryl bromide **S18** (35.2 mg, 0.200 mmol, 1.00 equiv), *rac*-BINAP (6.2 mg, 10 μmol, 5.0 mol%), and K_2CO_3 (56 mg, 0.40 mmol, 2.0 equiv). The vial was transferred into a nitrogen-filled glovebox. $Pd(PPh_3)_4$ (12 mg, 10 μmol, 5.0 mol%), dry MeCN (1 mL, c = 0.1 M), butadiene (1.0 mL, 1.0 M in MeCN, 1.0 mmol, 5.0 equiv), and morpholine (20.9 mg, 20.8 μL, 0.240 mmol, 1.20 equiv) were added. The vial was sealed with a Teflon-lined screw cap, stirred for 5 min without irradiation, and then irradiated with 450 nm LEDs for 12 h at 25 °C. Subsequently, silica gel (5–10 mL) was added, and the reaction mixture was concentrated to dryness under reduced pressure. The resulting residue was purified by chromatography on silica gel (EtOAc/Et_3N = 50:1) to afford **18** as a light yellow oil in 76% yield (35.9 mg).

R_f = 0.19 (EtOAc/Et_3N = 50:1).

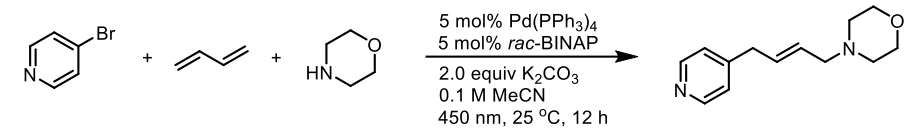
NMR Spectroscopy:

^{1}H NMR (500 MHz, $CDCl_3$, 23 ºC, δ): 8.00 (d, *J* = 2.3 Hz, 1H), 7.60 – 7.51 (m, 1H), 6.84 (dd, *J* = 8.4, 2.8 Hz, 1H), 5.77 – 5.67 (m, 1H), 5.60 – 5.50 (m, 1H), 3.69 (t, *J* = 4.7 Hz, 4H), 3.35 (d, *J* = 6.5 Hz, 2H), 2.96 (d, *J* = 6.6 Hz, 2H), 2.41 (t, *J* = 4.7 Hz, 4H).

^{13}C NMR (125 MHz, $CDCl_3$, 23 ºC, δ): 162.5 (d, *J* = 237.4 Hz), 147.2 (d, *J* = 14.4 Hz), 141.3 (d, *J* = 7.7 Hz), 133.2 (d, *J* = 4.6 Hz), 131.9, 128.8, 109.3 (d, *J* = 37.5 Hz), 67.0, 61.0, 53.7, 35.0.

HRMS-EI (m/z) calc'd for $C_{13}H_{17}N_2OF$ $[M]^+$, 236.1319; found, 236.1321; deviation: –0.6 ppm.

Allylamine 19



S19, 0.2 mmol | 5.0 equiv | 1.2 equiv | **45% yield** | **19**

To a 4-mL borosilicate vial containing a Teflon-coated magnetic stirring bar were added aryl bromide **S19** (31.6 mg, 0.200 mmol, 1.00 equiv), *rac*-BINAP (6.2 mg, 10 μmol, 5.0 mol%), and K_2CO_3 (56 mg, 0.40 mmol, 2.0 equiv). The vial was transferred into a nitrogen-filled glovebox. $Pd(PPh_3)_4$ (12 mg, 10 μmol, 5.0 mol%), dry MeCN (1 mL, c = 0.1 M), butadiene (1.0 mL, 1.0 M in MeCN, 1.0 mmol, 5.0 equiv), and morpholine (20.9 mg, 20.8 μL, 0.240 mmol, 1.20 equiv) were added. The vial was sealed with a Teflon-lined screw cap, stirred for 5 min without irradiation, and then irradiated with 450 nm LEDs for 12 h at 25 °C. Subsequently, silica gel (5–10 mL) was added, and the reaction mixture was concentrated to dryness under reduced pressure. The resulting residue was purified by chromatography on silica gel (EtOAc/Et_3N = 20:1) to afford **19** as a yellow oil in 45% yield (19.6 mg).

R_f = 0.19 (EtOAc/Et_3N = 20:1).

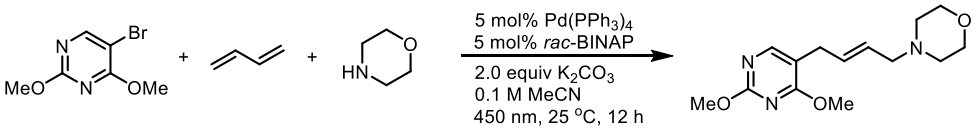
NMR Spectroscopy:

^{1}H NMR (500 MHz, $CDCl_3$, 23 ºC, δ): 8.67 (d, *J* = 5.0 Hz, 2H), 7.27 (d, *J* = 5.0 Hz, 2H), 5.91 (dt, *J* = 14.2, 6.7 Hz, 1H), 5.77 (dt, *J* = 14.6, 6.7 Hz, 1H), 3.88 (t, *J* = 4.6 Hz, 4H), 3.53 (d, *J* = 6.6 Hz, 2H), 3.15 (d, *J* = 6.6 Hz, 2H), 2.60 (t, *J* = 4.6 Hz, 4H).

^{13}C NMR (125 MHz, $CDCl_3$, 23 ºC, δ): 150.0, 149.2, 131.2, 129.2, 124.0, 67.0, 61.1, 53.7, 38.2.

HRMS-EI (m/z) calc'd for $C_{13}H_{18}N_2O$ $[M]^+$, 218.1414; found, 218.1414; deviation: –0.2 ppm.

Allylamine 20



S20, 0.2 mmol | 5.0 equiv | 1.2 equiv | **74% yield** | **20**

To a 4-mL borosilicate vial containing a Teflon-coated magnetic stirring bar were added aryl bromide **S20** (43.8 mg, 0.200 mmol, 1.00 equiv), *rac*-BINAP (6.2 mg, 10 μmol, 5.0 mol%), and K_2CO_3 (56 mg, 0.40 mmol, 2.0 equiv). The vial was transferred into a nitrogen-filled glovebox. $Pd(PPh_3)_4$ (12 mg, 10 μmol, 5.0 mol%),

dry MeCN (1 mL, c = 0.1 M), butadiene (1.0 mL, 1.0 M in MeCN, 1.0 mmol, 5.0 equiv), and morpholine (20.9 mg, 20.8 μL, 0.240 mmol, 1.20 equiv) were added. The vial was sealed with a Teflon-lined screw cap, stirred for 5 min without irradiation, and then irradiated with 450 nm LEDs for 12 h at 25 °C. Subsequently, silica gel (5–10 mL) was added, and the reaction mixture was concentrated to dryness under reduced pressure. The resulting residue was purified by chromatography on silica gel (EtOAc/Et_3N = 50:1) to afford **20** as a yellow oil in 74% yield (41.3 mg).

R_f = 0.23 (EtOAc/Et_3N = 50:1).

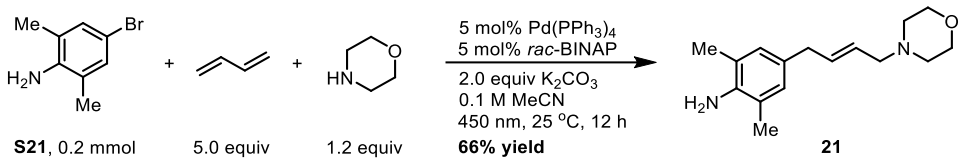
NMR Spectroscopy:

^{1}H NMR (500 MHz, $CDCl_3$, 23 ºC, δ): 8.0 (s, 1H), 5.7 (dt, *J* = 14.2, 6.5 Hz, 1H), 5.5 (dt, *J* = 15.3, 6.7 Hz, 1H), 3.9 (d, *J* = 3.7 Hz, 6H), 3.7 (t, *J* = 4.7 Hz, 4H), 3.2 (d, *J* = 6.4 Hz, 2H), 2.9 (dd, *J* = 6.8, 1.2 Hz, 2H), 2.4 (t, *J* = 4.9 Hz, 4H).

^{13}C NMR (125 MHz, $CDCl_3$, 23 ºC, δ): 169.3, 164.4, 157.0, 131.0, 128.2, 113.6, 67.1, 61.1, 54.7, 54.0, 53.6, 29.4.

HRMS-EI (m/z) calc'd for $C_{14}H_{21}N_3O_3$ $[M]^+$, 279.1577; found, 279.1577; deviation: +0.2 ppm.

Allylamine 21



To a 4-mL borosilicate vial containing a Teflon-coated magnetic stirring bar were added aryl bromide **S21** (40.0 mg, 0.200 mmol, 1.00 equiv), *rac*-BINAP (6.2 mg, 10 μmol, 5.0 mol%), and K_2CO_3 (56 mg, 0.40 mmol, 2.0 equiv). The vial was transferred into a nitrogen-filled glovebox. $Pd(PPh_3)_4$ (12 mg, 10 μmol, 5.0 mol%), dry MeCN (1 mL, c = 0.1 M), butadiene (1.0 mL, 1.0 M in MeCN, 1.0 mmol, 5.0 equiv), and morpholine (20.9 mg, 20.8 μL, 0.240 mmol, 1.20 equiv) were added. The vial was sealed with a Teflon-lined screw cap, stirred for 5 min without irradiation, and then irradiated with 450 nm LEDs for 12 h at 25 °C. Subsequently, silica gel (5–10 mL) was added, and the reaction mixture was concentrated to dryness under reduced pressure. The resulting residue was purified by chromatography on silica gel (hexanes/EtOAc/Et_3N = 10:5:1) to afford **1** as a light brown oil in 66% yield (34.6 mg).

R_f = 0.19 (hexanes/EtOAc/Et_3N = 10:5:1).

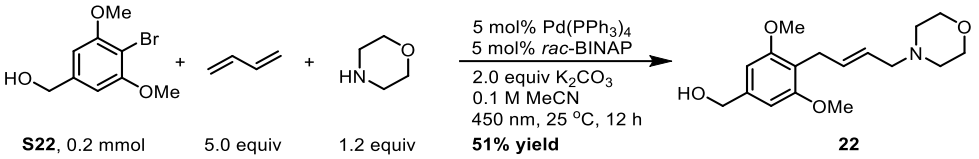
NMR Spectroscopy:

^{1}H NMR (500 MHz, $CDCl_3$, 23 ºC, δ): 6.75 (s, 2H), 5.80 – 5.69 (m, 1H), 5.59 – 5.49 (m, 1H), 3.73 (t, *J* = 4.7 Hz, 4H), 3.48 (s, 2H), 3.23 (d, *J* = 6.8 Hz, 2H), 2.97 (d, *J* = 6.8 Hz, 2H), 2.45 (t, *J* = 4.9 Hz, 4H), 2.16 (s, 6H).

^{13}C NMR (125 MHz, $CDCl_3$, 23 ºC, δ): 140.9, 134.8, 129.6, 128.4, 126.3, 122.0, 67.0, 61.3, 53.6, 38.2, 17.7.

HRMS-EI (m/z) calc'd for $C_{16}H_{24}N_2O$ $[M]^+$, 260.1883; found, 260.1884; deviation: –0.2 ppm.

Allylamine 22



S22, 0.2 mmol | 5.0 equiv | 1.2 equiv | **51% yield** | **22**

To a 4-mL borosilicate vial containing a Teflon-coated magnetic stirring bar were added aryl bromide **S22** (43.0 mg, 0.200 mmol, 1.00 equiv), *rac*-BINAP (6.2 mg, 10 μmol, 5.0 mol%), and K_2CO_3 (56 mg, 0.40 mmol, 2.0 equiv). The vial was transferred into a nitrogen-filled glovebox. $Pd(PPh_3)_4$ (12 mg, 10 μmol, 5.0 mol%), dry MeCN (1 mL, c = 0.1 M), butadiene (1.0 mL, 1.0 M in MeCN, 1.0 mmol, 5.0 equiv), and morpholine (20.9 mg, 20.8 μL, 0.240 mmol, 1.20 equiv) were added. The vial was sealed with a Teflon-lined screw cap, stirred for 5 min without irradiation, and then irradiated with 450 nm LEDs for 12 h at 25 °C. Subsequently, silica gel (5–10 mL) was added, and the reaction mixture was concentrated to dryness under reduced pressure. The resulting residue was purified by chromatography on silica gel (EtOAc/MeOH/Et_3N = 100:5:1) to afford **22** as a light yellow oil in 51% yield (31.2 mg).

R_f = 0.20 (EtOAc/MeOH/Et_3N = 100:5:1).

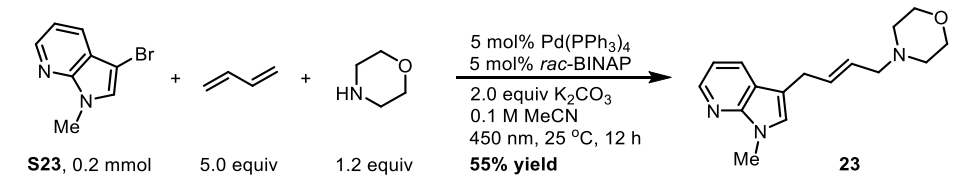
NMR Spectroscopy:

^{1}H NMR (500 MHz, $CDCl_3$, 23 °C, δ): 6.56 (s, 2H), 5.74 – 5.64 (m, 1H), 5.50 – 5.40 (m, 1H), 4.65 (s, 2H), 3.81 (s, 6H), 3.70 (t, *J* = 4.7 Hz, 4H), 3.37 (d, *J* = 6.3 Hz, 2H), 2.90 (d, *J* = 7.5 Hz, 2H), 2.39 (s, 4H).

^{13}C NMR (125 MHz, $CDCl_3$, 23 °C, δ): 158.2, 140.5, 132.9, 125.5, 115.7, 102.4, 66.9, 65.5, 61.2, 55.7, 53.4, 25.9.

HRMS-ESIpos (m/z) calc'd for $C_{17}H_{26}NO_4$ $[M+H]^+$, 308.1856; found, 308.1857; deviation: –0.1 ppm.

Allylamine 23



S23, 0.2 mmol | 5.0 equiv | 1.2 equiv | **55% yield** | **23**

To a 4-mL borosilicate vial containing a Teflon-coated magnetic stirring bar were added aryl bromide **S23** (42.2 mg, 0.200 mmol, 1.00 equiv), *rac*-BINAP (6.2 mg, 10 μmol, 5.0 mol%), and K_2CO_3 (56 mg, 0.40 mmol, 2.0 equiv). The vial was transferred into a nitrogen-filled glovebox. $Pd(PPh_3)_4$ (12 mg, 10 μmol, 5.0 mol%), dry MeCN (1 mL, c = 0.1 M), butadiene (1.0 mL, 1.0 M in MeCN, 1.0 mmol, 5.0 equiv), and morpholine (20.9 mg, 20.8 μL, 0.240 mmol, 1.20 equiv) were added. The vial was sealed with a Teflon-lined screw cap, stirred for 5 min without irradiation, and then irradiated with 450 nm LEDs for 12 h at 25 °C. Subsequently, silica gel (5–10 mL) was added, and the reaction mixture was concentrated to dryness under reduced pressure. The resulting residue was purified by chromatography on silica gel (hexanes/EtOAc/Et_3N = 5:20:1) to afford **23** as a yellow oil in 55% yield (29.8 mg).

R_f = 0.19 (hexanes/EtOAc/Et_3N = 5:20:1).

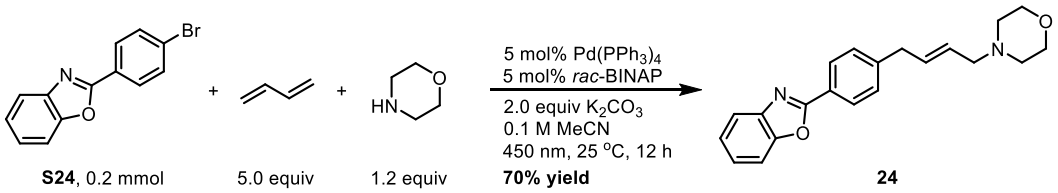
NMR Spectroscopy:

^{1}H NMR (500 MHz, $CDCl_3$, 23 ºC, δ): 8.31 (d, *J* = 4.7 Hz, 1H), 7.83 (d, *J* = 7.8 Hz, 1H), 7.00 (dd, *J* = 7.9, 4.7 Hz, 1H), 6.94 (s, 1H), 5.82 (dt, *J* = 13.7, 6.4 Hz, 1H), 5.60 (dt, *J* = 14.6, 6.6 Hz, 1H), 3.83 (s, 3H), 3.70 (t, *J* = 4.6 Hz, 4H), 3.47 (d, *J* = 6.4 Hz, 2H), 2.97 (d, *J* = 6.6 Hz, 2H), 2.49 – 2.36 (m, 4H).

^{13}C NMR (125 MHz, $CDCl_3$, 23 ºC, δ): 148.1, 142.9, 133.0, 127.1, 126.9, 126.4, 120.1, 114.8, 111.5, 66.9, 61.1, 53.6, 31.0, 28.4.

HRMS-EI (m/z) calc'd for $C_{16}H_{21}N_3O$ $[M]^+$, 271.1679; found, 271.1677; deviation: +0.7 ppm.

Allylamine 24



S24, 0.2 mmol | 5.0 equiv | 1.2 equiv | **70% yield** | **24**

To a 4-mL borosilicate vial containing a Teflon-coated magnetic stirring bar were added aryl bromide **S24** (54.8 mg, 0.200 mmol, 1.00 equiv), *rac*-BINAP (6.2 mg, 10 μmol, 5.0 mol%), and K_2CO_3 (56 mg, 0.40 mmol, 2.0 equiv). The vial was transferred into a nitrogen-filled glovebox. $Pd(PPh_3)_4$ (12 mg, 10 μmol, 5.0 mol%), dry MeCN (1 mL, c = 0.1 M), butadiene (1.0 mL, 1.0 M in MeCN, 1.0 mmol, 5.0 equiv), and morpholine (20.9 mg, 20.8 μL, 0.240 mmol, 1.20 equiv) were added. The vial was sealed with a Teflon-lined screw cap, stirred for 5 min without irradiation, and then irradiated with 450 nm LEDs for 12 h at 25 °C. Subsequently, silica gel (5–10 mL) was added, and the reaction mixture was concentrated to dryness under reduced pressure. The resulting residue was purified by chromatography on silica gel (hexanes/EtOAc/Et_3N = 10:5:1) to afford **24** as a light yellow oil in 70% yield (46.6 mg).

R_f = 0.18 (hexanes/EtOAc/Et_3N = 10:5:1).

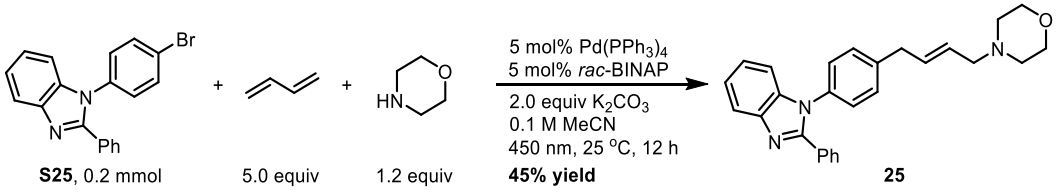
NMR Spectroscopy:

^{1}H NMR (500 MHz, $CDCl_3$, 23 ºC, δ): 8.20 (d, *J* = 8.3 Hz, 2H), 7.82 – 7.75 (m, 1H), 7.62 – 7.55 (m, 1H), 7.40 – 7.32 (m, 4H), 5.88 – 5.76 (m, 1H), 5.68 – 5.57 (m, 1H), 3.74 (t, *J* = 4.7 Hz, 4H), 3.48 (d, *J* = 6.7 Hz, 2H), 3.01 (d, *J* = 6.8 Hz, 2H), 2.46 (t, *J* = 4.7 Hz, 4H).

^{13}C NMR (125 MHz, $CDCl_3$, 23 ºC, δ): 163.1, 150.7, 144.2, 142.2, 132.4, 129.1, 128.3, 127.8, 125.1, 125.0, 124.5, 119.9, 110.5, 67.0, 61.1, 53.6, 38.8.

HRMS-ESIpos (m/z) calc'd for $C_{21}H_{23}N_2O_2$ $[M+H]^+$, 335.1754; found, 335.1753; deviation: +0.2 ppm.

Allylamine 25



S25, 0.2 mmol | 5.0 equiv | 1.2 equiv | **45% yield** | **25**

To a 4-mL borosilicate vial containing a Teflon-coated magnetic stirring bar were added aryl bromide **S25**

(70.0 mg, 0.200 mmol, 1.00 equiv), *rac*-BINAP (6.2 mg, 10 μmol, 5.0 mol%), and K_2CO_3 (56 mg, 0.40 mmol, 2.0 equiv). The vial was transferred into a nitrogen-filled glovebox. $Pd(PPh_3)_4$ (12 mg, 10 μmol, 5.0 mol%), dry MeCN (1 mL, c = 0.1 M), butadiene (1.0 mL, 1.0 M in MeCN, 1.0 mmol, 5.0 equiv), and morpholine (20.9 mg, 20.8 μL, 0.240 mmol, 1.20 equiv) were added. The vial was sealed with a Teflon-lined screw cap, stirred for 5 min without irradiation, and then irradiated with 450 nm LEDs for 12 h at 25 °C. Subsequently, silica gel (5–10 mL) was added, and the reaction mixture was concentrated to dryness under reduced pressure. The resulting residue was purified by chromatography on silica gel (EtOAc/Et_3N = 50:1) to afford **25** as a yellow oil in 45% yield (36.8 mg).

R_f = 0.32 (EtOAc/Et_3N = 50:1).

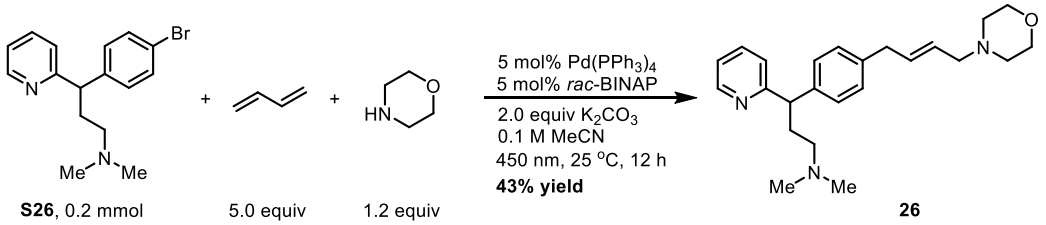
NMR Spectroscopy:

^{1}H NMR (500 MHz, $CDCl_3$, 23 ºC, δ): 7.88 (d, *J* = 8.0 Hz, 1H), 7.57 (d, *J* = 7.1 Hz, 2H), 7.37 – 7.28 (m, 6H), 7.26 – 7.20 (m, 4H), 5.83 (dt, *J* = 15.2, 6.7 Hz, 1H), 5.63 (dt, *J* = 15.2, 6.7 Hz, 1H), 3.74 (t, *J* = 4.7 Hz, 4H), 3.47 (d, *J* = 6.6 Hz, 2H), 3.03 (d, *J* = 6.7 Hz, 2H), 2.47 (t, *J* = 4.6 Hz, 4H).

^{13}C NMR (125 MHz, $CDCl_3$, 23 ºC, δ): 152.4, 143.0, 140.8, 137.3, 135.0, 130.0, 129.9, 129.5, 129.4, 128.3, 127.4, 123.3, 122.9, 119.8, 110.5, 66.9, 61.0, 53.5, 38.4.

HRMS-ESIpos (m/z) calc'd for $C_{27}H_{28}N_3O$ $[M+H]^+$, 410.2227; found, 410.2228; deviation: –0.2 ppm.

Brompheniramine-derived allylamine 26



S26, 0.2 mmol 5.0 equiv 1.2 equiv **26**

To a 4-mL borosilicate vial containing a Teflon-coated magnetic stirring bar were added brompheniramine **S26** (63.8 mg, 0.200 mmol, 1.00 equiv), *rac*-BINAP (6.2 mg, 10 μmol, 5.0 mol%), and K_2CO_3 (56 mg, 0.40 mmol, 2.0 equiv). The vial was transferred into a nitrogen-filled glovebox. $Pd(PPh_3)_4$ (12 mg, 10 μmol, 5.0 mol%), dry MeCN (1 mL, c = 0.1 M), butadiene (1.0 mL, 1.0 M in MeCN, 1.0 mmol, 5.0 equiv), and morpholine (20.9 mg, 20.8 μL, 0.240 mmol, 1.20 equiv) were added. The vial was sealed with a Teflon-lined screw cap, stirred for 5 min without irradiation, and then irradiated with 450 nm LEDs for 12 h at 25 °C. Subsequently, silica gel (5–10 mL) was added, and the reaction mixture was concentrated to dryness under reduced pressure. The resulting residue was purified by chromatography on silica gel (EtOAc/Et_3N = 10:1) to afford **26** as a light yellow oil in 43% yield (32.6 mg).

R_f = 0.12 (EtOAc/Et_3N = 10:1).

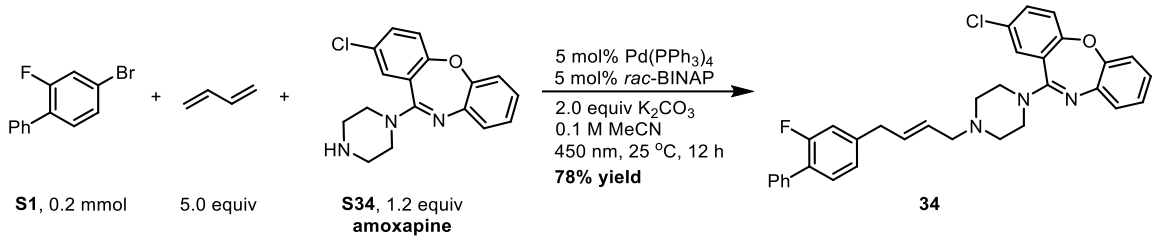
NMR Spectroscopy:

^{1}H NMR (500 MHz, $CDCl_3$, 23 ºC, δ): 8.55 (dd, *J* = 4.3, 1.3 Hz, 1H), 7.54 (td, *J* = 7.7, 1.8 Hz, 1H), 7.26 (d, *J* = 8.1 Hz, 2H), 7.15 (d, *J* = 7.8 Hz, 1H), 7.11 – 7.04 (m, 3H), 5.74 (dt, *J* = 15.1, 6.7 Hz, 1H), 5.58 – 5.48 (m, 1H), 4.11 (t, *J* = 6.9 Hz, 1H), 3.71 (t, *J* = 4.7 Hz, 4H), 3.32 (d, *J* = 6.7 Hz, 2H), 2.95 (d, *J* = 6.7 Hz, 2H), 2.42 (t, *J* = 4.7 Hz, 4H), 2.20 (s, 6H).

^{13}C NMR (125 MHz, $CDCl_3$, 23 ºC, δ): 163.8, 149.4, 141.5, 138.3, 136.5, 133.5, 128.7, 128.1, 127.4, 122.9, 121.4, 67.1, 61.2, 58.0, 53.7, 51.1, 45.5, 38.5, 32.9.

HRMS-ESIpos (m/z) calc'd for $C_{24}H_{34}N_3O$ $[M+H]^+$, 380.2696; found, 380.2696; deviation: +0.1 ppm.

Amoxapine-derived allylamine 34



To a 4-mL borosilicate vial containing a Teflon-coated magnetic stirring bar were added aryl bromide **S1** (50.0 mg, 0.200 mmol, 1.00 equiv), *rac*-BINAP (6.2 mg, 10 μmol, 5.0 mol%), and K_2CO_3 (56 mg, 0.40 mmol, 2.0 equiv). The vial was transferred into a nitrogen-filled glovebox. $Pd(PPh_3)_4$ (12 mg, 10 μmol, 5.0 mol%), dry MeCN (1 mL, c = 0.1 M), butadiene (1.0 mL, 1.0 M in MeCN, 1.0 mmol, 5.0 equiv), and amoxapine **S34** (75.3 mg, 0.240 mmol, 1.20 equiv) were added. The vial was sealed with a Teflon-lined screw cap, stirred for 5 min without irradiation, and then irradiated with 450 nm LEDs for 12 h at 25 °C. Subsequently, silica gel (5–10 mL) was added, and the reaction mixture was concentrated to dryness under reduced pressure. The resulting residue was purified by chromatography on silica gel (hexanes/EtOAc = 1:1) to afford **34** as a light yellow oil in 78% yield (84.0 mg).

R_f = 0.22 (hexanes/EtOAc = 1:1).

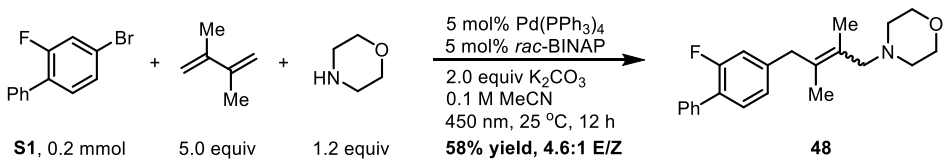
NMR Spectroscopy:

^{1}H NMR (500 MHz, $CDCl_3$, 23 ºC, δ): 7.57 (d, *J* = 8.3 Hz, 2H), 7.47 (t, *J* = 7.7 Hz, 2H), 7.44 – 7.35 (m, 3H), 7.35 (d, *J* = 2.6 Hz, 1H), 7.21 (d, *J* = 8.6 Hz, 1H), 7.18 (dd, *J* = 7.8, 1.7 Hz, 1H), 7.16 – 7.08 (m, 2H), 7.09 – 7.04 (m, 1H), 7.05 – 6.98 (m, 2H), 5.84 (dt, *J* = 15.2, 6.7 Hz, 1H), 5.68 (dt, *J* = 15.2, 6.6 Hz, 1H), 3.60 (s, 4H), 3.46 (d, *J* = 6.7 Hz, 2H), 3.11 (d, *J* = 6.6 Hz, 2H), 2.61 (s, 4H).

^{13}C NMR (125 MHz, $CDCl_3$, 23 ºC, δ): 159.7 (d, *J* = 248.0 Hz), 159.3, 158.9, 151.8, 141.8 (d, *J* = 7.3 Hz), 140.2, 135.8, 132.5, 130.7 (d, *J* = 3.8 Hz), 130.2, 129.1, 129.0 (d, *J* = 2.9 Hz), 128.4, 128.3, 127.5, 127.1, 126.8 (d, *J* = 13.5 Hz), 125.8, 125.1, 124.5, 124.5, 122.7, 120.1, 116.1 (d, *J* = 23.1 Hz), 60.7, 52.9, 47.4, 38.3.

HRMS-ESIpos (m/z) calc'd for $C_{33}H_{30}ClFN_3O$ $[M+H]^+$, 538.2056; found, 538.2060; deviation: –0.9 ppm.

Allylamine 48



To a 4-mL borosilicate vial containing a Teflon-coated magnetic stirring bar were added aryl bromide **S1** (50.0 mg, 0.200 mmol, 1.00 equiv), *rac*-BINAP (6.2 mg, 10 μmol, 5.0 mol%), and K_2CO_3 (56 mg, 0.40 mmol,

2.0 equiv). The vial was transferred into a nitrogen-filled glovebox. $Pd(PPh_3)_4$ (12 mg, 10 μmol, 5.0 mol%), dry MeCN (2 mL, c = 0.1 M), 2,3-dimethylbuta-1,3-diene (82.2 mg, 113 μL, 1.00 mmol, 5.00 equiv), and morpholine (20.9 mg, 20.8 μL, 0.240 mmol, 1.20 equiv) were added. The vial was sealed with a Teflon-lined screw cap, stirred for 5 min without irradiation, and then irradiated with 450 nm LEDs for 12 h at 25 °C. Subsequently, silica gel (5–10 mL) was added, and the reaction mixture was concentrated to dryness under reduced pressure. The resulting residue was purified by chromatography on silica gel (hexanes/EtOAc/Et_3N = 30:10:1) to afford **48** as a light yellow oil in 58% yield (39.1 mg).

R_f = 0.23 (hexanes/EtOAc/Et_3N = 30:10:1).

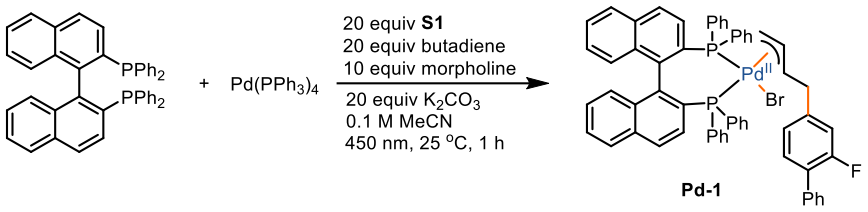
NMR Spectroscopy:

^{1}H NMR (500 MHz, $CDCl_3$, 23 ºC, δ): 7.59 – 7.55 (m, 2H), 7.46 (t, *J* = 7.7 Hz, 2H), 7.40 – 7.33 (m, 2H), 7.02 (dd, *J* = 7.9, 1.6 Hz, 1H), 6.95 (dd, *J* = 11.9, 1.6 Hz, 1H), 3.74 (t, *J* = 4.6 Hz, 4H), 3.48 (s, 2H), 3.03 (s, 2H), 2.45 (t, *J* = 4.5 Hz, 4H), 1.89 (d, *J* = 1.5 Hz, 3H), 1.73 (d, *J* = 1.5 Hz, 3H).

^{13}C NMR (125 MHz, $CDCl_3$, 23 ºC, δ): 159.8 (d, *J* = 247.7 Hz), 142.2 (d, *J* = 7.4 Hz), 135.8, 130.8, 130.5 (d, *J* = 3.8 Hz), 128.9 (d, *J* = 2.9 Hz), 128.4, 127.6, 127.4, 126.5 (d, *J* = 13.2 Hz), 124.4 (d, *J* = 3.1 Hz), 115.8 (d, *J* = 23.0 Hz), 67.2, 61.4, 53.6, 40.2, 18.4, 17.9.

HRMS-EI (m/z) calc'd for $C_{22}H_{26}NOF$ $[M]^+$, 339.1993; found, 339.1994; deviation: –0.4 ppm.

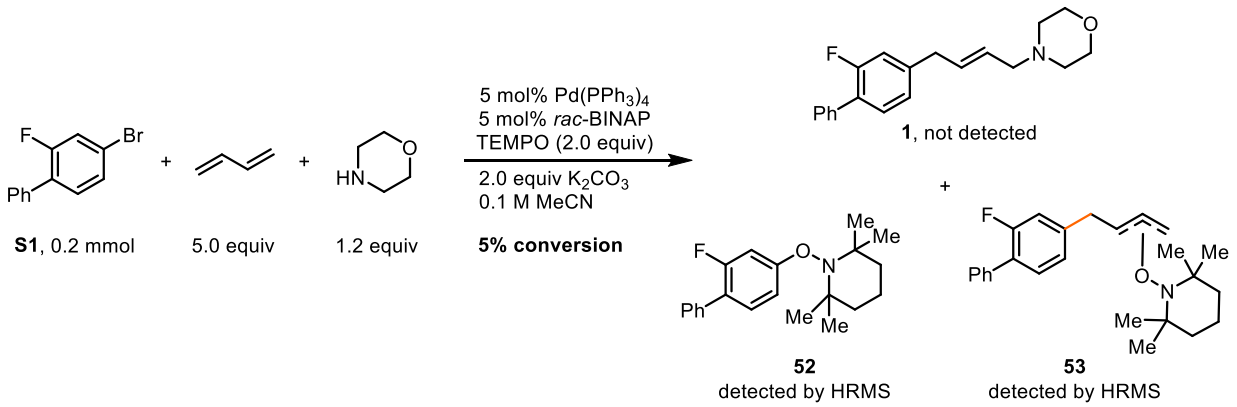
III.2.2 Detection of allyl Pd(II) species by ESI-MS



To a 4-mL borosilicate vial containing a Teflon-coated magnetic stirring bar were added aryl bromide **S1** (50.0 mg, 0.200 mmol, 20.0 equiv), *rac*-BINAP (6.2 mg, 10 μmol, 1.0 equiv), and K_2CO_3 (28 mg, 0.20 mmol, 20 equiv). The vial was transferred into a nitrogen-filled glovebox. $Pd(PPh_3)_4$ (12 mg, 10 μmol, 1.0 equiv), dry MeCN (1 mL, c = 0.1 M), butadiene (0.20 mL, 1.0 M in MeCN, 0.20 mmol, 20 equiv), and morpholine (11 mg, 11 μL, 0.10 mmol, 10 equiv) were added. The vial was sealed with a Teflon-lined screw cap, stirred for 5 min without irradiation, and then irradiated with 450 nm LEDs for 1 h at 25 °C. Then the reaction mixture was cooled down to –78 °C and measured by high-resolution mass spectrometry (HRMS). Allyl Pd(II) species **Pd-1** was detected.

HRMS-ESIpos (m/z) of **Pd-1** calc'd for $C_{60}H_{46}FP_2Pd$ $[M–Br]^+$, 953.2088; found, 953.2090; deviation: –0.2 ppm.

III.2.3 Radical trapping experiment with TEMPO



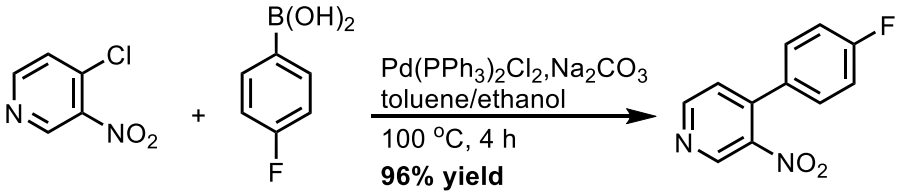
To a 4-mL borosilicate vial containing a Teflon-coated magnetic stirring bar were added aryl bromide **S1** (50.0 mg, 0.200 mmol, 1.00 equiv), *rac*-BINAP (6.2 mg, 10 μmol, 5.0 mol%), TEMPO (62.5 mg, 0.400 mmol, 2.00 equiv), and K_2CO_3 (56 mg, 0.40 mmol, 2.0 equiv). The vial was transferred into a nitrogen-filled glovebox. $Pd(PPh_3)_4$ (12 mg, 10 μmol, 5.0 mol%), dry MeCN (1 mL, c = 0.1 M), butadiene (1.0 mL, 1.0 M in MeCN, 1.0 mmol, 5.0 equiv), and morpholine (20.9 mg, 20.8 μL, 0.240 mmol, 1.20 equiv) were added. The vial was sealed with a Teflon-lined screw cap, stirred for 5 min without irradiation, and then irradiated with 450 nm LEDs for 12 h at 25 °C. Then the reaction mixtures was measured by high-resolution mass spectrometry (HRMS). The reaction conversion was approximately 5%, and the 1,4-aminoarylation product **1** was not observed. Both **52** and **53** were detected by HRMS.

HRMS-ESIpos (m/z) of **52** calc'd for $C_{21}H_{27}FNO$ $[M+H]^+$, 328.2071; found, 328.2071; deviation: +0.2 ppm.

HRMS-ESIpos (m/z) of **53** calc'd for $C_{25}H_{33}FNO$ $[M+H]^+$, 382.2541; found, 328.2541; deviation: –0.1 ppm.

III.3 Synthesis of Fluorinated Substrates

III.3.1 Synthesis of 4-(4-fluorophenyl)-3-nitropyridine S55



S55

4-(4-Fluorophenyl)-3-nitropyridine (S55) was synthesized following a reported literature procedure with minor modifications.[171] A 50 mL round-bottom flask equipped with a magnetic stir bar was charged with 4-chloro-3-nitropyridine (0.8 g, 5.0 mmol, 1.0 equiv.), 4-fluorophenylboronic acid (1.0 g, 7.5 mmol, 1.5 equiv.), and Na_2CO_3 (6.30 mL, 12.5 mmol, 2.50 equiv., 2.00 M aqueous solution) in toluene (16 mL) and ethanol (3 mL). The mixture was degassed, and bis(triphenylphosphine)palladium(II) chloride (0.18 g, 0.25 mmol, 0.05 equiv.) was added. The reaction mixture was stirred at 100 °C for 4 hours. After cooling to room temperature, the mixture was transferred to a separatory funnel containing saturated aqueous $NaHCO_3$ (20 mL). The aqueous layer was extracted with ethyl acetate (3 × 20 mL). The combined organic layers were washed with brine (25 mL), dried over Na_2SO_4, filtered, and concentrated under reduced pressure. The crude product was purified by column chromatography on silica gel, eluting with pentane/EtOAc (10:3(v/v)), affording 1.0 g (96% yield) of the title compound **S55 (4-(4-fluorophenyl)-3-nitropyridine)** as a yellow solid.

R_f = 0.20 (pentane/EtOAc = 10:3 (v/v)).

NMR Spectroscopy:

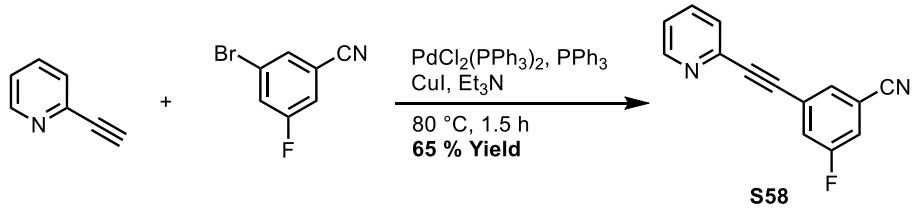
^{1}H NMR (500 MHz, $CDCl_3$, 23 ºC, δ): 9.02 (s, 1H), 8.76 (d, *J* = 5.0 Hz, 1H), 7.35 (d, *J* = 5.0 Hz, 1H), 7.29 (dd, *J* = 8.8, 5.1 Hz, 2H), 7.10 (t, *J* = 8.6 Hz, 2H).

^{13}C NMR (125 MHz, $CDCl_3$, 23 ºC, δ): 164.42, 162.43, 152.86, 145.37, 145.23, 142.77, 130.49 (d, *J* = 3.5 Hz), 129.65 (d, *J* = 8.4 Hz), 125.67, 116.28, 116.10.

^{19}F NMR (471 MHz, $CDCl_3$, 23 ºC, δ): –110.98 (td, *J* = 8.7, 4.4 Hz).

HRMS-ESIpos (m/z) calc'd for $C_{11}H_7O_2N_2F$ $[M]^+$, 218.0486; found, 218.0487; deviation: –0.5 ppm.

III.3.2 Synthesis of 3-Fluoro-5-[(pyridin-3-yl)ethynyl]benzonitrile (FPEB) S58



S58
FPEB

3-Fluoro-5-[(pyridin-3-yl)ethynyl]benzonitrile (FPEB, S58) was synthesized following a reported literature procedure with minor modifications.[158] A flame-dried 50 mL round-bottom flask equipped with a Teflon-coated magnetic stir bar was charged with 2-ethynylpyridine (0.5 g, 5.0 mmol, 1.0 equiv.), 3-dibromo-5-fluorobenzonitrile (3.0 g, 15 mmol, 3.0 equiv.), trans-dichlorobis(triphenylphosphine)palladium(II) (0.35 g, 0.50 mmol, 0.10 equiv.), CuI (0.48 g, 2.50 mmol, 0.50 equiv.), PPh_3 (0.26 g, 1.00 mmol, 0.20 equiv.), and Et_3N (10.1 g, 14.0 mL, 100 mmol, 20.0 equiv.). The mixture was heated at 80 °C for 1.5 h. After cooling to 25 ºC the reaction mixture was diluted with saturated aqueous NH_4Cl (10 mL) and extracted with DCM (4 × ~30 mL). The combined organic layers were dried over Na_2SO_4 and concentrated under reduced pressure. The residue was dissolved in 50 mL of hexanes/EtOAc (4:1), filtered through a silica gel column, and washed three times with 20 mL hexanes/EtOAc (4:1), and then concentrated under reduced pressure. The crude product was purified by chromatography on silica gel, eluting with hexanes/EtOAc (5:2, v/v), to afford 0.72 g (65% yield) of the title compound **S58 (FPEB)** as a yellow solid.

R_f = 0.22 (Hexanes/ethyl acetate = 5:2 (v/v)).

NMR Spectroscopy:

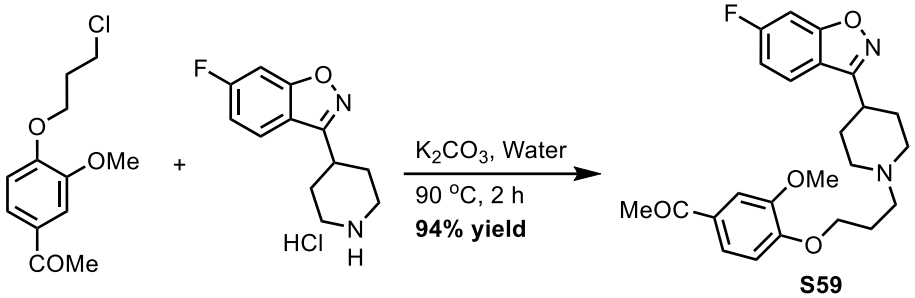
^{1}H NMR (500 MHz, $CDCl_3$, 23 ºC, δ): 8.65 (d, *J* = 4.7 Hz, 1H), 7.73 (t, *J* = 7.7 Hz, 1H), 7.66 (s, 1H), 7.53 (dd, *J* = 15.6, 8.2 Hz, 1H), 7.36 (d, *J* = 7.8 Hz, 1H), 7.34 – 7.29 (m, 1H).

^{13}C NMR (125 MHz, $CDCl_3$, 23 ºC, δ): 162.0 (d, *J* = 251.5 Hz), 150.5, 142.3, 136.5, 131.6 (d, *J* = 3.5 Hz), 127.7, 126.2 (d, *J* = 10.0 Hz), 123.8, 123.6 (d, *J* = 23.0 Hz), 119.6 (d, *J* = 24.6 Hz), 116.9 (d, *J* = 3.5 Hz), 114.5 (d, *J* = 10.2 Hz), 91.8, 85.2 (d, *J* = 3.1 Hz).

^{19}F NMR (471 MHz, $CDCl_3$, 23 ºC, δ): –108.9 (t, *J* = 8.2 Hz).

HRMS-ESIpos (m/z) calc'd for $C_{14}H_7N_2F$ $[M]^+$, 222.0588; found, 222.0589; deviation: –0.5 ppm.

III.3.3 Synthesis of Iloperidone S59



S59
Iloperidone

Iloperidone (S59) was synthesized following a reported literature procedure with minor modifications.[172] A 100 mL round-bottom flask equipped with a magnetic stir bar was charged with 6-fluoro-3-(4-piperidinyl)-1,2-benzoisoxazole hydrochloride (2.4 g, 9.3 mmol, 1.0 equiv.) and 1-[4-(3-chloropropoxy)-3-methoxyphenyl]ethyl ketone (2.3 g, 9.3 mmol, 1.0 equiv.). A solution of potassium carbonate (3.9 g, 28 mmol, 3.0 equiv.) in water (30 mL) was added, and the reaction mixture was heated to 90 °C and stirred for 2 h. After cooling to room temperature, the mixture was filtered, and the filter cake was washed with water followed by methanol to afford crude product. The crude product was purified by column chromatography on silica gel, eluting with EtOAc/MeOH (19:1(v/v)), affording 3.6 g (94% yield) of the title compound **S59 (Iloperidone)** as a white solid.

R_f = 0.30 (EtOAc/MeOH = 19:1 (v/v)).

NMR Spectroscopy:

^{1}H NMR (500 MHz, $CDCl_3$, 23 ºC, δ): 7.67 (dd, J = 8.8, 5.1 Hz, 1H), 7.55 (dd, J = 8.4, 2.0 Hz, 1H), 7.52 (d, J = 2.0 Hz, 1H), 7.22 (dd, J = 8.5, 2.1 Hz, 1H), 7.04 (td, J = 8.9, 2.1 Hz, 1H), 6.92 (d, J = 8.4 Hz, 1H), 4.18 (t, J = 6.7 Hz, 2H), 3.91 (s, 3H), 3.06 (qd, J = 8.1, 5.0 Hz, 3H), 2.58 (t, J = 7.1 Hz, 2H), 2.55 (s, 3H), 2.17 (dt, J = 11.2, 6.9 Hz, 2H), 2.06 (ddt, J = 12.9, 9.5, 5.4 Hz, 6H).

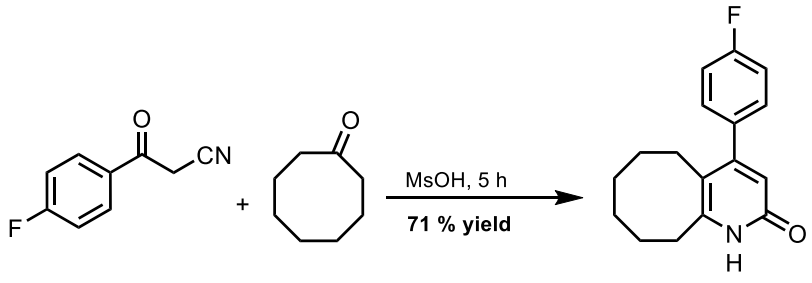
^{13}C NMR (125 MHz, $CDCl_3$, 23 ºC, δ): 196.91, 165.18, 163.96 (d, J = 13.6 Hz), 163.19, 161.21, 152.98, 149.35, 130.49, 123.33, 122.64 (d, J = 11.2 Hz), 117.43, 112.41 (d, J = 25.2 Hz), 111.34, 110.58, 97.54 (d, J = 26.5 Hz), 67.50, 56.14, 55.20, 53.69, 34.69, 30.70, 26.52 (d, J = 50.1 Hz).

^{19}F NMR (471 MHz, $CDCl_3$, 23 ºC, δ): -109.66 (td, J = 8.7, 5.2 Hz).

HRMS-ESIpos (m/z) calc'd for $C_{24}H_{28}O_4N_2F$ $[M+H]^+$, 427.2028; found, 427.2026; deviation: 0.3 ppm.

III.3.4 Synthesis of Blonanserin S60

Precursor for Blonanserin, S60a



S60a

The precursor for blonanserin (S60a) was synthesized following a reported literature procedure with minor

modifications.[173] A 50 mL round-bottom flask equipped with a Teflon-coated magnetic stir bar was charged with 3-(4-fluorophenyl)-3-oxopropanenitrile (3.50 g, 21.5 mmol, 1.00 equiv.), methanesulfonic acid (8.25 g, 85.8 mmol, 4.00 equiv.), and water (0.46 mL, 25.7 mmol, 1.20 equiv.). The mixture was heated to 65 °C and stirred for 3 hours. Cyclooctanone (3.00 g, 23.6 mmol, 1.10 equiv.) was then added at the same temperature, and the reaction mixture was heated to 110 °C and stirred for 2 hours. The reaction was cooled to room temperature, diluted with dichloromethane (10 mL), and water (10 mL) was added. The organic layer was separated, and the aqueous layer was extracted with DCM (3 × ~30 mL). The combined organic layers were dried over Na_2SO_4 and concentrated under reduced pressure. The crude product was purified by column chromatography on silica gel, eluting with DCM/MeOH (25:1, (v/v)), affording 4.1 g (71% yield) of the title compound **S60a** as a white solid.

R_f = 0.22 (DCM/MeOH = 25:1 (v/v)).

NMR Spectroscopy:

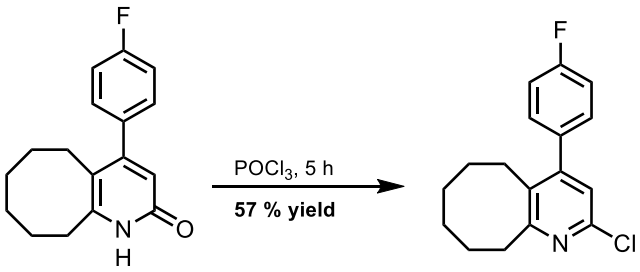
^{1}H NMR (500 MHz, $CDCl_3$, 23 ºC, δ): 13.37 (br, 1H), 7.22 (dd, *J* = 8.7, 5.3 Hz, 2H), 7.09 (t, *J* = 8.6 Hz, 2H), 6.31 (s, 1H), 2.85 – 2.79 (m, 2H), 2.47 – 2.42 (m, 2H), 1.84 (td, *J* = 5.8, 2.7 Hz, 2H), 1.50 – 1.43 (m, 2H), 1.42 – 1.26 (m, 4H).

^{13}C NMR (125 MHz, $CDCl_3$, 23 ºC, δ): 164.6, 163.5, 161.6, 156.3, 147.8, 135.7 (d, *J* = 3.5 Hz), 129.8 (d, *J* = 8.2 Hz), 117.6, 116.9, 115.3 (d, *J* = 21.4 Hz), 31.0, 30.5, 30.1 , 26.3, 25.8 (d, *J* = 17.2 Hz).

^{19}F NMR (471 MHz, $CDCl_3$, 23 ºC, δ): –114.3 (ddd, *J* = 13.9, 8.7, 5.3 Hz).

HRMS-ESIpos (m/z) calc'd for $C_{14}H_7FN_2$ $[M]^+$, 272.1445; found, 272.1445; deviation: 0.0 ppm.

Precursor for Blonanserin, S60b



S60a **S60b**

The precursor for blonanserin (S60b) was synthesized following a reported literature procedure with minor modifications.[173] A 50 mL round-bottom flask equipped with a Teflon-coated magnetic stir bar was charged with **S60a** (2.0 g, 7.4 mmol, 1.0 equiv.) and phosphoryl chloride (6.7 mL, 74 mmol, 10 equiv.). The mixture was heated to reflux and stirred for 5 h. After cooling to room temperature, the reaction mixture was slowly poured into ice water and then neutralized with sat. $NaHCO_3$ (20 mL). The aqueous suspension was extracted with DCM (4 × ~20 mL). The combined organic layers were dried over Na_2SO_4 and concentrated under reduced pressure. The crude product was purified by column chromatography on silica gel, eluting with hexanes/EtOAc (5:2, (v/v)), affording 1.2 g (57% yield) of the title compound **S60b** as a white solid.

R_f = 0.12 (hexanes/EtOAc = 5:2 (v/v)).

NMR Spectroscopy:

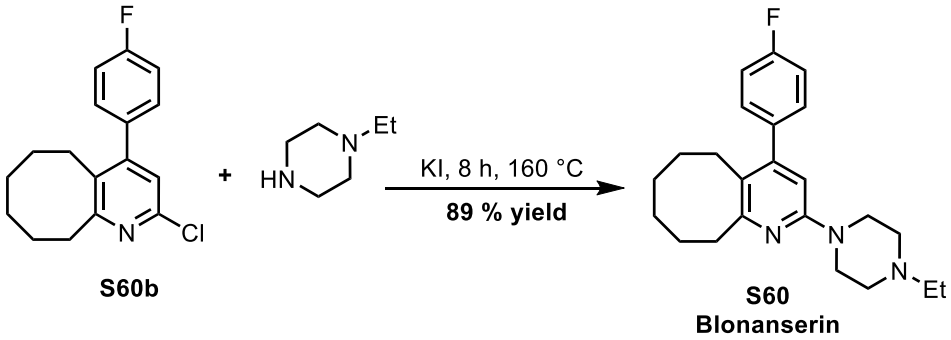
^{1}H NMR (500 MHz, $CDCl_3$, 23 ºC, δ): 7.23 – 7.16 (m, 2H), 7.09 (t, *J* = 8.7 Hz, 2H), 6.96 (s, 1H), 3.00 – 2.94 (m, 2H), 2.67 – 2.63 (m, 2H), 1.85 – 1.74 (m, 2H), 1.47 – 1.36 (m, 4H), 1.36 – 1.28 (m, 2H).

^{13}C NMR (125 MHz, $CDCl_3$, 23 ºC, δ): 163.6, 162.9, 161.6, 151.8, 147.7, 134.9 (d, *J* = 3.5 Hz), 132.5, 130.1, 122.8, 115.5 (d, *J* = 21.5 Hz), 35.3, 30.9 (d, *J* = 59.0 Hz), 26.8, 26.5, 25.7.

^{19}F NMR (471 MHz, $CDCl_3$, 23 ºC, δ): –113.7 (tt, *J* = 8.3, 5.4 Hz).

HRMS-ESIpos (m/z) calc'd for $C_{17}H_{17}FN_1Cl$ $[M]^+$, 289.1028; found, 289.1031; deviation: –1.0 ppm.

Blonanserin, S60



S60b **S60 Blonanserin**

The blonanserin (S60) was synthesized following a reported literature procedure with minor modifications.[174] A 50 mL round-bottom flask equipped with a Teflon-coated magnetic stir bar was charged with **S60b** (2.0 g, 7.0 mmol, 1.0 equiv.), potassium iodide (1.3 g, 7.7 mmol, 1.1 equiv.), and ethylpiperazine (2.70 mL, 21.0 mmol, 3.00 equiv.). The mixture was heated to reflux and stirred for 8 h. The reaction was cooled to room temperature, diluted with dichloromethane (10 mL), and water (10 mL) was added. The aqueous suspension was extracted with DCM (4 × ~20 mL). The combined organic layers were dried over Na_2SO_4 and concentrated under reduced pressure. The crude product was purified by column chromatography on silica gel, eluting with DCM/MeOH/Et_3N (20:1:0.2, (v/v/v)), affording 2.3 g (89% yield) of the title compound **S60 (Blonanserin)** as a yellow solid.

R_f = 0.19 (DCM/MeOH/Et_3N = 20:1:0.2, (v/v/v)).

NMR Spectroscopy:

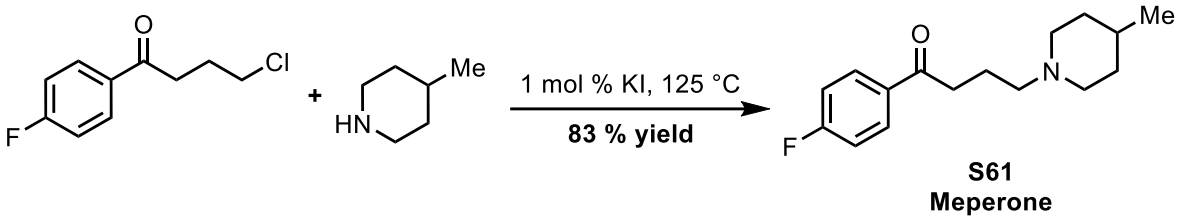
^{1}H NMR (500 MHz, $CDCl_3$, 23 ºC, δ): 7.21 (dd, *J* = 8.7, 5.5 Hz, 2H), 7.07 (t, *J* = 8.7 Hz, 2H), 6.29 (s, 1H), 3.58 – 3.48 (m, 4H), 2.92 – 2.83 (m, 2H), 2.56 (q, *J* = 5.0 Hz, 6H), 2.46 (q, *J* = 7.2 Hz, 2H), 1.78 (m, *J* = 3.5 Hz, 2H), 1.47 – 1.40 (m, 2H), 1.40 – 1.30 (m, 4H), 1.13 (t, *J* = 7.2 Hz, 3H).

^{13}C NMR (125 MHz, $CDCl_3$, 23 ºC, δ): 163.19, 161.24, 160.05, 157.40, 150.49, 137.55 (d, *J* = 3.5 Hz), 130.22 (d, *J* = 7.9 Hz), 123.01, 115.01 (d, *J* = 21.3 Hz), 106.05, 52.90, 52.61, 45.66, 35.69, 31.63, 30.73, 26.65 (d, *J* = 17.2 Hz), 25.94, 12.13.

^{19}F NMR (471 MHz, $CDCl_3$, 23 ºC, δ): –115.42 (td, *J* = 8.7, 4.3 Hz).

HRMS-ESIpos (m/z) calc'd for $C_{23}H_{30}FN_3$ $[M]^+$, 367.2418; found, 367.2421; deviation: –0.7 ppm.

III.3.5 Synthesis of Melperone, S61



S61
Meperone

Melperone (S61) was synthesized following a reported literature procedure with minor modifications.[175] A 50 mL round-bottom flask equipped with a magnetic stir bar was charged with 4-chloro-1-(4-fluorophenyl)butan-1-one (1.0 g, 5.0 mmol, 1.0 equiv.), 4-methylpiperidine (1.2 mL, 10 mmol, 2.0 equiv.), and potassium iodide (8.30 mg, 0.05 mmol, 0.01 equiv.) in toluene (17 mL). The reaction mixture was stirred at 125 ºC for 25 h. The reaction was cooled to room temperature, diluted with dichloromethane (10 mL), and water (10 mL) was added. The aqueous suspension was extracted with DCM (3 × ~20 mL). The combined organic layers were dried over Na_2SO_4 and concentrated under reduced pressure. The crude product was purified by column chromatography on silica gel, eluting with hexanes/EtOAc/Et_3N (10:2:0.1, (v/v/v)), affording 2.3 g (83% yield) of the title compound **S61 (Melperone)** as a yellow solid.

R_f = 0.10 hexanes/EtOAc/Et_3N (10:2:0.1, (v/v/v)).

NMR Spectroscopy:

^{1}H NMR (500 MHz, $CDCl_3$, 23 ºC, δ): 7.99 (dd, *J* = 8.9, 5.4 Hz, 2H), 7.11 (t, *J* = 8.6 Hz, 2H), 2.95 (t, *J* = 7.2 Hz, 2H), 2.84 (d, *J* = 11.7 Hz, 2H), 2.36 (t, *J* = 7.2 Hz, 2H), 1.97 – 1.84 (m, 4H), 1.58 (d, *J* = 14.3 Hz, 2H), 1.32 (m, *J* = 10.5, 5.3 Hz, 1H), 1.15 (qd, *J* = 11.8, 3.7 Hz, 2H), 0.89 (d, *J* = 6.6 Hz, 3H).

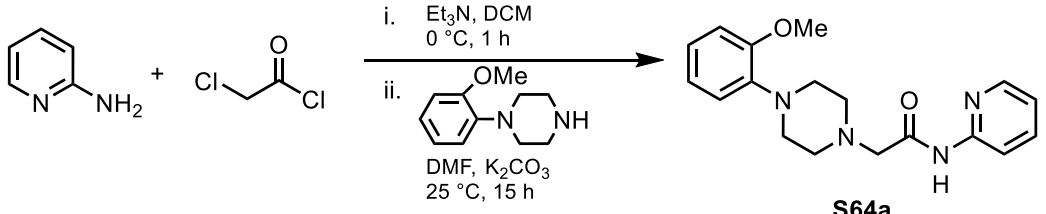
^{13}C NMR (125 MHz, $CDCl_3$, 23 ºC, δ): 198.76, 166.75, 164.73, 133.77 (d, *J* = 2.8 Hz), 130.83 (d, *J* = 9.1 Hz), 115.76, 115.59, 58.27, 54.08, 36.55, 34.46, 30.97, 22.08 (d, *J* = 4.1 Hz).

^{19}F NMR (471 MHz, $CDCl_3$, 23 ºC, δ): –105.91 (t, *J* = 9.1 Hz).

HRMS-ESIpos (m/z) calc'd for $C_{16}H_{23}FNO$ $[M+H]^+$, 264.1758; found, 264.1757; deviation: 0.4 ppm.

III.3.6 Synthesis of p-MPPF, S64

Synthesis of precursor for p-MPPF, S64a



S64a

The precursor for p-MPPF (S64a) was synthesized following a reported literature procedure with minor modifications.[176] A flame-dried 50 mL round-bottom flask equipped with a Teflon-coated magnetic stir bar was charged with 2-aminopyridine (0.53 mL, 6.0 mmol, 1.0 equiv.) and Et_3N (1.0 mL, 7.2 mmol, 1.2 equiv.) in DCM (12 mL) and cooled to 0 °C in an ice bath, Chloroacetyl chloride (0.6 mL, 7.2 mmol, 1.2 equiv.) was added dropwise at 0 °C in an ice bath. The mixture was stirred for 1 hour at 0 °C, after which cold water (8 mL) was added. The organic layer was separated, and the aqueous layer was extracted with DCM(3 × ~10 mL). The combined organic layers were dried over Na_2SO_4 and concentrated under reduced pressure,

affording a grey-tan solid. The crude product was combined with 1-(2-methoxyphenyl)piperazine (1.34 g, 6.60 mmol, 1.10 equiv.) and K_2CO_3 (2.6 g, 18 mmol, 3.0 equiv.) in DMF (12 mL) and stirred at room temperature for 15 hours. The reaction was quenched with water (20 mL), and the mixture was extracted with DCM (4 × ~30 mL). The combined organic layers were dried over Na_2SO_4 and concentrated under reduced pressure. The crude product was purified by column chromatography on silica gel, eluting with hexanes/EtOAc (2:1, v/v), to afford 1.3 g (67% yield) of the title compound **S64a** as a colorless oil.

R*f* = 0.14 (Hexanes/ethyl acetate = 2:1 (v/v)).

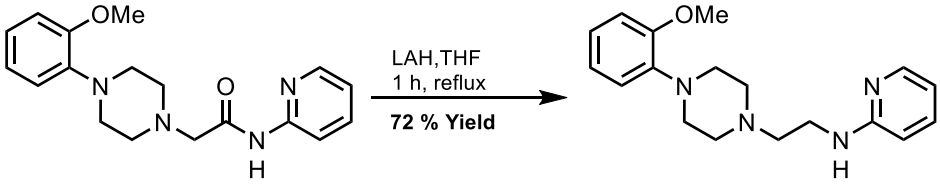
NMR Spectroscopy:

^{1}H NMR (500 MHz, $CDCl_3$, 23 ºC, δ): 9.63 (s, 1H), 8.30 (d, J = 3.7 Hz, 1H), 8.26 (d, J = 8.4 Hz, 1H), 7.70 (td, J = 7.9, 1.9 Hz, 1H), 7.07 – 6.98 (m, 2H), 6.97 – 6.89 (m, 2H), 6.86 (d, J = 9.3 Hz, 1H), 3.85 (s, 3H), 3.23 (s, 2H), 3.17 (br, 4H), 2.82 (t, J = 4.9 Hz, 4H)..

^{13}C NMR (125 MHz, $CDCl_3$, 23 ºC, δ): 169.2, 152.3, 151.1, 148.0, 140.9, 138.3, 123.2, 121.1, 119.9, 118.4, 113.9, 111.3, 62.3, 55.4, 53.9, 50.7.

HRMS-ESIpos (m/z) calc'd for $C_{18}H_{22}O_2N_4$ $[M+H]^+$, 327.1816; found, 327.1815; deviation: 0.1 ppm.

Synthesis of precursor for p-MPPF, S64b



S64a **S64b**

The precursor for p-MPPF (S64b) was synthesized following a reported literature procedure with minor modifications.[176] A flame-dried 100 mL round-bottom flask equipped with a Teflon-coated magnetic stir bar was charged with LAH (304 mg, 8.00 mmol, 3.20 equiv.) in THF (16 mL) under an inert atmosphere. A solution of compound **S2.1** (816 mg, 2.50 mmol, 1.00 equiv.) in THF (16 mL) was added dropwise at room temperature under stirring. The mixture was refluxed for 1 hour and then cooled to room temperature. Water (0.3 mL) was added carefully, followed by NaOH (1.0 M, 0.3 mL) and additional water (0.3 mL) successively. The mixture was stirred at room temperature for 10 minutes and then filtered. The mixture was extracted with DCM (3 × ~30 mL). The combined organic layers were dried over Na_2SO_4 and concentrated under reduced pressure. The crude product was purified by column chromatography on silica gel, eluting with DCM/MeOH/Et_3N (25:1:0.2, v/v/v), affording 0.56 g (72% yield) of the title compound **S64b** as a colorless oil.

R*f* = 0.14 (DCM/MeOH/Et_3N = 25:1:0.2 (v/v/v)).

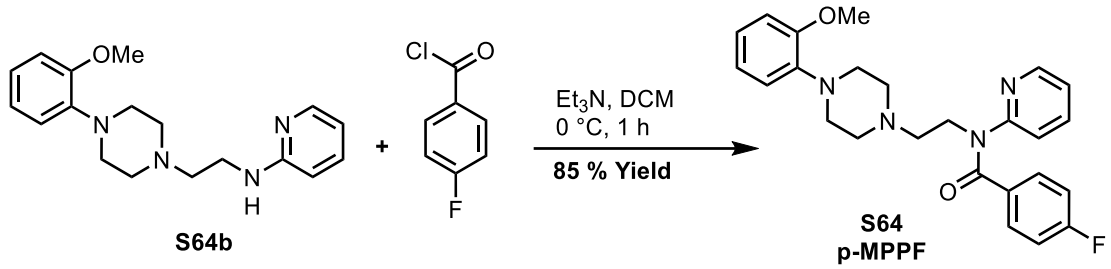
NMR Spectroscopy:

^{1}H NMR (500 MHz, $CDCl_3$, 23 ºC, δ) 8.09 (d, *J* = 5.4 Hz, 1H), 7.41 (td, *J* = 8.7, 7.2, 2.0 Hz, 1H), 7.00 (td, *J* = 7.9, 6.7, 2.4 Hz, 1H), 6.97 – 6.89 (m, 2H), 6.86 (d, *J* = 7.9 Hz, 1H), 6.56 (td, *J* = 7.1, 5.0 Hz, 1H), 6.41 (d, *J* = 8.4 Hz, 1H), 5.13 (br, 1H), 3.86 (s, 3H), 3.38 (q, *J* = 5.1 Hz, 2H), 3.10 (s, 4H), 2.70 (t, *J* = 6.0 Hz, 6H).

^{13}C NMR (125 MHz, $CDCl_3$, 23 ºC, δ): 159.0, 152.4, 148.3, 141.4, 137.4, 123.0, 121.1, 118.3, 112.8, 111.3, 107.1, 56.9, 55.5, 53.3, 50.8, 38.7.

HRMS-ESIpos (m/z) calc'd for $C_{18}H_{25}ON_4$ $[M+H]^+$, 313.2023; found, 313.2022; deviation: 0.2 ppm.

Synthesis of p-MPPF S64



p-MPPF (S64) was synthesised following a reported literature procedure with minor modifications.[176] A flame-dried 50 mL round-bottom flask equipped with a Teflon-coated magnetic stir bar was charged with **S2.2** (0.47 g, 1.5 mmol, 1.0 equiv.) and Et_3N (0.5 ml, 3.6 mmol, 2.4 equiv.) in DCM (10 mL) and cooled to 0 °C in an ice bath. A solution of the 4-fluorobenzoyl chloride (0.20 mL, 1.8 mmol, 1.2 equiv.) in DCM (5 mL) was added dropwise at 0 °C. The mixture was stirred at room temperature for 1 hour, after which water (10 mL) was added. The organic layer was separated, and the aqueous layer was extracted with DCM (3 × ~20 mL). The combined organic layers were dried over Na_2SO_4 and concentrated under reduced pressure. The crude product was purified by column chromatography on silica gel, eluting with DCM/MeOH (20:1, v/v), affording 0.65 g (85% yield) of the title compound **S64 (p-MPPF)** as a colorless oil.

$\mathbf{R_f}$ = 0.22 (DCM/MeOH = 20:1 (v/v)).

NMR Spectroscopy:

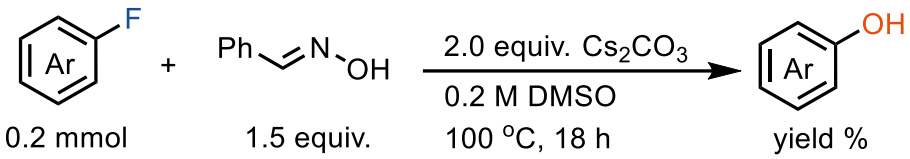
^{1}H NMR (500 MHz, $CDCl_3$, 23 ºC, δ) 8.39 (dd, *J* = 5.0, 2.3 Hz, 1H), 7.38 (td, *J* = 7.6, 2.0 Hz, 1H), 7.31 (dd, *J* = 8.9, 5.3 Hz, 2H), 6.99 (dd, *J* = 7.6, 4.9 Hz, 1H), 6.96 – 6.89 (m, 1H), 6.89 – 6.77 (m, 5H), 6.73 (d, *J* = 7.9 Hz, 1H), 4.26 (t, *J* = 6.7 Hz, 2H), 3.80 (s, 3H), 2.90 (br, 4H), 2.73 (t, *J* = 6.7 Hz, 2H), 2.61 (s, 4H).

^{13}C NMR (125 MHz, $CDCl_3$, 23 ºC, δ): 169.5, 164.5, 162.5, 156.5, 152.2, 148.7, 141.3, 137.1, 132.3 (d, *J* = 3.2 Hz), 131.0 (d, *J* = 8.6 Hz), 122.8 (d, *J* = 5.0 Hz), 120.9 (d, *J* = 4.0 Hz), 118.0, 115.0 (d, *J* = 21.8 Hz), 111.2, 56.4, 55.3, 53.3, 50.6, 45.6.

^{19}F NMR (471 MHz, $CDCl_3$, 23 ºC, δ): –109.3 (tt, *J* = 9.5, 5.2 Hz).

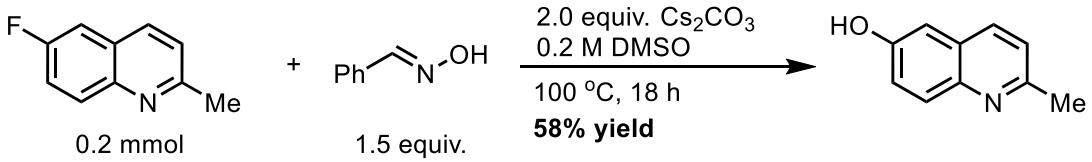
HRMS-ESIpos (m/z) calc'd for $C_{25}H_{28}O_2N_4F$ $[M+H]^+$, 435.2191; found, 435.2192; deviation: –0.4 ppm.

III.4 General Procedure for Radical Hydroxylation



An oven-dried 4 mL screw-cap reaction vial equipped with a Teflon-coated magnetic stir bar was charged with Cs_2CO_3 (130 mg, 0.40 mmol, 2.00 equiv.), benzaldoxime (36.3 mg, 0.30 mmol, 2.00 equiv.), and the corresponding aryl fluoride (0.2 mmol, 1.0 equiv.) and dry DMSO (1.0 mL, c = 0.20 M) at 25 °C. The reaction mixture was stirred and heated at 100 °C in a metal heating block for 18 h. After completion, the reaction mixture was diluted with dichloromethane or ethyl acetate (10 mL) and poured into a mixture of water (5 mL) and brine (5 mL). The mixture was neutralized with a sat. NH_4Cl solution (5 ml). The organic phase was separated, and the aqueous layer was extracted with DCM or EtOAc (3 ×~20 mL). The combined organic layers were dried over Na_2SO_4 and concentrated under reduced pressure. The crude product was purified by column chromatography to afford the desired phenol product.

2-Methylquinoline phenol derivative 54



An oven-dried 4 mL screw-cap reaction vial equipped with a Teflon-coated magnetic stir bar was charged with Cs_2CO_3 (130 mg, 0.40 mmol, 2.00 equiv.), benzaldoxime (36.3 mg, 0.30 mmol, 1.50 equiv.), and **S54** (80.6 mg, 0.20 mmol, 1.00 equiv.) and dry DMSO (1.0 mL, c = 0.20 M) at 25 °C. The reaction mixture was stirred and heated at 100 °C in a metal heating block for 18 h. After completion, the reaction mixture was diluted with dichloromethane or ethyl acetate (10 mL) and poured into a mixture of water (5 mL) and brine (5 mL). The mixture was neutralized with a sat. NH_4Cl solution (5 ml). The organic phase was separated, and the aqueous layer was extracted with DCM or EtOAc (3 ×~20 mL). The combined organic layers were dried over Na_2SO_4 and concentrated under reduced pressure. The crude product was purified by column chromatography on silica gel, eluting with (DCM/MeOH = 20:1 (v/v)), affording 31.8 mg (58 % yield) of the title compound **54** as a yellow solid.

R_f = 0.13 (DCM/MeOH = 20:1 (v/v).

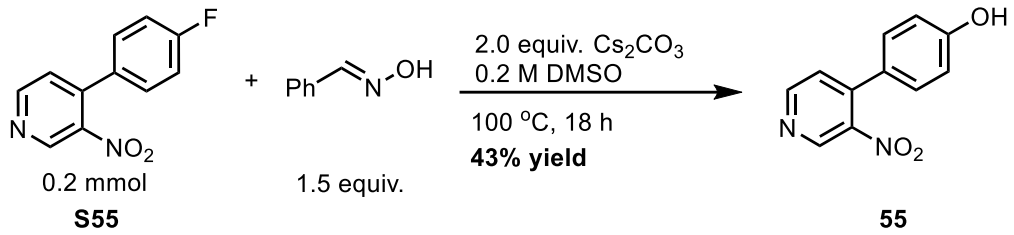
NMR Spectroscopy:

^{1}H NMR (500 MHz, DMSO-d_6, 23 ºC, δ): 9.83 (s, 1H), 8.01 (d, *J* = 8.4 Hz, 1H), 7.75 (d, *J* = 9.0 Hz, 1H), 7.30 – 7.22 (m, 2H), 7.09 (d, *J* = 2.6 Hz, 1H), 2.57 (s, 3H).

^{13}C NMR (125 MHz, DMSO-d_6, 23 ºC, δ): 154.96, 154.76, 142.48, 134.38, 129.57, 127.37, 122.02, 121.53, 108.31, 24.47.

HRMS-ESIpos (m/z) calc'd for $C_{10}H_9NO$ $[M]^+$, 159.0679; found, 159.0681; deviation: –1.2 ppm.

2-Nitro-4-fluorophenylpyridine phenol derivative 55



An oven-dried 4 mL screw-cap reaction vial equipped with a Teflon-coated magnetic stir bar was charged with Cs_2CO_3 (130 mg, 0.40 mmol, 2.00 equiv.), benzaldoxime (36.3 mg, 0.30 mmol, 1.50 equiv.), and **S55** (43.6 mg, 0.20 mmol, 1.00 equiv.) and dry DMSO (1.0 mL, c = 0.20 M) at 25 °C. The reaction mixture was stirred and heated at 100 °C in a metal heating block for 18 h. After completion, the reaction mixture was diluted with dichloromethane or ethyl acetate (10 mL) and poured into a mixture of water (5 mL) and brine (5 mL). The mixture was neutralized with a sat. NH_4Cl solution (5 ml). The organic phase was separated, and the aqueous layer was extracted with DCM or EtOAc (3 ×~20 mL). The combined organic layers were dried over Na_2SO_4 and concentrated under reduced pressure. The crude product was purified by column chromatography on silica gel, eluting with (hexanes/EtOAc = 10:3 (v/v)), affording 18.6 mg (43 % yield) of the title compound **55** as a yellow solid.

$\mathbf{R_f}$ = 0.11 (hexanes/EtOAc = 10:3 (v/v).

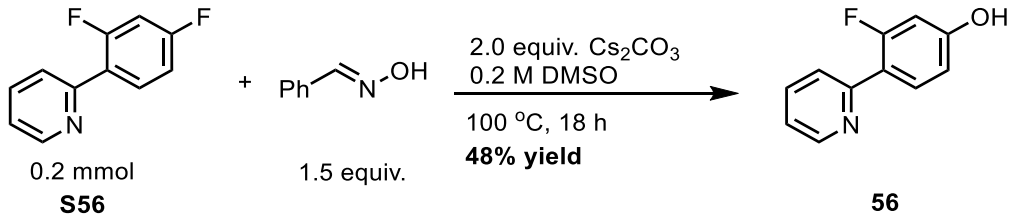
NMR Spectroscopy:

^{1}H NMR (500 MHz, DMSO-d_6, 23 ºC, δ): 9.98 (s, 1H), 9.06 (s, 1H), 8.81 (d, *J* = 5.2 Hz, 1H), 7.61 (d, *J* = 5.0 Hz, 2H), 7.26 (d, *J* = 8.7 Hz, 2H), 6.89 (d, *J* = 8.6 Hz, 2H).

^{13}C NMR (125 MHz, DMSO-d_6, 23 ºC, δ): 158.98, 152.83, 145.39, 144.78, 142.27, 129.32, 125.49, 124.23, 116.00.

HRMS-ESIpos (m/z) calc'd for $C_{11}H_8N_2O_3$ $[M]^+$, 216.0529; found, 216.0532; deviation: –1.1 ppm.

3-(2,4-difluorophenyl)pyridine phenol derivative 56



An oven-dried 4 mL screw-cap reaction vial equipped with a Teflon-coated magnetic stir bar was charged with Cs_2CO_3 (130 mg, 0.40 mmol, 2.00 equiv.), benzaldoxime (36.3 mg, 0.30 mmol, 1.50 equiv.), and **S56** (38.2 mg, 0.20 mmol, 1.00 equiv.) and dry DMSO (1.0 mL, c = 0.20 M) at 25 °C. The reaction mixture was stirred and heated at 100 °C in a metal heating block for 18 h. After completion, the reaction mixture was diluted with dichloromethane or ethyl acetate (10 mL) and poured into a mixture of water (5 mL) and brine (5 mL). The mixture was neutralized with a sat. NH_4Cl solution (5 ml). The organic phase was separated, and the aqueous layer was extracted with DCM or EtOAc (3 ×~20 mL). The combined organic layers were dried over Na_2SO_4 and concentrated under reduced pressure. The crude product was purified by column

chromatography on silica gel, eluting with (hexanes/EtOAc = 4:1 (v/v)), affording 18.2 mg (48 % yield) of the title compound **56** as a yellow solid.

R_f = 0.12 (hexanes/EtOAc = 4:1 (v/v).

NMR Spectroscopy:

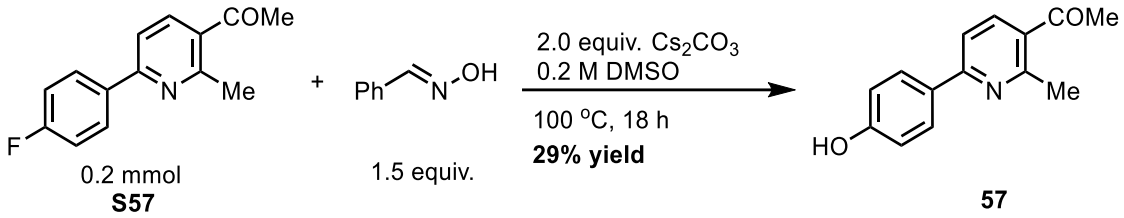
^{1}H NMR (500 MHz, CD_3Cl, 23 ºC, δ): 9.42 (s, 1H), 8.64 (ddd, J = 5.0, 1.9, 0.9 Hz, 1H), 7.79 (td, J = 7.8, 1.8 Hz, 1H), 7.74 – 7.68 (m, 1H), 7.60 (t, J = 8.7 Hz, 1H), 7.30 – 7.23 (m, 1H), 6.56 – 6.47 (m, 2H).

^{13}C NMR (125 MHz, CD_3Cl, 23 ºC, δ): 162.17, 160.19, 159.54 (d, J = 12.1 Hz), 153.76, 148.92, 137.36, 131.51 (d, J = 4.7 Hz), 124.92 (d, J = 7.7 Hz), 122.22, 112.33 (d, J = 2.9 Hz), 103.83 (d, J = 25.6 Hz).

^{19}F NMR (471 MHz, CD_3Cl, 23 ºC, δ): -115.66 (ddd, J = 12.3, 8.8, 2.6 Hz).

HRMS-ESIpos (m/z) calc'd for $C_{11}H_8N_2O_3$ $[M]^+$, 216.0529; found, 216.0532; deviation: –1.2 ppm.

Methylpyridine phenol derivative 57



An oven-dried 4 mL screw-cap reaction vial equipped with a Teflon-coated magnetic stir bar was charged with Cs_2CO_3 (130 mg, 0.40 mmol, 2.00 equiv.), benzaldoxime (36.3 mg, 0.30 mmol, 1.50 equiv.), and **S57** (45.8 mg, 0.20 mmol, 1.00 equiv.) and dry DMSO (1.0 mL, c = 0.2 M) at 25 °C. The reaction mixture was stirred and heated at 100 °C in a metal heating block for 18 h. After completion, the reaction mixture was diluted with dichloromethane or ethyl acetate (10 mL) and poured into a mixture of water (5 mL) and brine (5 mL). The mixture was neutralized with a sat. NH_4Cl solution (5 ml). The organic phase was separated, and the aqueous layer was extracted with DCM or EtOAc (3 ×~20 mL). The combined organic layers were dried over Na_2SO_4 and concentrated under reduced pressure. The crude product was purified by column chromatography on silica gel, eluting with (pentane/EtOAc/Et_3N = 20:8:0.1 (v/v/v)), affording 13.2 mg (29 % yield) of the title compound **57** as a yellow solid.

R_f = 0.17 (pentane/EtOAc/Et_3N = 20:8:0.1 (v/v/v)).

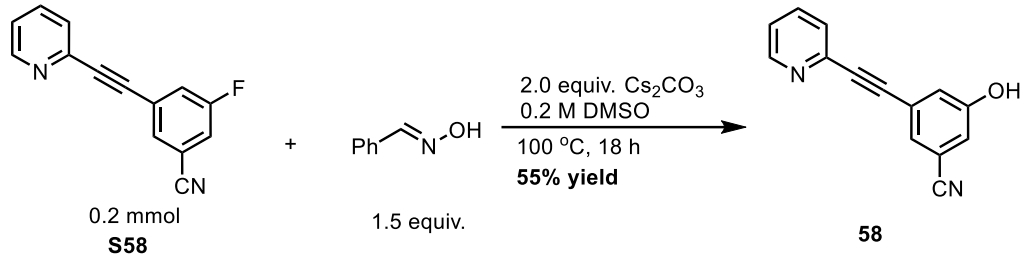
NMR Spectroscopy:

^{1}H NMR (500 MHz, DMSO-*d_6*, 23 ºC, δ): 9.88 (s, 1H), 8.22 (d, *J* = 8.2 Hz, 1H), 8.02 (d, *J* = 8.8 Hz, 1H), 7.79 (d, *J* = 8.2 Hz, 1H), 6.88 (d, *J* = 8.9 Hz, 1H), 2.68 (s, 3H), 2.58 (s, 3H).

^{13}C NMR (125 MHz, DMSO-*d_6*, 23 ºC, δ): 200.01, 159.31, 157.14, 157.00, 138.78, 129.52, 128.58, 128.49, 115.95, 115.60, 29.32, 24.99.

HRMS-ESIpos (m/z) calc'd for $C_{14}H_{13}NO_2$ $[M]^+$, 227.0941; found, 227.0942; deviation: –0.7 ppm.

FPEB Phenol derivative 58



An oven-dried 4 mL screw-cap reaction vial equipped with a Teflon-coated magnetic stir bar was charged with Cs_2CO_3 (130 mg, 0.40 mmol, 2.00 equiv.), benzaldoxime (36.3 mg, 0.30 mmol, 1.50 equiv.), and **S58** (44.4 mg, 0.20 mmol, 1.00 equiv.) and dry DMSO (1.0 mL, c = 0.2 M) at 25 °C. The reaction mixture was stirred and heated at 100 °C in a metal heating block for 18 h. After completion, the reaction mixture was diluted with dichloromethane or ethyl acetate (10 mL) and poured into a mixture of water (5 mL) and brine (5 mL). The mixture was neutralized with a sat. NH_4Cl solution (5 ml). The organic phase was separated, and the aqueous layer was extracted with DCM or EtOAc (3 ×~20 mL). The combined organic layers were dried over Na_2SO_4 and concentrated under reduced pressure. The crude product was purified by column chromatography on silica gel, eluting with hexanes/EtOAc (5:2, (v/v)), affording 24 mg (55 % yield) of the title compound **P1** as a yellow solid.

R_f = 0.10 (hexanes/EtOAc = 5:2 (v/v)).

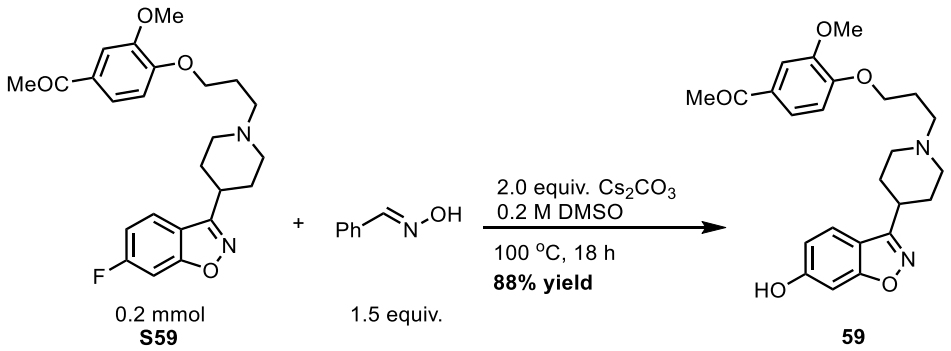
NMR Spectroscopy:

^{1}H NMR (500 MHz, DMSO-*d*$_6$, 23 ºC, δ): 10.61 (s, 1H), 8.65 – 8.60 (m, 1H), 7.87 (td, *J* = 7.7, 1.8 Hz, 1H), 7.67 (d, *J* = 7.8 Hz, 1H), 7.51 (d, *J* = 1.5 Hz, 1H), 7.45 (ddd, *J* = 7.8, 4.9, 1.1 Hz, 1H), 7.25 (dt, *J* = 12.4, 2.0 Hz, 2H).

^{13}C NMR (125 MHz, DMSO-*d*$_6$, 23 ºC, δ): 158.02, 150.26, 141.68, 136.91, 127.66, 125.72, 123.94 (d, *J* = 9.7 Hz), 122.98, 119.65, 117.91, 113.03, 89.94, 86.16.

HRMS-ESIpos (m/z) calc'd for $C_{14}H_8FN_2O$ $[M]^+$, 220.0631; found, 220.0633; deviation: –0.8 ppm.

Iloperidone phenol derivative 59



An oven-dried 4 mL screw-cap reaction vial equipped with a Teflon-coated magnetic stir bar was charged with Cs_2CO_3 (130 mg, 0.40 mmol, 2.00 equiv.), benzaldoxime (36.3 mg, 0.30 mmol, 1.50 equiv.), and **S59** (85.3 mg, 0.20 mmol, 1.00 equiv.) and dry DMSO (1.0 mL, c = 0.20 M) at 25 °C. The reaction mixture was stirred and heated at 100 °C in a metal heating block for 18 h. After completion, the reaction mixture was diluted with dichloromethane or ethyl acetate (10 mL) and poured into a mixture of water (5 mL) and brine

(5 mL). The mixture was neutralized with a sat. NH_4Cl solution (5 ml). The organic phase was separated, and the aqueous layer was extracted with DCM or EtOAc (3 ×~20 mL). The combined organic layers were dried over Na_2SO_4 and concentrated under reduced pressure. The crude product was purified by column chromatography on silica gel, eluting with DCM/MeOH (10:1, (v/v)), affording 74.7 mg (88 % yield) of the title compound **59** as a white solid.

R_f = 0.13 (DCM/MeOH = 10:1 (v/v)).

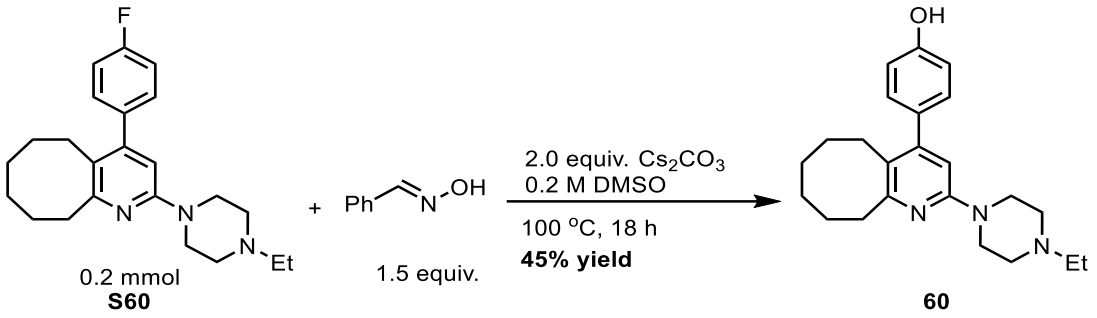
NMR Spectroscopy:

^{1}H NMR (500 MHz, DMSO-d_6, 23 ºC, δ): 10.28 (s, 1H), 7.64 (d, *J* = 8.7 Hz, 2H), 7.58 (d, *J* = 6.4 Hz, 1H), 7.43 (s, 1H), 7.04 (d, *J* = 8.4 Hz, 2H), 6.90 (s, 1H), 6.81 (d, *J* = 8.5 Hz, 1H), 4.08 (t, *J* = 6.5 Hz, 4H), 3.80 (s, 5H), 3.01 – 2.92 (m, 3H), 2.49 – 2.42 (m, 2H), 2.07 (t, *J* = 10.9 Hz, 3H), 1.99 – 1.87 (m, 4H), 1.86 – 1.75 (m, 2H).

^{13}C NMR (125 MHz, DMSO-d_6, 23 ºC, δ): 196.29, 164.27, 160.84, 160.12, 152.49, 148.66, 129.78, 123.10, 122.49, 113.73, 112.75, 111.70, 110.42, 94.72, 66.80, 55.54, 54.57, 53.07, 33.62, 30.24, 26.27 (d, *J* = 5.4 Hz).

HRMS-ESIpos (m/z) calc'd for $C_{24}H_{29}N_2O_5$ $[M+H]^+$, 425.2071; found, 425.2071; deviation: –0.1 ppm

Blonanserin phenol derivative 60



An oven-dried 4 mL screw-cap reaction vial equipped with a Teflon-coated magnetic stir bar was charged with Cs_2CO_3 (130 mg, 0.40 mmol, 2.00 equiv.), benzaldoxime (36.3 mg, 0.30 mmol, 1.50 equiv.), and **S60** (73.5 mg, 0.20 mmol, 1.00 equiv.) and dry DMSO (1.0 mL, c = 0.20 M) at 25 °C. The reaction mixture was stirred and heated at 100 °C in a metal heating block for 18 h. After completion, the reaction mixture was diluted with dichloromethane or ethyl acetate (10 mL) and poured into a mixture of water (5 mL) and brine (5 mL). The mixture was neutralized with a sat. NH_4Cl solution (5 ml). The organic phase was separated, and the aqueous layer was extracted with DCM or EtOAc (3 ×~20 mL). The combined organic layers were dried over Na_2SO_4 and concentrated under reduced pressure. The crude product was purified by column chromatography on silica gel, eluting with DCM/MeOH (25:2, (v/v)), affording 32.9 mg (45 % yield) of the title compound **60** as a yellow solid.

R_f = 0.18 (DCM/MeOH = 25:2 (v/v)).

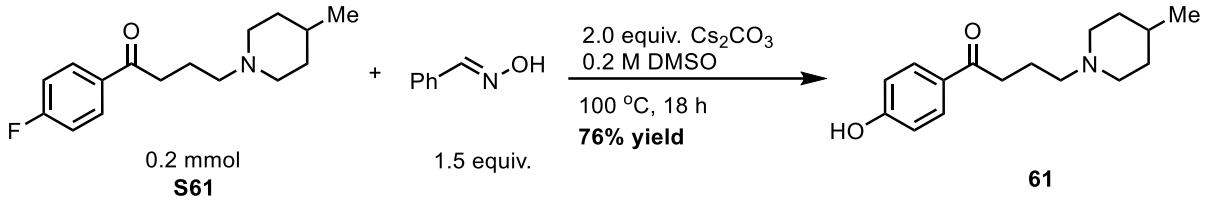
NMR Spectroscopy:

^{1}H NMR (500 MHz, DMSO-d_6, 23 ºC, δ): 9.49 (s, 1H), 7.05 (d, J = 8.5 Hz, 2H), 6.79 (d, J = 8.4 Hz, 2H), 6.32 (s, 1H), 3.40 (m, 4H), 2.78 (t, J = 6.1 Hz, 2H), 2.55 (t, J = 5.9 Hz, 2H), 2.44 (br, 3H), 2.40 – 2.31 (m, 2H), 1.67 (m, 2H), 1.41 – 1.30 (m, 4H), 1.30 – 1.24 (m, 2H), 1.02 (t, J = 7.2 Hz, 3H).

^{13}C NMR (125 MHz, DMSO-d_6, 23 ºC, δ): 158.55, 156.72, 156.64, 151.08, 131.40, 129.37, 121.95, 114.83, 105.85, 52.22, 51.69, 44.72, 34.95, 31.06, 30.28, 26.00, 25.84, 25.40, 11.90.

HRMS-ESIpos (m/z) calc'd for $C_{23}H_{31}N_3O$ [M]$^+$, 365.2462; found, 365.2463; deviation: –0.5 ppm.

Melperone phenol derivative 61



0.2 mmol **S61** 1.5 equiv. **61**

An oven-dried 4 mL screw-cap reaction vial equipped with a Teflon-coated magnetic stir bar was charged with Cs_2CO_3 (130 mg, 0.40 mmol, 2.00 equiv.), benzaldoxime (36.3 mg, 0.30 mmol, 1.50 equiv.), and **S61** (52.7 mg, 0.20 mmol, 1.00 equiv.) and dry DMSO (1.0 mL, c = 0.2 M) at 25 °C. The reaction mixture was stirred and heated at 100 °C in a metal heating block for 18 h. After completion, the reaction mixture was diluted with dichloromethane or ethyl acetate (10 mL) and poured into a mixture of water (5 mL) and brine (5 mL). The mixture was neutralized with a sat. NH_4Cl solution (5 ml). The organic phase was separated, and the aqueous layer was extracted with DCM or EtOAc (3 ×~20 mL). The combined organic layers were dried over Na_2SO_4 and concentrated under reduced pressure. The crude product was purified by column chromatography on silica gel, eluting with (DCM/MeOH = 25:2 (v/v)), affording 39.7 mg (76 % yield) of the title compound **61** as a yellow solid.

R_f = 0.10 (DCM/MeOH = 25:2 (v/v)).

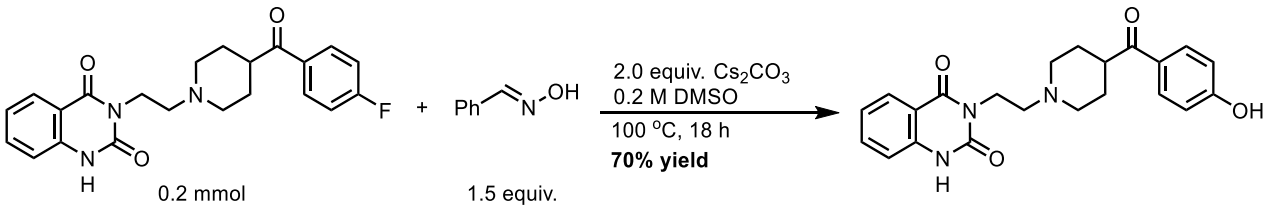
NMR Spectroscopy:

^{1}H NMR (500 MHz, DMSO-d_6, 23 ºC, δ): 7.82 (d, *J* = 8.7 Hz, 2H), 6.83 (d, *J* = 8.9 Hz, 2H), 2.86 (t, *J* = 7.1 Hz, 2H), 2.75 (d, *J* = 11.6 Hz, 2H), 2.25 (t, *J* = 7.2 Hz, 2H), 1.81 (t, *J* = 11.6 Hz, 2H), 1.73 (p, *J* = 7.2 Hz, 2H), 1.50 (d, *J* = 11.7 Hz, 2H), 1.25 (m, 1H), 1.03 (qd, *J* = 12.0, 3.8 Hz, 2H), 0.84 (d, *J* = 6.5 Hz, 2H).

^{13}C NMR (125 MHz, DMSO-d_6, 23 ºC, δ): 197.93, 161.95, 130.34, 128.43, 115.13, 57.49, 53.34, 35.13, 33.90, 30.37, 21.83, 21.76.

HRMS-ESIpos (m/z) calc'd for $C_{16}H_{23}NO_2$ [M+H]$^+$, 262.1802; found, 262.1803; deviation: –0.5 ppm.

Ketanserin phenol derivative 62



0.2 mmol **S62** 1.5 equiv. **62**

An oven-dried 4 mL screw-cap reaction vial equipped with a Teflon-coated magnetic stir bar was charged with Cs_2CO_3 (130 mg, 0.40 mmol, 2.00 equiv.), benzaldoxime (36.3 mg, 0.30 mmol, 1.50 equiv.), and **S62** (79.1 mg, 0.20 mmol, 1.00 equiv.) and dry DMSO (1.0 mL, c = 0.20 M) at 25 °C. The reaction mixture was stirred and heated at 100 °C in a metal heating block for 18 h. After completion, the reaction mixture was diluted with dichloromethane or ethyl acetate (10 mL) and poured into a mixture of water (5 mL) and brine

(5 mL). The mixture was neutralized with a sat. NH_4Cl solution (5 ml). The organic phase was separated, and the aqueous layer was extracted with DCM or EtOAc (3 ×~20 mL). The combined organic layers were dried over Na_2SO_4 and concentrated under reduced pressure. The crude product was purified by column chromatography on silica gel, eluting with (DCM/MeOH/Et3N = 20:1:0.1 (v/v/v)), affording 55.1 mg (70 % yield) of the title compound **62** as a yellow solid.

R_f = 0.10 (DCM/MeOH/Et_3N = 20:1:0.1 (v/v).

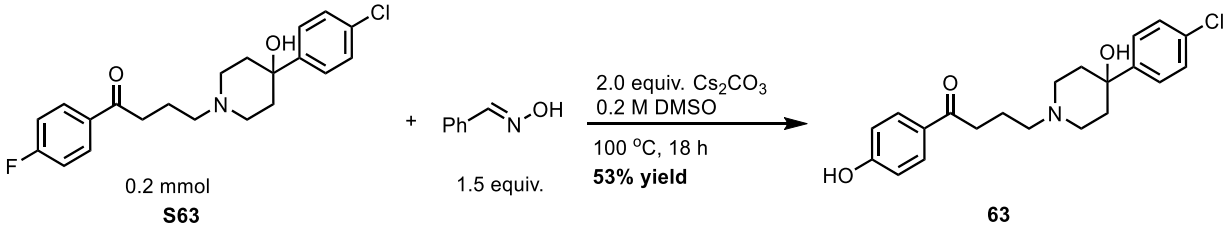
NMR Spectroscopy:

^{1}H NMR (500 MHz, DMSO-*d*$_6$, 23 ºC, δ): 11.44 (s, 1H), 10.37 (s, 1H), 7.92 (d, J = 6.4 Hz, 1H), 7.84 (d, J = 8.8 Hz, 2H), 7.64 (t, J = 7.7 Hz, 1H), 7.23 – 7.16 (m, 2H), 6.85 (d, J = 8.9 Hz, 2H), 4.04 (t, J = 7.0 Hz, 2H), 3.36 (t, J = 7.2 Hz, 1H), 3.03 (s, 2H), 2.58 (s, 2H), 2.19 (s, 2H), 1.70 (d, J = 11.3 Hz, 2H), 1.56 (t, J = 12.5 Hz, 2H).

^{13}C NMR (125 MHz, DMSO-*d*$_6$, 23 ºC, δ): 200.45, 162.06, 161.93, 150.16, 139.42, 134.91, 130.68, 127.36, 127.07, 122.45, 115.36, 115.11, 113.76, 55.13, 54.90, 52.74, 48.63, 41.93, 37.32, 28.45.

HRMS-ESIpos (m/z) calc'd for $C_{22}H_{24}N_3O_4$ $[M+H]^+$, 394.1761; found, 394.1763; deviation: –0.3 ppm.

Haloperidol phenol derivative 63



An oven-dried 4 mL screw-cap reaction vial equipped with a Teflon-coated magnetic stir bar was charged with Cs_2CO_3 (130 mg, 0.40 mmol, 2.00 equiv.), benzaldoxime (36.3 mg, 0.30 mmol, 1.50 equiv.), and **S63** (75.2 mg, 0.20 mmol, 1.00 equiv.) and dry DMSO (1.0 mL, c = 0.20 M) at 25 °C. The reaction mixture was stirred and heated at 100 °C in a metal heating block for 18 h. After completion, the reaction mixture was diluted with dichloromethane or ethyl acetate (10 mL) and poured into a mixture of water (5 mL) and brine (5 mL). The mixture was neutralized with a sat. NH_4Cl solution (5 ml). The organic phase was separated, and the aqueous layer was extracted with DCM or EtOAc (3 ×~20 mL). The combined organic layers were dried over Na_2SO_4 and concentrated under reduced pressure. The crude product was purified by column chromatography on silica gel, eluting with (DCM/MeOH/Et_3N = 20:1:0.1 (v/v/v)), affording 39.6 mg (53 % yield) of the title compound **63** as a yellow solid.

R_f = 0.10 (DCM/MeOH/Et_3N = 20:1:0.1 (v/v/v)).

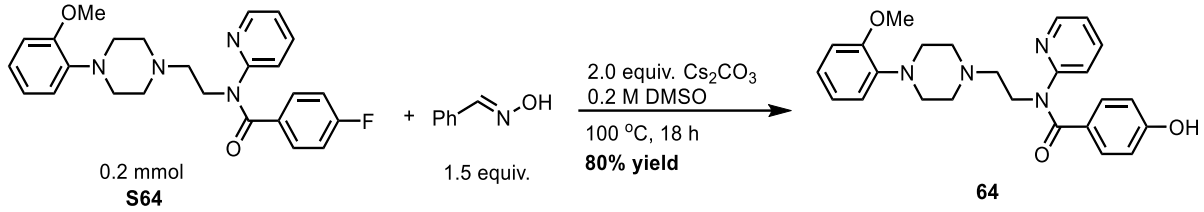
NMR Spectroscopy:

^{1}H NMR (500 MHz, DMSO-*d*$_6$, 23 ºC, δ): 7.86 (d, J = 8.3 Hz, 2H), 7.39 (d, J = 8.3 Hz, 2H), 7.32 (d, J = 8.2 Hz, 2H), 6.86 (d, J = 8.3 Hz, 2H), 5.73 (s, 4H), 3.18 (s, 1H), 2.89 (t, J = 6.9 Hz, 2H), 2.61 (d, J = 10.8 Hz, 2H), 2.50 (br, 1H), 2.39 – 2.32 (m, 4H), 1.78 (m, 4H), 1.50 (d, J = 12.9 Hz, 2H).

^{13}C NMR (125 MHz, DMSO-*d*$_6$, 23 ºC, δ): 197.92, 161.86, 149.16, 130.74, 130.39, 128.68, 127.64, 126.77, 115.14, 69.54, 57.35, 54.86, 48.93, 37.79, 35.16.

HRMS-ESIpos (m/z) calc'd for $C_{21}H_{25}NClO_3$ $[M+H]^+$, 374.1518; found, 374.1519; deviation: –0.3 ppm.

p-MPPF phenol derivative 64



An oven-dried 4 mL screw-cap reaction vial equipped with a Teflon-coated magnetic stir bar was charged with Cs_2CO_3 (130 mg, 0.40 mmol, 2.00 equiv.), benzaldoxime (36.3 mg, 0.30 mmol, 1.50 equiv.), and **S64** (86.9 mg, 0.2 mmol, 1.0 equiv.) and dry DMSO (1.0 mL, c = 0.2 M) at 25 °C. The reaction mixture was stirred and heated at 100 °C in a metal heating block for 18 h. After completion, the reaction mixture was diluted with dichloromethane or ethyl acetate (10 mL) and poured into a mixture of water (5 mL) and brine (5 mL). The mixture was neutralized with a sat. NH_4Cl solution (5 ml). The organic phase was separated, and the aqueous layer was extracted with DCM or EtOAc (3 ×~20 mL). The combined organic layers were dried over Na_2SO_4 and concentrated under reduced pressure. The crude product was purified by column chromatography on silica gel, eluting with DCM/MeOH (20:1, (v/v)), affording 69.2 mg (80 % yield) of the title compound **64** as a white solid.

$\mathbf{R_f}$ = 0.16 (DCM/MeOH = 20:1 (v/v)).

NMR Spectroscopy:

^{1}H NMR (500 MHz, CD_3Cl, 23 ºC, δ): 8.40 (dd, *J* = 4.9, 1.1 Hz, 1H), 7.38 (td, *J* = 7.5, 2.0 Hz, 1H), 7.16 (d, *J* = 8.7 Hz, 2H), 7.03 – 6.94 (m, 2H), 6.92 – 6.80 (m, 3H), 6.76 (d, *J* = 8.1 Hz, 1H), 6.56 (d, *J* = 8.7 Hz, 2H), 4.27 (t, *J* = 6.9 Hz, 2H), 3.82 (s, 3H), 2.93 (br, 3H), 2.74 (t, *J* = 6.9 Hz, 2H), 2.64 (s, 3H), 2.62 (s, 2H).

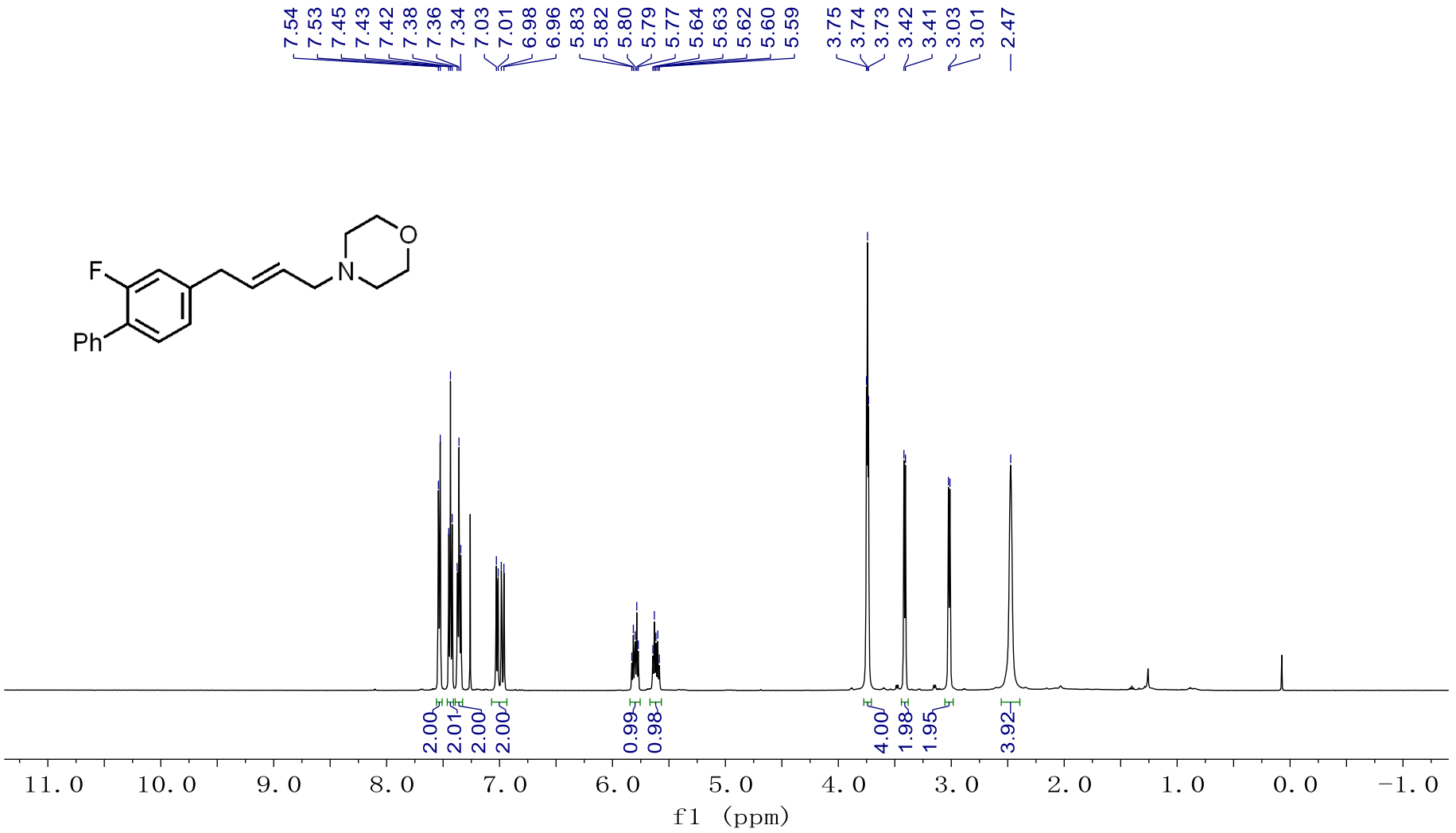
^{13}C NMR (125 MHz, $CDCl_3$, 23 ºC, δ): 170.97, 158.81, 156.73, 152.24, 148.47, 141.26, 137.14, 130.92, 126.97, 122.94 (d, J = 7.2 Hz), 120.95, 120.76, 118.16, 115.11, 111.21, 56.37, 55.35, 53.28, 50.49, 45.58, 40.78.

HRMS-ESIpos (m/z) calc'd for $C_{25}H_{29}N_4O_3$ $[M+H]^+$, 433.2233; found, 433.2234; deviation: 0.2 ppm.

IV. SPECTROSCOPIC DATA

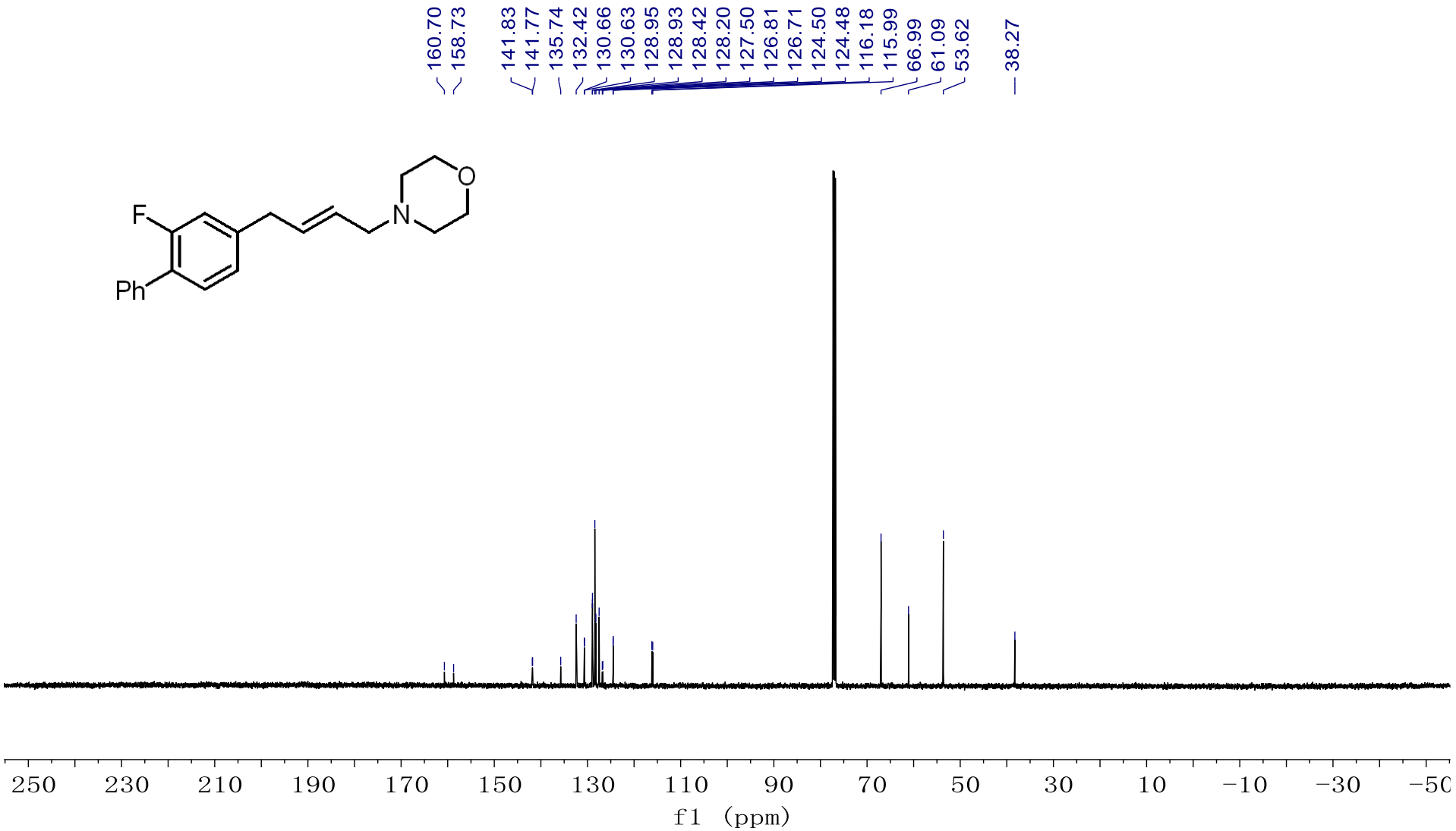
^{1}H NMR of allylamine 1

$CDCl_3$, 23 ºC



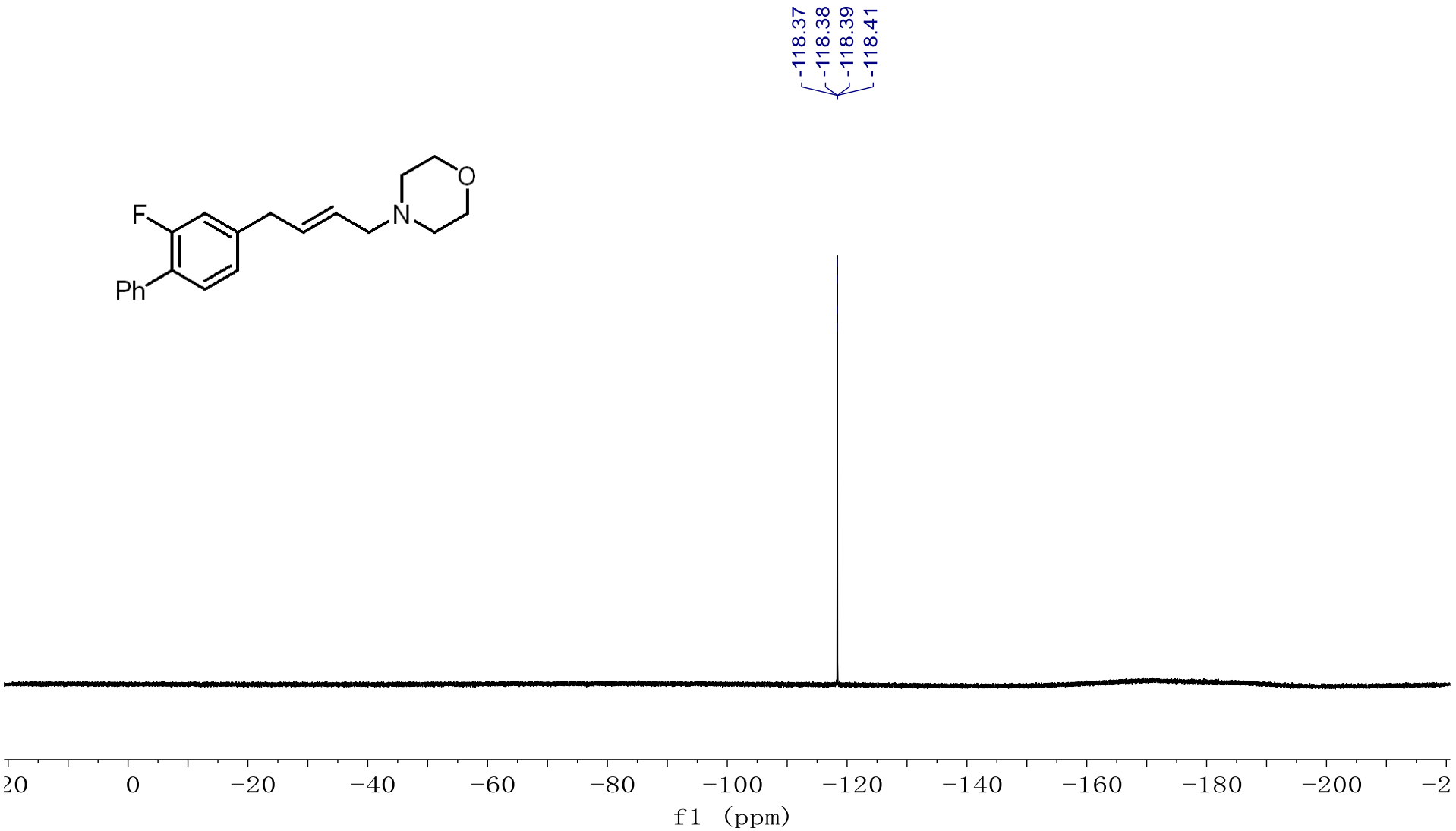
^{13}C NMR of allylamine 1

$CDCl_3$, 23 ºC



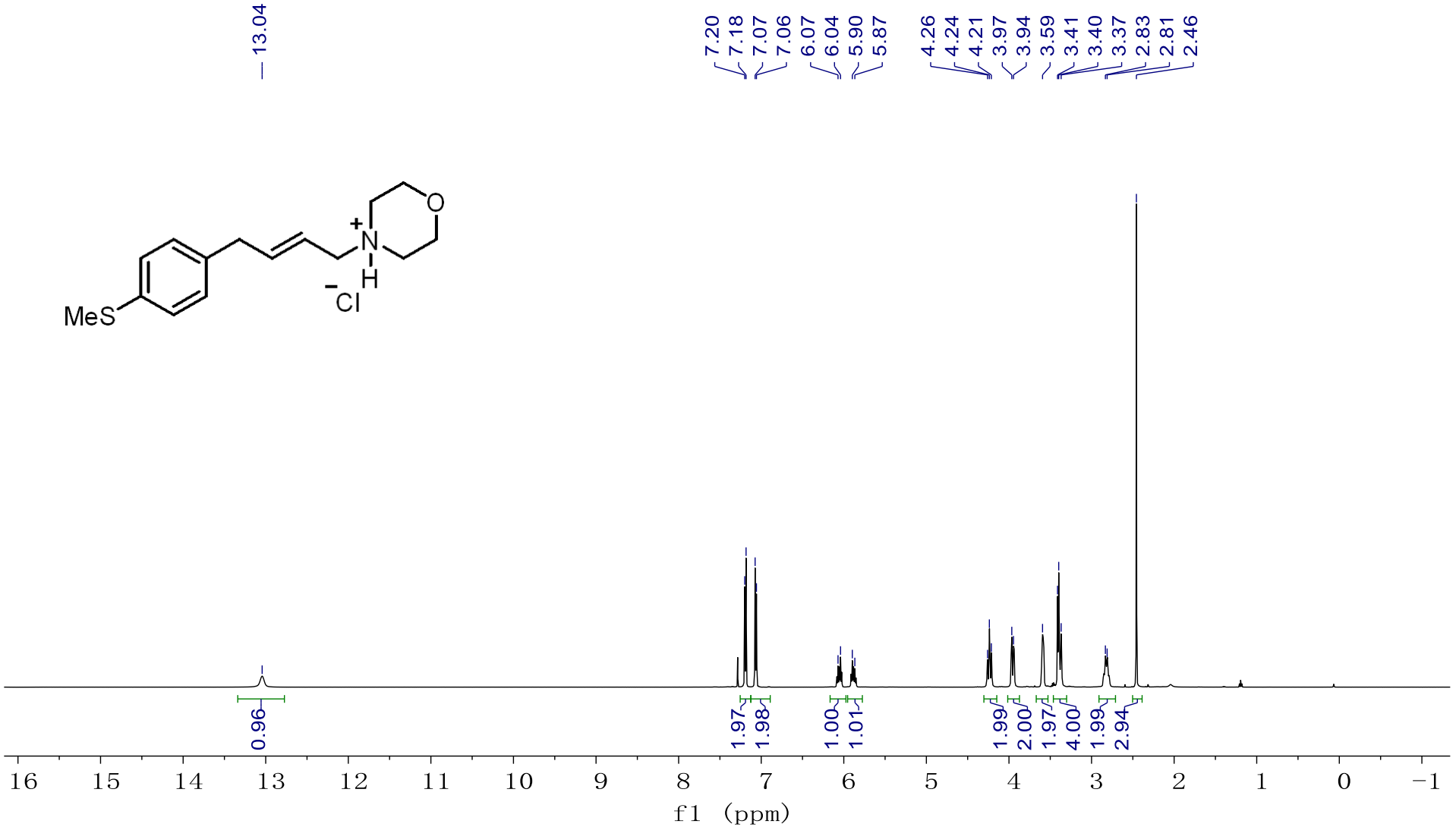
^{19}F NMR of allylamine 1

$CDCl_3$, 23 ºC



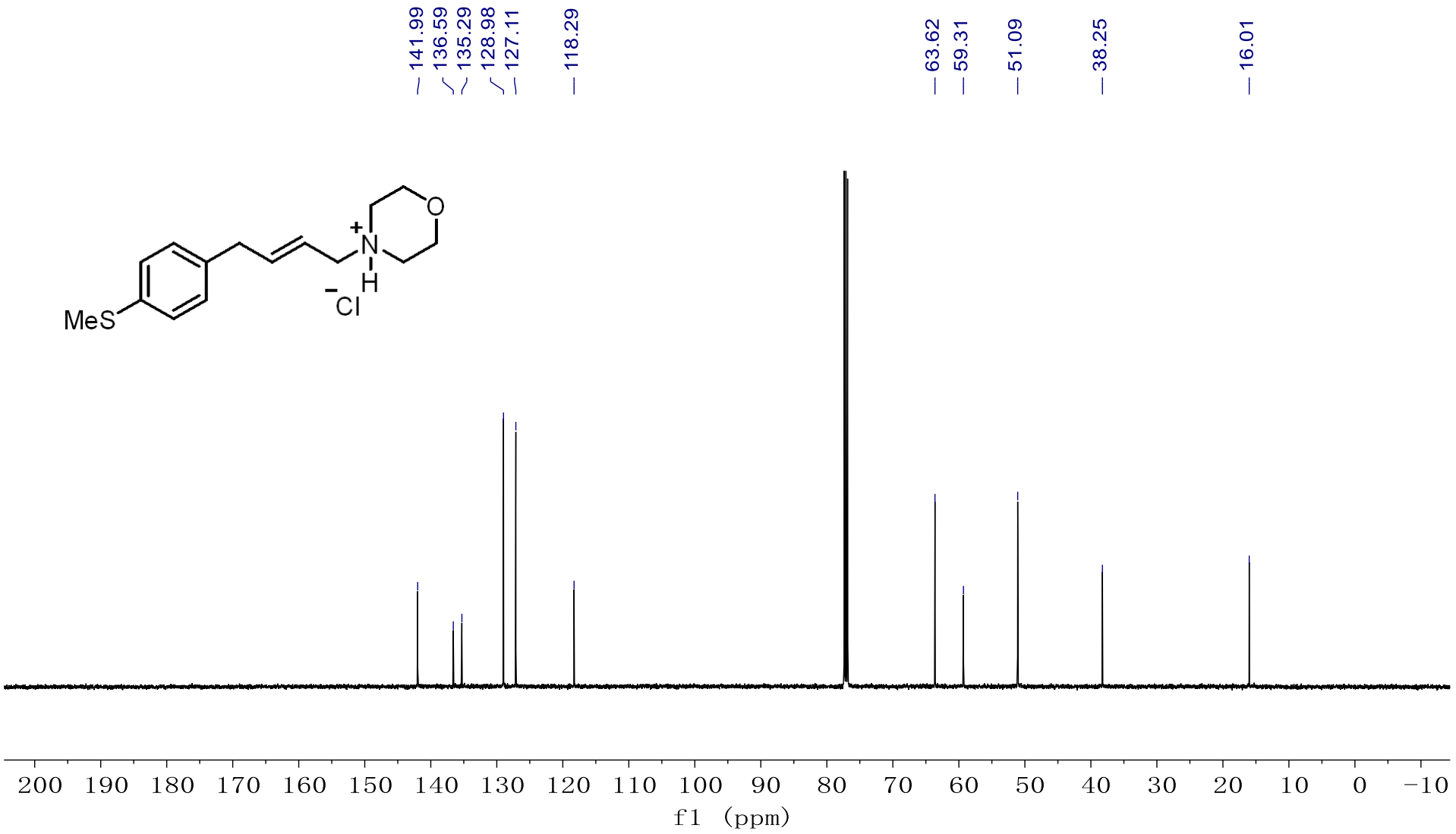
^{1}H NMR of allylamine hydrochloride 5/HCl

$CDCl_3$, 23 ºC



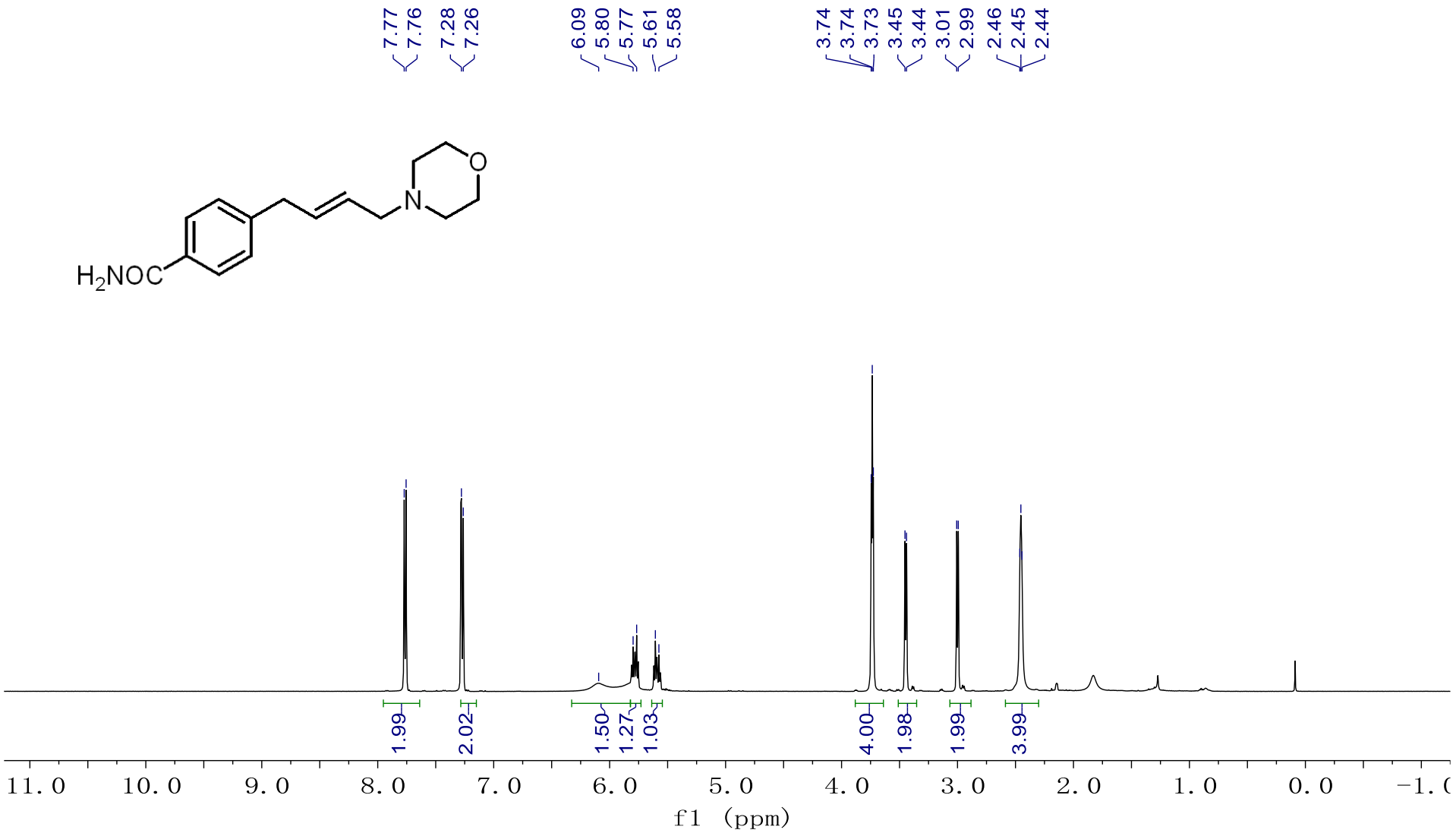
^{13}C NMR of allylamine hydrochloride 5/HCl

$CDCl_3$, 23 ºC



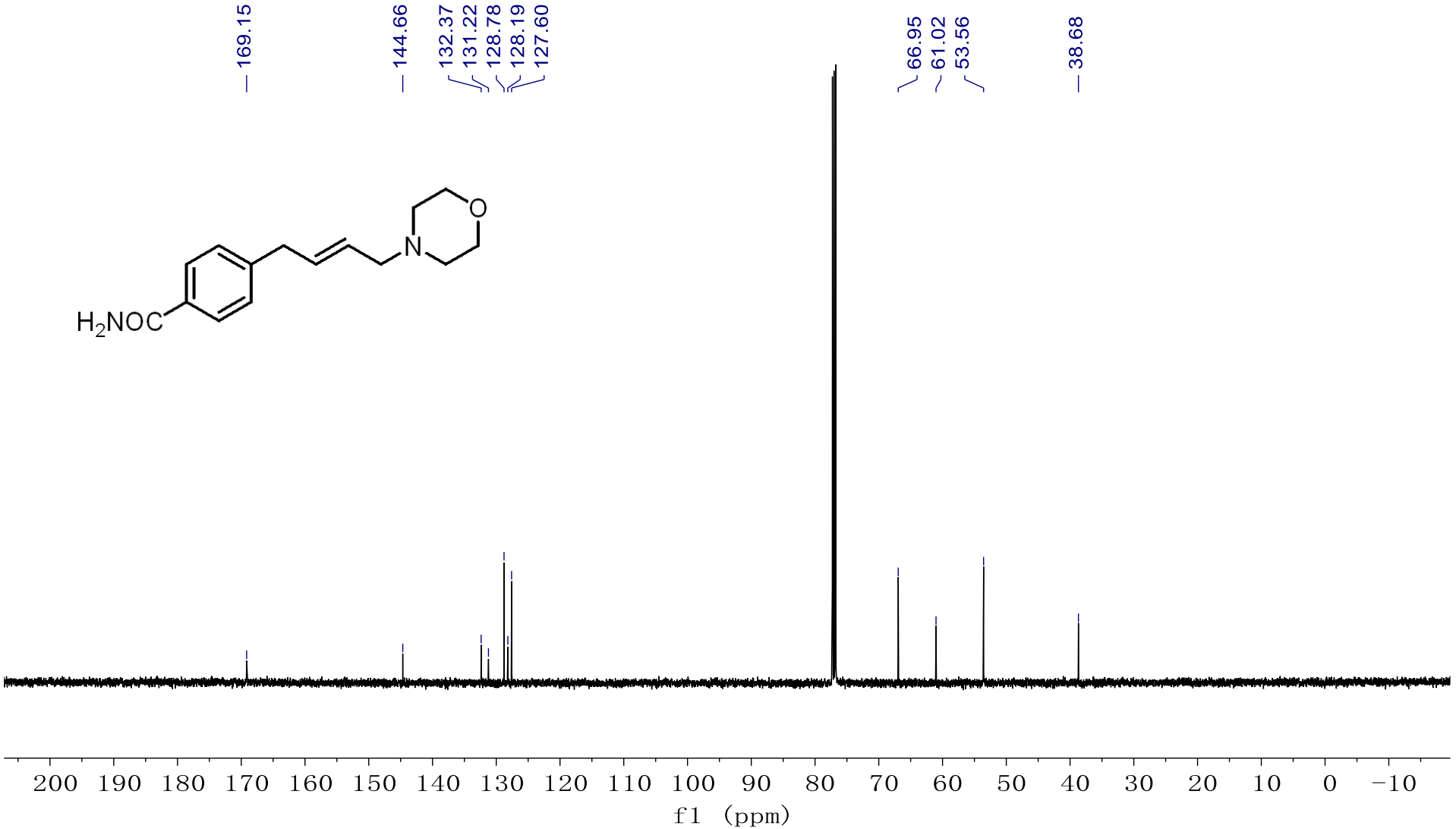
^{1}H NMR of allylamine 6

$CDCl_3$, 23 ºC



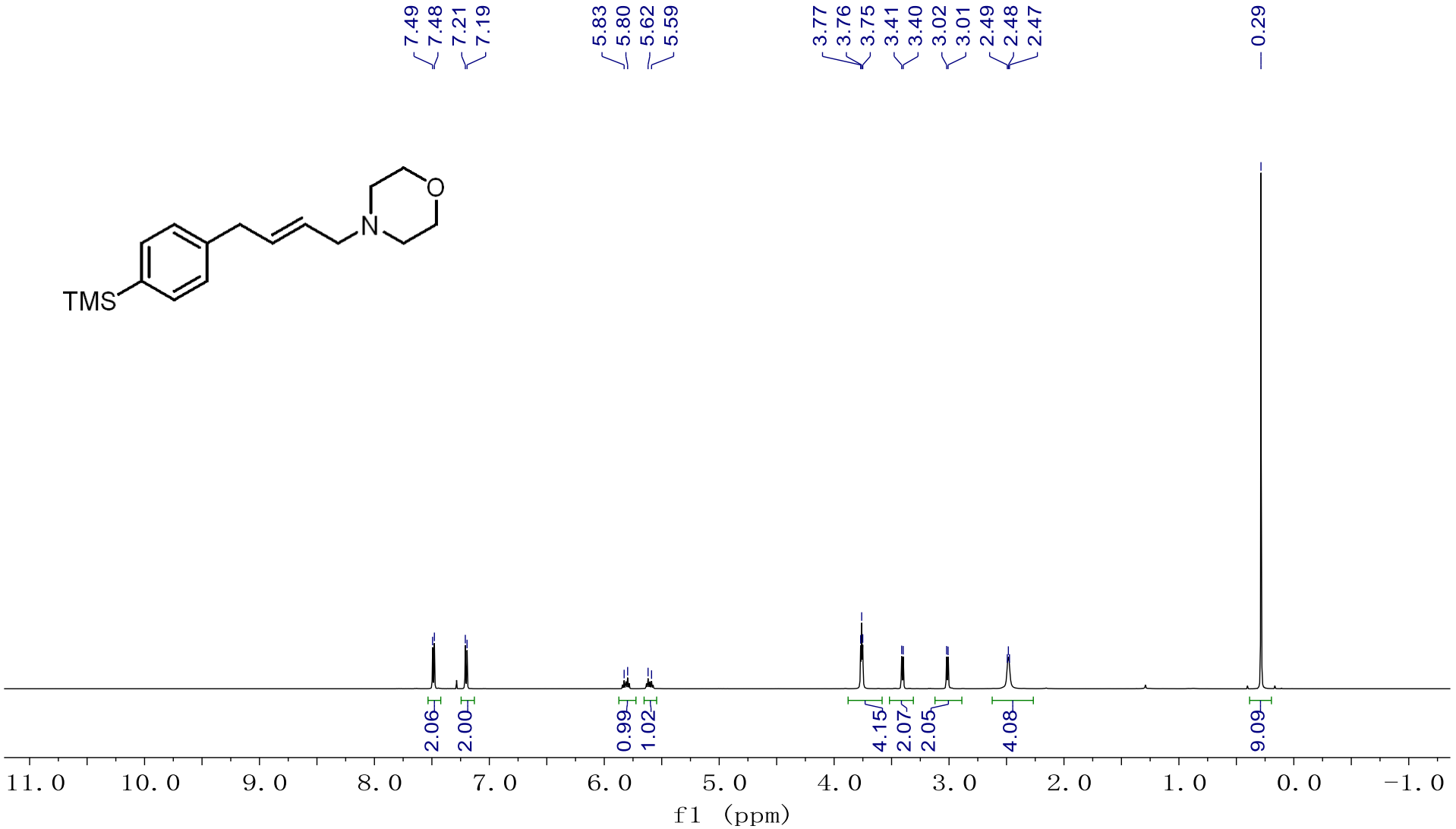
^{13}C NMR of allylamine 6

$CDCl_3$, 23 ºC



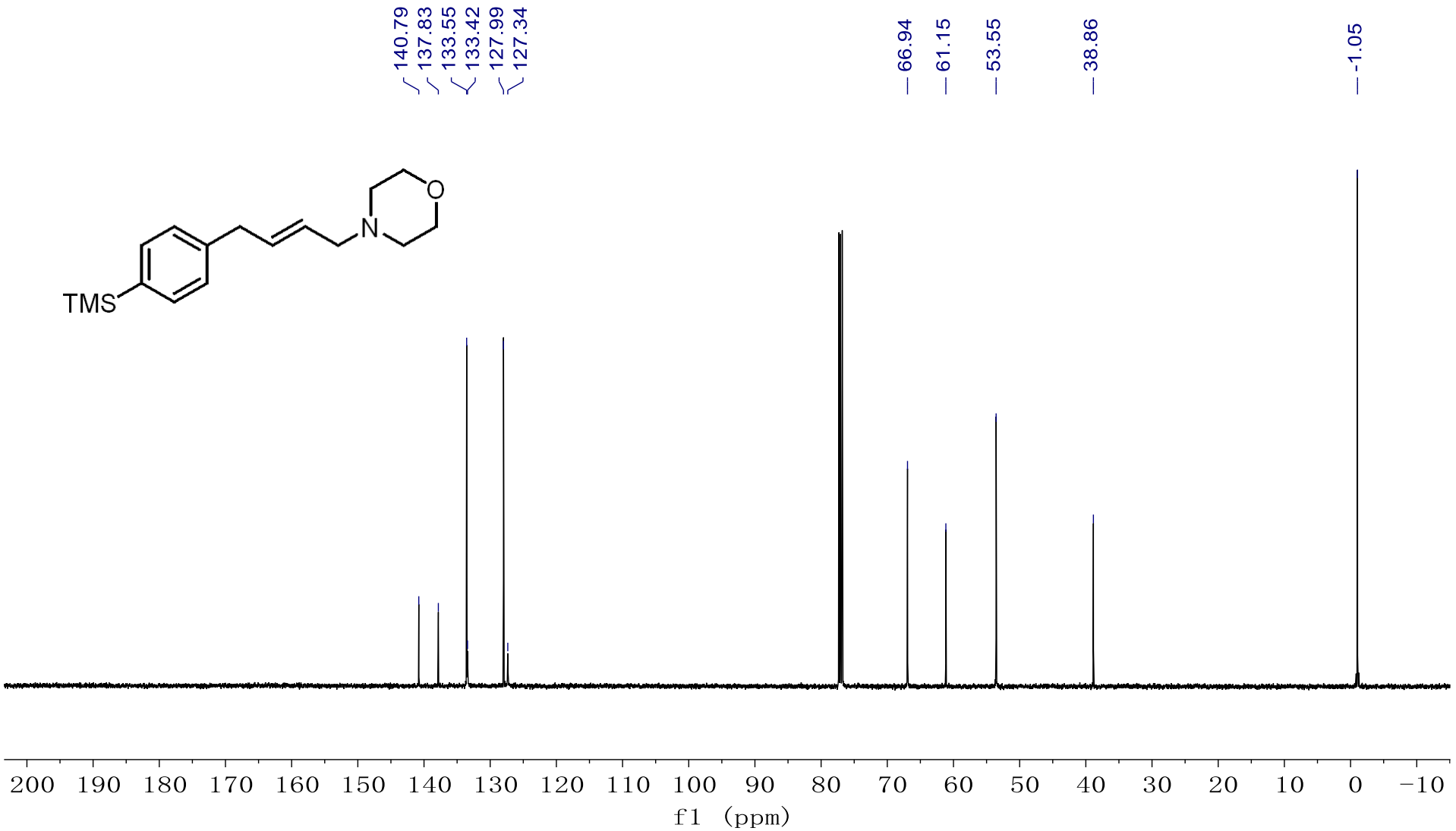
^{1}H NMR of allylamine 7

$CDCl_3$, 23 ºC



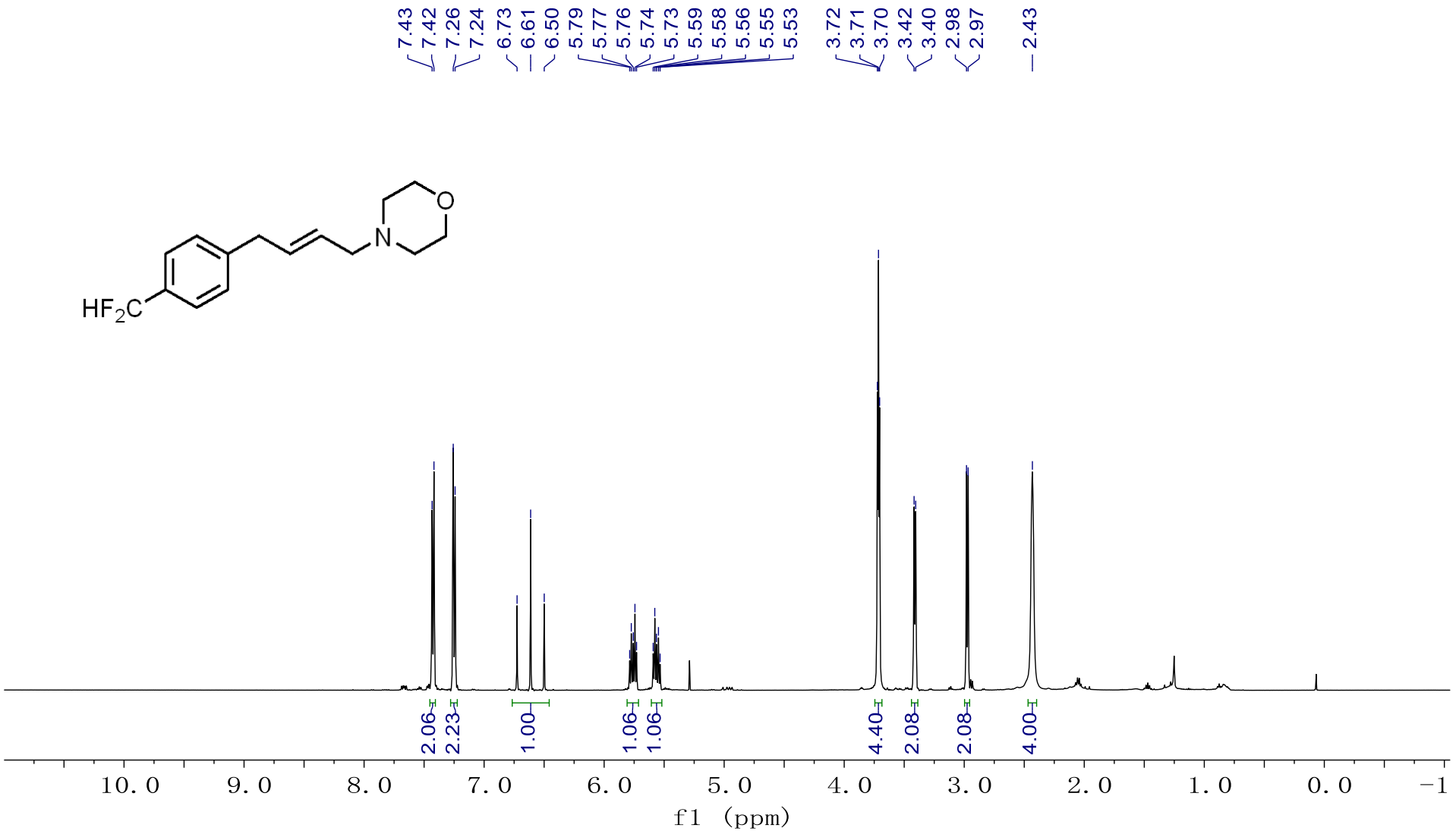
^{13}C NMR of allylamine 7

$CDCl_3$, 23 ºC



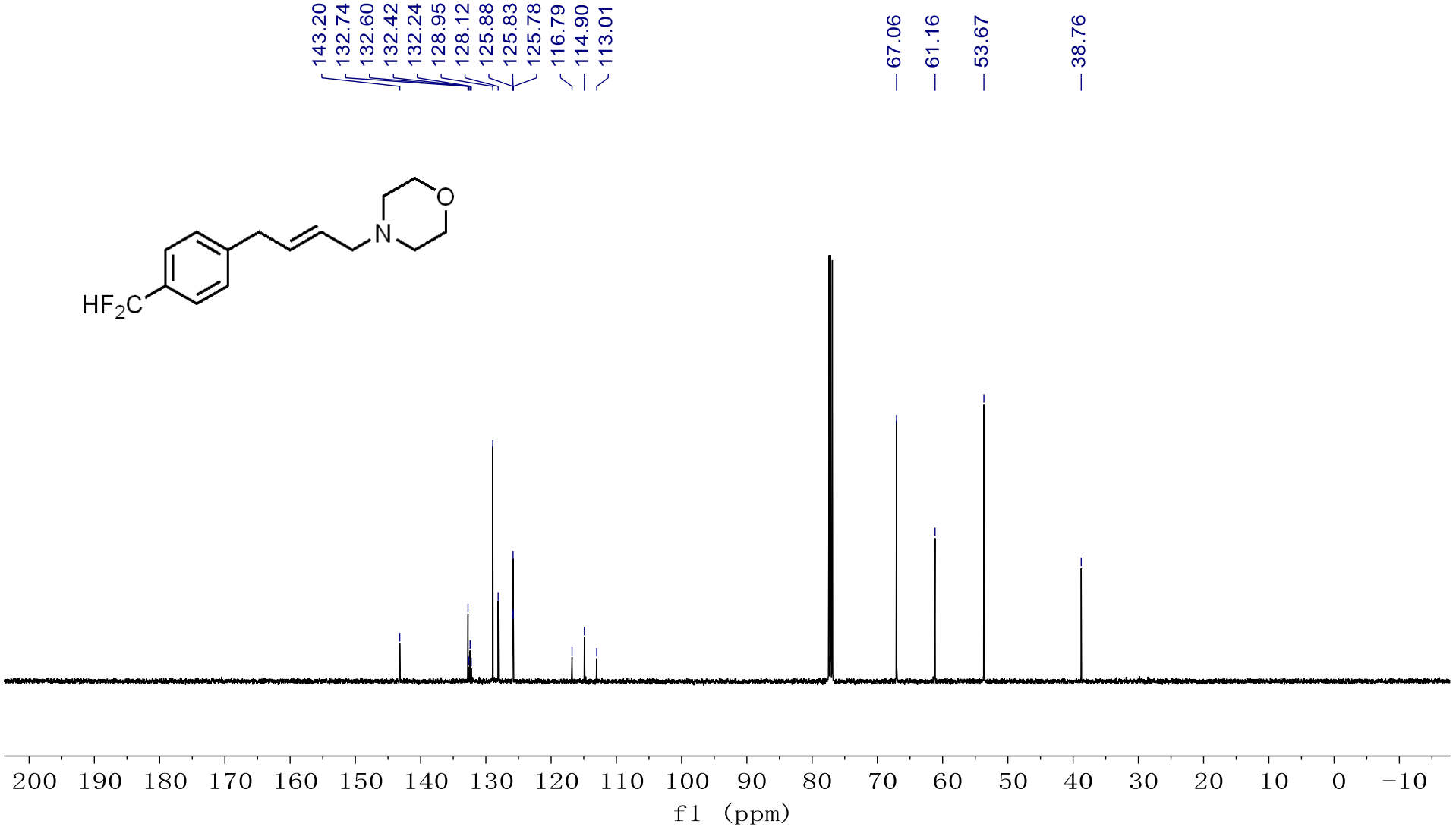
^{1}H NMR of allylamine 8

$CDCl_3$, 23 ºC



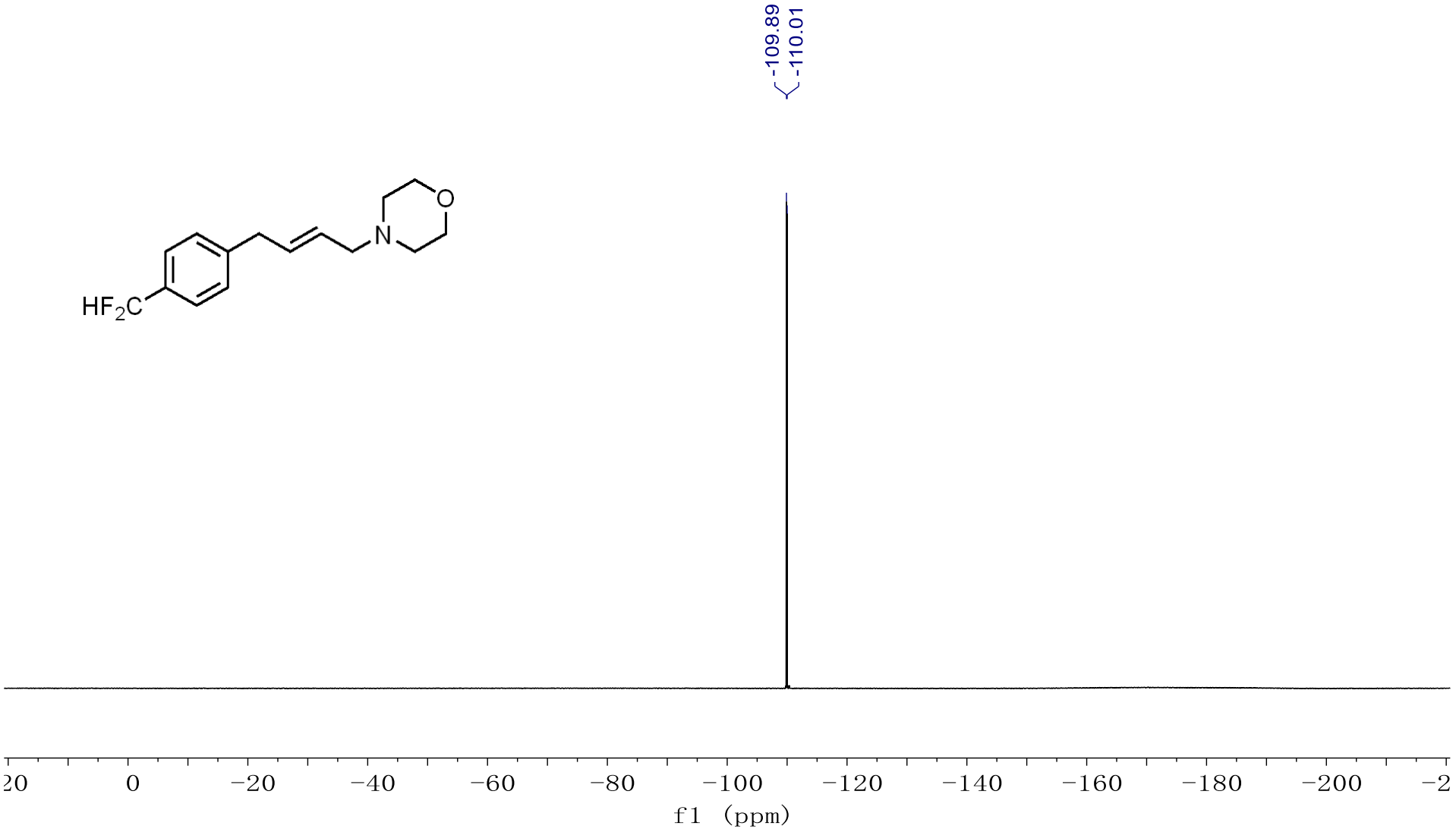
^{13}C NMR of allylamine 8

$CDCl_3$, 23 ºC



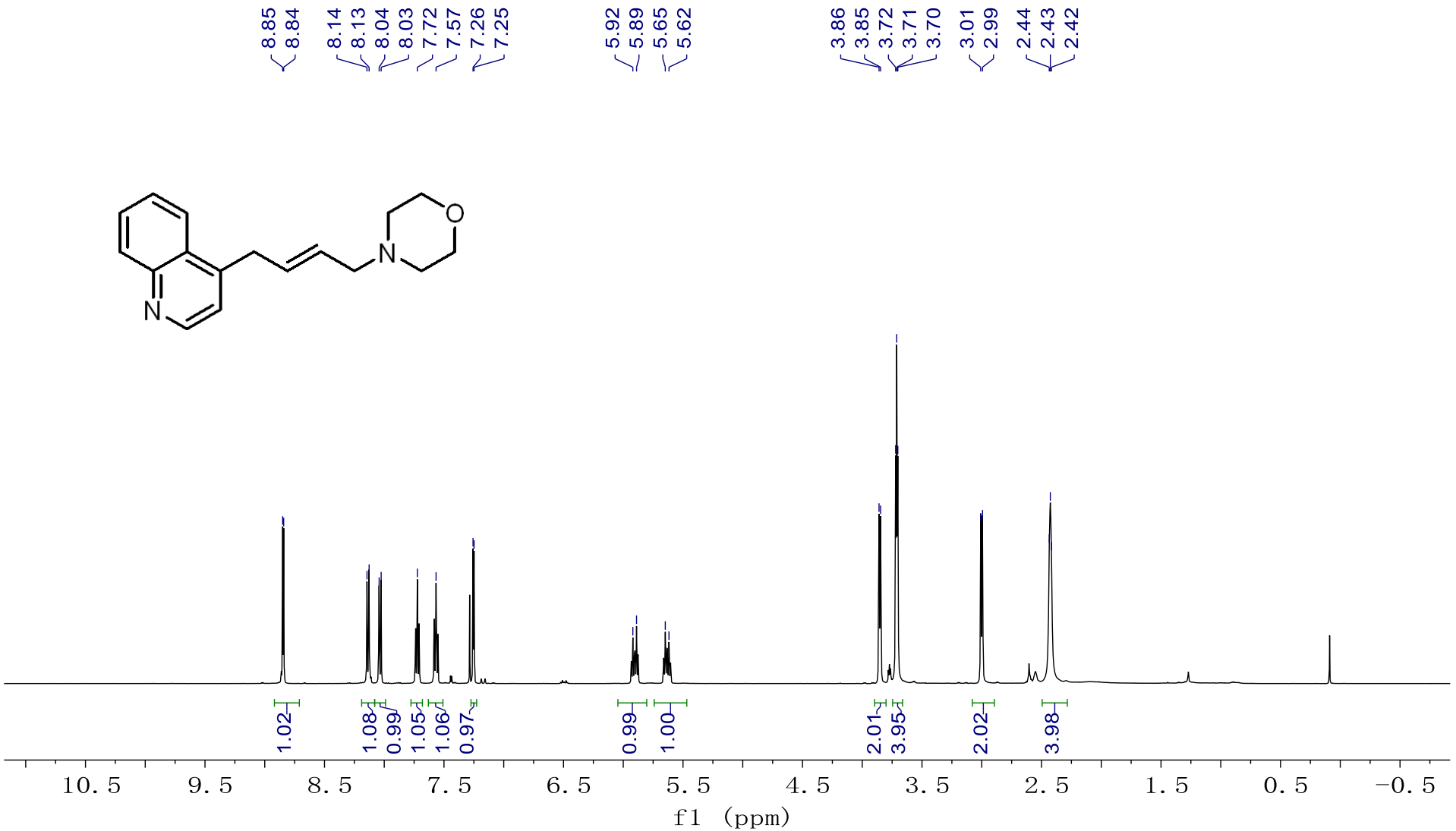
^{19}F NMR of allylamine 8

$CDCl_3$, 23 ºC



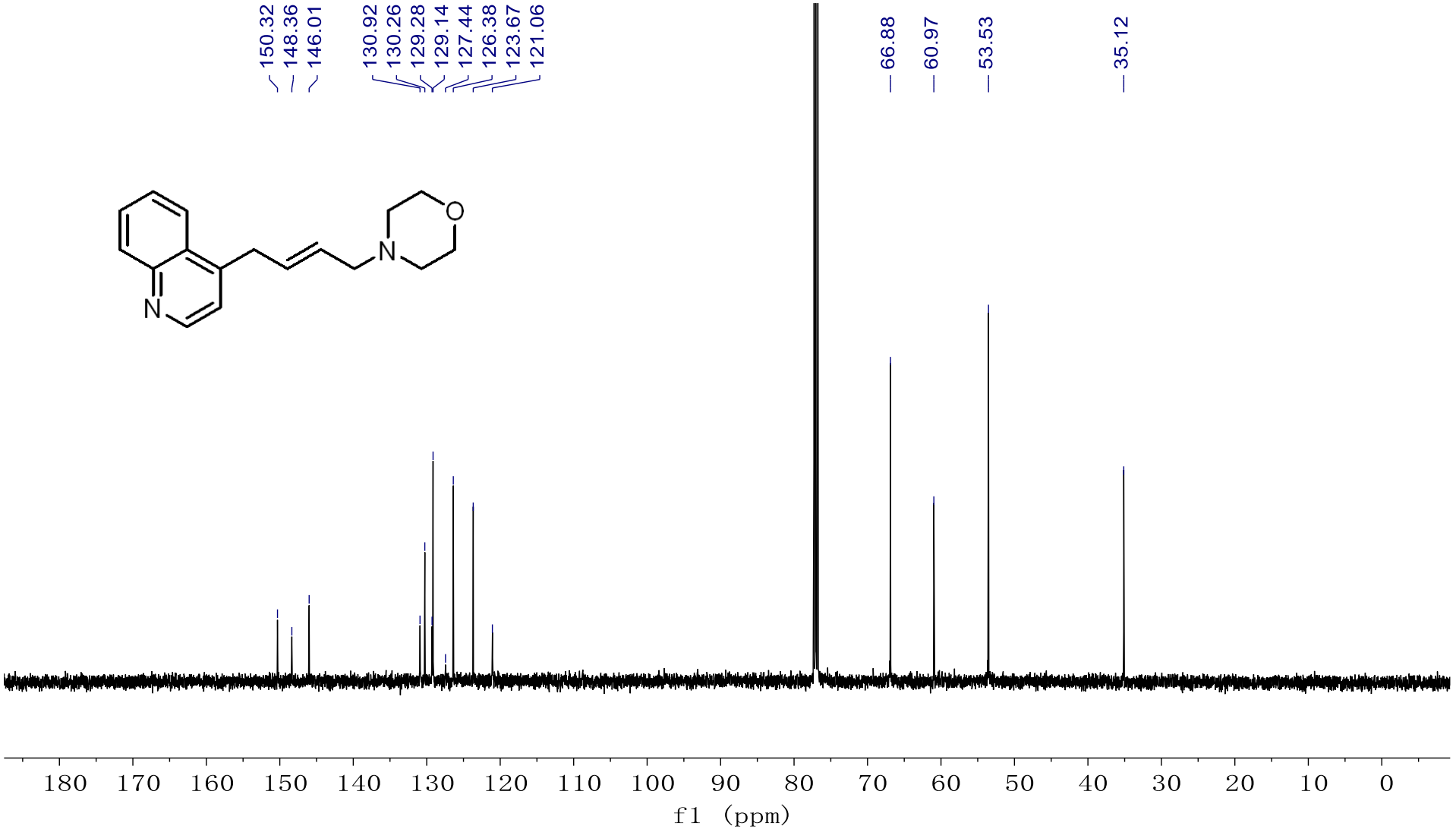
^{1}H NMR of allylamine 12

$CDCl_3$, 23 ºC



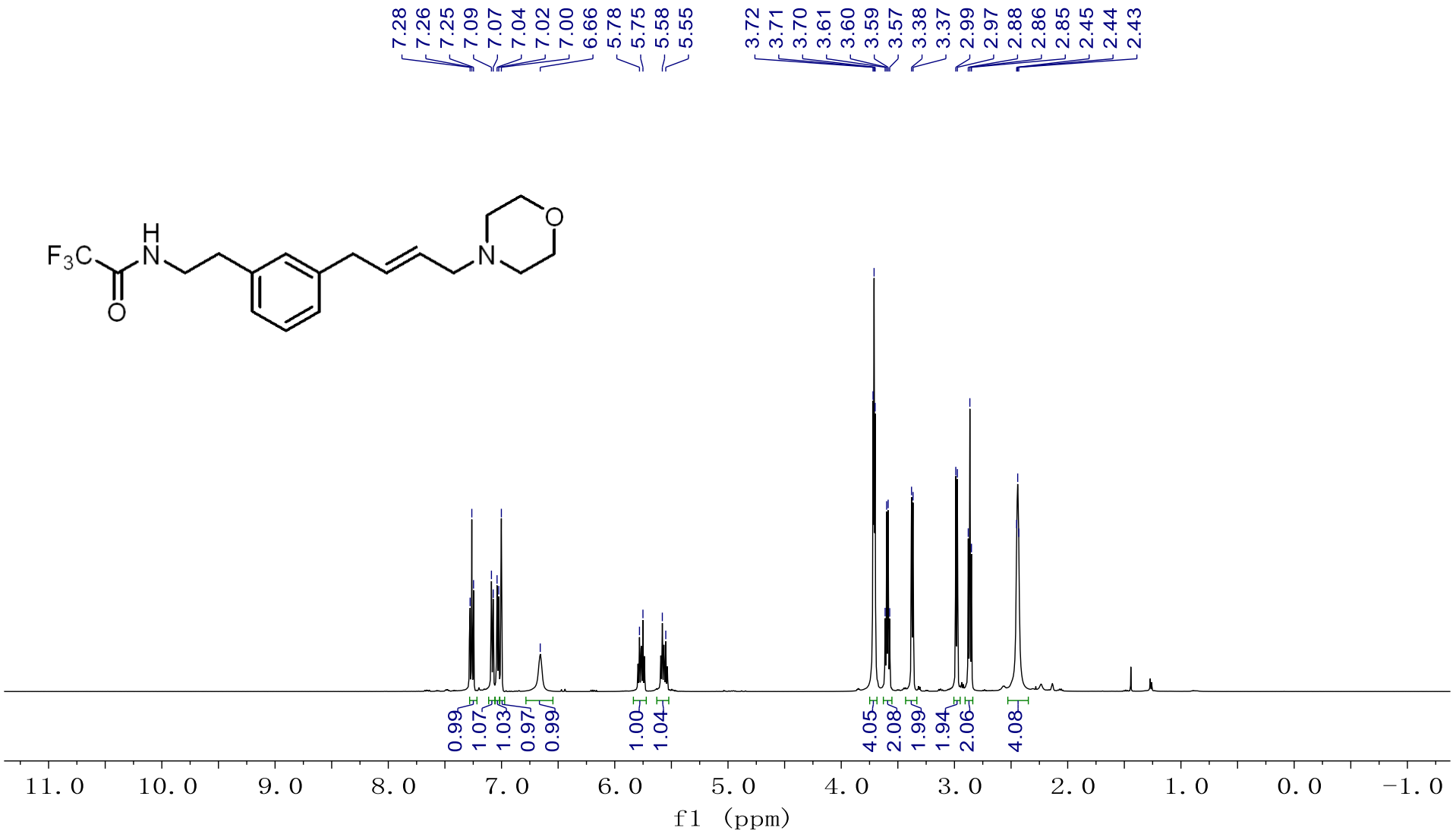
^{13}C NMR of allylamine 12

$CDCl_3$, 23 ºC



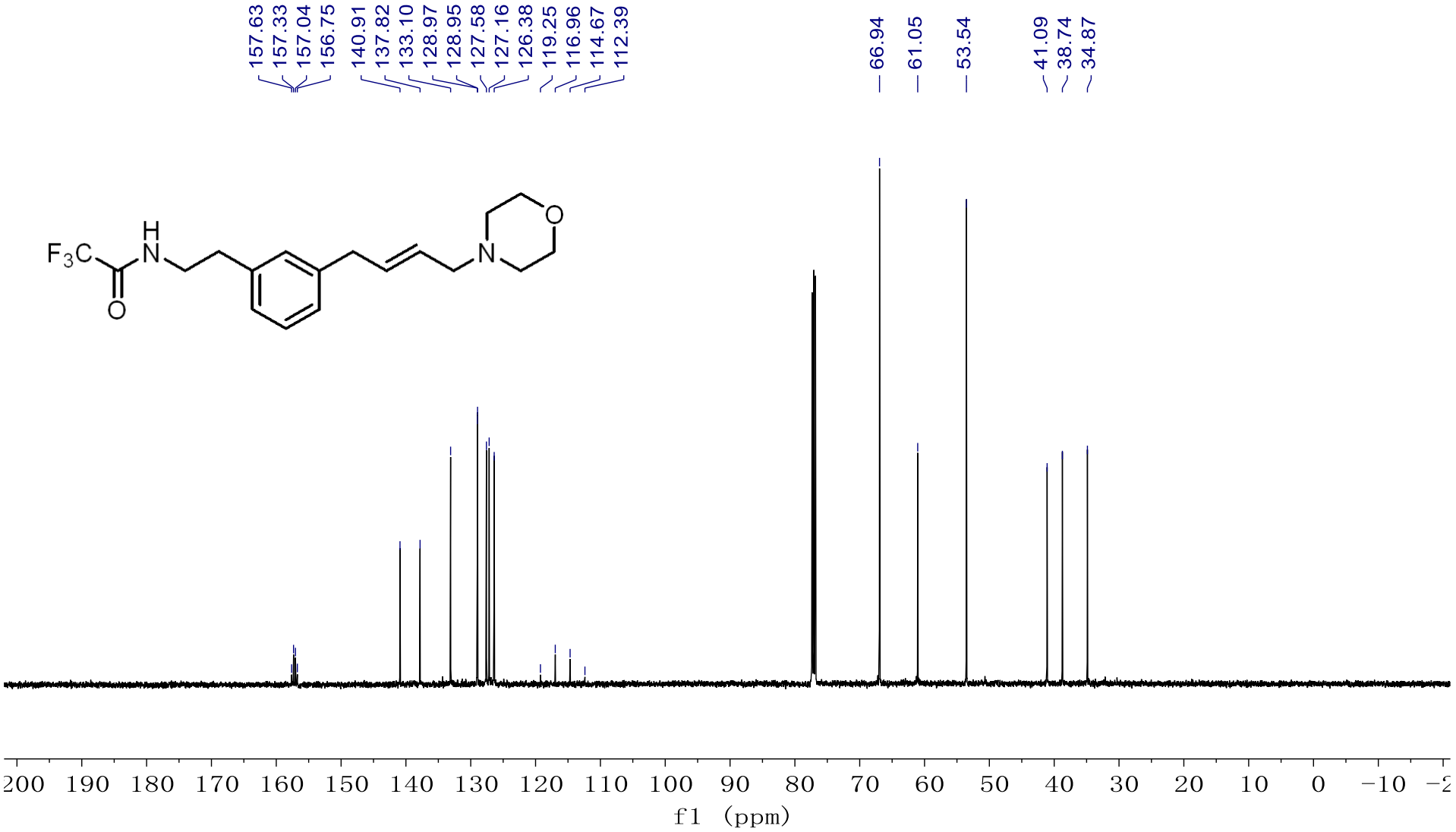
^{1}H NMR of allylamine 15

$CDCl_3$, 23 ºC



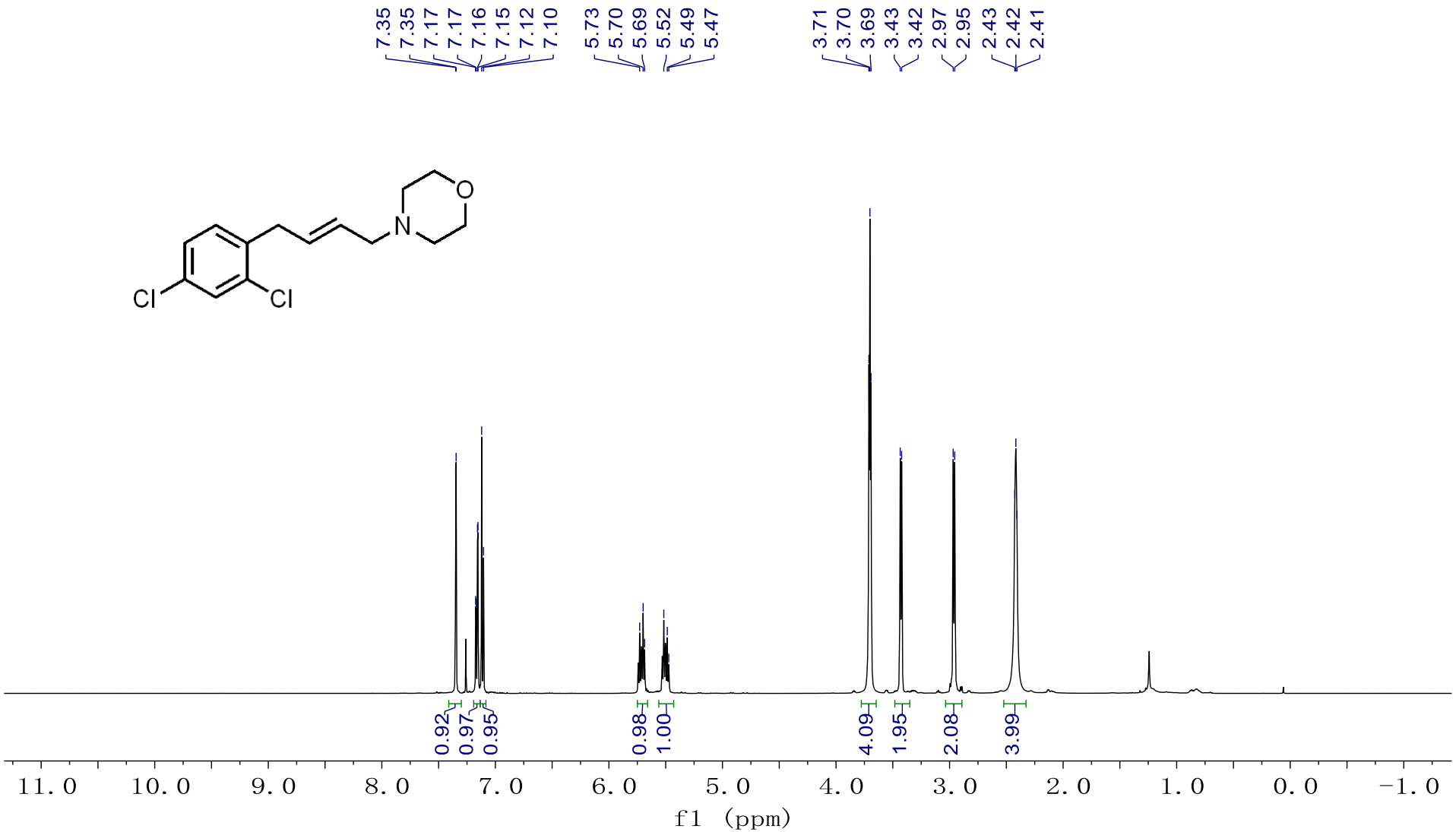
^{13}C NMR of allylamine 15

$CDCl_3$, 23 ºC



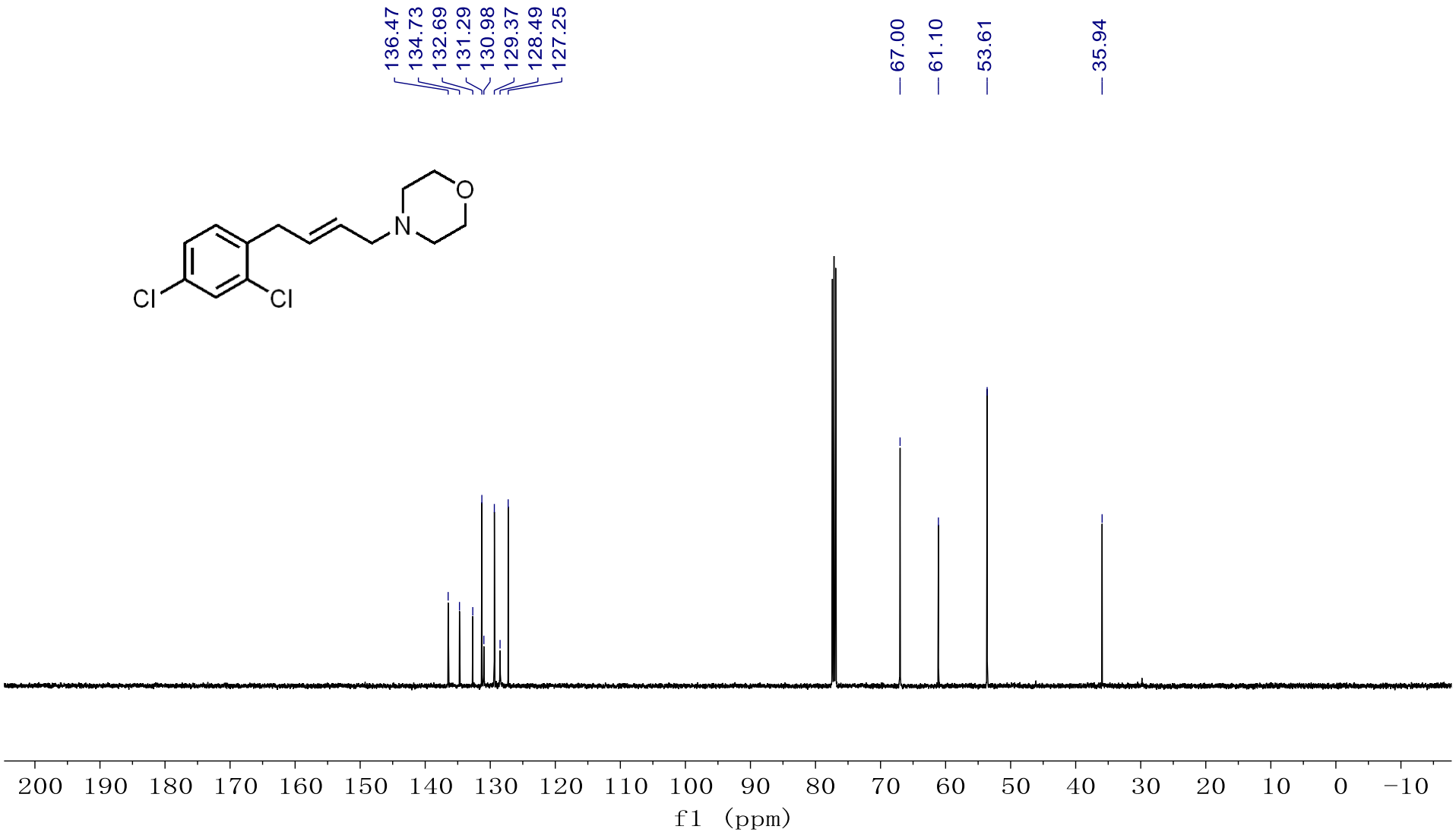
^{1}H NMR of allylamine 16

$CDCl_3$, 23 ºC



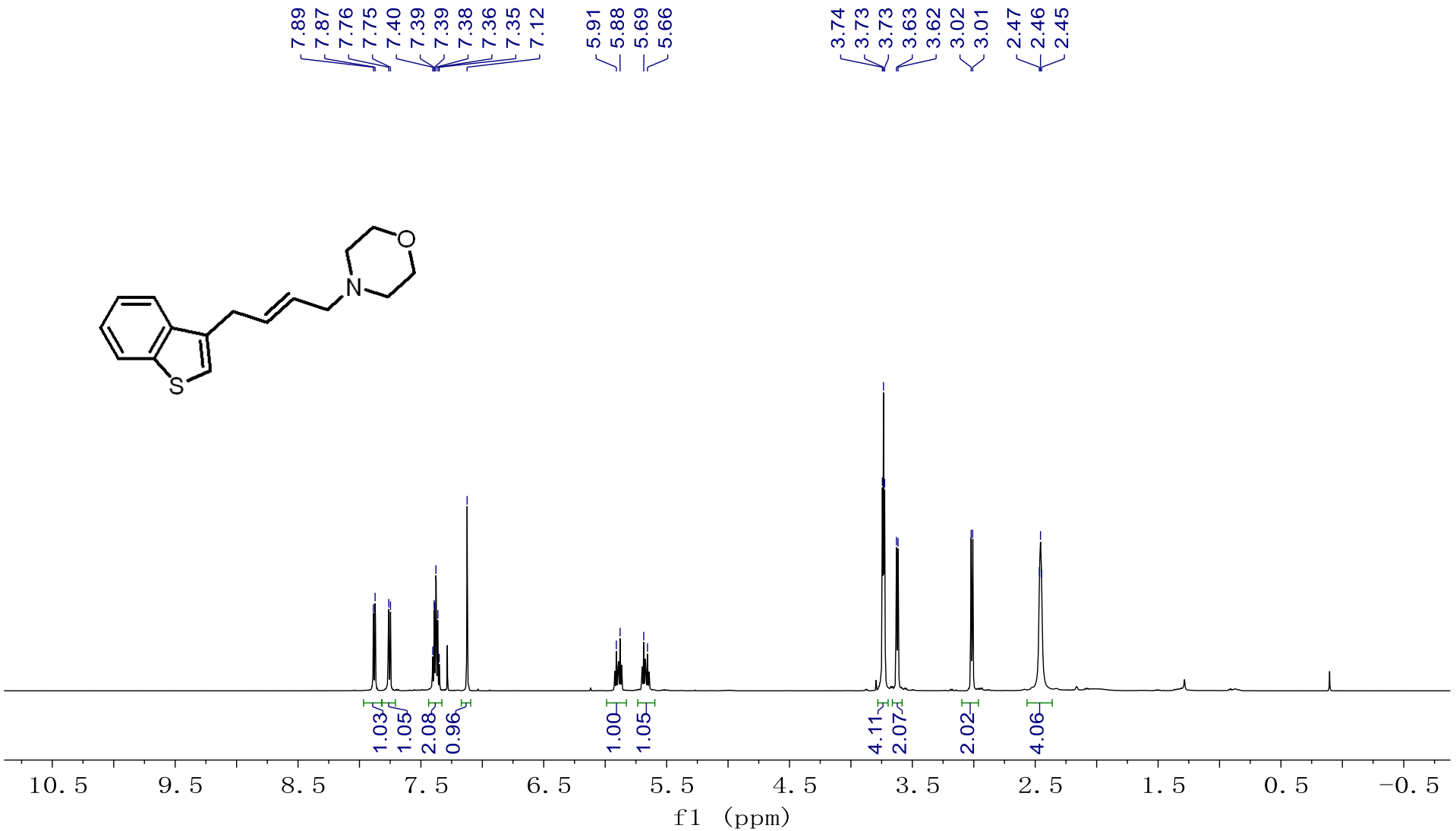
^{13}C NMR of allylamine 16

$CDCl_3$, 23 ºC



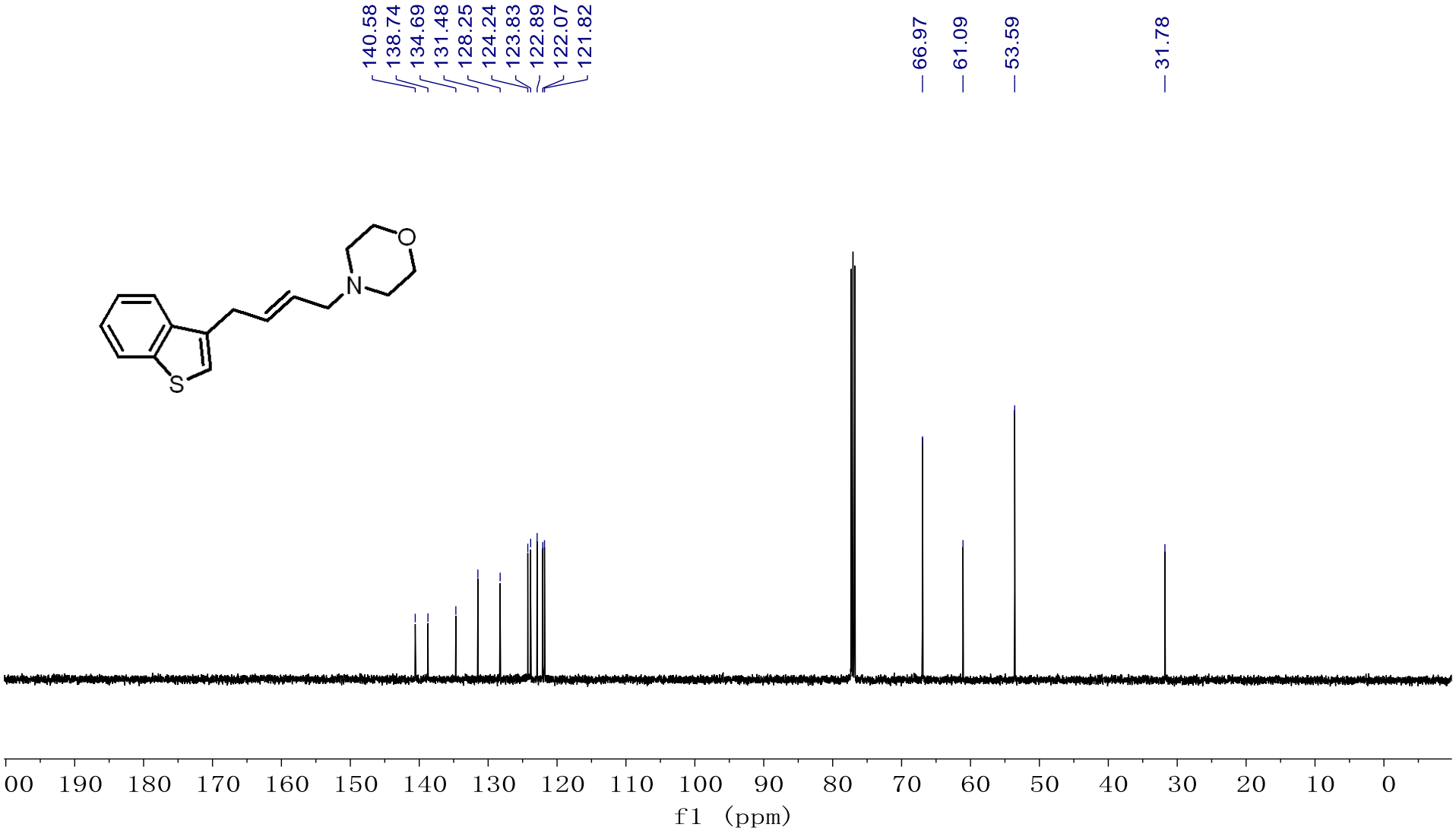
^{1}H NMR of allylamine 17

$CDCl_3$, 23 ºC



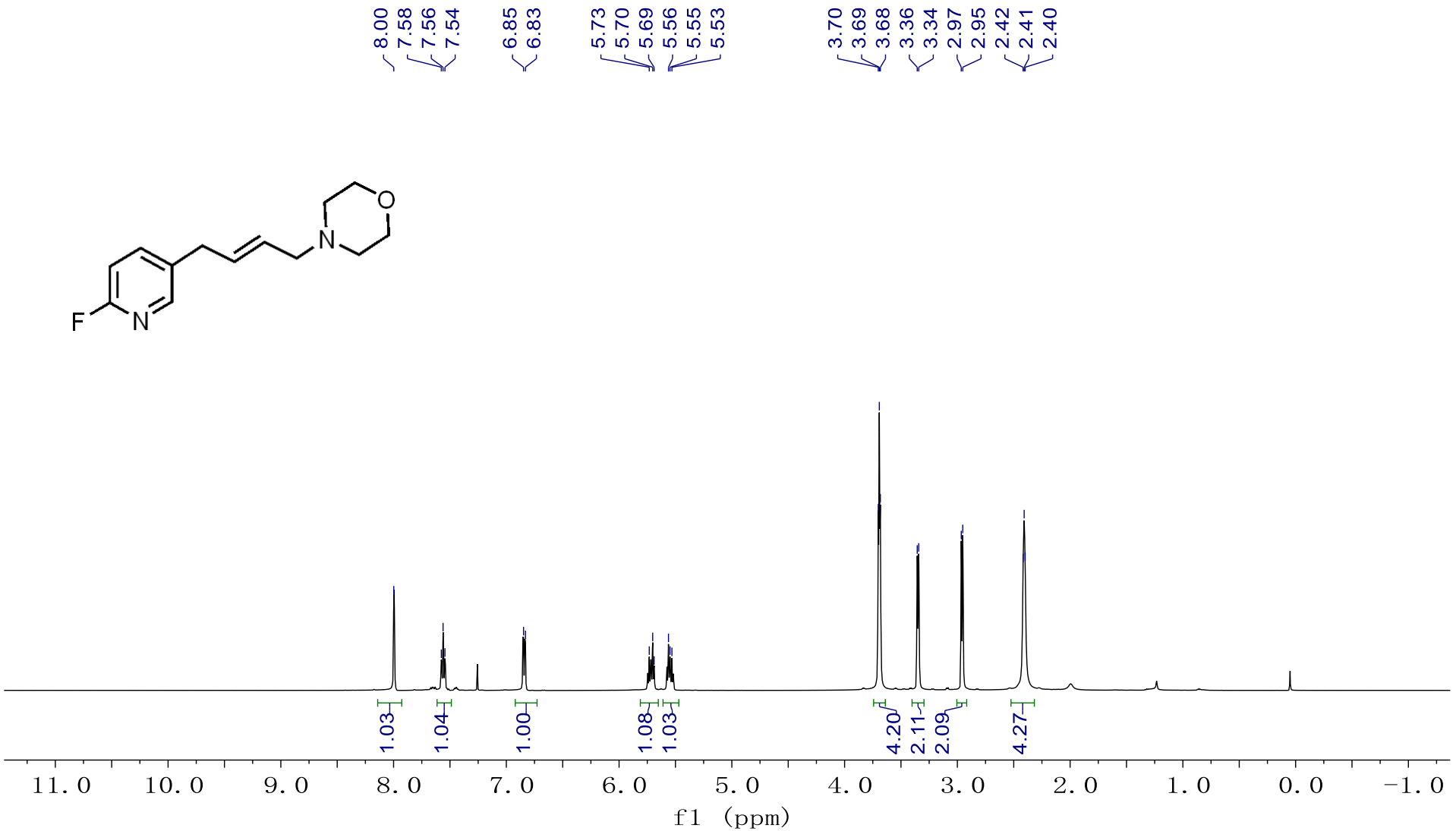
^{13}C NMR of allylamine 17

$CDCl_3$, 23 ºC



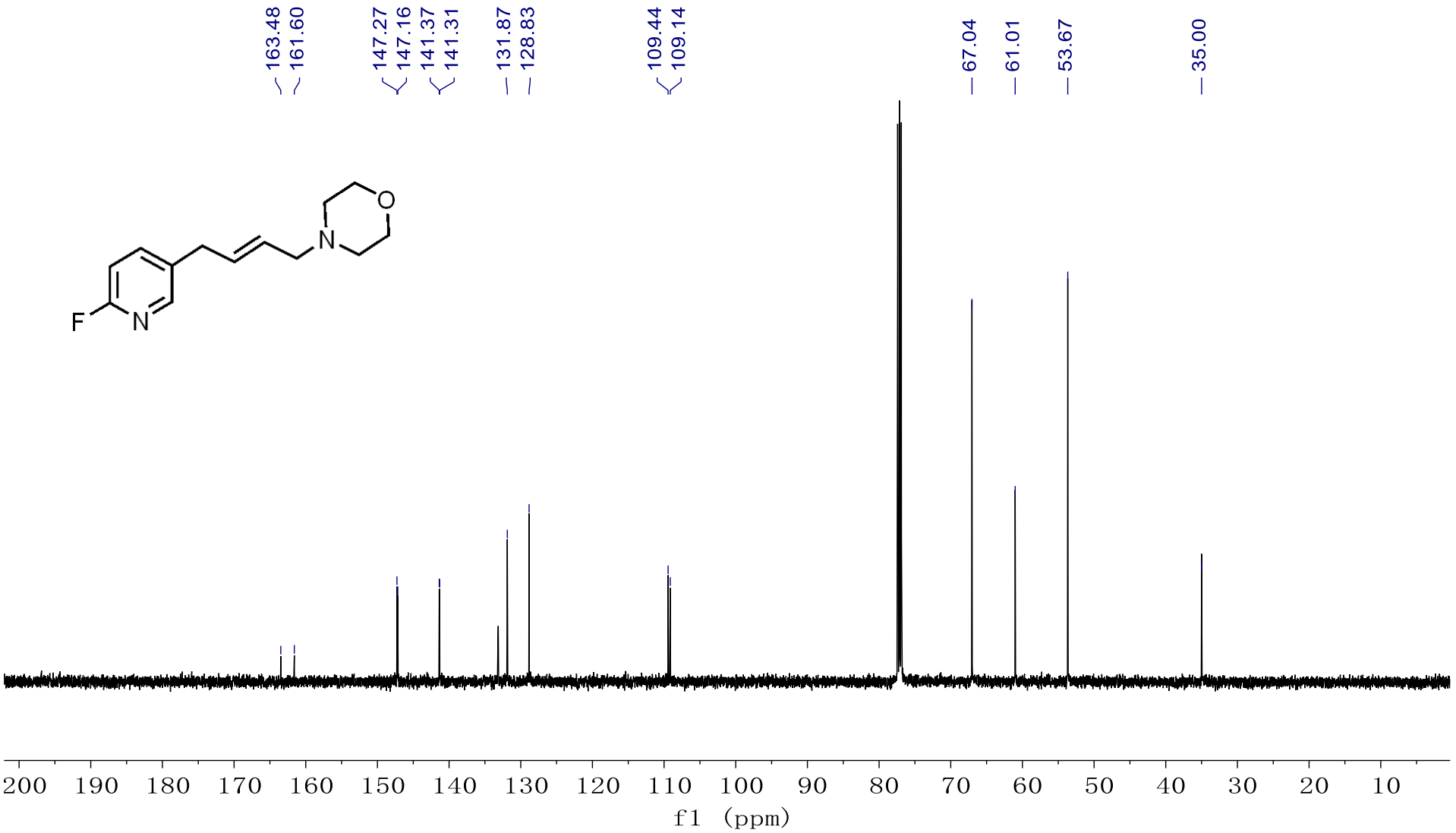
^{1}H NMR of allylamine 18

$CDCl_3$, 23 ºC



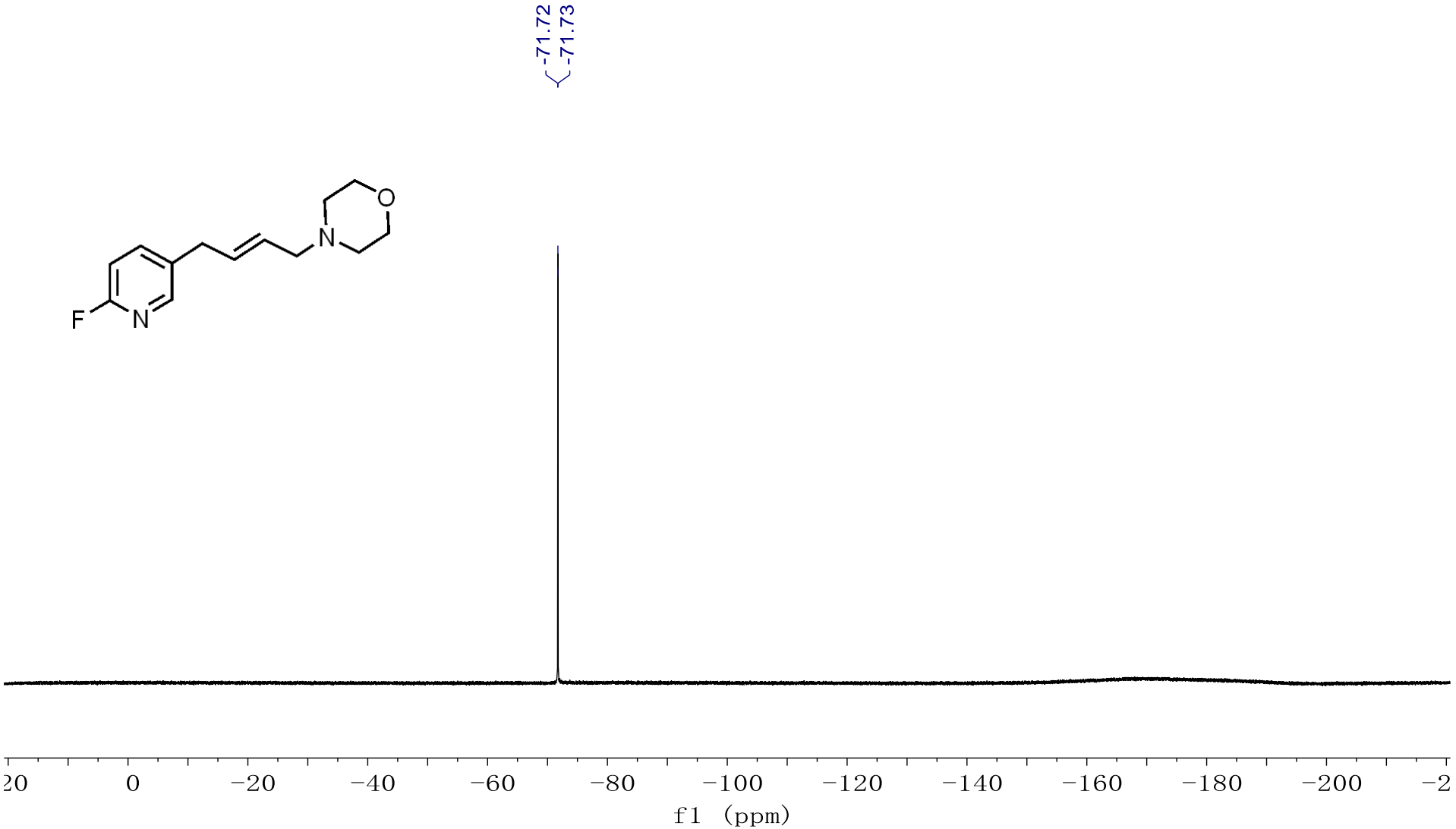
^{13}C NMR of allylamine 18

$CDCl_3$, 23 ºC



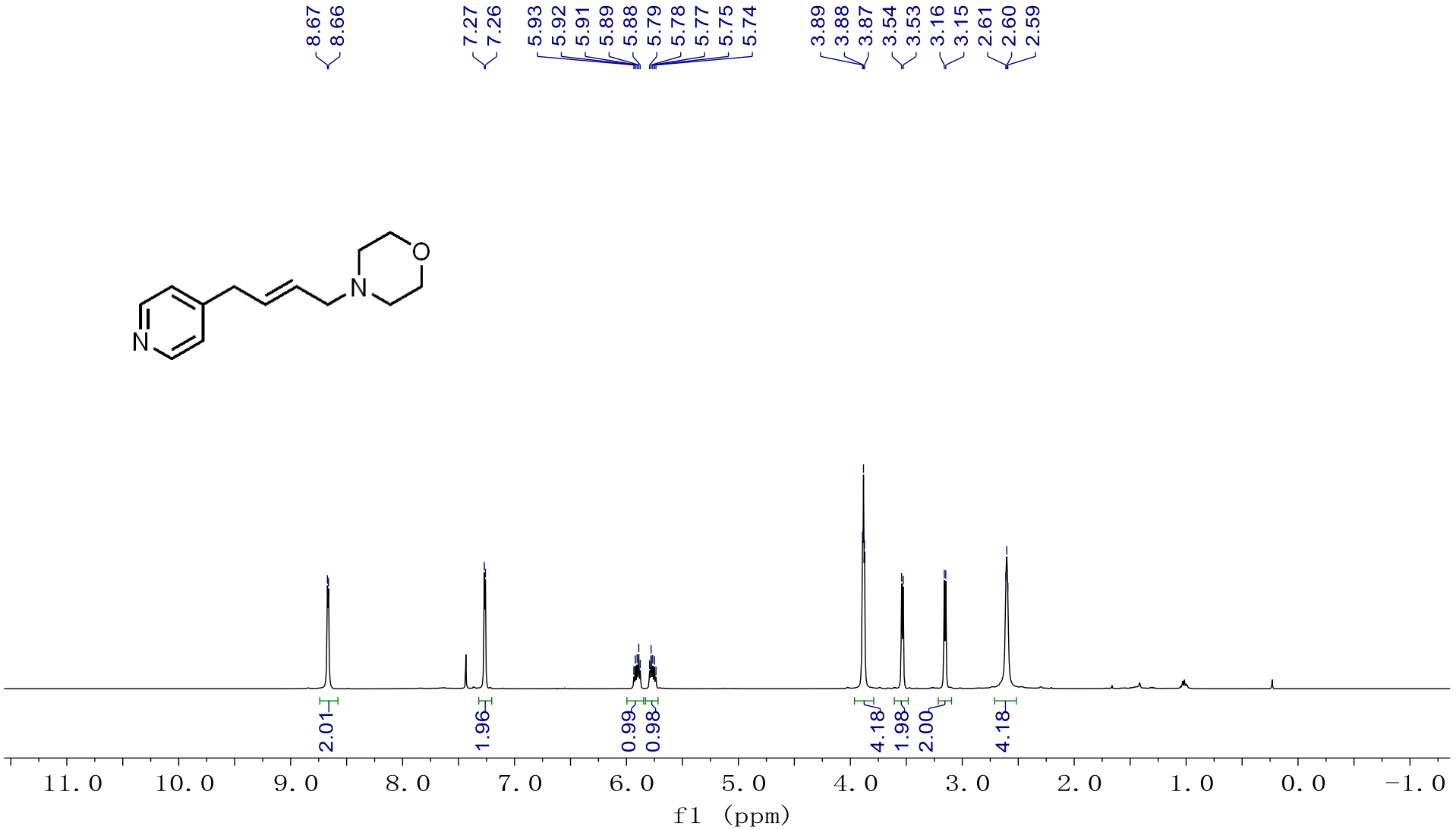
^{19}F NMR of allylamine 18

$CDCl_3$, 23 ºC



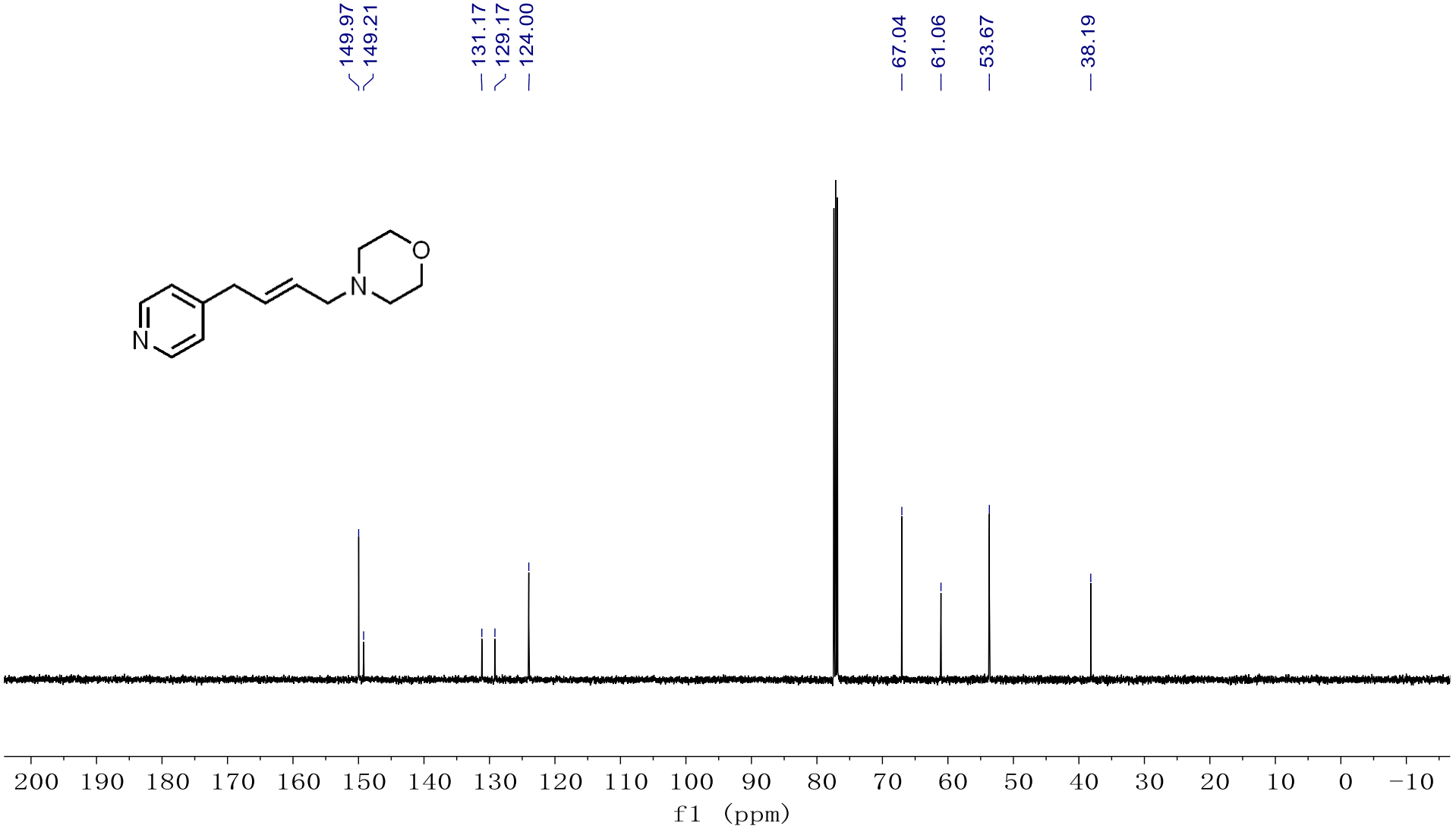
^{1}H NMR of allylamine 19

$CDCl_3$, 23 ºC



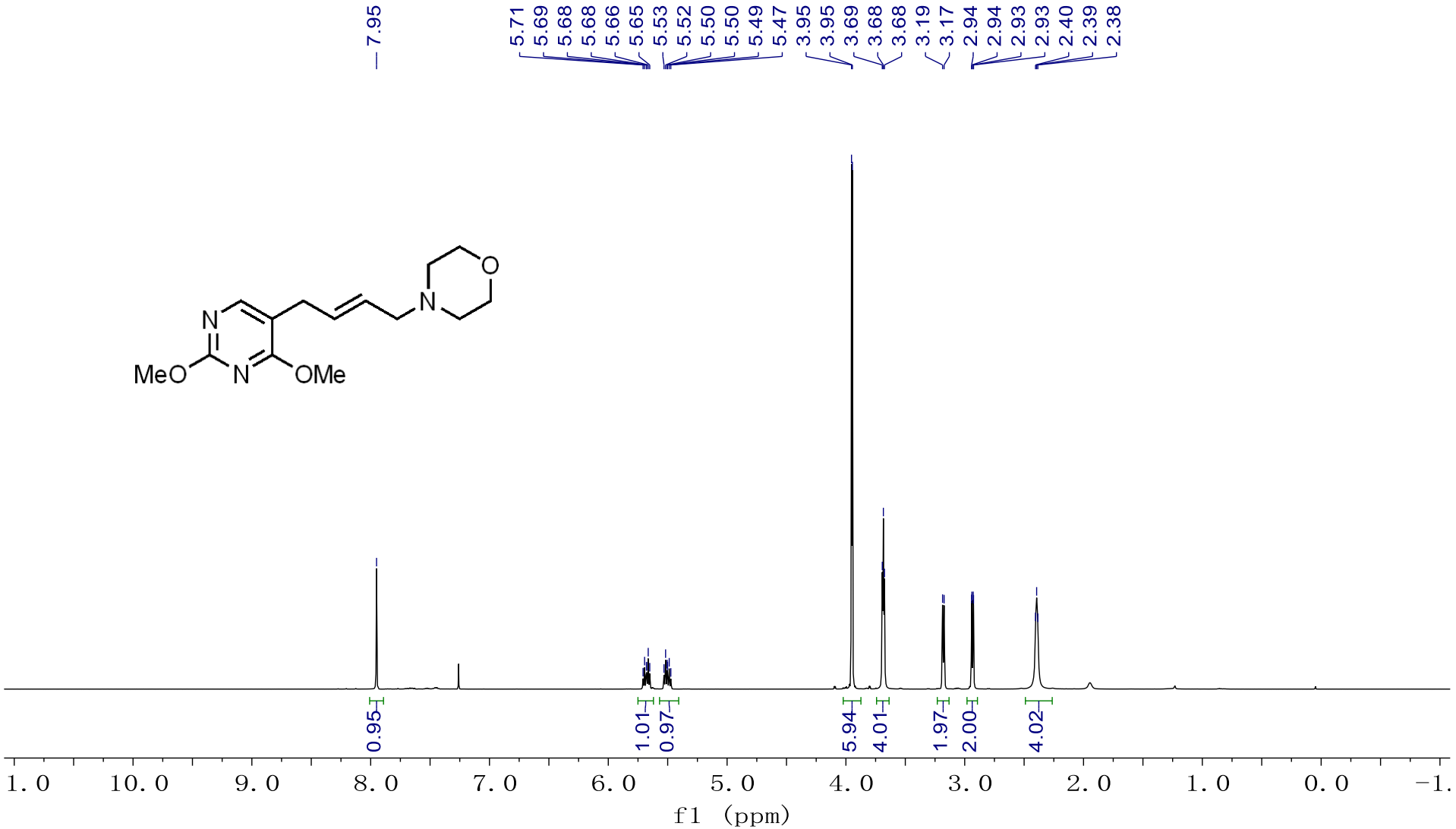
^{13}C NMR of allylamine 19

$CDCl_3$, 23 ºC



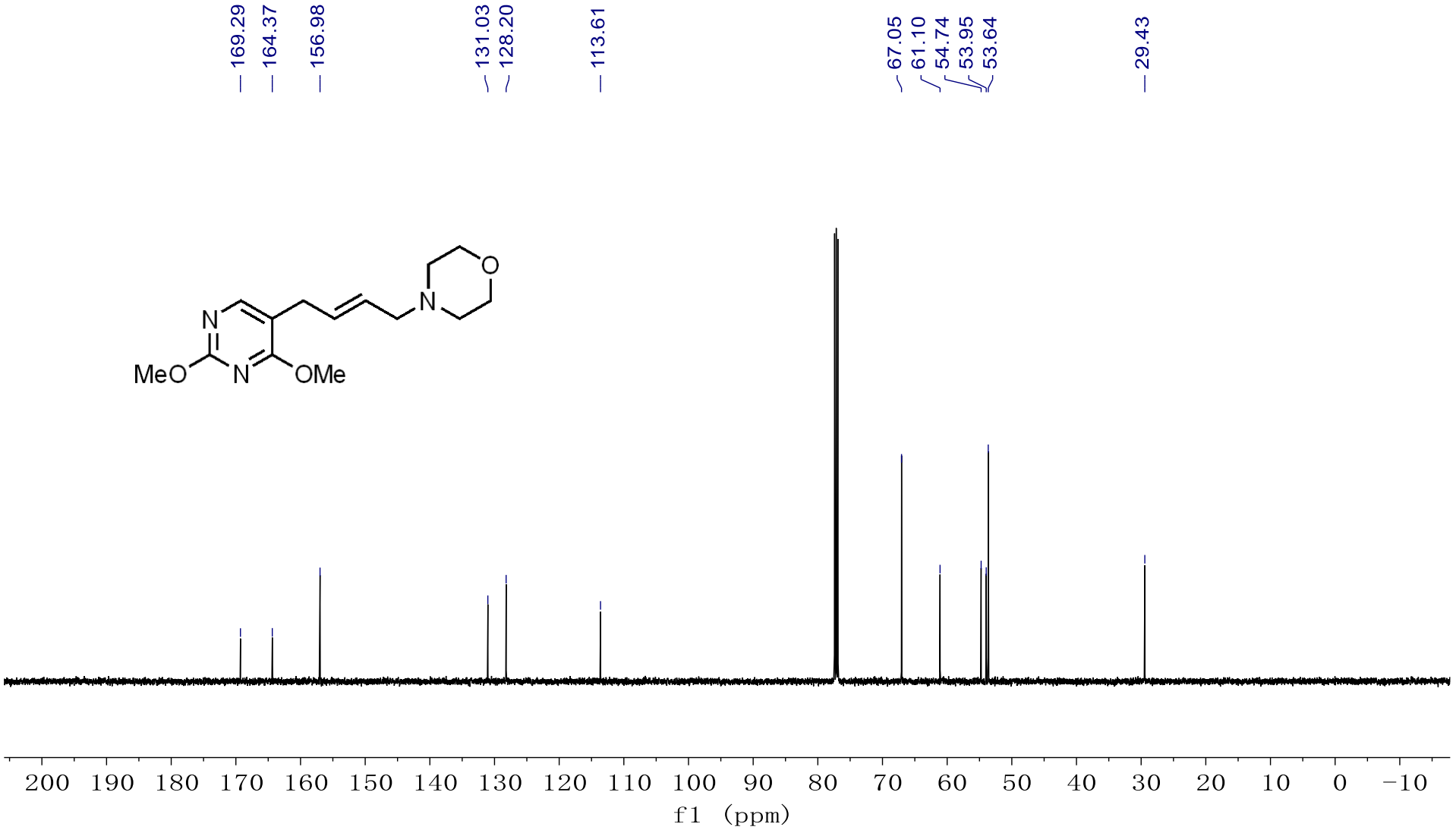
^{1}H NMR of allylamine 20

$CDCl_3$, 23 ºC



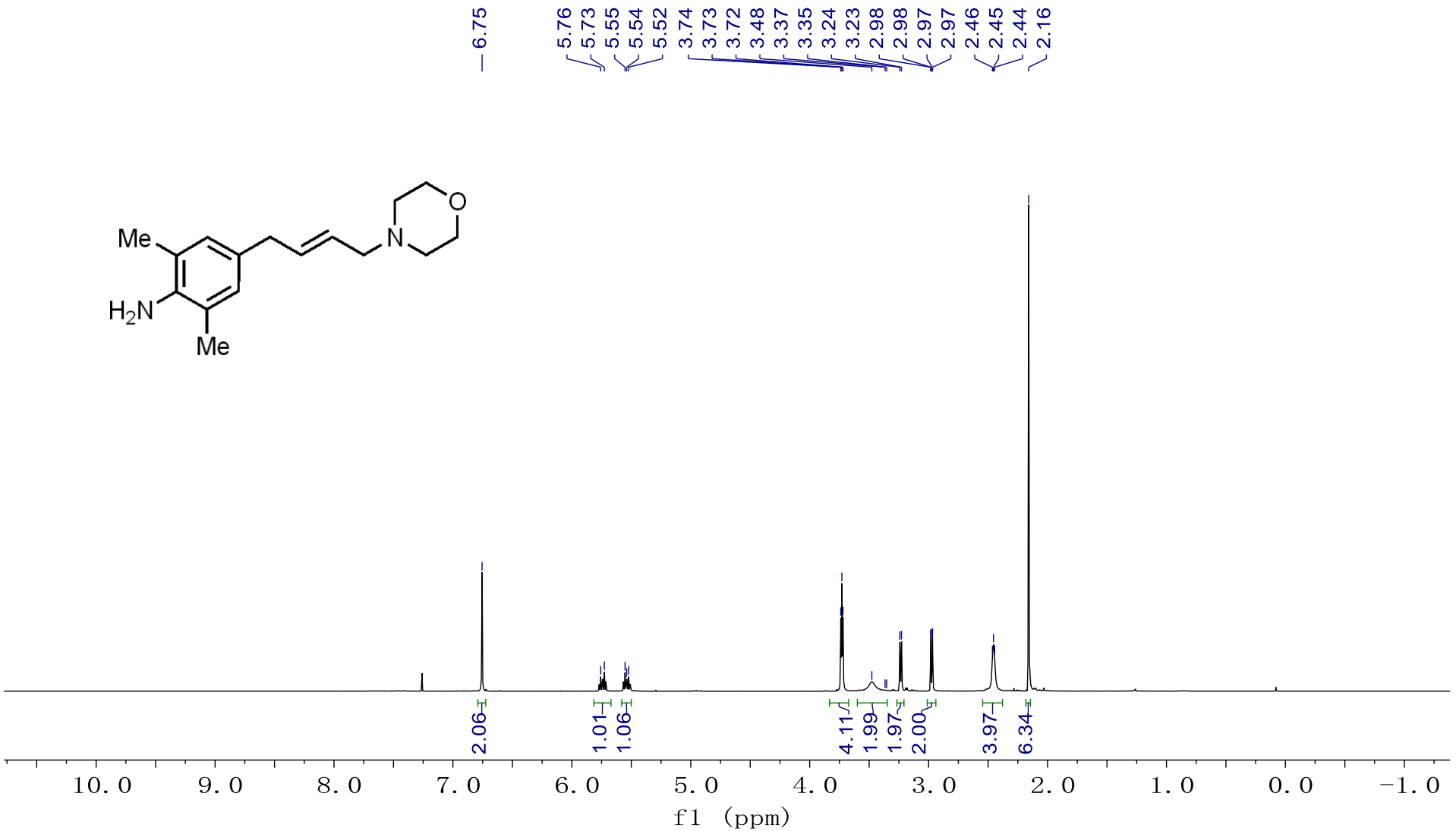
^{13}C NMR of allylamine 20

$CDCl_3$, 23 ºC



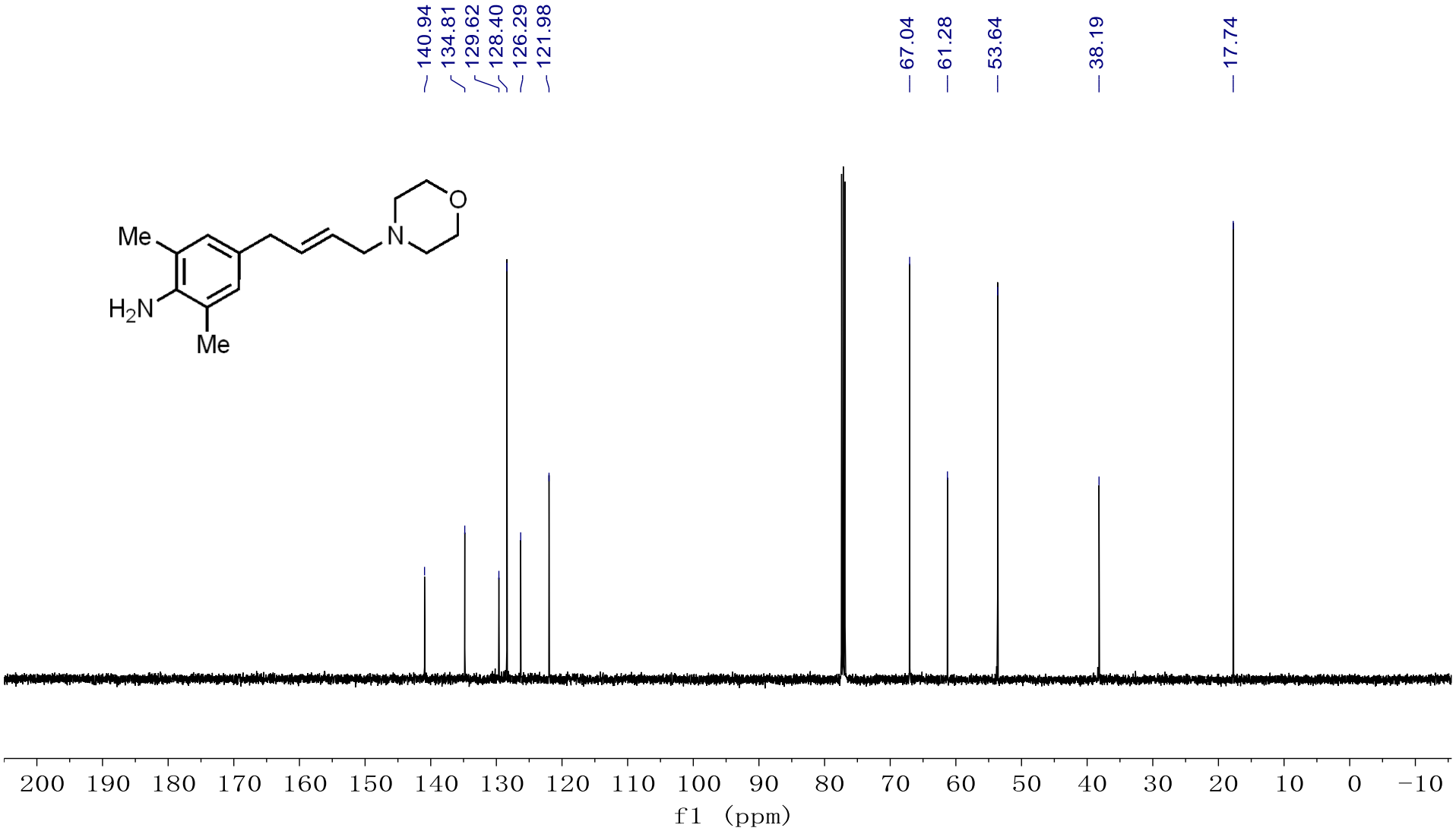
^{1}H NMR of allylamine 21

$CDCl_3$, 23 ºC



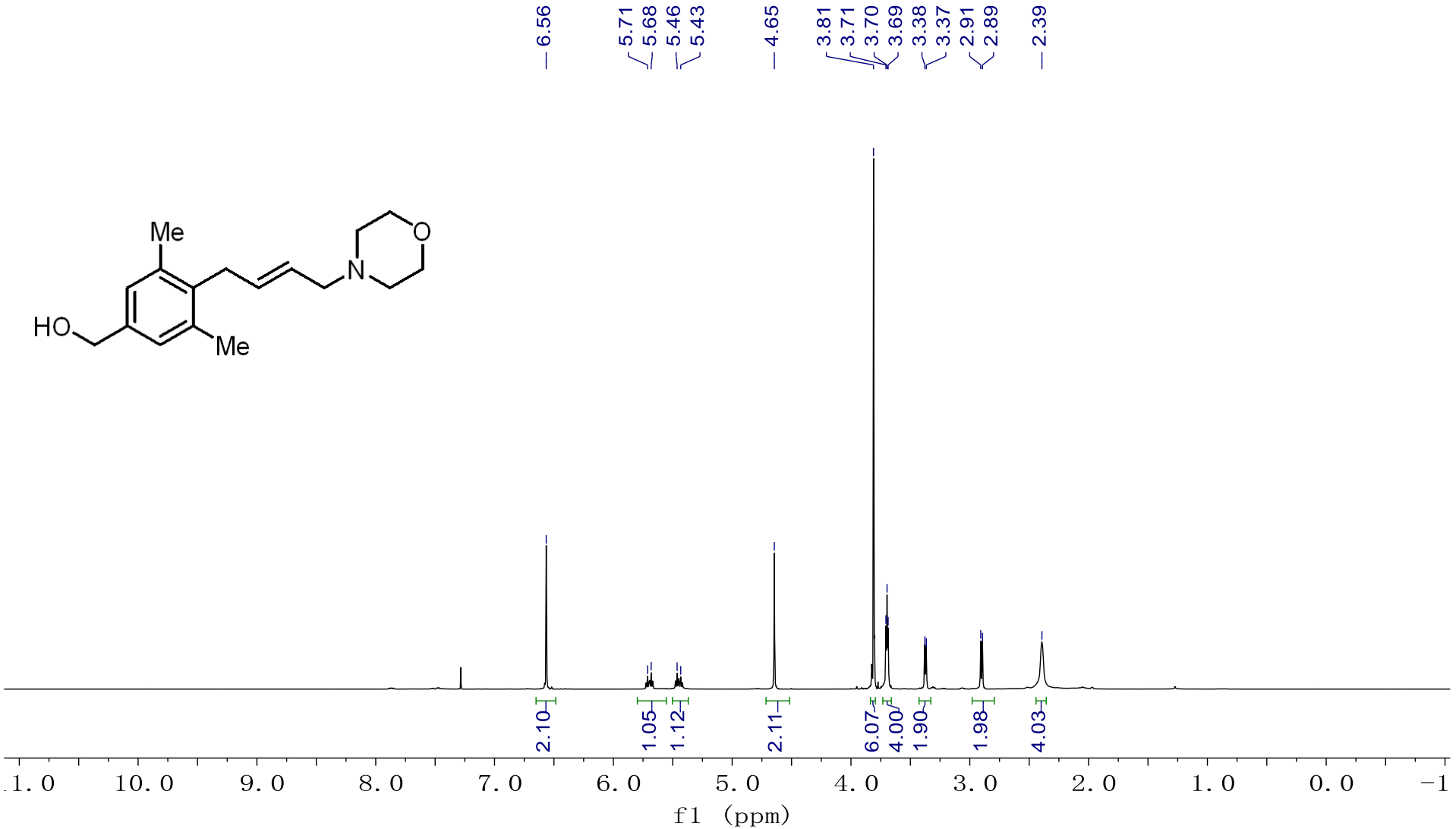
^{13}C NMR of allylamine 21

$CDCl_3$, 23 ºC



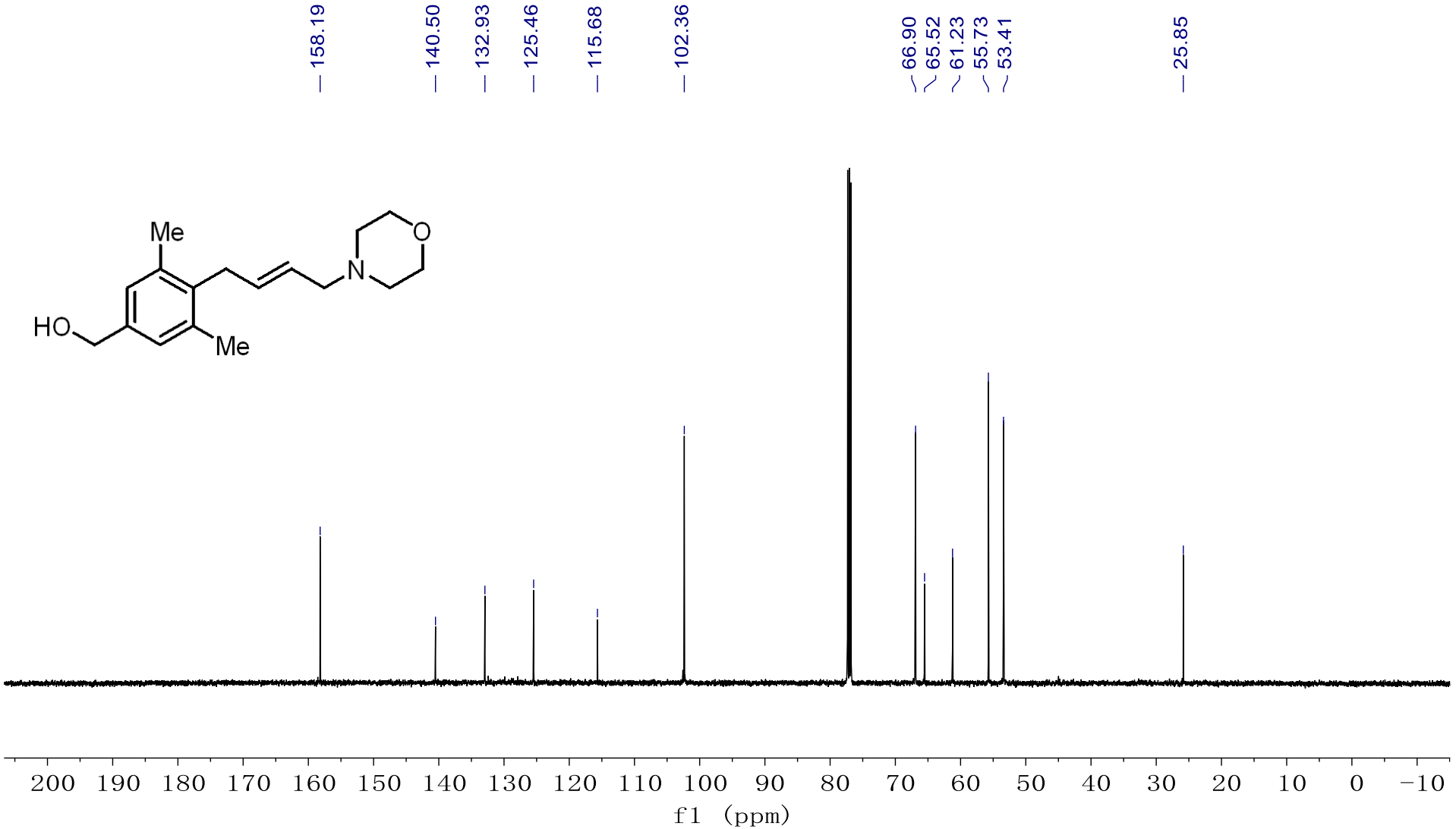
^{1}H NMR of allylamine 22

$CDCl_3$, 23 ºC



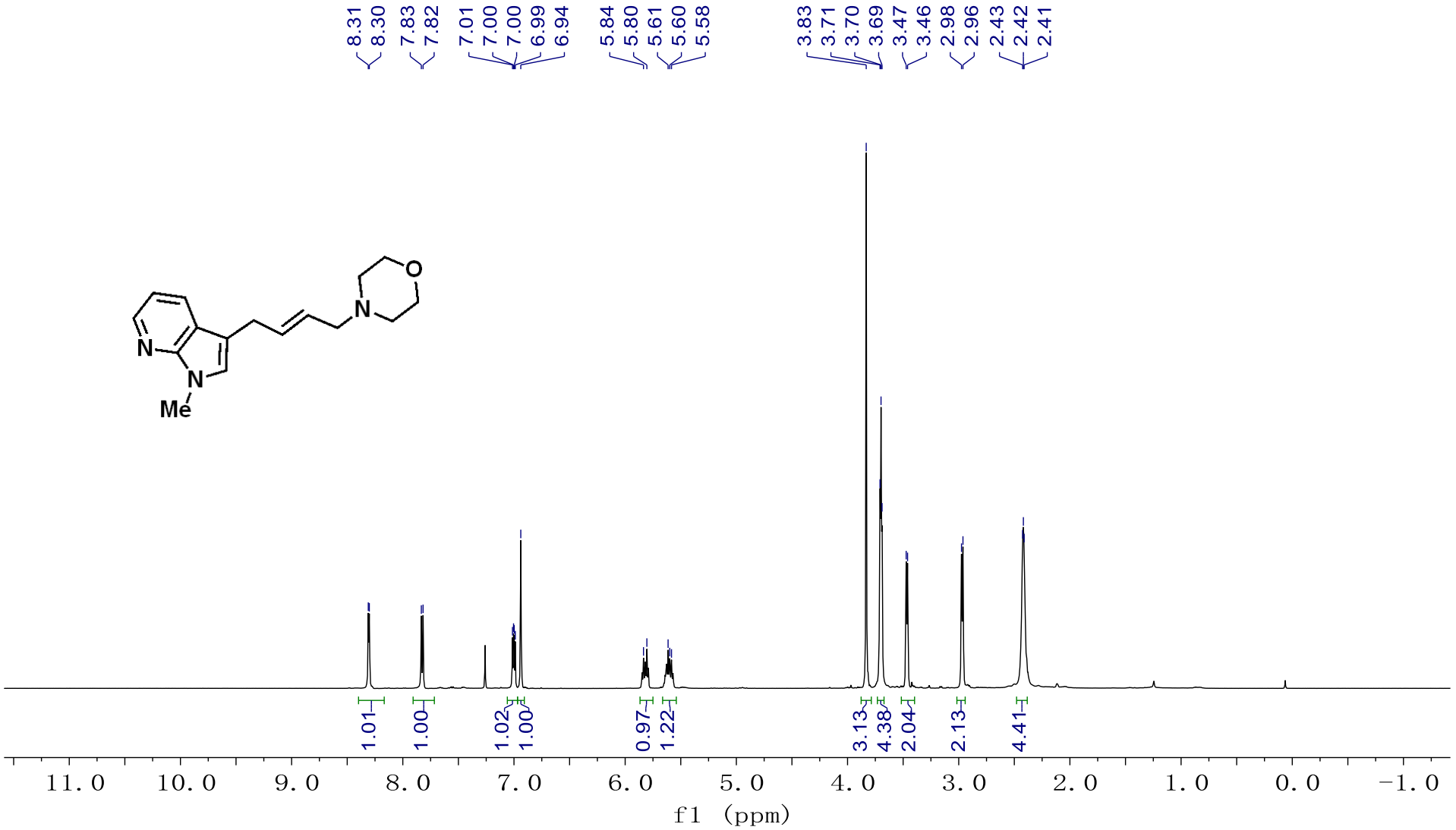
^{13}C NMR of allylamine 22

$CDCl_3$, 23 ºC



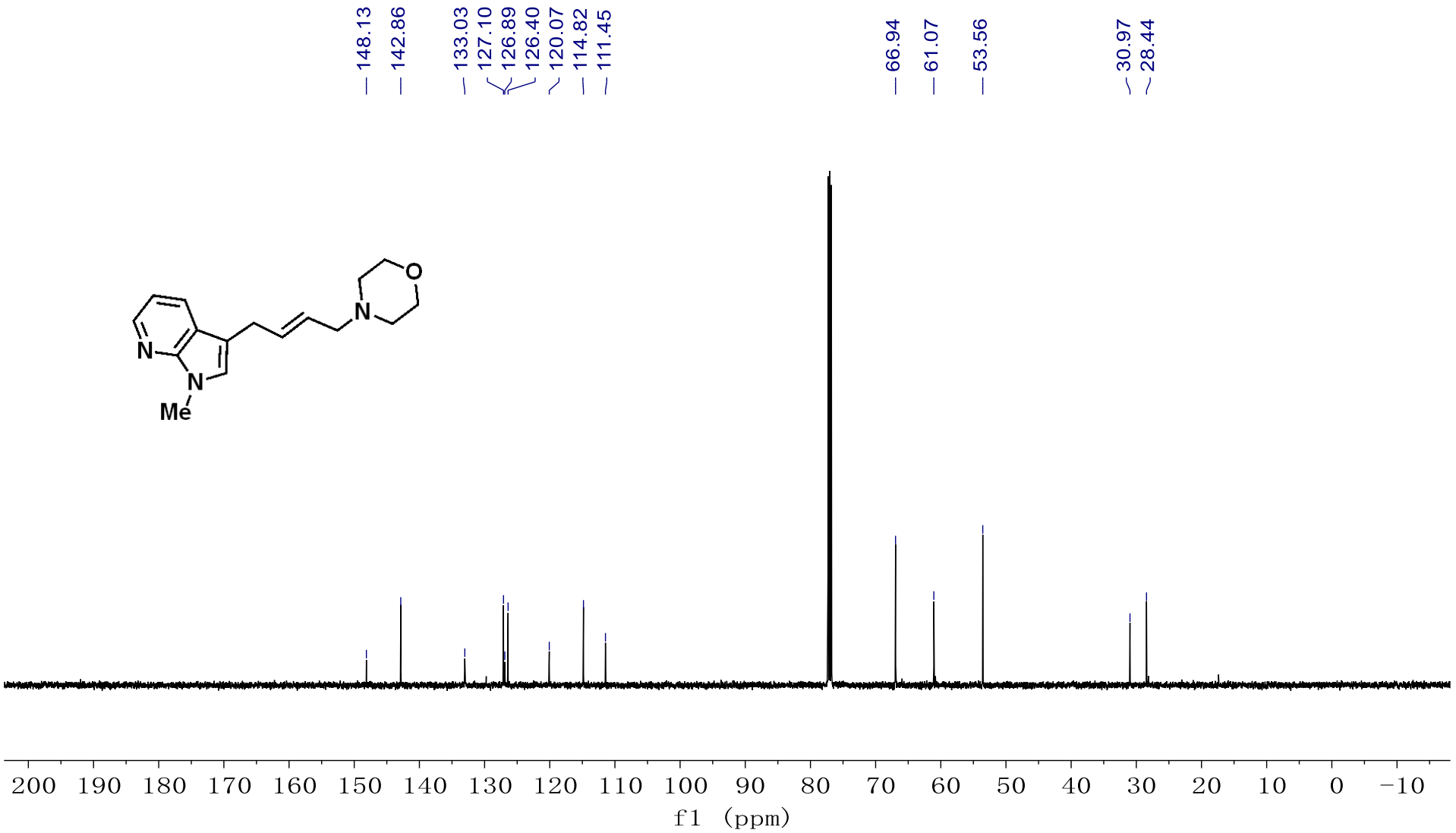
^{1}H NMR of allylamine 23

$CDCl_3$, 23 ºC



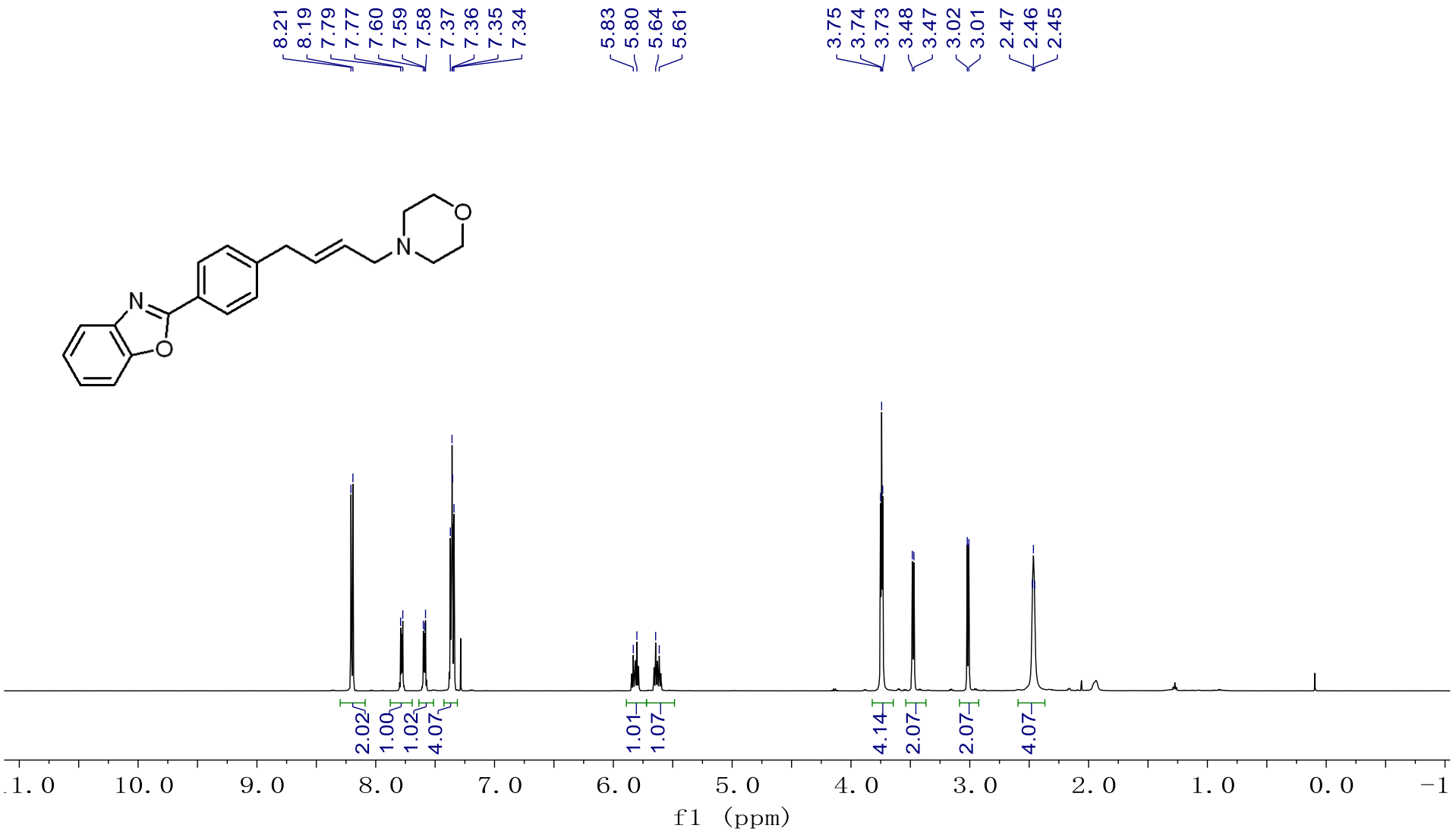
^{13}C NMR of allylamine 23

$CDCl_3$, 23 ºC



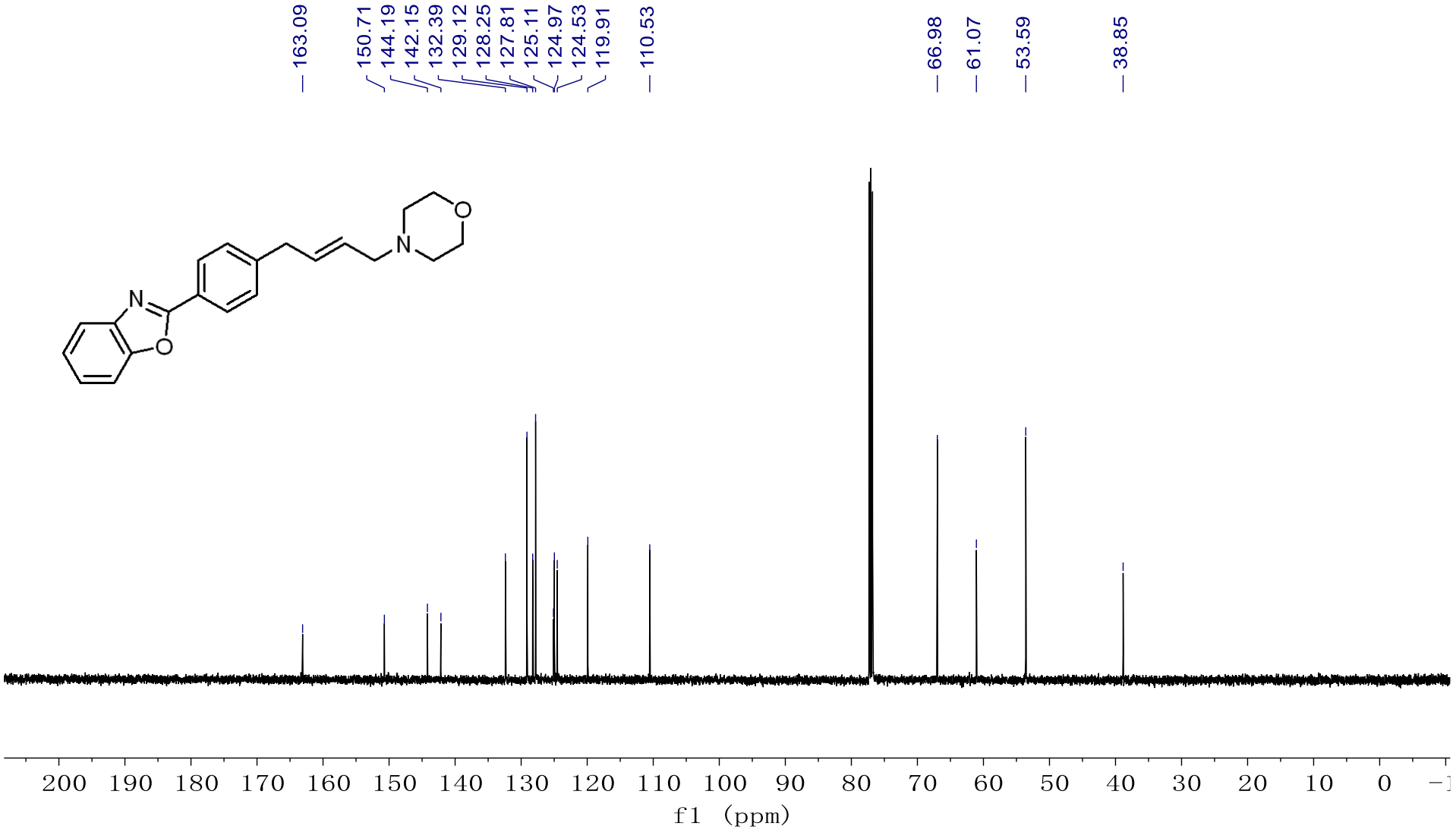
^{1}H NMR of allylamine 24

$CDCl_3$, 23 ºC



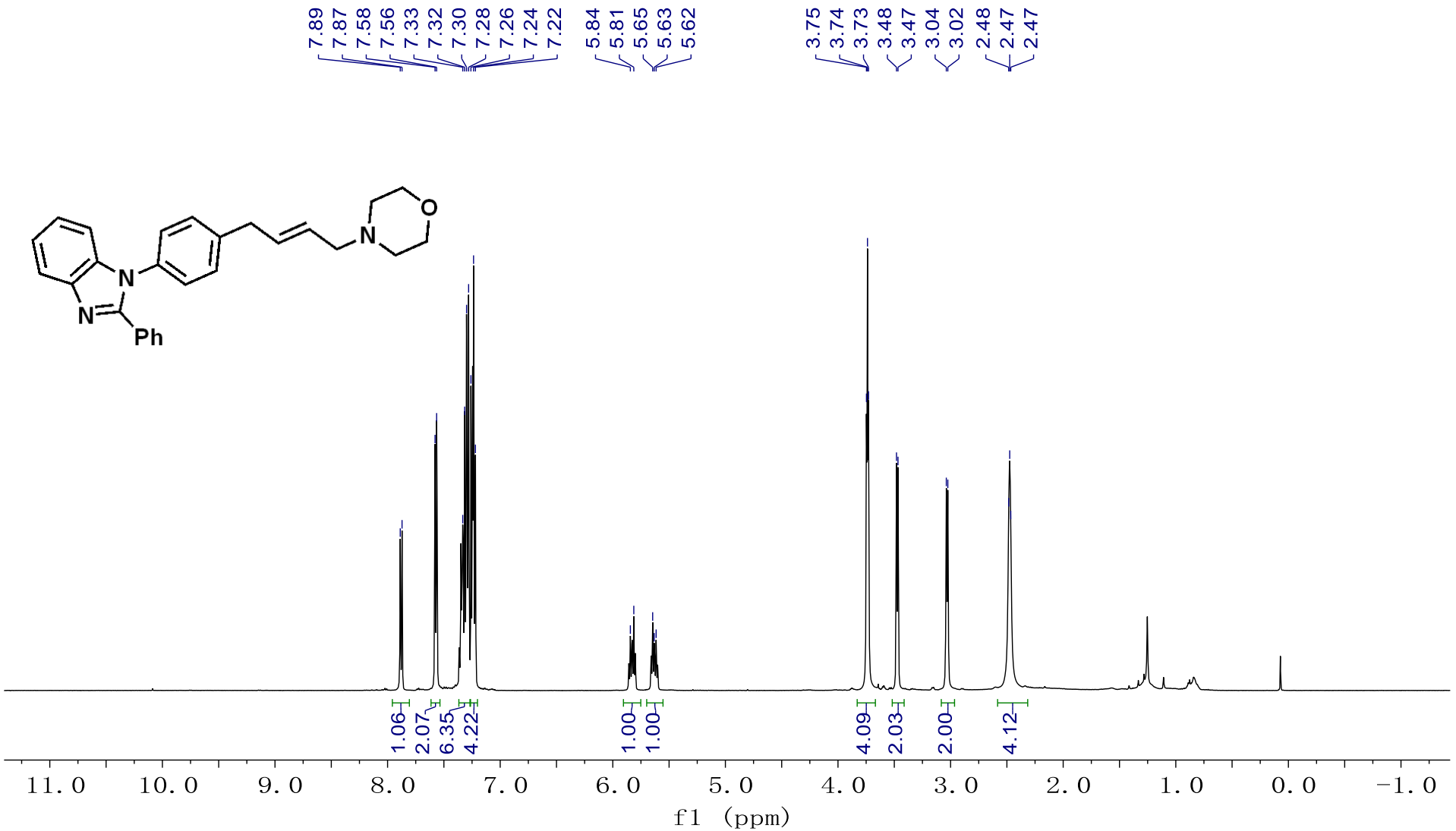
^{13}C NMR of allylamine 24

$CDCl_3$, 23 ºC



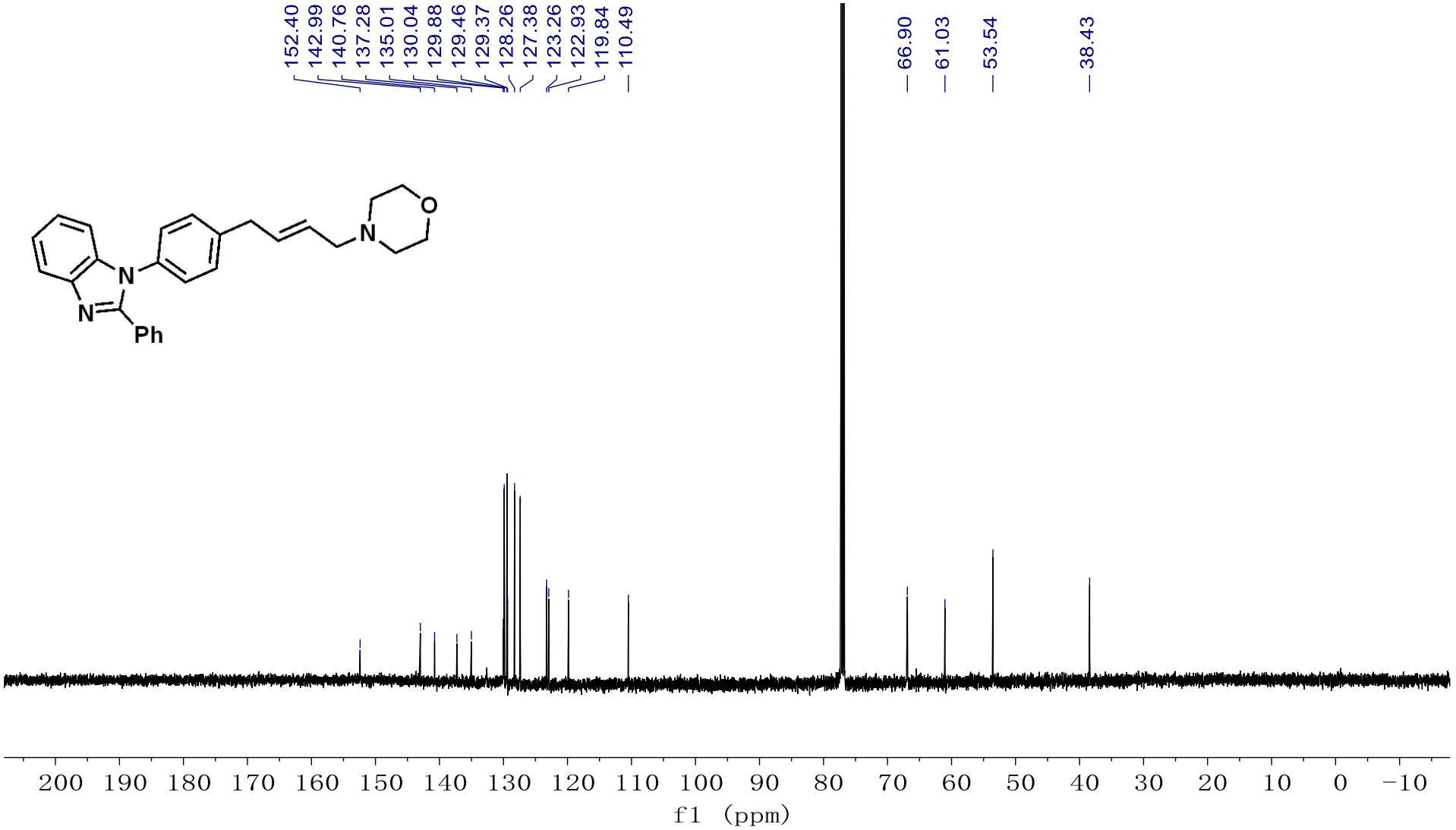
^{1}H NMR of allylamine 25

$CDCl_3$, 23 ºC



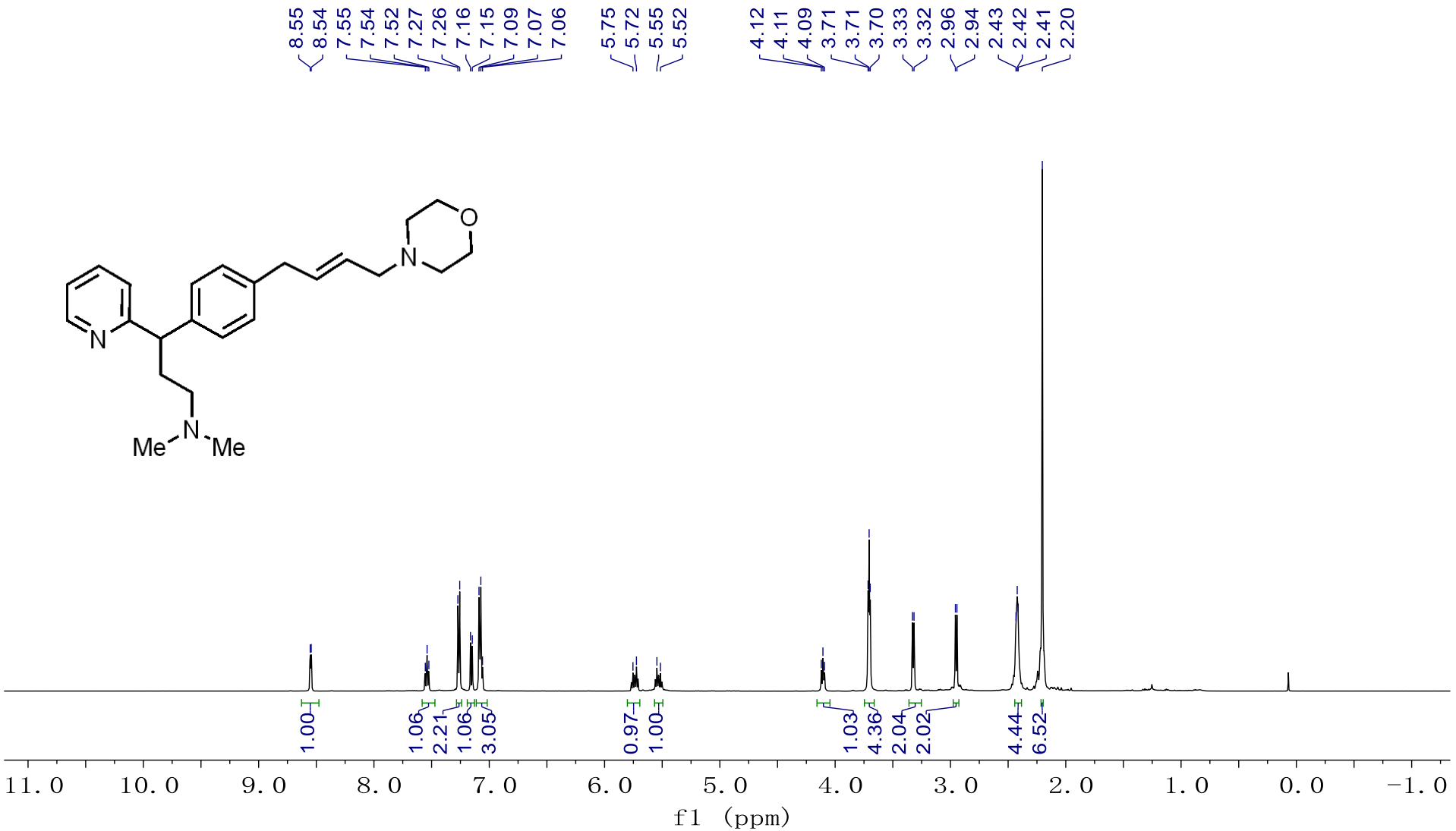
^{13}C NMR of allylamine 25

$CDCl_3$, 23 ºC



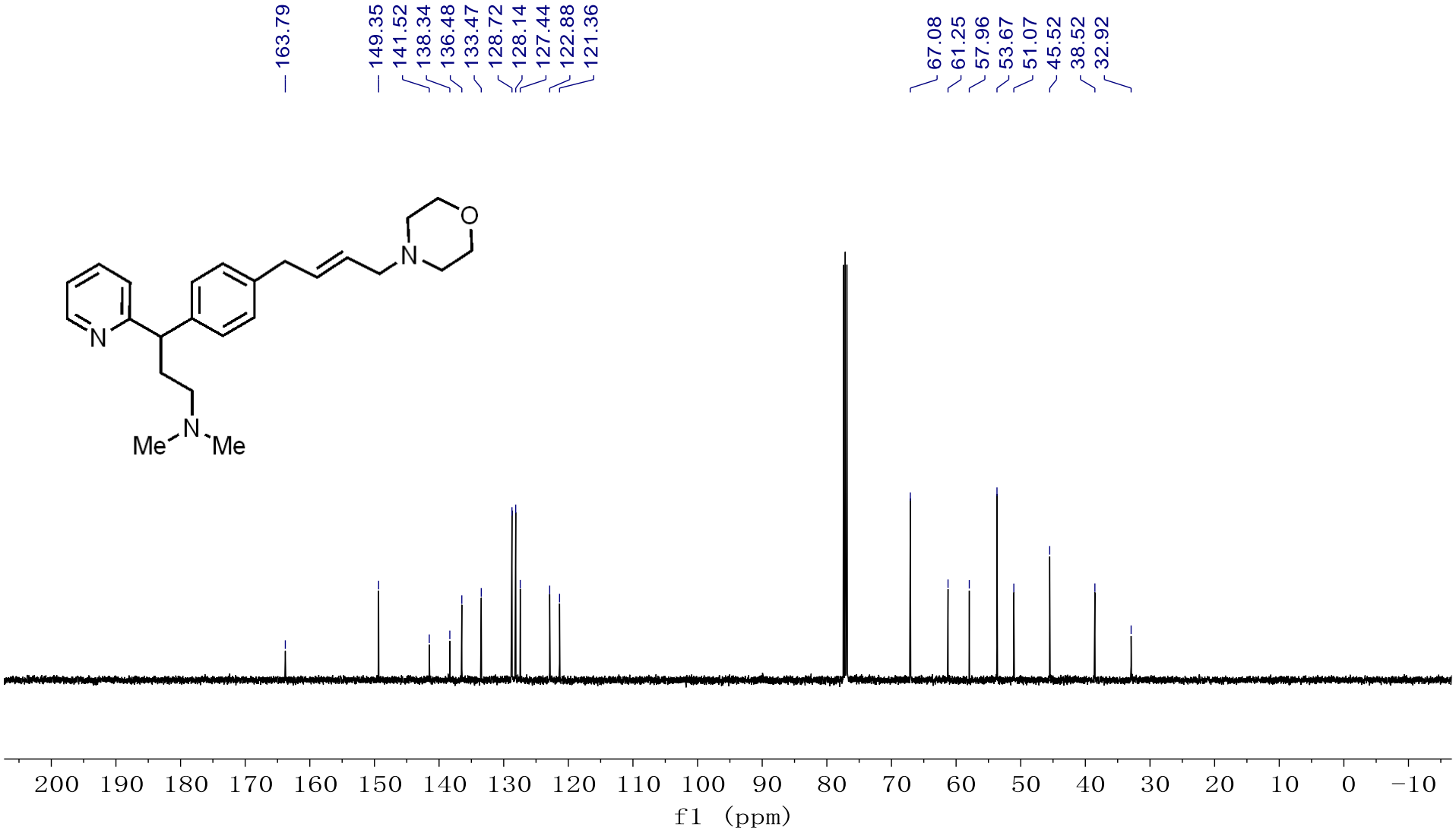
^{1}H NMR of brompheniramine-derived allylamine 26

$CDCl_3$, 23 ºC



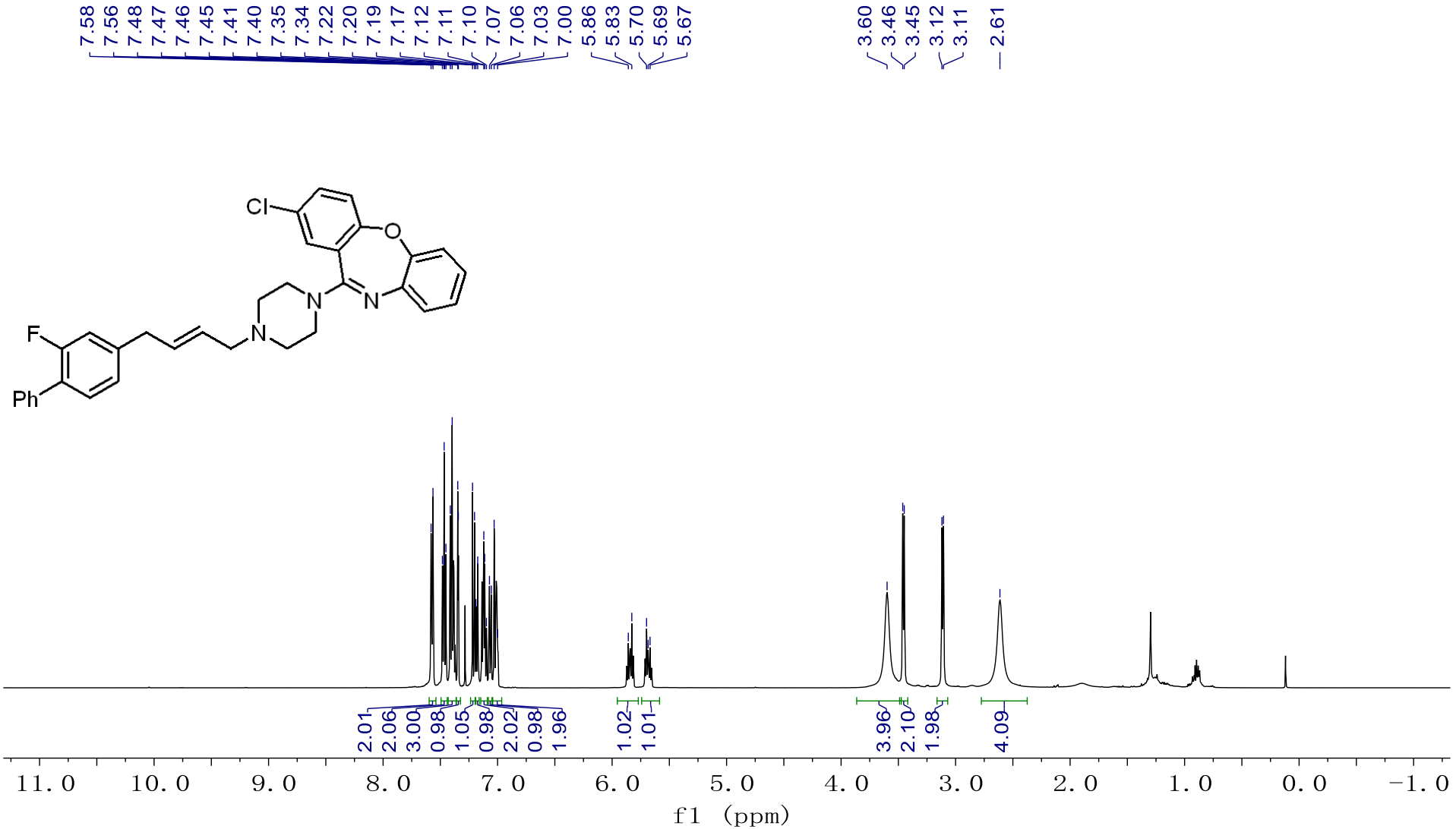
^{13}C NMR of brompheniramine-derived allylamine 26

$CDCl_3$, 23 ºC



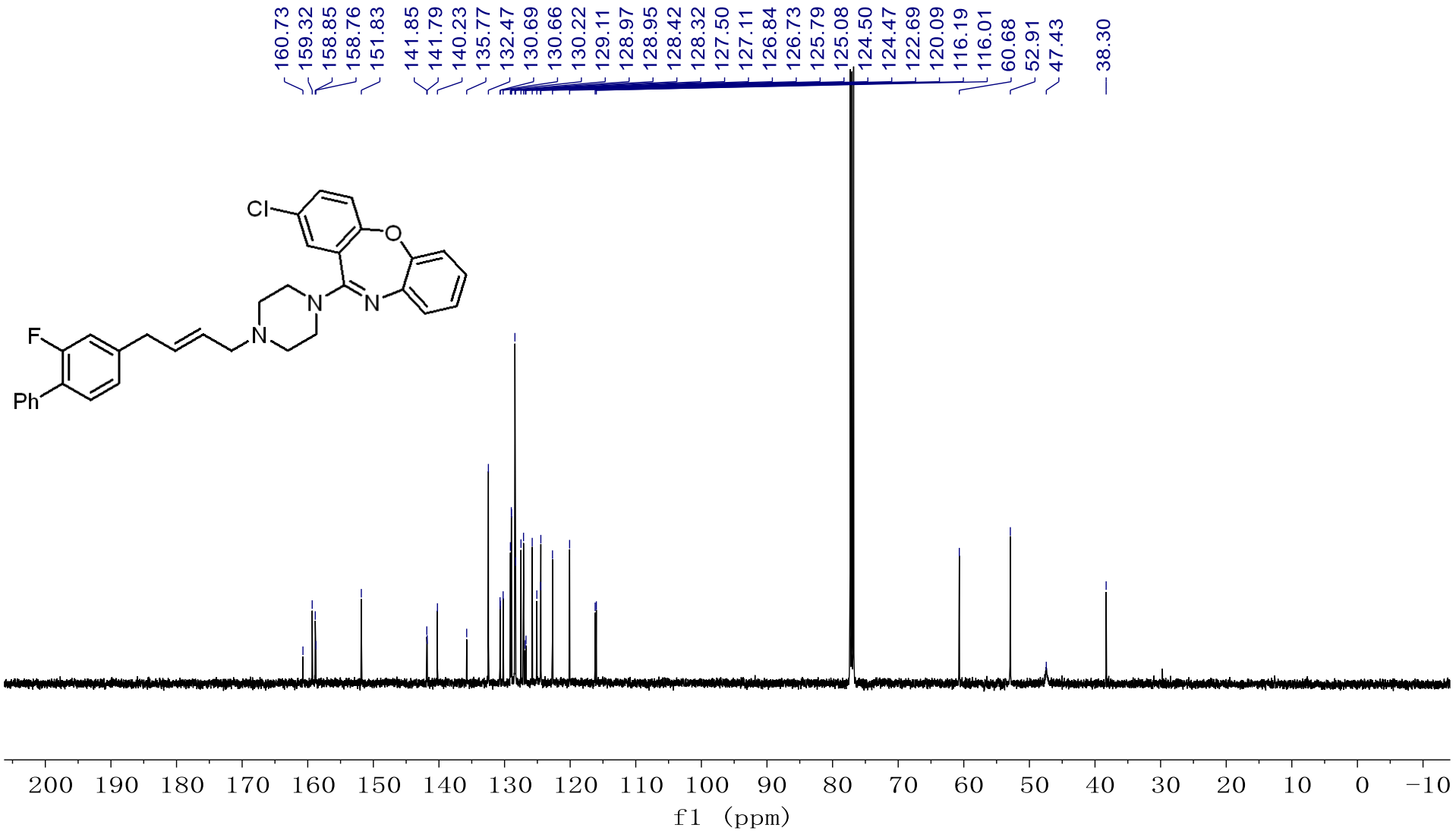
^{1}H NMR of amoxapine-derived allylamine 34

$CDCl_3$, 23 ºC



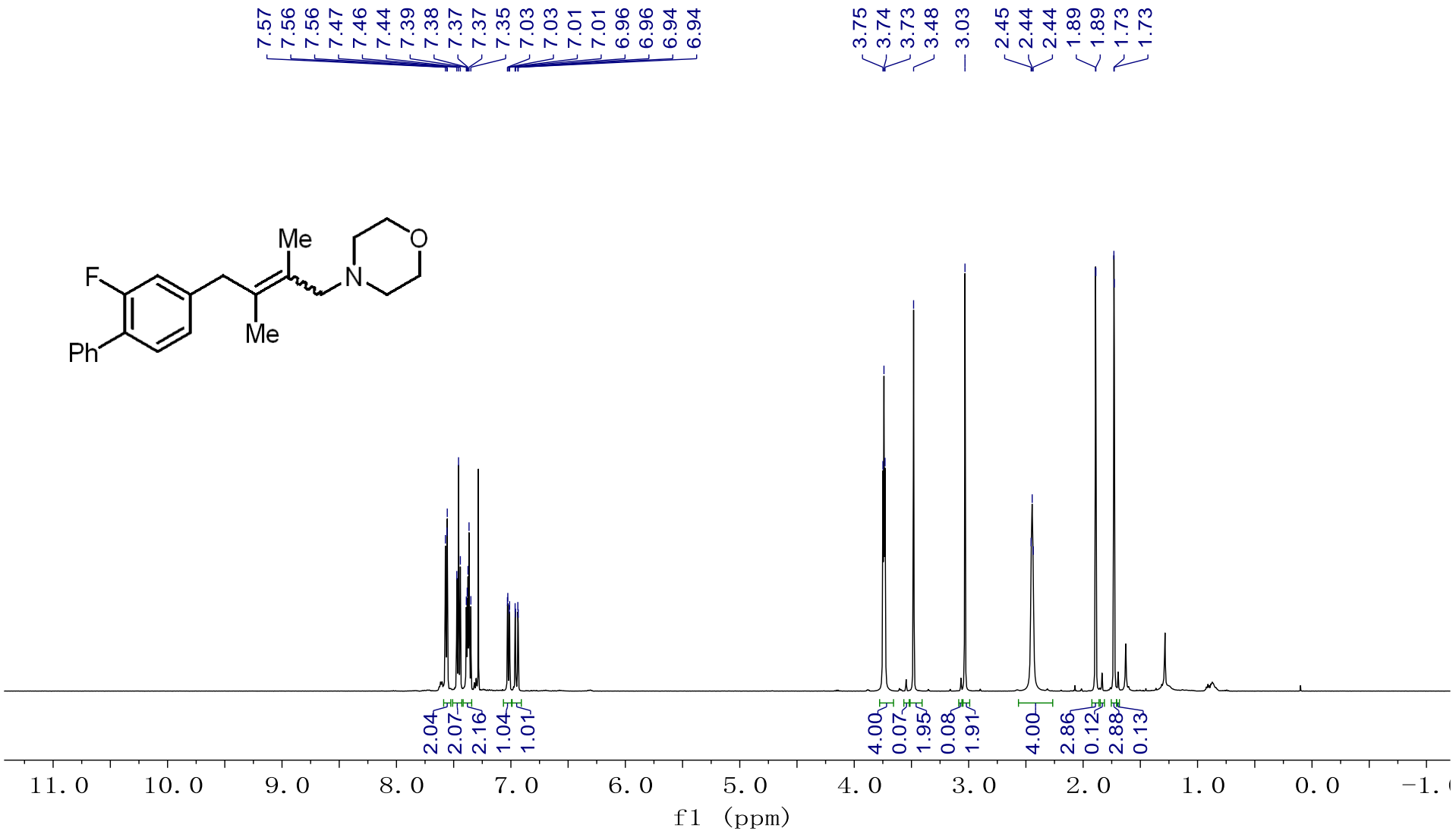
^{13}C NMR of amoxapine-derived allylamine 34

$CDCl_3$, 23 ºC



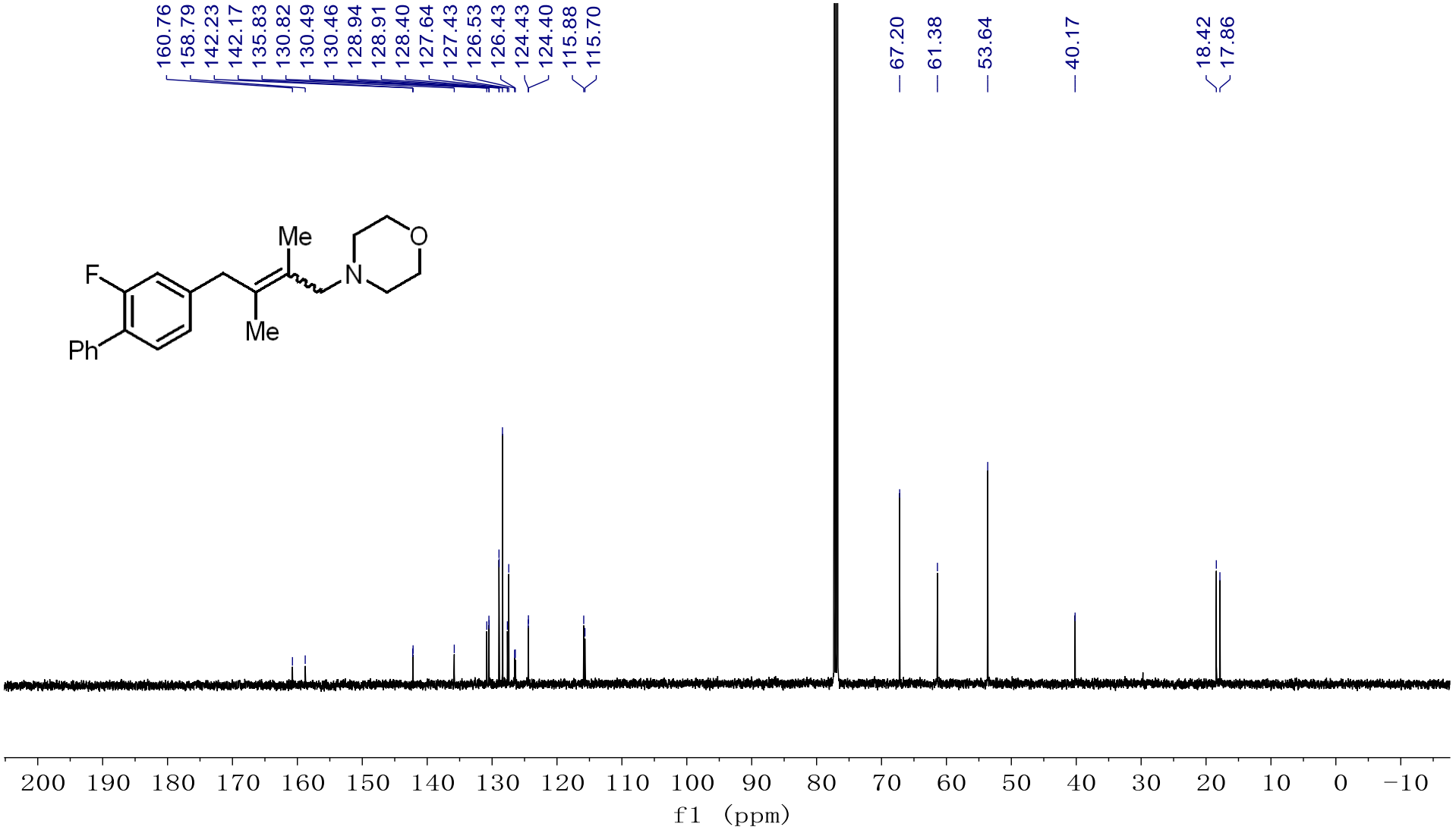
^{1}H NMR of allylamine 48

$CDCl_3$, 23 ºC



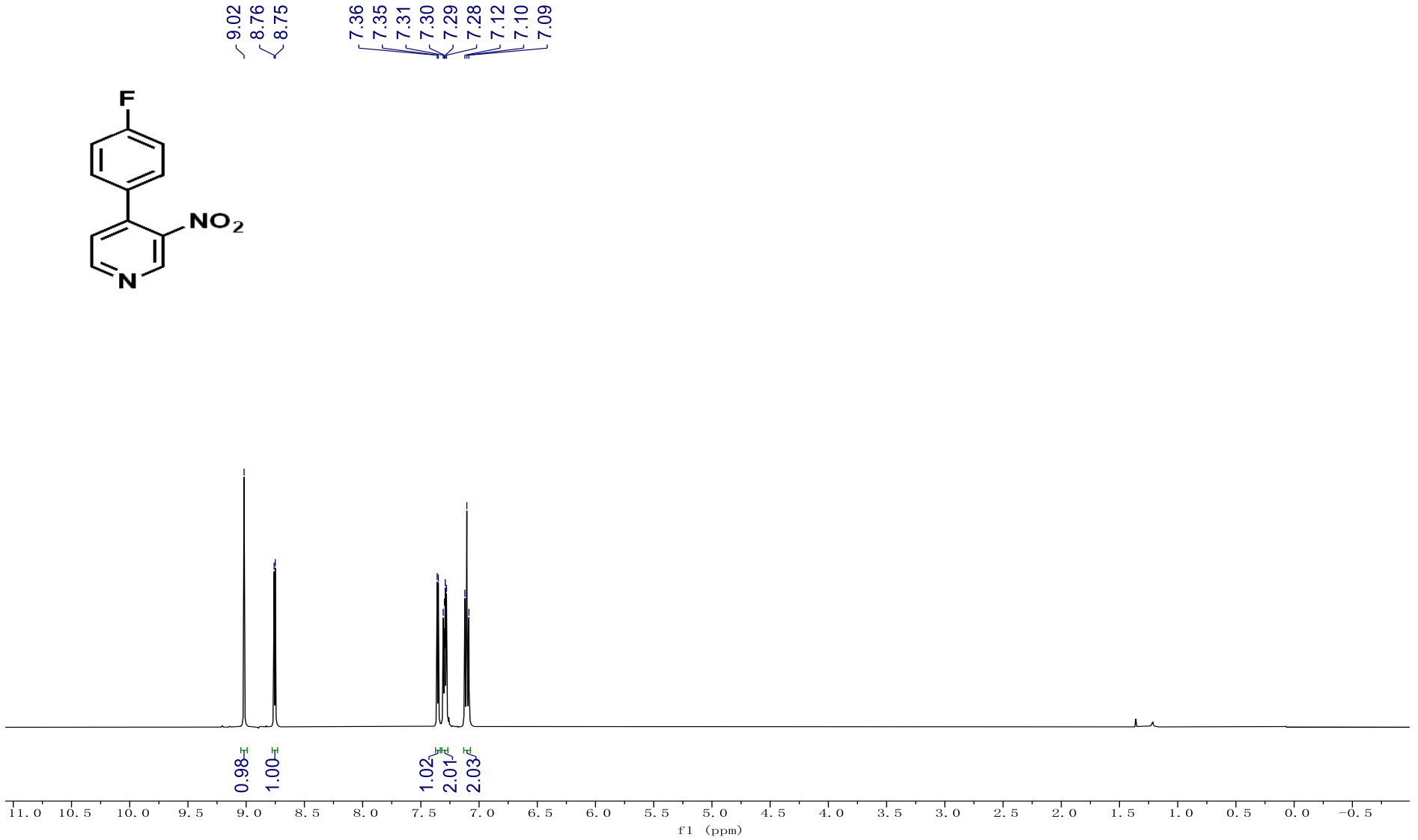
^{13}C NMR of allylamine 48

$CDCl_3$, 23 ºC



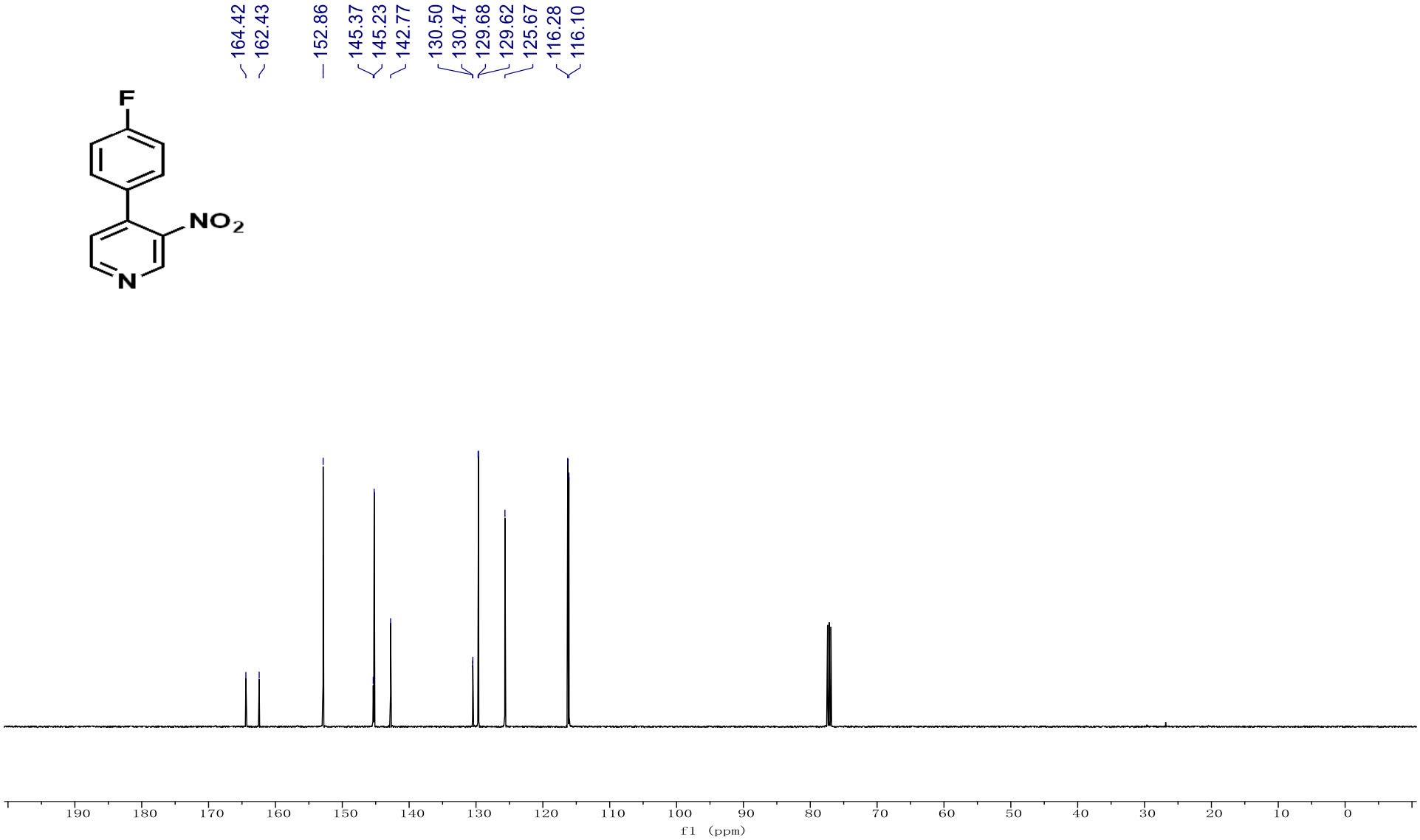
^{1}H NMR of 4-(4-fluorophenyl)-3-nitropyridine, S55

$CDCl_3$, 23 °C



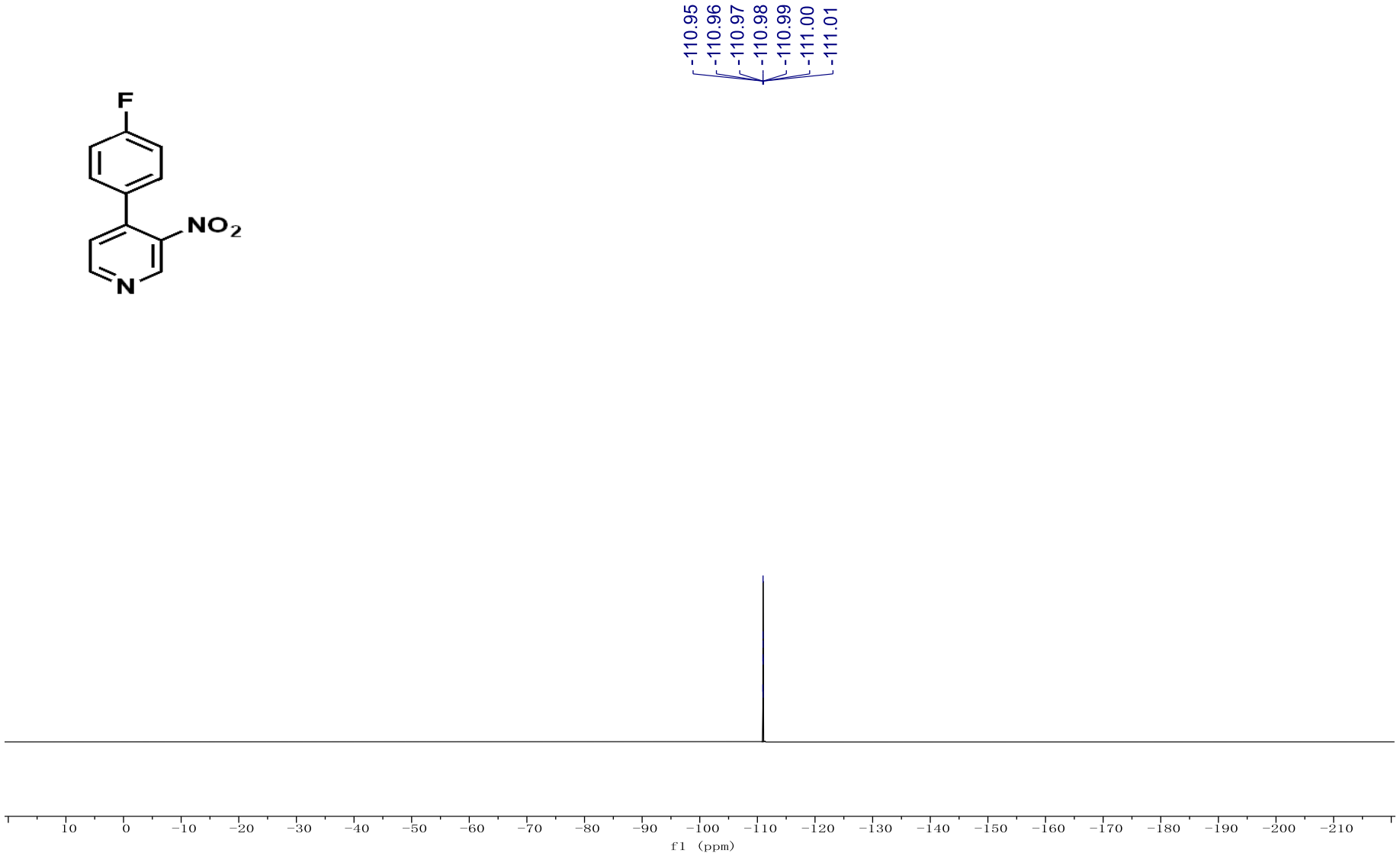
^{13}C NMR of 4-(4-fluorophenyl)-3-nitropyridine, S55

$CDCl_3$, 23 °C



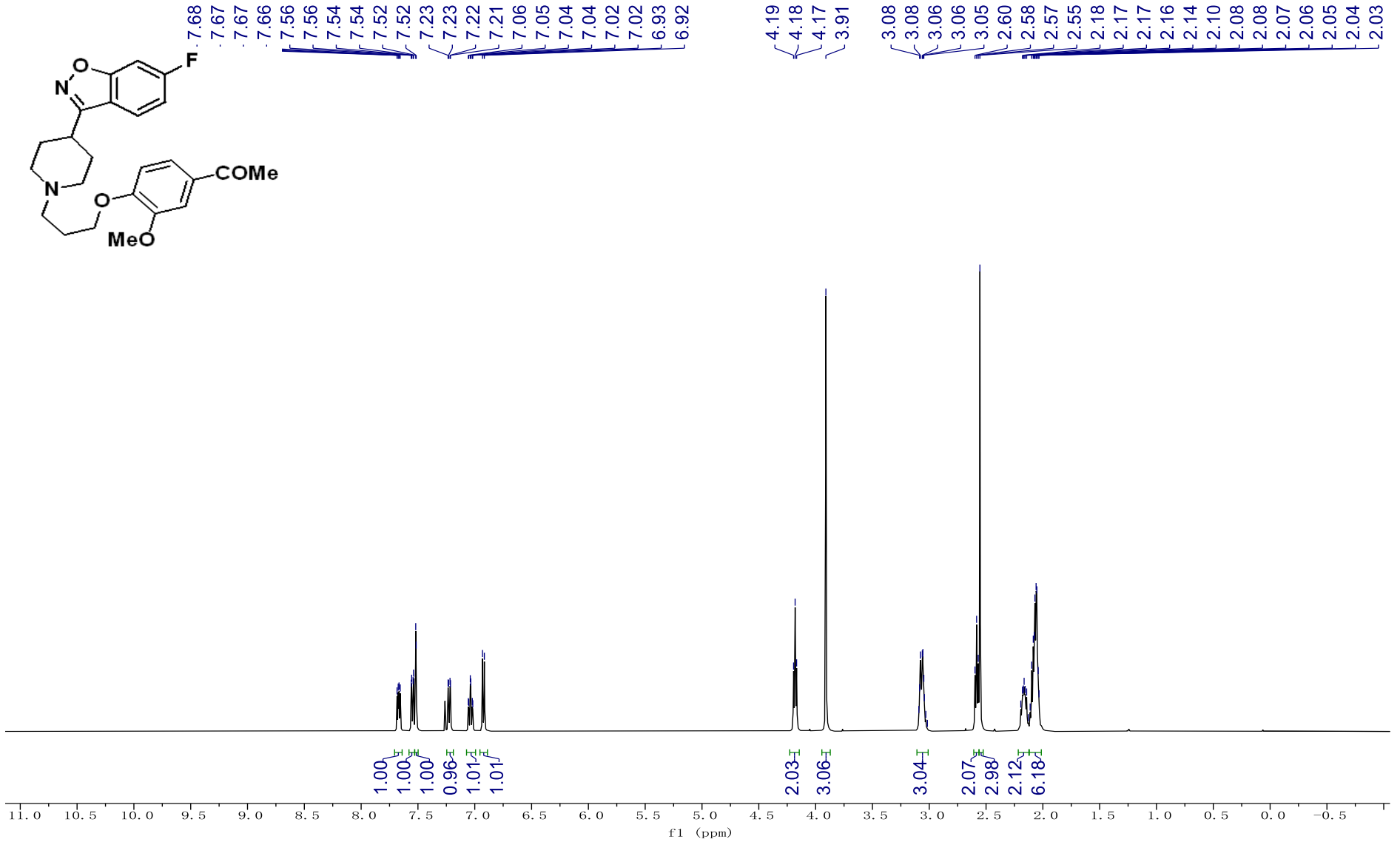
^{19}F NMR of 4-(4-fluorophenyl)-3-nitropyridine, S55

$CDCl_3$, 23 °C



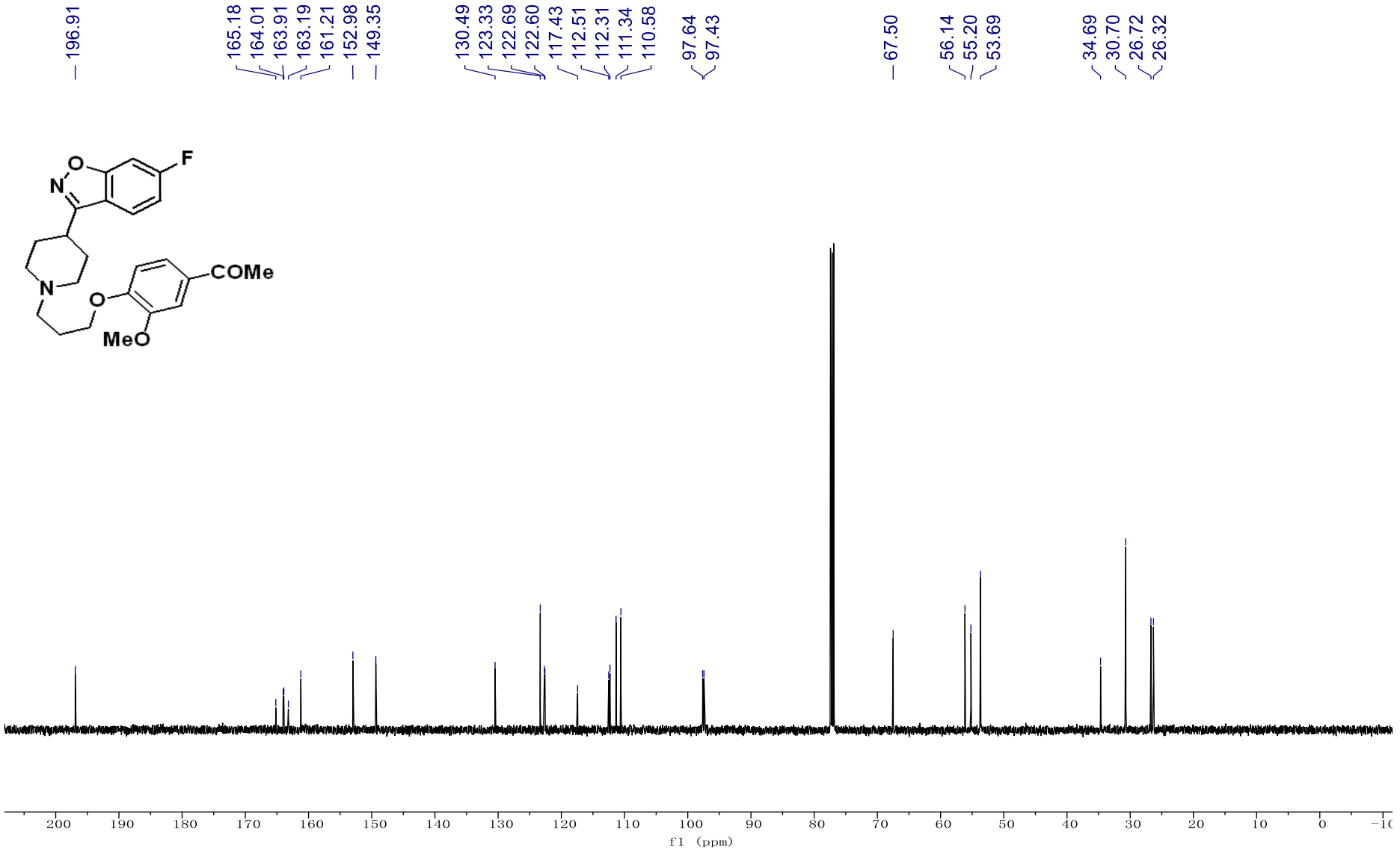
^{1}H NMR of Iloperidone, S59

$CDCl_3$, 23 °C



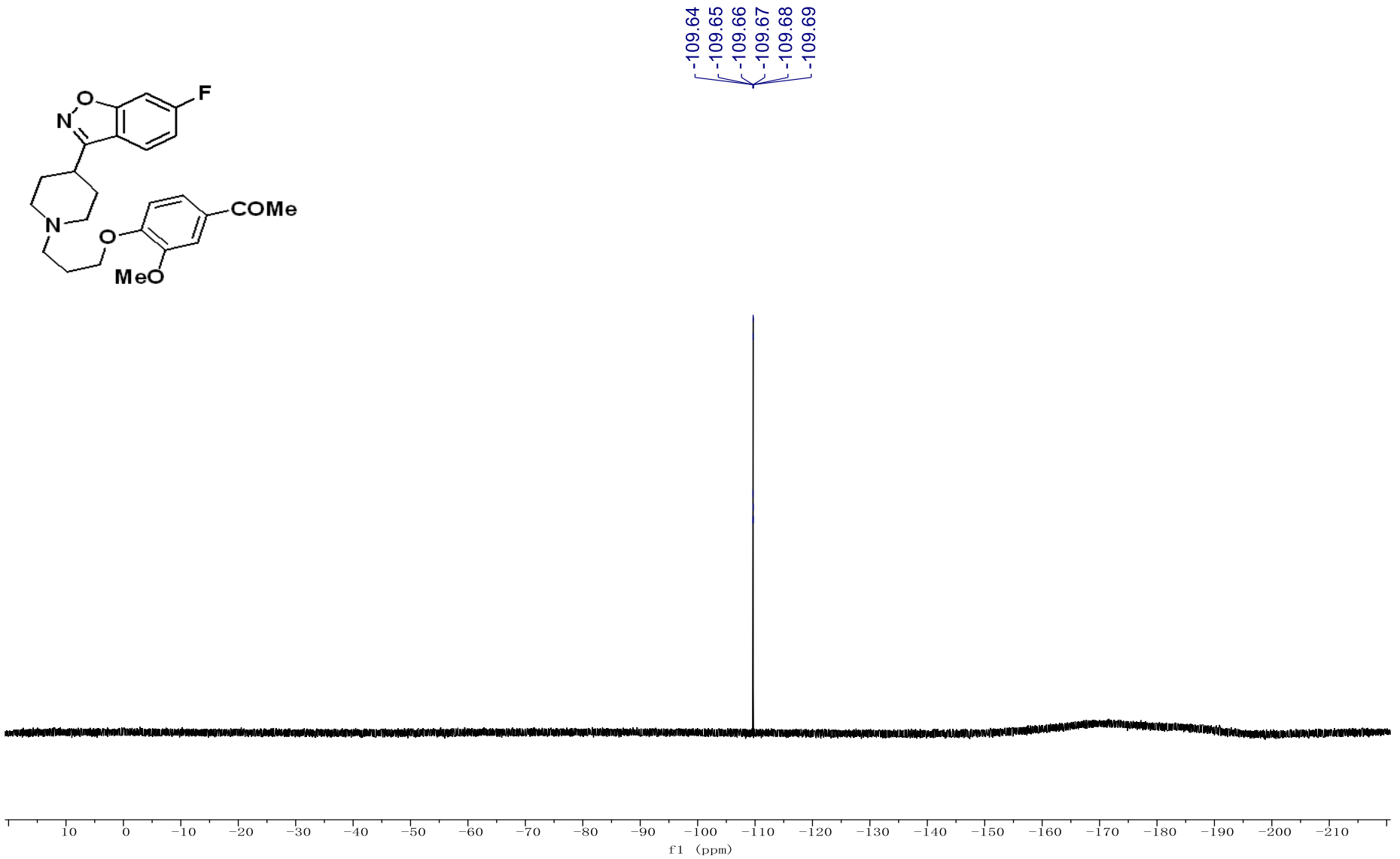
^{13}C NMR of Iloperidone, S59

$CDCl_3$, 23 °C



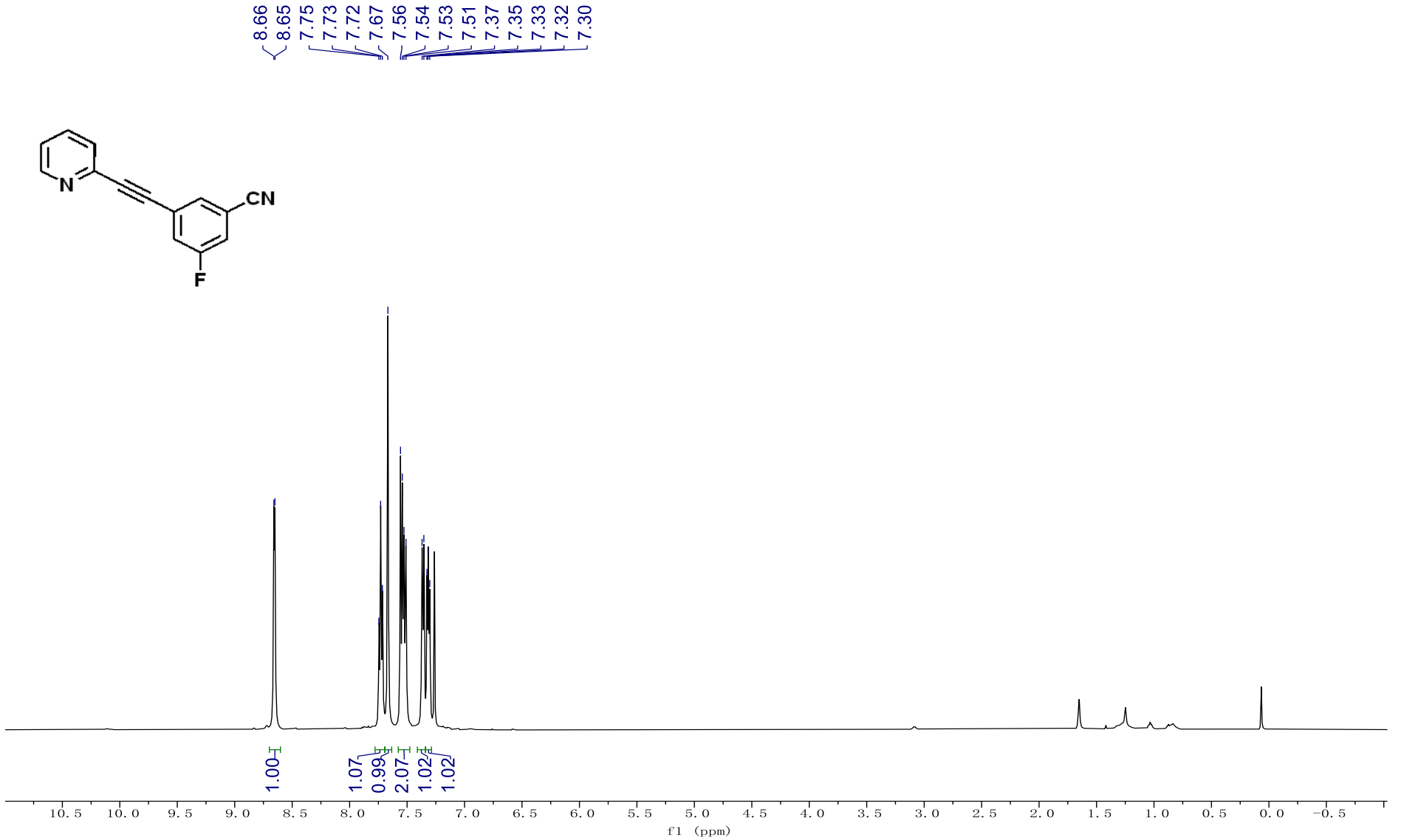
^{19}F NMR of Iloperidone, S59

$CDCl_3$, 23 °C



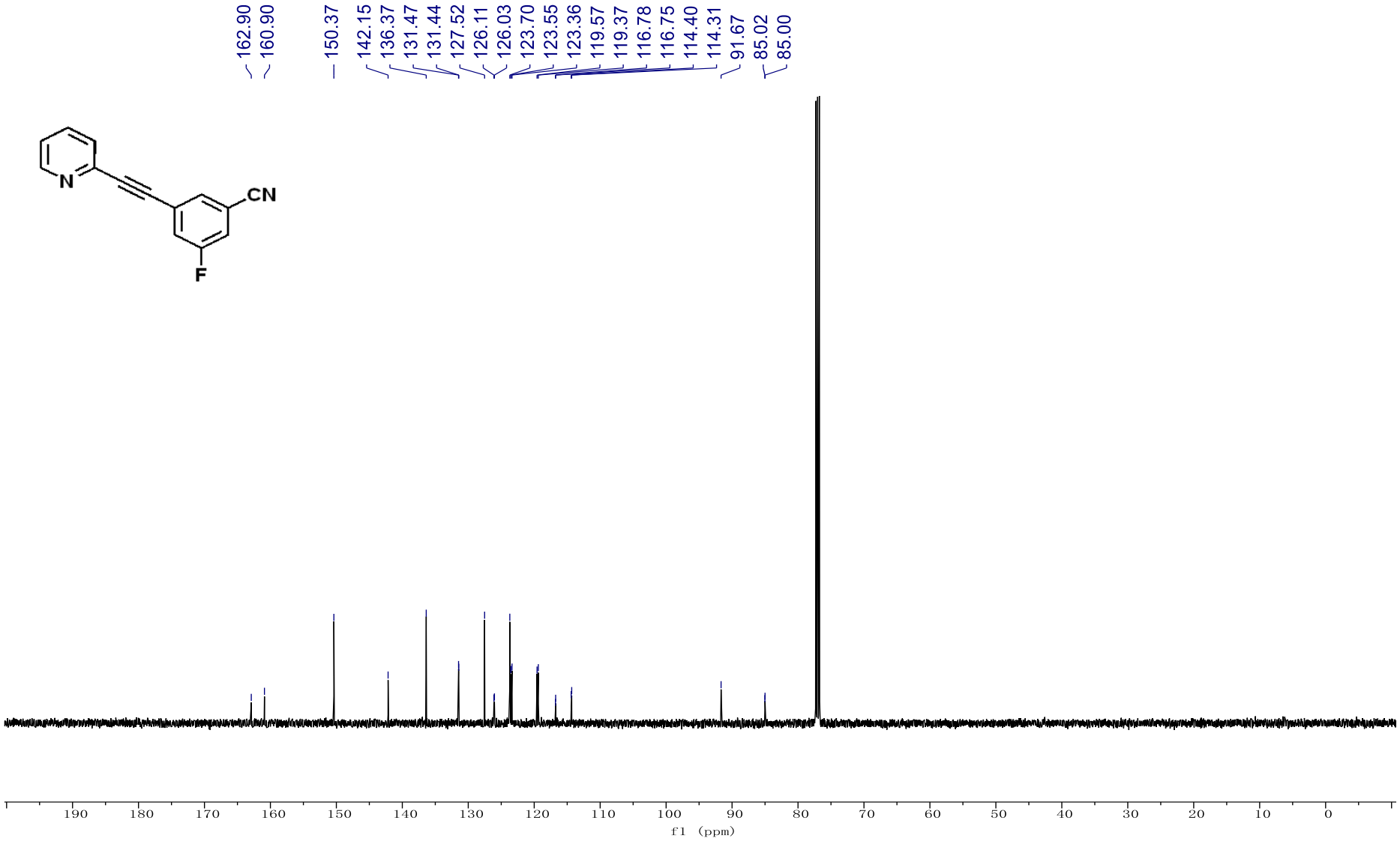
^{1}H NMR of 3-Fluoro-5-[(pyridin-3-yl)ethynyl]benzonitrile (FPEB) S58

$CDCl_3$, 23 °C



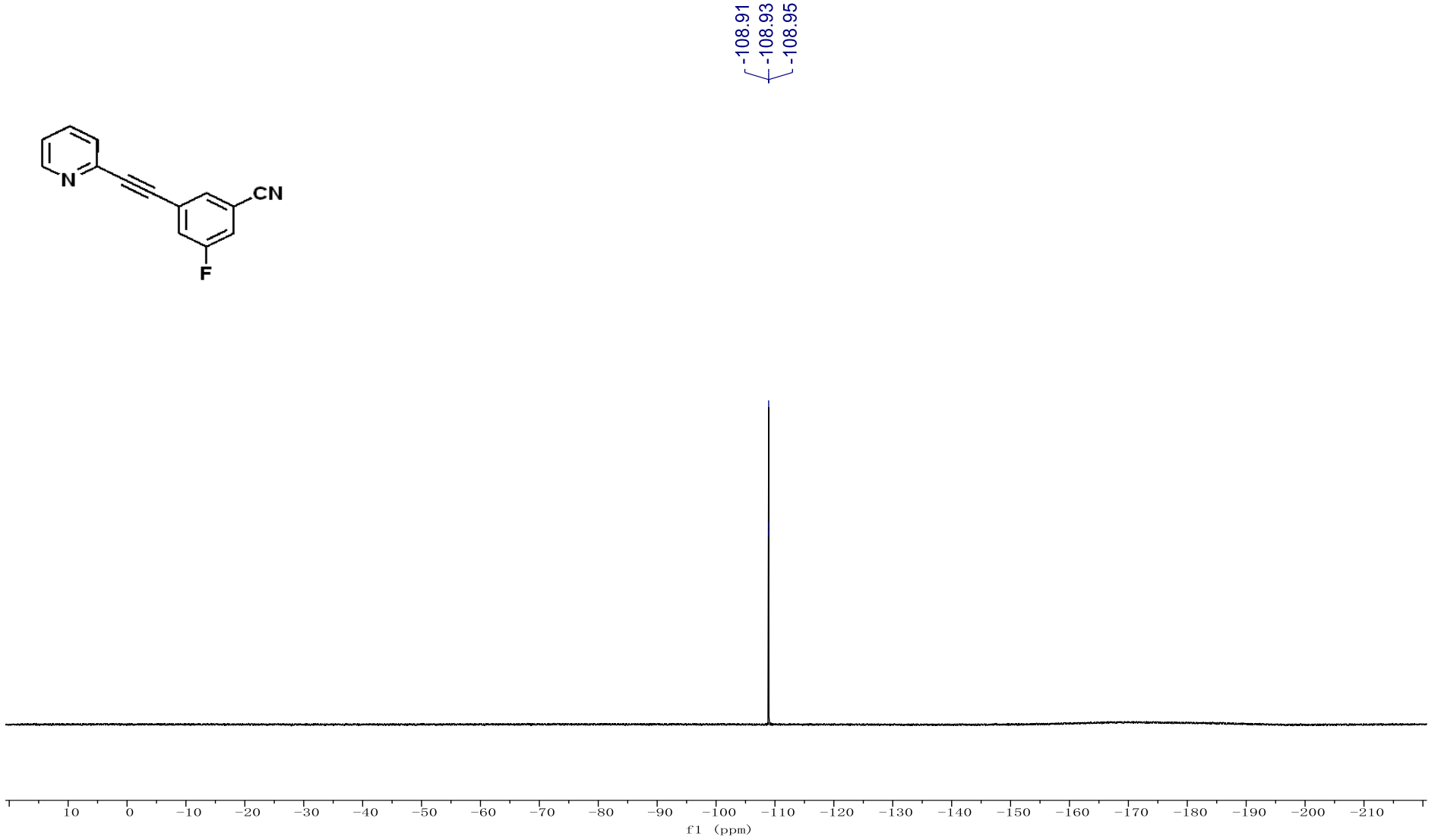
^{13}C NMR of 3-Fluoro-5-[(pyridin-3-yl)ethynyl]benzonitrile (FPEB) S58

$CDCl_3$, 23 °C



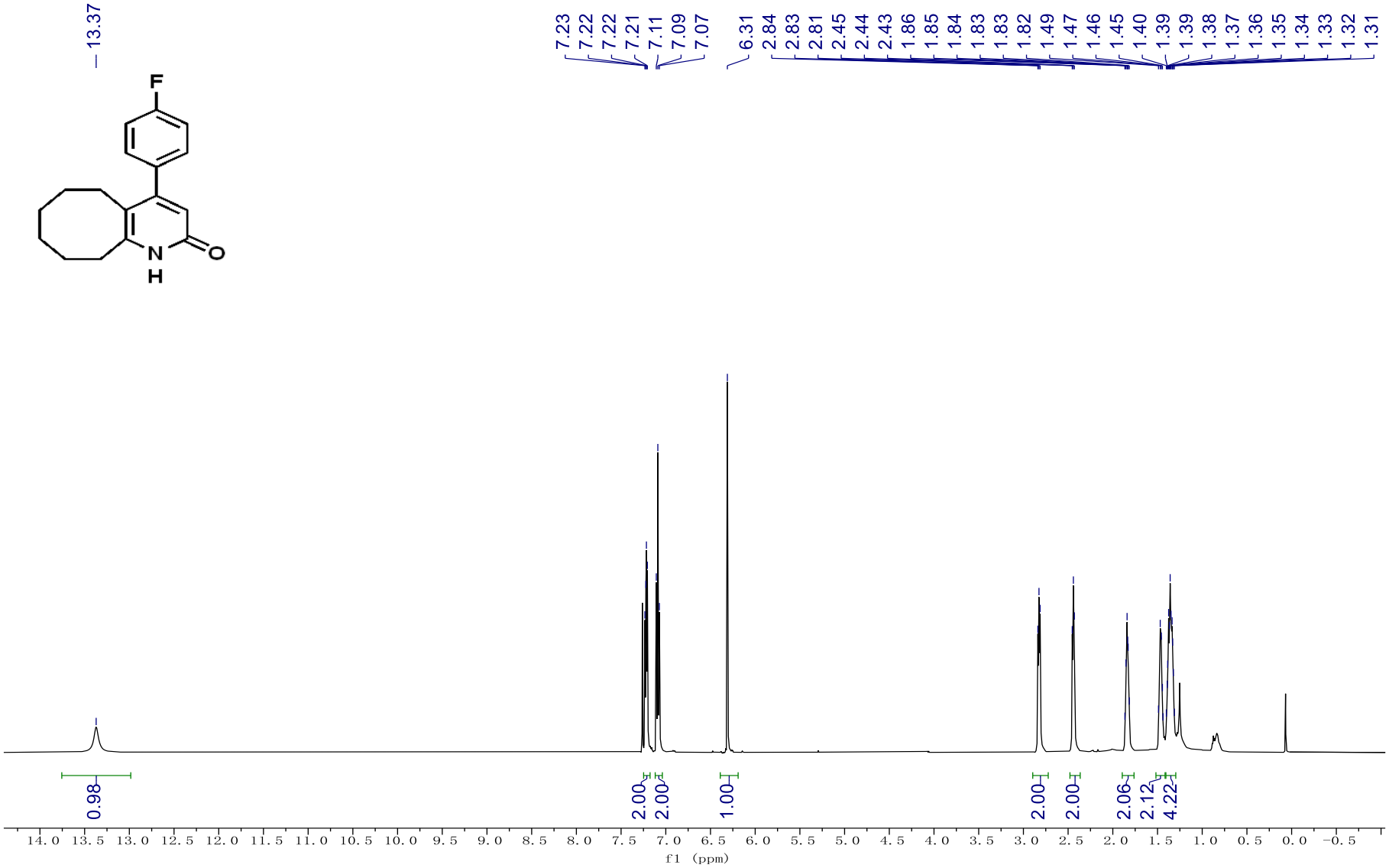
^{19}F NMR of 3-Fluoro-5-[(pyridin-3-yl)ethynyl]benzonitrile (FPEB) S58

$CDCl_3$, 23 °C



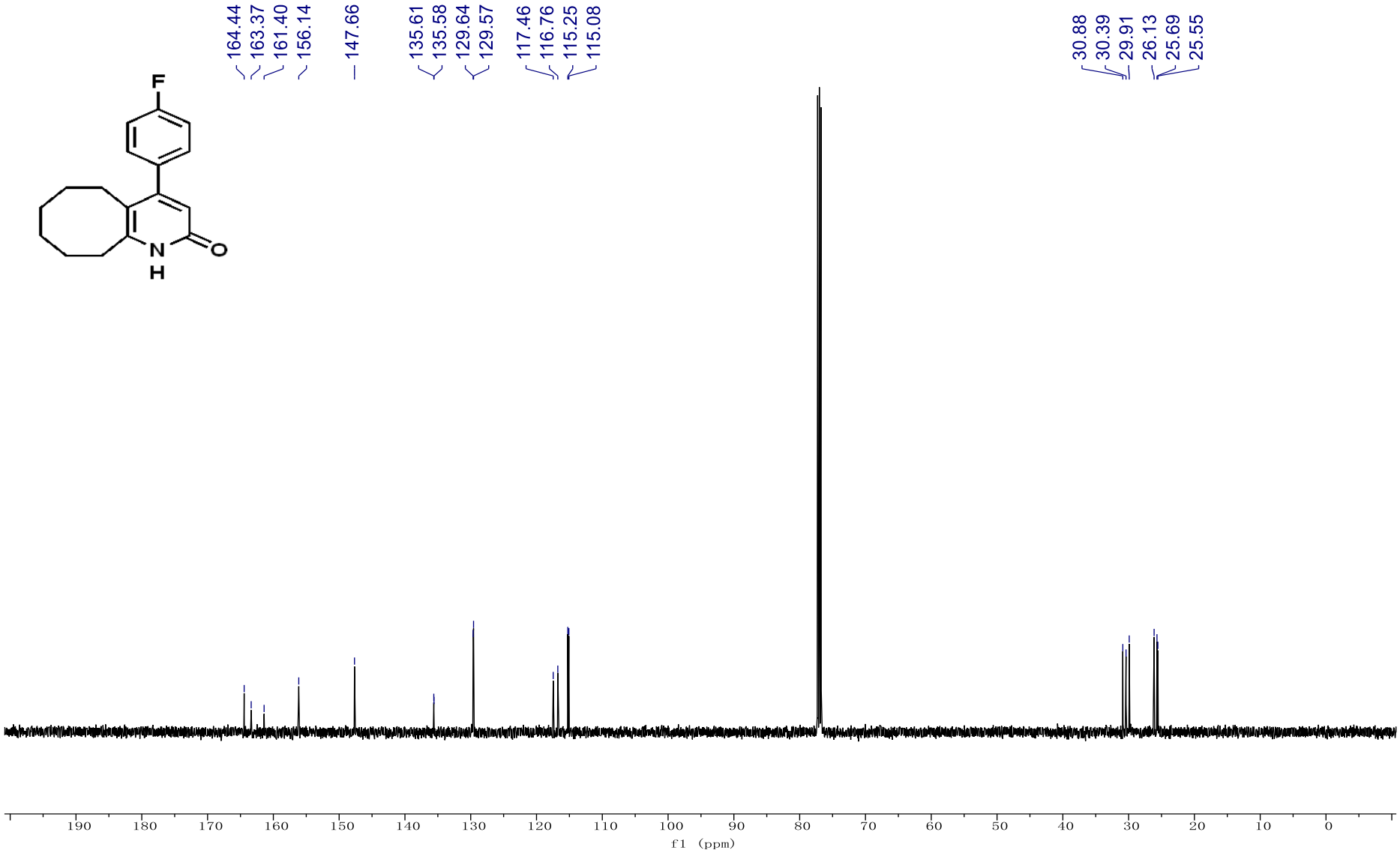
^{1}H NMR of Precursor for Blonanserin S60a

$CDCl_3$, 23 °C



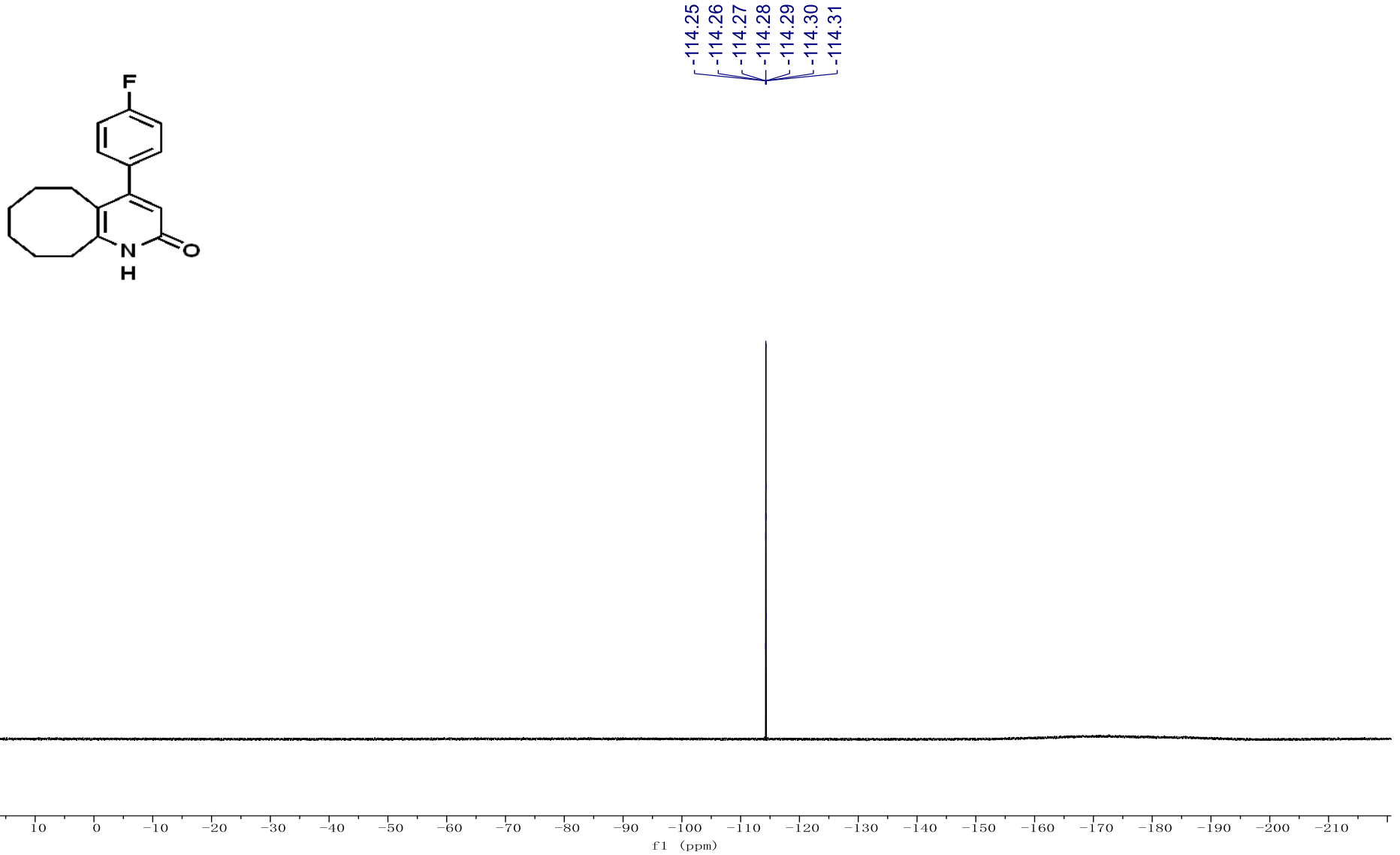
^{13}C NMR of Precursor for Blonanserin S60a

$CDCl_3$, 23 °C



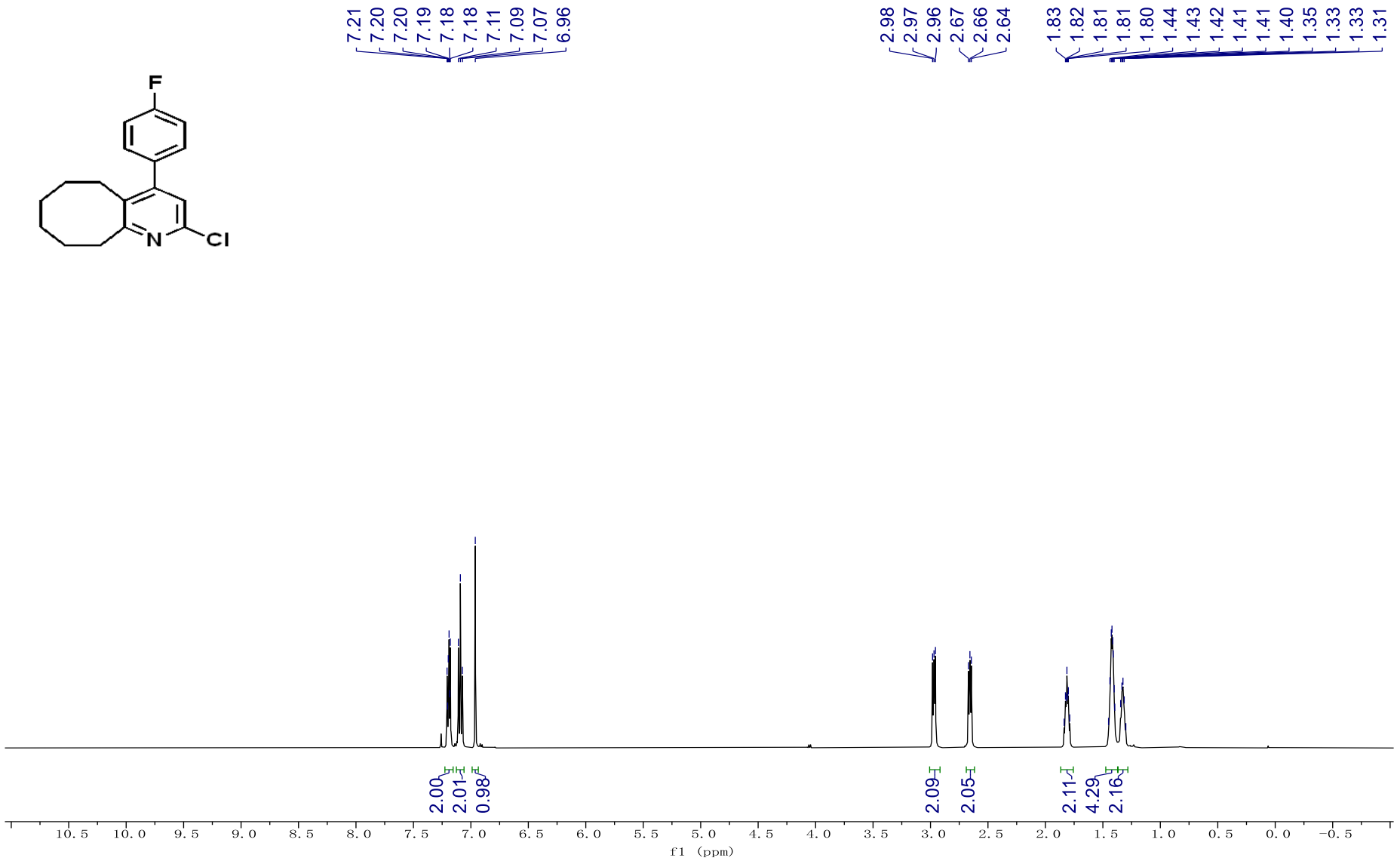
^{19}F NMR of Precursor for Blonanserin S60a

$CDCl_3$, 23 °C



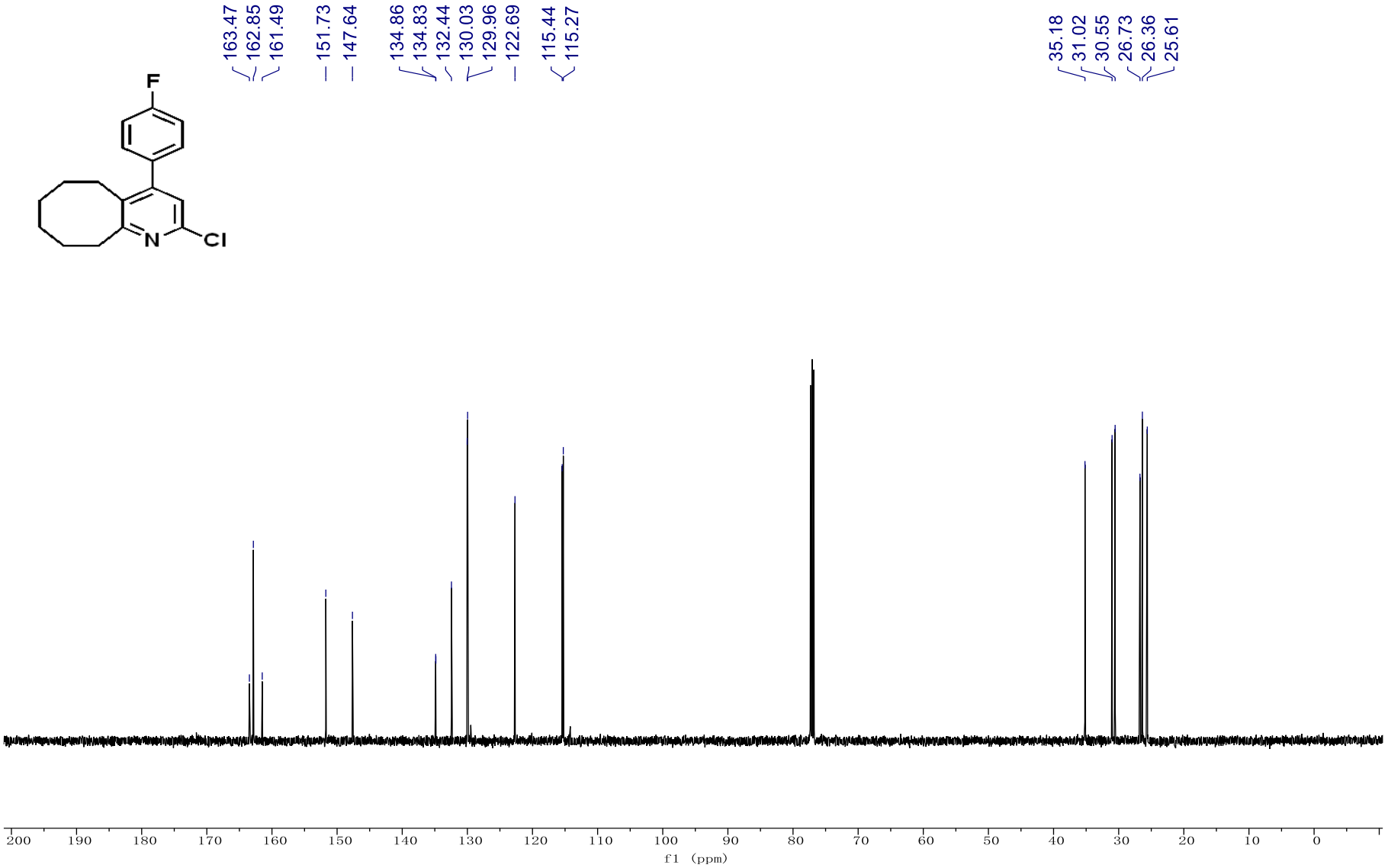
^{1}H NMR of Precursor for Blonanserin S60b

$CDCl_3$, 23 °C



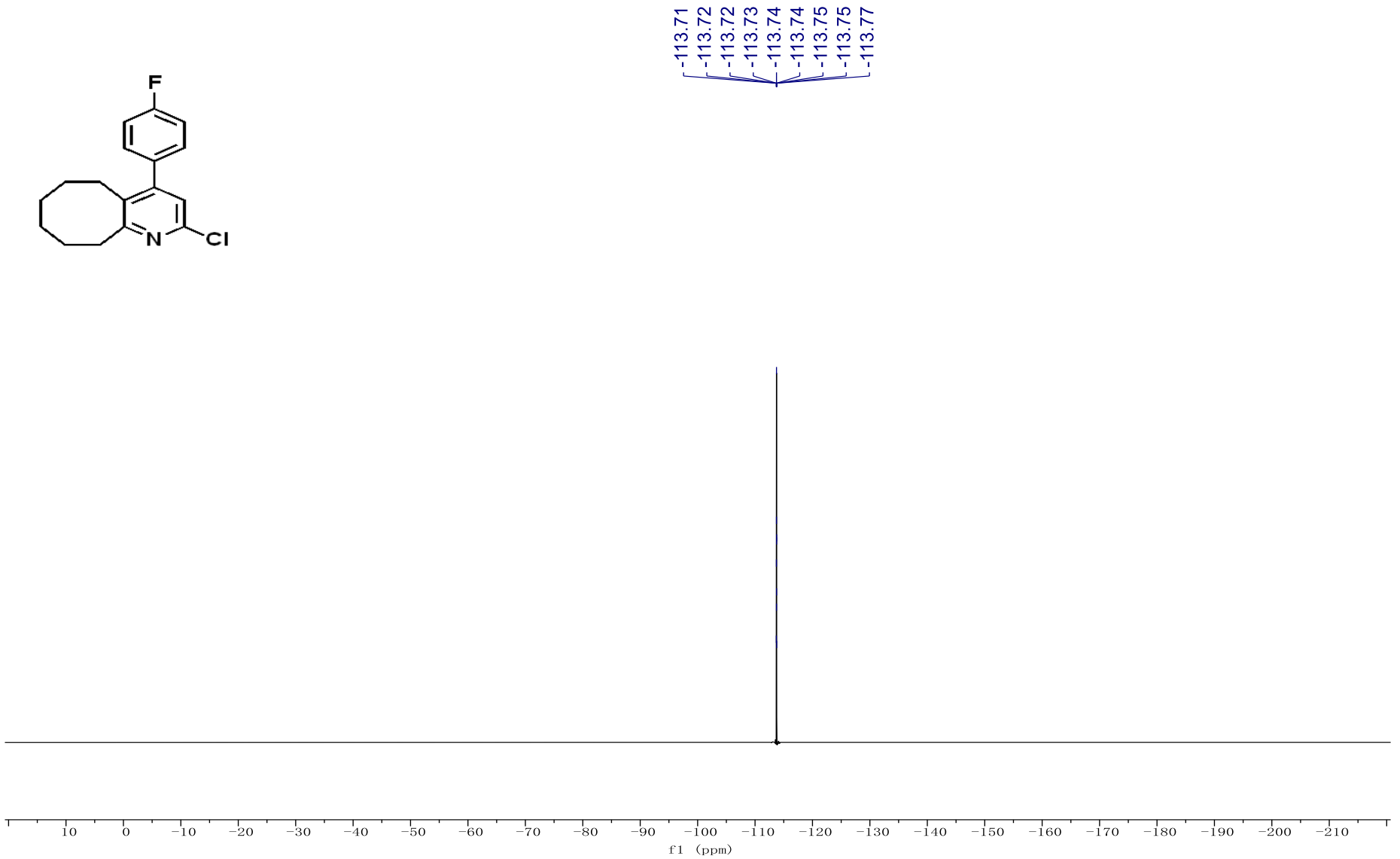
^{13}C NMR of Precursor for Blonanserin S60b

$CDCl_3$, 23 °C



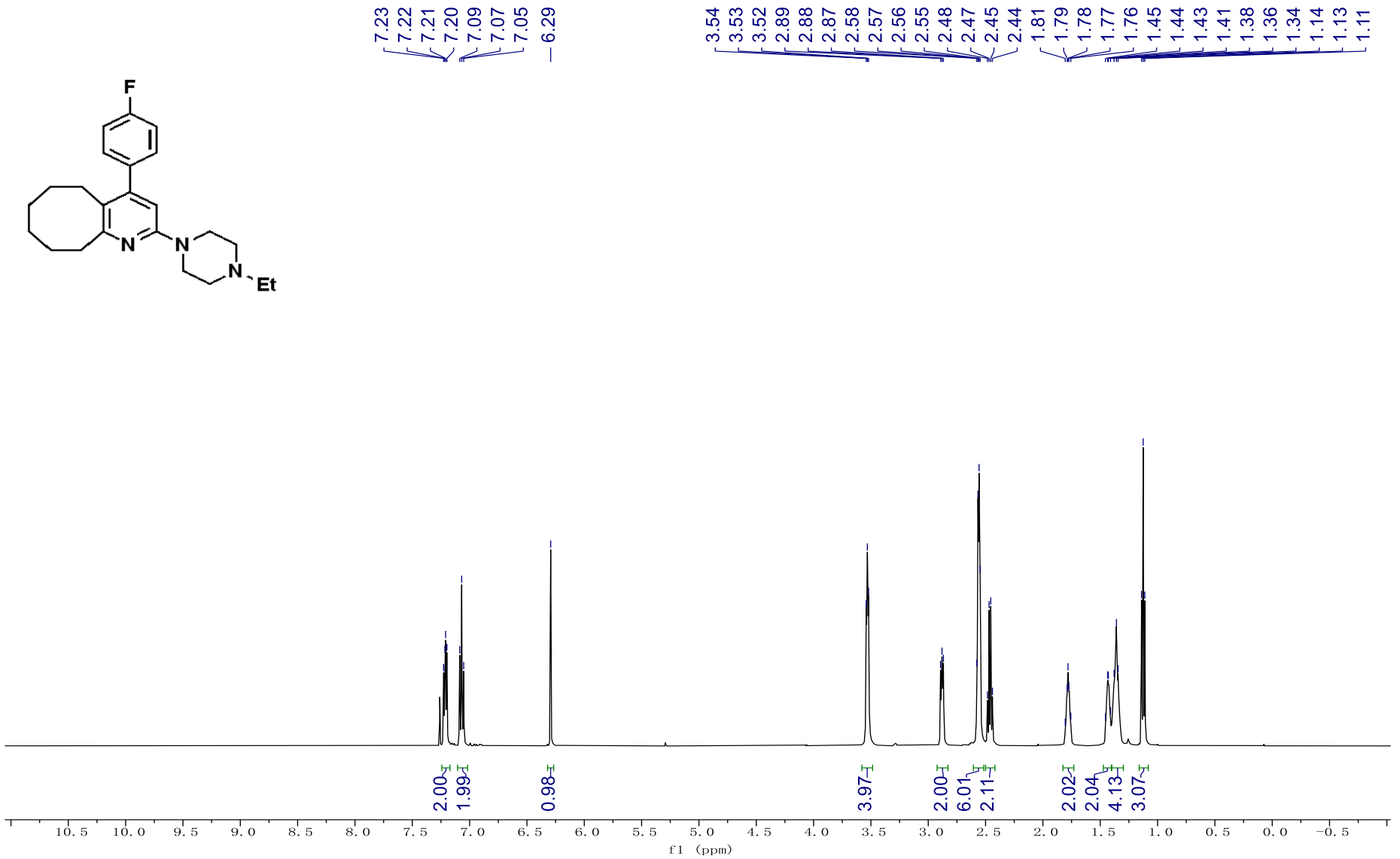
^{19}F NMR of Precursor for Blonanserin S60b

$CDCl_3$, 23 °C



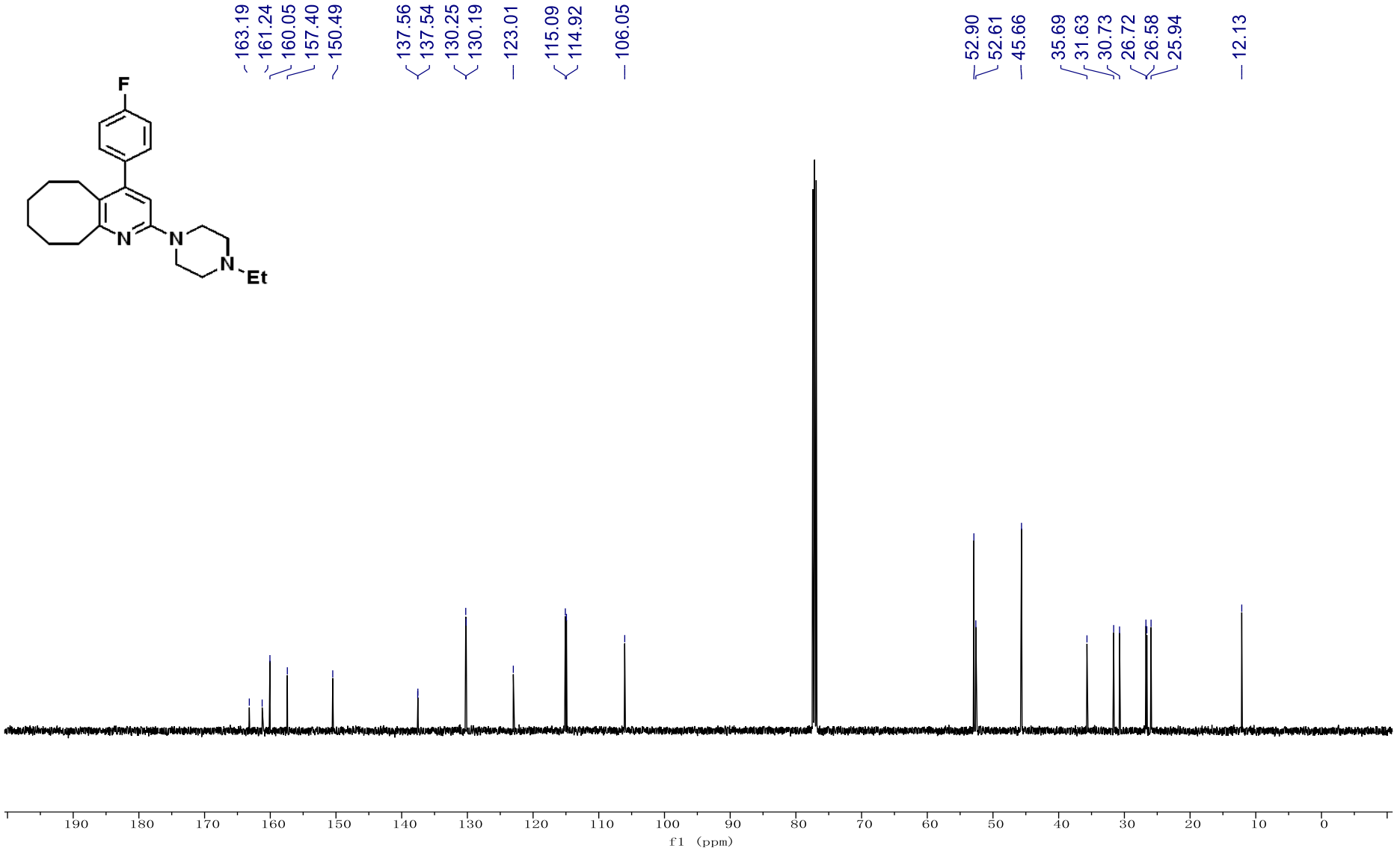
^{1}H NMR Blonanserin S60

$CDCl_3$, 23 °C



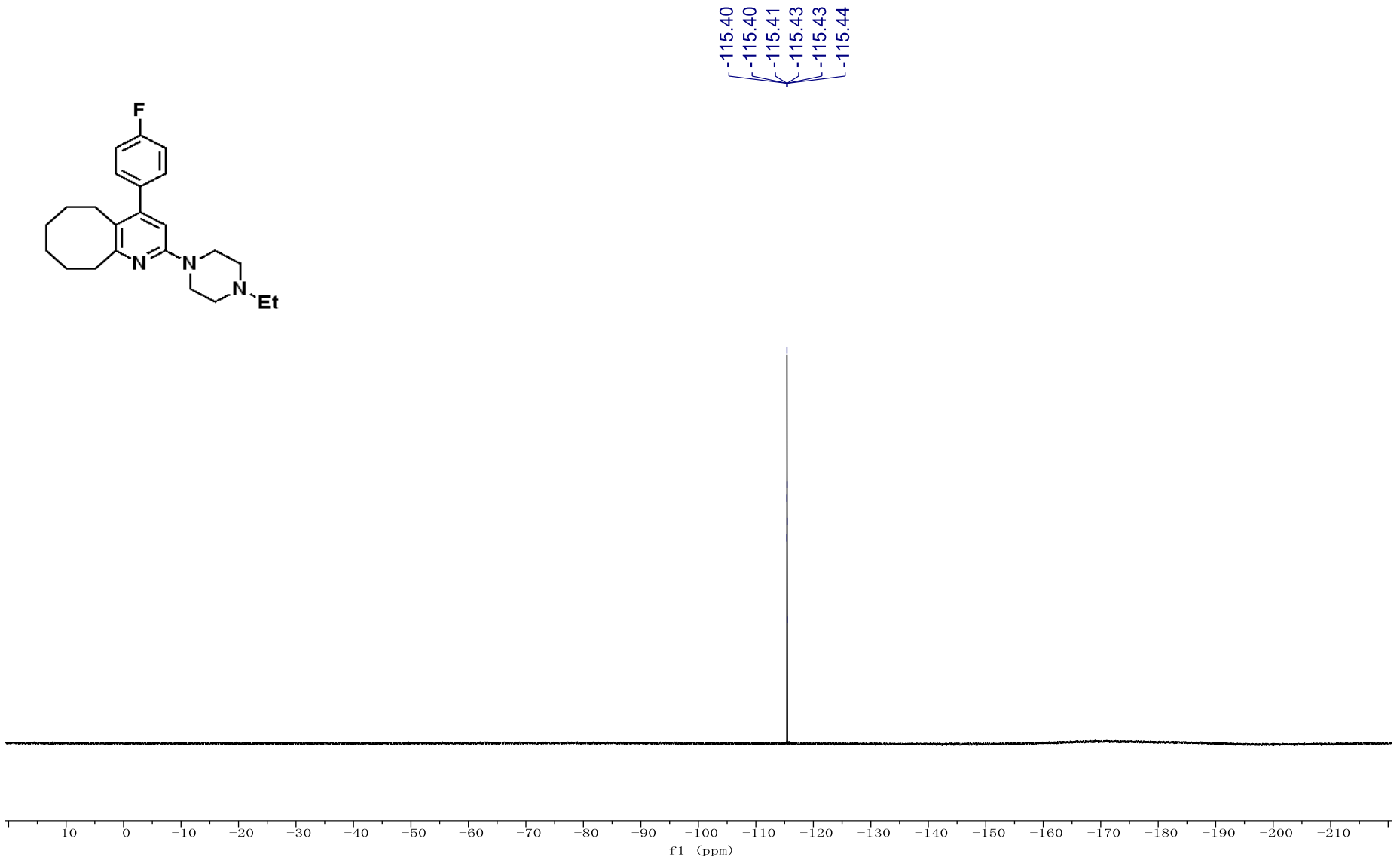
^{13}C NMR of Blonanserin S60

$CDCl_3$, 23 °C



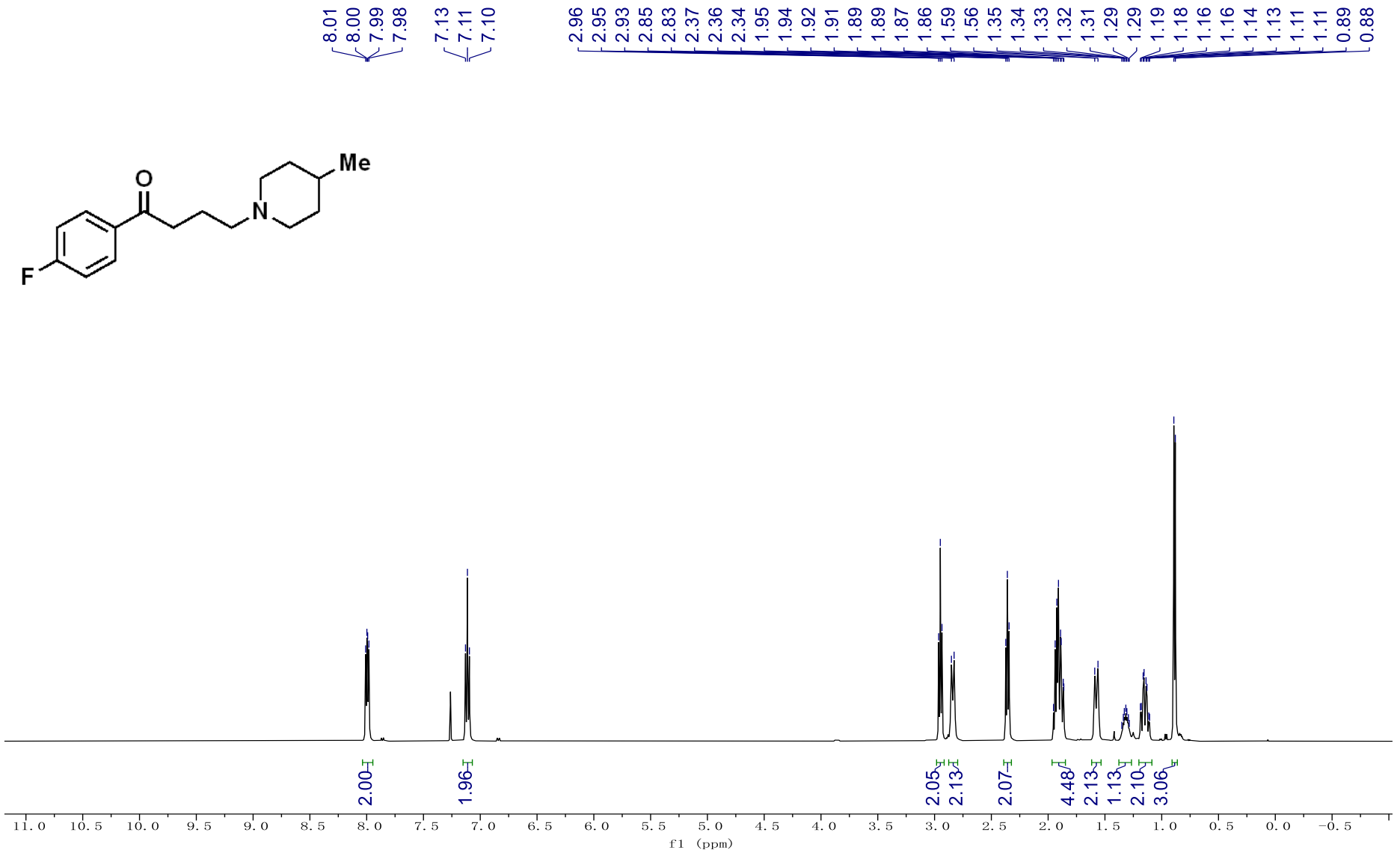
^{19}F NMR of Blonanserin S60

$CDCl_3$, 23 °C



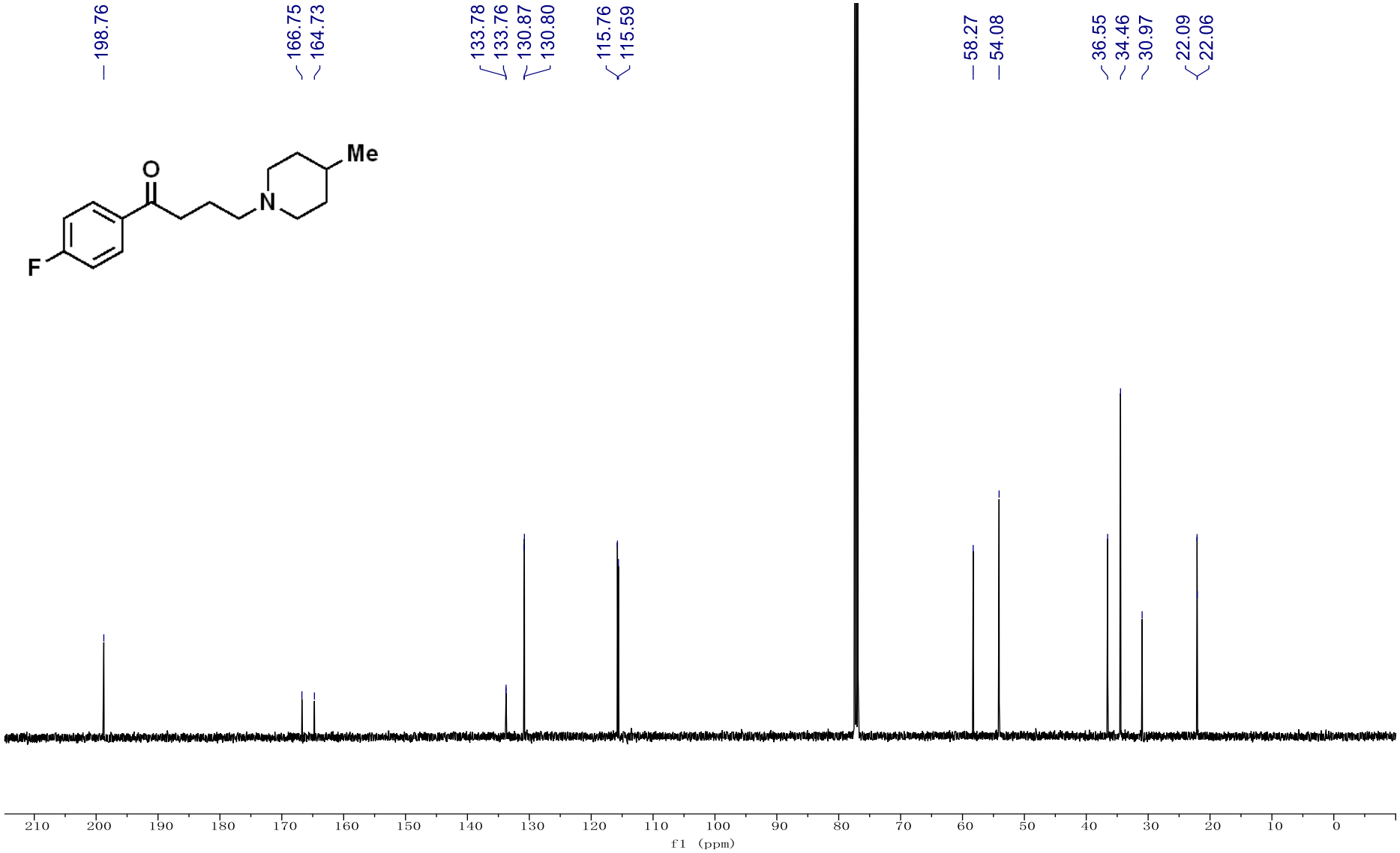
^{1}H NMR of Melperone S61

$CDCl_3$, 23 °C



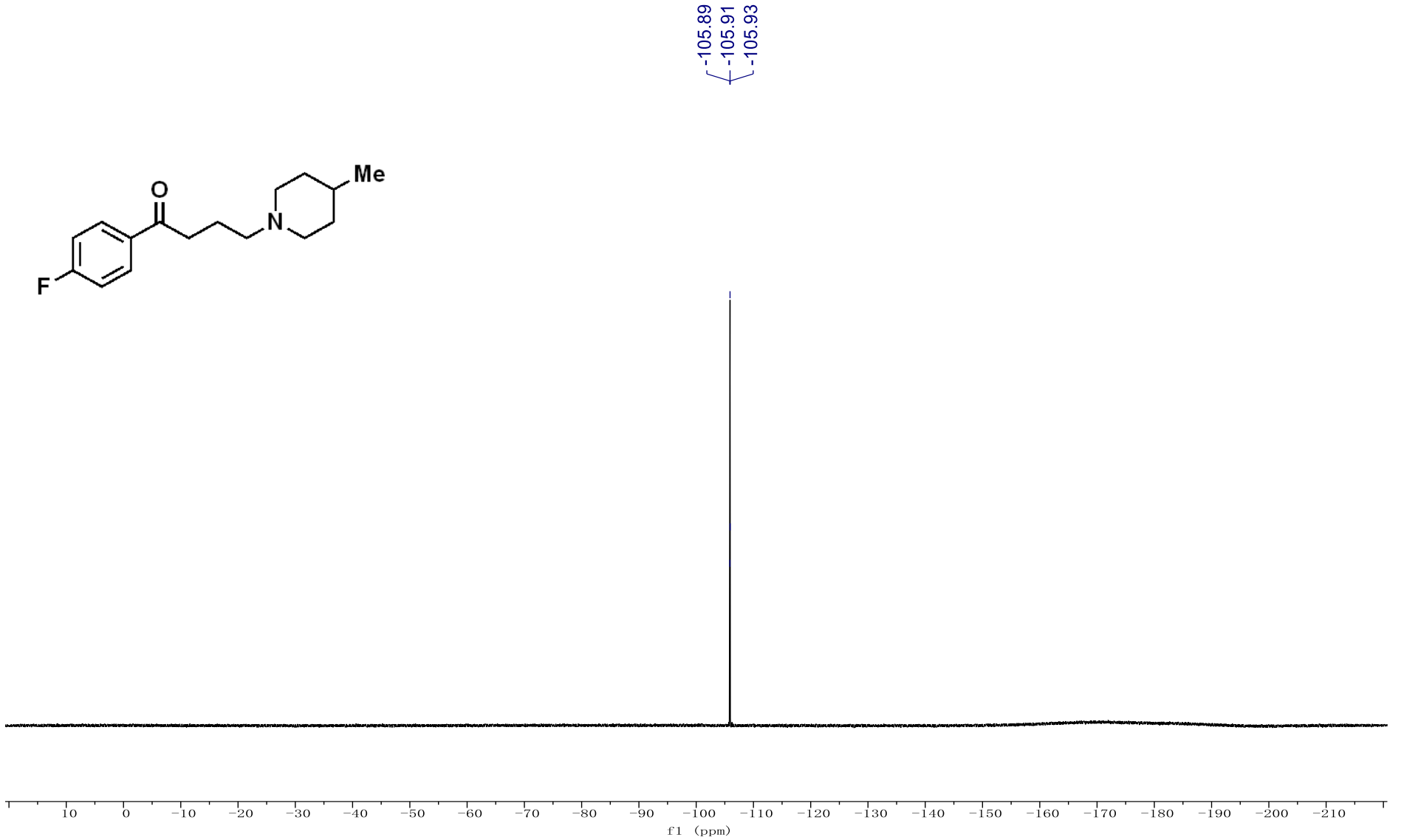
^{13}C NMR of Melperone S61

$CDCl_3$, 23 °C



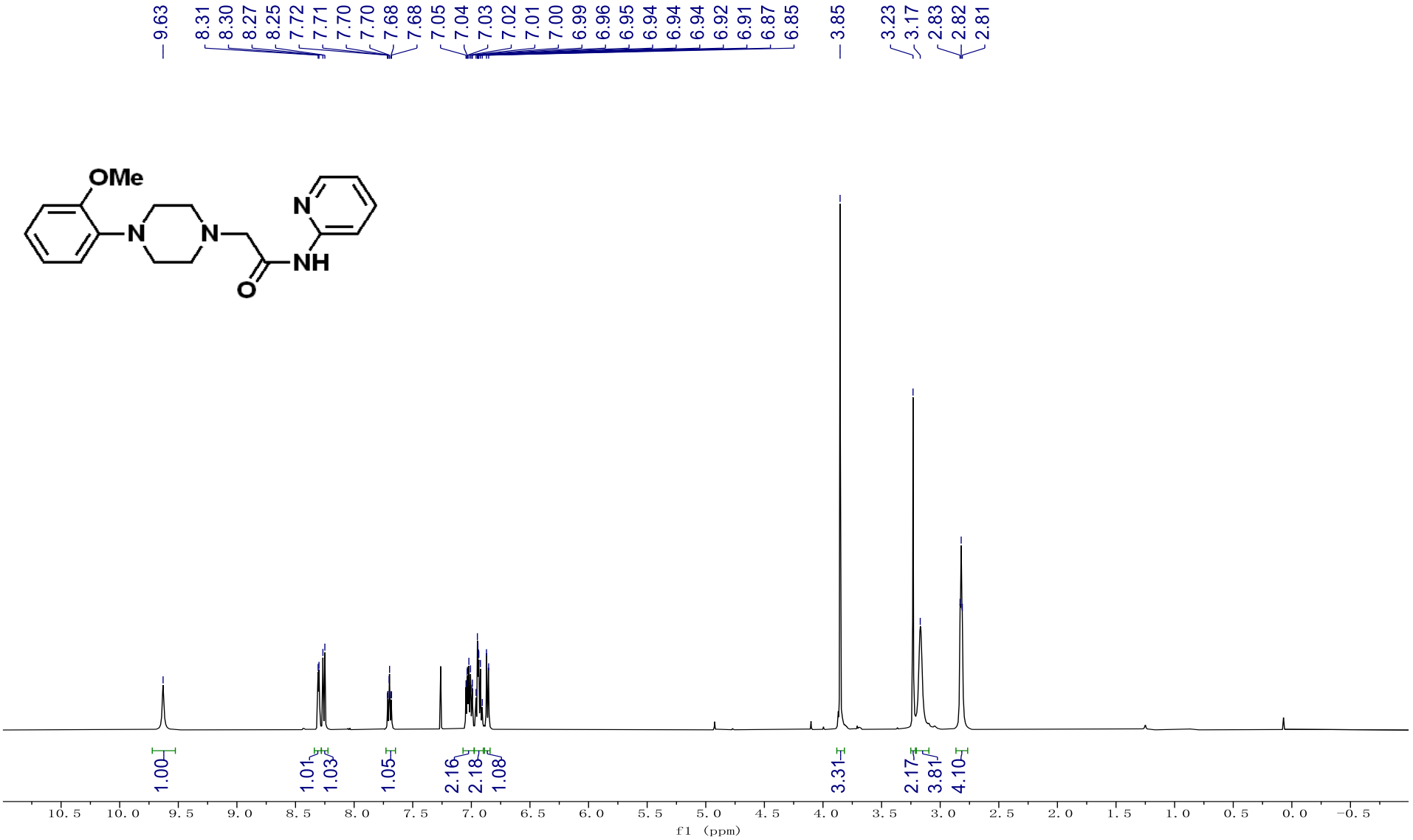
^{19}F NMR of Melperone S61

$CDCl_3$, 23 °C



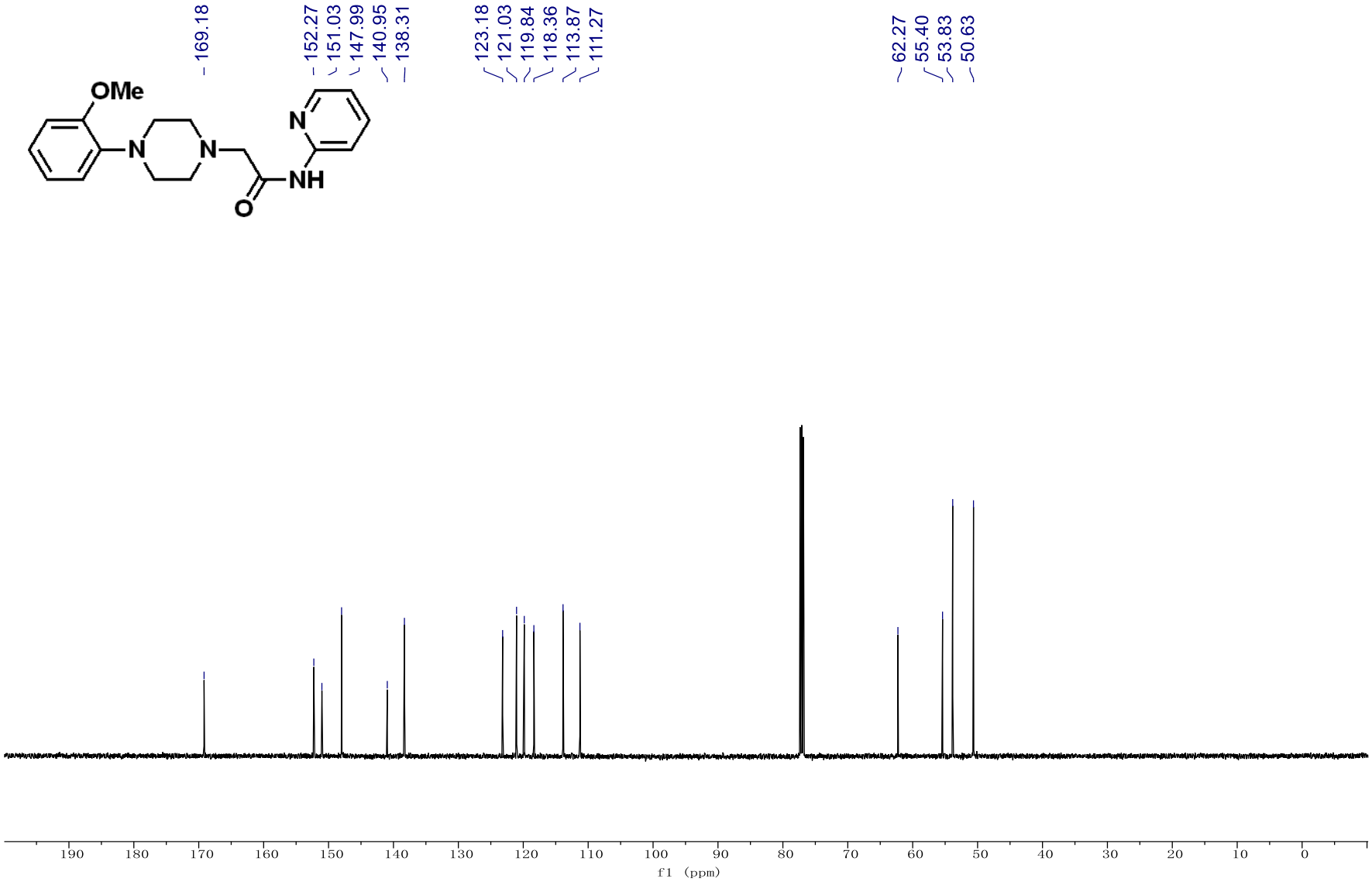
^{1}H NMR of S64a

$CDCl_3$, 23 °C



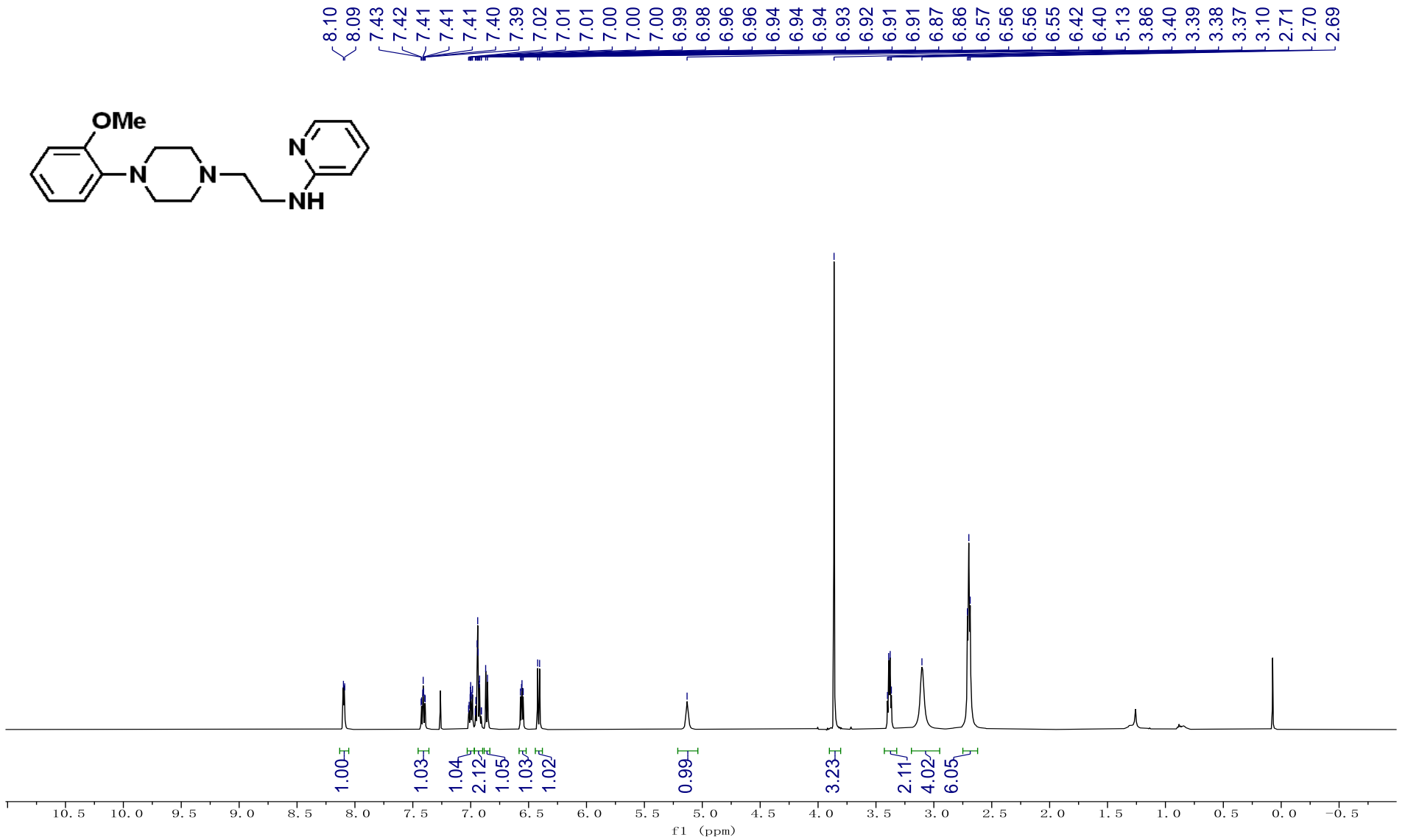
^{13}C NMR of S64a

$CDCl_3$, 23 °C



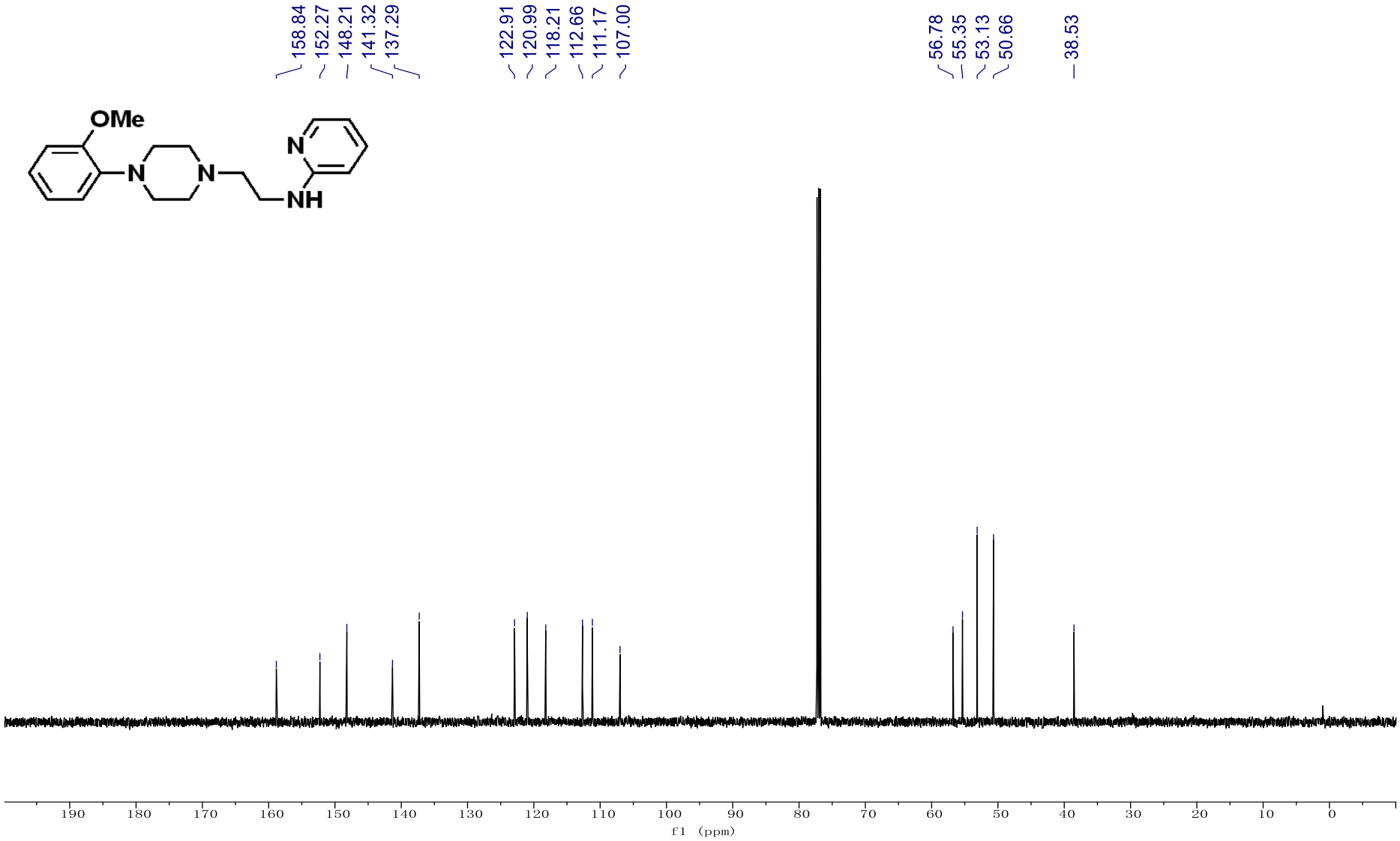
^{1}H NMR of S64b

$CDCl_3$, 23 °C



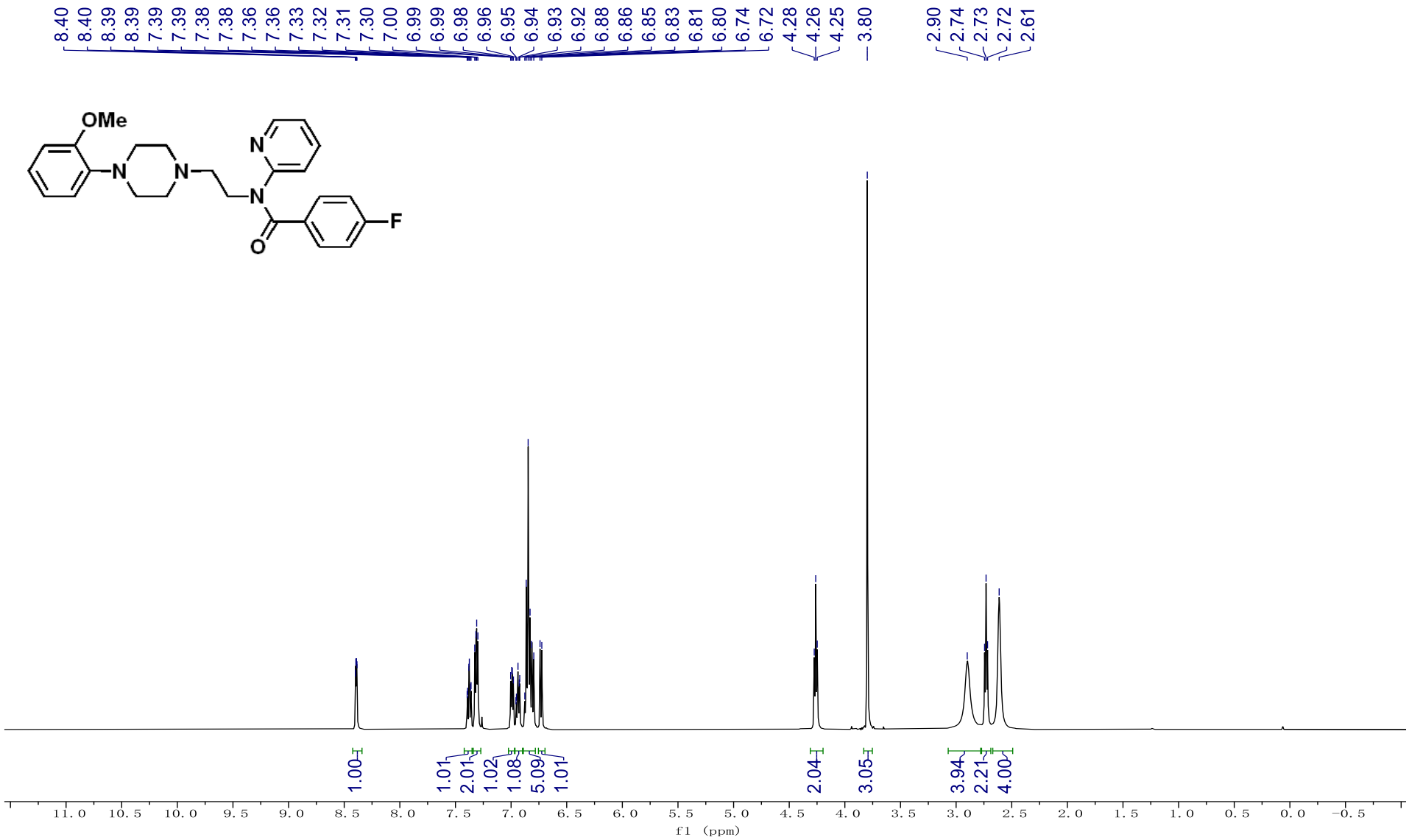
^{13}C NMR of S64b

$CDCl_3$, 23 °C



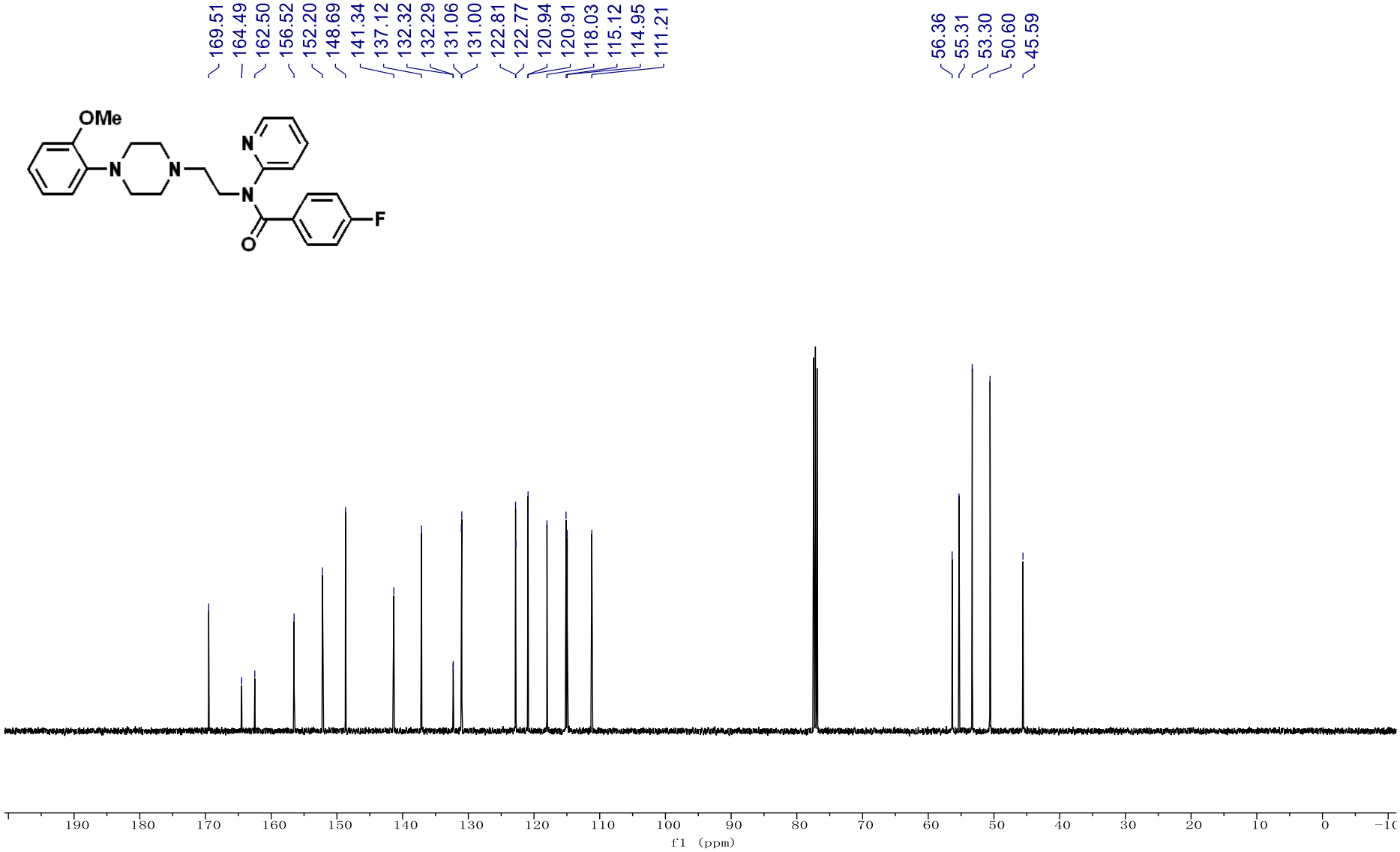
^{1}H NMR of 2'-methoxyphenyl-(N-2'-pyridinyl)-p-fluoro-benzamidoethyipiperazine (p-MPPF) S64

$CDCl_3$, 23 °C



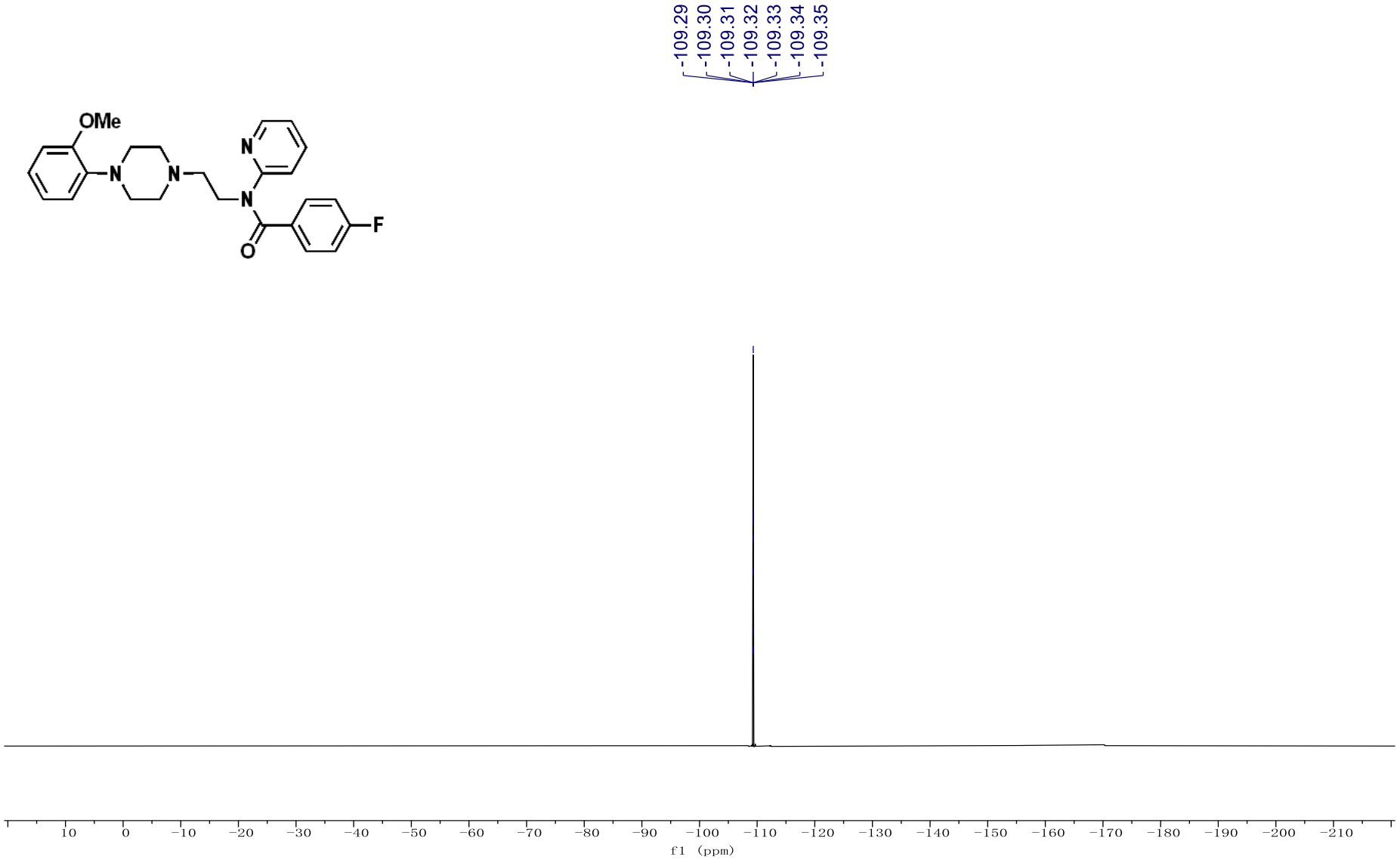
^{13}C NMR of 2'-methoxyphenyl-(N-2'-pyridinyl)-p-fluoro-benzamidoethyipiperazine (p-MPPF) S64

$CDCl_3$, 23 °C



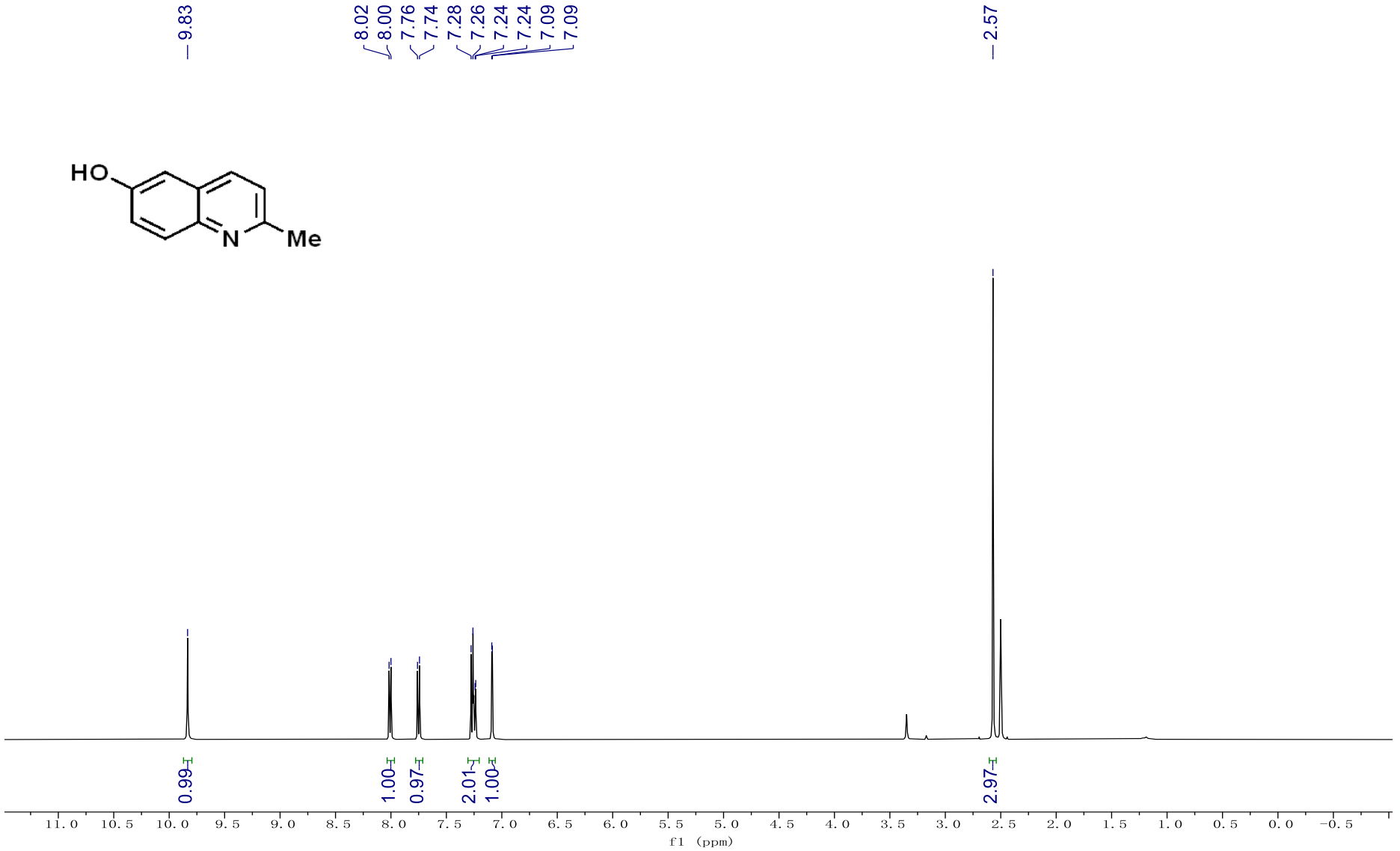
^{19}F NMR of 2'-methoxyphenyl-(N-2'-pyridinyl)-p-fluoro-benzamidoethyipiperazine (p-MPPF) S64

$CDCl_3$, 23 °C



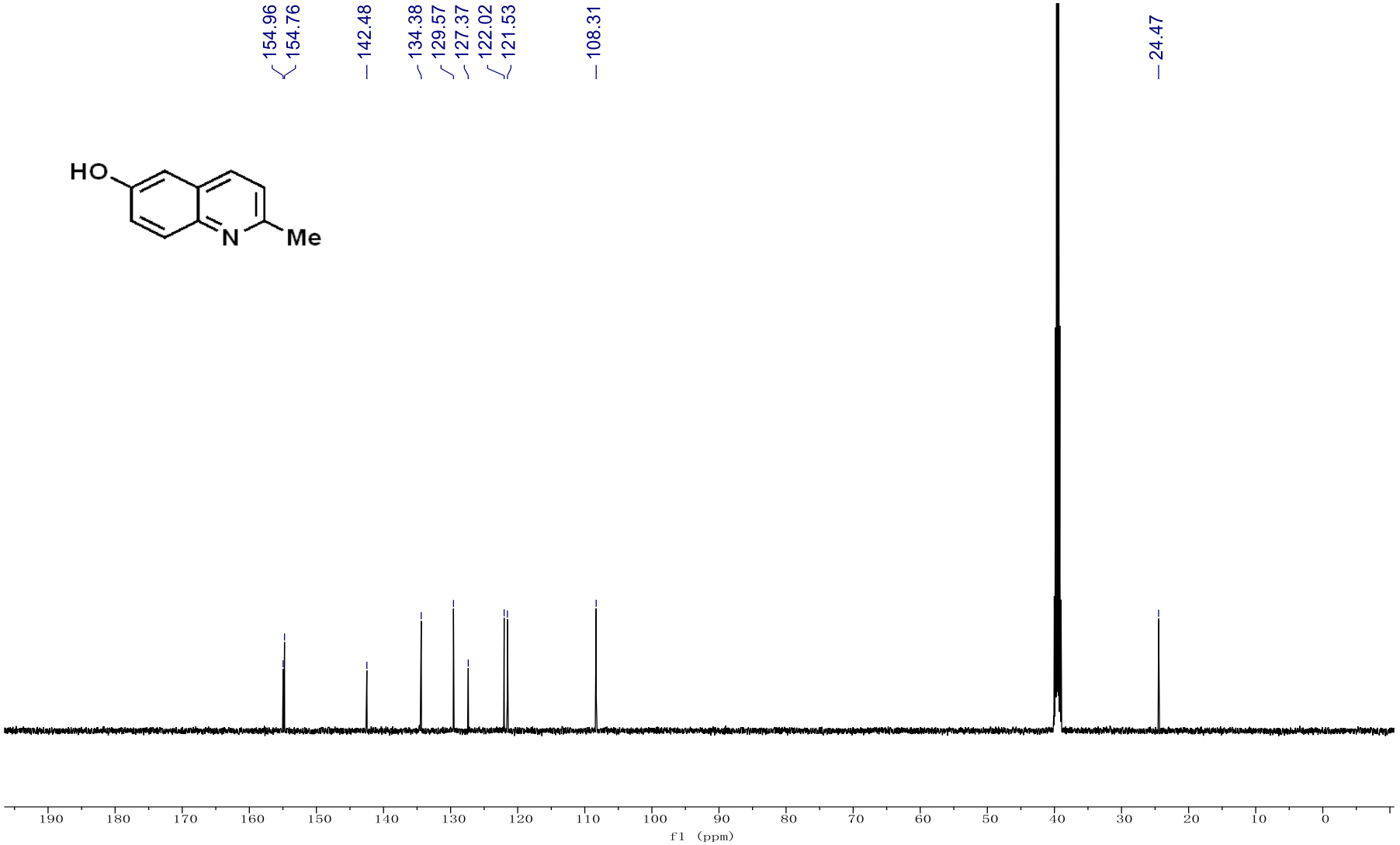
^{1}H NMR of Phenol 54

DMSO-d_6, 23 °C



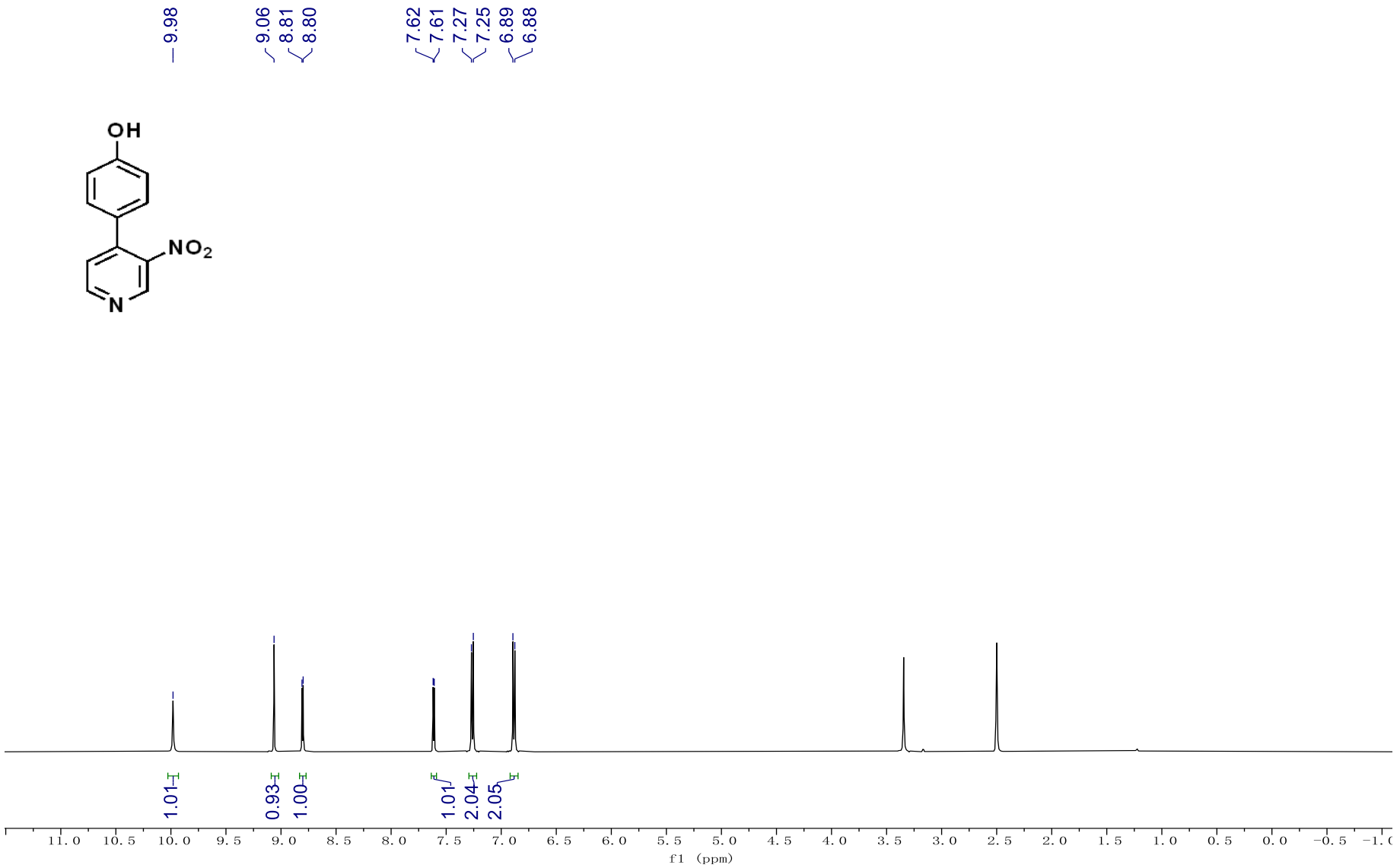
^{13}C NMR of Phenol 54

DMSO-d_6, 23 °C



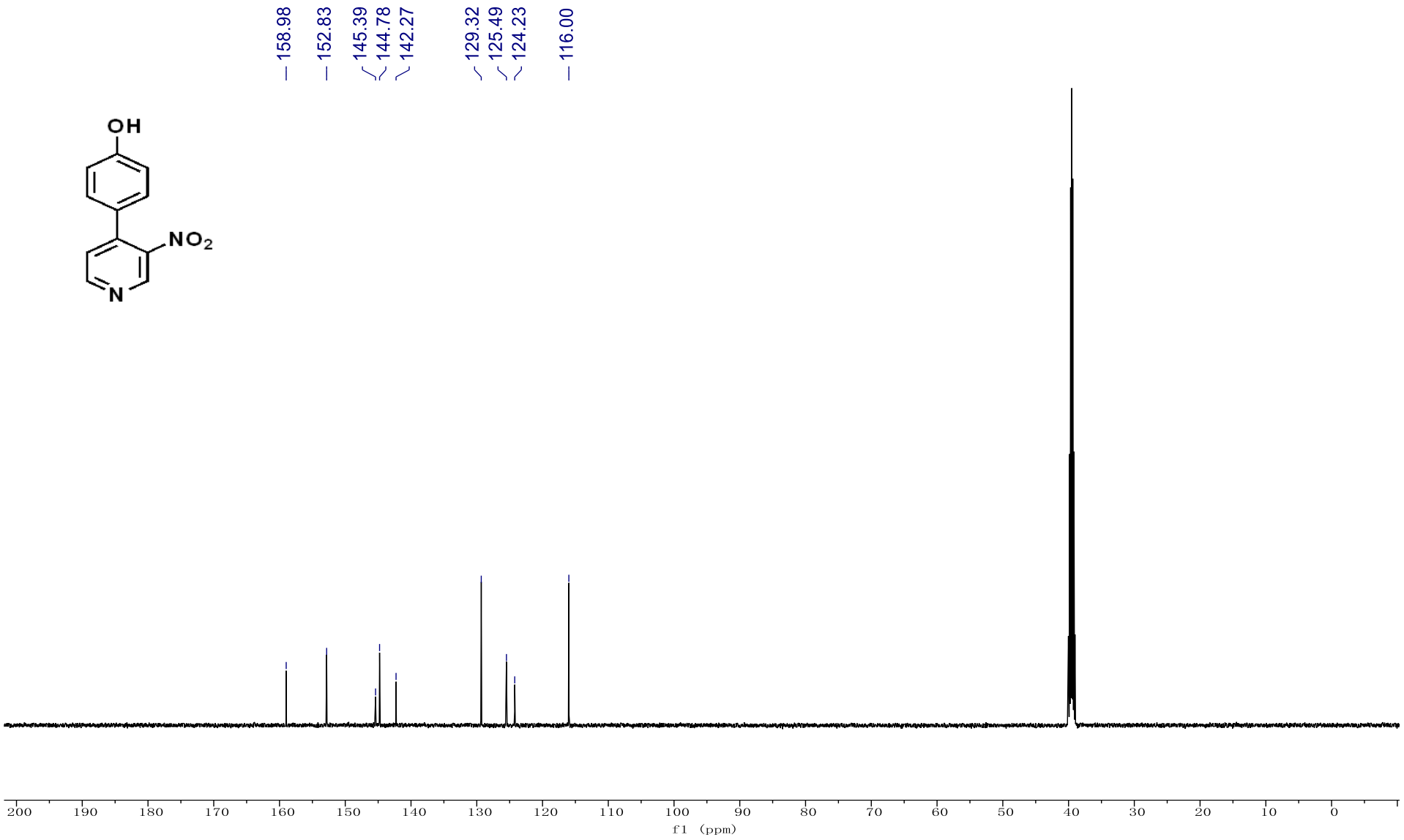
^{1}H NMR of Phenol 55

DMSO-d_6, 23 °C



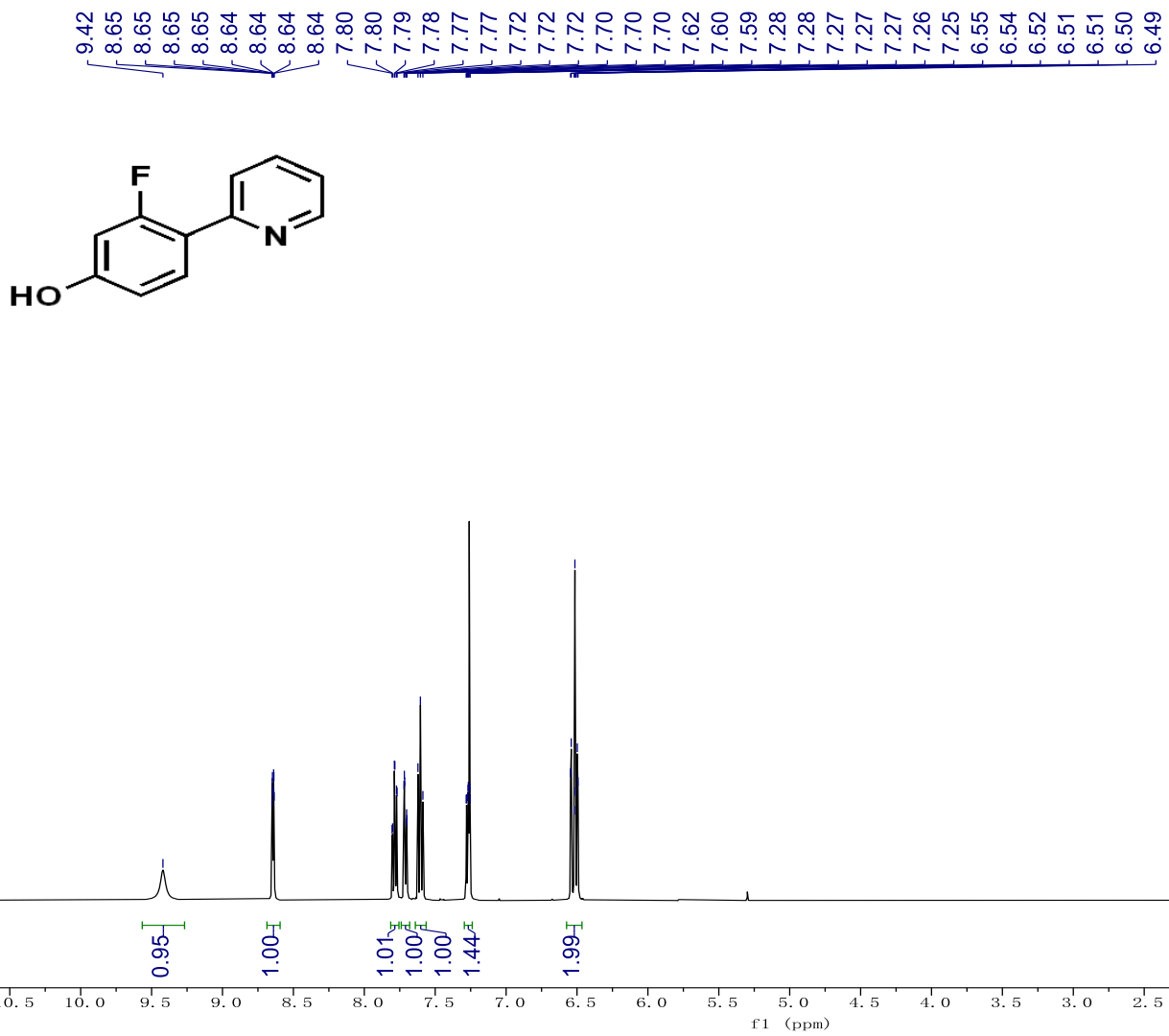
^{13}C NMR of Phenol 55

DMSO-d_6, 23 °C



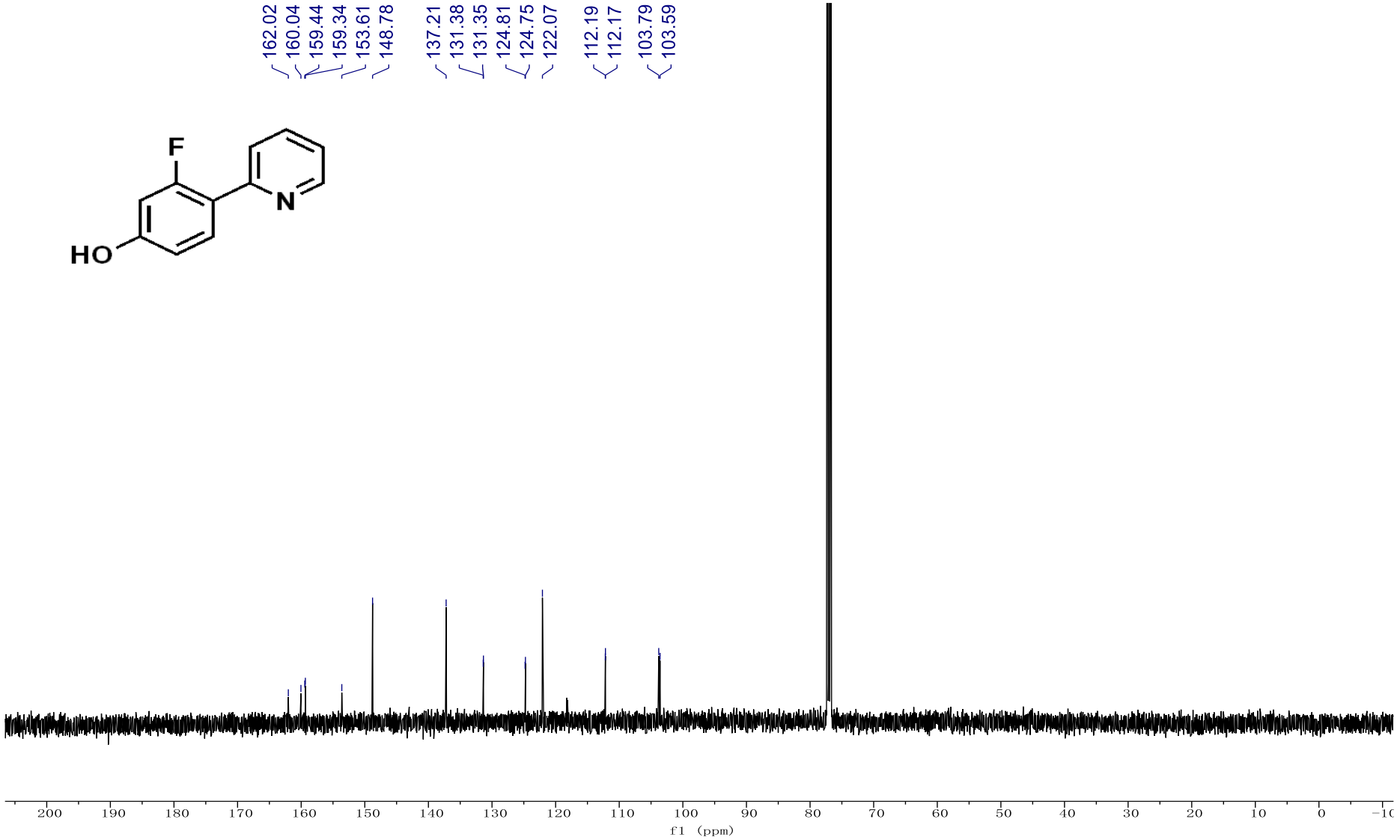
1H NMR of Phenol 56

$CDCl_3$, 23 °C



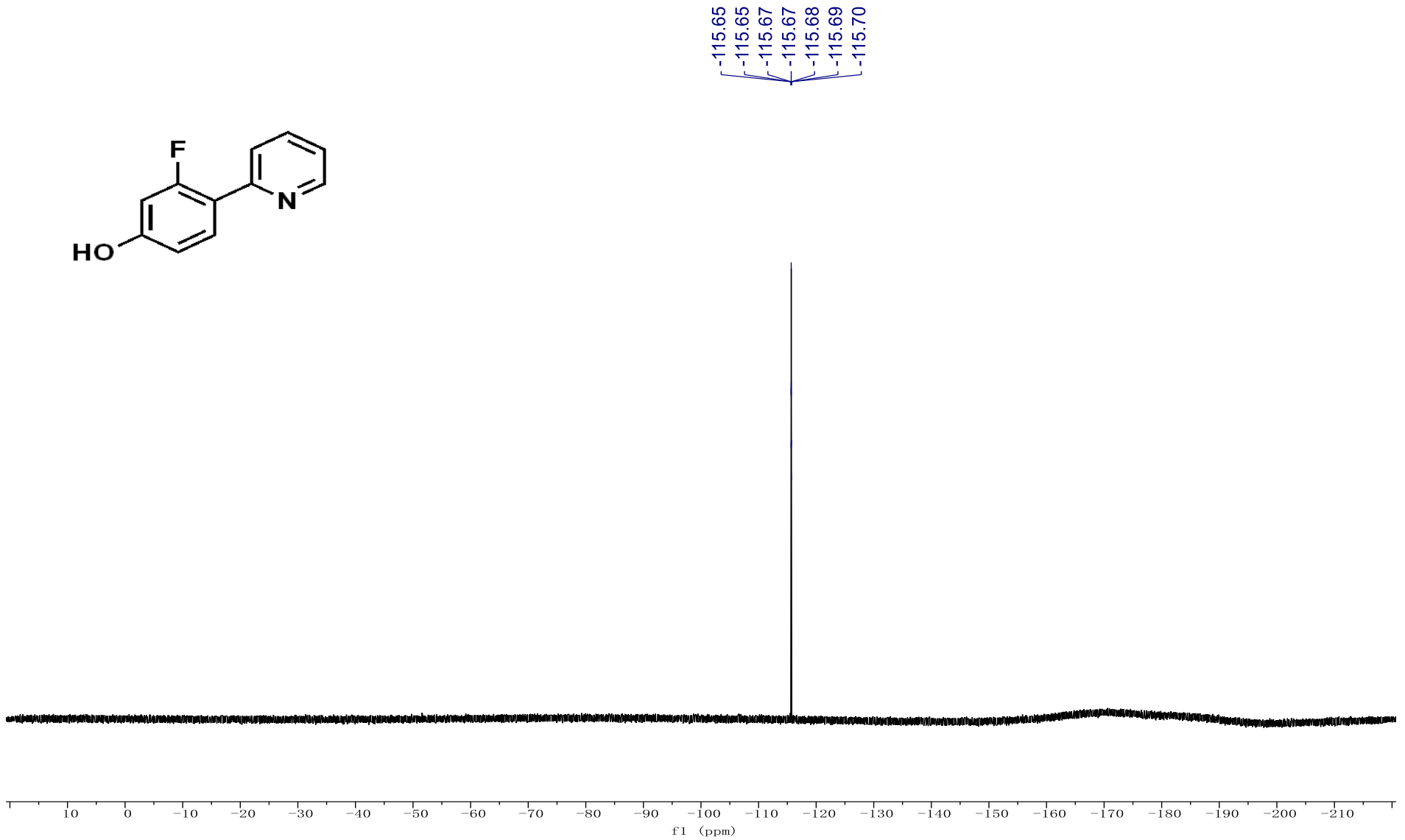
^{13}C NMR of Phenol 56

$CDCl_3$, 23 °C



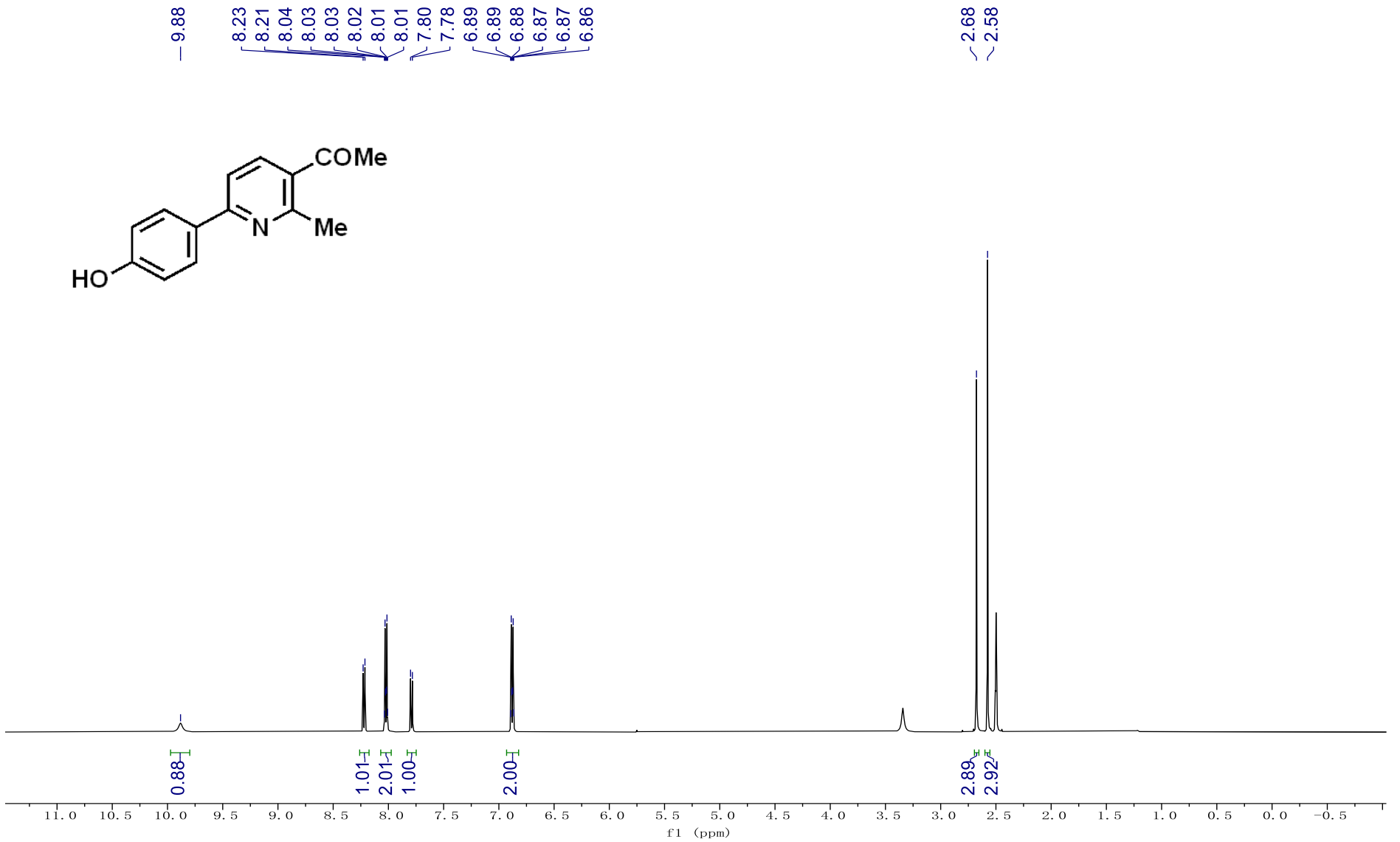
^{19}F NMR of Phenol 56

$CDCl_3$, 23 °C



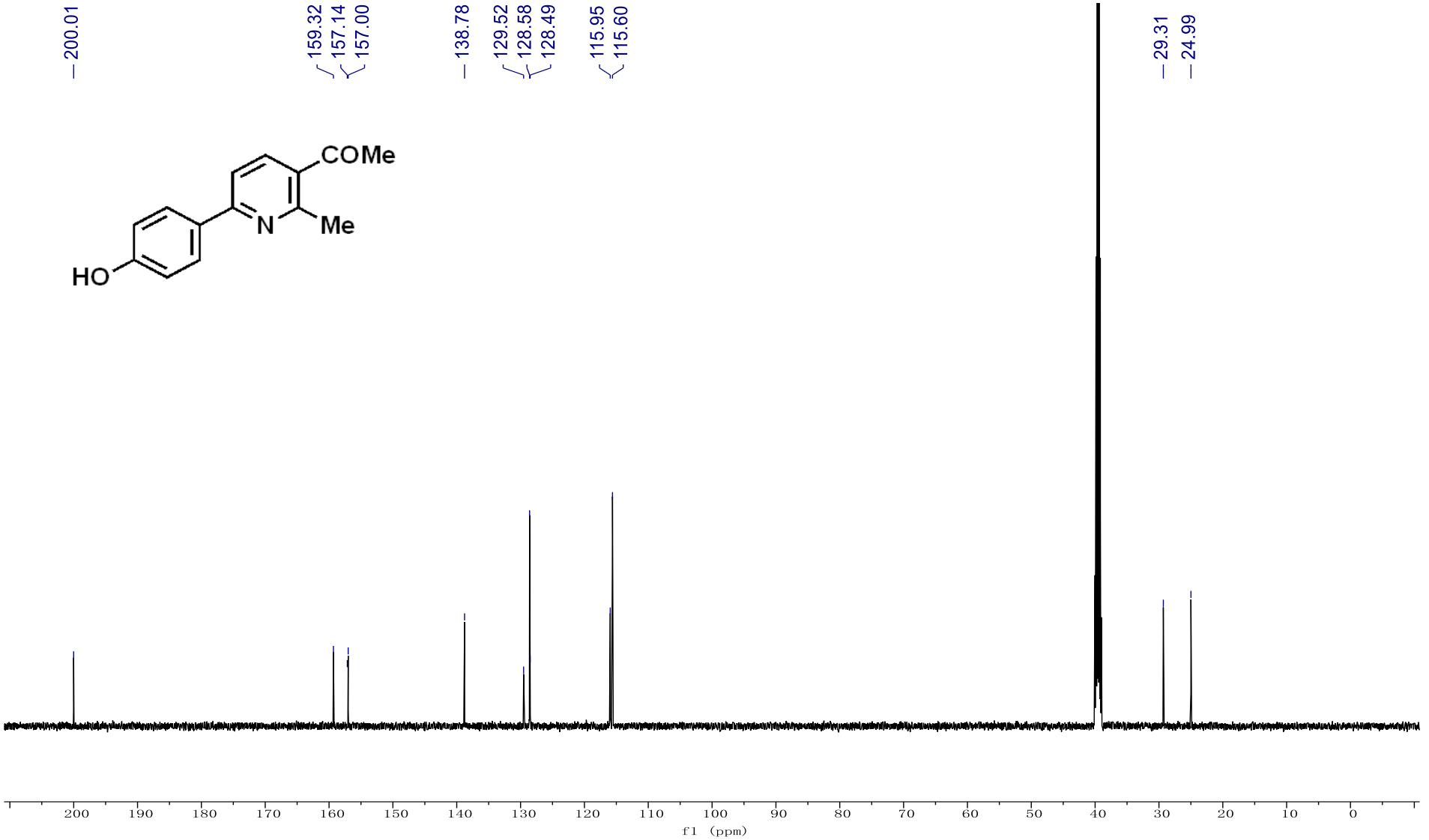
^{1}H NMR of Phenol 57

DMSO-d_6, 23 °C



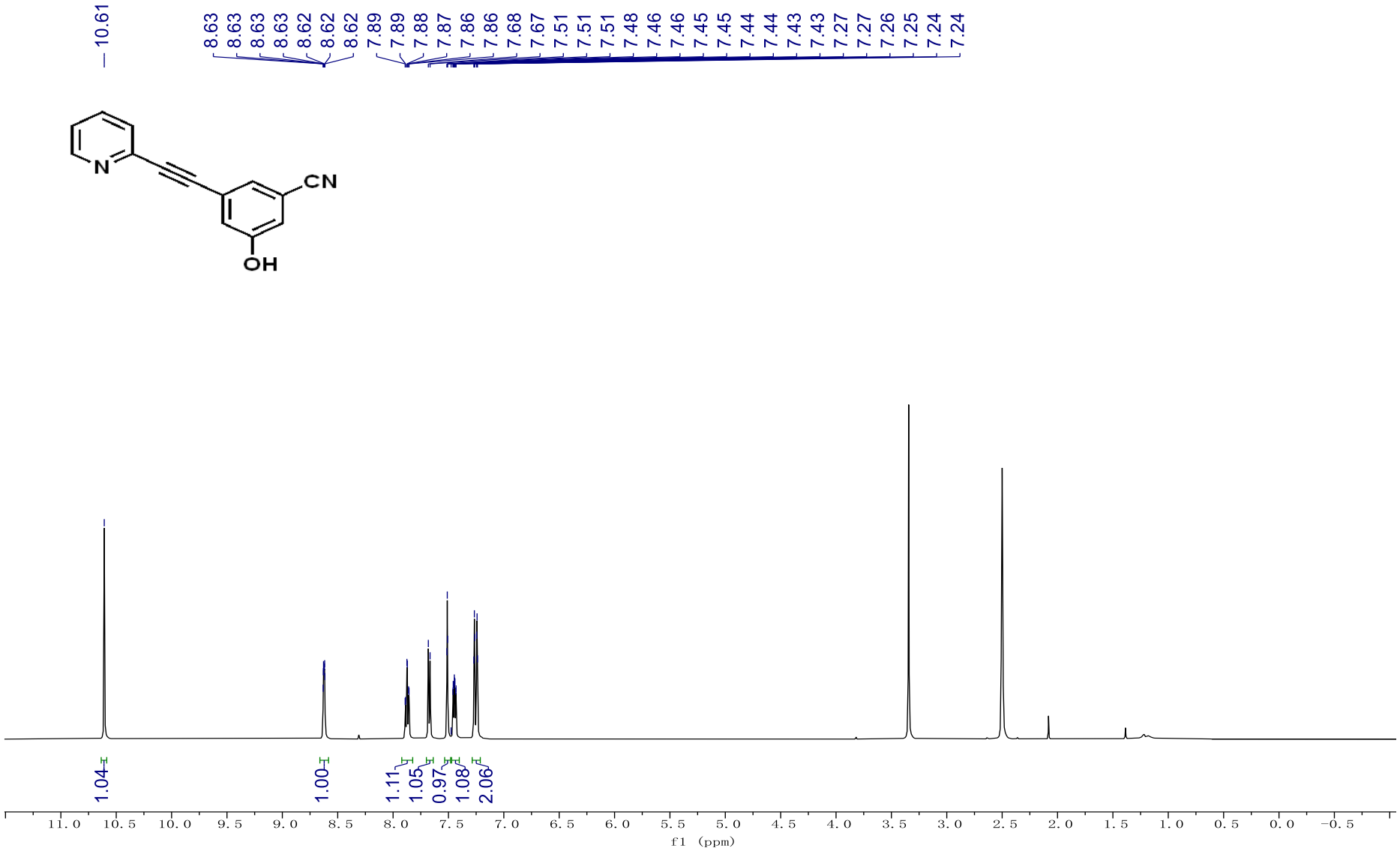
^{13}C NMR of Phenol 57

DMSO-d_6, 23 °C



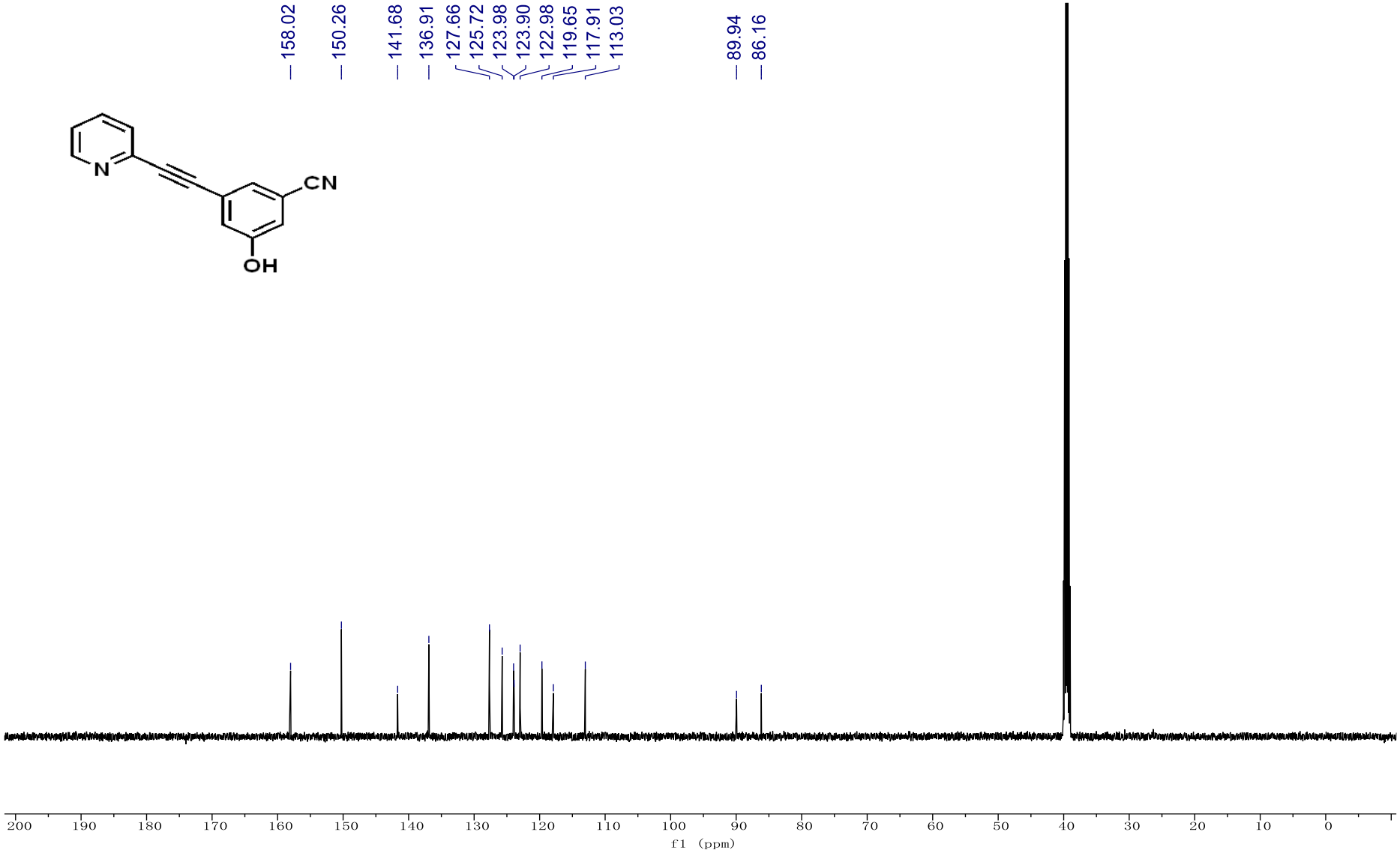
^{1}H NMR of Phenol 58

DMSO-d_6, 23 °C



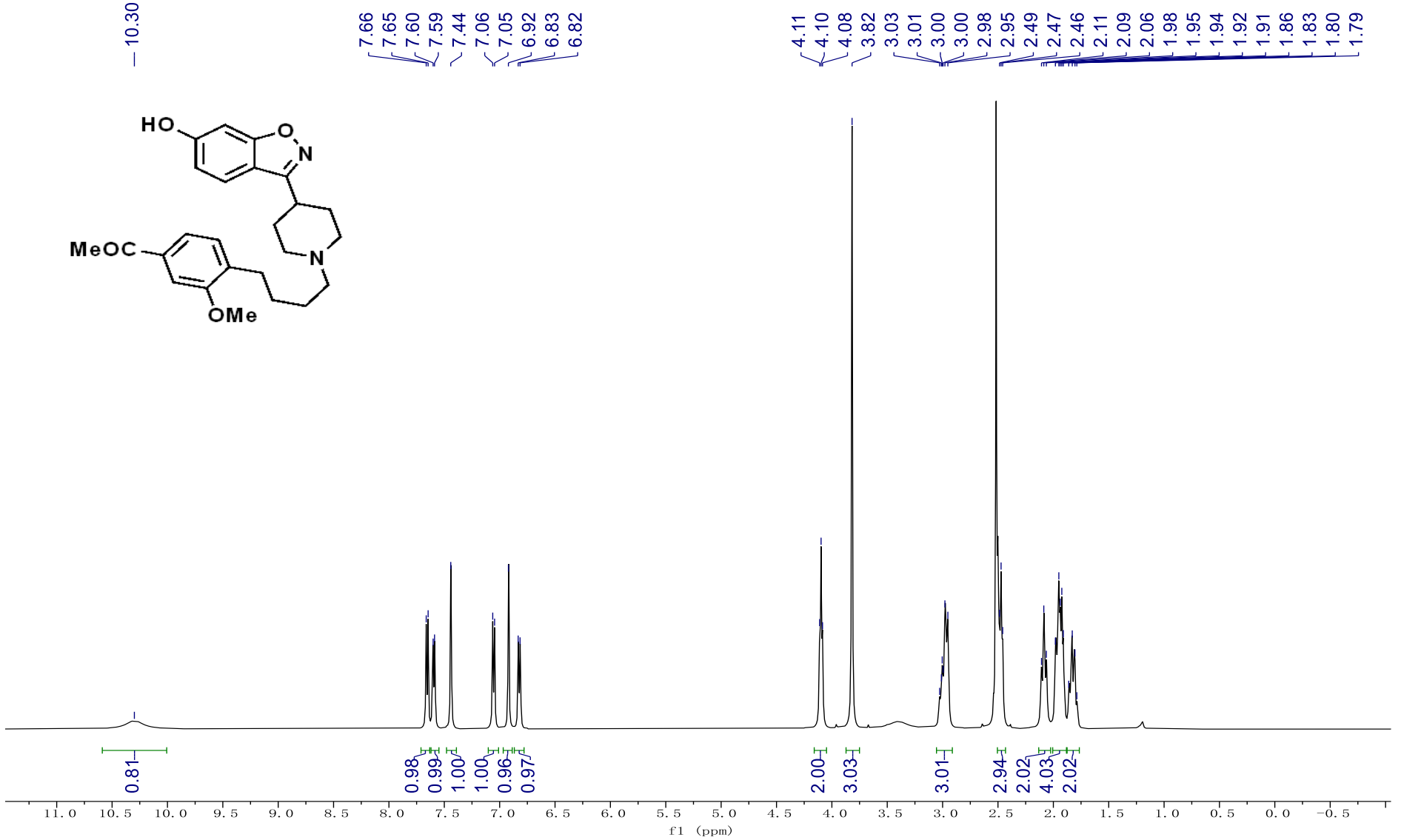
^{13}C NMR of Phenol 58

DMSO-d_6, 23 °C



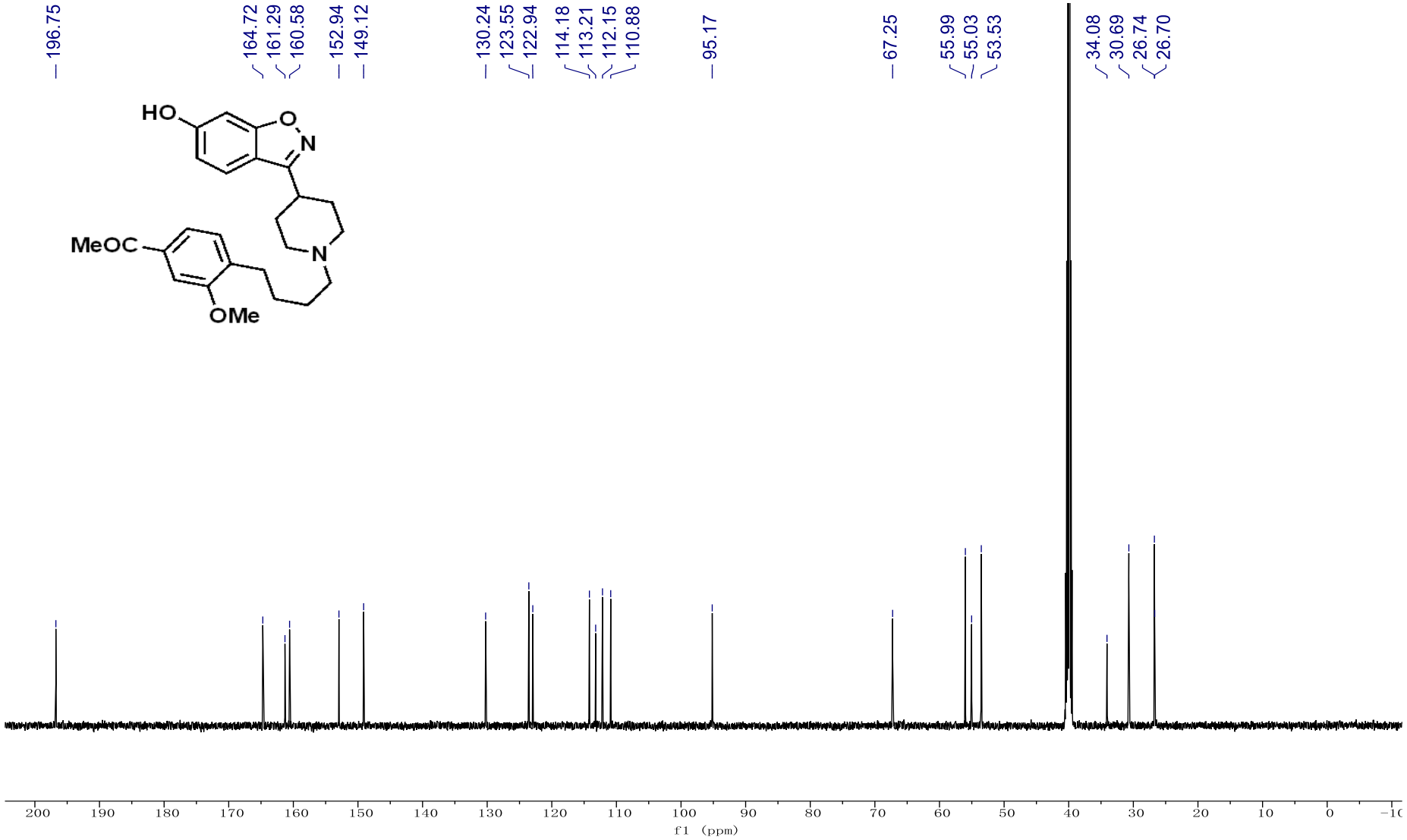
^{1}H NMR of Phenol 59

DMSO-d_6, 23 °C



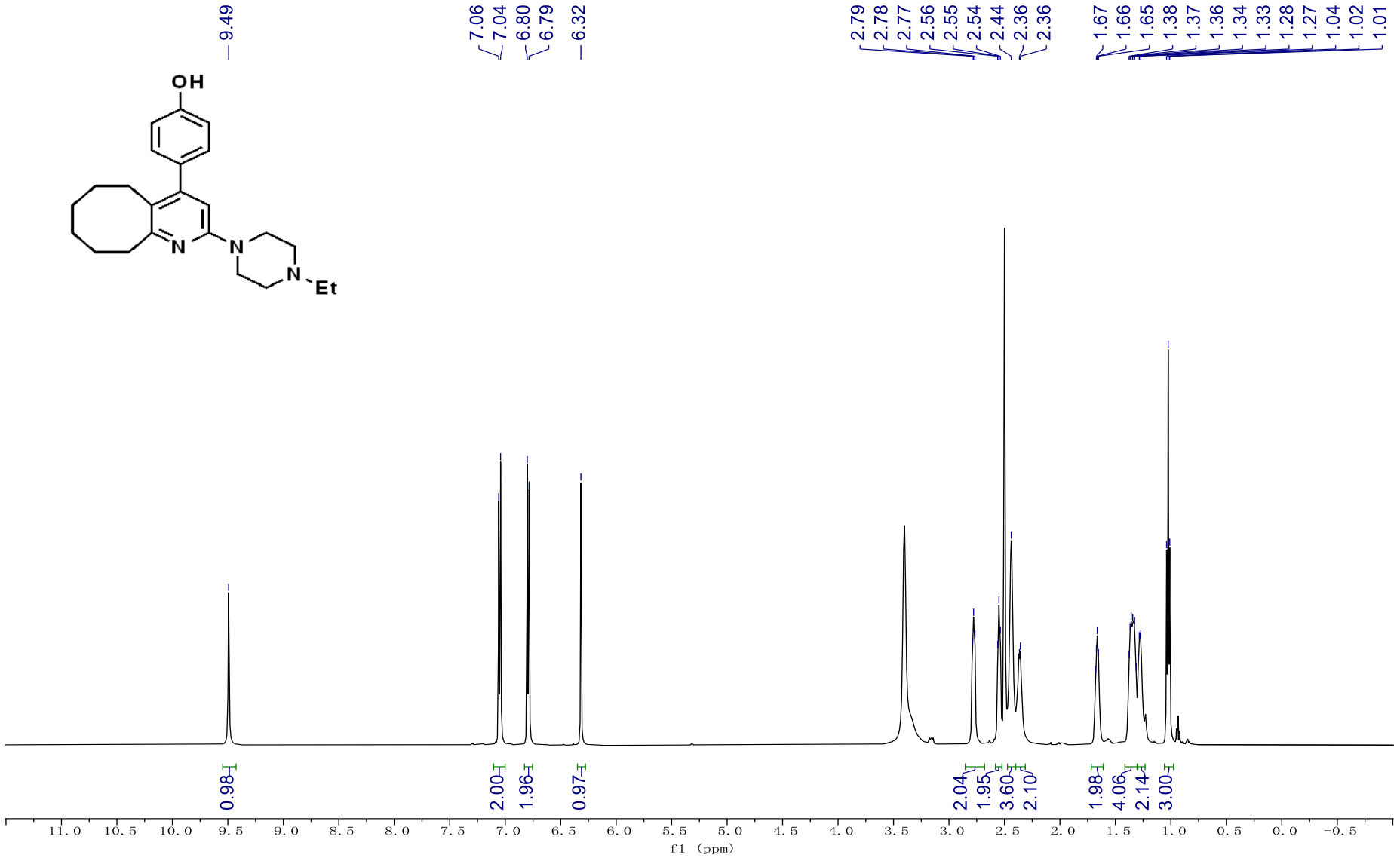
^{13}C NMR Phenol 59

DMSO-d_6, 23 °C



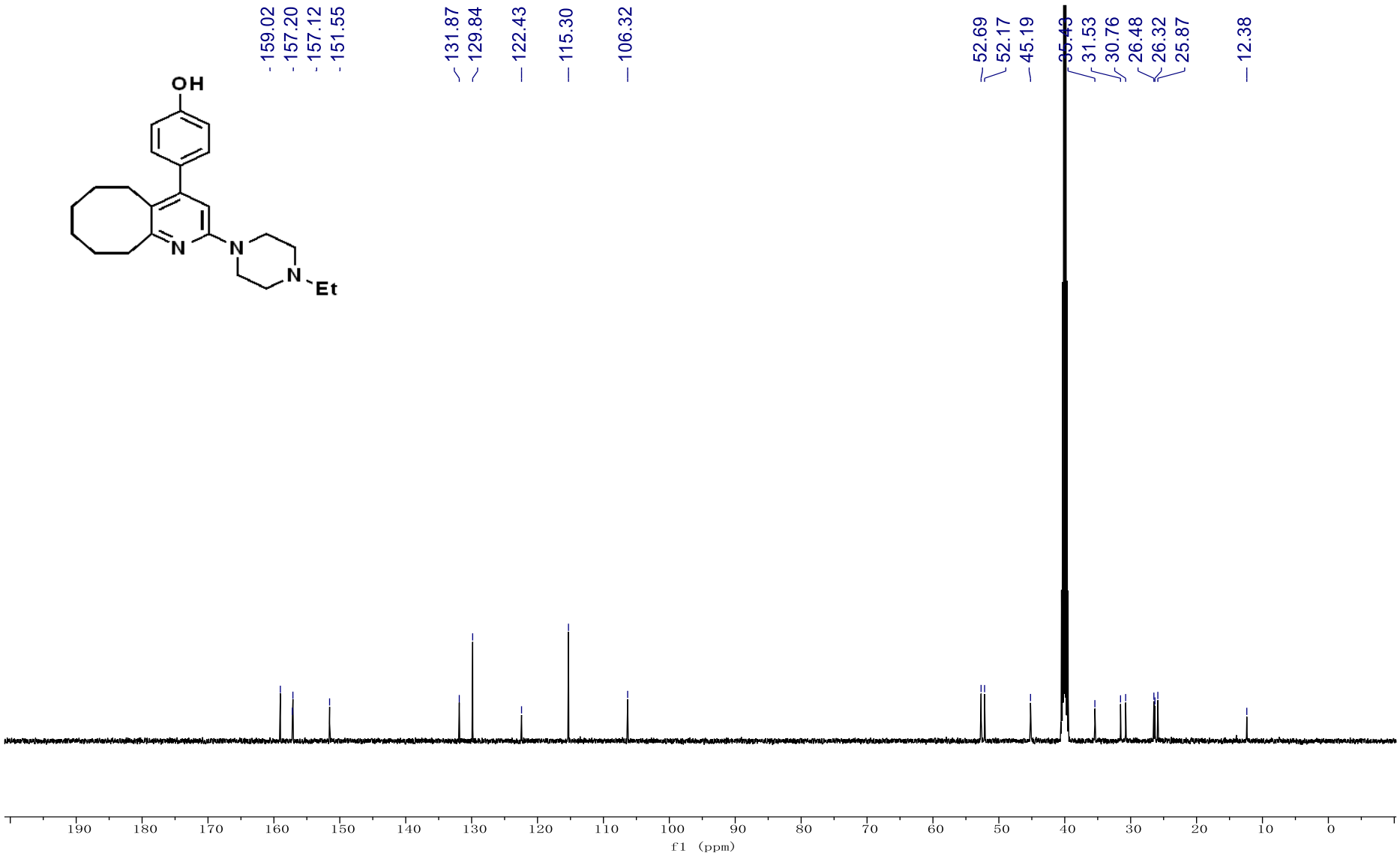
^{1}H NMR of Phenol 60

DMSO-d_6, 23 °C



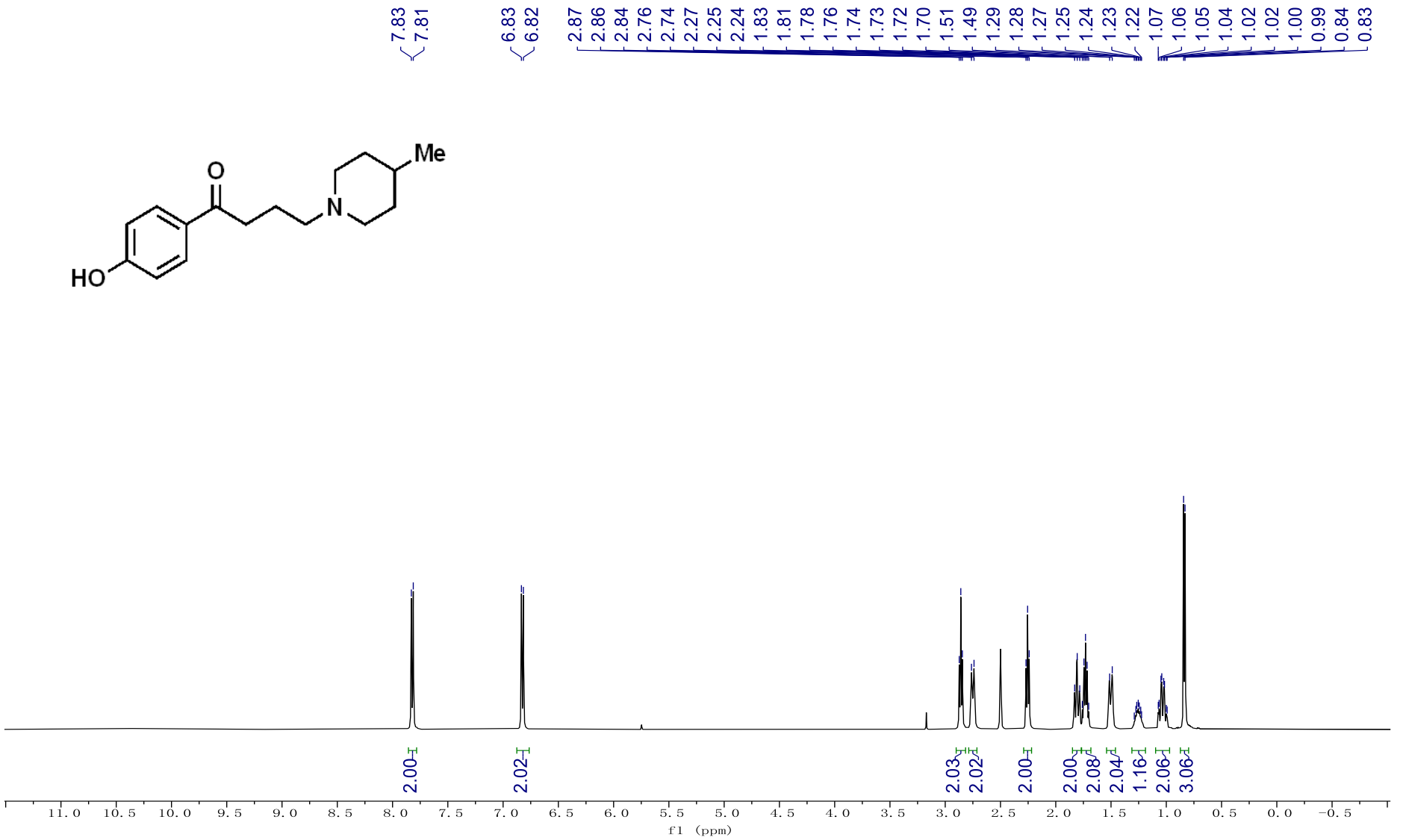
^{13}C NMR of Phenol 60

DMSO-d_6, 23 °C



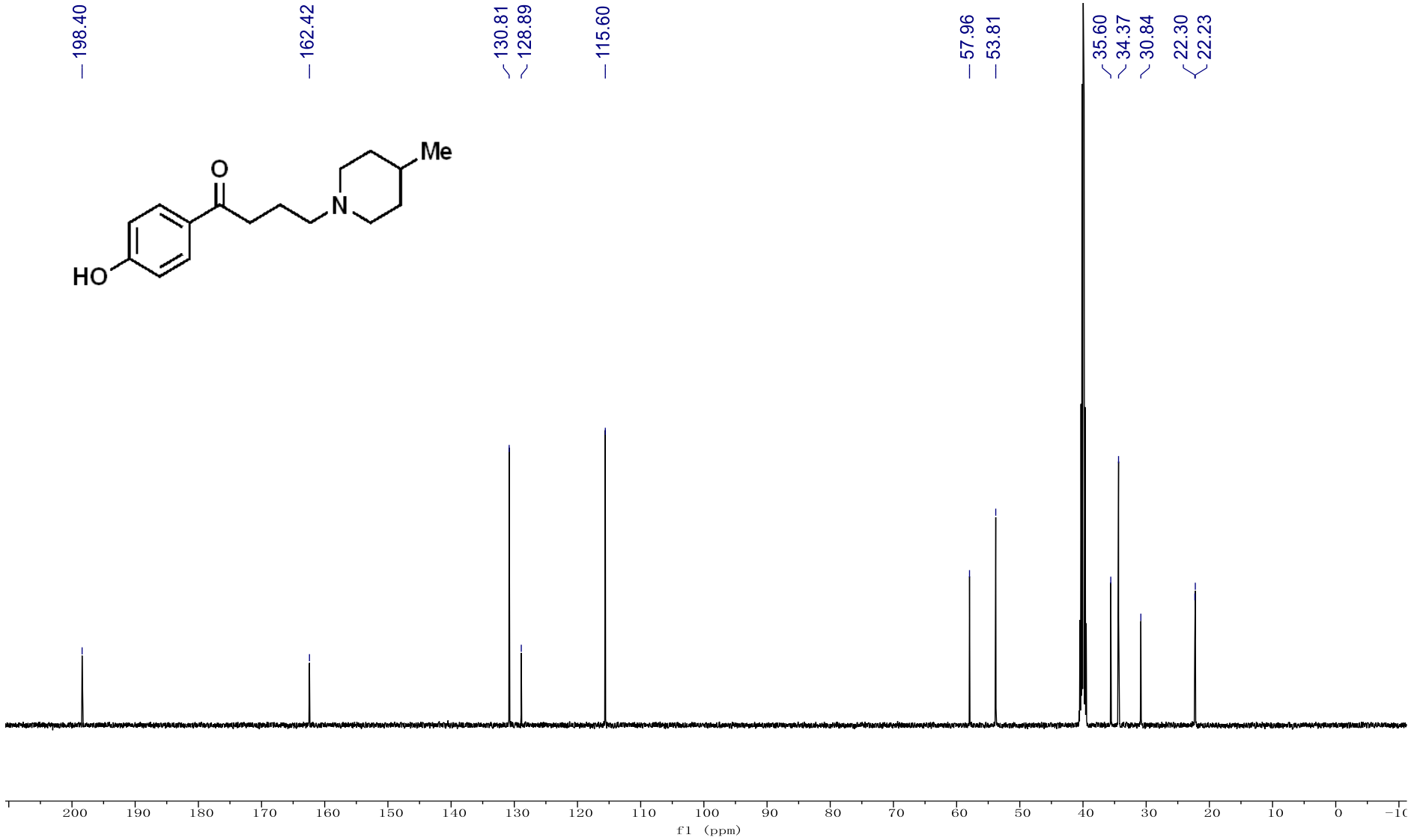
^{1}H NMR of Phenol 61

DMSO-d_6, 23 °C



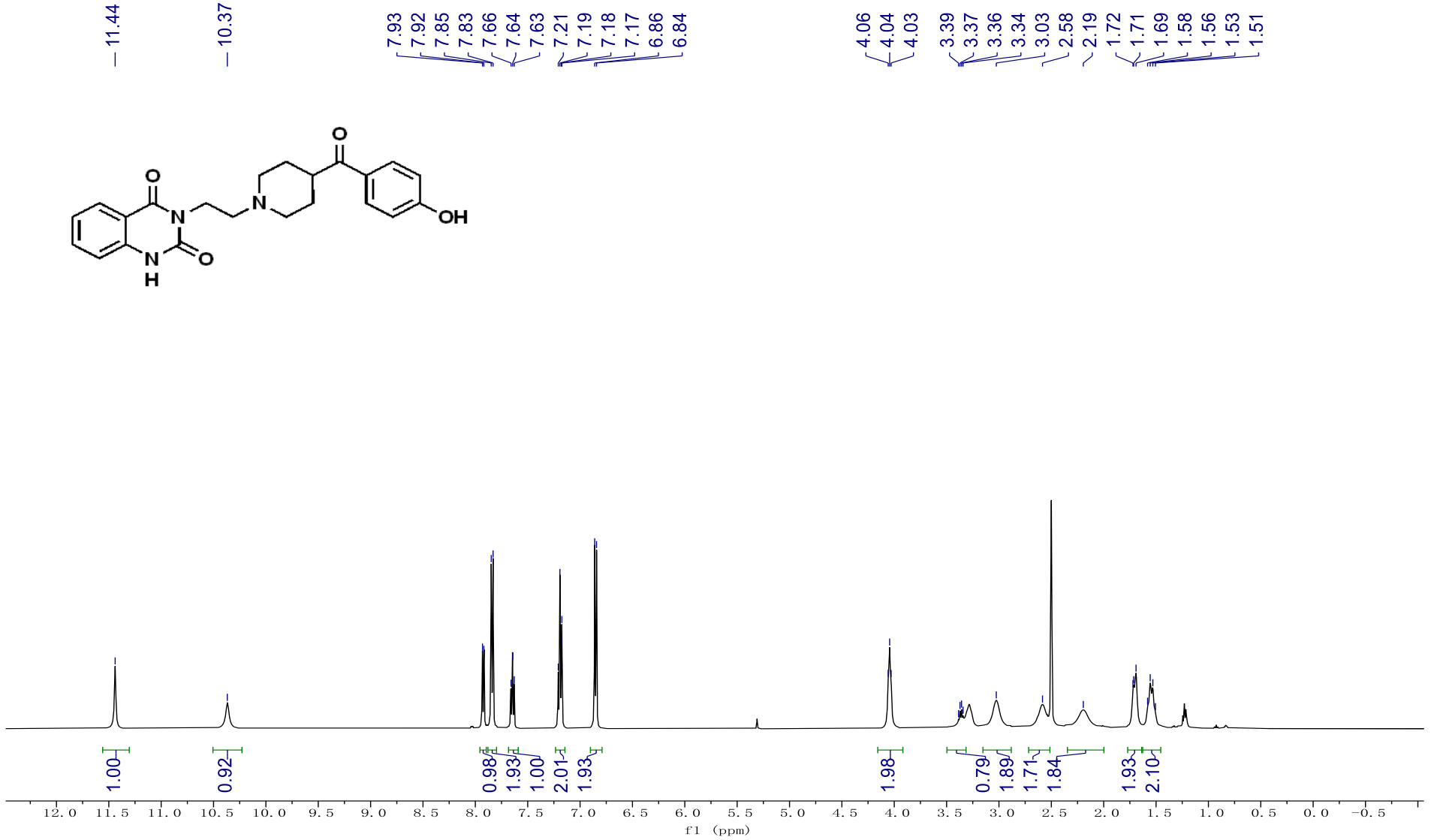
^{13}C NMR of Phenol 61

DMSO-d_6, 23 °C



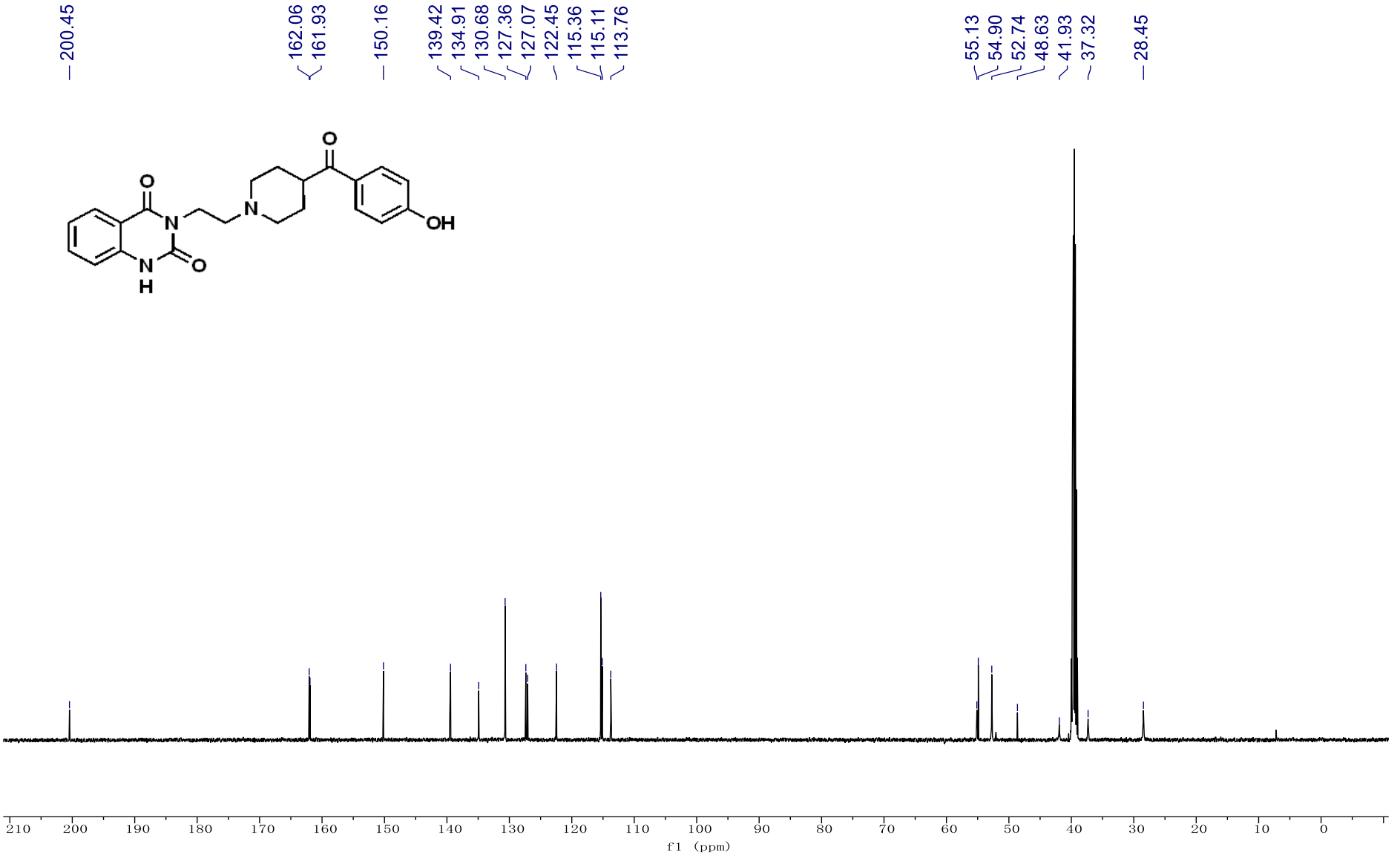
^{1}H NMR of Phenol 62

DMSO-d_6, 23 °C



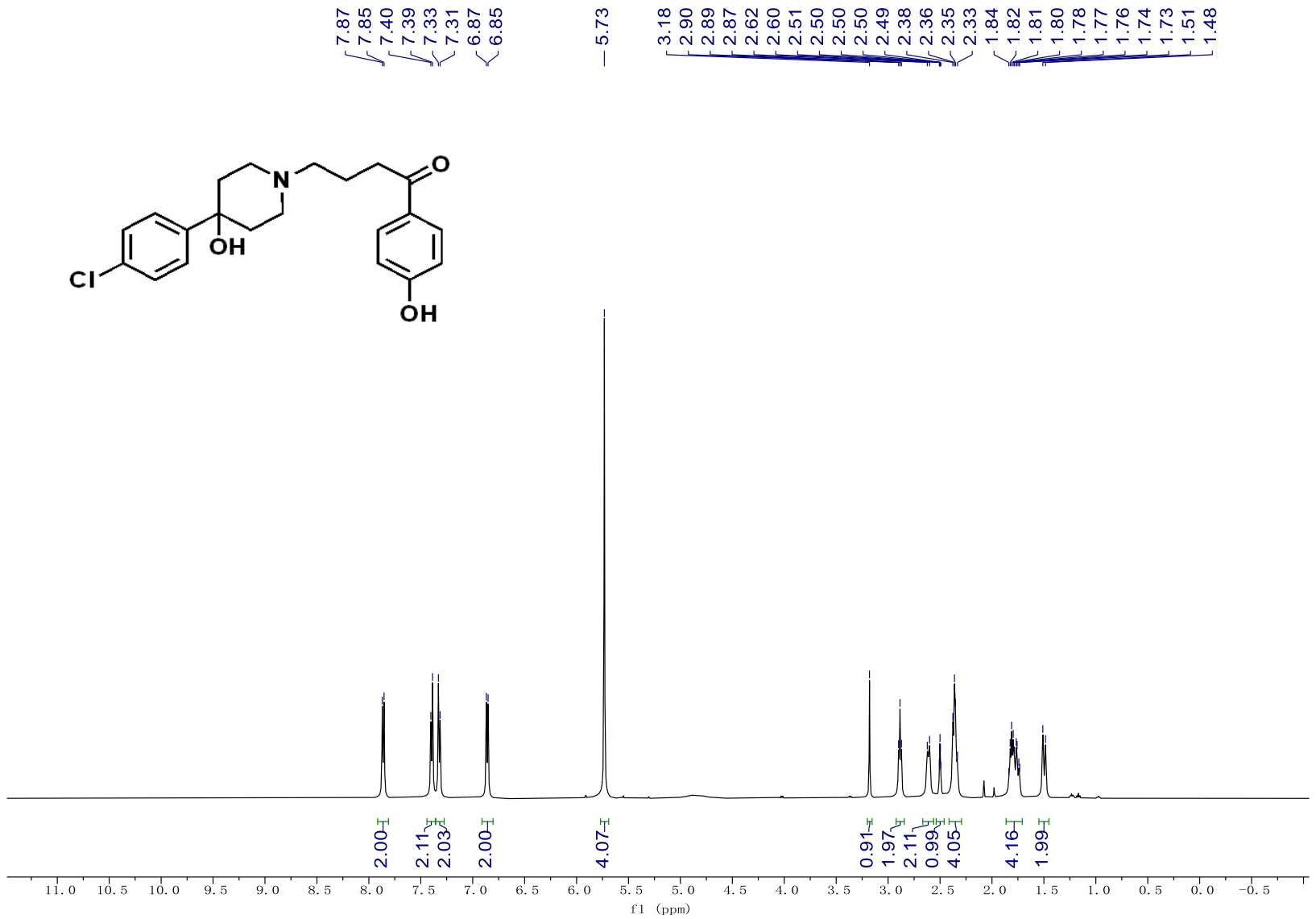
^{13}C NMR of Phenol 62

DMSO-d_6, 23 °C



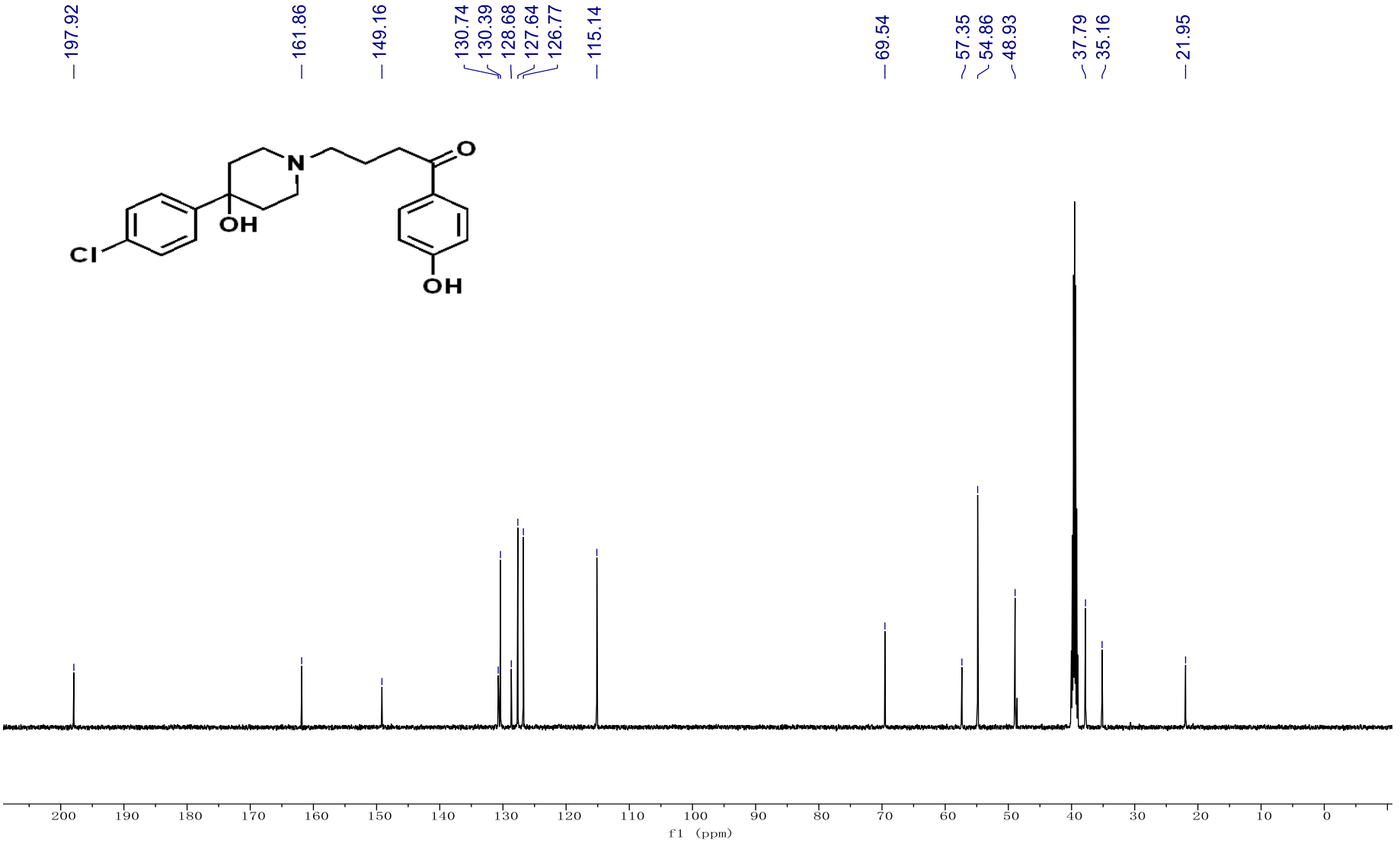
^{1}H NMR of Phenol 63

DMSO-d_6, 23 °C



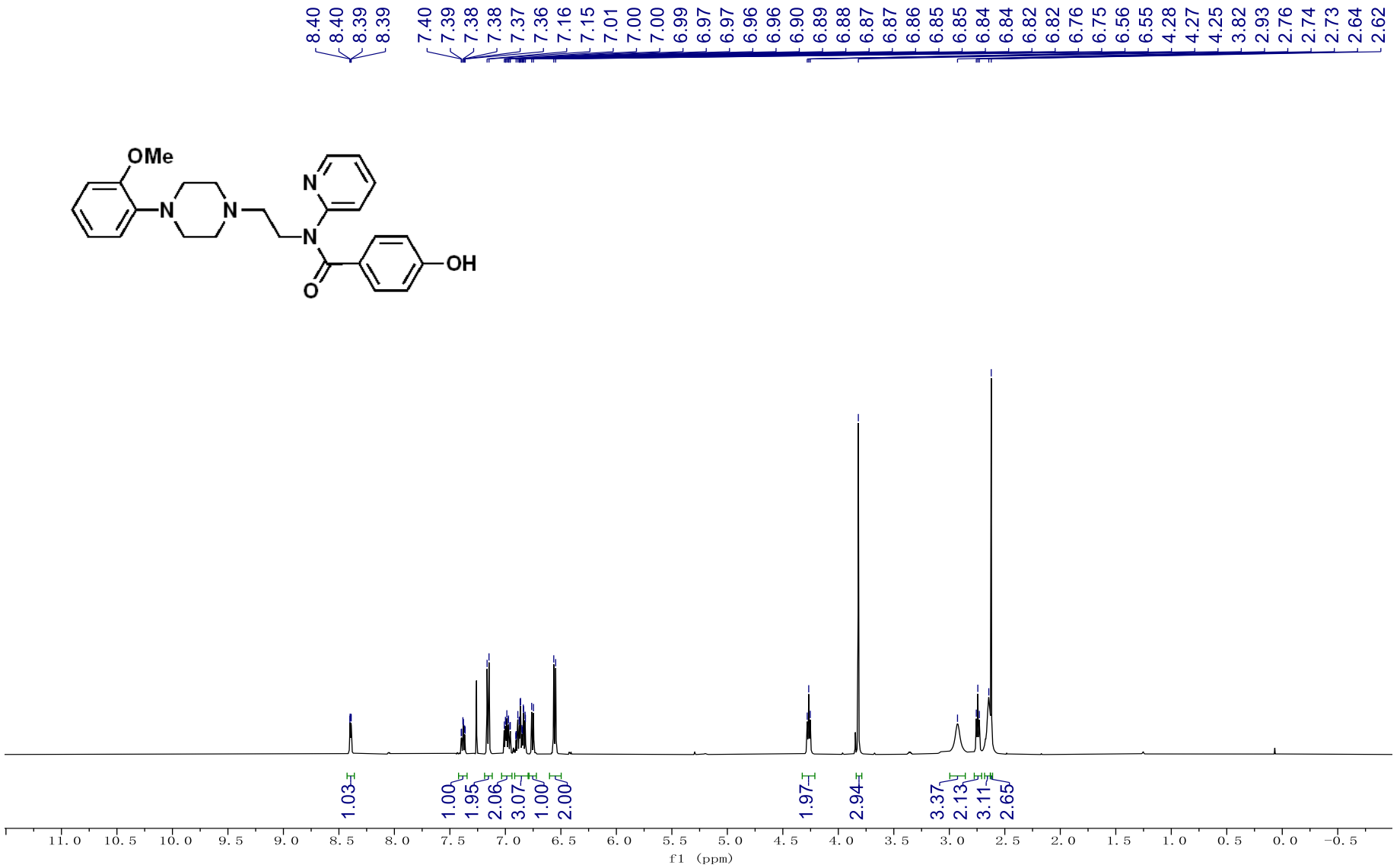
^{13}C NMR of Phenol 63

DMSO-d_6, 23 °C



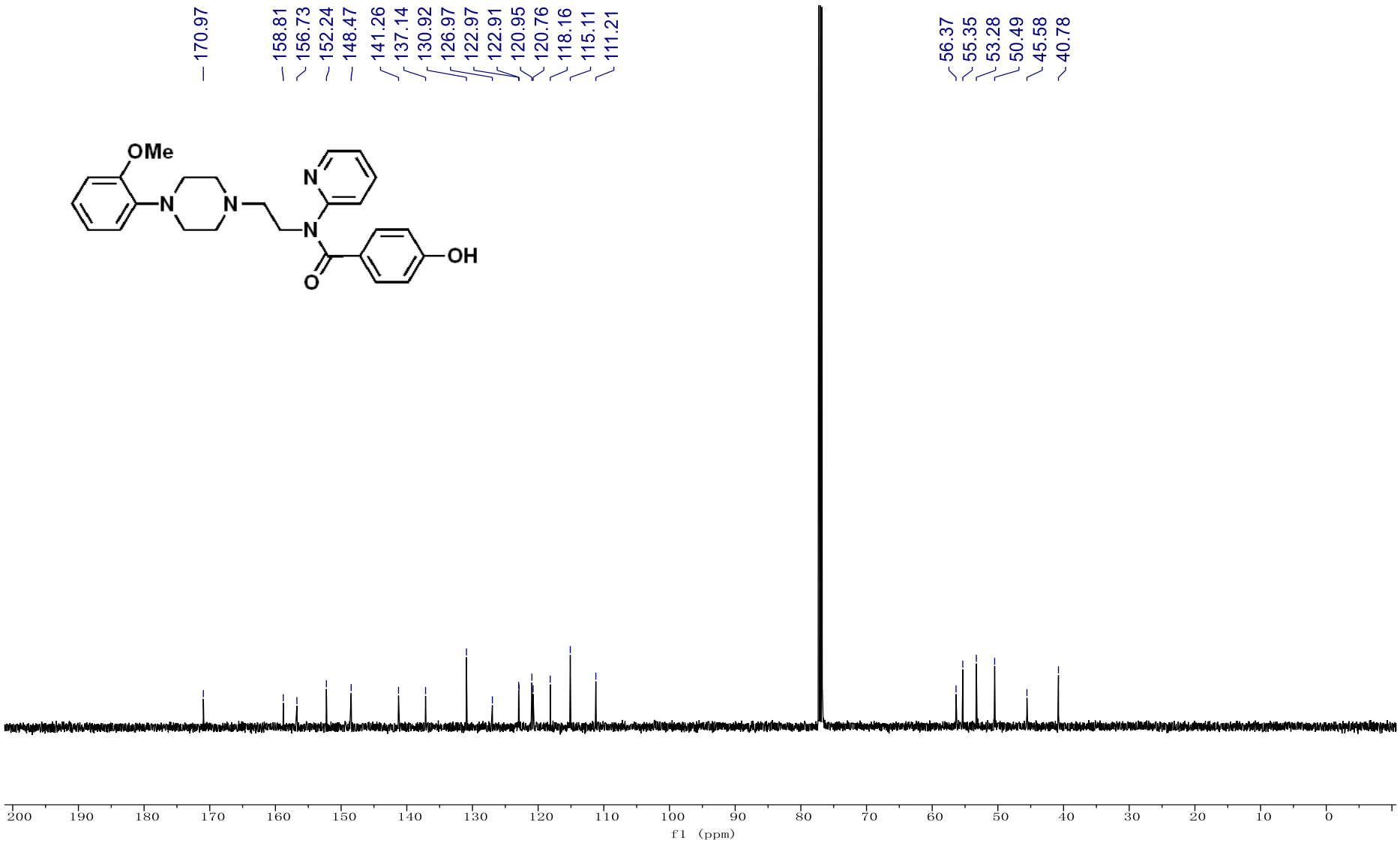
^{1}H NMR of Phenol 64

$CDCl_3$, 23 °C



^{13}C NMR of Phenol 64

$CDCl_3$, 23 °C



V. REFERENCES

(1) Roth, H. D. The Beginnings of Organic Photochemistry. *Angew. Chem. Int. Ed. Engl.* **1989**, *28* (9), 1193–1207.

(2) Barber, J. Photosynthetic Energy Conversion: Natural and Artificial. *Chem. Soc. Rev.* **2009**, *38* (1), 185–196.

(3) Scheele, C. W. *Chemische Abhandlung von der Luft und dem Feuer*; Magn. Swederus: Uppsala, Leipzig, **1777**.

(4) Grotthuss, T. V. Über die chemische Wirksamkeit des Lichts und der Electricität. *Ann. Phys.* **1819,** *61*, 50–74.

(5) Draper, J. W. On some analogies between the phenomena of the chemical rays, and those of radiant heat. *Philos. Mag.* **1841,** *19*, 195–210.

(6) Ciamician, G.; Silber, P. Chemische Lichtwirkungen. *Ber. Dtsch. Chem. Ges.* **1907,** *40*, 2415–2424.

(7) Ciamician, G.; Silber, P. Chemische Lichtwirkungen. *Ber. Dtsch. Chem. Ges.* **1903,** *36*, 4266–4272.

(8) Ciamician, G.; Silber, P. Chemische Lichtwirkungen. XVIII. *Ber. Dtsch. Chem. Ges.* **1910,** *43*, 1536–1541.

(9) Ciamician, G.; Silber, P. Chemische Lichtwirkungen. *Ber. Dtsch. Chem. Ges.* **1903,** *36*, 1575–1583.

(10) Schramm, J. Ueber den Einfluss des Lichtes auf den Verlauf chemischer Reaktionen bei der Einwirkung der Halogene auf aromatische Verbindungen. *Ber. Dtsch. Chem. Ges.* **1885,** *18*, 606–609.

(11) Perkin, W. H. LVIII.—On the isomeric acids obtained from coumarin and the ethers of hydride of salicyl. *J. Chem. Soc.* **1881,** *39*, 409–452.

(12) Fritzsche, C. J. Über die festen Kohlenwasserstoffe des Steinkohlentheers. *J. Prakt. Chem.* **1867,** *101*, 333–343.

(13) Liebermann, C. T. Über Polythymochinon. *Ber. Dtsch. Chem. Ges.* **1877,** *10*, 2177–2179.

(14) Draper, J. W. On some analogies between the phenomena of the chemical rays, and those of radiant heat. *Philos. Mag.* **1841,** *19*, 195–210.

(15) Stern, O.; Volmer, M. Bemerkungen zum photochemischen Äquivalentgesetz vom Standpunkt der Bohr-Einsteinschen Auffassung der Lichtabsorption. *Z. Wiss. Photogr. Photophys. Photochem.* **1920,** *19*, 275–287.

(16) Einstein, A. Strahlungs-Emission und -Absorption nach der Quantentheorie. *Verh. Dtsch. Phys. Ges.* **1916,** *18*, 318–323.

(17) Ciamician, G.; Silber, P. Chemische Lichtwirkungen. *Ber. Dtsch. Chem. Ges.* **1901,** *34*, 2040–2046.

(18) Ciamician, G.; Silber, P. Chemische Lichtwirkungen. *Ber. Dtsch. Chem. Ges.* **1908,** *41*, 1928–1935.

(19) Ciamician, G.; Silber, P. Chemische Lichtwirkungen. XX. *Ber. Dtsch. Chem. Ges.* **1911,** *44*, 1554–1558.

(20) GCiamician, G.; Silber, P. Chemische Lichtwirkungen. XXVII. Autooxydationen V. *Ber. Dtsch. Chem. Ges.* **1913,** *46*, 3077–3084.

(21) Norrish, R. G. W. Photochemistry and Absorption Spectrum of Acetone. *Nature* **1934**, *133* (3370), 837–837.

(22) Ciamician, G.; Silber, P. Chemische Lichtwirkungen. XXXIII. *Ber. Dtsch. Chem. Ges.* **1915,** *48*, 190–195.

(23) Ciamician, G. The Photochemistry of the Future. *Science* **1912**, *36* (926), 385–394.

(24) Turro, N. J.; Ramamurthy, V.; Scaiano, J. C. *Modern Molecular Photochemistry of Organic Molecules*, 1st ed.; University Science Books: Mill Valley, CA, 2010; p 1053.

(25) Klán, P.; Wirz, J. A crash course in photophysics and a classification of primary photoreactions. In *Photochemistry of Organic Compounds*; Wiley-Blackwell: Oxford, 2009; pp 25–72.

(26) Turro, N. J.; Schuster, G. Photochemical reactions as a tool in organic syntheses. *Science* **1975,** *187*, 303–312.

(27) Skubi, K. L.; Blum, T. R.; Yoon, T. P. Dual Catalysis Strategies in Photochemical Synthesis. *Chem. Rev.* **2016**, *116* (17), 10035–10074.

(28) König, B. Photocatalysis in Organic Synthesis – Past, Present, and Future. *Eur J Org Chem* **2017**, *2017* (15), 1979–1981.

(29) Prier, C. K.; Rankic, D. A.; MacMillan, D. W. C. Visible Light Photoredox Catalysis with Transition Metal Complexes: Applications in Organic Synthesis. *Chem. Rev.* **2013**, *113* (7), 5322–5363.
(30) Goti, G.; Manal, K.; Sivaguru, J.; Dell'Amico, L. The Impact of UV Light on Synthetic Photochemistry and Photocatalysis. *Nat. Chem.* **2024**, *16* (5), 684–692.
(31) Beeler, A. B. Introduction: Photochemistry in Organic Synthesis. *Chem. Rev.* **2016**, *116* (17), 9629–9630.
(32) Klán, P.; Wirz, J. Chemistry of excited molecules. In *Photochemistry of Organic Compounds*; Wiley-Blackwell: Oxford, 2009; pp 227–453.
(33) Turro, N. J.; Dalton, J. C.; Dawes, K.; Farrington, G.; Hautala, R.; Morton, D.; Niemczyk, M.; Schore, N. Molecular photochemistry of alkanones in solution: α-cleavage, hydrogen abstraction, cycloaddition, and sensitization reactions. *Acc. Chem. Res.* **1972,** *5*, 92–101.
(34) Kropp, P. J. Photochemistry of Alkenes in Solution. *Pure and Applied Chemistry* **1970**, *24* (3), 585–598.
(35) Melchiorre, P. Introduction: Photochemical Catalytic Processes. *Chem. Rev.* **2022**, *122* (2), 1483–1484.
(36) Kozlowski, M.; Yoon, T. Editorial for the Special Issue on Photocatalysis. *J. Org. Chem.* **2016**, *81* (16), 6895–6897.
(37) Klessinger, M.; Michl, J. *Excited States and Photochemistry of Organic Molecules*; VCH: New York, 1995; p 564.
(38) Balzani, V.; Campagna, S. *Photochemistry and Photophysics of Coordination Compounds I*. *Top. Curr. Chem.* **2007,** *280*; Springer: Berlin, Heidelberg.
(39) Juris, A.; Balzani, V.; Barigelletti, F.; Campagna, S.; Belser, P.; Von Zelewsky, A. Ru(II) Polypyridine Complexes: Photophysics, Photochemistry, Eletrochemistry, and Chemiluminescence. *Coordination Chemistry Reviews* **1988**, *84*, 85–277.
(40) Arias-Rotondo, D. M.; McCusker, J. K. The Photophysics of Photoredox Catalysis: A Roadmap for Catalyst Design. *Chem. Soc. Rev.* **2016**, *45* (21), 5803–5820.
(41) Twilton, J.; Le, C.; Zhang, P.; Shaw, M. H.; Evans, R. W.; MacMillan, D. W. C. The merger of transition metal and photocatalysis. *Nat. Rev. Chem.* **2017,** *1*, 0052.
(42) Reischauer, S.; Pieber, B. Emerging concepts in photocatalytic organic synthesis. *iScience* **2021,** *24*, 102209.
(43) Cheung, K. P. S.; Sarkar, S.; Gevorgyan, V. Visible light-induced transition metal catalysis. *Chem. Rev.* **2022,** *122*, 1543–1625.
(44) Strieth-Kalthoff, F.; James, M. J.; Teders, M.; Pitzer, L.; Glorius, F. Energy transfer catalysis mediated by visible light: principles, applications, directions. *Chem. Soc. Rev.* **2018,** *47*, 7190–7202.
(45) Capaldo, L.; Quadri, L. L.; Ravelli, D. Photocatalytic hydrogen atom transfer: the philosopher's stone for late-stage functionalization? *Green Chem.* **2020,** *22*, 3376–3396.
(46) Gentry, E. C.; Knowles, R. R. Synthetic applications of proton-coupled electron transfer. *Acc. Chem. Res.* **2016,** *49*, 1546–1556.
(47) Chan, A. Y.; Perry, I. B.; Bissonnette, N. B.; Buksh, B. F.; Edwards, G. A.; Frye, L. I.; Garry, O. L.; Lavagnino, M. N.; Li, B. X.; Liang, Y.; Mao, E.; Millet, A.; Oakley, J. V.; Reed, N. L.; Sakai, H. A.; Seath, C. P.; MacMillan, D. W. C. Metallaphotoredox: the merger of photoredox and transition metal catalysis. *Chem. Rev.* **2022,** *122*, 1485–1542.
(48) Chuentragool, P.; Kurandina, D.; Gevorgyan, V. Catalysis with palladium complexes photoexcited by visible light. *Angew. Chem. Int. Ed.* **2019,** *58*, 11586–11598.
(49) Sarkar, S.; Cheung, K. P. S.; Gevorgyan, V. Recent advances in visible light induced palladium catalysis. *Angew. Chem. Int. Ed.* **2024,** *63*, e202311972.
(50) Hedstrand, D. M.; Kruizinga, W. H.; Kellogg, R. M. Light induced and dye accelerated reductions of phenacyl onium salts by 1,4-dihydropyridines. *Tetrahedron Lett.* **1978,** *19*, 1255–1258.
(51) Cano-Yelo, H.; Deronzier, A. Photocatalysis of the Pschorr reaction by tris-(2,2′-bipyridyl)ruthenium(II) in the phenanthrene series. *J. Chem. Soc., Perkin Trans. 2* **1984,** 1093–1098.
(52) Fukuzumi, S.; Mochizuki, S.; Tanaka, T. Photocatalytic reduction of phenacyl halides by 9,10-dihydro-10-methylacridine: control between the reductive and oxidative quenching pathways of tris(bipyridine)ruthenium complex utilizing an acid catalysis. *J. Phys. Chem.* **1990,** *94*, 722–726.
(53) Okada, K.; Okamoto, K.; Morita, N.; Okubo, K.; Oda, M. Photosensitized decarboxylative Michael

addition through N-(acyloxy)phthalimides via an electron-transfer mechanism. *J. Am. Chem. Soc.* **1991,** *113*, 9401–9402.

(54) Shaw, M. H.; Twilton, J.; MacMillan, D. W. C. Photoredox catalysis in organic chemistry. *J. Org. Chem.* **2016,** *81*, 6898–6926.

(55) Nicewicz, D. A.; MacMillan, D. W. C. Merging photoredox catalysis with organocatalysis: the direct asymmetric alkylation of aldehydes. *Science* **2008,** *322*, 77–80.

(56) Ischay, M. A.; Anzovino, M. E.; Du, J.; Yoon, T. P. Efficient visible light photocatalysis of [2+2] enone cycloadditions. *J. Am. Chem. Soc.* **2008,** *130*, 12886–12887.

(57) Narayanam, J. M. R.; Tucker, J. W.; Stephenson, C. R. J. Electron-transfer photoredox catalysis: development of a tin-free reductive dehalogenation reaction. *J. Am. Chem. Soc.* **2009,** *131*, 8756–8757.

(58) Strieth-Kalthoff, F.; Glorius, F. Triplet energy transfer photocatalysis: unlocking the next level. *Chem* **2020,** *6*, 1888–1903.

(59) Grutsch, P. A.; Kutal, C. Charge-transfer sensitization of the valence photoisomerization of norbornadiene to quadricyclene by an orthometalated transition-metal complex. *J. Am. Chem. Soc.* **1986,** *108*, 3108–3110.

(60) Lu, Z.; Yoon, T. P. Visible light photocatalysis of [2+2] styrene cycloadditions by energy transfer. *Angew. Chem. Int. Ed.* **2012,** *51*, 10329–10332.

(61) Singh, K.; Staig, S. J.; Weaver, J. D. Facile synthesis of *Z*-alkenes via uphill catalysis. *J. Am. Chem. Soc.* **2014,** *136*, 5275–5278.

(62) Metternich, J. B.; Gilmour, R. A bio-inspired, catalytic E → Z isomerization of activated olefins. *J. Am. Chem. Soc.* **2015,** *137*, 11254–11257.

(63) Dutta, S.; Erchinger, J. E.; Strieth-Kalthoff, F.; Kleinmans, R.; Glorius, F. Energy transfer photocatalysis: exciting modes of reactivity. *Chem. Soc. Rev.* **2024,** *53*, 1068–1089.

(64) Kleinmans, R.; Pinkert, T.; Dutta, S.; Paulisch, T. O.; Keum, H.; Daniliuc, C. G.; Glorius, F. Intermolecular [2π+2σ]-photocycloaddition enabled by triplet energy transfer. *Nature* **2022,** *605*, 477–482.

(65) Cai, Y.; Roy, T. K.; Zähringer, T. J. B.; Lansbergen, B.; Kerzig, C.; Ritter, T. Arylthianthrenium salts for triplet energy transfer catalysis. *J. Am. Chem. Soc.* **2024,** *146*, 30474–30482.

(66) Murray, P. R. D.; Cox, J. H.; Chiappini, N. D.; Roos, C. B.; McLoughlin, E. A.; Hejna, B. G.; Nguyen, S. T.; Ripberger, H. H.; Ganley, J. M.; Tsui, E.; Shin, N. Y.; Koronkiewicz, B.; Qiu, G.; Knowles, R. R. Photochemical and electrochemical applications of proton-coupled electron transfer in organic synthesis. *Chem. Rev.* **2022,** *122*, 2017–2291.

(67) Capaldo, L.; Ravelli, D.; Fagnoni, M. Direct photocatalyzed hydrogen atom transfer (HAT) for aliphatic C–H bonds elaboration. *Chem. Rev.* **2022,** *122*, 1875–1924.

(68) Capaldo, L.; Ravelli, D. Hydrogen atom transfer (HAT): a versatile strategy for substrate activation in photocatalyzed organic synthesis. *Eur. J. Org. Chem.* **2017,** *2017*, 2056–2071.

(69) Ganley, J. M.; Murray, P. R. D.; Knowles, R. R. Photocatalytic generation of aminium radical cations for C–N bond formation. *ACS Catal.* **2020,** *10*, 11712–11738.

(70) Dherange, B. D.; Yuan, M.; Kelly, C. B.; Reiher, C. A.; Grosanu, C.; Berger, K. J.; Gutierrez, O.; Levin, M. D. Direct deaminative functionalization. *J. Am. Chem. Soc.* **2023,** *145*, 17–24.

(71) Tarantino, K. T.; Liu, P.; Knowles, R. R. Catalytic ketyl-olefin cyclizations enabled by proton-coupled electron transfer. *J. Am. Chem. Soc.* **2013,** *135*, 10022–10025.

(72) Rono, L. J.; Yayla, H. G.; Wang, D. Y.; Armstrong, M. F.; Knowles, R. R. Enantioselective photoredox catalysis enabled by proton-coupled electron transfer: development of an asymmetric aza-pinacol cyclization. *J. Am. Chem. Soc.* **2013,** *135*, 17735–17738.

(73) Parasram, M.; Chuentragool, P.; Sarkar, D.; Gevorgyan, V. Photoinduced formation of hybrid aryl Pd-radical species capable of 1,5-HAT: selective catalytic oxidation of silyl ethers into silyl enol ethers. *J. Am. Chem. Soc.* **2016,** *138*, 6340–6343.

(74) DiRocco, D. A.; Rovis, T. Catalytic asymmetric α-acylation of tertiary amines mediated by a dual catalysis mode: N-heterocyclic carbene and photoredox catalysis. *J. Am. Chem. Soc.* **2012,** *134*, 8094–8097.

(75) Pirnot, M. T.; Rankic, D. A.; Martin, D. B. C.; MacMillan, D. W. C. Photoredox activation for the direct β-arylation of ketones and aldehydes. *Science* **2013,** *339*, 1593–1596.

(76) Du, J.; Skubi, K. L.; Schultz, D. M.; Yoon, T. P. A dual-catalysis approach to enantioselective [2+2] photocycloadditions using visible light. *Science* **2014,** *344*, 392–396.
(77) Tyson, E. L.; Niemeyer, Z. L.; Yoon, T. P. Redox mediators in visible light photocatalysis: photocatalytic radical thiol–ene additions. *J. Org. Chem.* **2014,** *79*, 1427–1436.
(78) Zuo, Z.; Ahneman, D. T.; Chu, L.; Terrett, J. A.; Doyle, A. G.; MacMillan, D. W. C. Merging photoredox with nickel catalysis: coupling of α-carboxyl sp3-carbons with aryl halides. *Science* **2014,** *345*, 437–440.
(79) Kalyani, D.; McMurtrey, K. B.; Neufeldt, S. R.; Sanford, M. S. Room-temperature C–H arylation: merger of Pd-catalyzed C–H functionalization and visible-light photocatalysis. *J. Am. Chem. Soc.* **2011,** *133*, 18566–18569.
(80) Johansson Seechurn, C. C. C.; Kitching, M. O.; Colacot, T. J.; Snieckus, V. Palladium-catalyzed cross-coupling: a historical contextual perspective to the 2010 Nobel Prize. *Angew. Chem. Int. Ed.* **2012,** *51*, 5062–5085.
(81) Banerjee, S.; Chakrabarti, S.; Bouley, B. S.; Wahlmeier, A. J.; Mirica, L. M. Mononuclear palladium(I) and palladium(III) coordination compounds. *Coord. Chem. Rev.* **2025,** *535*, 216605.
(82) Rudolph, A.; Lautens, M. Secondary alkyl halides in transition-metal-catalyzed cross-coupling reactions. *Angew. Chem. Int. Ed.* **2009,** *48*, 2656–2670.
(83) Scheffold, R.; Orlinski, R. Synthesis and reactions of porphine-type metal complexes. 15. Carbon–carbon bond formation by light assisted B12-catalysis. Nucleophilic acylation of Michael olefins. *J. Am. Chem. Soc.* **1983,** *105*, 7200–7202.
(84) Weiss, M. E.; Kreis, L. M.; Lauber, A.; Carreira, E. M. Cobalt-catalyzed coupling of alkyl iodides with alkenes: deprotonation of hydridocobalt enables turnover. *Angew. Chem. Int. Ed.* **2011,** *50*, 11125–11128.
(85) Kreis, L. M.; Krautwald, S.; Pfeiffer, N.; Martin, R. E.; Carreira, E. M. Photocatalytic synthesis of allylic trifluoromethyl substituted styrene derivatives in batch and flow. *Org. Lett.* **2013,** *15*, 1634–1637.
(86) Ravetz, B. D.; Wang, J. Y.; Ruhl, K. E.; Rovis, T. Photoinduced ligand-to-metal charge transfer enables photocatalyst-independent light-gated activation of Co(II). *ACS Catal.* **2019,** *9*, 200–204.
(87) Li, Z.; Wang, X.; Xia, S.; Jin, J. Ligand-accelerated iron photocatalysis enabling decarboxylative alkylation of heteroarenes. *Org. Lett.* **2019,** *21*, 4259–4265.
(88) Huang, L.; Rudolph, M.; Rominger, F.; Hashmi, A. S. K. Photosensitizer-free visible-light-mediated gold-catalyzed 1,2-difunctionalization of alkynes. *Angew. Chem. Int. Ed.* **2016,** *55*, 4808–4813.
(89) Lei, W.-L.; Wang, T.; Feng, K.-W.; Wu, L.-Z.; Liu, Q. Visible-light-driven synthesis of 4-alkyl/aryl-2-aminothiazoles promoted by in situ generated copper photocatalyst. *ACS Catal.* **2017,** *7*, 7941–7945.
(90) Xu, P.; López-Rojas, P.; Ritter, T. Radical decarboxylative carbometalation of benzoic acids: a solution to aromatic decarboxylative fluorination. *J. Am. Chem. Soc.* **2021,** *143*, 5349–5354.
(91) Su, W.; Xu, P.; Ritter, T. Decarboxylative hydroxylation of benzoic acids. *Angew. Chem. Int. Ed.* **2021,** *60*, 24012–24017.
(92) Shields, B. J.; Kudisch, B.; Scholes, G. D.; Doyle, A. G. Long-lived charge-transfer states of nickel(II) aryl halide complexes facilitate bimolecular photoinduced electron transfer. *J. Am. Chem. Soc.* **2018,** *140*, 3035–3039.
(93) Ting, S. I.; Garakyaraghi, S.; Taliaferro, C. M.; Shields, B. J.; Scholes, G. D.; Castellano, F. N.; Doyle, A. G. 3d-d excited states of Ni(II) complexes relevant to photoredox catalysis: spectroscopic identification and mechanistic implications. *J. Am. Chem. Soc.* **2020,** *142*, 5800–5810.
(94) Caspar, J. V. Long-lived reactive excited states of zero-valent phosphine, phosphite, and arsine complexes of nickel, palladium and platinum. *J. Am. Chem. Soc.* **1985,** *107*, 6718–6719.
(95) Harvey, P. D.; Gray, H. B. Low-lying singlet and triplet electronic excited states of binuclear (d^{10}-d^{10}) palladium(0) and platinum(0) complexes. *J. Am. Chem. Soc.* **1988,** *110*, 2145–2147.
(96) Harvey, P. D.; Schaefer, W. P.; Gray, H. B. Emission properties of tetrahedral bis[bis(diphenylphosphino)propane]palladium and -platinum complexes. Crystal and molecular structure of $Pt(dppp)_2$. *Inorg. Chem.* **1988,** *27*, 1101–1104.
(97) Kakizoe, D.; Nishikawa, M.; Ohkubo, T.; Sanga, M.; Iwamura, M.; Nozaki, K.; Tsubomura, T. Photophysical properties of simple palladium(0) complexes bearing triphenylphosphine derivatives. *Inorg. Chem.* **2021,** *60*, 9516–9528.
(98) Fredricks, M. A.; Drees, M.; Köhler, K. Acceleration of the rate of the Heck reaction through UV- and

visible-light-induced palladium(II) reduction. *ChemCatChem* **2010,** *2*, 1467–1476.

(99) Abdiaj, I.; Huck, L.; Mateo, J. M.; de la Hoz, A.; Gomez, M. V.; Díaz-Ortiz, A.; Alcázar, J. Photoinduced palladium-catalyzed Negishi cross-couplings enabled by the visible-light absorption of palladium–zinc complexes. *Angew. Chem. Int. Ed.* **2018,** *57*, 13231–13236.

(100) Kurandina, D.; Parasram, M.; Gevorgyan, V. Visible light-induced room-temperature Heck reaction of functionalized alkyl halides with vinyl arenes/heteroarenes. *Angew. Chem. Int. Ed.* **2017,** *56*, 14212–14216.

(101) Kurandina, D.; Rivas, M.; Radzhabov, M.; Gevorgyan, V. Heck reaction of electronically diverse tertiary alkyl halides. *Org. Lett.* **2018,** *20*, 357–360.

(102) Koy, M.; Sandfort, F.; Tlahuext-Aca, A.; Quach, L.; Daniliuc, C. G.; Glorius, F. Palladium-catalyzed decarboxylative Heck-type coupling of activated aliphatic carboxylic acids enabled by visible light. *Chem. Eur. J.* **2018,** *24*, 4552–4555.

(103) Huang, H.-M.; Bellotti, P.; Pflüger, P. M.; Schwarz, J. L.; Heidrich, B.; Glorius, F. Three-component, interrupted radical Heck/allylic substitution cascade involving unactivated alkyl bromides. *J. Am. Chem. Soc.* **2020,** *142*, 10173–10183.

(104) Cheung, K. P. S.; Kurandina, D.; Yata, T.; Gevorgyan, V. Photoinduced palladium-catalyzed carbofunctionalization of conjugated dienes proceeding via radical-polar crossover scenario: 1,2-aminoalkylation and beyond. *J. Am. Chem. Soc.* **2020,** *142*, 9932–9937.

(105) Bellotti, P.; Koy, M.; Gutheil, C.; Heuvel, S.; Glorius, F. Three-component three-bond forming cascade via palladium photoredox catalysis. *Chem. Sci.* **2021,** *12*, 1810–1817.

(106) Cai, Y.; Gaurav, G.; Ritter, T. 1,4-Aminoarylation of butadienes via photoinduced palladium catalysis. *Angew. Chem. Int. Ed.* **2024,** *63*, e202311250.

(107) Patel, B. A.; Dickerson, J. E.; Heck, R. F. Palladium-catalyzed arylation of conjugated dienes. *J. Org. Chem.* **1978,** *43*, 5018–5020.

(108) O'Connor, J. M.; Stallman, B. J.; Clark, W. G.; Shu, A. Y. L.; Spada, R. E.; Stevenson, T. M.; Dieck, H. A. Some aspects of palladium-catalyzed reactions of aryl and vinylic halides with conjugated dienes in the presence of mild nucleophiles. *J. Org. Chem.* **1983,** *48*, 807–809.

(109) Cioc, R. C.; Ruijter, E.; Orru, R. V. A. Multicomponent reactions: advanced tools for sustainable organic synthesis. *Green Chem.* **2014,** *16*, 2958–2975.

(110) Cheung, K. P. S.; Fang, J.; Mukherjee, K.; Mihranyan, A.; Gevorgyan, V. Asymmetric intermolecular allylic C–H amination of alkenes with aliphatic amines. *Science* **2022,** *378*, 1207–1213.

(111) Trost, B. M. New rules of selectivity: allylic alkylations catalyzed by palladium. *Acc. Chem. Res.* **1980,** *13*, 385–393.

(112) Yang, J.; Wang, P.; Neumann, H.; Jackstell, R.; Beller, M. Industrially applied and relevant transformations of 1,3-butadiene using homogeneous catalysts. *Ind. Chem. Mater.* **2023,** *1*, 155–174.

(113) Faßbach, T. A.; Vorholt, A. J.; Leitner, W. The telomerization of 1,3-dienes – a reaction grows up. *ChemCatChem* **2019,** *11*, 1153–1166.

(114) Huang, H.-M.; Koy, M.; Serrano, E.; Pflüger, P. M.; Schwarz, J. L.; Glorius, F. Catalytic radical generation of π-allylpalladium complexes. *Nat. Catal.* **2020,** *3*, 393–400.

(115) Costentin, C.; Robert, M.; Savéant, J.-M. Fragmentation of aryl halide π anion radicals. Bending of the cleaving bond and activation vs driving force relationships. *J. Am. Chem. Soc.* **2004,** *126*, 16051–16057.

(116) Roth, H.; Romero, N.; Nicewicz, D. Experimental and calculated electrochemical potentials of common organic molecules for applications to single-electron redox chemistry. *Synlett* **2016,** *27*, 714–723.

(117) Ghosh, I.; Ghosh, T.; Bardagi, J. I.; König, B. Reduction of aryl halides by consecutive visible light-induced electron transfer processes. *Science* **2014,** *346*, 725–728.

(118) Molloy, B. B.; Steinberg, M. I. Quaternary ammonium antiarrhythmic drugs. U.S. Patent US4289787A, Sept 15, 1981.

(119) Morgan, T. K.; Wohl, R. A.; Lumma, W. C.; Wan, C. N.; Davey, D. D.; Gomez, R. P.; Marisca, A. J.; Briggs, M.; Sullivan, M. E.; Wong, S. S. Synthesis and class III antiarrhythmic activity of (phenyl-2-butenyl)ammonium salts. Effect of conformation on activity. *J. Med. Chem.* **1986,** *29*, 1398–1405.

(120) Kancherla, R.; Muralirajan, K.; Maity, B.; Zhu, C.; Krach, P. E.; Cavallo, L.; Rueping, M. Oxidative addition to palladium(0) made easy through photoexcited-state metal catalysis: experiment and

computation. *Angew. Chem. Int. Ed.* **2019,** *58*, 3412–3416.
(121) Mayr, H.; Patz, M. Scales of nucleophilicity and electrophilicity: a system for ordering polar organic and organometallic reactions. *Angew. Chem. Int. Ed. Engl.* **1994,** *33*, 938–957.
(122) Molloy, B. B.; Steinberg, M. I. Quaternary ammonium antiarrhythmic drugs. U.S. Patent US4289787A, Sept 15, 1981.
(123) Preshlock, S.; Tredwell, M.; Gouverneur, V. ^{18}F-labeling of arenes and heteroarenes for applications in positron emission tomography. *Chem. Rev.* **2016,** *116*, 719–766.
(124) Wrenn, F. R.; Good, M. L.; Handler, P. The use of positron-emitting radioisotopes for the localization of brain tumors. *Science* **1951,** *113*, 525–527.
(125) Ter-Pogossian, M. M.; Phelps, M. E.; Hoffman, E. J.; Mullani, N. A. A positron-emission transaxial tomograph for nuclear imaging (PETT). *Radiology* **1975,** *114*, 89–98.
(126) Zhang, S.; Wang, X.; Gao, X.; Chen, X.; Li, L.; Li, G.; Liu, C.; Miao, Y.; Wang, R.; Hu, K. Radiopharmaceuticals and their applications in medicine. *Signal Transduct. Target. Ther.* **2025,** *10*, 1.
(127) Miller, P. W.; Long, N. J.; Vilar, R.; Gee, A. D. Synthesis of ^{11}C, ^{18}F, ^{15}O, and ^{13}N radiolabels for positron emission tomography. *Angew. Chem. Int. Ed.* **2008,** *47*, 8998–9033.
(128) Conti, M.; Eriksson, L. Physics of pure and non-pure positron emitters for PET: a review and a discussion. *EJNMMI Phys.* **2016,** *3*, 8.
(129) Brooks, A. F.; Topczewski, J. J.; Ichiishi, N.; Sanford, M. S.; Scott, P. J. H. Late-stage [^{18}F]fluorination: new solutions to old problems. *Chem. Sci.* **2014,** *5*, 4545–4553.
(130) Jacobson, O.; Kiesewetter, D. O.; Chen, X. Fluorine-18 radiochemistry, labeling strategies and synthetic routes. *Bioconjugate Chem.* **2015,** *26*, 1–18.
(131) Cai, L.; Lu, S.; Pike, V. W. Chemistry with [^{18}F]fluoride ion. *Eur. J. Org. Chem.* **2008,** *2008*, 2853–2873.
(132) Campbell, M. G.; Mercier, J.; Genicot, C.; Gouverneur, V.; Hooker, J. M.; Ritter, T. Bridging the gaps in ^{18}F PET tracer development. *Nat. Chem.* **2017,** *9*, 1–3.
(133) Hamacher, K.; Coenen, H. H.; Stöcklin, G. Efficient stereospecific synthesis of no-carrier-added 2-[^{18}F]-fluoro-2-deoxy-D-glucose using aminopolyether supported nucleophilic substitution. *J. Nucl. Med.* **1986,** *27*, 235–238.
(134) Bunnett, J. F.; Zahler, R. E. Aromatic nucleophilic substitution reactions. *Chem. Rev.* **1951,** *49*, 273–412.
(135) Coenen, H. H.; Ermert, J. Direct nucleophilic ^{18}F-fluorination of electron rich arenes: present limits of no-carrier-added reactions. *Curr. Radiopharm.* **2010,** *3*, 163–173.
(136) Watson, D. A.; Su, M.; Teverovskiy, G.; Zhang, Y.; García-Fortanet, J.; Kinzel, T.; Buchwald, S. L. Formation of ArF from LPdAr(F): catalytic conversion of aryl triflates to aryl fluorides. *Science* **2009,** *325*, 1661–1664.
(137) Lee, E.; Kamlet, A. S.; Powers, D. C.; Neumann, C. N.; Boursalian, G. B.; Furuya, T.; Choi, D. C.; Hooker, J. M.; Ritter, T. A fluoride-derived electrophilic late-stage fluorination reagent for PET imaging. *Science* **2011,** *334*, 639–642.
(138) Lee, E.; Hooker, J. M.; Ritter, T. Nickel-mediated oxidative fluorination for PET with aqueous [^{18}F]fluoride. *J. Am. Chem. Soc.* **2012,** *134*, 17456–17458.
(139) Tredwell, M.; Preshlock, S. M.; Taylor, N. J.; Gruber, S.; Huiban, M.; Passchier, J.; Mercier, J.; Génicot, C.; Gouverneur, V. A general copper-mediated nucleophilic ^{18}F fluorination of arenes. *Angew. Chem. Int. Ed.* **2014,** *53*, 7751–7755.
(140) Pike, V. W.; Aigbirhio, F. I. Reactions of cyclotron-produced [^{18}F]fluoride with diaryliodonium salts — a novel single-step route to no-carrier-added [^{18}F]fluoroarenes. *J. Chem. Soc., Chem. Commun.* **1995,** 2215–2216.
(141) Ross, T. L.; Ermert, J.; Hocke, C.; Coenen, H. H. Nucleophilic ^{18}F-fluorination of heteroaromatic iodonium salts with no-carrier-added [^{18}F]fluoride. *J. Am. Chem. Soc.* **2007,** *129*, 8018–8025.
(142) Rotstein, B. H.; Stephenson, N. A.; Vasdev, N.; Liang, S. H. Spirocyclic hypervalent iodine(III)-mediated radiofluorination of non-activated and hindered aromatics. *Nat. Commun.* **2014,** *5*, 4365.
(143) Gendron, T.; Sander, K.; Cybulska, K.; Benhamou, L.; Sin, P. K. B.; Khan, A.; Wood, M.; Porter, M. J.; Årstad, E. Ring-closing synthesis of dibenzothiophene sulfonium salts and their use as leaving groups for aromatic ^{18}F-fluorination. *J. Am. Chem. Soc.* **2018,** *140*, 11125–11132.

(144) Xu, P.; Zhao, D.; Berger, F.; Hamad, A.; Rickmeier, J.; Petzold, R.; Kondratiuk, M.; Bohdan, K.; Ritter, T. Site-selective late-stage aromatic [^{18}F]fluorination via aryl sulfonium salts. *Angew. Chem. Int. Ed.* **2020,** *59*, 1956–1960.

(145) Tang, P.; Wang, W.; Ritter, T. Deoxyfluorination of phenols. *J. Am. Chem. Soc.* **2011,** *133*, 11482–11484.

(146) Neumann, C. N.; Ritter, T. Facile C–F bond formation through a concerted nucleophilic aromatic substitution mediated by the PhenoFluor reagent. *Acc. Chem. Res.* **2017,** *50*, 2822–2833.

(147) Neumann, C. N.; Hooker, J. M.; Ritter, T. Concerted nucleophilic aromatic substitution with ^{19}F− and ^{18}F−. *Nature* **2016,** *534*, 369–373.

(148) Beyzavi, H.; Mandal, D.; Strebl, M. G.; Neumann, C. N.; D'Amato, E. M.; Chen, J.; Hooker, J. M.; Ritter, T. ^{18}F-deoxyfluorination of phenols via Ru π-complexes. *ACS Cent. Sci.* **2017,** *3*, 944–948.

(149) Rickmeier, J.; Ritter, T. Site-specific deoxyfluorination of small peptides with [^{18}F]fluoride. *Angew. Chem. Int. Ed.* **2018,** *57*, 14207–14211.

(150) Zoratti, M.; Bunnett, J. F. Mechanism of the nonaryne hydroxydehalogenation of unactivated aryl halides. *J. Org. Chem.* **1980,** *45*, 1769–1776.

(151) Kang, Q.; Lin, Y.; Li, Y.; Xu, L.; Li, K.; Shi, H. Catalytic S_NAr hydroxylation and alkoxylation of aryl fluorides. *Angew. Chem. Int. Ed.* **2021,** *60*, 20391–20399.

(152) Fier, P. S.; Maloney, K. M. Synthesis of complex phenols enabled by a rationally designed hydroxide surrogate. *Angew. Chem. Int. Ed.* **2017,** *56*, 4478–4482.

(153) Fier, P. S.; Maloney, K. M. Reagent design and ligand evolution for the development of a mild copper-catalyzed hydroxylation reaction. *Org. Lett.* **2017,** *19*, 3033–3036.

(154) Greener, A. J.; Ubysz, P.; Owens-Ward, W.; Smith, G.; Ocaña, I.; Whitwood, A. C.; Chechik, V.; James, M. J. Radical–anion coupling through reagent design: hydroxylation of aryl halides. *Chem. Sci.* **2021,** *12*, 14641–14646.

(155) Wong, D. F.; Waterhouse, R.; Kuwabara, H.; Kim, J.; Brašić, J. R.; Chamroonrat, W.; Stabins, M.; Holt, D. P.; Dannals, R. F.; Hamill, T. G.; Mozley, P. D. ^{18}F-FPEB, a PET radiopharmaceutical for quantifying metabotropic glutamate 5 receptors: a first-in-human study of radiochemical safety, biokinetics, and radiation dosimetry. *J. Nucl. Med.* **2013,** *54*, 388–396.

(156) Lim, K.; Labaree, D.; Li, S.; Huang, Y. Preparation of the metabotropic glutamate receptor 5 ($mGluR_5$) PET tracer [^{18}F]FPEB for human use: an automated radiosynthesis and a novel one-pot synthesis of its radiolabeling precursor. *Appl. Radiat. Isot.* **2014,** *94*, 349–354.

(157) Mossine, A. V.; Brooks, A. F.; Makaravage, K. J.; Miller, J. M.; Ichiishi, N.; Sanford, M. S.; Scott, P. J. H. Synthesis of [^{18}F]arenes via the copper-mediated [^{18}F]fluorination of boronic acids. *Org. Lett.* **2015,** *17*, 5780–5783.

(158) Preshlock, S.; Calderwood, S.; Verhoog, S.; Tredwell, M.; Huiban, M.; Hienzsch, A.; Gruber, S.; Wilson, T. C.; Taylor, N. J.; Cailly, T.; Schedler, M.; Collier, T. L.; Passchier, J.; Smits, R.; Mollitor, J.; Hoepping, A.; Mueller, M.; Genicot, C.; Mercier, J.; Gouverneur, V. Enhanced copper-mediated ^{18}F-fluorination of aryl boronic esters provides eight radiotracers for PET applications. *Chem. Commun.* **2016,** *52*, 8361–8364.

(159) Makaravage, K. J.; Brooks, A. F.; Mossine, A. V.; Sanford, M. S.; Scott, P. J. H. Copper-mediated radiofluorination of arylstannanes with [^{18}F]KF. *Org. Lett.* **2016,** *18*, 5440–5443.

(160) Aznavour, N.; Zimmer, L. [^{18}F]MPPF as a tool for the in vivo imaging of 5-HT1A receptors in animal and human brain. *Neuropharmacology* **2007,** *52*, 695–707.

(161) Sanabria-Bohórquez, S. M.; Biver, F.; Damhaut, P.; Wikler, D.; Veraart, C.; Goldman, S. Quantification of 5-HT_{1A} receptors in human brain using p-MPPF kinetic modelling and PET. *Eur. J. Nucl. Med.* **2002,** *29*, 76–81.

(162) Richelson, E.; Souder, T. Binding of antipsychotic drugs to human brain receptors. *Life Sci.* **2000,** *68*, 29–39.

(163) Baron, J. C.; Samson, Y.; Crouzel, C.; Berridge, M.; Chretien, L.; Deniker, P.; Comar, D.; Agid, Y. Pharmacologic studies in man with PET: an investigation using ^{11}C-labeled ketanserin, a 5-HT_2 receptor antagonist. In *Cerebral Blood Flow and Metabolism Measurement*; Hartmann, A., Hoyer, S., Eds.; Springer: Berlin, Heidelberg, 1985; pp 471–480.

(164) Moerlein, S. M.; Perlmutter, J. S. Central serotonergic S2 binding in *Papio anubis* measured in vivo with N-ω-[^{18}F]fluoroethylketans erin and PET. *Neurosci. Lett.* **1991,** *123*, 23–26.

(165) Arnett, C. D.; Shiue, C.; Wolf, A. P.; Fowler, J. S.; Logan, J.; Watanabe, M. Comparison of three ^{18}F-labeled butyrophenone neuroleptic drugs in the baboon using positron emission tomography. *J. Neurochem.* **1985,** *44*, 835–844.

(166) Farde, L. Positron emission tomographic analysis of central D1 and D2 dopamine receptor occupancy in patients treated with classical neuroleptics and clozapine: relation to extrapyramidal side effects. *Arch. Gen. Psychiatry* **1992,** *49*, 538.

(167) Tateno, A.; Arakawa, R.; Okumura, M.; Fukuta, H.; Honjo, K.; Ishihara, K.; Nakamura, H.; Kumita, S.; Okubo, Y. Striatal and extrastriatal dopamine D_2 receptor occupancy by a novel antipsychotic, blonanserin: a PET study with [^{11}C]raclopride and [^{11}C]FLB 457 in schizophrenia. *J. Clin. Psychopharmacol.* **2013,** *33*, 162–169.

(168) Müller, K.; Faeh, C.; Diederich, F. Fluorine in pharmaceuticals: looking beyond intuition. *Science* **2007,** *317*, 1881–1886.

(169) Hagmann, W. K. The many roles for fluorine in medicinal chemistry. *J. Med. Chem.* **2008,** *51*, 4359–4369.

(170) Rizzo, C.; Amata, S.; Pibiri, I.; Pace, A.; Buscemi, S.; Palumbo Piccionello, A. FDA-approved fluorinated heterocyclic drugs from 2016 to 2022. *Int. J. Mol. Sci.* **2023,** *24*, 7728.

(171) Hartz, R. A.; Ahuja, V. T.; Sivaprakasam, P.; Xiao, H.; Krause, C. M.; Clarke, W. J.; Kish, K.; Lewis, H.; Szapiel, N.; Ravirala, R.; Mutalik, S.; Nakmode, D.; Shah, D.; Burton, C. R.; Macor, J. E.; Dubowchik, G. M. Design, structure–activity relationships, and in vivo evaluation of potent and brain-penetrant imidazo[1,2-b]pyridazines as glycogen synthase kinase-3β (GSK-3β) inhibitors. *J. Med. Chem.* **2023,** *66*, 4231–4252.

(172) Solanki, P. V.; Uppelli, S. B.; Pandit, B. S.; Mathad, V. T. Improved and efficient process for the production of highly pure iloperidone: a psychotropic agent. *Org. Process Res. Dev.* **2014,** *18*, 342–348.

(173) Ochi, T.; Sakamoto, M.; Minamida, A.; Suzuki, K.; Ueda, T.; Une, T.; Toda, H.; Matsumoto, K.; Terauchi, Y. Syntheses and properties of the major hydroxy metabolites in humans of blonanserin AD-5423, a novel antipsychotic agent. *Bioorg. Med. Chem. Lett.* **2005,** *15*, 1055–1059.

(174) Sudarshan Rao, K.; Nageswara Rao, K.; Uma Sankara Sastry, T.; Muralikrishna, P.; Jayashree, A. An investigation into formation of impurities during synthesis of blonanserin. *Asian J. Chem.* **2014,** *26*, 5928–5830.

(175) Cabrero-Antonino, J. R.; Leyva-Pérez, A.; Corma, A. Regioselective hydration of alkynes by iron(III) Lewis/Brønsted catalysis. *Chem. Eur. J.* **2012,** *18*, 11107–11114.

(176) Zhuang, Z.-P.; Kung, M.-P.; Kung, H. F. Synthesis and evaluation of 4-(2′-methoxyphenyl)-1-[2′-[N-(2″-pyridinyl)-p-iodobenzamido]ethyl]piperazine (p-MPPI): a new iodinated 5-HT_{1A} ligand. *J. Med. Chem.* **1994,** *37*, 1406–1407.

VI. APPENDIX

Declaration of Authorship (Eidesstattliche Erklärung)

I, Gaurav Gaurav declare that this thesis and the work presented in it are my own and has been generated by me as the result of my own original research.

Hiermit erkläre ich an Eides statt / I do solemnely swear that:

1. This work was done wholly or mainly while in candidature for the doctoral degree at this faculty and university;

2. Where any part of this thesis has previously been submitted for a degree or any other qualification at this university or any other institution, this has been clearly stated;

3. Where I have consulted the published work of others or myself, this is always clearly attributed;

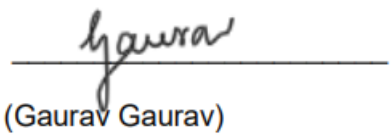
4. Where I have quoted from the work of others or myself, the source is always given. This thesis is entirely my own work, with the exception of such quotations;

5. I have acknowledged all major sources of assistance;

6. Where the thesis is based on work done by myself jointly with others, I have made clear exactly what was done by others and what I have contributed myself;

7. Parts of this work have been published before as: See “Note” page: XI.

Mülheim an der Ruhr, 27-May-2026.



(Gaurav Gaurav)

VII. LIST OF PUBLICATIONS

- Cai, Y.; **Gaurav, G.**; Ritter, T. 1,4-Aminoarylation of Butadienes via Photoinduced Palladium Catalysis, *Angew. Chem. Int. Ed.* **2024**, *63*, e202311250
- Cai, Y.; Dawor, M.; **Gaurav, G.**; Ritter, T. Kharasch-Type Haloalkylation of Alkenes by Photoinduced Copper Catalysis. *J. Am. Chem. Soc.* **2025**, *147*, 18438–18444.

VIII. CURRICULUM VITAE

Gaurav Gaurav

gauravjobs89@gmail.com
Place of Birth: New Delhi, India

EDUCATION

- *PhD. in Chemistry* *(2022 – 2025)*
  Max-Planck-Institut für Kohlenforschung, Mülheim an der Ruhr
  (Advisor: Prof. Dr. Tobias Ritter)
- *MSc. Chemistry* *(2020 – 2022)*
  Indian Institutes of Technology Delhi (IITD) (First Division)
- *BSc. Chemistry* *(2017 – 2020)*
  University of Delhi, Hansraj College (First Division)

PROFESSIONAL EXPERIENCE

Doctoral Researcher *Mülheim, Germany*
(MPI - Kohlenforschung, Supervisor - Prof. Dr. Tobias Ritter) *(2022 – 2025)*

- 1,4-Aminoarylation of 1,3-dienes via photoexcited Pd catalysis: independently synthesized 20+ allylamine products; conducted mechanistic studies including TEMPO trapping, Telemerozation studies, HRMS detection of the π-allylPd(II) intermediate.
- Phenol synthesis from fluorinated drug scaffolds as precursors for ^{18}F-radiodeoxyfluorination: independently conceived and executed a metal-free radical $S_{RN}1$ hydroxylation strategy using benzaldoxime as hydroxide surrogate (29–88% yield, 11 substrates). Manuscript in preparation.
- Kharasch-type haloalkylation via photoinduced Cu catalysis: contributed to mechanistic investigations of excited-state Cu activation.

MSc. Student *Delhi, India*
(IIT Delhi, Supervisor - Prof. Dr. Janakiram Vaitla) *(2020 – 2022)*

- Synthesized and characterized vinyl sulfoxonium ylides, employing them as key intermediates for the construction of indolizine and fused furan heterocycles
- Designed and executed a retrosynthetic strategy toward the total synthesis of the natural product Lepadiformine A, preparing key intermediates on a gram scale

PUBLICATIONS

- 1,4-Aminoarylation of Butadienes via Photoinduced Palladium Catalysis
  (*Angew. Chem. Int. Ed.* **2024**, *63*, e202311250)
- Kharasch-Type Haloalkylation of Alkenes by Photoinduced Copper Catalysis
  (*J. Am. Chem. Soc.* ***2025***, *147*, 22, 18438–18444)

SCHOLASTIC ACHIEVEMENT

- Achieved an outstanding grade – **10.00/10.00** for Master's Thesis in Master's Program
- Ranked **AIR-126 (top 0.35%)** among 35,784 candidates in CSIR-NET June 2021 National Chemistry Exam
- Ranked **AIR-446 (top 2.7%)** among 16,687 candidates in IIT Joint Admission Test (JAM) 2020
- Selected for **Project Associate-I** at CSIR-CDRI Lucknow for **antiviral drug discovery** program
- Awarded Junior Research Fellowship by **DRDO** for **high-energy materials** research at IIT Kharagpur